Onslow Bay Physical / Dynamical Experiments

Summer 1976
Data Report

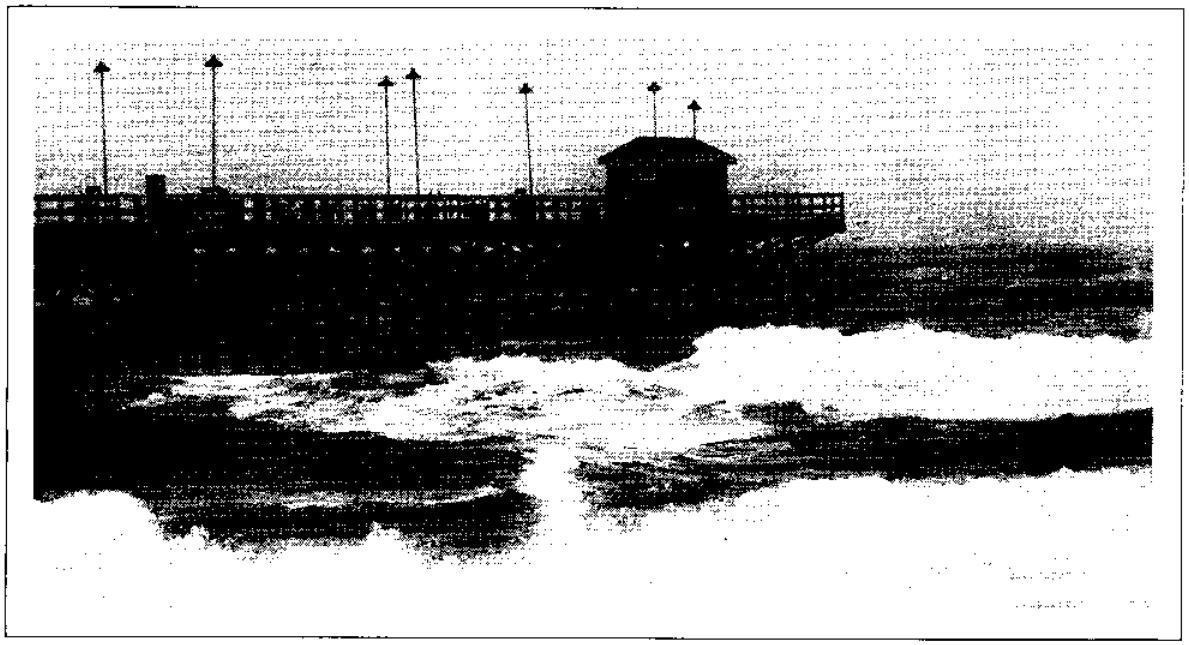

By L. J. Pietrafesa, R. D'Amato,
C. Gabriel, R. J. Sawyer, Jr.,
D. A. Brooks, P. Blankinship
and R. H. Weisberg

UNC Sea Grant Publication UNC-SG-78-16

North Carolina State University
Department for Marine Science and Engineering
Report No. 78-5

Copies are available from: UNC Sea Grant
105 1911 Building
North Carolina State University
Raleigh, N.C. 27607

Onslow Bay

Physical/Dynamical Experiments

Summer, 1976

Data Report

by

L. J. Pietrafesa, R. D'Amato,

C. Gabriel, R. J. Sawyer, Jr.,

D. A. Brooks, P. Blankinship

and

R. H. Weisberg

This work was partially supported by the Department of Energy under Contract No. E(38-1)-902 and the Office of Sea Grant, NOAA, U.S. Dept. of Commerce, under Grant No. 04-6-158-44054, and the State of North Carolina, Dept. of Administration. The U.S. Government is authorized to produce and distribute reprints for governmental purposes notwithstanding any copyright that may appear hereon.

Department of Energy
Contract No. E(38-1)-902

UNC Sea Grant Publication
UNC-SG-78-16

Department for Marine Science and Engineering
Report No. 78-5

August, 1978

ACKNOWLEDGMENTS

The authors would like to thank all those who have participated in this project to date. These include the Captain, Art Jordan, and crew, particularly, Mitch Malpus, of the R/V Advance II. Also, much credit is given to the scientists, technicians and graduate and undergraduate students without whose assistance, both at sea and back at the University, the existing data would not have been collected and processed.

The list includes:

Larry Atkinson
Jack Blanton
Marcus Bowen
Nancy Bowen
Eileen Hofmann
John Klinck
Tom Lee
Dave Leech
Chuck McClain
Kerry Parker
Jim Singer

Table of Contents

List of Tables

List of Figures

List of Figures (Cont'd)

List of Figures (Cont'd)

List of Figures (Cont'd) Page

List of Figures (Cont'd)

List of Figures (Cont'd)

List of Figures (Cont'd)

List of Figures (Cont'd)

List of Figures (Cont'd)

List of Figures (Cont'd)

List of Figures (Cont'd)

List of Figures (Cont'd)

List of Figures (Cont'd)

List of Figures (Cont'd) Page

List of Figures (Cont'd)

List of Figures (Cont'd)

List of Figures (Cont'd)

List of Figures (Cont'd)

List of Figures (Cont'd)

List of Figures (Cont'd)

Introduction

In August, 1975 a set of Summer and Fall studies were begun in Onslow Bay, N. C. These studies constituted part of the North Carolina State University (NCSU) - Skidaway Institute of Oceanography (SKIO) combined efforts to contemporaneously measure: the temperature and salinity, i.e., hydrography; the current speeds and direction at several locations; and sea level and meteorology local and regional to Onslow Bay, North Carolina. Personnel from SKIO also measured various biological parameters along the hydrographic grid (cf. Figure 3). This work constituted the initial effort of a multi-discipline, multi-institutional program partially sponsored by the Department of Energy and in part by the National Oceanographic and Atmospheric Administration and the University of North Carolina - Sea Grant College Program, to study the continental shelf processes affecting the oceanography of the South Atlantic Bight and is detailed in Pietrafesa, et. al., (1978). The immediate problems being addressed were those of understanding the processes by which nutrients are transported onto the North Carolina Shelf from offshore and to establish possible transport pathways for effluents discharged into North Carolina coastal waters.

Cruises were conducted to deploy (retrieve) fixed position current meter moorings (Figure 7) and to make detailed hydrographic and biological parametric measurements in Onslow Bay. The results of the latter surveys are presented in a series of SKIO data reports: Atkinson, et. al., (1976a, b), Dunstan, et. al. (1976), Atkinson, et. al. (1977) and Singer, et. al. (1977).

Endeco 105 current meters were used to measure speed and direction at specified temporal intervals and spatial locations.

The essential part of the 1975 Summer-Fall experiment was a fixed-level array of 4 Endeco 105-film recording current meters and 4 General Oceanics film - recording thermographs. Two moorings were set at the "focal points", locations A and B (Figure 2) of the cuspate shaped Onslow Bay. The current meters were set two to a mooring at depths of 10 and 25 meters from the surface in 28 meters of water, at each of the mooring sites, A and B. The array was designed to observe the propagation of phenomena across and along the inner to mid-shelf and to establish insights into the physics of the vertical and horizontal modal structure of the horizontal currents.

The data from the upper part of the water column were collected to address the "possibility of siting ocean-out-falls" problem (Pietrafesa, 1974) while the lower elements were specific to the "intrusion" (Pietrafesa and Atkinson, 1975) problem. More generally, Onslow Bay was chosen as an initial study site in the context of a study of the whole of the continental margin of the South Atlantic Bight because it is the more densely populated region of the North Carolina coast and, consequently, the waste disposal problem is more critical there than elsewhere. The reason for siting the study of the intrusion of nutrients

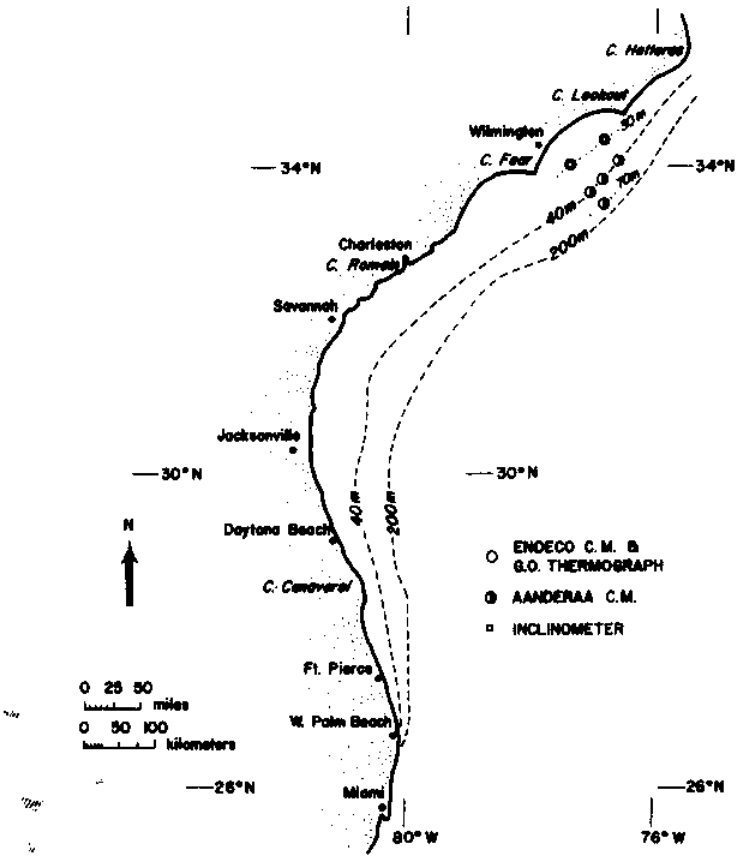

Figure 1 South Atlantic Bight

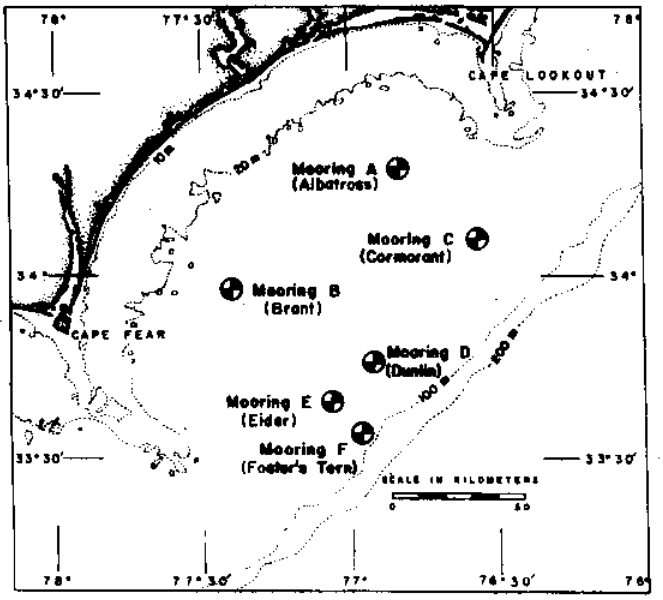

Figure 2 Onslow Bay, North Carolina-Study Area

onto the continental shelf of the South Atlantic Bight in Onslow Bay was primarily based on the fact that there is/has been more historical data, i.e., background information needed to plan such a study, collected in Onslow Bay than anywhere else in the South Atlantic Bight.

Encouraged by the relative success of the 1975 pilot study, Atkinson and Pietrafesa conducted a more extensive and comprehensive field experiment in Onslow Bay during the period June thru September, 1976. The objectives of this second year experiment included both the direct measurement of the along-shelf, cross-shelf and vertical structure of the "late Spring-Summer-early Fall" current, temperature, conductivity and pressure fields from fixed point, vertical moorings and a continuation of the hydrographic and biological sampling, along the 1975 grid (Figure 3) by SKIO personnel. The mooring locations and vertical configurations are shown in Figures 1 and 4. A total of 8 Endeco and General Oceanic current meters and thermographs were used at the 30 meter locations (sites A and B) and 8 Aanderaa RCM-4, with temperature, pressure and conductivity sensors, were used at the three 45 meter and one 70 meter sites (C, D, E and F). Several major and minor quasisynoptic hydrographic and biological surveys were made during the moored array experiment to study the variability of the shelf water and biological properties and to better determine the spatial and temporal distributions therein. Meteorological and coastal sea level data were collected from the stations listed in Tables 1 and 2.

Additionally: the moorings were re-established in December, 1976 and were retrieved in late April, 1977; and the deployment - retrieval scenario was conducted again during the period July-December, 1977 (as shown in Figures 5 and 6). From December, 1977, through the present a reduced array has been deployed. Drs. T.N. Lee (University of Miami) and Pietrafesa have co-ordinated a series of Georgia Bight - Carolina Capes experiments. These experiments will yield the first major alongshore South Atlantic Bight physical data.

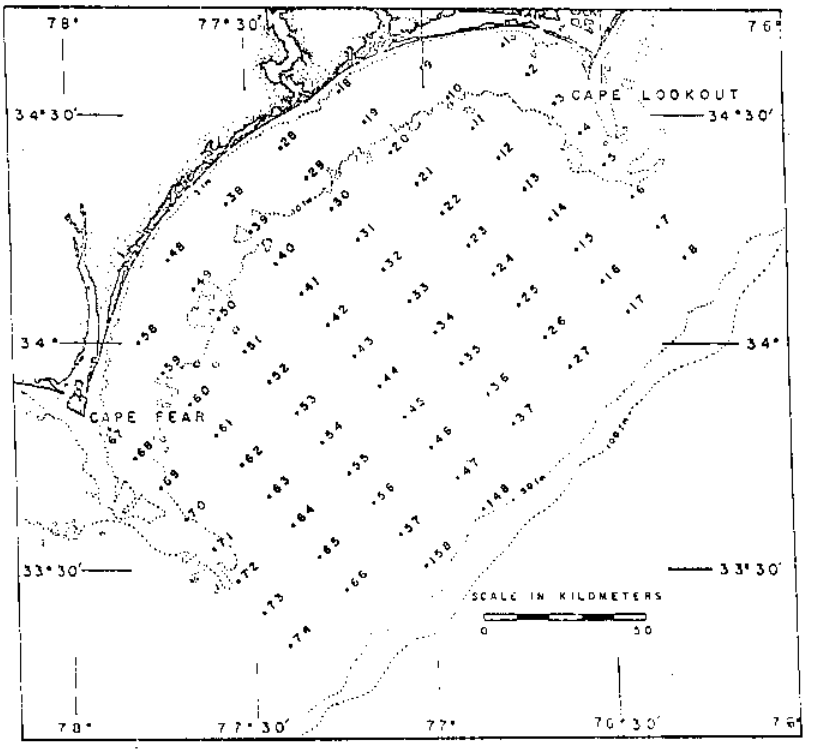

Figure 3 SKIO/NCSU hydrography/biological grid

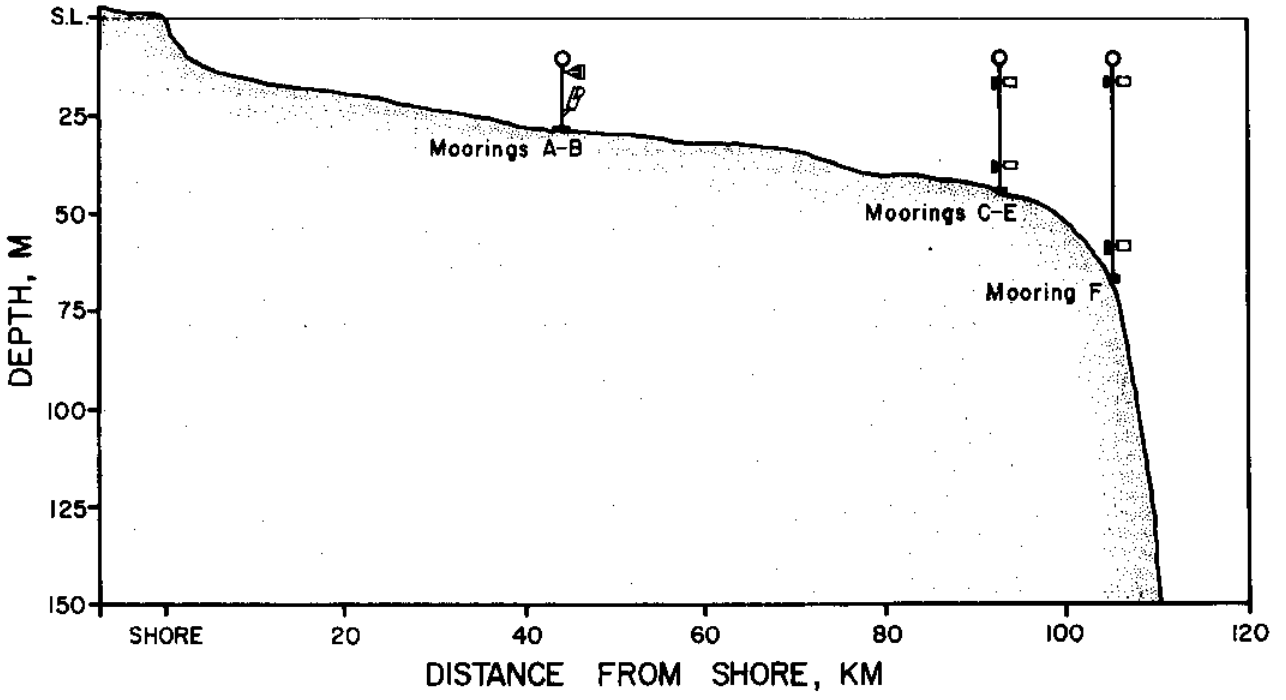

Figure 4 Vertical section of instrument depths

Table 1

Meteorological Stations

Station	Latitude	Longitude
Cape Hatteras, N.C.	35°16'N	75°33'W
Wilmington, N.C.	34°14'N	77°57'W
Charleston, S.C.	32°46'N	79°56'W
Savannah, Ga.	32°05'N	81°06'W

Table 2

Sea Level Stations

Station	Latitude	Longitude
Beaufort, N.C.	34°43.2'N	76°40.2'W
Beaufort Inlet, N.C.	34°41.6'N	76°42.7'W
Wilmington, N.C.	34°13.6'N	77°57.2'W
Frying Pan Shoals, N.C.	33°29.1'N	77°35.4'W
Charleston, S.C.	32°46'N	79°56'W

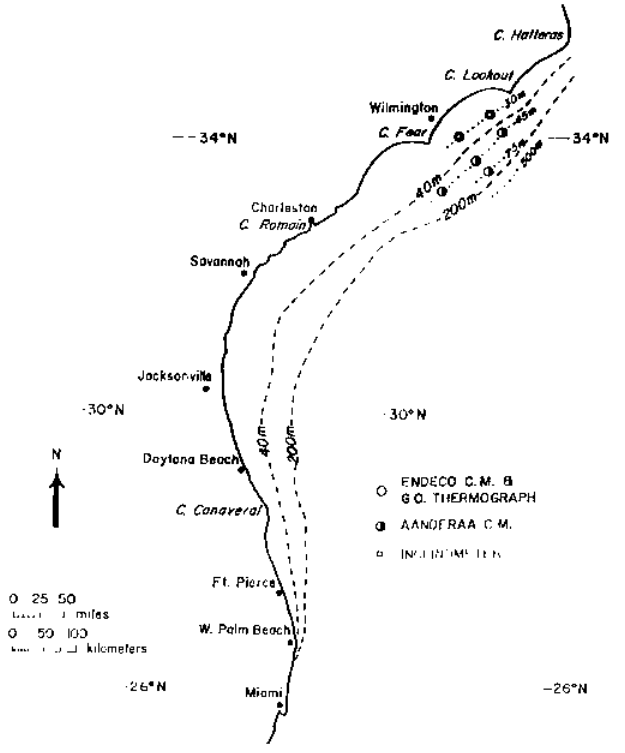

Figure 5 Mooring site locations for Fall-Winter, 1976 experiment.

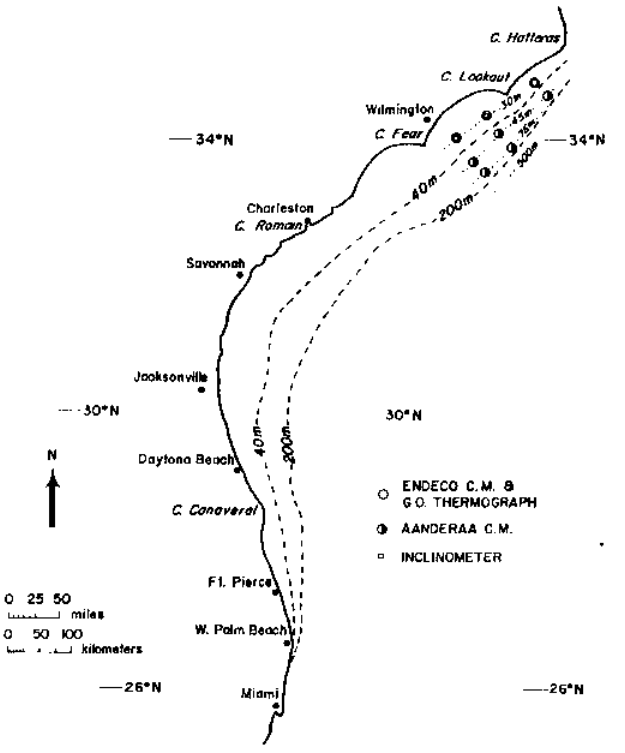

Figure 6 Mooring site locations for Summer, 1977 experiment

Equipment and Mooring Description

The moorings, established at sites A-F during the summer of 1976, had a taut line (wire) configuration. One or more subsurface floats were used to keep a bottom anchored cable taut. Fixed level recording equipment was attached to and suspended (away) from the cable. For mooring A and B a bottom anchored, auxiliary surface marker was located some distance from the main mooring line. The bottom "auxiliary" anchor was connected to the "main" anchor by a polypropylene ground line, which floats approximately a meter from the ocean floor. Moorings C-F did not have a surface marker. These moorings made use of AMF acoustic releases which served the dual function of helping locate and retrieve the mooring. The mooring configurations is depicted in Figure 7.

The operational logistics of installing moorings A-F were initiated in such a way as to maximize repeatability of location in subsequent experiments. The R/V Advance II was used during all deployment and retrieval phases of this 1976 experiment and mooring position locations (Table 3) were taken by the ship's Loran A system at the time of installation. The absolute error (accuracy) of the position is estimated to be less than $\pm$ 1 minute of latitude and longitude. The relative error (precision) is estimated to be less than $\pm$ 0.5 minute in either co-ordinate. Depths were taken by fathometer and are accurate to within $\pm$ 0.5 meters.

The recording instruments used on the shallow moorings (i.e. moorings A and B) were Endeco - 105 current meters, General Oceanics Model 2010 Inclinometer current meters and General Oceanics 3070, Thermographs; all film recording devices. The recording instruments used on the deep moorings (i.e. mooring C-F) were Aanderaa magnetic tape recording current meters and General Oceanics 3070 thermographs. Table 3 gives instrument types and depths used on all moorings. The specifications of the instruments are given in Table 4.

The Aanderaa recording current meter, model RCM4 is a self-contained instrument designed to record speed, direction and temperature of ocean currents below the wave zone. Sensors for depth and conductivity are also used. The RCM4 is capable of 2000 meters depth. The RCM design is based upon a savonious rotor current velocity sensor, a magnetic compass for directional determination, and a thermistor for temperature sensing. The depth sensor is a bourdon tube driving a potentiometer, and conductivity is determined by an induction type sensor. An electro-mechanical encoder (analog to digital converter) samples and converts the different parameters to binary signals which are recorded on 1/4" magnetic tape. The measuring cycles of the RCM4 are controlled by a quartz clock for timing accuracy. Power is supplied by batteries capable of recording 600 feet of magnetic tape, or approximately 100 days using a 15 minute sampling interval. The RCM4 consists of two main parts, the recording unit and the vane assembly. The vane assembly has a spindle which is shackled to the mooring line. The RCM4 is then able to "weathercock" and align itself with the correct direction.

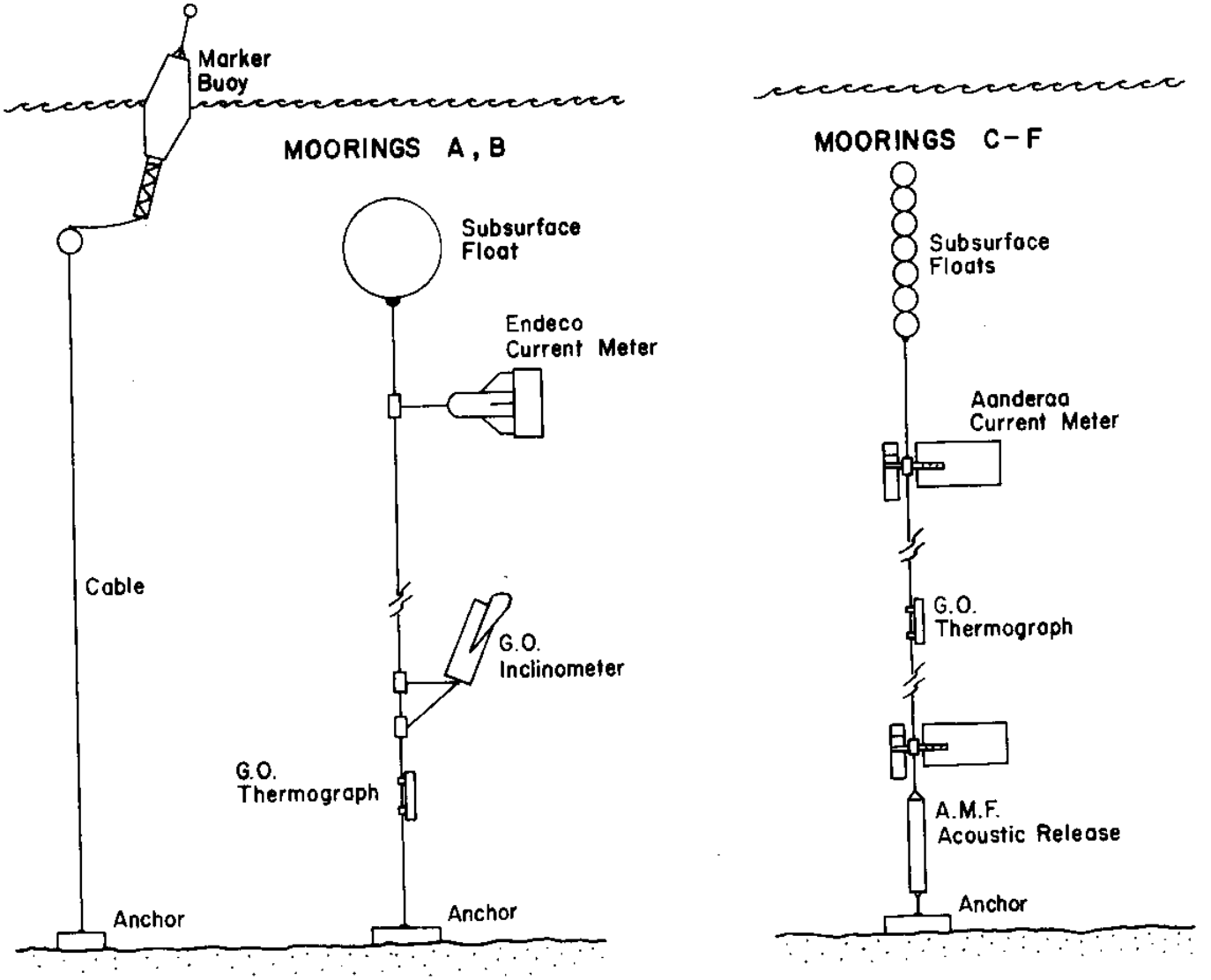

Figure 7 Fixed position current meter moorings

Table 3

Instrument Moorings and Element Locations

Mooring	Date	Lat./Long.	Loran A	Water Depth, m	Instr. Depth, m	Instr. Type	Inst. #
A (Albatross)	8 July, 25 Aug. '76	34°18'N 76°50.6'W	4855 2060	30	12 25 26	Endeco C.M. Inclimometer Thermograph	316 M 8
B (Brant)	7 July, 25 Aug. '76	33°58.2'N 77°25.8'W	4894 2493	30	12 25 26	Endeco C.M. Inclimometer Thermograph	247 2 5
C (Cormorant)	22 June, 21 Sept. '76	34°06.8'N 76°35.6'W	4780 2030	40	22 28.5 35	Aanderaa Thermograph Aanderaa	2254 4 1905
D (Dunlin)	8 July, 21 Sept. '76	33°46.7'N 76°55.1'W	4777 2325	40	22 28.5 35	Aanderaa Thermograph Aanderaa	2259 7 1908
E (Eider)	22 June, 21 Sept. '76	33°39'N 77°03'W	4774 2445	40	22 28.5 35	Aanderaa Thermograph Aanderaa	2256 3 1907
F (Foster's Tern)	8 July, 21 Sept. '76	33°34.6'N 76°56'W	4743 2432	70	22 65	Aanderaa Aanderaa	2255 1906

Table 4

SPECIFICATIONS: ENDECO Type 105 in-situ Tethered Current Meter

1. CURRENT VELOCITY

Sensor Type:	Ducted Impeller
Sensitivity:	53.7 RPM/knot
Speed Range:	0 - 1.75 knots (0-90.1 cm/sec) at one Reading/60 minutes
	0 - 3.5 knots (0-180.2 cm/sec) at one Reading/30 minutes
	0 - 7.0 knots (0-360.4 cm/sec) at one Reading/15 minutes
Impeller Threshold:	Less than .05 knot (2.57 cm/sec)
Resolution:	.05 knot
Speed Accuracy:	$\pm$3 percent of Full Scale

2. CURRENT DIRECTION

Magnetic Direction:	0 - 360^{o}
Sensitivity:	$\pm5^{o}$ at 0.05 knot (2.57 cm/sec)
Resolution:	$\pm1^{o}$
Accuracy:	2 percent above 0.05 knot, when referenced to computer calibration

3. TILT

The instrument orients to the flow thus eliminating the need for tilt indication or correction.

4. RECORDING TIME AND RATE

Number of Readings:	3600
Recording Rate:	1 Reading/15 minutes 1 Reading/30 minutes 1 Reading/60 minutes 30 minutes used in this study
Time Reference Mark:	24-hour Light Emitting Diode indication provided by timer

Type 105

Table 4 (Cont'd.

Maximum Recording Period:	75 days at 1 Reading/30 minutes
Time Stability:	$\pm$1.5 second/day at 20°C $\pm$4 second/day from -5 to +30°C
Timer Type:	ENDECO Type 124 Crystal Timer
5. RECORDER	
Method:	Direct photographic time exposure of sensor outputs
Light Source:	Light Emitting Diodes continuously energized
Format:	Analog/Bar Graph
Film Type:	50 feet - 16mm Tri-X Cine Kodak Magazine, Modified
Power:	Four, 1-1/2 volt standard "D" size cells (Use only carbon-zinc batteries in non-ferrous cases)
6. OPERATING ENVIRONMENT	
Operating Medium:	Salt, fresh, or polluted water
Operating Temperature Range:	-2° to 45°C (28° to 113°F)
Storage Temperature Range:	-24° to 65°C (-29° to 149°F)
Maximum Depth:	500 feet (pressure cases to 10,000 psi available)
7. INSTRUMENT HOUSING	
Material:	P.V.C. Plastic
Finish:	All surfaces painted for resistance to marine growth
Hardware:	300 Series Stainless Steel and Plastic
8. PHYSICAL SIZE	
Weight:	27 pounds (in air)

Type 105 Table 4 (Cont'd.)

Buoyancy:	Approximately neutral; adjustable for salt, fresh, or polluted water
Dimensions:	30" long X 16" diameter
Shipping Weight:	45 pounds
Shipping Crate Dimensions:	38" long X 22" diameter

SPECIFICATIONS: Aanderaa Recording Current Meter Model RCM4

Measuring System:	Self-balancing bridge with sequential measuring of six channels and recording on magnetic tape. A ten bit binary word is used for each channel.
Measuring Speed:	4 seconds each channel. The channels are:
Reference:	This is a fixed reading that acts as a control on the performance of the RCM, and also as an identification of individual instruments.
Temperature:	
Sensor Type:	Thermistor (Fenwal GB32 JM18)
Wide Range:	-0.34°C to 32.17°C
Accuracy:	±0.15°C
Resolution:	0.1% of range selected
63% Response Time:	Slow Response, 60 seconds (standard).
Conductivity:	
Sensor Type:	inductive cell
Range:	0 to 70 mmho, (standard)
Resolution:	0.1% of range.
Depth:	
Sensor Type:	Bourdon Tube driving a potentiometer
Range:	0-100 PSI, or 0-200 PSI
Accuracy:	1% of range
Resolution:	0.1% of range

Current Direction:	
Sensor Type:	Magnetic compass with needle clamped on to potentiometer ring.
Resolution:	0.35^{o}
Accuracy:	$\pm 7.5^{o}$, speed within 2.5 to 5 cm/sec, or 100 to 200 cm/sec. $\pm 5^{o}$, speed within 5 to 100 cm/sec.
Maximum Compass Tilt:	12^{o} from horizontal
Current Speed:	
Principle:	Rotor with magnetic coupling through instrument case. The number of rotations during the period between two samplings are counted by an electronic counter (Rotor Counter 2246) This counter has a pre-circuit with choice between three dividing factors 1, 4, and 16 rev/count, suited for sampling intervals 2.5, 10 and 40 min. respectively. Standard is 4 rev/count.
Range:	2.5 to 250 cm/sec.
Accuracy:	± 1 cm/sec, or $\pm 2\%$ of the actual speed, whichever is greatest.
Starting Velocity:	1.5 cm/sec.
Clock:	
Type:	Quartz crystal clock.
Accuracy:	Better than ± 2 sec/day within 0^{o} to $20^{o}C$
Sampling Intervals:	0.5, 1, 2, 2.5, 5, 10, 15, 20, 40, 60 minutes, selected by change of Interval Selecting Plug. 15 min. used in this study.

Model RCM4

Table 4 (Cont'd.)

Recording System:	
Type:	Reel to reel 1/4" magnetic tape.
Coding:	10 bit binary words (short and long pulses) in serial from.
Storage Capacity:	10,000 samplings
Power:	
Main Battery:	Tudor 9T1 non-magnetic, 9 volts.
Size:	63 x 50 x 80 mm.
Capacity:	Sufficient for 10,000 samplings
Clock Battery:	Mallory TR113, 4.05 volts.
Size:	16.5 mm dia., 21 mm long.
Capacity:	More than one year.
Mooring:	Spindle designed for 14 mm maximum diameter wire or rope, and 2000 kg. maximum force. Gimbal mounting permits $\pm 27^{o}$ deviation between spindle and instrument.
Drag Force of RCM (typical values)	2.5 Kg. at 105 cm/sec. 5 Kg. at 155 cm/sec 10 Kg. at 195 cm/sec. 20 Kg. at 250 cm/sec.
External Materials:	
Pressure Case:	97.77% Cu, 1.73% Ni, 0.5% Si, alloy, nickel plated.
Vane:	8 mm. PVC.
Other Parts:	Stainless acid proof steel, or nickel plated bronze.

Model RCM4

Table 4 (Cont'd.)

Weight:	In Air	In Water
Recording Unit:	13.4 Kg.	9.2 Kg.
Vane Assembly:	12 Kg.	8.5 Kg.

Dimensions:

Overall Length:	1370 mm.
Overall Height:	750 mm.
Recording Unit:	128 mm dia., 510 mm height.
Vane Size:	370 x 1000 mm.

SPECIFICATIONS: General Oceanics Model 2010 Current Meter

Weight:	5.6 kgs. (12.3 lbs.) in air (Model 2010)
Buoyancy in Seawater:	1.0 kgs. (2.2 lbs.) positive
Exposed Materials:	Polyvinyl chloride (Model 2010) and end caps; high density polyethylene vanes; stainless steel hardware.
Dimensions:	11.4 cm. (4 1/2") O.D. x 51 cm. (20") long housing; 20.3 cm. (8") diameter circular sector right angle vanes tapered to housing base.
Depth Rating:	50 meters
Inclinometer Range:	0 to 90° from vertical.
Inclinometer Accuracy:	$\pm 1^{\circ}$
Speed Range:	0.05 to 1.6 knots.
Speed Accuracy:	$\pm$3% of full scale (0.05 knot)
Directional Range:	0 to 360°
Directional Accuracy:	$\pm 5^{\circ}$ at inclinations over 10° (0.25 knot)
Time Reference:	Battery powered calendar watch with second, minute, and hour hands plus date window
Watch Accuracy:	$\pm$0.035% (30 seconds per 24 hours)
Data Recording Medium:	Super 8 movie film (Tri-X, B. & W.) available in 50 ft. pre-load cartridges; approx. 3500 data frames at 6 frames/inch (first and last 50 frames used as leader)
Data Interval:	Selectable by interchangeable timing plugs for 1, 5, 15, 30 or 60 minutes between photographs; ten second cycle without timing plugs for test and checkout. A 30 minute range was used in this study.

Table 4 (Cont'd.)

Main Battery Supply:	Eighteen manganese-alkaline penlight cells (Mallory MN 1500 size AA, or equal)
Battery Operating Life:	Five months or, if sooner, 11,000 data records. (Watch battery, one year.)
Mounting:	Swivel eye at base of housing for mooring to ballast weight or mid-wire frame.

SPECIFICATIONS: General Oceanics Model 3070 Film Recording Thermograph

Weight:	3 Kgs. (6 1/2 lbs.) in air; approximately 1 kg. (2.2 lbs.) positively buoyant in water.
Exposed Materials:	Rigid polyvinyl chloride (PVC) housing, end caps, and thermometer bulb guard; stainless steel hardware and thermometer bulb.
Dimensions:	11.4 cm. (4 1/2") O.D x 38 cm. (15") overall length less thermometer bulb guard piece.
Depth Rating:	50 meters (72 psi).
Temperature Range:	0° to 55° C
Accuracy:	$\pm$1% of full scale (.55° C).
Time Reference:	Battery powered calendar watch with second, minute, and hour hands plus date window.
Watch Accuracy:	$\pm$0.0035% (30 seconds per 24 hours)
Date Interval:	Selectable at 5, 15, 30, or 60 minutes. Timing intervals chosen by changing timing plugs in data logger circuit. a 30 minute range was used in this study.
Main Battery Supply:	16 manganese-alkaline penlight cells. (Mallory MN 1500, size AA, or equal)
Operating Life:	5 months or, if sooner, 11,000 camera operations. (Watch battery, one year)

The Endeco-105 current meter is of the axial flow, ducted impeller, film recording type and is tethered to the taut line mooring. It is specifically designed for continental shelf and estuarine environmental monitoring. The E-105 (Figure 7) records analog signals from direction and speed transducers on 16 millimeter photographic film. The ducted impeller acts as the speed sensor with an internal conversion of its rotation converted to a light trace on the film. The light trace, which is generated by sensor output, is lengthened or shortened at a rate proportional to the speed of the current. A light bar, whose length is representative of the current speed integrated over the timing interval, is produced by the advancing light trace. The length of the displacement of the light trace divided by the time interval yields the speed, averaged over the timing interval. Consecutive thirty-minute time exposures are taken of the continuous light traces and a timing pulse is provided by a crystal timer (accuracy of 1 part in 420) every 24 hours. Instantaneous instrument direction is given by the displacement of a light trace from a datum line. The directional light trace is generated by a magnetic compass coupled with an analog encoder. The time integrated signal appears as a bar of light which varies in intensity along its length as a function of the length of time that the instrument is aligned in a particular direction. The displacement of the point of maximum intensity from the datum line then yields the average direction for the thirty minute period of actual recording.

The General Oceanics Model 2010 Inclinometer Current Meter consists of a buoyant, cylindrical housing containing a directional inclinometer and a super 8 cartridge camera which sense and record the inclination and compass heading of the instrument. It was attached to a midwire frame for this current profile study. Two vanes affixed to the housing assist orientation and stabilization of the Model 2010 within the current stream. The data recording camera is triggered to photograph the directional inclinometer at regular intervals (30 min. used) by a completely solid state electronic clock.

The directional inclinometer is a spherically shaped component mounted on the inner face of the lower housing end cap. The inclinometer design utilizes a transparent, fluid-filled outer housing containing a neutrally buoyant inner sphere. A small circular target at the top of the transparent outer housing can be viewed against a grid of precision latitude and longitude lines scribed on the free inner sphere. When photographed by the camera, this target mark enables direct reading of the instrument attitude and azimuth by its position relative to the latitude and longitude lines.

The Model 2010 incorporates a standard movie camera to photograph the directional inclinometer. A battery powered watch is mounted above and offset from the inclinometer. This watch is photographed in each frame by means of a split lens on the camera. The camera exposes and advances the film a single frame when triggered by a solenoid actuator. The actuator is fired by a simple, solid state circuit which also operates a small light bulb to illuminate the inclinometer while the camera shutter is open.

The General Oceanics Model 3070 film recording thermograph is a self-contained instrument for measurement and recording of air and water temperatures over extended periods of time. The Model 3070 sensor is a large dial thermometer mounted on one end cap of the cylindrical instrument housing. The bimetallic sensing element of the thermometer protrudes through the end cap out into the environment for quick response to temperature changes. This thermometer bulb is protected by a small guard piece with a number of through-holes for easy circulation of air or water. The thermometer dial is photographed at periodic intervals (30 min. interval used) by a film data logger at the opposite end of the housing. A battery powered calendar watch is mounted in the center of the thermometer dial to provide an accurate time and date reference for each film frame.

Mooring Deployment and Recovery

Deployment

Prior to the cruise, all wire, flotation and anchoring components are set up for each mooring. The wire is pre-cut and terminated appropriately. The flotation is assembled as several bouyancy units. The anchor and its hardware, including chain, swivel and eye hook on the anchor, are combined. The components of each mooring are labeled.

The moorings are transported, loaded and secured on the ship. As each mooring site come up, the appropriate components are laid out and assembled on the fantail. The current meters are given a final check prior to putting them "in-line" on the wire. The release mechanism is attached and an in-air acoustic check is made. The entire mooring line is then scrutinized item by item to insure proper assembly.

As we approach the desired drop site, we begin to trail out the mooring over the stern, starting with the top. The ship is "bumped" ahead 1/3 on one engine by signals relayed from the fantail. This slow forward motion of the ship allows us to keep the mooring stretched as it is being played out. As the last of the mooring goes over, the acoustic release is gently lowered and allowed to hang from the mooring anchor. This anchor is then lowered to the water surface and held there by a deck-controlled quick release. We should at this time be over the drop site. If this is the case the release is pulled and the anchor and mooring drop away. Simultaneously a mark is given to the bridge to record the Loran A location. Also any other fixes at the deployment position such as Loran C and radar are recorded.

With the mooring in position the ship is immediately stopped and the hydrophone is lowered to interogate the acoustic release. After it has been found to be operating satisfactorily, the hydrophone is brought up and we proceed to the next mooring site.

Recovery

All bridge personnel are informed prior to recovery as to what ship maneuvers will be required. The ship is brought to the same Loran A location at which a mooring was deployed. After the ship comes to a full stop the hydrophone is lowered and an attempt to interogate the mooring is made. If no contact is made or if the return signal is weak, the ship is maneuvered in a pattern so as to optimize the chances of getting a return signal. If the signal is strong an attempt will be made to release the mooring. Weather, amount of daylight and sea state are checked to ascertain that a released mooring can be brought on board. With these conditions met all available personnel are called to a watch position on the upper decks. The release signal is sent. If the release mechanism responds that it has released, the work is sent out to begin a visual search for the free-floating mooring.

When the mooring is sighted, the ship maneuvers in on it from a down wind position. The bridge attempts to bring the stern in close proximity to the mooring. A grapnel line is thrown and usually after repeated attempts the mooring is hooked and pulled to the side of the ship. All ship locomotion ceases when the mooring is hooked. The mooring is then pulled in by hand, taking extreme care with the current meters and release mechanism. When all of the mooring is on board, the ship proceeds to the next site as a crew begins disassembling the mooring. The current meters are removed first. They are cleaned, taken inside, checked for damage, opened, turned off and inspected for amount of data collected. The tape from each meter is removed, labeled as to reference number, date, meter location, etc. and wrapped in aluminum foil. The tapes are then ready to be sent for processing. The meters are then closed up and stored for the return trip to Raleigh.

Calibration Techniques

Speed

Although the manner in which one obtains speed data differs widely among instruments, the same basic method of calibration may be used. The instrument may be a savonious rotor, inclinometer, impeller or hot film. All of these types may be calibrated in the same manner on a towed cart in a water channel when the speed of the cart is known.

This method, as used at N. C. State University, utilizes the facilities of EPA located in the Research Triangle Park. The facility consists of a 35 meter long, 2.4 meter wide and 1.2 meter deep channel with an overhead track capable of variable speeds from 0 to 50 cm/sec. Higher speeds are possible by setting up an opposing current.

Any number of points may be taken to establish the calibration curve depending on the resolution required. About every 10 cm/sec gives a satisfactory curve. Additional points at 5 cm/sec intervals can be used to "fill in" uncertain areas.

The actual method used consists of rigidly attaching the current meter to the cart. The meter is immersed in the tank to a depth of approximately 10 cm below the surface, 1 meter from the nearest sidewall. All supporting structures for the meter when immersed in the tank are designed to be down current of the meter so as not to interfere with the flow around the meter. This may be checked from time to time by introducing dye in front of the meter while the cart is in motion.

With the meter in place on the frame, test runs are ready to begin. Starting at a slow speed, the cart travels the 25 meter length of the test section. The meter is tilted back out of the water when returning the cart to the start position to prevent inducing unnecessary turbulence in the channel. Each successive run is at a greater speed up to the 50 cm/sec limit.

This would complete the speed calibration for a given meter. The data is plotted and a speed calibration curve is obtained.

Direction

The Aanderaa meters have a mechanical compass. The compass produces a coded electrical signal, by means of a potentiometer, which is recorded on magnetic tape. The 10 bit binary code yields a number from 0 to 1023. Thus a resolution of approximately 1/3 degree is possible. The Aanderaa specification sheet lists the accuracy of the compass as better than $\pm$ 2 degrees (meter out of the case). In the case, the accuracy is $\pm$ 7.5 degrees with a current of 2.5 to 5 cm/sec or 100 to 200 cm/sec and $\pm$ 5 degrees with a current of 5 to 100 cm/sec.

A non-magnetic stand was built by us and set on a concrete base in a remote area of the coast for the purpose of calibrating the meters. This stand is located near the State marine resource facility at Fort Fisher. The stand consists of a vertical base with a flat disk on top. A sheet of Teflon® (registered Dupont trademark) is placed on the disk. A cross piece with a matching disk is placed on top of the Teflon® sheet. Thirty six holes are drilled in the lower plate at 10 degree intervals. The upper plate has a single hole in it to allow a pin to slide through to the lower plate. This locks the frame in a given position. There is no noticable give in the pin at any setting. The cross piece consists of two aluminum I-beams at 90 degrees. This makes a stand with four arms allowing four meters to be calibrated simultaneously. Each arm is approximately two feet long. Each meter is placed on a pin at the end of an arm. This mounting is similar to that on the Aanderaa vane. The position of the stand was determined relative to true North by shooting Polaris and turning the angle to the zero or starting position of the stand. To go through a calibration series, the crosspiece is rotated 10 degrees and allowed to record for three minutes. This is continued through all 36 positions.

This completes the compass calibration procedure. The data is plotted to correct future field data (see Fig. 8).

Pressure

A Heise pressure gauge is connected directly to the pressure sensor on the Aanderaa. With a hydraulic hand pump connected to this system, the pressure is increased in 10 psi increments up to the rated maximum pressure of the individual sensor. This is usually 100 or 200 psi. At each 10 psi step the coded Aanderaa value is noted and recorded. This value is determined by counting the ten binary pins and converting it into a number from 0 to 1023. This number may then be plotted against the Heise gauge reading to give a calibration curve for each sensor (Fig. 8).

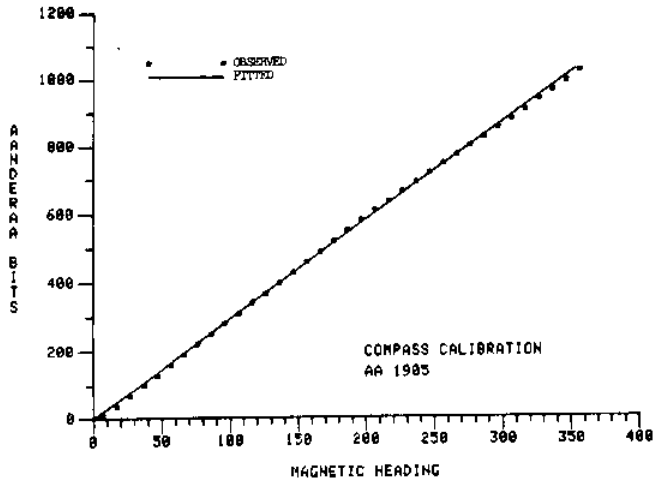

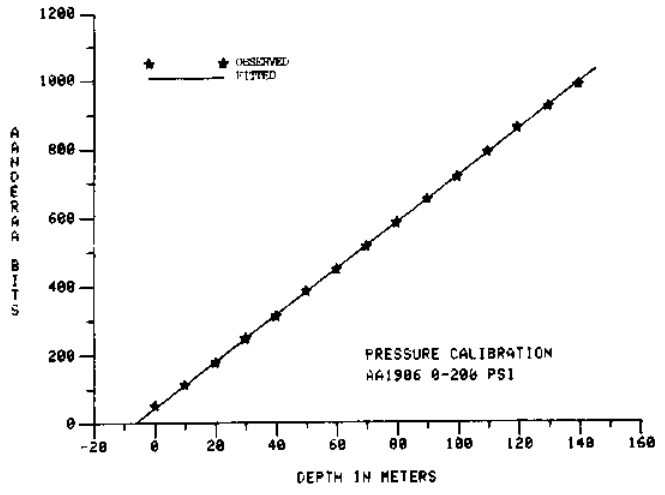

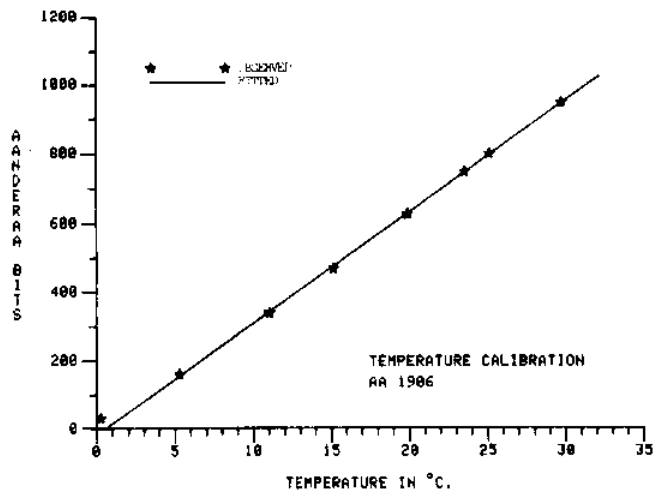

Figure 8 Sample Aanderaa calibration curves

Temperature and Conductivity

We presently use the calibration formula provided with each sensor from Aanderaa for conductivity. For temperature a small constant temperature bath was used to generate a temperature calibration curve for each sensor (see Figure 8). A constant temperature-salinity bath is being constructed at the present time to enable us to calibrate these parameters in the future.

Data Processing

Standard NCSU time series analysis programs based on both the FESTSA system (Brooks, 1976) and the programs of Dr. R.W. Weisberg of N.C.S.U. have been used to process the current and meteorological raw data.

Aanderaa Current Meters

The original Aanderaa data consisted of 10-bit binary words recorded on 1/4 inch magnetic tape. As this format was not computer-compatible, the original data tapes were sent to the University of Miami/RSMAS for decoding. As each reel was transcribed, the data frames were expanded to include frame count and flags for hardware-detectable errors, (Lee 1977). The expanded data files were returned to NCSU on standard 9-track tape, where they were transferred to disk files for convenient access. A primary editing pass was made to correct hardware-detected errors, after which the calibration vector for each meter were applied. The calibrated data was then converted to card-image format and plotted. These plots were visually scanned, and any errors detected were corrected by a second editing pass. The resulting files were then converted to FESTSA format for use in all further processing.

The calibrated data with an interval of 15 minutes was filtered using program CURFIL. A three-hour low pass filter (3HRLP) was first applied to reduce high frequency noise due to gravity wave aliasing and other contamination. The 3HRLP operation results in a data loss of 8 hours from each end of the record. The 3HRLP data were subsampled hourly. A 40 HRLP filter was then applied to the 3HRLP to separate the tidal and subtidal frequency bands, resulting in additional data loss of four days at each end. An hourly 3-40HRLP series was created by subtraction, and the 40HRLP series was then decimated to six-hourly samples for further analysis. The 40HRLP filter attenuation at the daily tidal frequency (1CPD) is greater than 10^6 (Fig. 9). The six hour interval was chosen to be commensurate with the filtered meteorological data. Table 5 gives the particulars on data sets.

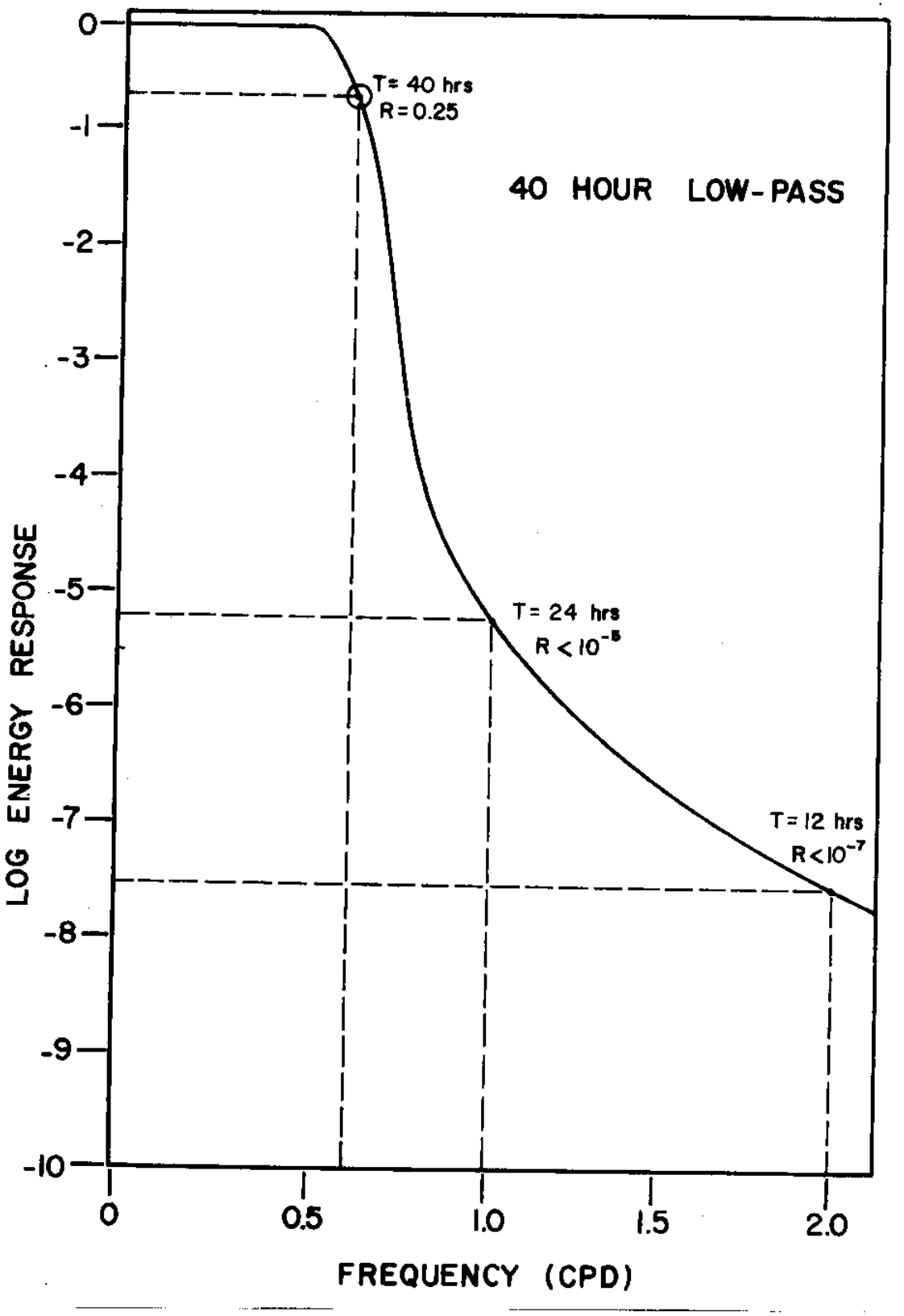

Figure 9 Filter energy response envelope, 40HRLP

Table 5

Data Particulars

Mooring	Meter	Unfiltered Data				Filtered Data			
		Start time EST	End time EST	# of points	Δt (hr)	Start time EST	End time EST	# of points	Δt(hrs)
A	316	1830 hrs. 8 July	1330 hrs. 25 Aug.	2295	.50	0230 hrs. 13 July	0230 hrs. 21 Aug.	157	6
B	247	1730 hrs. 7 July	0600 hrs. 25 Aug.	2329	.50	0130 hrs. 12 July	1930 hrs. 20 Aug.	160	6
C	2254	1730 hrs. 22 Jun.'76	2130 hrs. 18 Sept.'76	8465	.25	0130 hrs. 27 Jan.'76	1330 hrs. 14 Sept.'76	319	6
	1905	1730 hrs. 22 Jun.'76	0415 hrs. 22 Aug.'76	5804	.25	0130 hrs. 27 Jun.'76	1930 hrs. 17 Aug.'76	208	6
D	2259	1445 hrs. 8 Jul.'76	1015 hrs. 21 Sept.'76	7183	.25	2245 hrs. 12 Jul.'76	2245 hrs. 16 Sep.'76	265	6
	1908	1445 hrs. 8 Jul.'76	0545 hrs. 21 Aug.'76	4189	.25	2245 hrs. 12 Jul.'76	1645 hrs. 16.Aug.'76	140	6
E	2256	0615 hrs. 22 Jun.'76	1130 hrs. 21 Sep.'76	8758	.25	1415 hrs. 26 Jun.'76	0215 hrs. 17 Sep.'76	331	6
	1907	0615 hrs. 22 Jun.'76	0630 hrs. 21 Sep.'76	8738	.25	1415 hrs. 26 Jun.'76	2015 hrs. 16 Sep.'76	330	6
F	2255	No data				No data			
	1906	1100 hrs. 8 Jul.'76	1230 hrs. 21 Sep.'76	7207	.25	1900 hrs. 12 Jul.'76	0100 hrs. 17 Sep.'76	266	6

The "Principal Axis" coordinate system was used for the current meter data (see Appendix A). This system maximizes the variance in any given direction and is calculated for each meter separately (see Fig. 10). First order statistics are presented in Table 6 for the topographically aligned rotation system (not used in this report) and Table 7 for the "Principal Axis" coordinate system.

Meteorological (MET) Data

Three-hourly values of surface wind speed, wind direction, atmospheric pressure, and temperature were obtained from NOAA, Environmental Data Service, Asheville, North Carolina. Wind vector and wind stress vector components were computed for the rotated coordinate system (y-axis rotated 56° clockwise to be qualitatively "alongshore", see Appendix A), with the positive vector sense in the direction toward which the wind blows. The wind stress vector components were computed from the wind vector components using a quadratic drag law with the drag coefficient $C_D=1.5\times10^{-3}$.

A 40HRLP filter (program METFIL) with an energy response identical to CURFIL (Fig. 9) was applied to the MET data, resulting in a 4-day data loss at each end of the time series. The 40HRLP data were subsampled six-hourly and adjusted to have the same start times as the 40HRLP current meter data.

Frequency Domain Presentations

Spectral representations of data in this report are given in two formats:

a) Graphs of variance (spectrum density times frequency) versus the logarithm of frequency. These are "quick look" calculations based on the fast Fourier transform (FFT). The FFT's of original data were smoothed by block averaging over five adjacent estimates, yielding about ten degrees of freedom for each averaged estimate. The FFT's of low passed data were not smoothed, yielding two degrees of freedom for each estimate.

b) Auto and cross spectra, phase and coherence squared computed for paired input time series. The spectral calculations were performed by Fourier transforming correlation functions. The maximum correlation lag, spectral bandwidth, degrees of freedom, and input time series names are shown on each figure. The first named time series corresponds to "spectrum x". Positive phase values indicate series y leading series x.

Figure Formats

A product listing is provided in Appendix B.

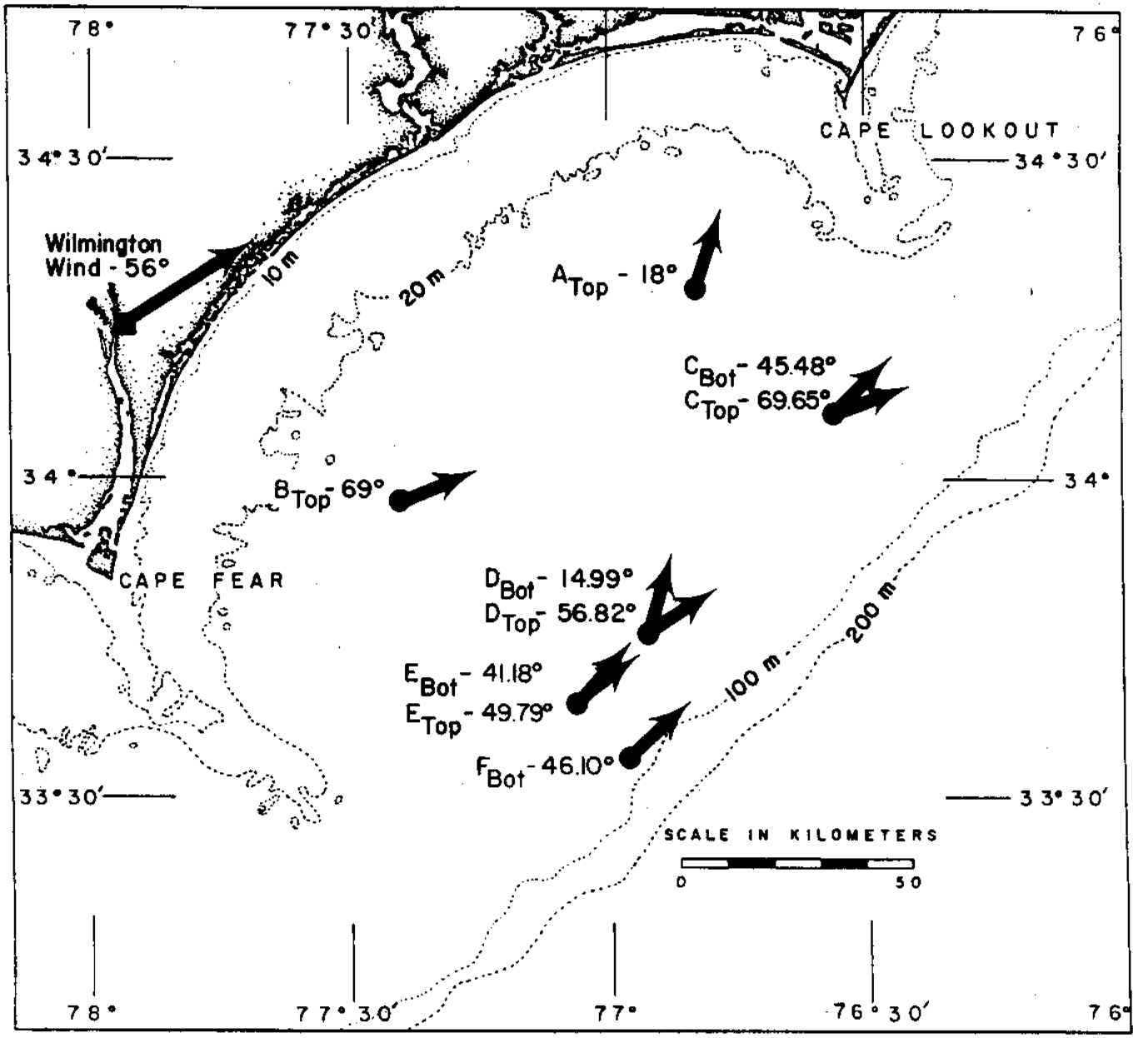

Figure 10 Principal Axis rotation angles for each current meter

Table 6

First Order Statistics (Rotation - 56°)

Meter	Meter Depth(m)	Min.	Max.	Mean	S.D.	Parameter Cm/sec
A_{top}(316)	12	-33.0	57.0	3.78	15.1	u
		-35.0	35.0	-1.1	10.9	v
B_{top}(247)	12	-29.0	32.0	0.13	9.9	u
		-42.0	37.0	-2.3	11.8	v
C_{top}(2254)	22	-42.11	51.35	0.18	12.42	u
		-26.09	52.68	9.55	13.64	v
C_{bottom}(1905_a)	35	-27.54	23.75	-1.60	10.32	u
		-26.31	35.80	7.14	10.14	v
D_{top}(2259)	22	-53.17	51.96	-2.45	18.07	u
		-16.87	72.61	4.70	20.37	v
D_{bottom}(1908)	35	-38.86	22.29	-2.72	9.80	u
		-18.20	28.42	3.16	6.46	v
E_{top}(2256)	22	-62.23	53.12	-1.86	15.58	u
		-55.90	91.03	8.41	20.70	v
E_{bottom}(1907)	35	-14.57	2.65	-0.18	1.10	u
		-1.50	24.69	0.37	1.27	v
F_{top}(2255)	22		- No Data -			u
						v
F_{bottom}(1906)	65	-27.00	76.79	1.48	8.80	u
		-56.21	42.93	-0.25	8.32	v

Table 7

First Order Statistics (Principal Axis angle = R)

Meter	Meter Depth(m)	Min.	Max.	Mean	S.D.	Parameter (Cm/sec)	R
A_{top}(316)	12	-39.0	58.0	2.30	16.0	u	18°
		-43.0	29.0	-3.18	9.4	v	
B_{top}(247)	12	-28.0	28.0	0.65	8.9	u	69°
		-44.0	38.0	-2.22	12.6	v	
C_{top}(2254)	22	-43.49	43.04	-2.14	11.67	u	69.65°
		-28.93	55.49	9.30	14.28	v	
C_{bottom}(1905_A)	35	-27.49	28.31	-0.3244	10.37	u	45.48°
		-27.31	37.89	7.32	10.09	v	
D_{top}(2259)	22	-53.57	51.68	-2.55	18.05	u	56.82°
		-57.24	72.59	4.66	20.38	v	
D_{bottom}(1908)	35	-20.00	22.14	-0.0082	6.99	u	14.99°
		-21.23	43.94	4.17	9.41	v	
E_{top}(2256)	22	-60.16	58.11	-1.00	15.52	u	49.79°
		-53.33	91.25	8.55	20.75	v	
E_{bottom}(1907)	35	- 9.16	8.72	-.086	1.03	u	41.18°
		- 1.50	24.10	.40	1.32	v	
F_{top}(2255)	22		-	No Data	-	u	
						v	
F_{bottom}(1906)	65	-27.23	79.60	1.42	8.70	u	46.10°
		-61.63	39.47	-0.49	8.42	v	

The current meter naming convention used in this report is

$$A(B,C,D,E,\text{or } F)_{\text{top (bottom)}}$$

where A(B,C,D,E,or F) identifies the mooring location and the top (bottom) subscript identifies the location of the instrument on the mooring string (see Table 3).

Preliminary Physical Dynamical Analysis

This report contains a preliminary description of currents measured in Onslow Bay N. C., the generic term for the continental shelf region between Cape Lookout and Cape Fear; data from six moorings maintained during the summer of 1976 are presented in this report. Their locations are shown in Figure 2. The Onslow Bay measurement program continues to be active and a complete listing of available data is contained in the referenced data reports. We've chosen the summer 1976 data set included within for description. Data are also available from winter and summer of 1975 (Pietrafesa, et. al., 1978) on a more limited basis. These will also be discussed briefly.

Water motions on the continental shelf are caused by numerous physical processes. Synoptic and seasonal scale motions occur in response to direct forcing by the weather (principally wind and atmospheric pressure) at synoptic scales and variations in thermohaline inputs (heat and salt) at seasonal scales. Synoptic variability occurs predominantly over the range of time scales spanning 2-10 days, the scales of the cyclonic and anticyclonic perturbations of the wind field. Other low frequency fluctuations occur in response to external forcing from the deep ocean e.g. eddies and Gulf Stream intrusions. Due to its sloping bottom the continental shelf region can support free modes of oscillation generally spanning similar time scales as the atmospheric forcing. The free modes are commonly referred to as quasi-geostrophic, topographic Rossby, or continental shelf waves and a review of these oscillations is given by Leblond and Mysak (1977). The combined low frequency oscillations observed at any position on the continental shelf is expected to reflect a complex mixture of these aforementioned processes.

At higher frequencies, the astronomically forced semi-diurnal tides propagating shoreward from the deep ocean are a dominant feature observed in the South Atlantic Bight continental shelf. Between these semi-diurnal tides and the lower frequency weather continuum three processes occur in varying degrees across the shelf: diurnal tides, inertial oscillations, and sea breeze. These all have time scales of roughly one day. Processes occurring at frequencies higher than the semi-diurnal tides include internal inertia-gravity waves, edge waves, and finally the surface gravity waves.

We will view the summer 1976 data from Onslow Bay with these processes in mind, not for the purposes of scientific analysis, but rather as a conceptual overview delineating which candidate processes may be important.

The mooring locations in Onslow Bay during the ERDA/Sea Grant sponsored summer 1976 measurements are shown in Figure 2 and the corresponding instrument positions and sampling lengths are given in Tables 2 and 5. Two different recording current meters: Aanderaa and Endeco, were used. These instruments as well as others have recently been intercompared by Beardsley et. al. (1977) and the results, for the present purposes, suggest that data from the two are qualitatively similar. The rectangular array had simulteneous records spanning 23 July to 22 Aug. These are presented in Figs. 17, 27, 38, 71, 104, 134, 164, 193, 194 and 222. Speeds are in cm/s with the u and v velocity components positively directed

offshore and alongshore respectively, the alongshore direction being approximately at 55.6 degrees clockwise from true north. The time series were all low pass filtered with a half power point of 3 hours to remove high frequency noise. The most apparent features are semi-diurnal tidal currents superimposed upon a low frequency background. The only qualitative differences between the Aanderaa recordings (moorings C and E) and the Endeco recordings (mooring A and B) are the decrease in speed with time on the Aanderaa's due to fouling by barnacles. This does not appreciably affect the general findings. Simultaneous recordings are also available at both the top and bottom locations of mooring C. These are shown in Figures 38 and 71 and records from moorings E (top) and F (bottom) are shown in Figures 164 and 222.

Mean velocity vectors are shown in Figures 304 and 305. Figure 305 contains vectors at moorings C, E, and F computed over the total available record length. Location C and E suggest an alongshore mean to the northeast compatible with the predominant wind direction during the summer. The slight offshore component in the upper level on mooring C and the corresponding onshore component at the lower level would seem capatible with the thermohaline convection brought about by river runoff. The situation is much more confusing however. Figure 304 shows upper level mean vectors computed over the common sampling duration of 7/23 - 8/22. Both B and E point toward the southeast, A points offshore, and C now has a slight onshore component. Clearly the record lengths are too short to compute statistically reliable mean values in the presence of energetic low frequency events. These results must be kept in mind when trying to interpret the progressive vector diagrams shown in Figs. 16, 26, 36, 69, 102, 132, 162, 191 and 220.

From speed histograms (Figs. 37, 70, 103, 133, 163, 192 and 221) typical speeds were observed to be around 10 cm/s at mooring C. Peak speeds of 58 cm/s and 35 cm/s occurred at the upper and lower levels respectively. An example of a polar histogram of current direction for mooring C top is given in Fig. 37.

Progressive vector diagrams are used in some studies to estimate water particle trajectories (Lagrangian measurements) from Eulerian data. An example of the PVD's is mooring C in Figs. 36 and 70. PVD's may be of use for estimating such quantities as tidal excursions which in this location are of a few kilometers in length.

Representative alongshore (aligned with the mean coastline at 55.6° true) and offshore kinetic energy density spectra from mooring C (top and bottom) are shown in Figures 61-63 and 94-96. Except for higher energy at the upper level both the upper and lower level spectra show similar features. Energy density decreases with increasing frequency to a combined diurnal tide and local inertial peak (local inertial period, 12 hr/sin 34° = 21.5 hrs.) followed by a pronounced semi-diurnal tidal peak and then a continuing decrease through the internal gravity wave range. Comparing alongshore with offshore energy levels we see a distinct, difference between the low frequency, presumably meteorologically driven, background and the tidal peak. The wind driven background has higher energy in the alongshore direction while the tidal currents have higher

energy directed offshore. No marked directional preference appears in the high frequency internal gravity wave portion of the spectrum.

Relative to any given current meter record, or velocity vector time series, the choice of a coordinate system oriented alongshore and offshore with respect to the coastline (or major bathymetric features) is quite arbitrary. A preferred coordinate system for many descriptive applications is one which maximizes the variance in a given direction thus giving the principal axis of variance. Depending upon the physical processes causing the observed water motions, the principal axis of variance (normal coordinates) may vary with location and frequency. The principal axis for a given vector time series may be obtained by rotating the covariance matrix until the cross-covariance between orthogonal velocity components is zero. These are shown in Figure 306 along with the root mean square (r.m.s. or standard deviation) of the velocity components relative to the normal coordinates. The computations were made using data low pass filtered to suppress the tides. Thus, the variance crosses represent only the low frequency portion of the spectrum where the motions are primarily induced by atmospheric forcing. Each mooring site contains one or two crosses: solid lines for the upper level and dashed lines for the lower level. The angle in parenthesis gives the rotation of the principal axis relative to true north and the numbers at the tips of the crosses are the standard deviations along the coordinate axis. Typical low frequency r.m.s. speeds are of order 10 cm/s. The principal axis exhibit topographic steering and the reduction in amplitude and rotation with depth is compatible with local Ekman dynamics.

The preceeding principal axis representation gives an overview of the low frequency motions. Since the principal axis may vary as a function of frequency (the physical processes giving rise to the motions differ) it is useful to construct a hodograph model. In so doing, the velocity vector time series are decomposed into clockwise and anticlockwise rotating motions of different amplitude and phase. The sum of these two polarized motions gives an ellipse whose semi-major axis is oriented along the principal axis of variance at that particular frequency. This form of analysis is generally referred to as rotary spectral analysis and a comprehensive description of the technique may be found in Mooers, 1973; Gonella, 1972; or Fofonoff, 1969. It is analogous to what was presented in Figs. 39, and 72, except here the principal axis are computed as a function of frequency instead of just an average over a rather large frequency band. Example of the anticlockwise and clockwise polarized kinetic energy density spectra is indicated in Figure 39 for the upper level on mooring C. No consistent polarization preference is evident for time scales longer than one pendulum day while at shorter time scales the preference is clearly for clockwise polarized motions compatible with the dynamics of inertia-gravity controlled oscillations. Various parameters are required to describe the hodograph ellipse; for example, the ellipse semi-major and semi-minor axis (analogous to the crosses shown in Figure 306), the ellipse orientation, and three different measures of coherency between the velocity component fluctuations; the minimum and maximum coherences and the ellipse stability. The minimum coherence is the coherence between velocity components measured relative to the normal coordinates; the maximum coherence is the coherence between velocity components measured

relative to coordinates rotated 45° to the normal coordinates and the ellipse stability gives the coherence between anticlockwise and clockwise rotating components, i.e. it is a measure of the stability of the ellipse orientation. An example of these parameters is given in Figure 39 for the upper level on mooring C. The bottom plate contained the maximum (solid line) and minimum (dots) coherence squared as a function of frequency. The middle plate gives the stability (solid line) and the semi-minor to semi-major axis ratio (dots) with negative axis ratio designating clockwise hodograph rotation and vice-versa. The upper plate gives the ellipse orientation as a function of frequency which is useful when the stability is high. Regions of high maximum coherence but low minimum coherence generally designate coherent rectilinear motions where the stability mimicks the maximum coherency (the quadrative spectrum is small). Regions of both high maximum and minimum coherence designate coherent elliptical motions. For this case the stability can be either high or low. For example, the orientation of a nearly circular motion is arbitrary, therefore, the stability would be low. Upon traversing from low to higher frequency motions in Figure 39, we see fairly coherent rectilinear motions at time scales longer than roughly 5 days oriented approximately along the principal axis shown in Figure 306. Note that orientation here is measured anticlockwise from the nominal offshore direction of 145.6° relative to true north. The units shown in the Figure have been normalized by π radians therefore one must multiply by π to get the radian measure. The motions are incoherent between time scales between 1 to 5 days except for a peak at about 32 hrs. A rather broad peak in both minimum and maximum coherence occurs spanning time scales of approximately 16-25 hours which incompasses the astronomical diurnal tidal species propagating onto the shelf from the deep ocean, local sea breeze effects, and local inertial period oscillations ($2\pi/f$ = 21.5 hrs.) as mentioned previously. The interaction between these three important processes is evident in the low ellipse stability and the varying orientation. The most coherent peak occurs centered at 12.41 hrs. which is the time scale of the principal lunar semi-diurnal tide. This is the only time scale where the motions are truly coherent and stable because it is the only time scale dominated by a regular deterministic process.

Redfield (1958) analyzed sea level records along the east coast of the U.S. to produce the co-tide and co-range lines and concluded that the principal lunar semi-diurnal tide (M_2) on the eastern U.S. continental shelf is a co-oscillation caused by the reflection of an incident oceanic wave by the coast. The portion of the oceanic wave transmitted onto the shelf reflects off the coast resulting in an increase in the tidal amplitude with distance from the continental slope. Hence, the mean tidal range at Savannah is 6.8 ft. whereas it decreases to 3.6 ft. at Cape Hatteras, since the shelf width at Savannah is larger than at Cape Hatteras. This type of reflected inertiagravity wave is called a Poincare wave. It has a maximum elevation slightly seaward of the coast and the associated water particle motions in the horizontal plane are elliptical, clockwise polarized, and oriented with the semi-major axis along the direction of propagation. The ratio of semi-minor to semi-major axis is theoretically predicted to be a pendulum day ($2\pi/f$) divided by the wave period (in this case 12.41 hr.) Thus the predicted axis ratio is 0.58 at the latitude of 34°N. The velocity data in Onslow Bay supports Redfields view. Figures 307 and 308

show the semi-diurnal tidal ellipses computed at all the mooring locations. Computations made from the entire record lengths are shown in Figure 308 and those made over the common length for the rectangular array are shown in Figure 307. The sense of rotation for all of the ellipses is clockwise, they are oriented onshore and their axis ratios are all close to the value predicted for a Poincare wave. At mooring C it is observed that the amplitude of the tidal current decreases with depth and the ellipse orientation is slightly rotated. Both of these effects may be attributed to bottom friction. A small phase shift (less than 1 hr.) also occurs between the upper and lower tidal current due to bottom friction.

Other tidal constituents were examined but only the principal lunar semi-diurnal M_2, the principal solar semi-diurnal S_2, and a shallow water harmonic M_4 were found to have amplitudes over 1 cm/s. In some cases the other tidal constituents did not even stand out above the background noise level. The three major constituents for Onslow Bay tidal currents are summarized in Table 8, from which Figures 307 and 308 were constructed. The S_2 tidal currents are very similar in orientation and axis ratio to the M_2 currents except for being much smaller in magnitude.

A preliminary look at the Onslow Bay velocity data from this experiment portrays the general character of water movements off the Carolina coasts. Except for the tidal oscillations, the picture is extremely complicated resulting from the superposition of numerous random processes operating over a broad range of frequencies.

Mean currents remain ill-defined. Velocity records of a months duration are too short to compute relatively small mean values in the presence of relatively large low frequency variability. Additional research is required (and has been conducted under DOE support, to date) to establish reliable mean fields and their seasonal variations.

The variance structure is summarized in Figures 40-42 and 73-75, which is a plot of the fluctuation kinetic energy distribution as a function of frequency for the upper and lower levels at mooring C. The ordinate gives the energy fraction contained over any frequency band. For example, the semi-diurnal tidal current comprises 39% (top) and 53% (bottom) of the variances at the two depths at that location. Other pertainent fractions are labeled on the figure.

Earlier, it was mentioned that the low frequency portion of the spectrum could be attributable to either direct atmospheric forcing, intrusions or eddies from the deep ocean boundary, or propagation of free modes of oscillation supported by the bottom topography i.e. continental shelf waves. A first impression from the data presented; particularly the velocity hodograph parameters, is that regular, coherent, wave like features on the continental shelf in Onslow Bay are of secondary importance to the transient wind induced motions and influence of the Gulf Stream.

TABLE 8

TIDAL CONSTITUENTS IN ONSLOW BAY OBSERVED DURING THE SUMMER OF 1976

Record	Length Hrs.	M_2 Orientation	M_2 Semi-Major CM/S	M_2 Axis Ratio	S_2 Orientation	S_2 Semi-Major CM/S	S_2 Axis Ratio	M_4 Orientation	M_4 Semi-Major CM/S	M_4 Axis Ratio
CT	1434	132	17.2	0.52	136	3.1	0.48	163	1.0	0.20
CB	"	137	13.2	0.43	136	2.3	0.39	163	0.8	0.12
ET	1784	138	16.3	0.55						
FB	"	152	6.8	0.26	163	2.1	0.29	136	1.3	0.25
AT	1123	138	14.5	0.45	143	2.3	0.52	073	2.4	0.35
BT	"	115	11.9	0.44	091	2.5	0.68	073	1.8	0.20
CT	"	133	9.4	0.55	136	2.5	0.52	163	0.6	0.10
ET	"	137	13.3	0.52	137	3.1	0.48	019	0.8	0.40

From the point of view of modelling, prediction of tidal currents appears to be tractable because of their regularity and orderliness. Prediction of the low frequency events will be much more difficult however since their driving functions tend to be random and nonstationary. Considerable diagnostic analysis will be required to define the important processes and their coupling with the shelf circulation before reliable predictive models can be realized. The DOE and U.N.C.-Sea Grant sponsored efforts represent a major step in acquiring such an understanding.

In summary, the velocity structure in Onslow Bay consists of low frequency atmospheric and deep ocean forced motions comprising about 45% of the variance (r.m.s. speed of order 10 cm/s) superimposed upon semi-diurnal tidal oscillations comprising about 53% of the variance (r.m.s. speed again of order 10 cm/s). The remainder of the variance is associated with internal gravity waves, along shore seiches and associated with the bordering shoals, and turbulence. Mean currents remain poorly defined with magnitudes smaller than the r.m.s. fluctuations. The deterministic tidal currents seem amenable to predictive modelling; however, considerable more work will be required to understand the low frequency motions which can play a dominant role in mass transport. For example, typical tidal excursions are roughly 1-2 km while the low frequency excursions will typically be roughly ten times larger. Furthermore, due to the transient as opposed to oscillatory nature of the low frequency motions, their particle excursions are more likely to lead to net transports.

Data Products

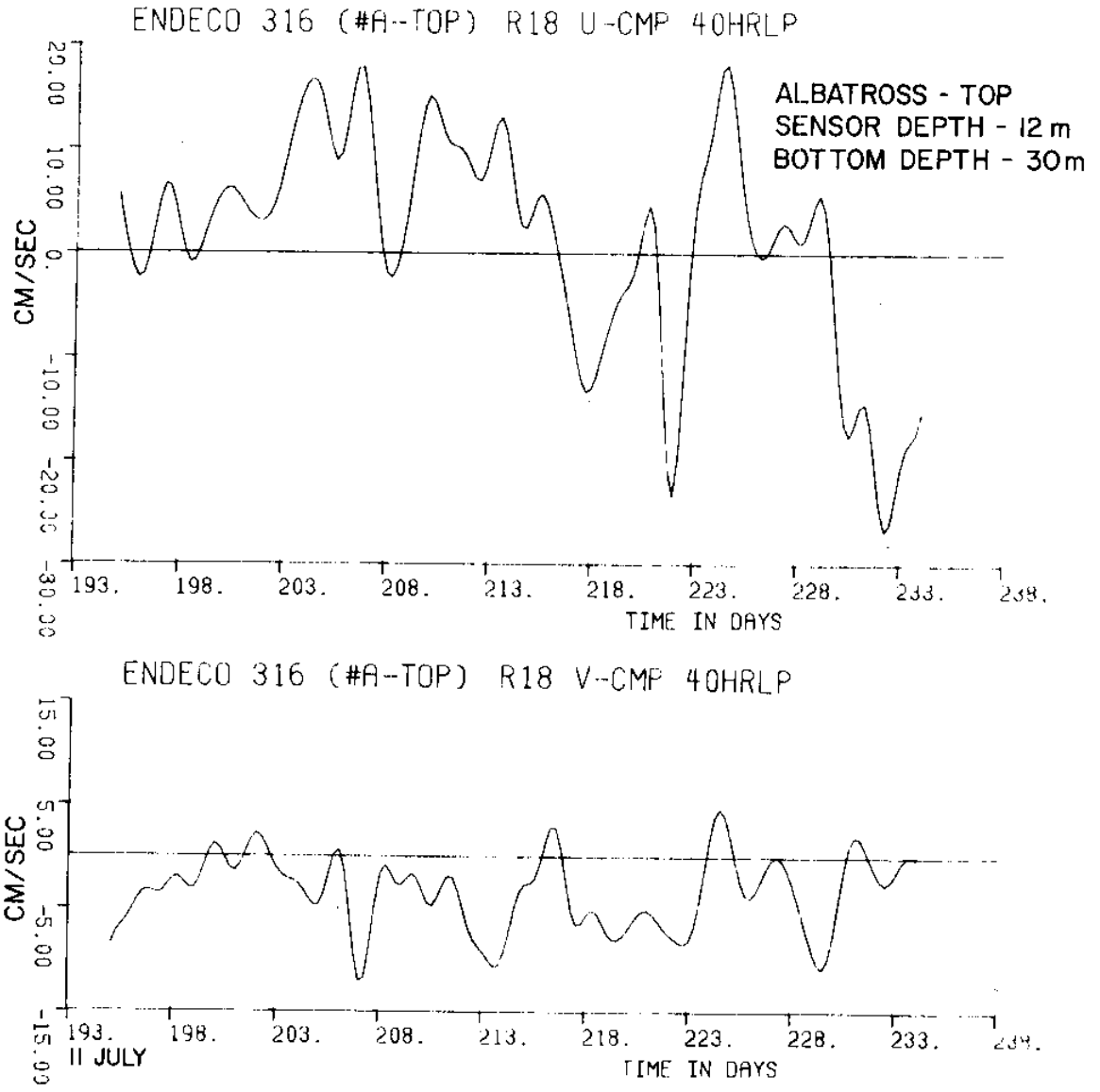

Figure 11 Low pass current velocity components and vectors from meter A(Albatross)$_{top}$

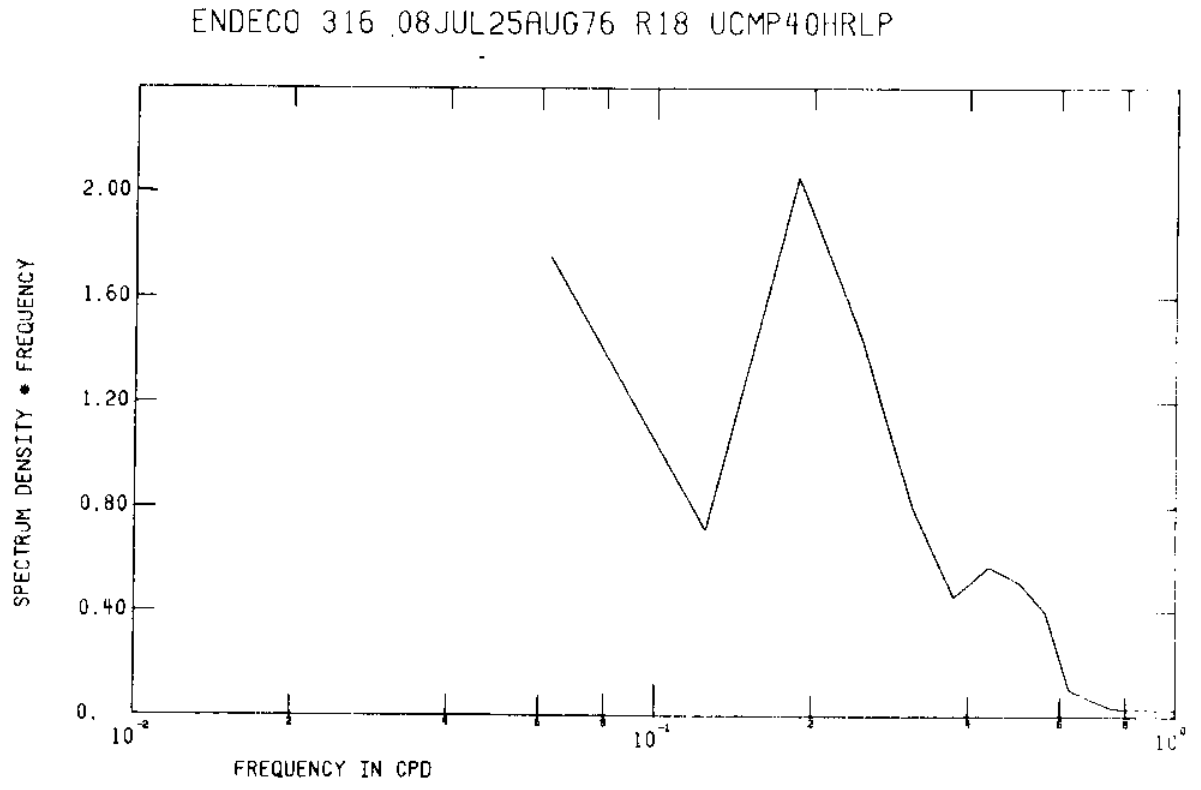

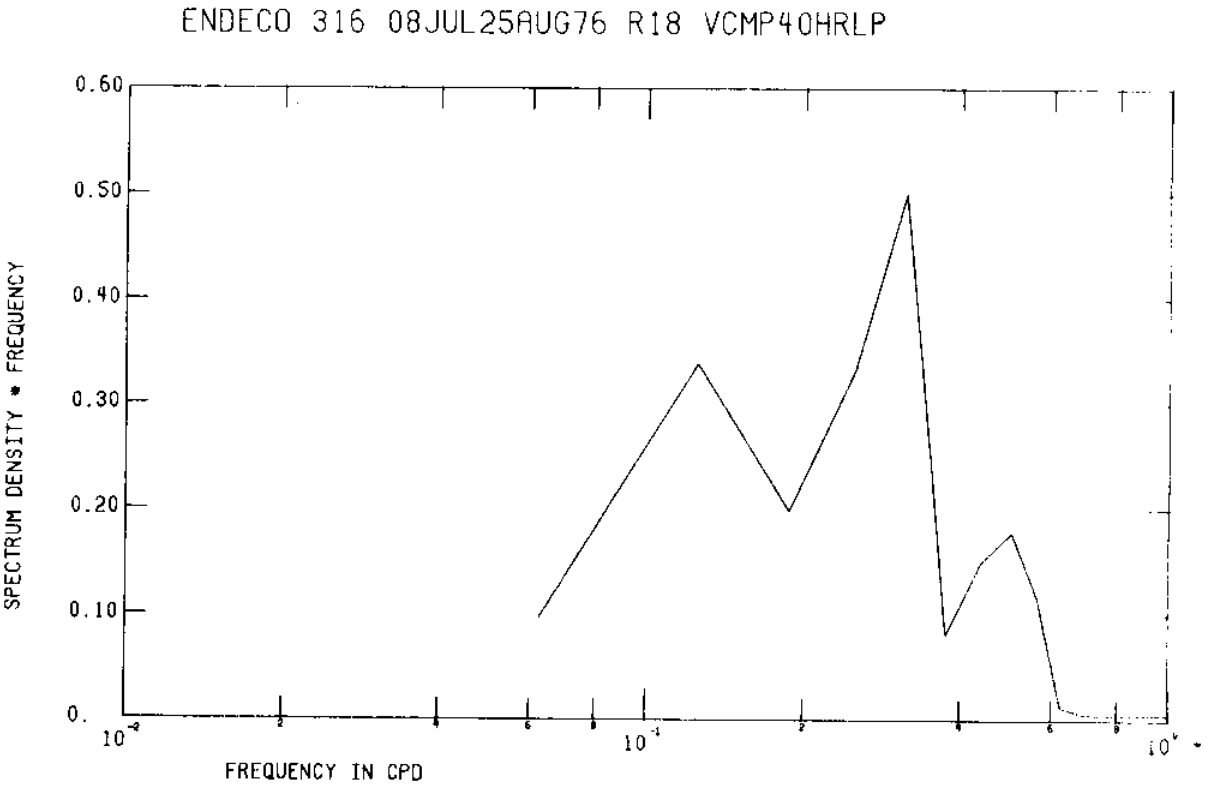

Figure 12 FFT of low pass current velocity components from meter A(Albatross)$_{top}$

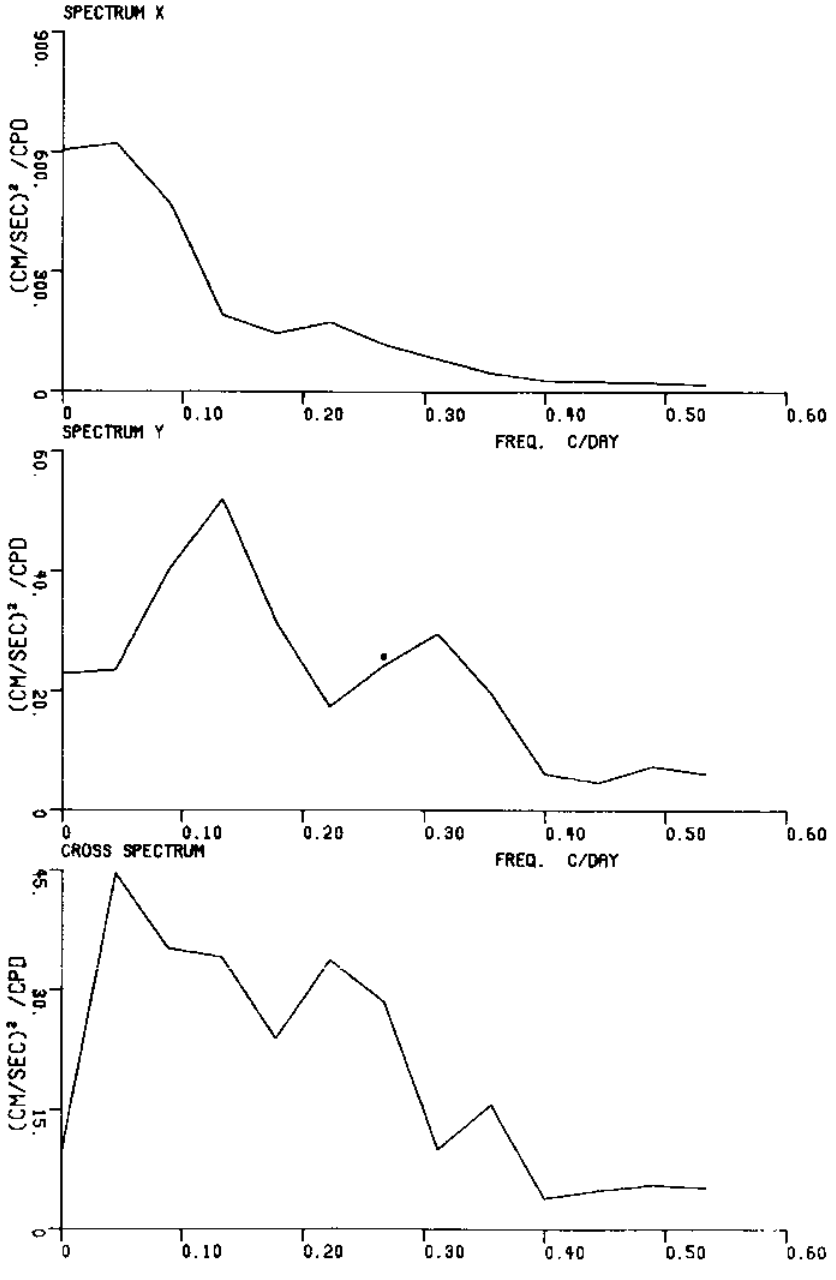

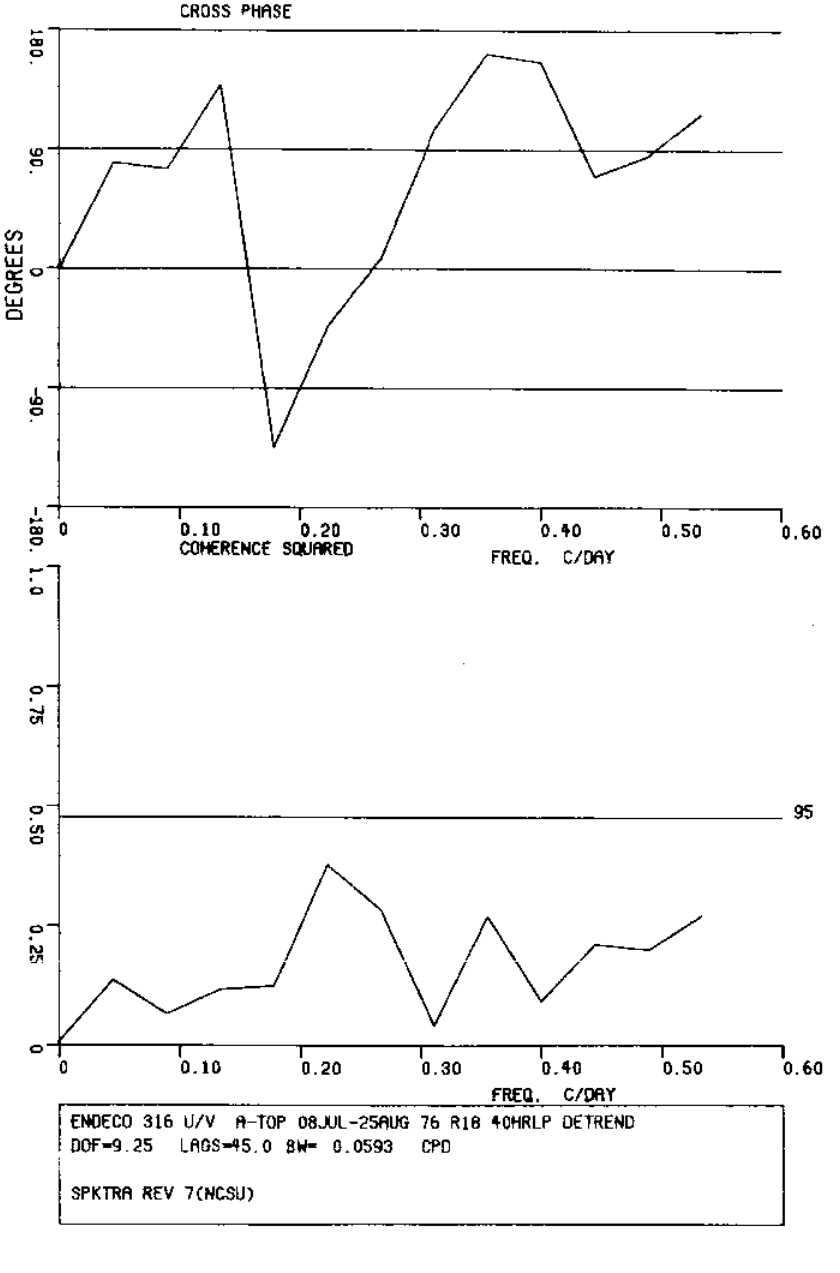

Figure 13 Spectra of low pass current velocity components from meter A(Albatross)$_{top}$

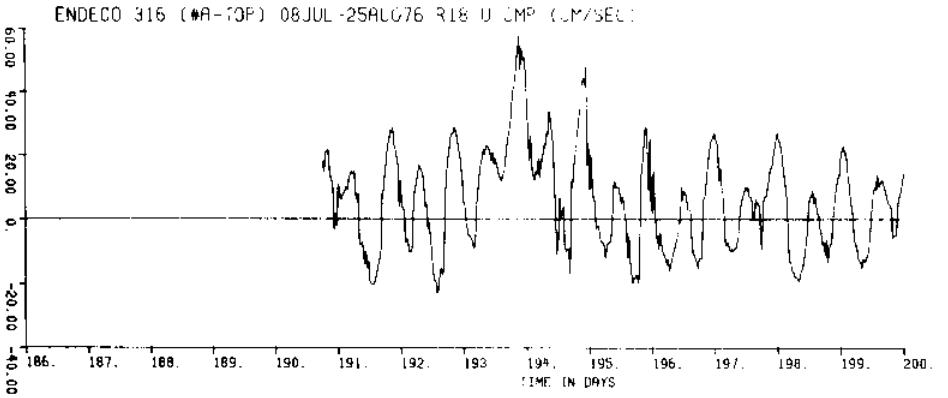

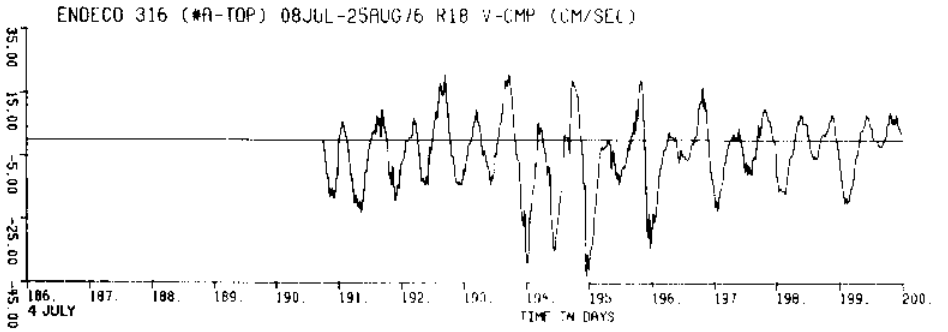

Figure 14 a

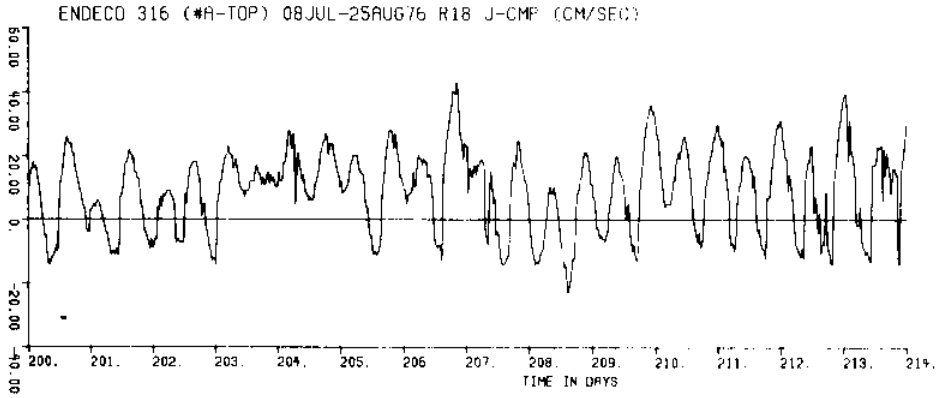

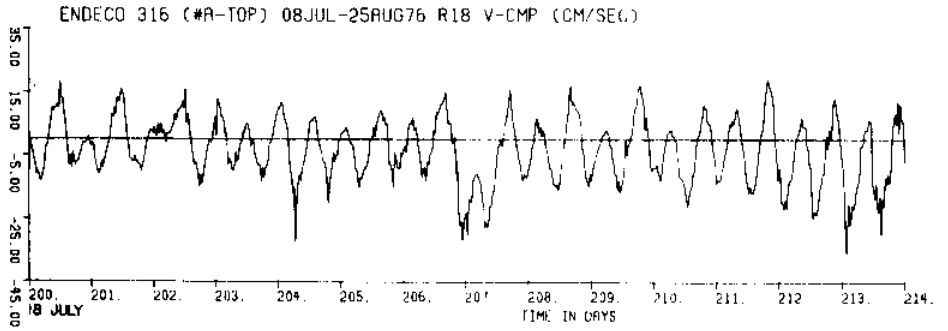

Figure 14 b

Figure 14 (a,b,c,d) Unfiltered current velocity components from meter A(Albatross)$_{top}$

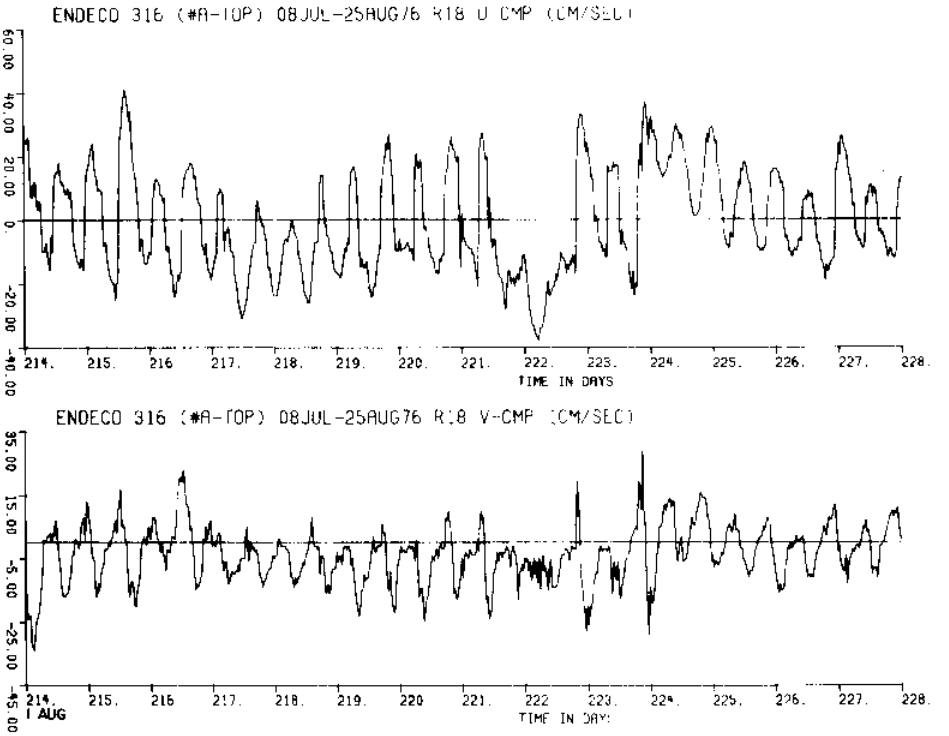

Figure 14 c

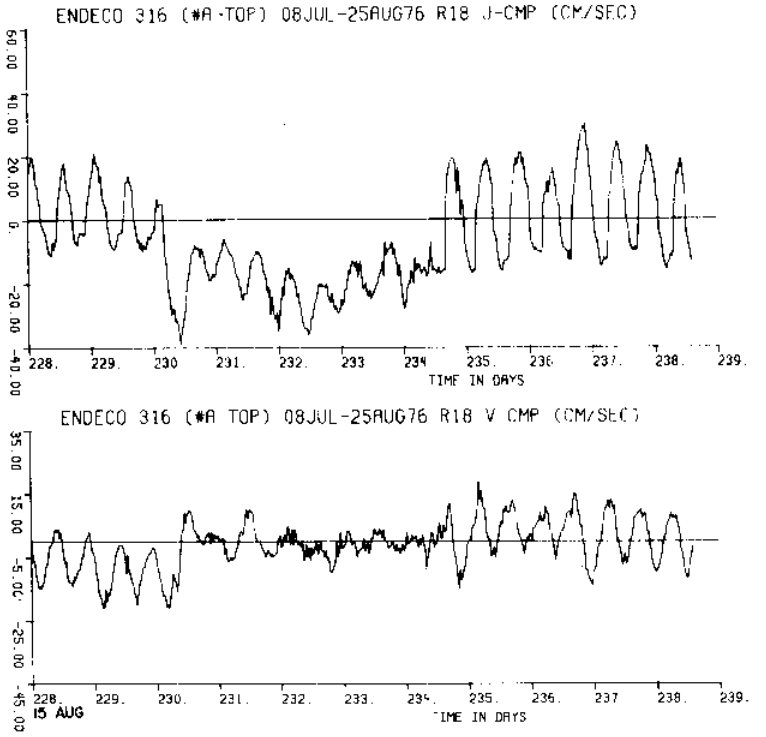

Figure 14 d

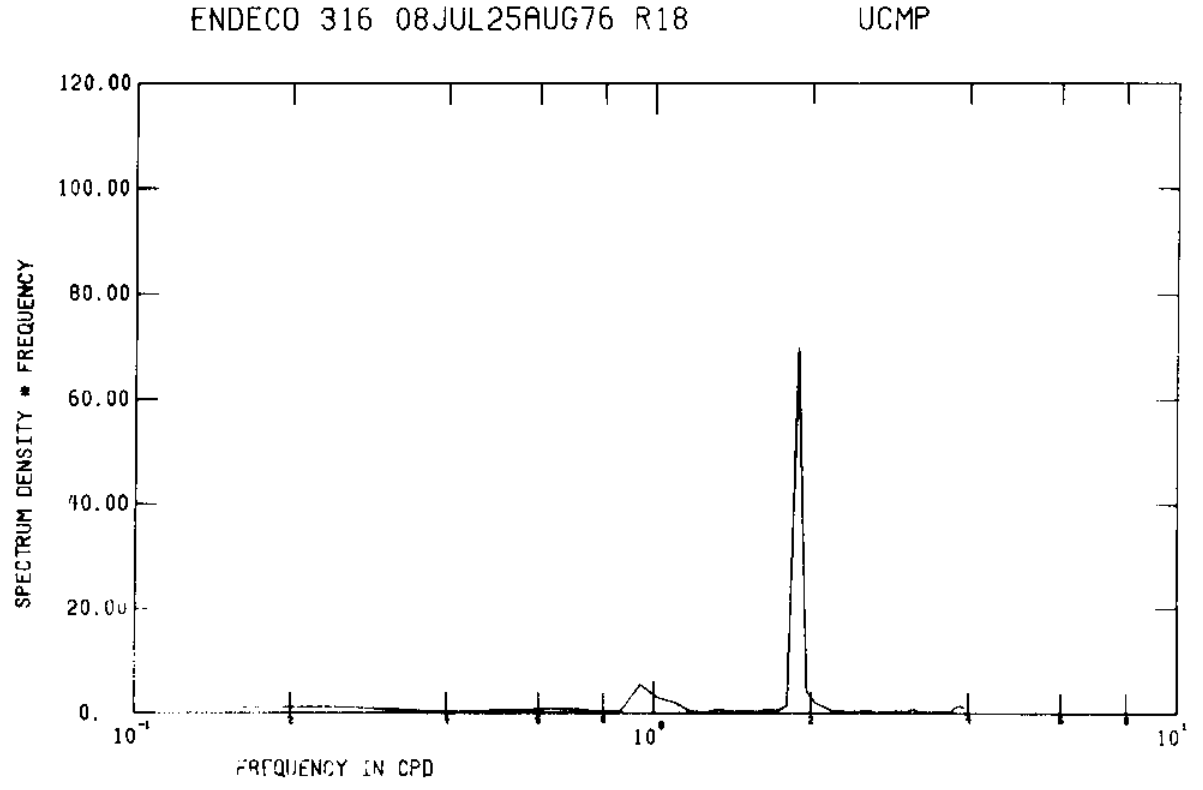

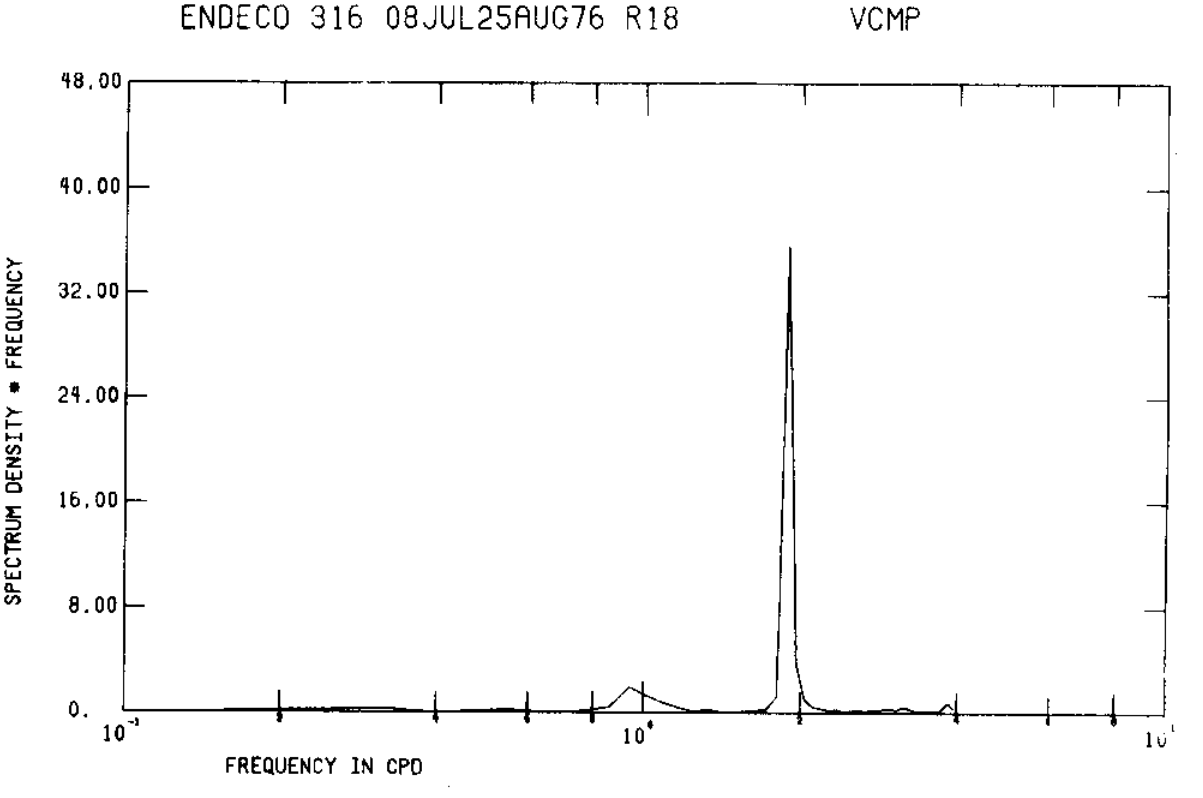

Figure 15 FFT of unfiltered current velocity components from meter A(Albatross)$_{top}$

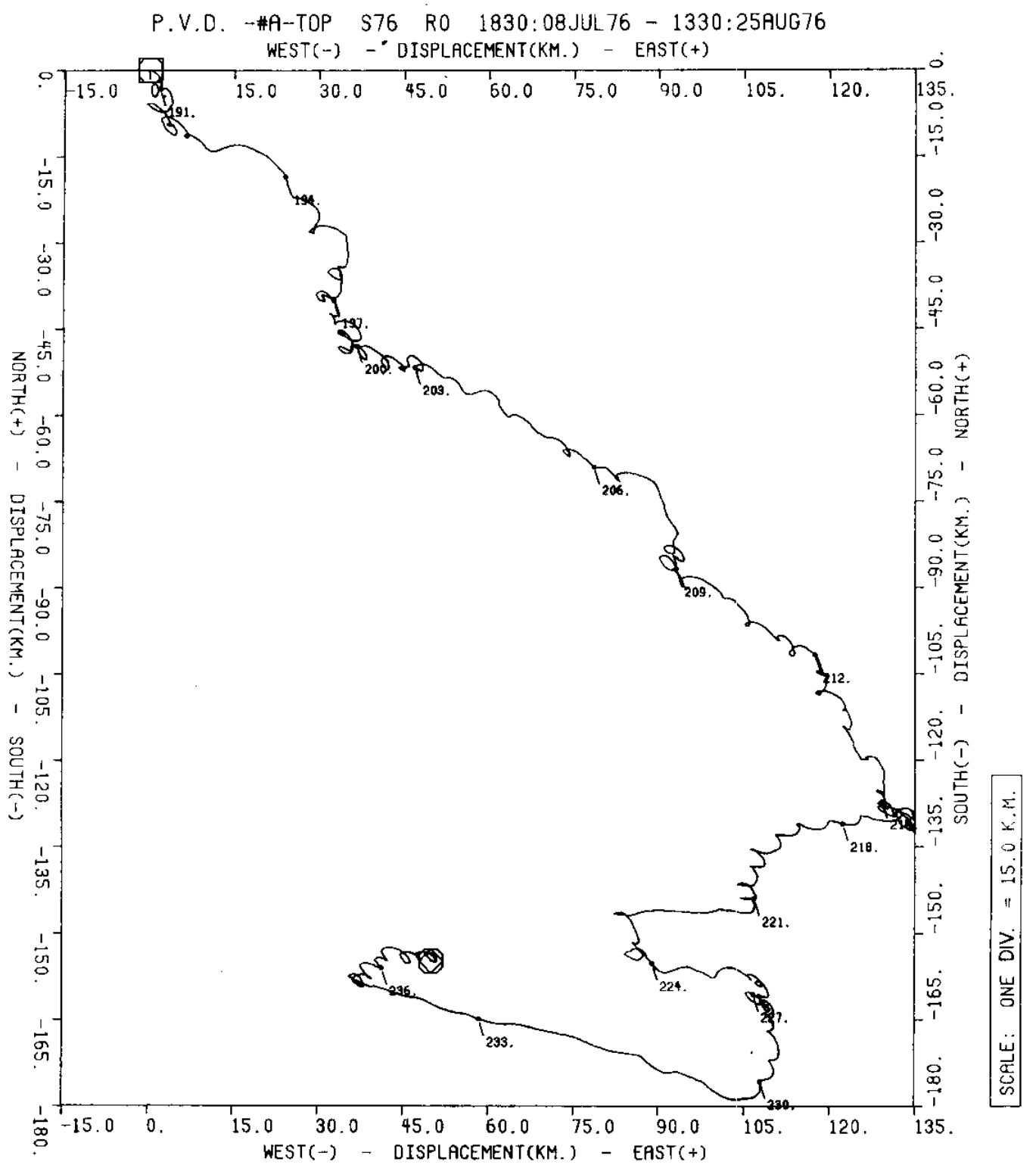

Figure 16 a

Figure 16 (a,b,c) Progressive vector diagrams of unfiltered current velocity from meter A(Albatross)$_{top}$

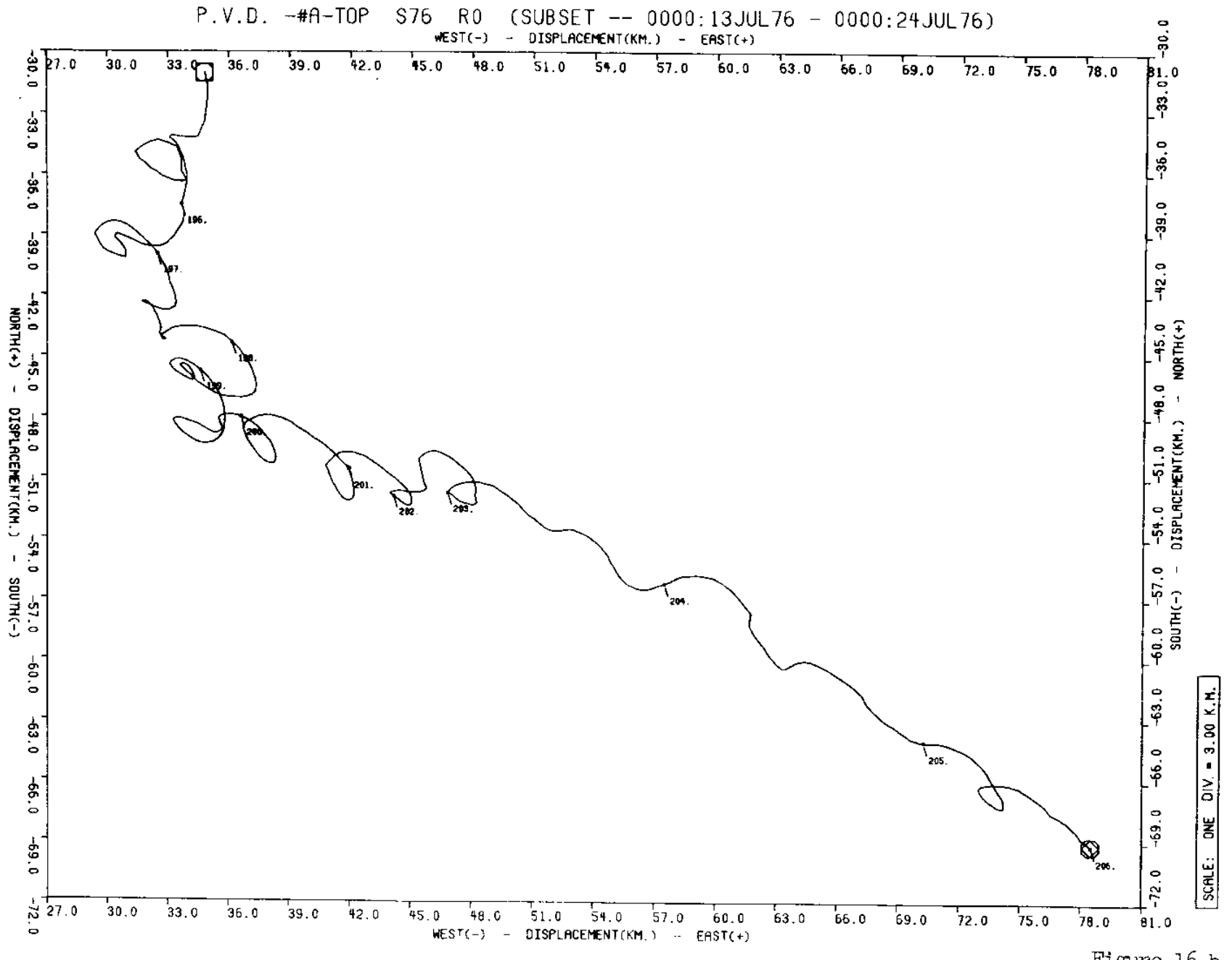
P.V.D. -#A-TOP S76 R0 (SUBSET -- 0000:13JUL76 - 0000:24JUL76)
WEST(-) - DISPLACEMENT(KM.) - EAST(+)
NORTH(+) - DISPLACEMENT(KM.) - SOUTH(-)
SOUTH(-) - DISPLACEMENT(KM.) - NORTH(+)
SCALE: ONE DIV. = 3.00 K.M.
196.
197.
198.
199.
200.
201.
202.
203.
204.
205.
206.

Figure 16 b

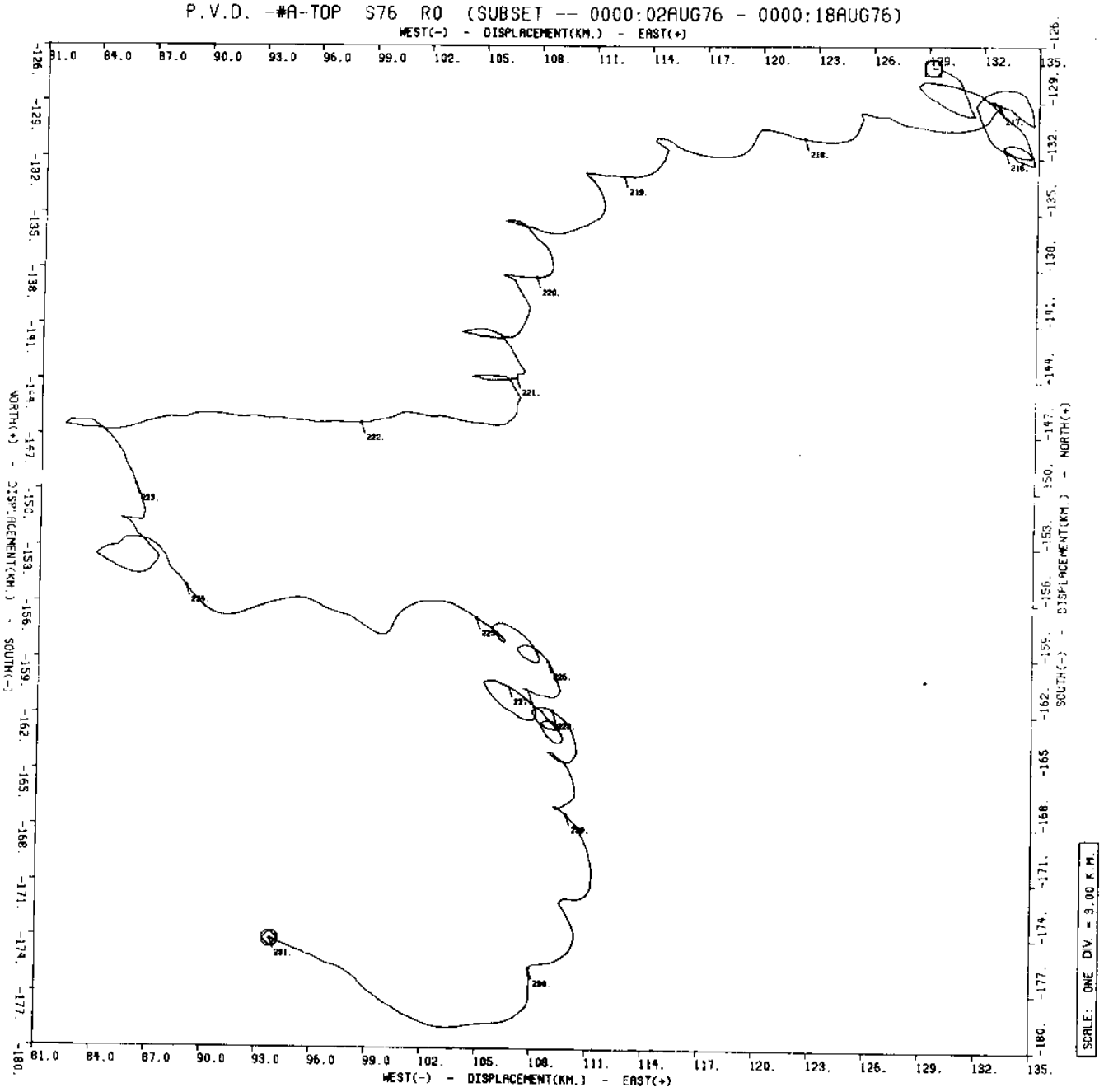
P.V.D. -#A-TOP S76 R0 (SUBSET -- 0000:02AUG76 - 0000:18AUG76)
WEST(-) - DISPLACEMENT(KM.) - EAST(+)
NORTH(+) - DISPLACEMENT(KM.) - SOUTH(-)
SCALE: ONE DIV. = 3.00 K.M.

Figure 16 c

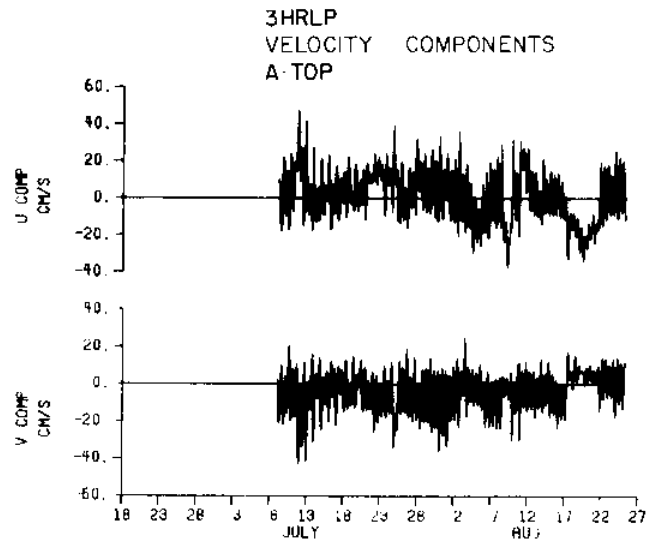

Figure 17 3HRLP velocity components for A_{top}

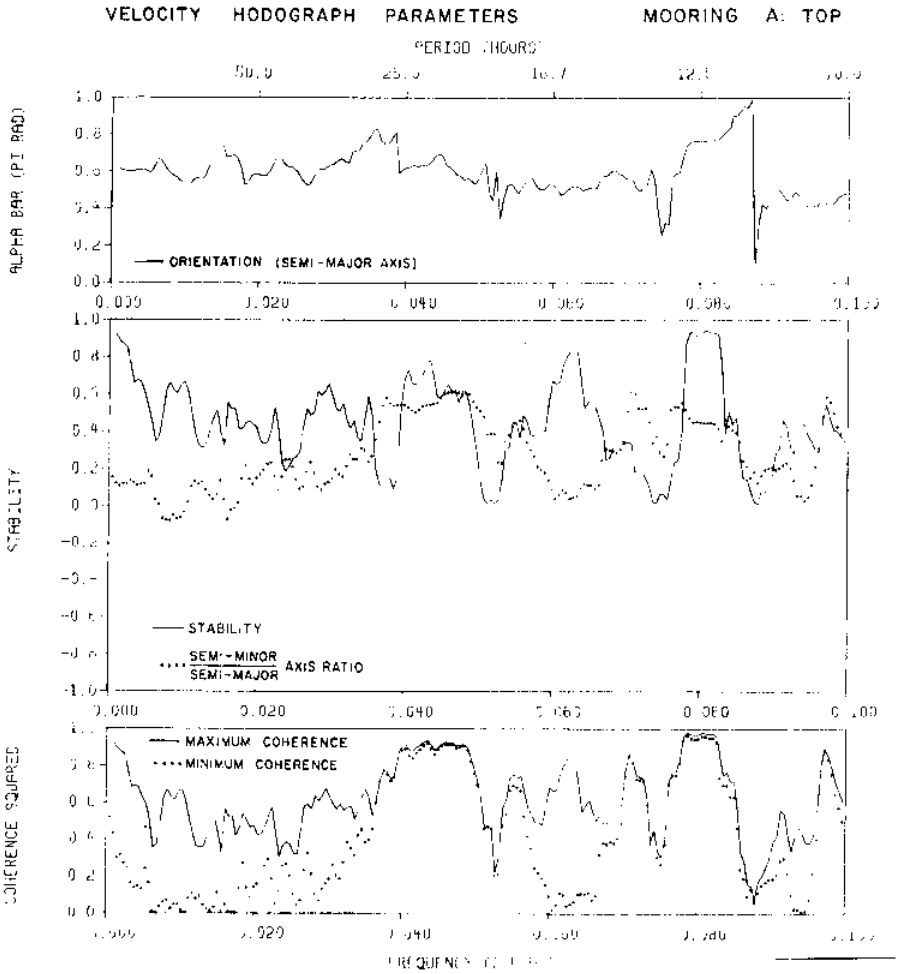

Figure 18 Hodograph parameters from meter A(Albatross)$_{top}$

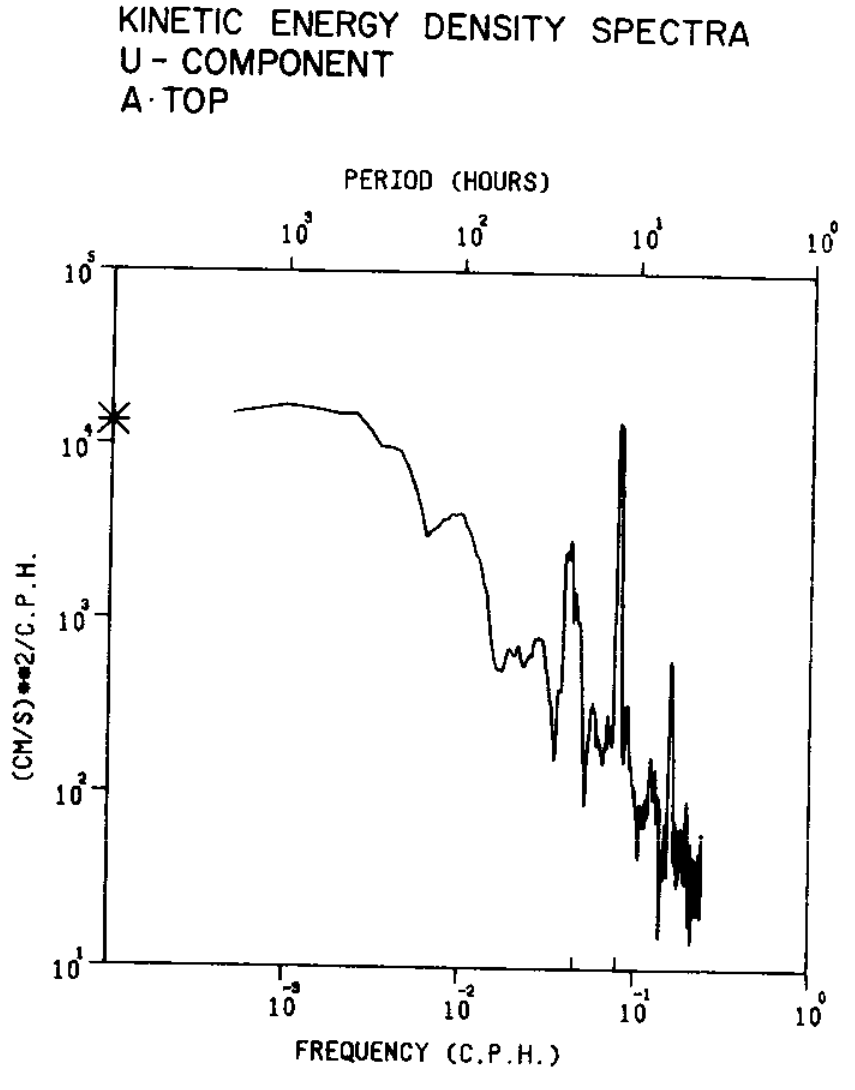

Figure 19 Kinetic energy density spectra for current velocity, u-component, A_{top}

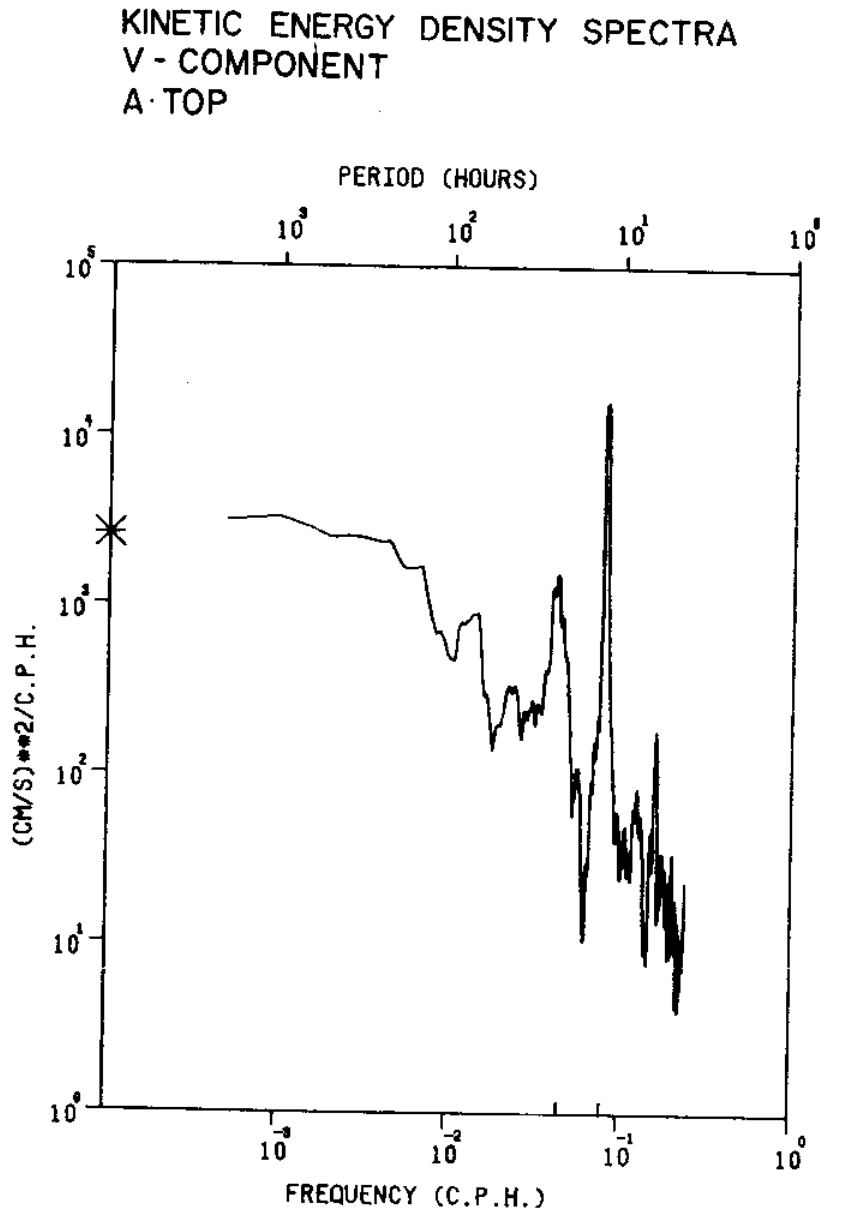

Figure 20 Kinetic energy density spectra for current velocity, v-component, A_{top}

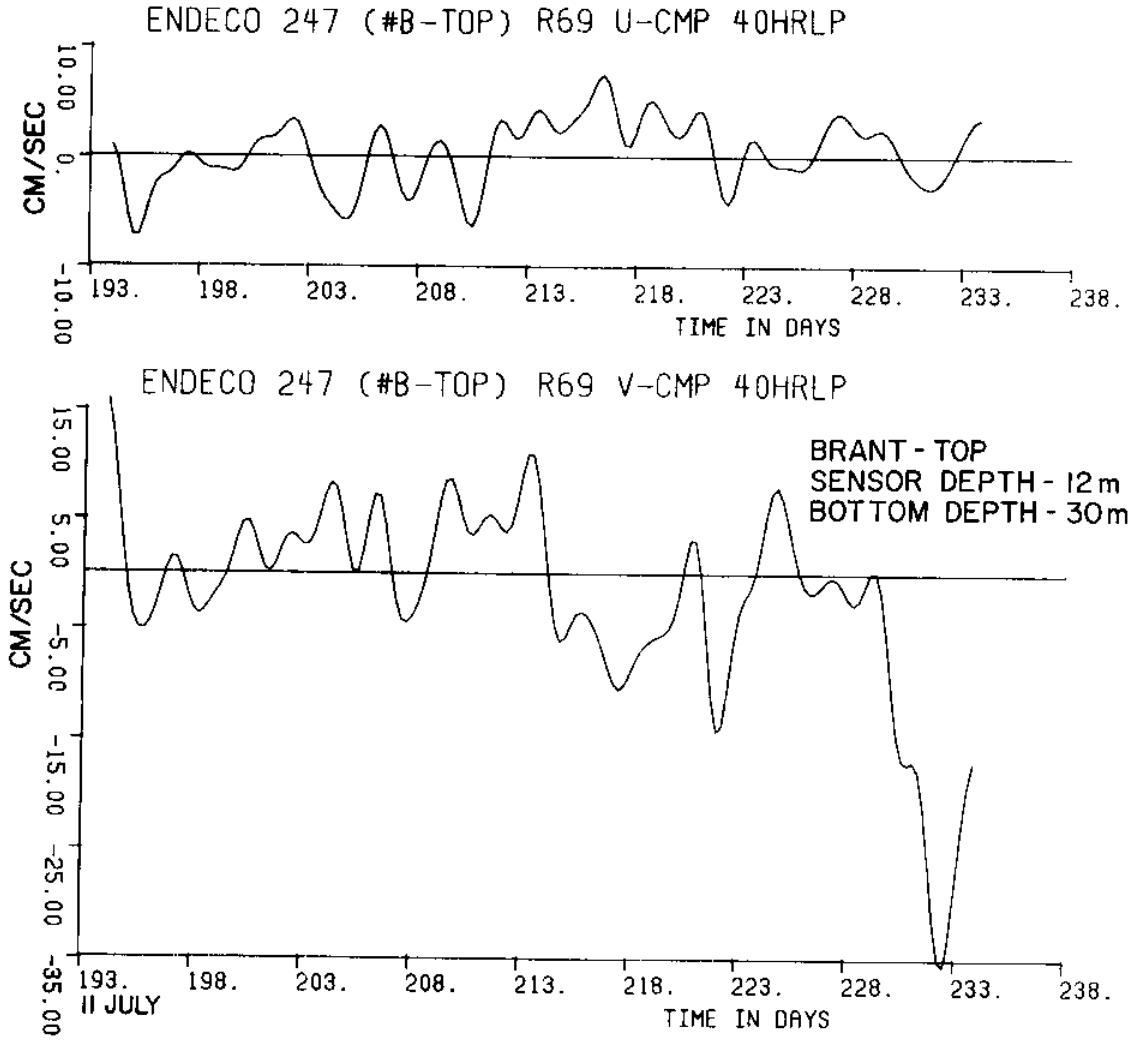

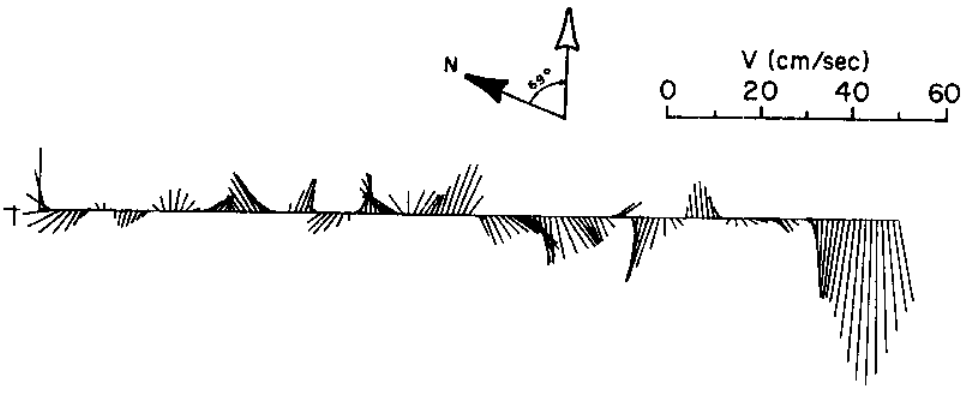

Figure 21 Low pass current velocity components and vectors from meter B(Brant)$_{top}$

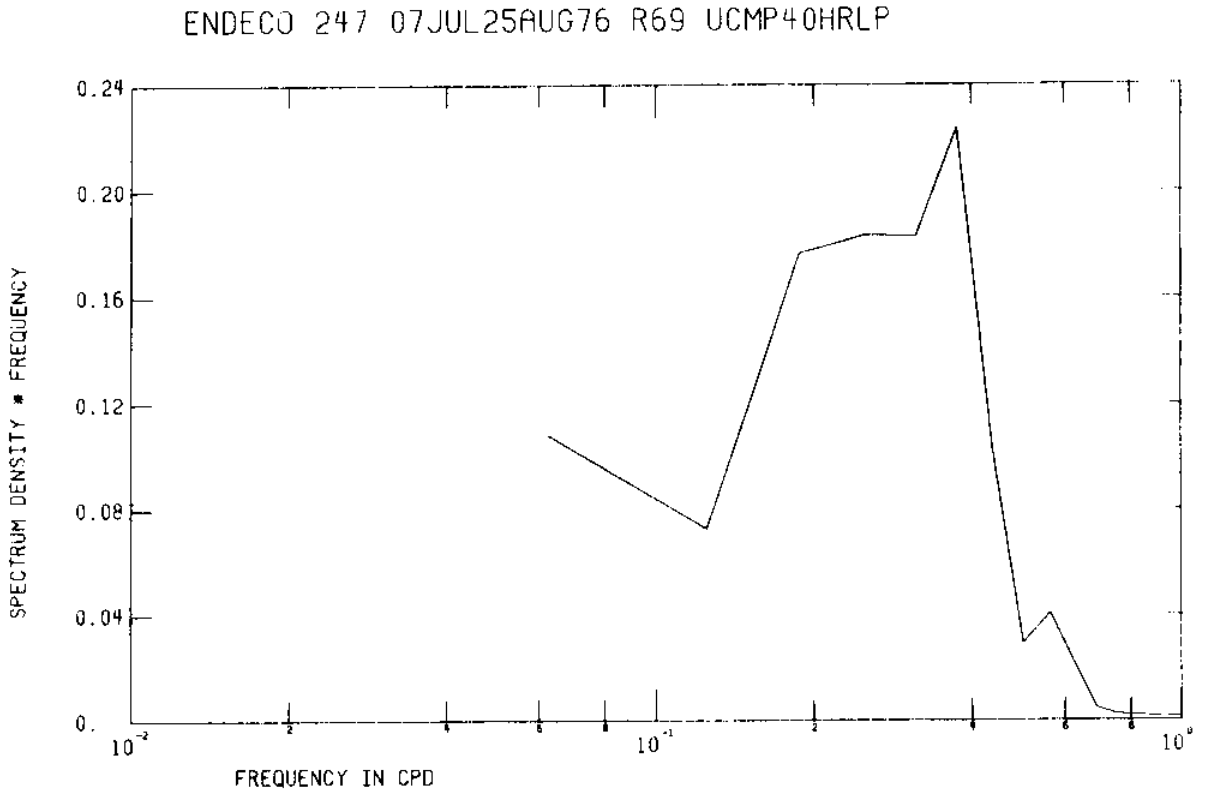

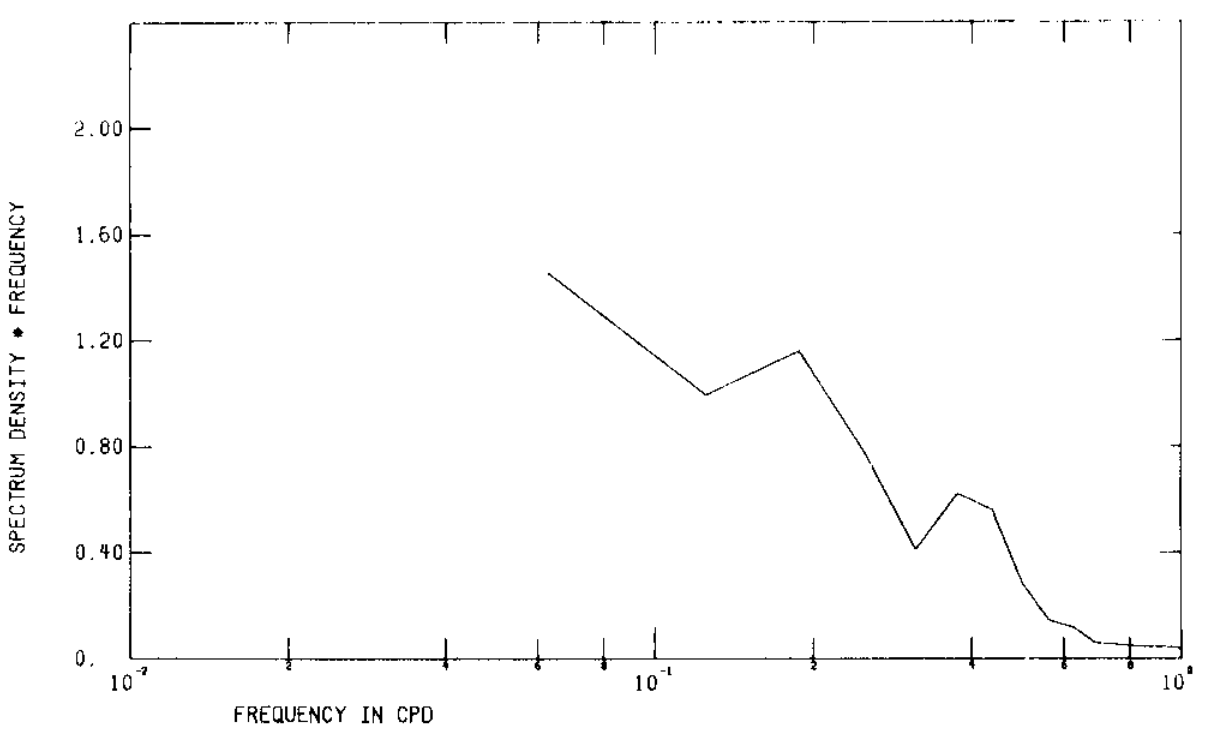

Figure 22 FFT of low pass current velocity components from meter $B(Brant)_{top}$

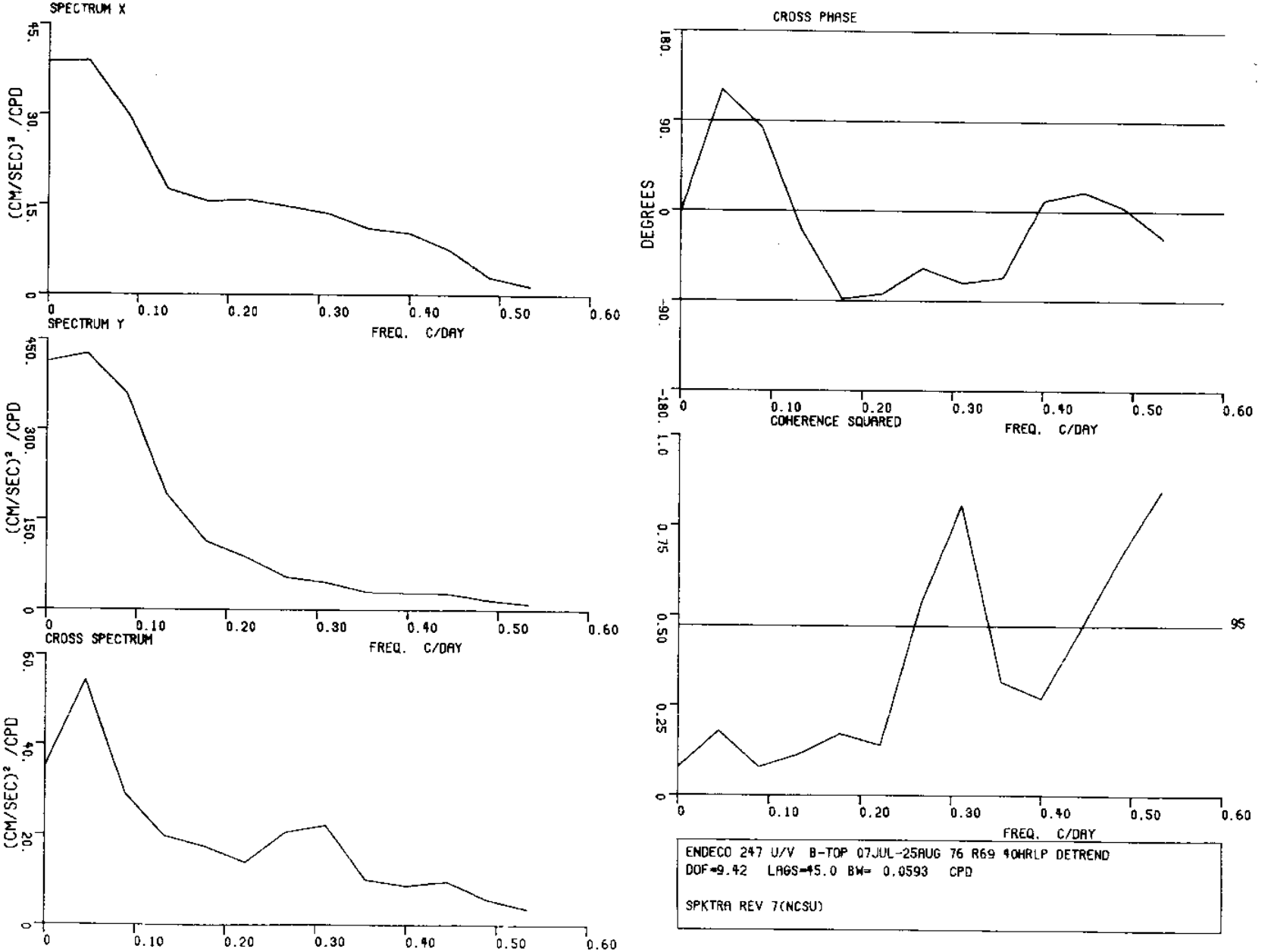

Figure 23 Spectra of low pass current velocity components from meter $B(Brant)_{top}$

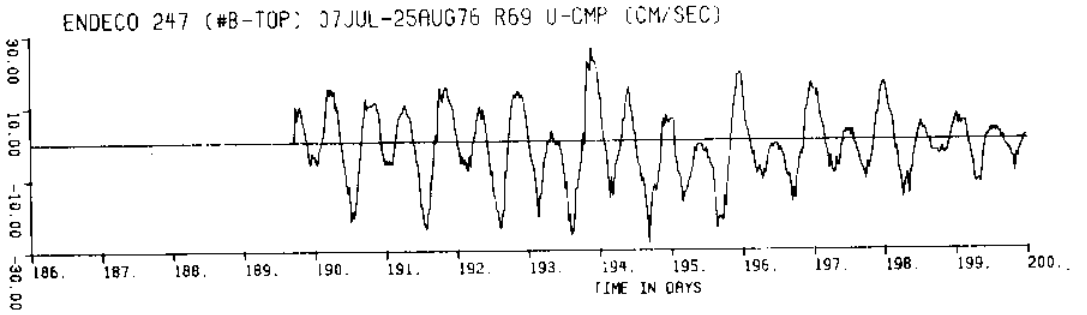

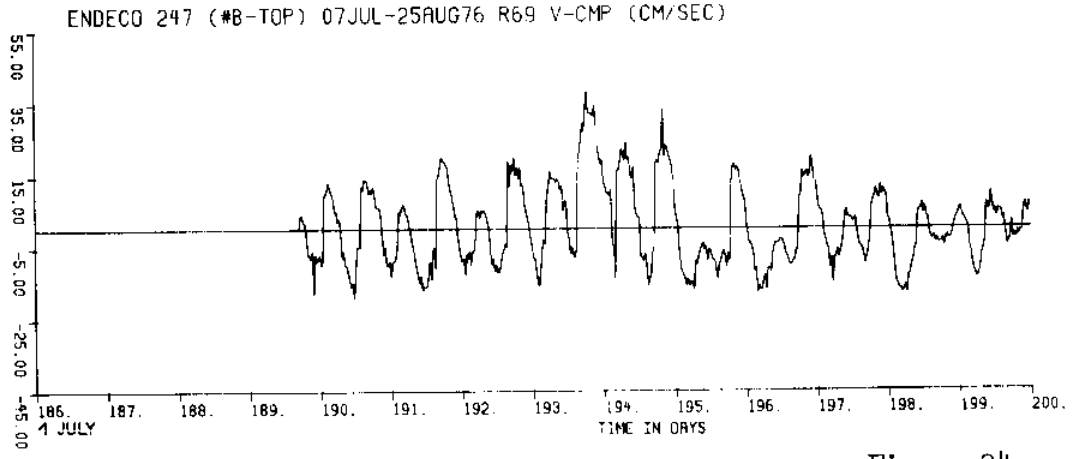

Figure 24 a

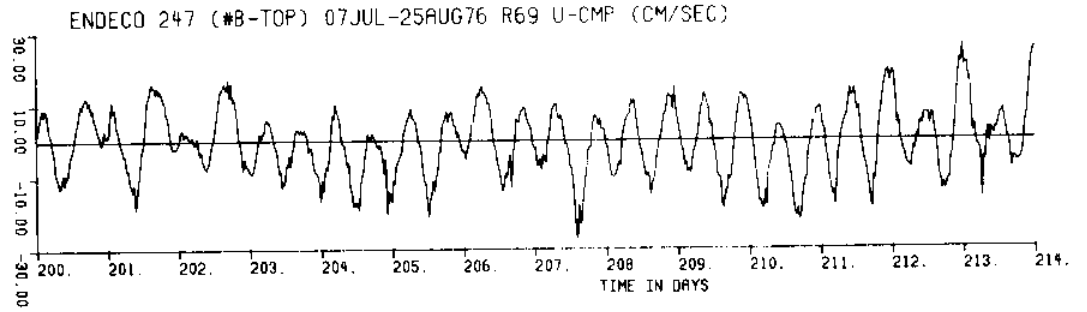

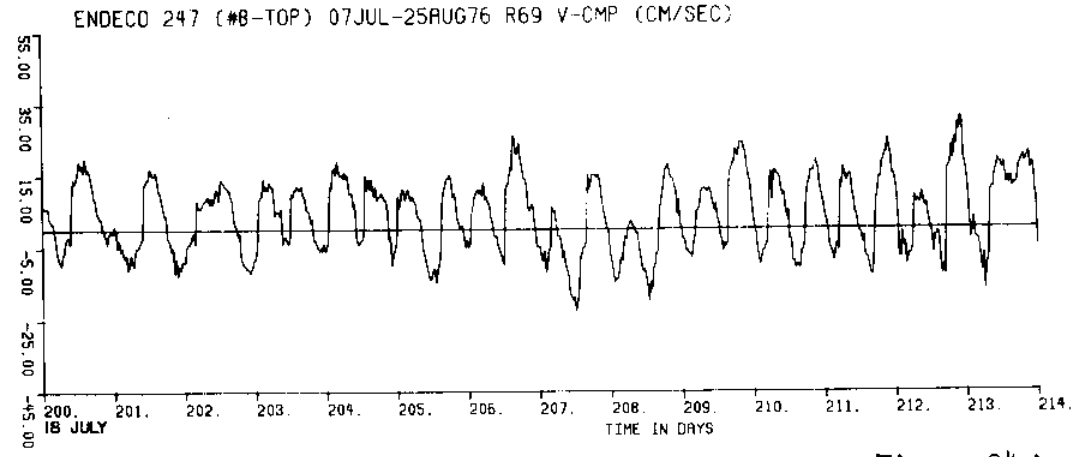

Figure 24 b

Figure 24 (a,b,c,d) Unfiltered current velocity components from meter $B(Brant)_{top}$

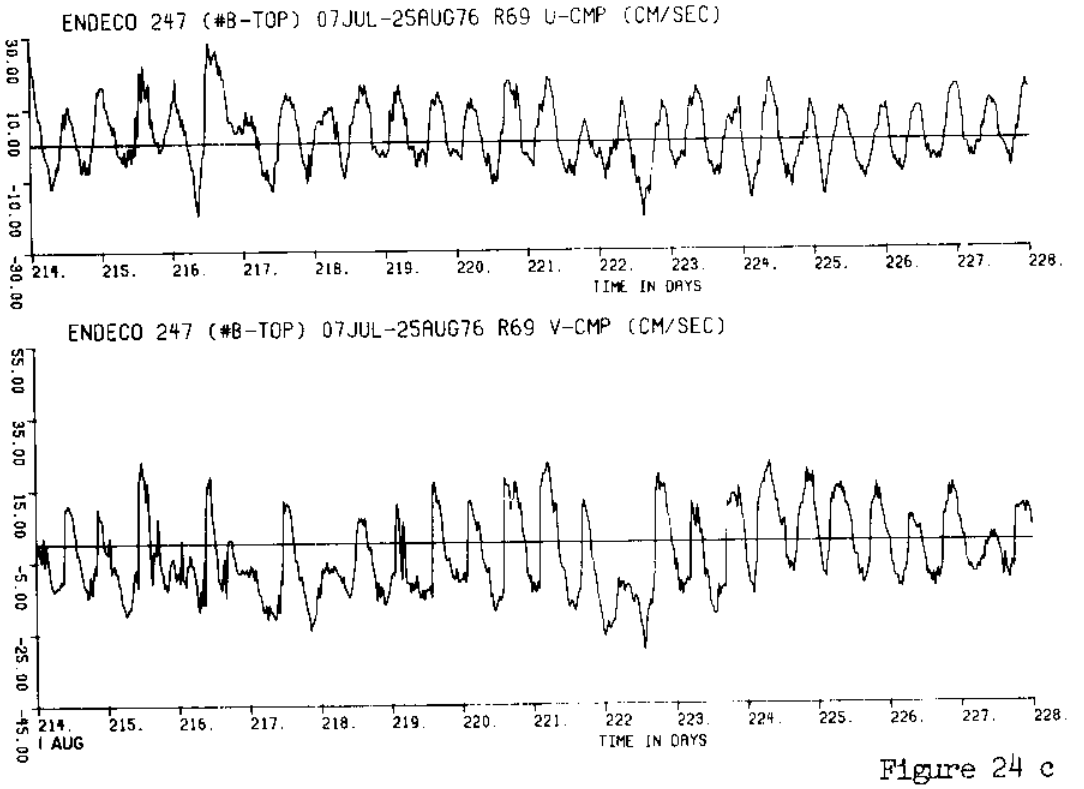

Figure 24 c

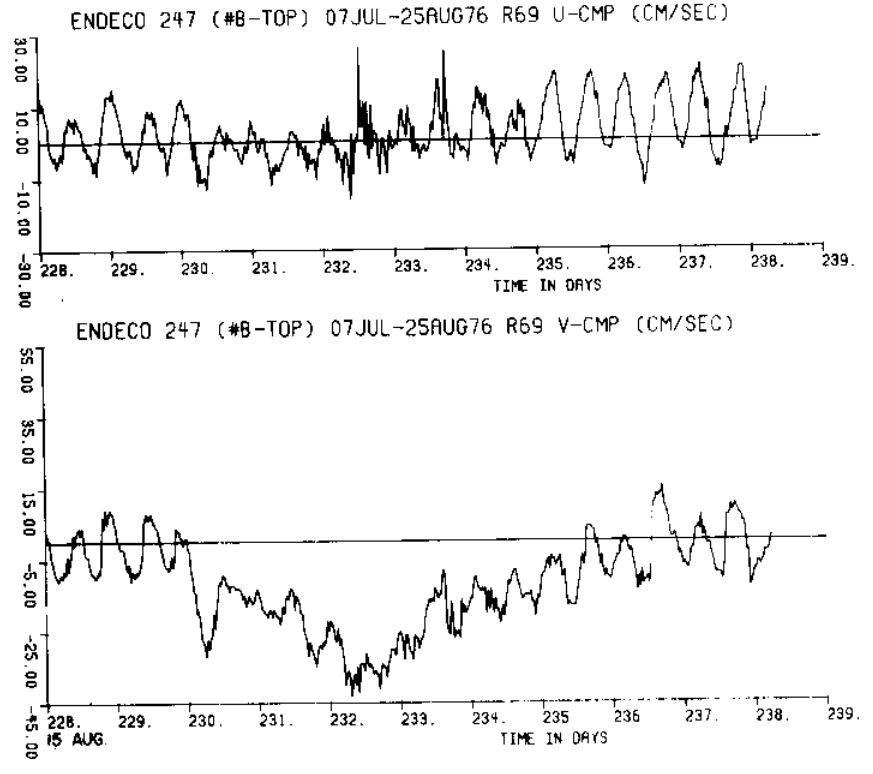

Figure 24 d

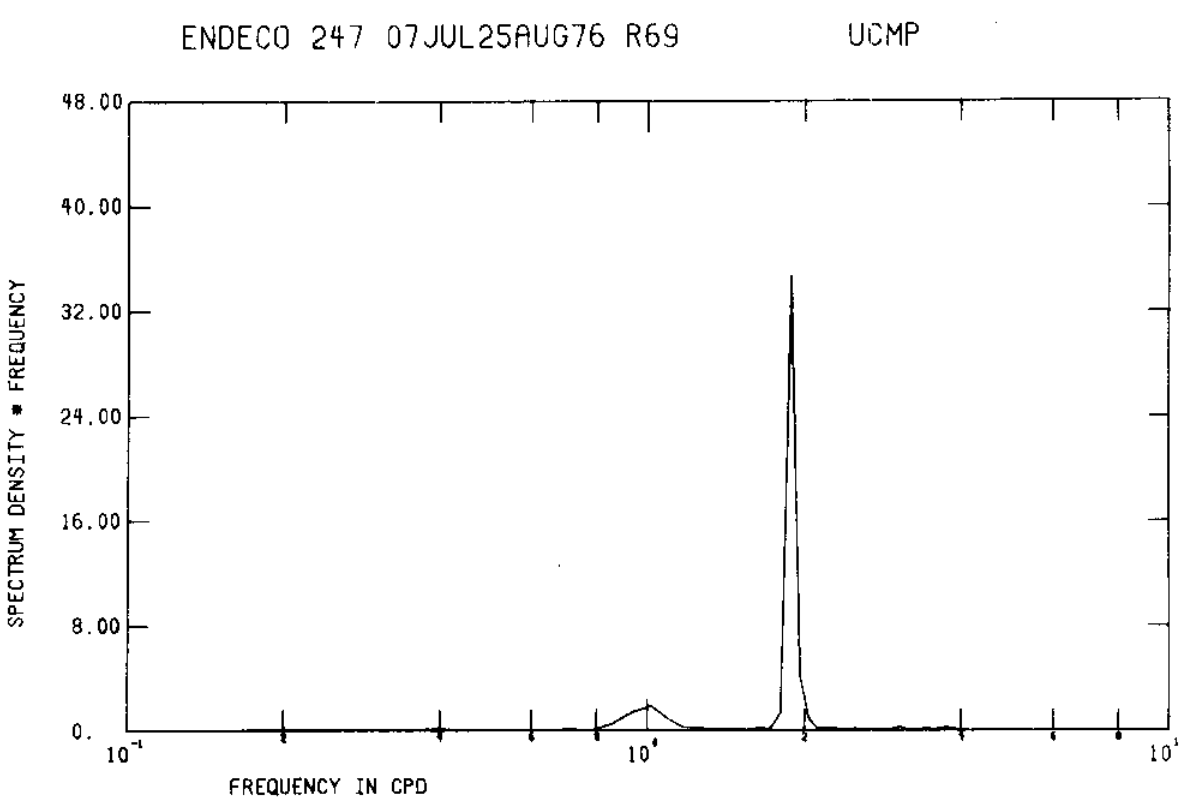

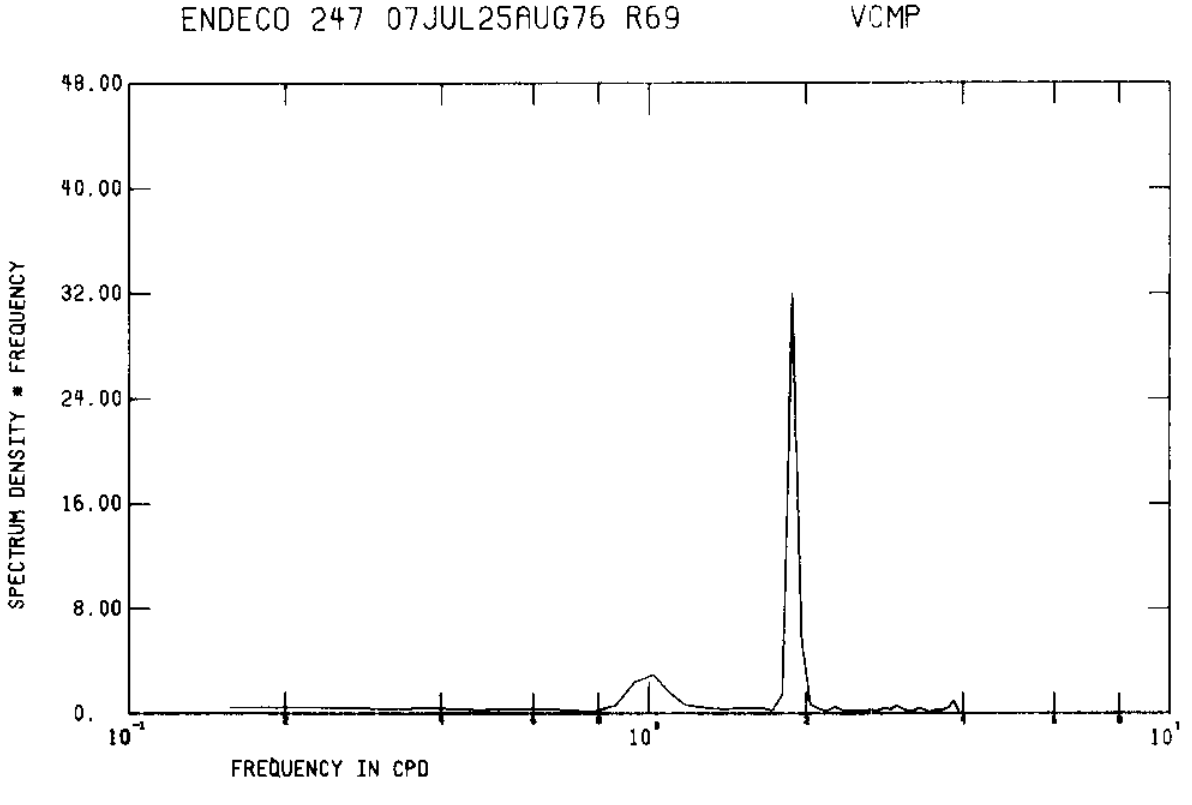

Figure 25 FFT of unfiltered current velocity components from meter $B(Brant)_{top}$

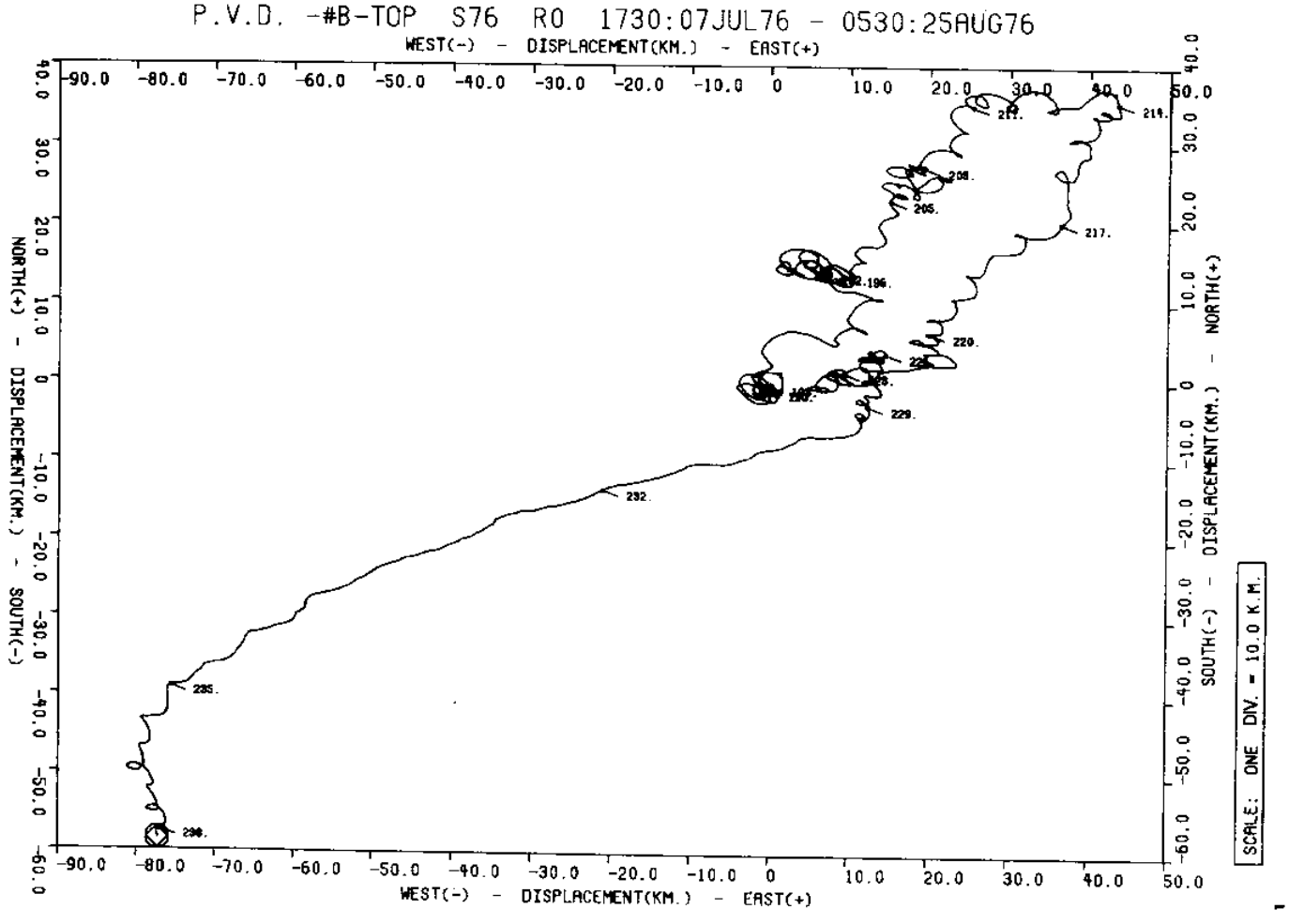

Figure 26 a

Figure 26 (a,b,c) Progressive vector diagrams of unfiltered current velocity from meter B(Brant)$_{top}$

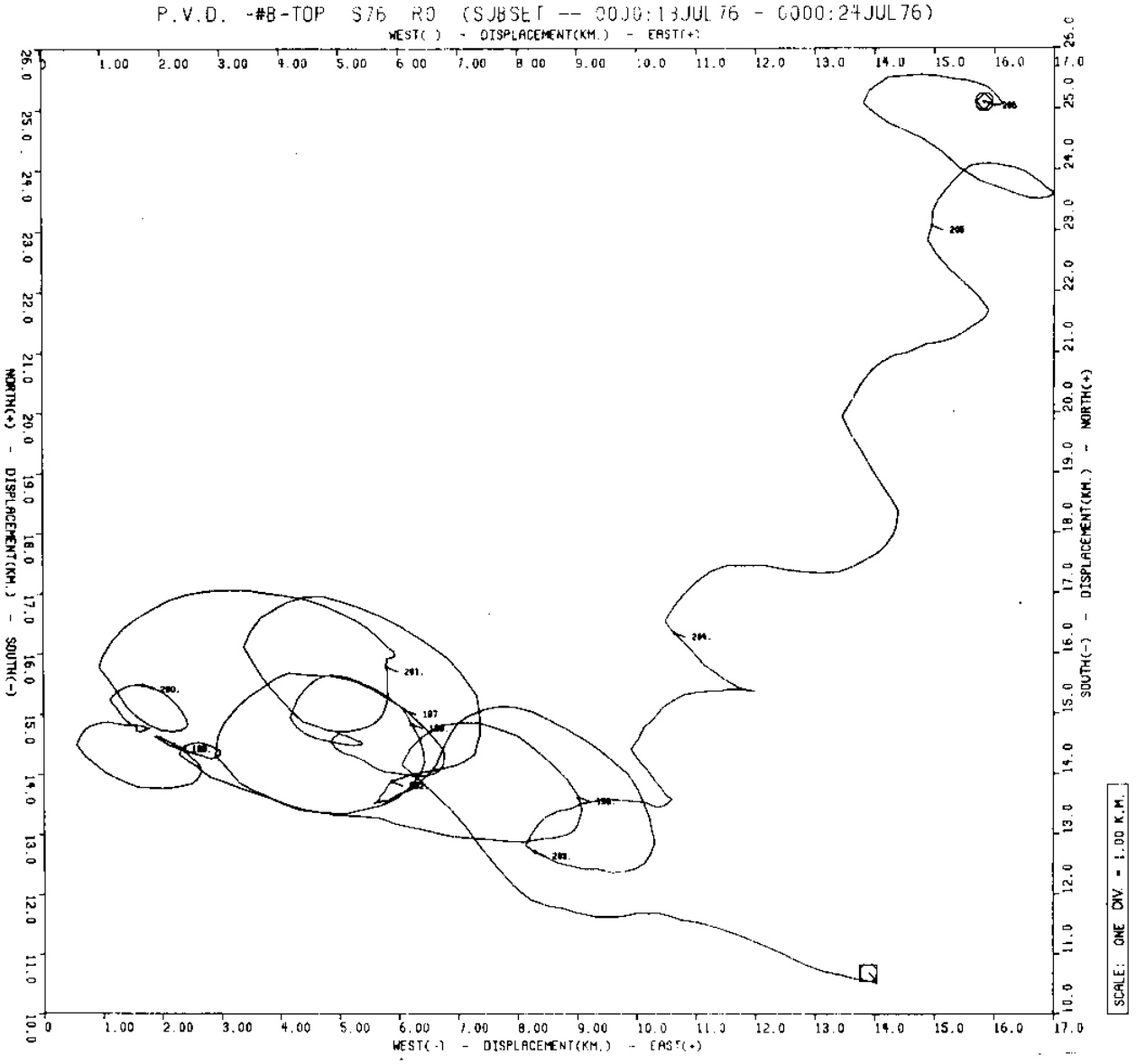
P.V.D. -#B-TOP S76 RD (SUBSET -- 0000:13JUL76 - 0000:24JUL76)
WEST( ) - DISPLACEMENT(KM.) - EAST(+)
WEST(-) - DISPLACEMENT(KM.) - EAST(+)
NORTH(+) - DISPLACEMENT(KM.) - SOUTH(-)
SOUTH(-) - DISPLACEMENT(KM.) - NORTH(+)
SCALE: ONE DIV. = 1.00 K.M.

Figure 26 b

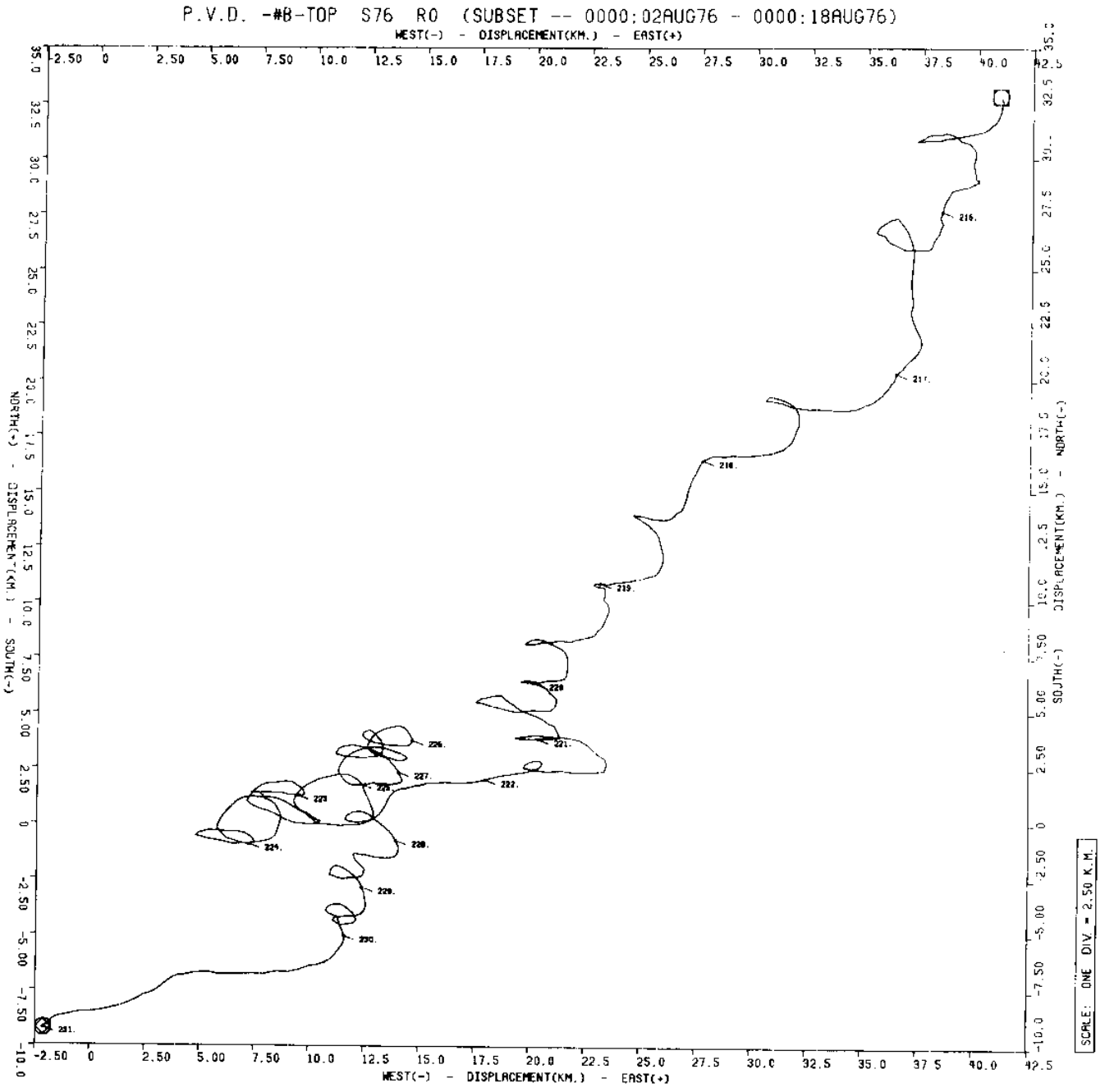
P.V.D. -#B-TOP S76 R0 (SUBSET -- 0000:02AUG76 - 0000:18AUG76)
WEST(-) - DISPLACEMENT(KM.) - EAST(+)
NORTH(+) - DISPLACEMENT(KM.) - SOUTH(-)
SCALE: ONE DIV = 2.50 K.M.

Figure 26 c

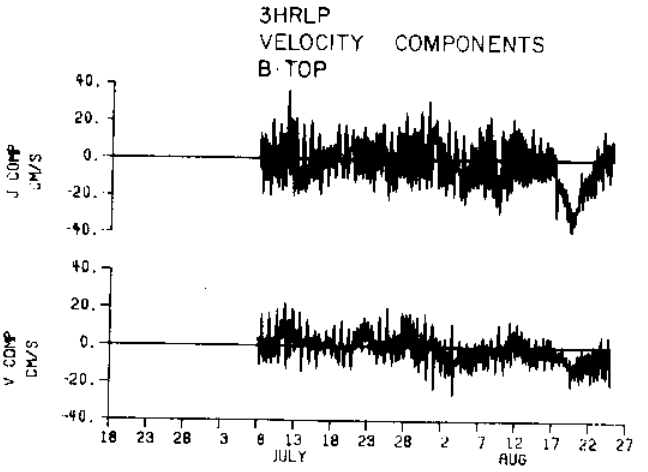

Figure 27 3HRLP velocity components for B_{top}

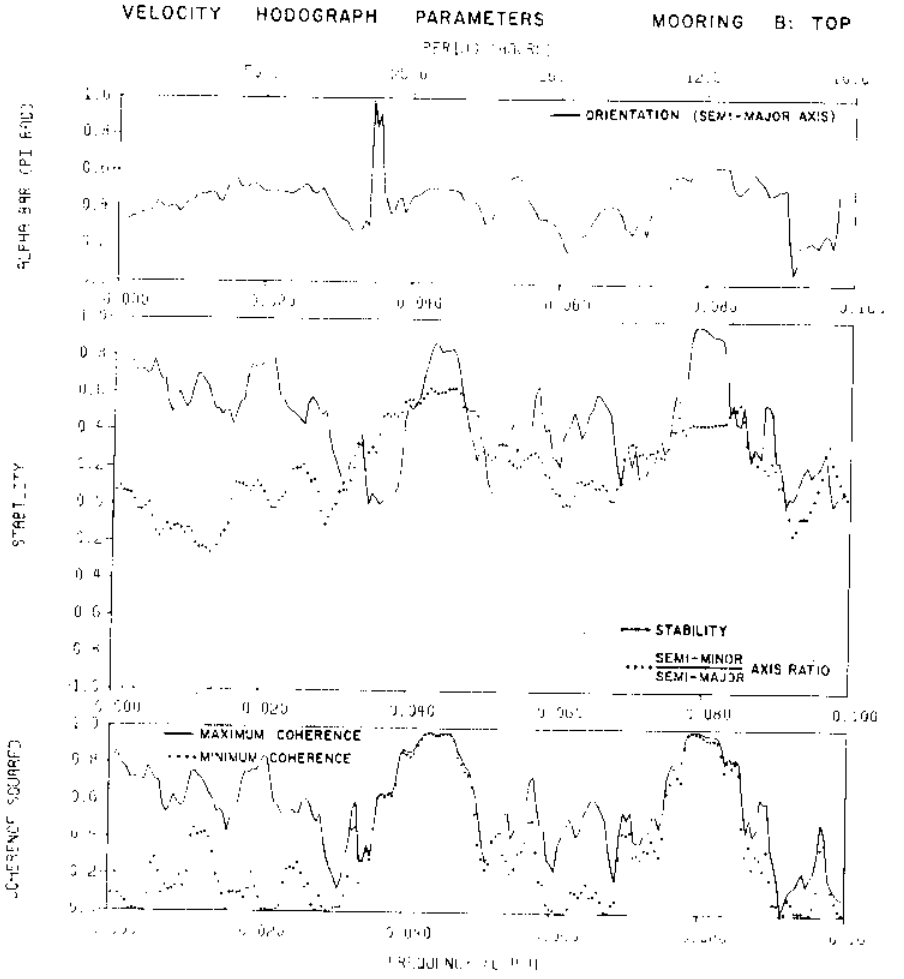

Figure 28 Hodograph parameters from meter B(Brant)$_{top}$

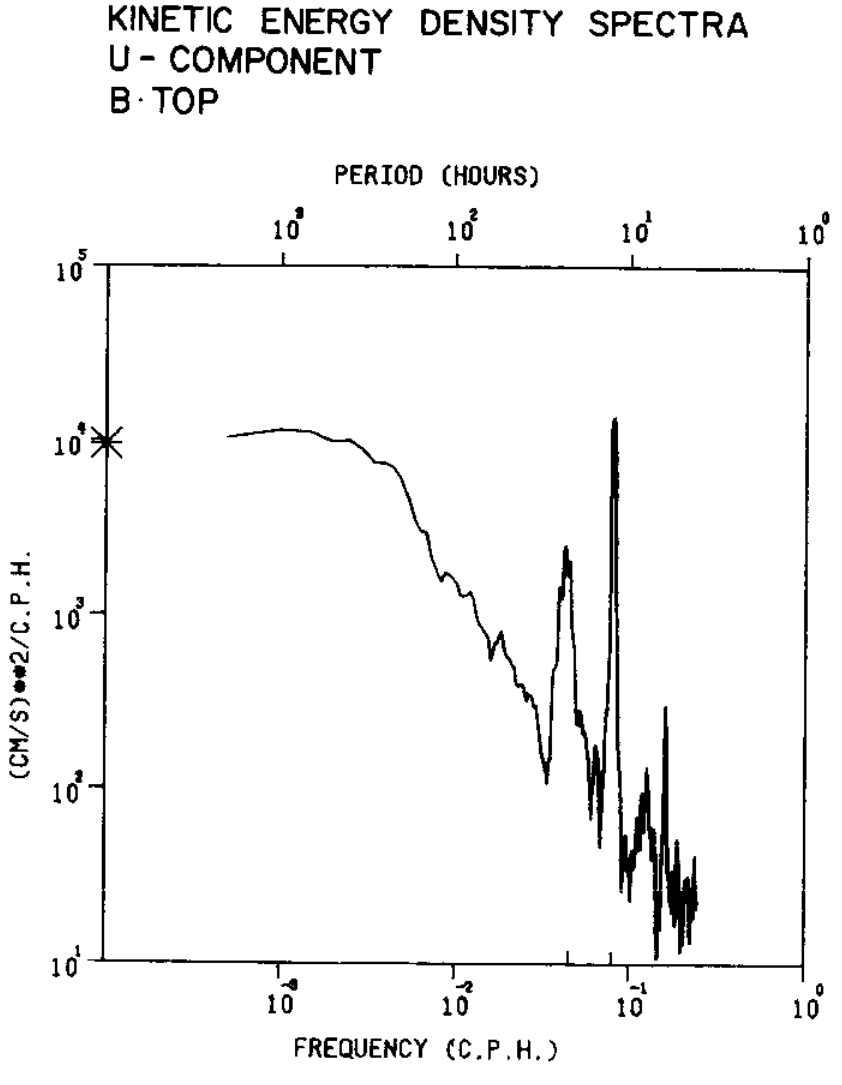

Figure 29

Kinetic energy density spectra for current velocity, u-component, B_{top}

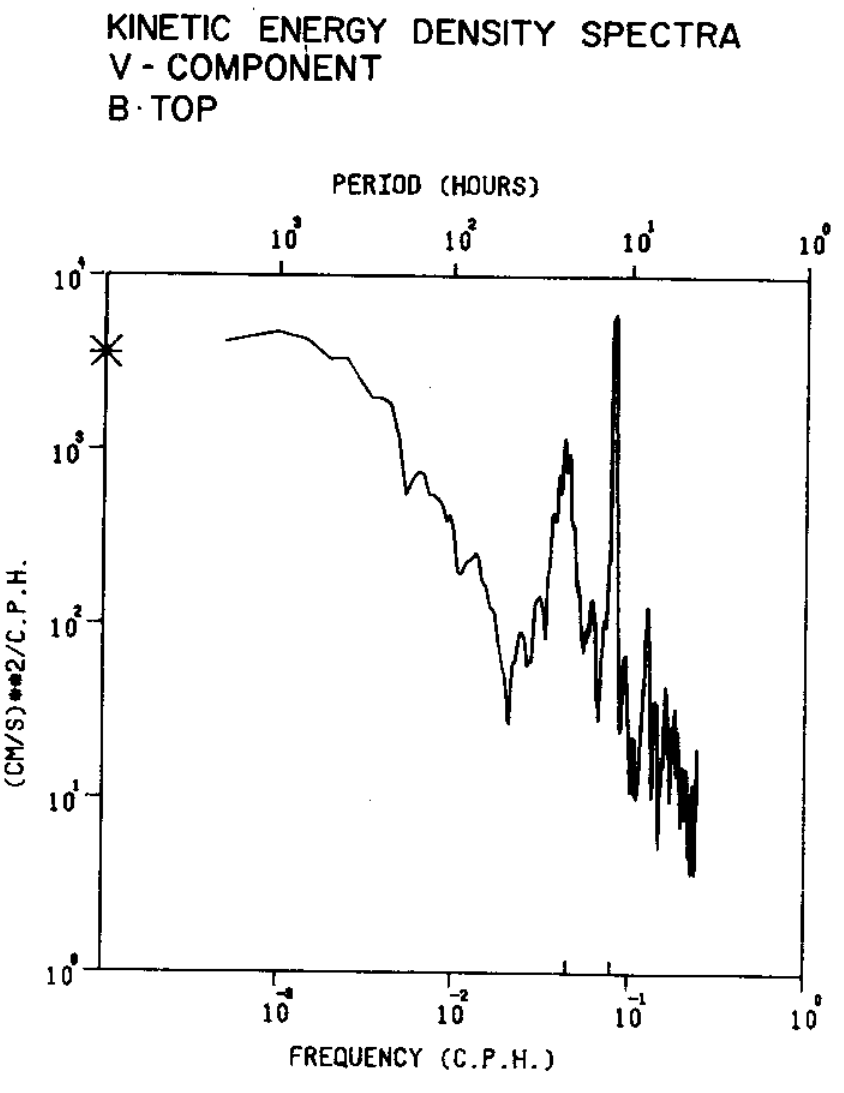

Figure 30

Kinetic energy density spectra for current velocity, v-component, B_{top}

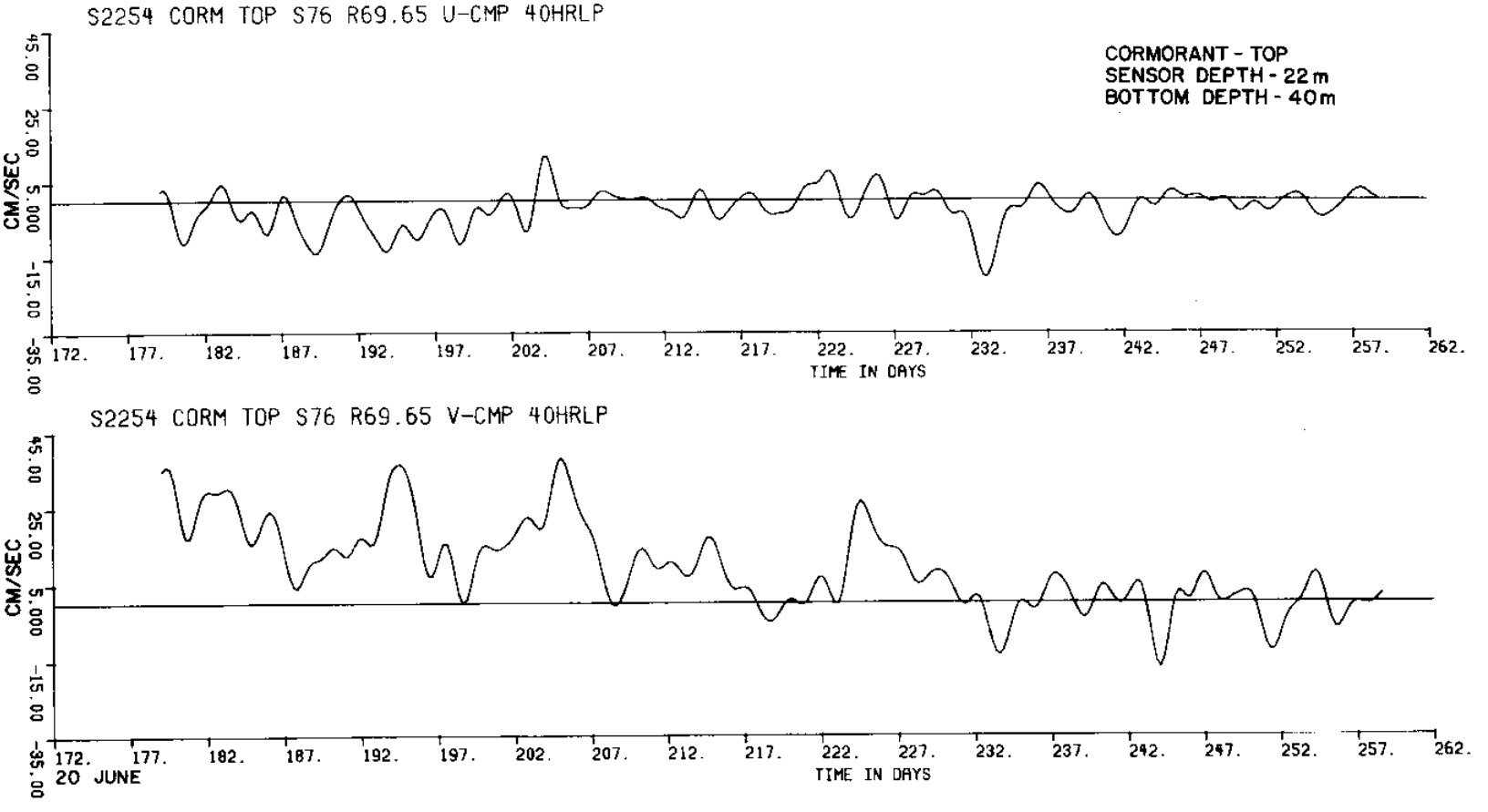

Figure 31 Low pass current velocity components and vectors from meter C(Cormorant)$_{top}$

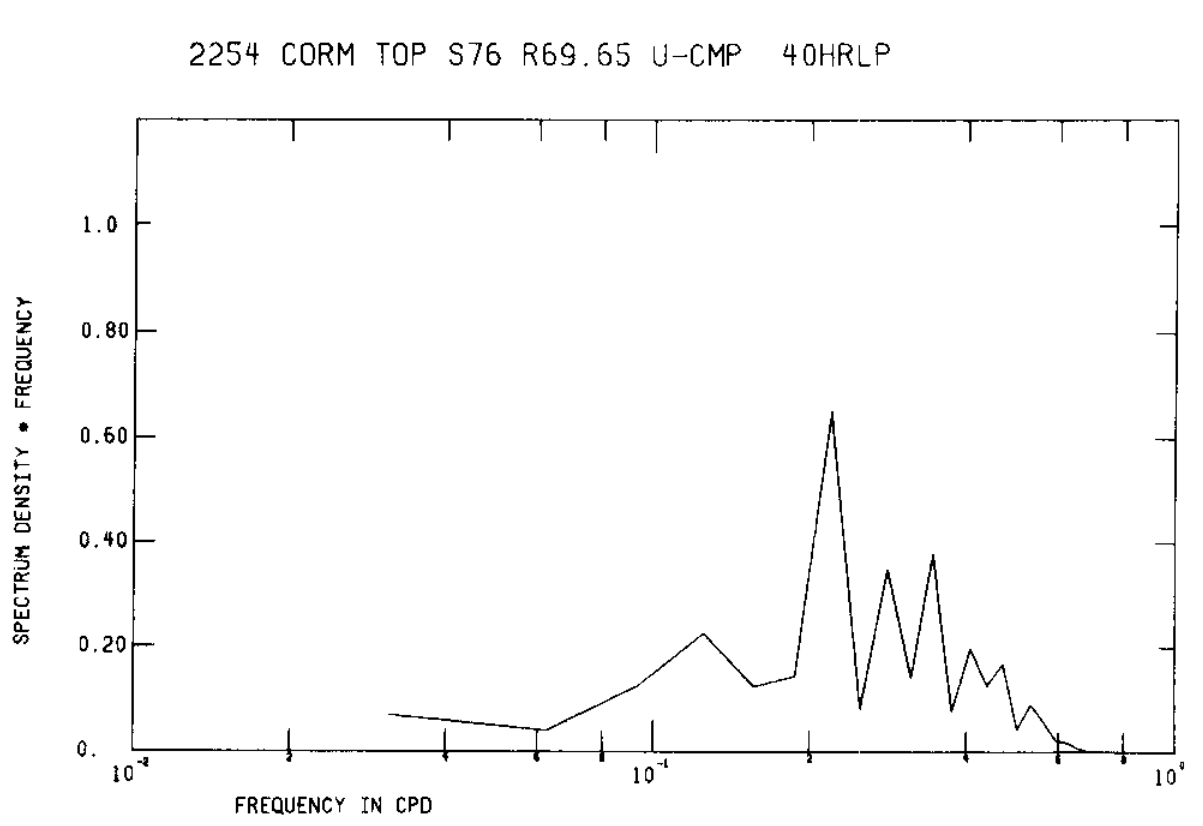

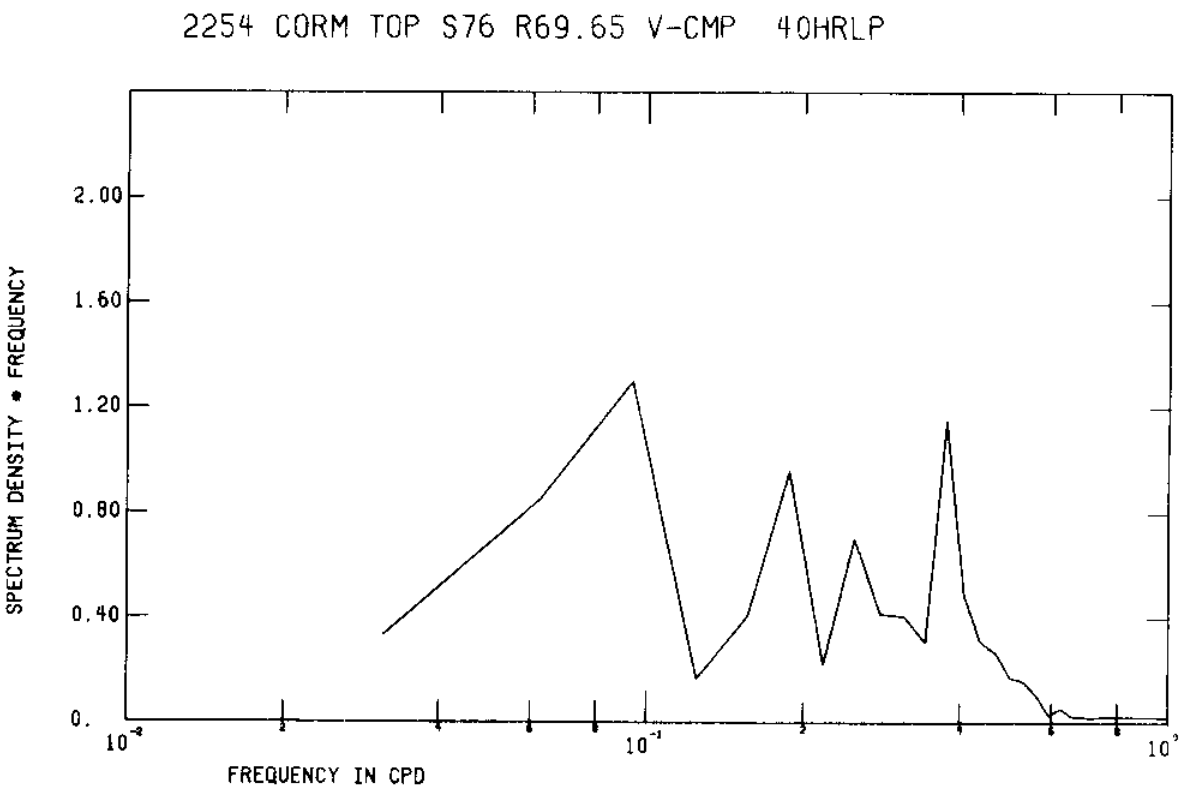

Figure 32 FFT of low pass current velocity components from meter C(Cormorant)$_{top}$

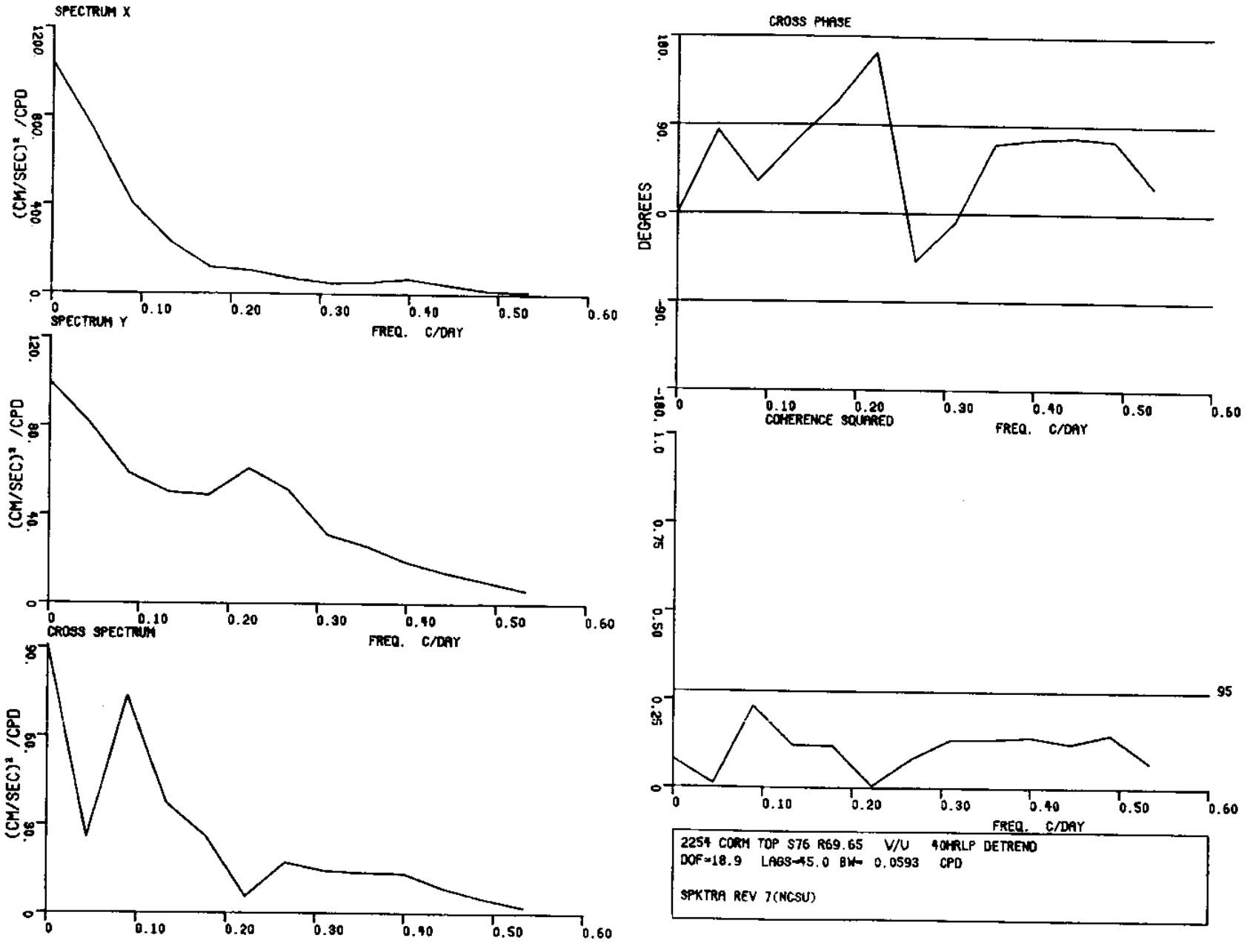

Figure 33 Spectra of low pass current velocity components from meter C(Cormorant)$_{top}$

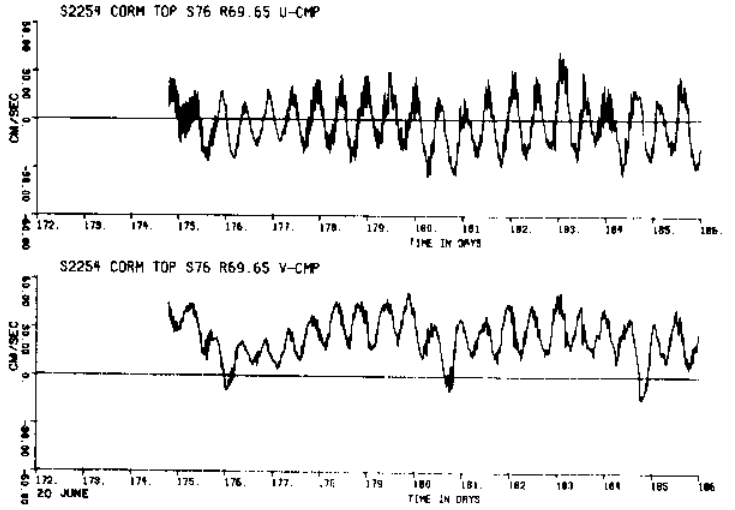

Figure 34 a

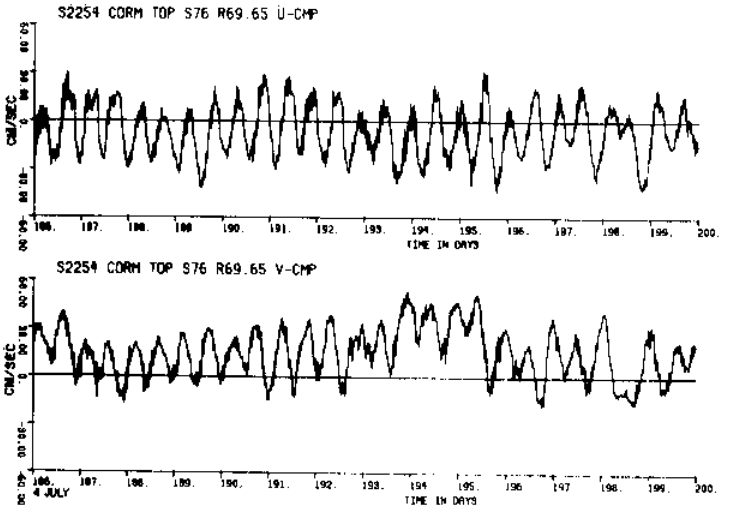

Figure 34 b

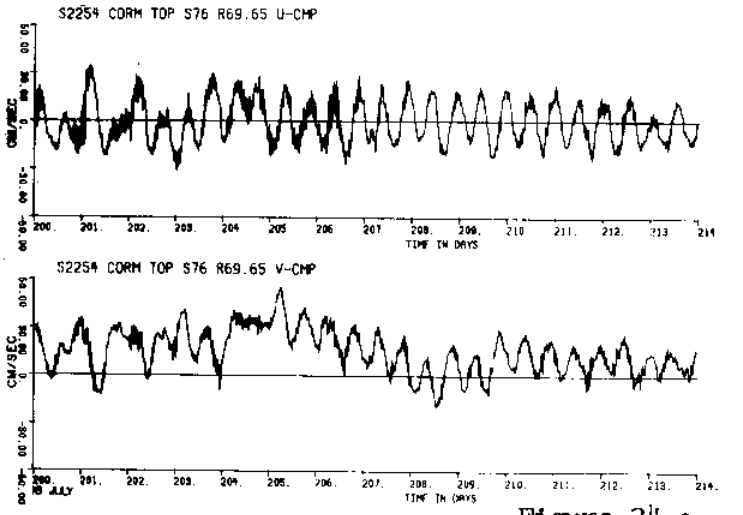

Figure 34 c

Figure 34 (a,b,c,d,e f,g) Unfiltered current velocity components from meter C(Cormorant)$_{top}$

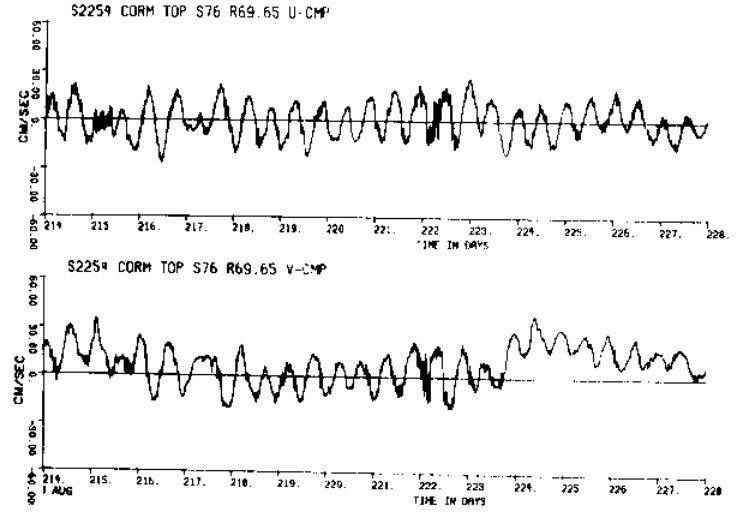

Figure 34 d

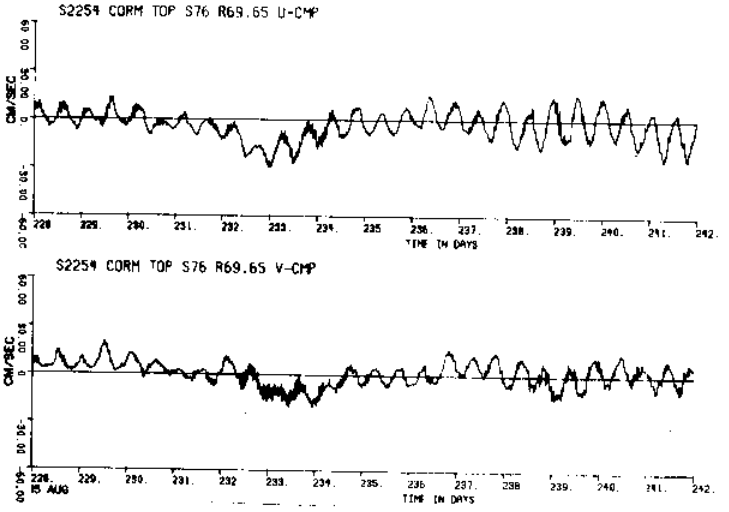

Figure 34 e

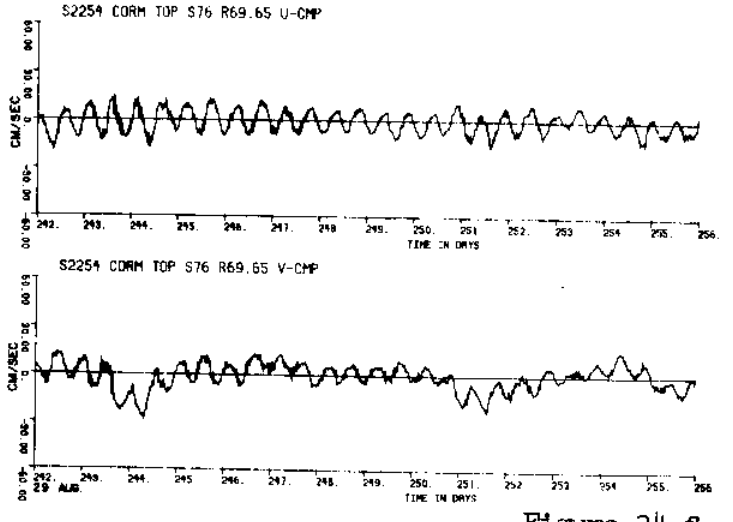

Figure 34 f

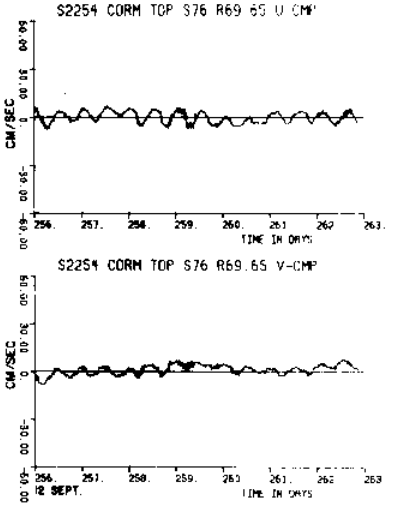
S2254 CORM TOP S76 R69 65 U CMP
CM/SEC
256.
257.
258.
259.
260.
261
262
263.
TIME IN DAYS
S2254 CORM TOP S76 R69.65 V-CMP
CM/SEC
12 SEPT.
TIME IN DAYS

Figure 34 g

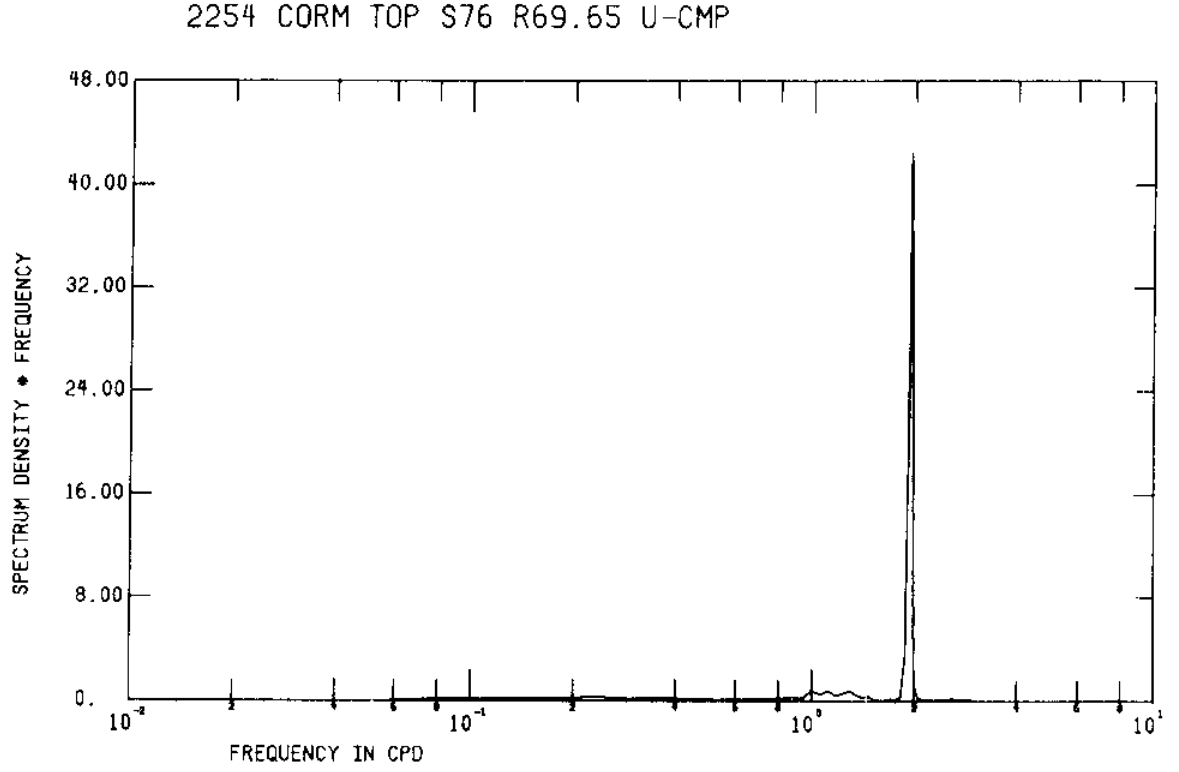

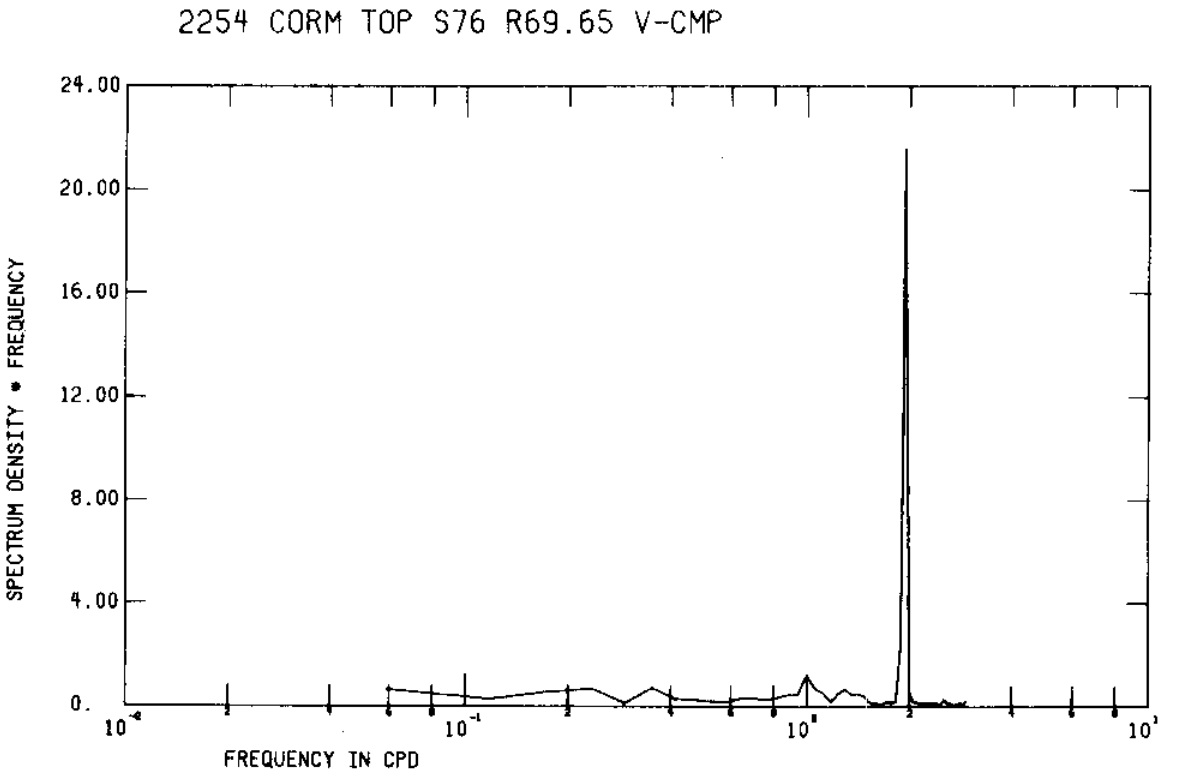

Figure 35 FFT of unfiltered current velocity components from meter C(Cormorant)$_{top}$

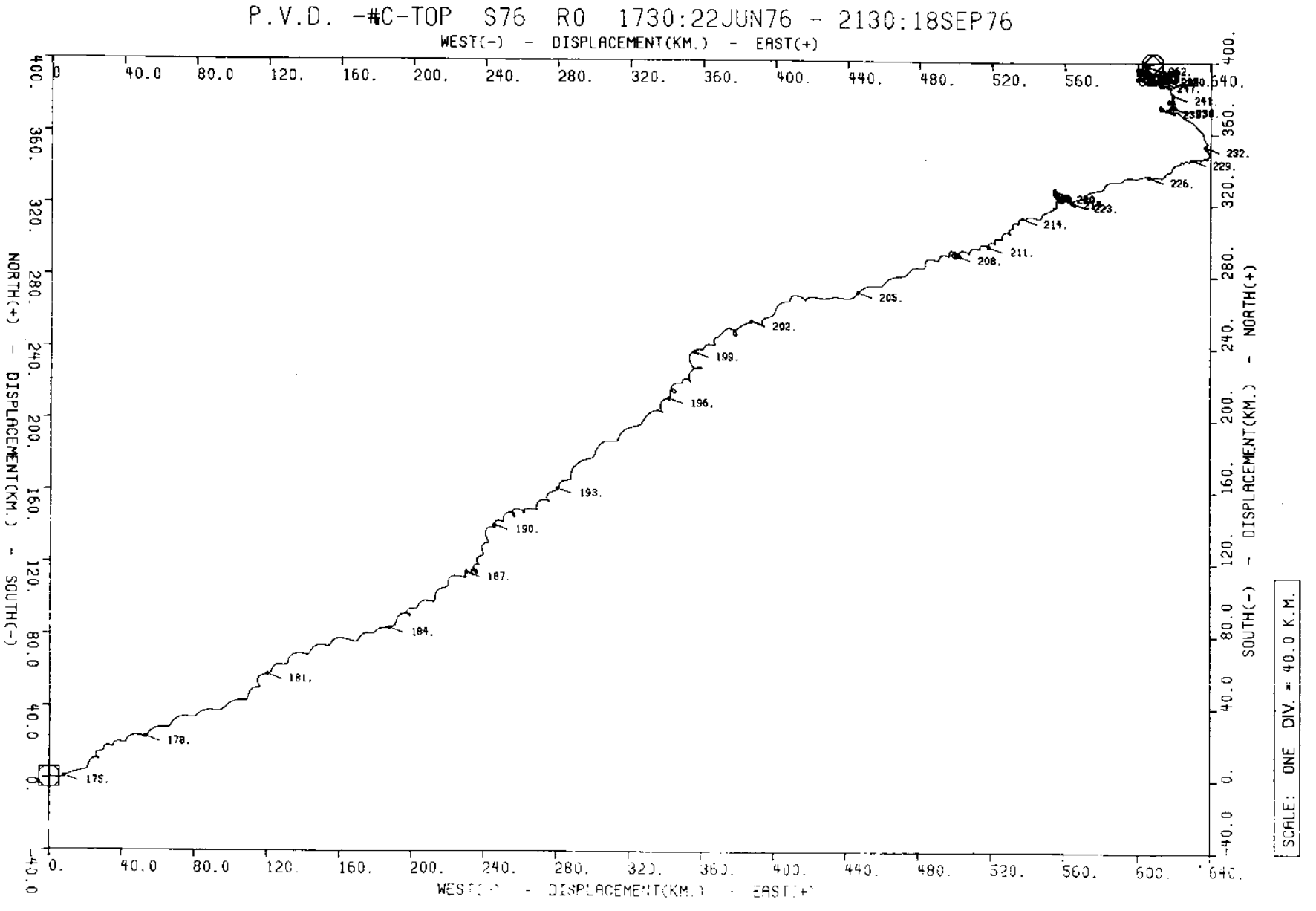

Figure 36 a

Figure 36 (a,b,c) Progressive vector diagrams of unfiltered current velocity from meter C(Cormorant)$_{top}$

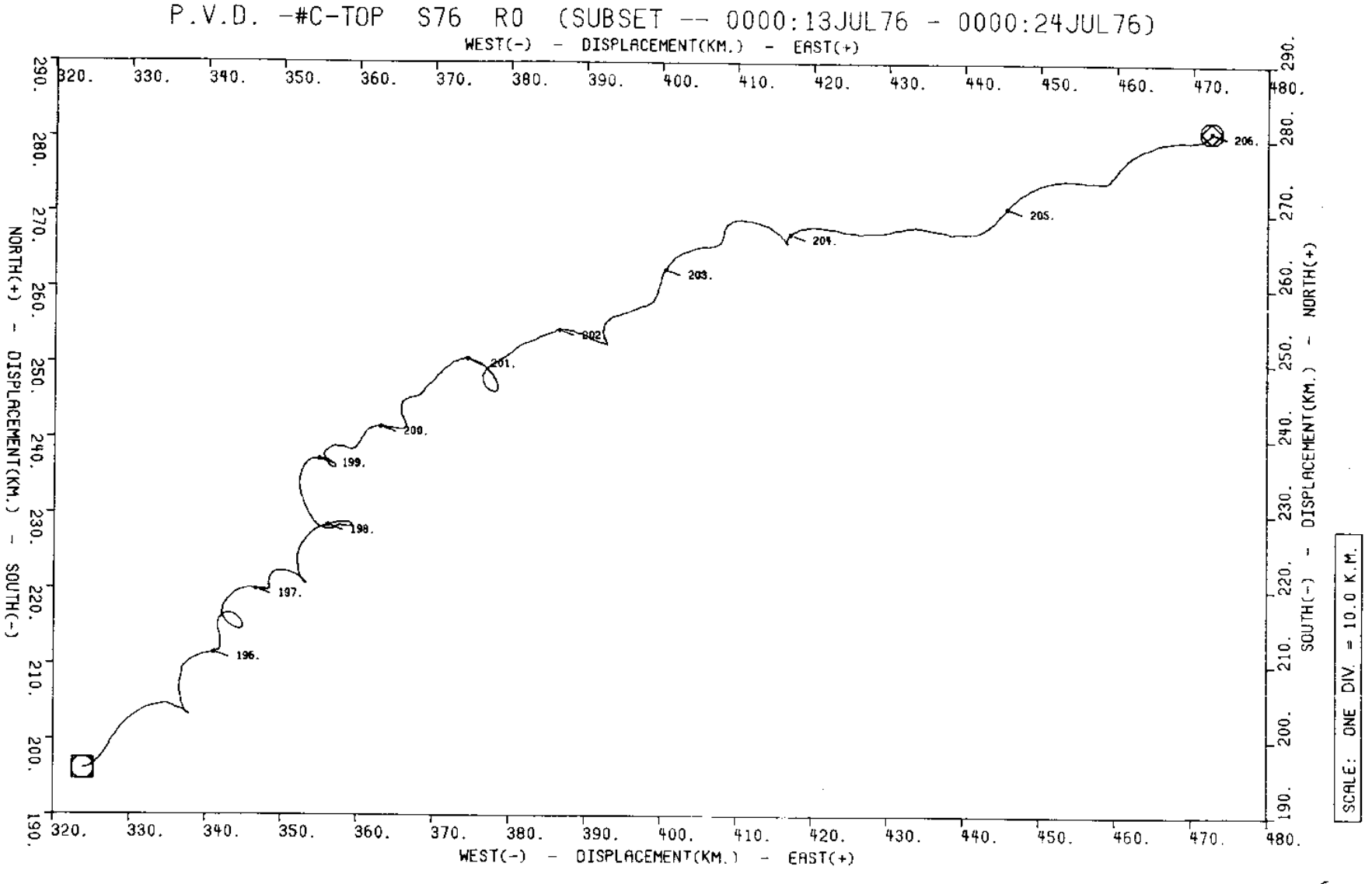
P.V.D. -#C-TOP S76 R0 (SUBSET -- 0000:13JUL76 - 0000:24JUL76)
WEST(-) - DISPLACEMENT(KM.) - EAST(+)
NORTH(+) - DISPLACEMENT(KM.) - SOUTH(-)
SOUTH(-) - DISPLACEMENT(KM.) - NORTH(+)
320. 330. 340. 350. 360. 370. 380. 390. 400. 410. 420. 430. 440. 450. 460. 470.
290. 280. 270. 260. 250. 240. 230. 220. 210. 200. 190.
480. 470. 460. 450. 440. 430. 420. 410. 400. 390. 380. 370. 360. 350. 340. 330. 320.
290. 280. 270. 260. 250. 240. 230. 220. 210. 200. 190.
196.
197.
198.
199.
200.
201.
202.
203.
204.
205.
206.
SCALE: ONE DIV. = 10.0 K.M.

Figure 36 b

P.V.D. -#C-TOP S76 R0 (SUBSET -- 0000:02AUG76 - 0000:18AUG76)
WEST(-) - DISPLACEMENT(KM.) - EAST(+)
NORTH(+) - DISPLACEMENT(KM.) - SOUTH(-)
SCALE: ONE DIV. = 6.00 K.M.
546.
552.
558.
564.
570.
576.
582.
588.
594.
600.
606.
612.
618.
624.
630.
636.
642.
354.
348.
342.
336.
330.
324.
318.
312.
220.
223.
224.
225.
226.
227.
228.
229.
230.

Figure 36 c

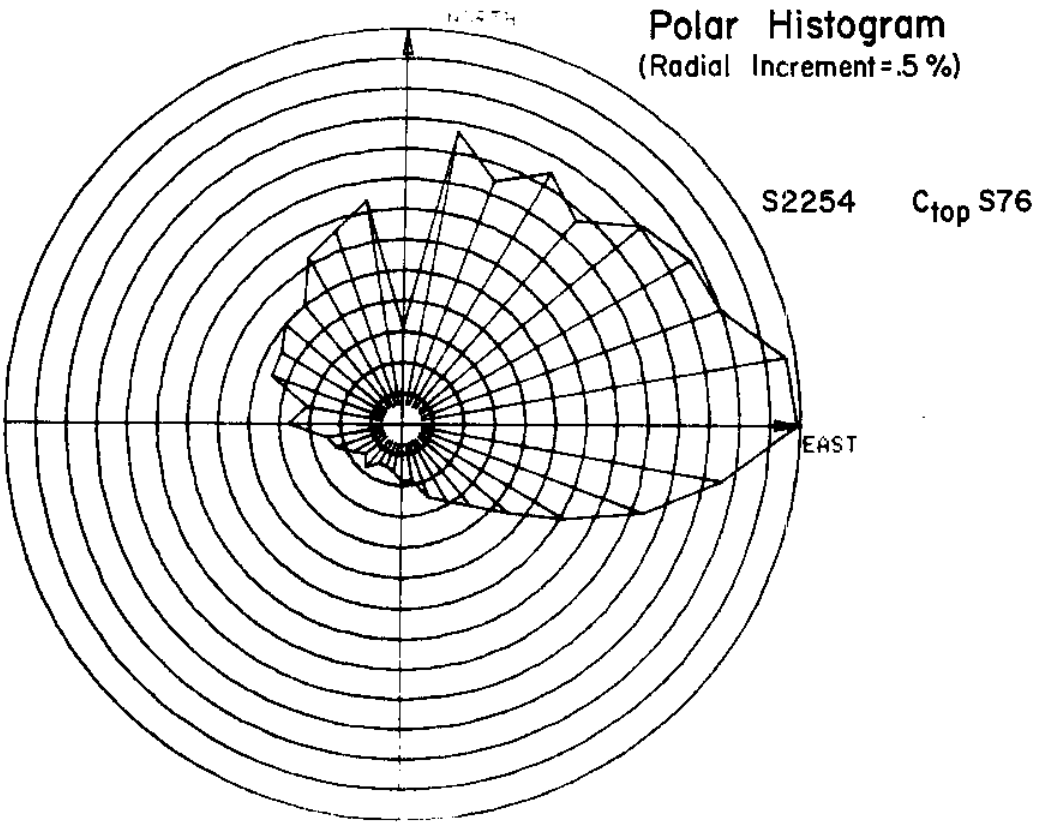

Figure 37 Histogram from meter C(Cormorant)$_{top}$

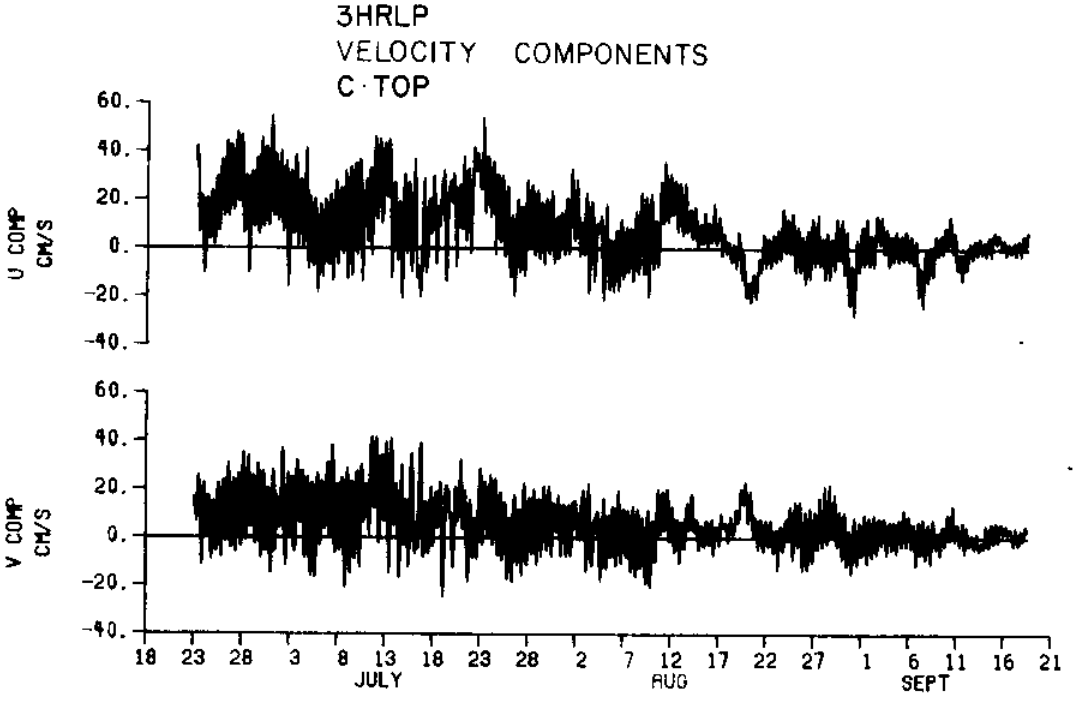

Figure 38 3HRLP velocity components for C_{top}

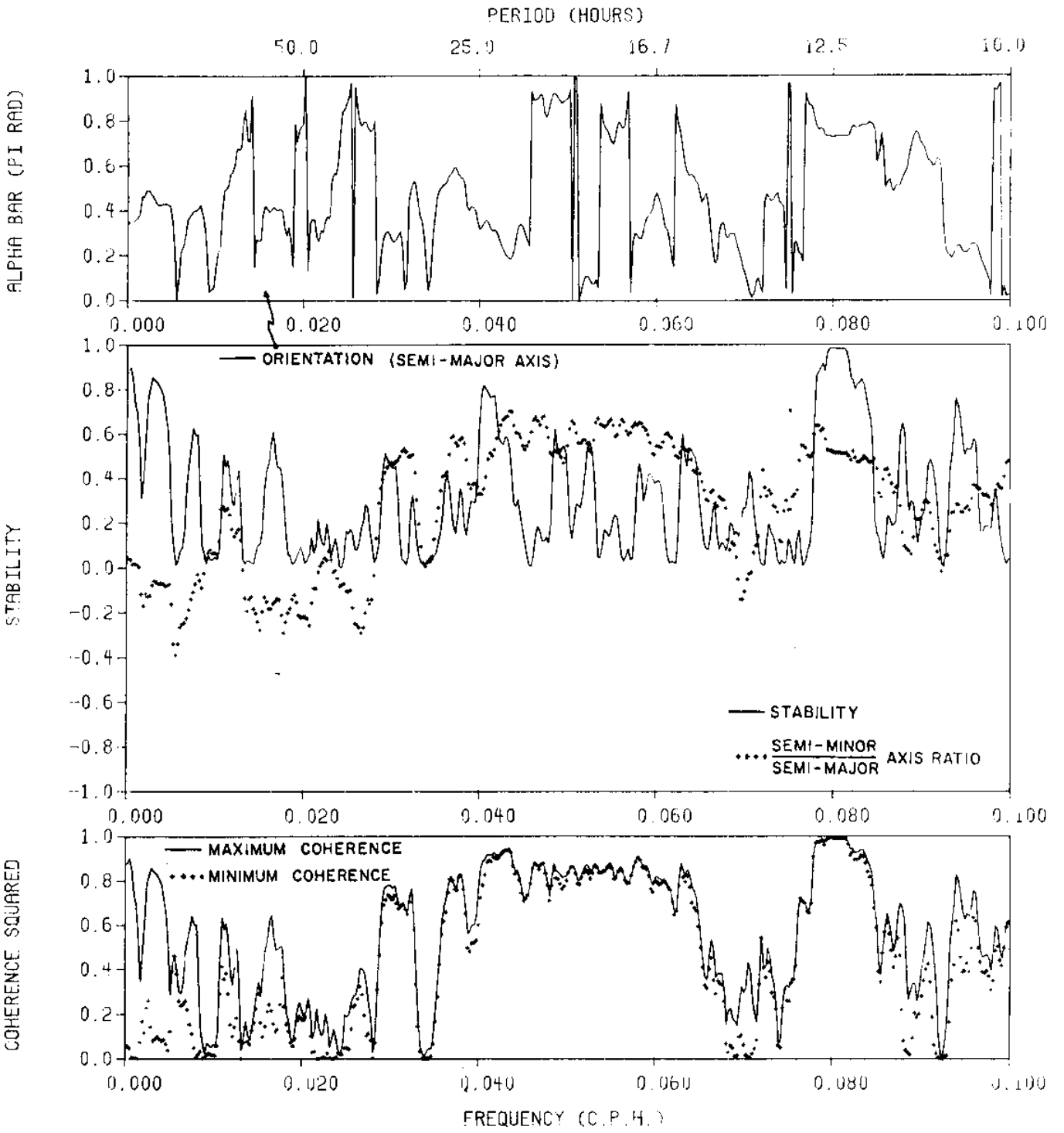

Figure 39 Hodograph parameters from meter C(Cormorant)$_{top}$

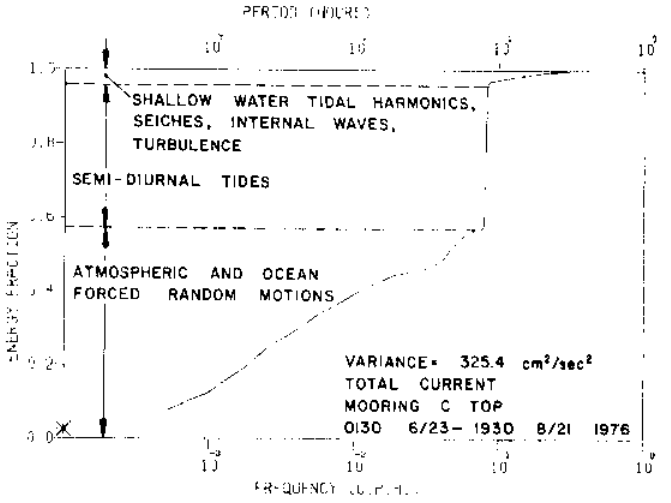

Figure 40 Energy fraction vs. frequency for C_{top} total current

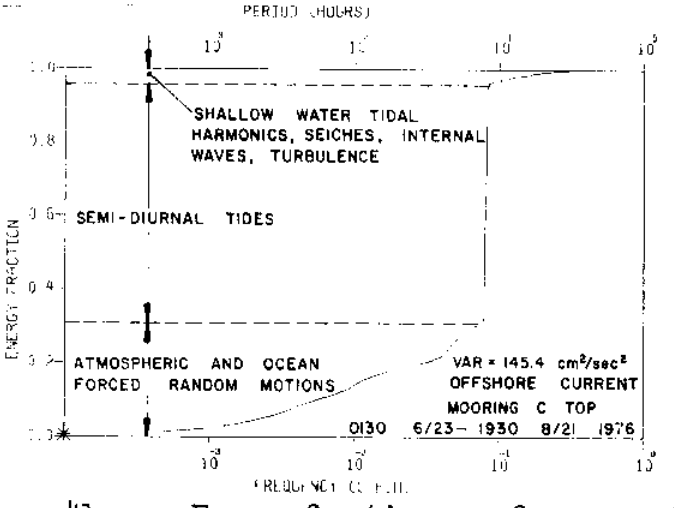

Figure 41 Energy fraction vs. frequency for C_{top} offshore current

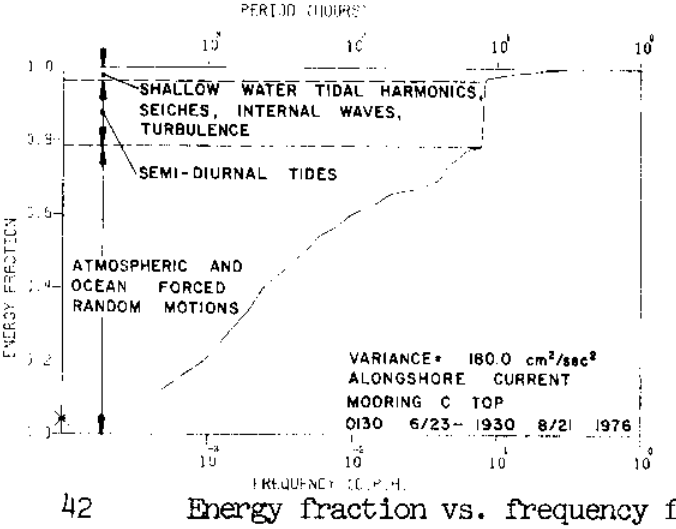

Figure 42 Energy fraction vs. frequency for C_{top} alongshore current

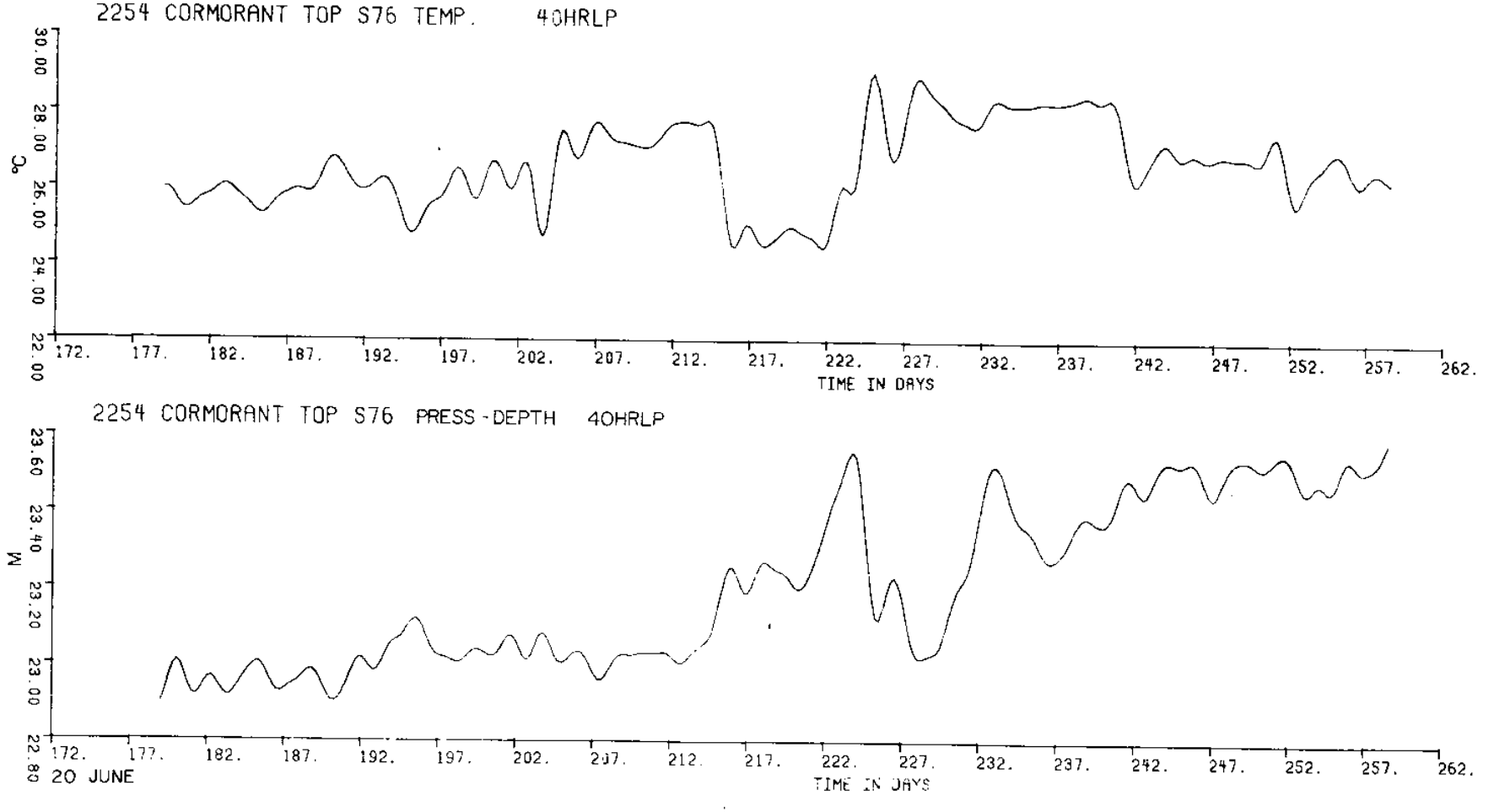

Figure 43 Low pass temperature and pressure from meter C(Cormorant)$_{top}$

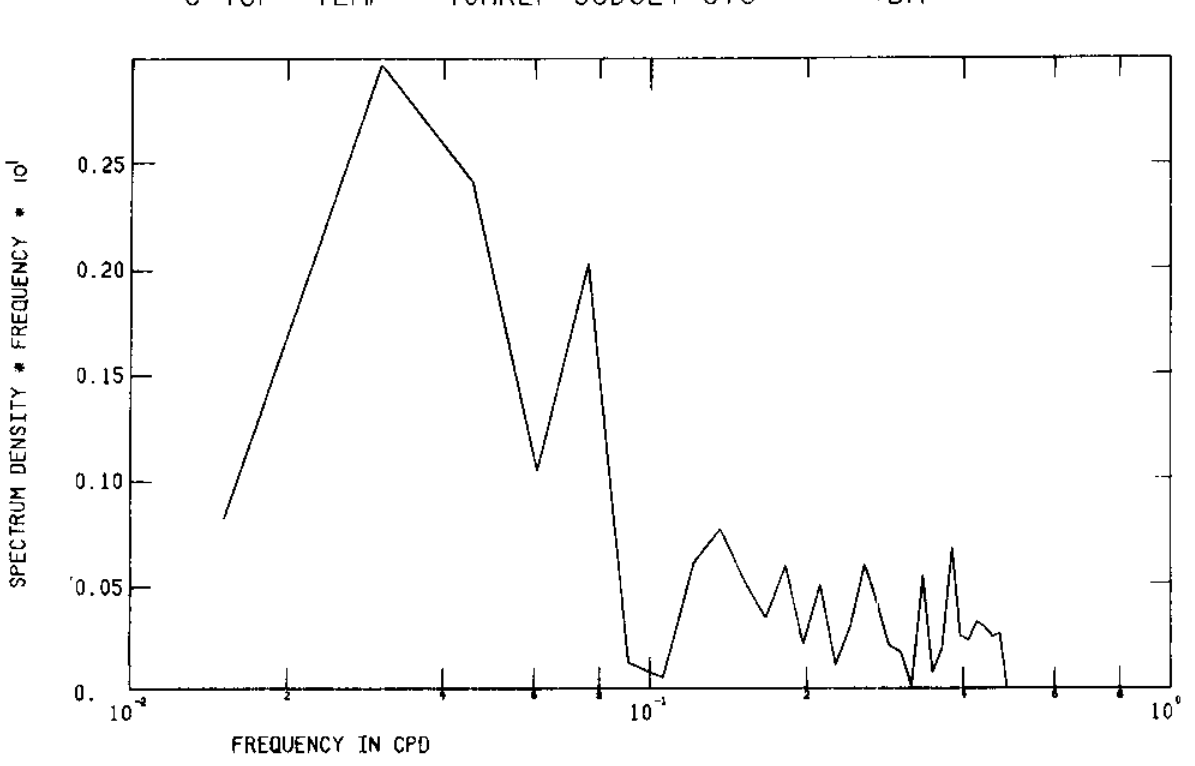

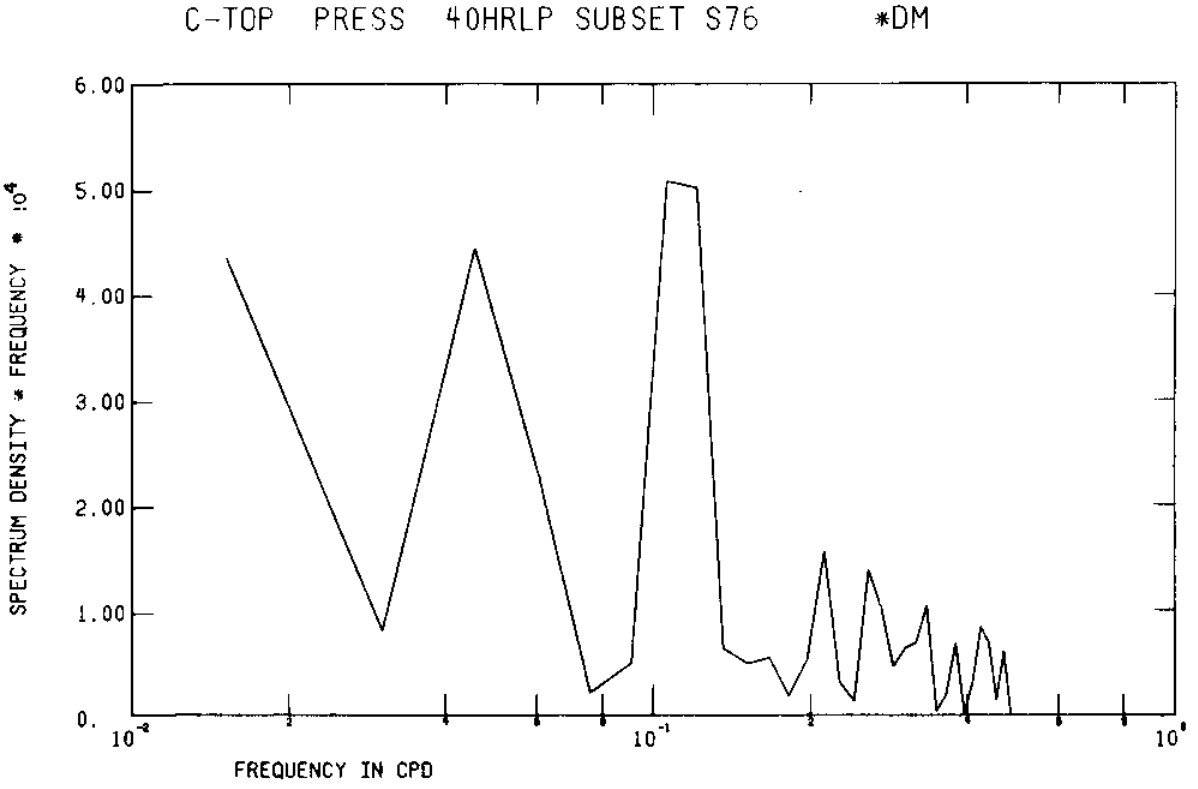

Figure 44 FFT of low pass temperature and pressure from meter C(Cormorant)$_{top}$

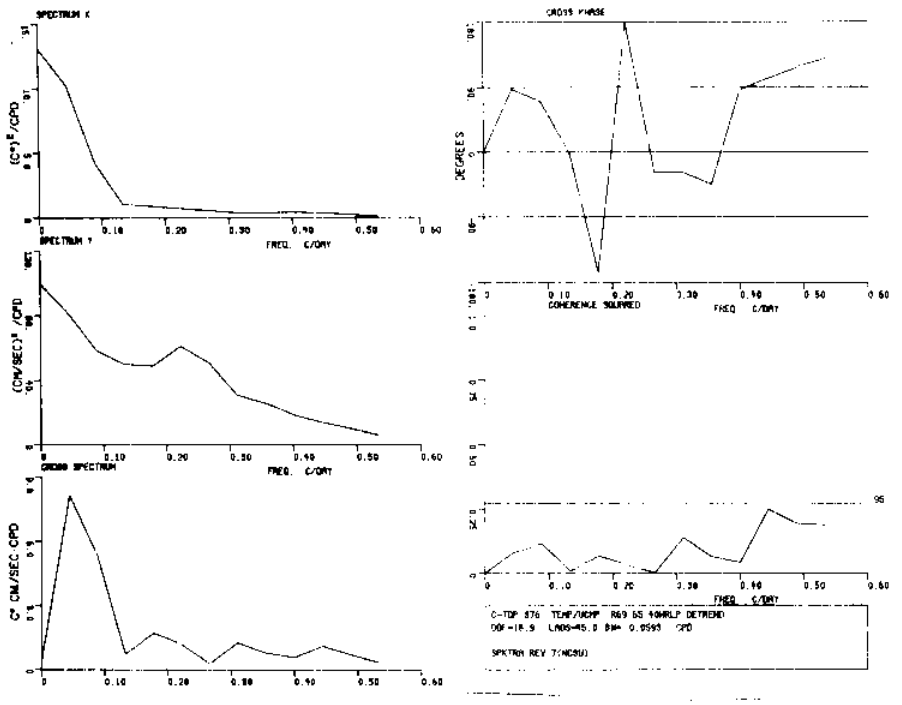

Figure 45 Spectra of temperature and the low pass current velocity u component, both from meter C(Cormorant)$_{top}$

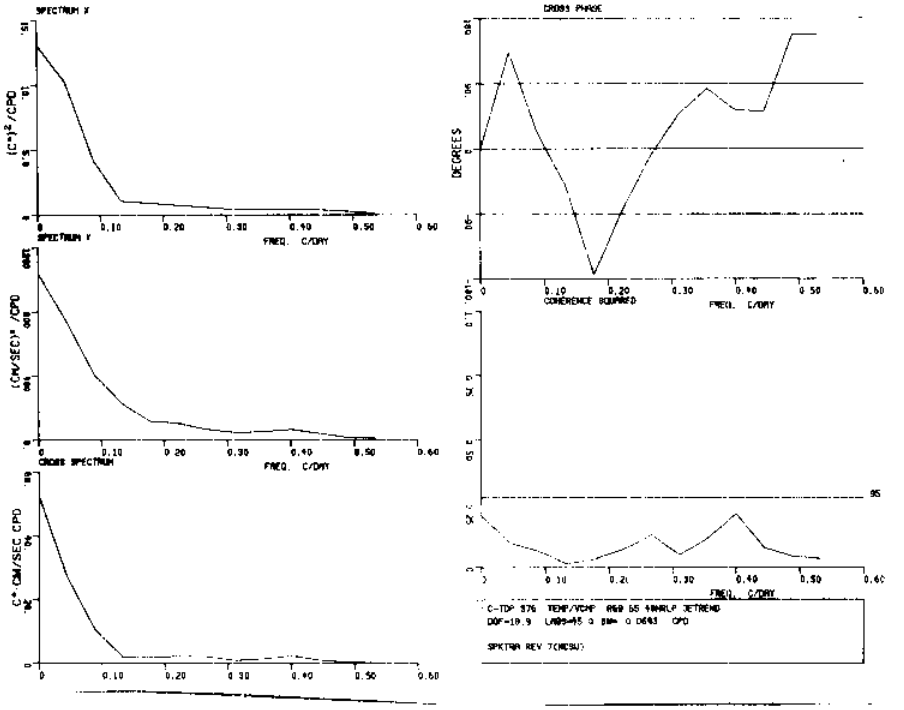

Figure 46 Spectra of temperature and the low pass current velocity v component, both from meter C(Cormorant)$_{top}$

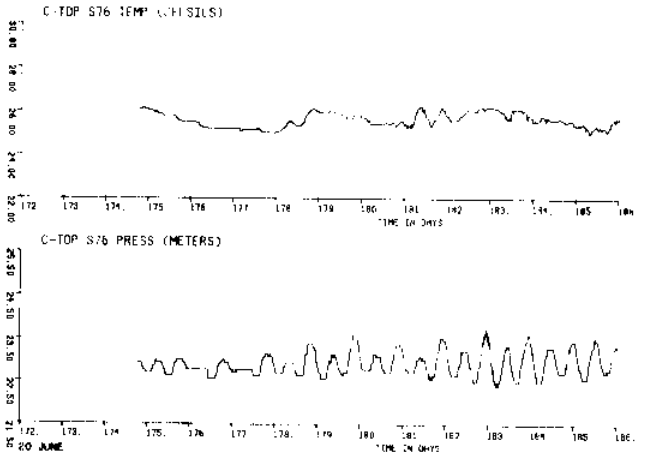

Figure 47 a

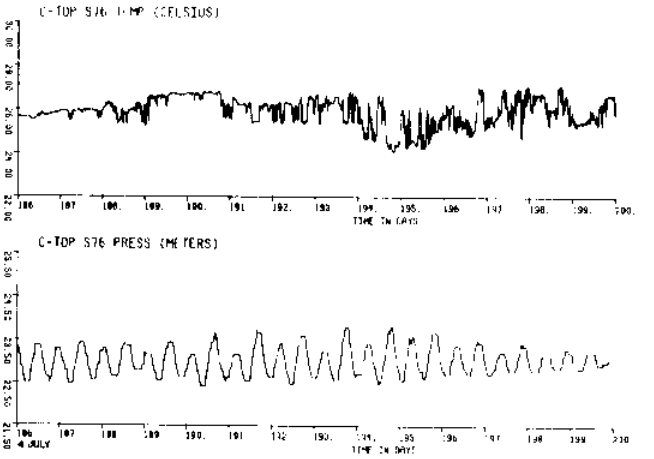

Figure 47 b

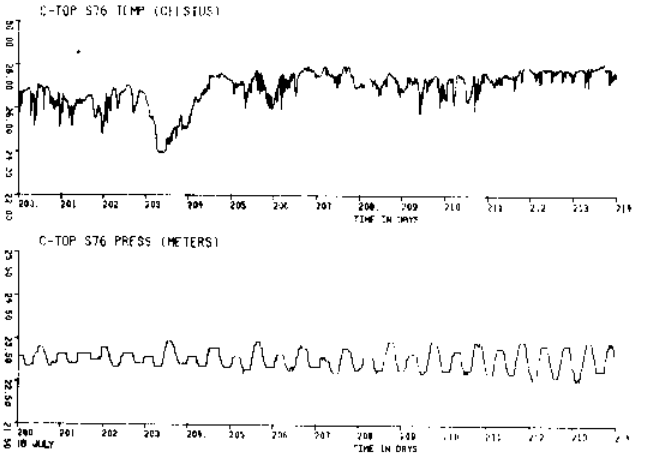

Figure 47 c

Figure 47 (a,b,c,d, e,f,g) Unfiltered temperature and pressure from meter C(Cormorant)$_{top}$

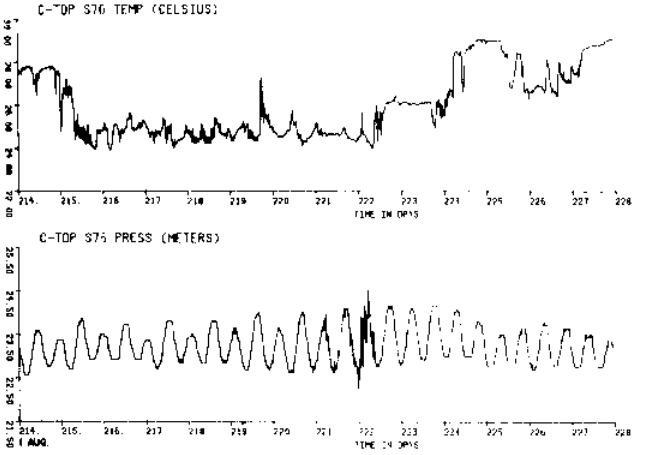

Figure 47 d

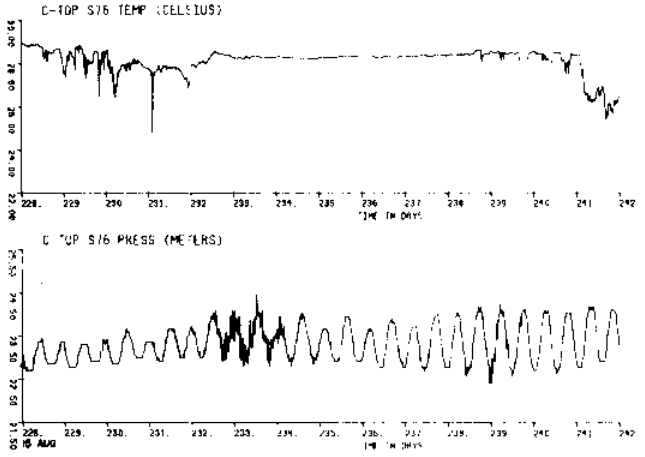

Figure 47 e

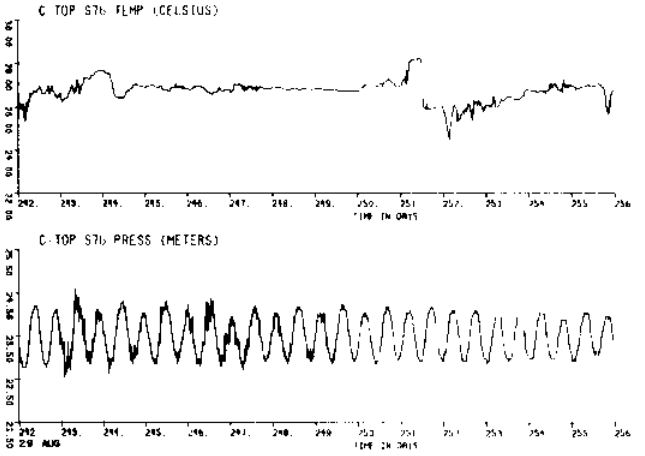

Figure 47 f

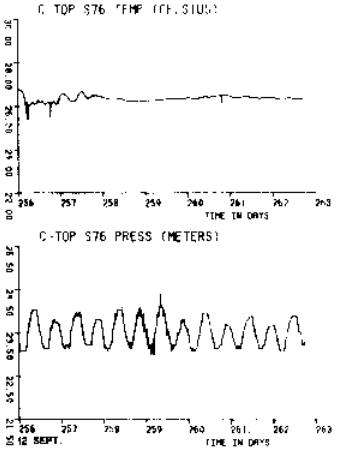
C TOP S76 TEMP (DEG.STUD)
TIME IN DAYS
C-TOP S76 PRESS (METERS)
12 SEPT.
TIME IN DAYS

Figure 47 g

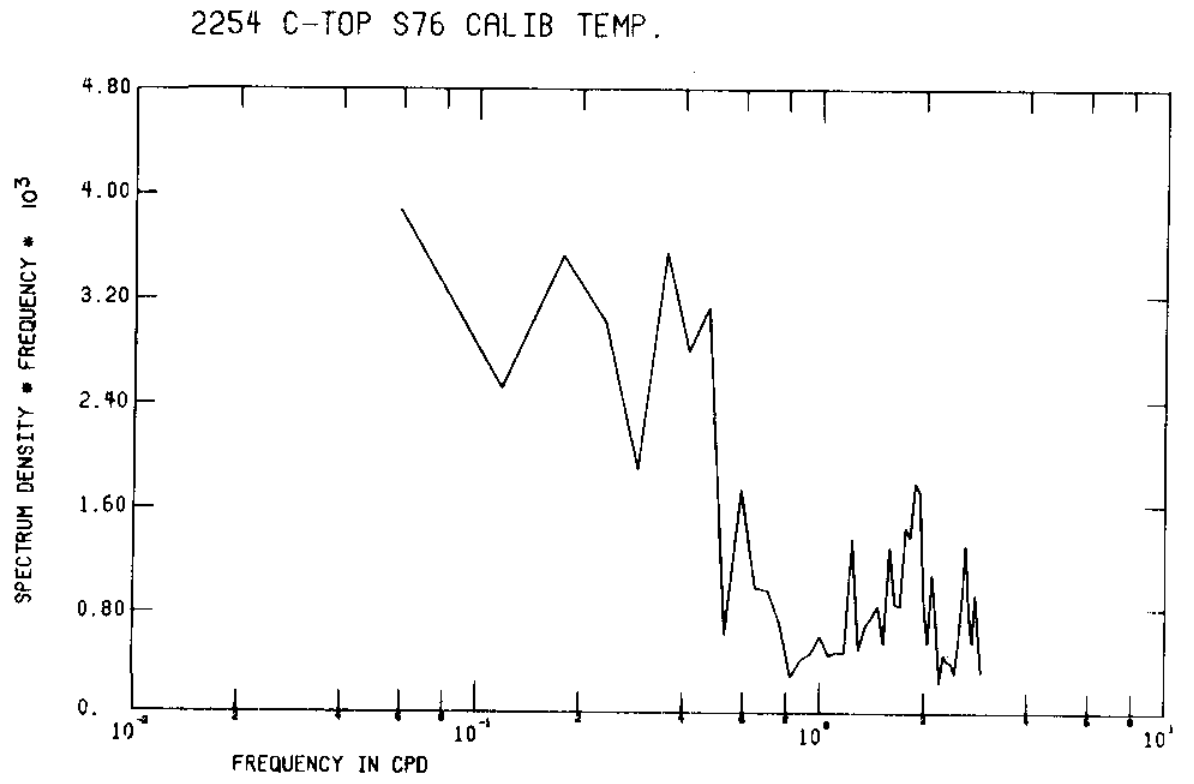

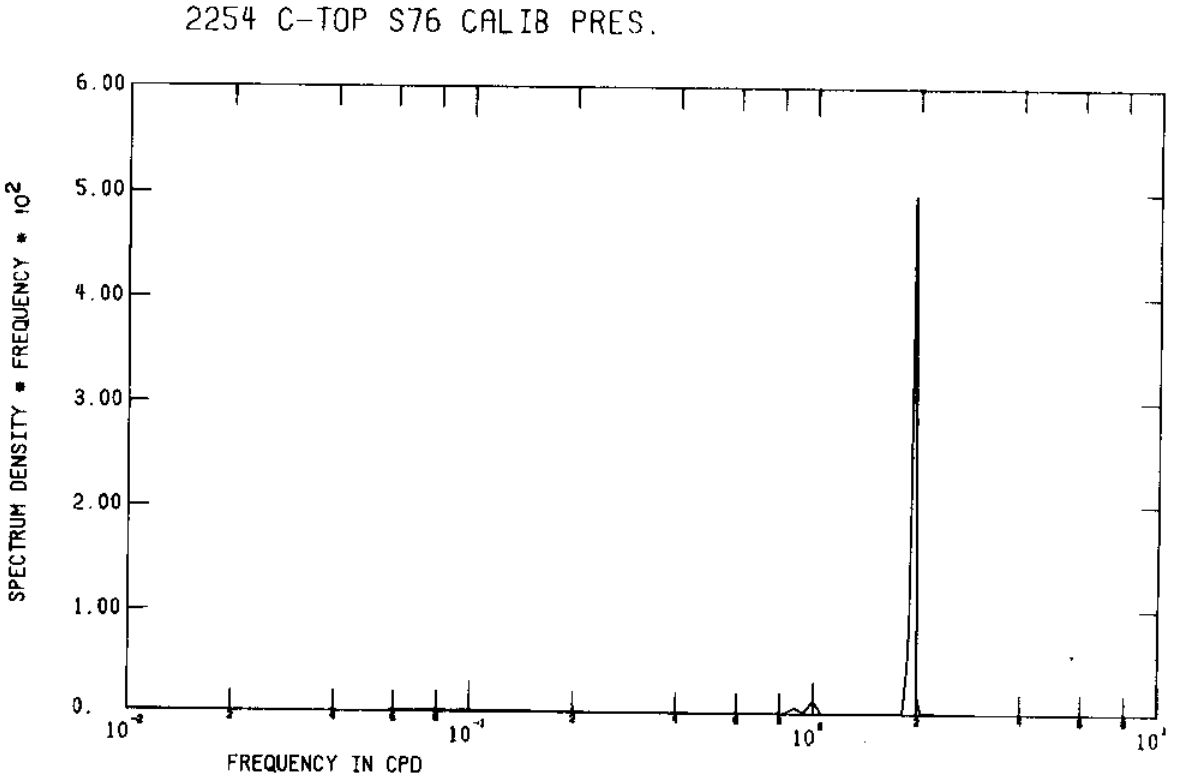

Figure 48 FFT of unfiltered temperature and pressure from meter C(Cormorant)$_{top}$

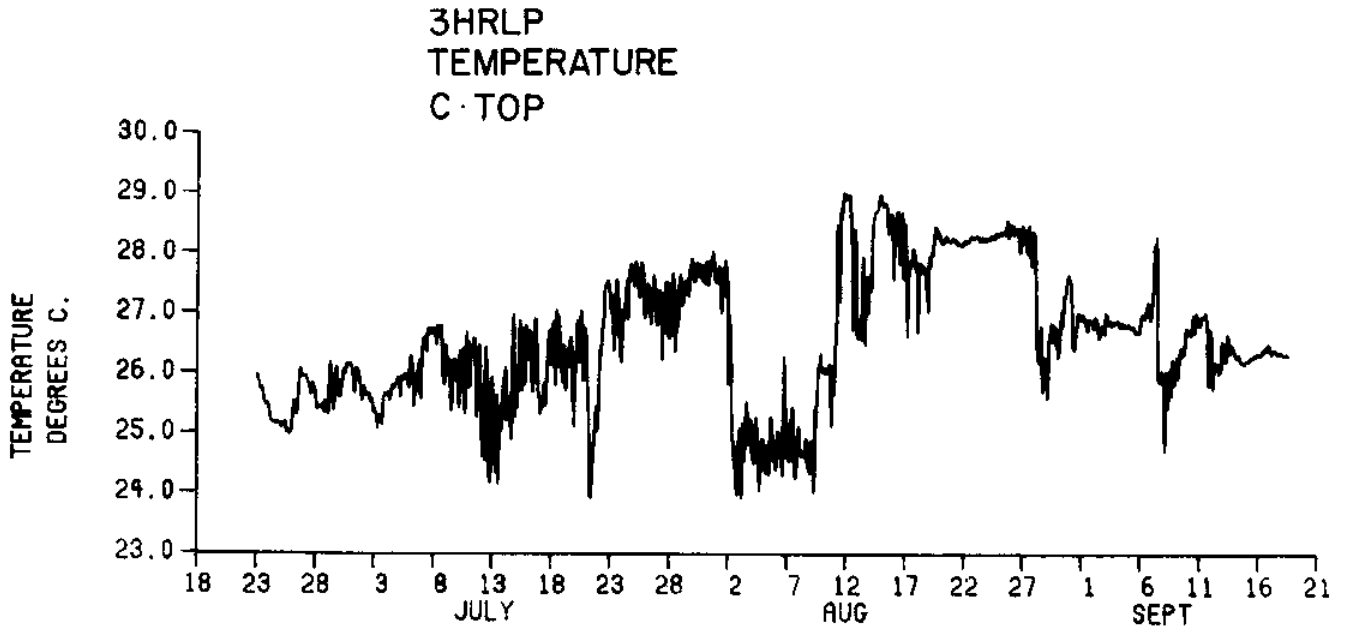

Figure 49 3HRLP temperature for C_{top}

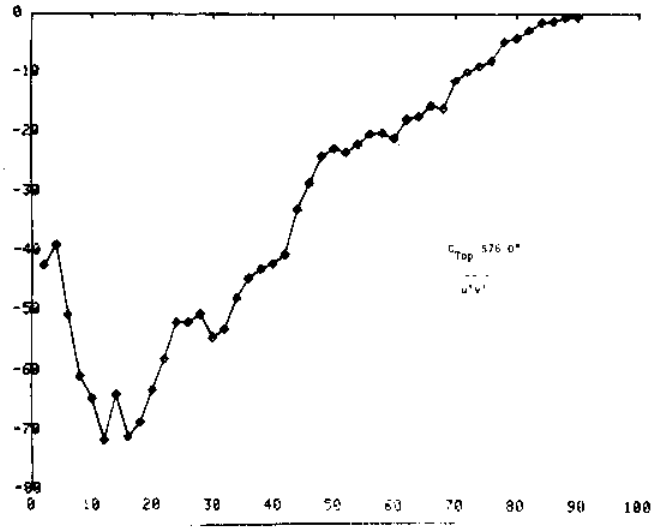

Figure 50 Momentum correlation variance in horizontal plane for C_{top} Summer, 1976 (cumulative)

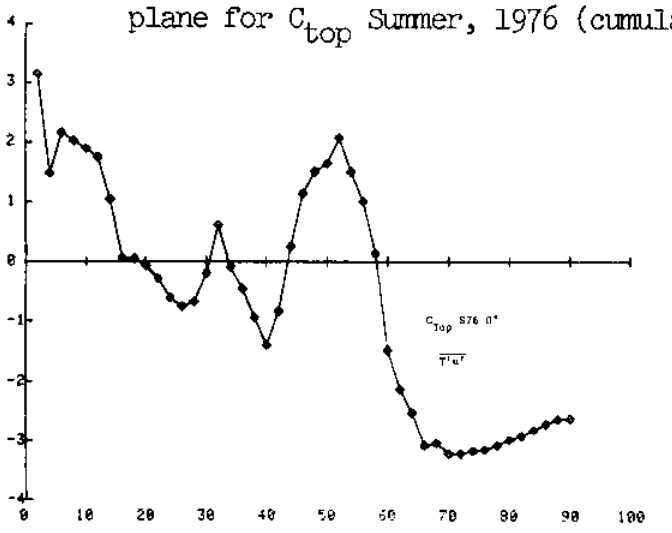

Figure 51 Heat correlation variance in x-direction for C_{top} Summer, 1976 (cumulative)

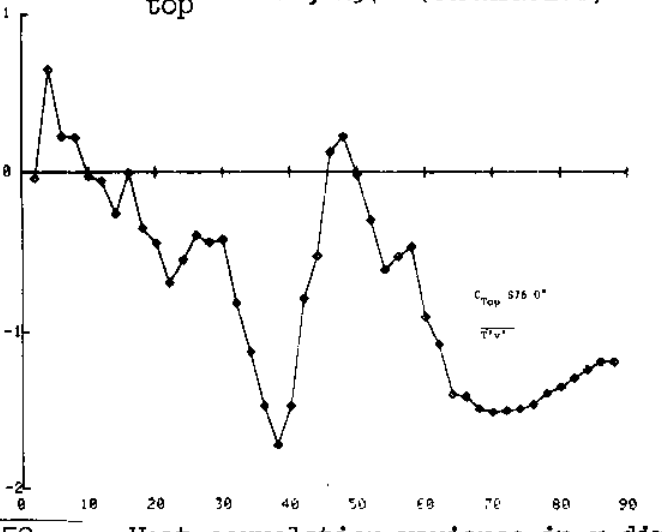

Figure 52 Heat correlation variance in y-direction for C_{top} Summer, 1976 (cumulative)

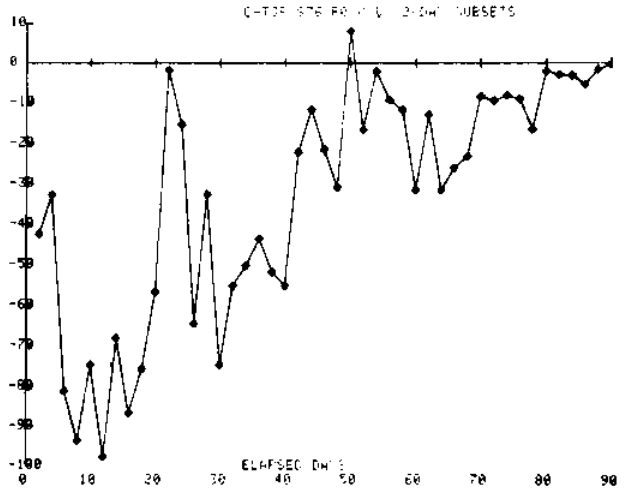

Figure 53 Momentum correlation variance in the horizontal plane for C_{top} Summer, 1976 (2-day subset)

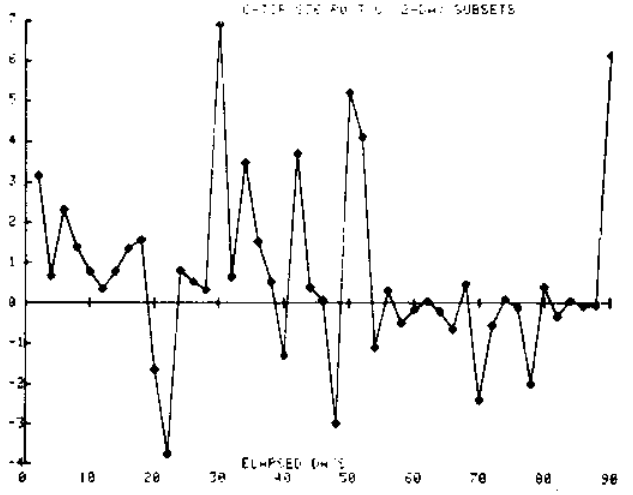

Figure 54 Heat correlation variance in the x-direction for C_{top} Summer, 1976 (2-day subset)

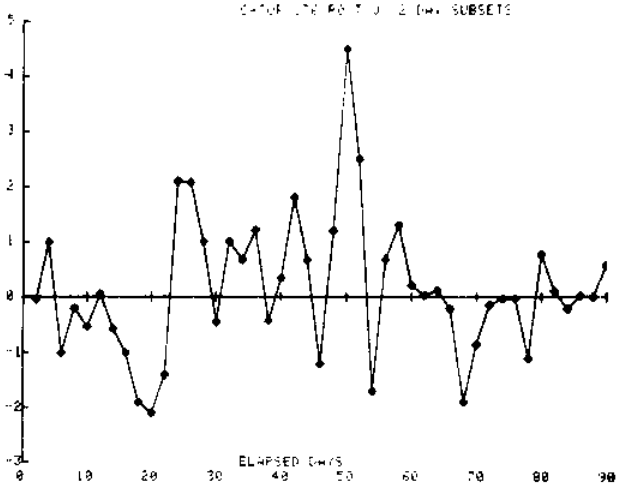

Figure 55 Heat correlation variance in the y-direction for C_{top} Summer, 1976 (2-day subset)

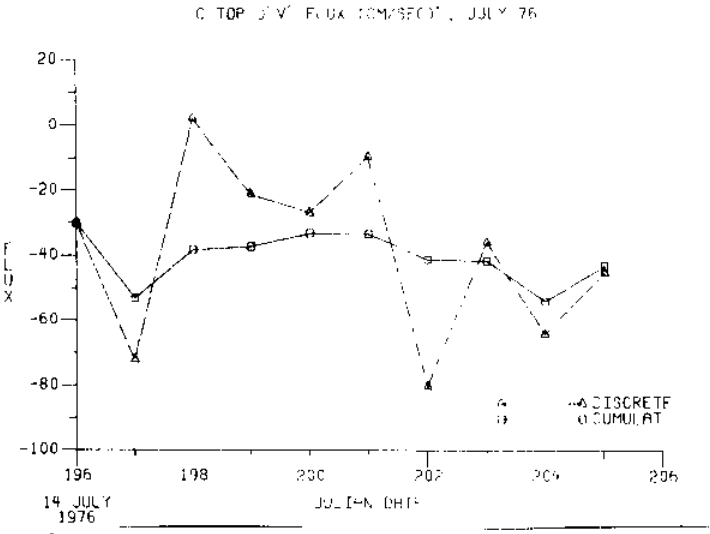

Figure 56 Momentum correlation variance in horizontal plane for C_{top}, July 14-23, 1976

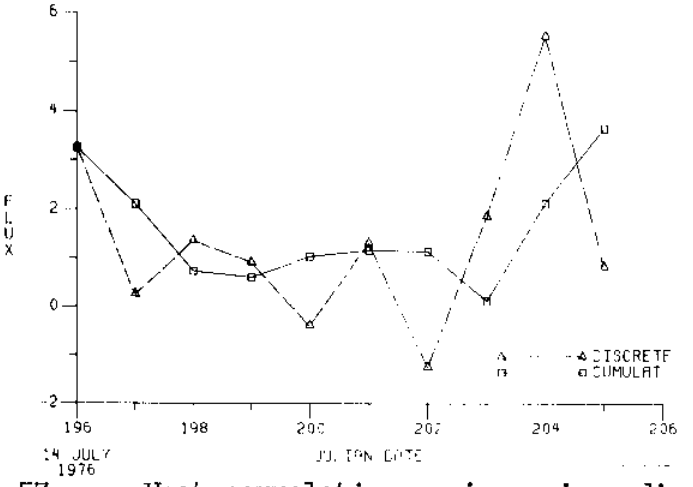

Figure 57 Heat correlation variance in x-direction for C_{top}, July 14-23, 1976

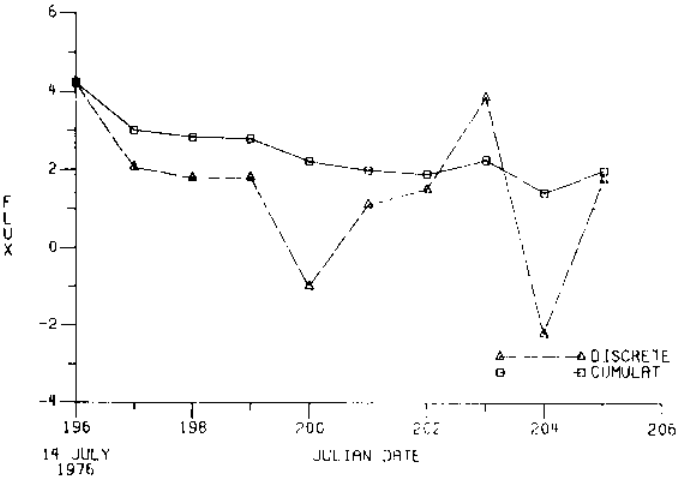

Figure 58 Heat correlation variance in y-direction for C_{top}, July 14-23, 1976

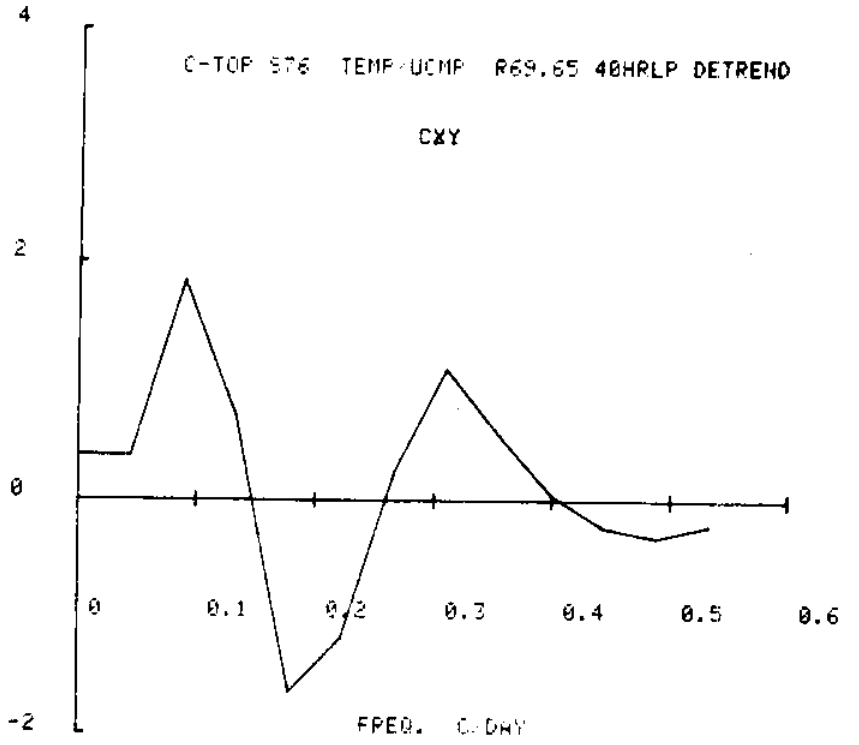

Figure 59 Cospectra of temperature vs. u-component for meter C_{top}

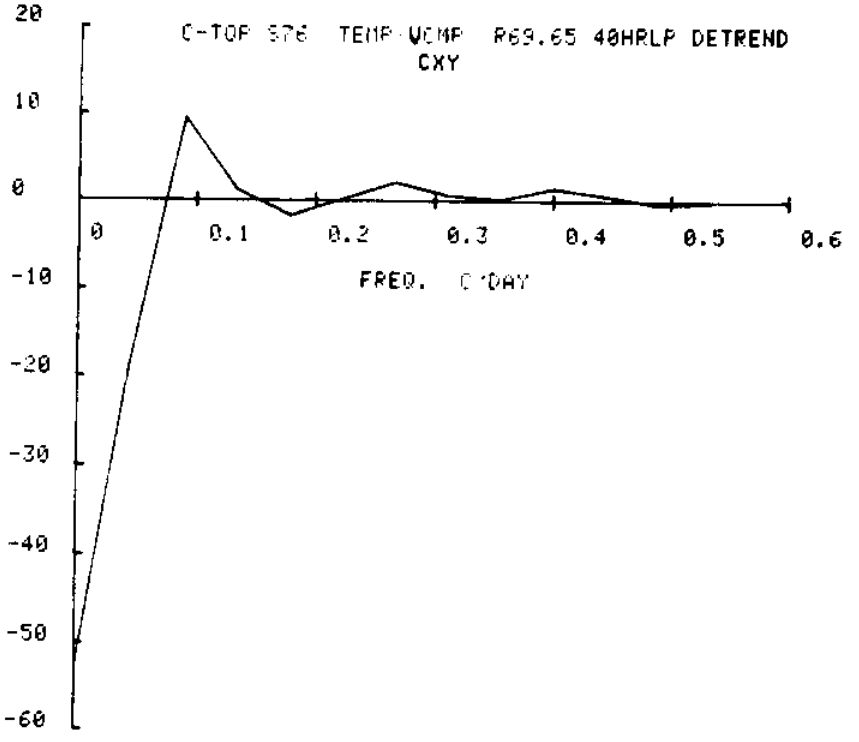

Figure 60 Cospectra of temperature vs. v-component for meter C_{top}

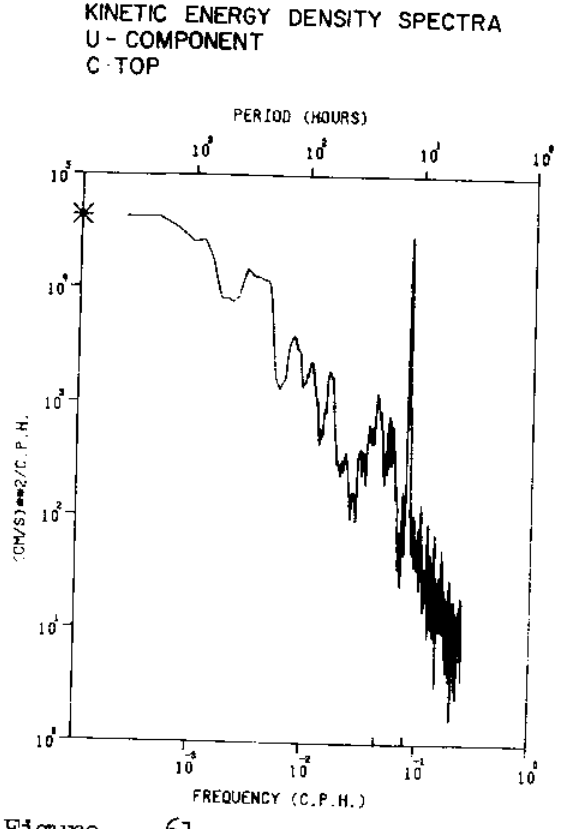

Figure 61

Kinetic energy density spectra for current velocity, u-component, C_{top}

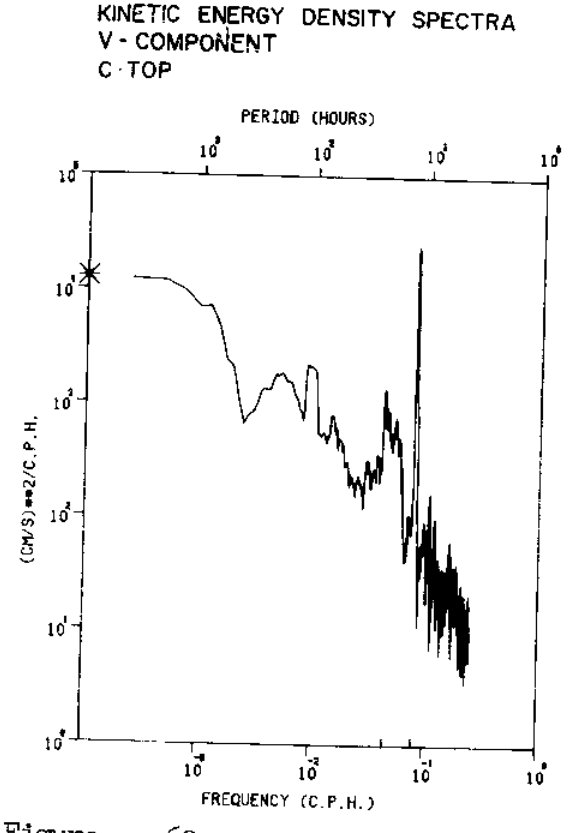

Figure 62

Kinetic energy density spectra for current velocity, v-component, C_{top}

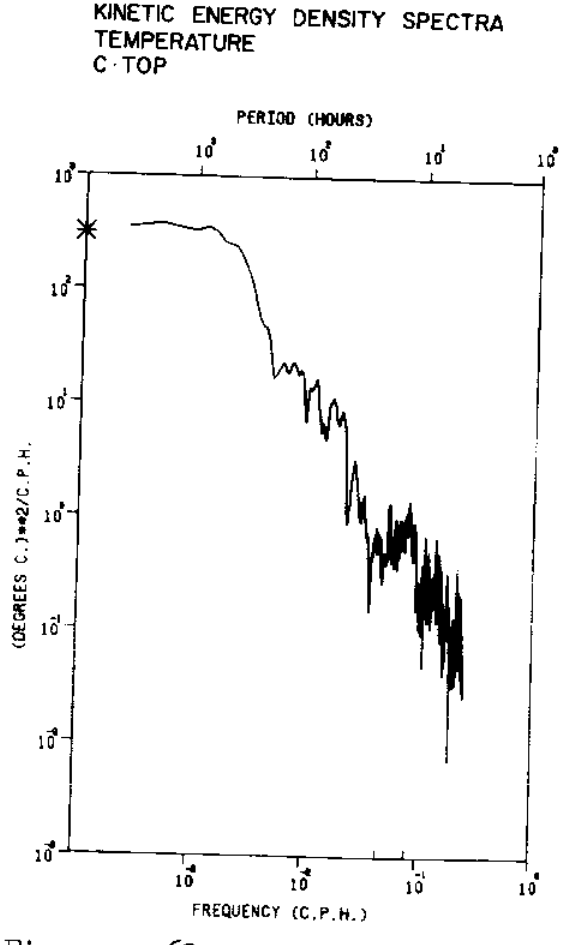

Figure 63

Kinetic energy density spectra for temperature at C_{top}

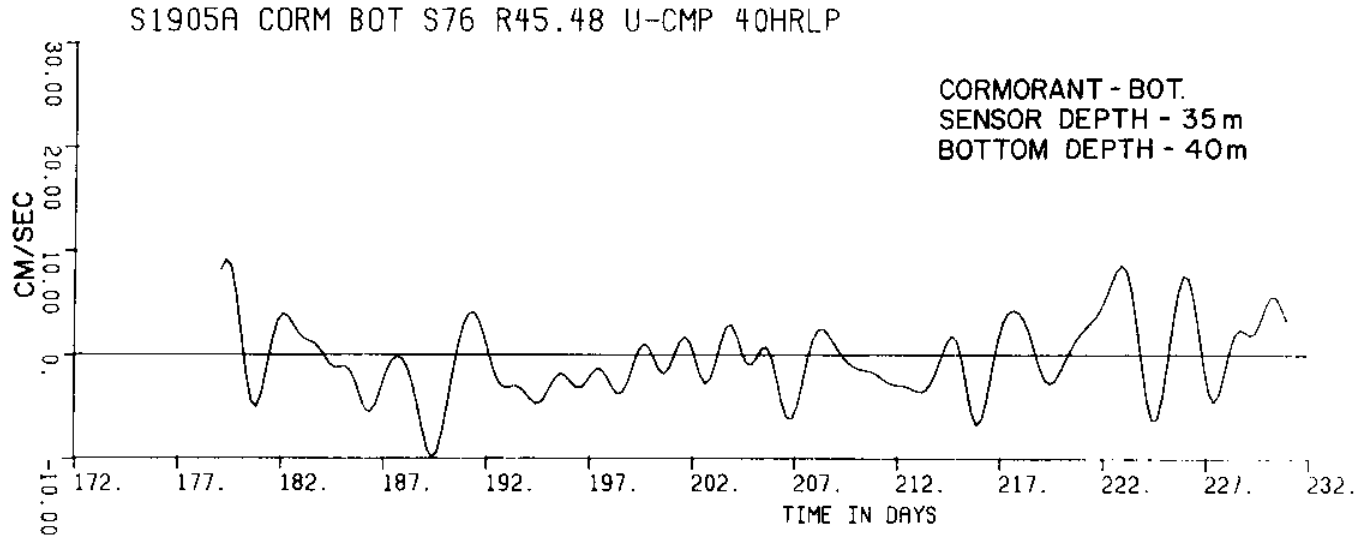

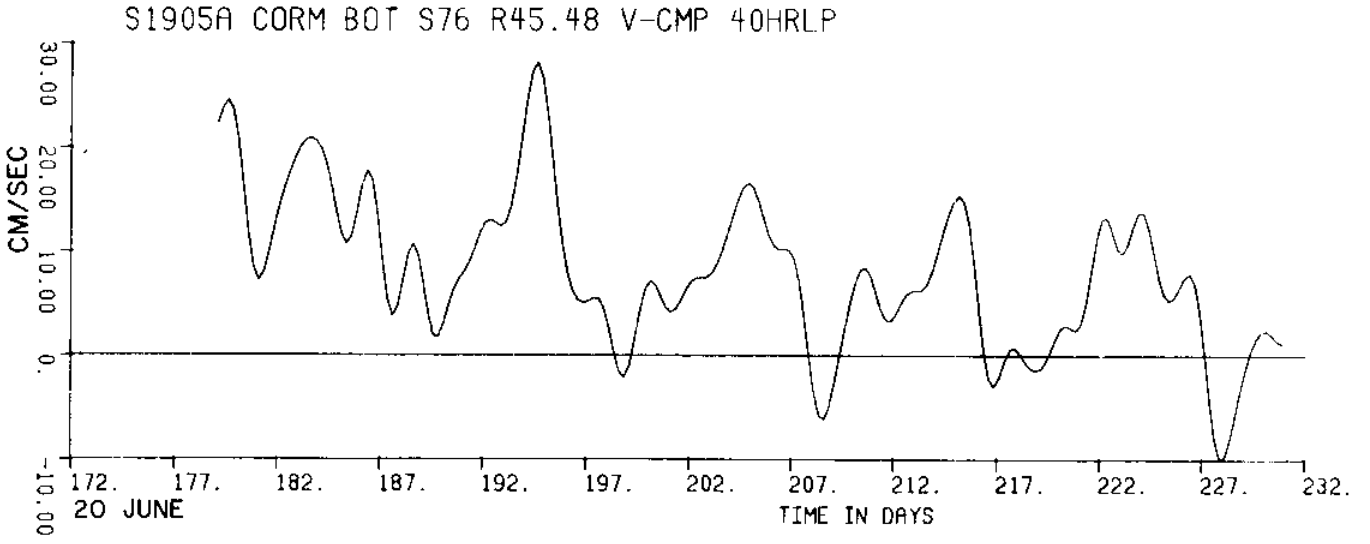

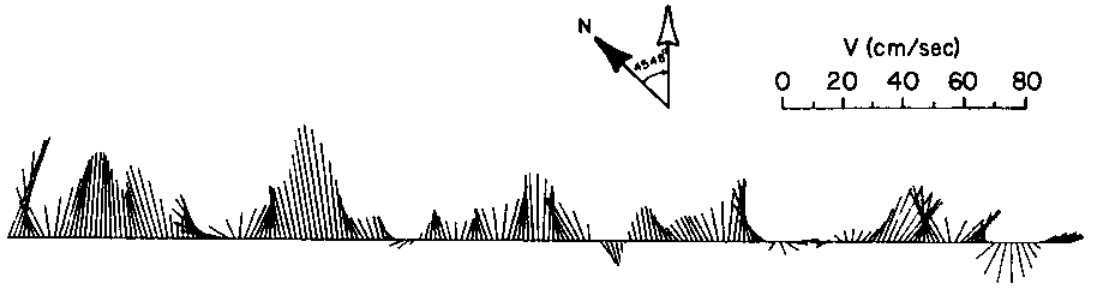

Figure 64 Low pass current velocity components and vectors from meter C(Cormorant)$_{bot}$

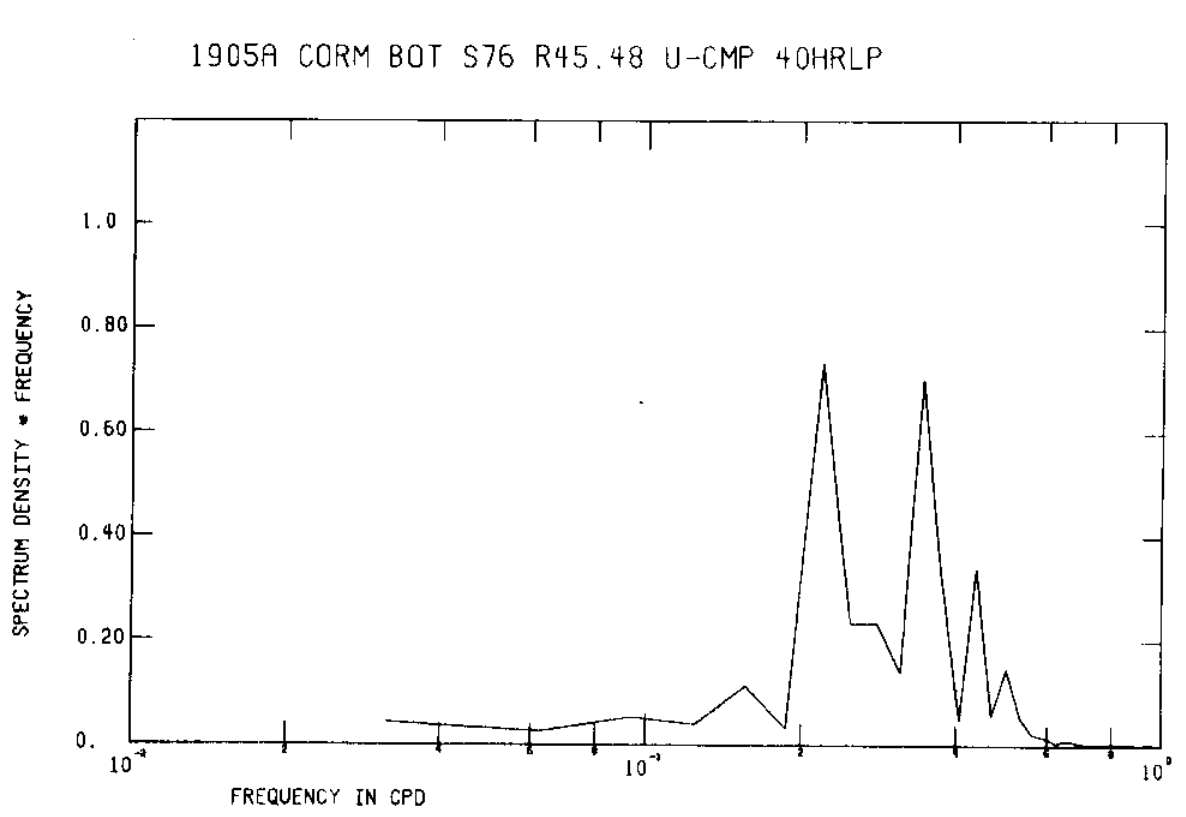

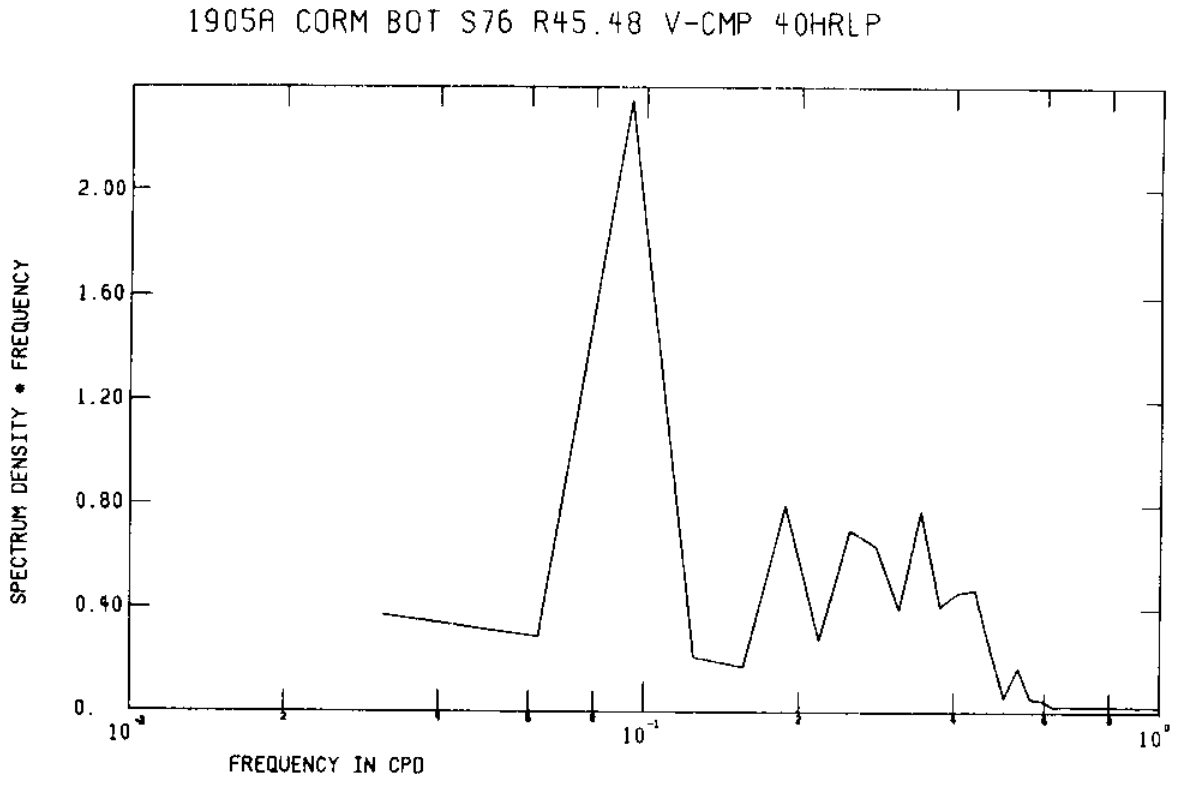

Figure 65 FFT of low pass current velocity components from meter C(Cormorant)$_{bot}$

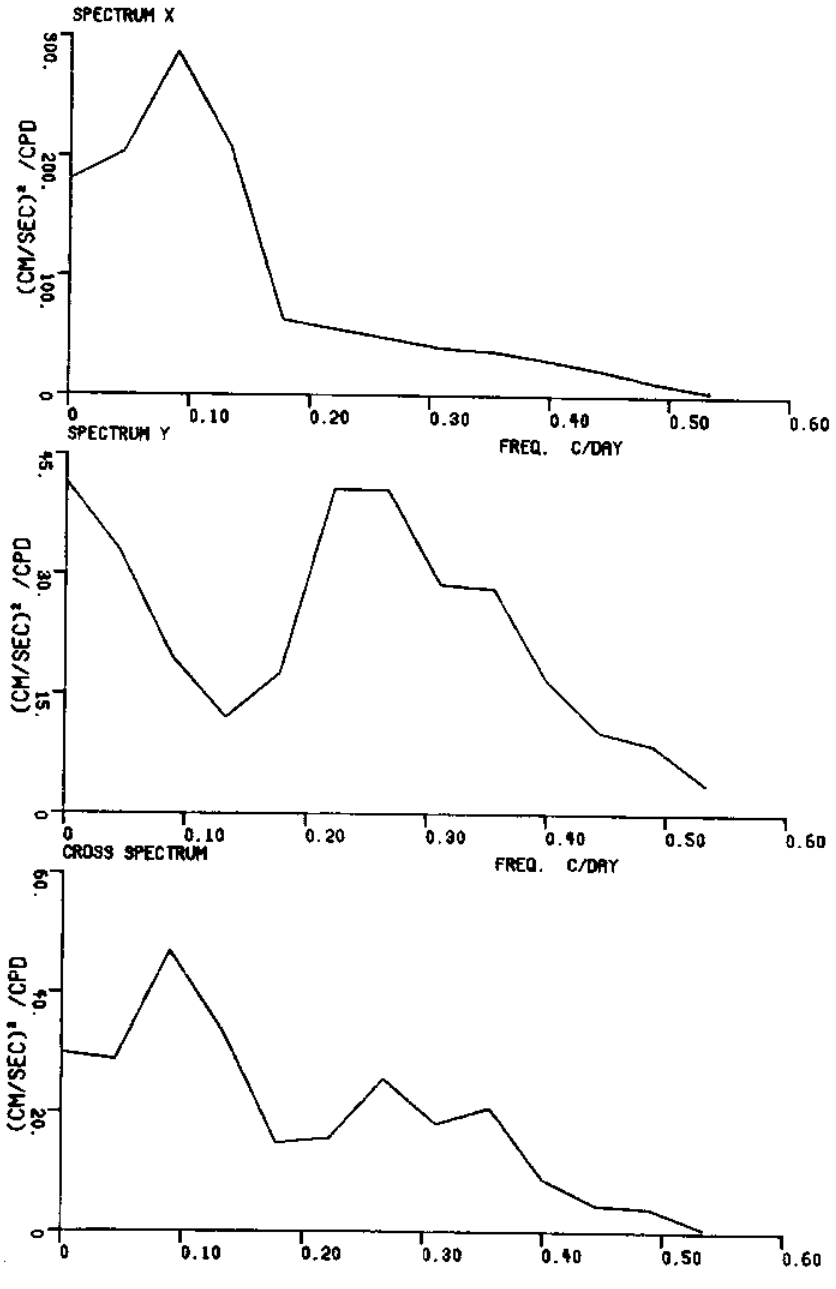

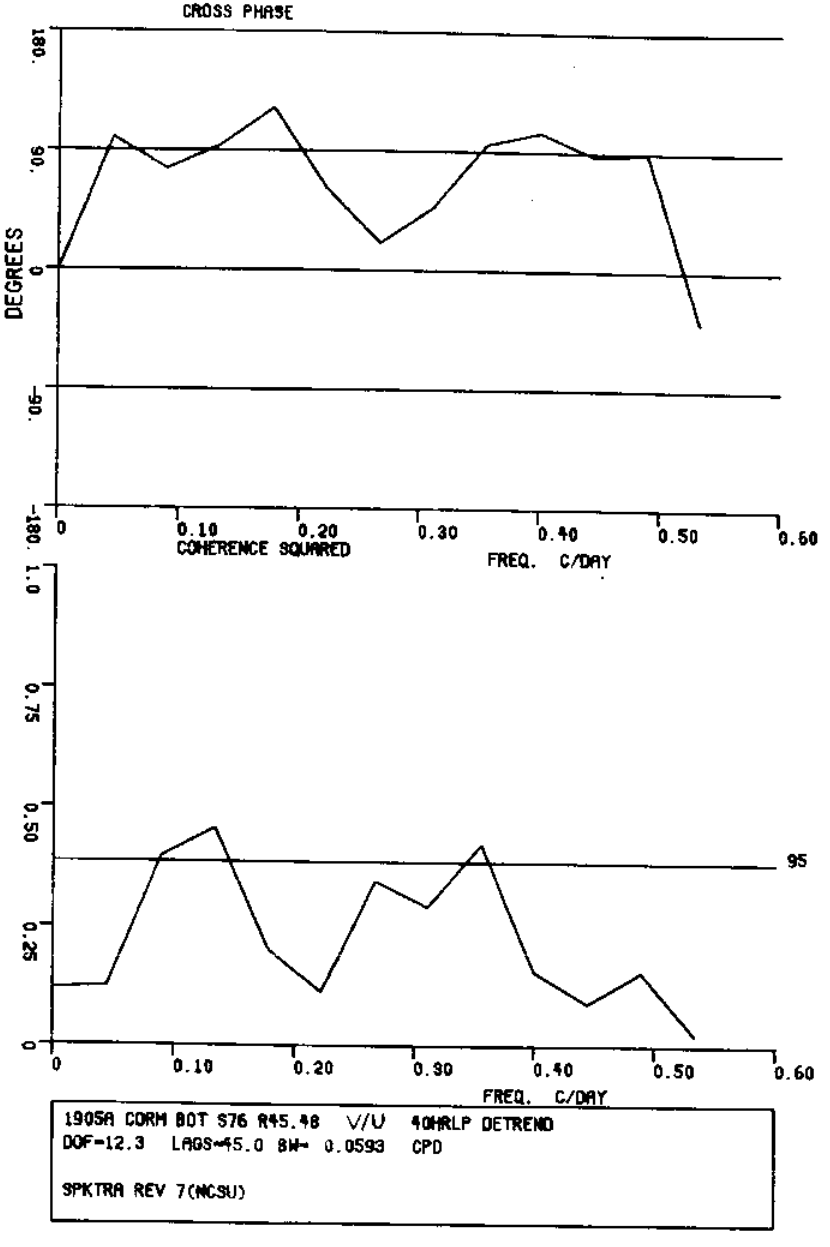

Figure 66 Spectra of low pass current velocity components from meter C(Cormorant)$_{bot}$

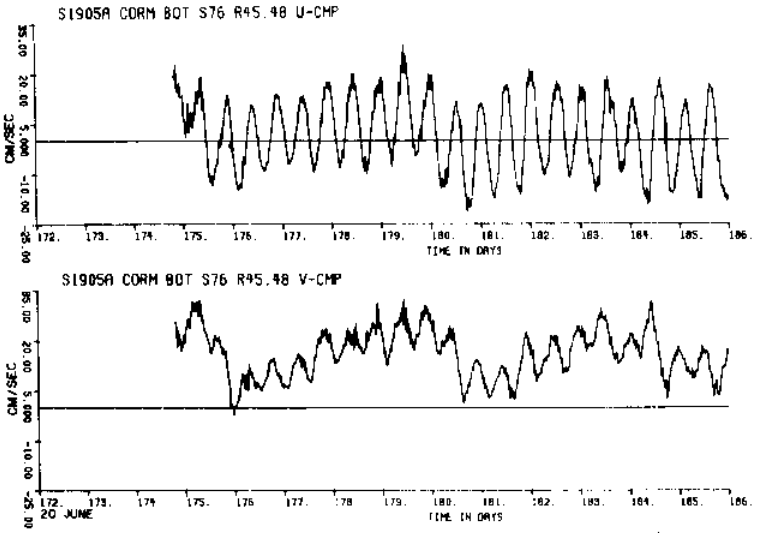

Figure 67 a

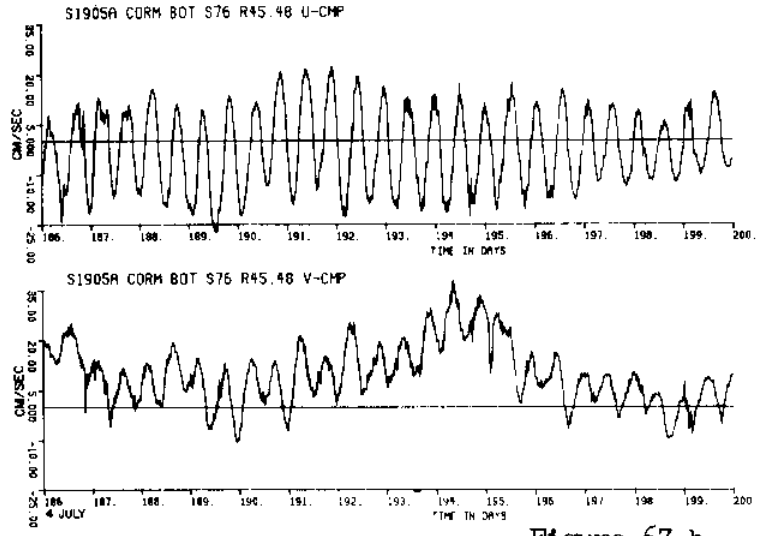

Figure 67 b

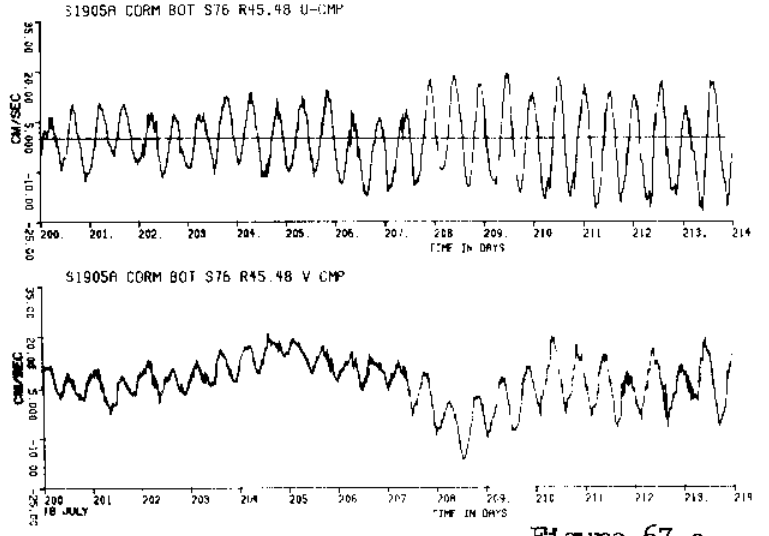

Figure 67 c

Figure 67 (a,b,c,d,e) Unfiltered current velocity components from meter C(Cormorant)$_{bot}$

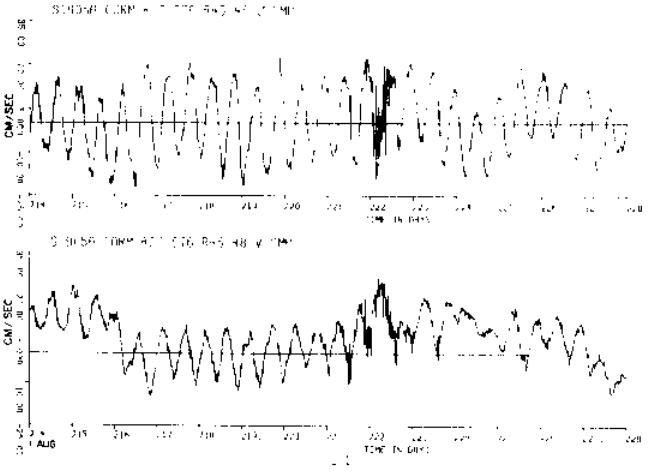

Figure 67 d

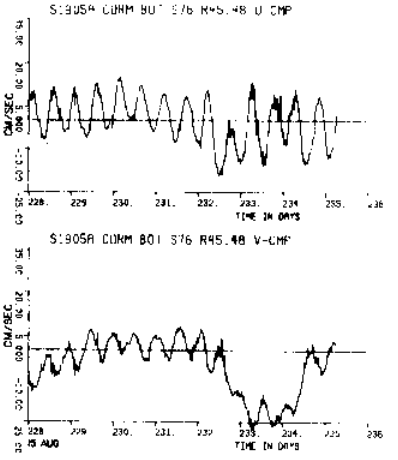

Figure 67 e

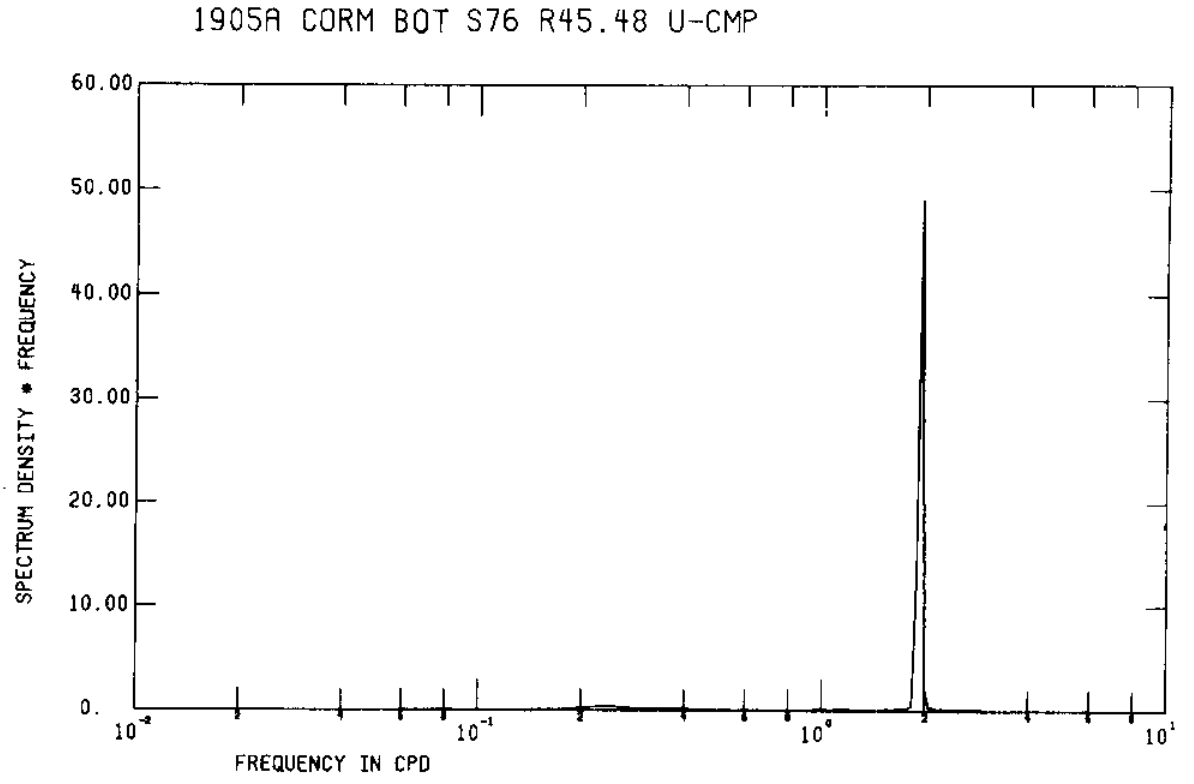

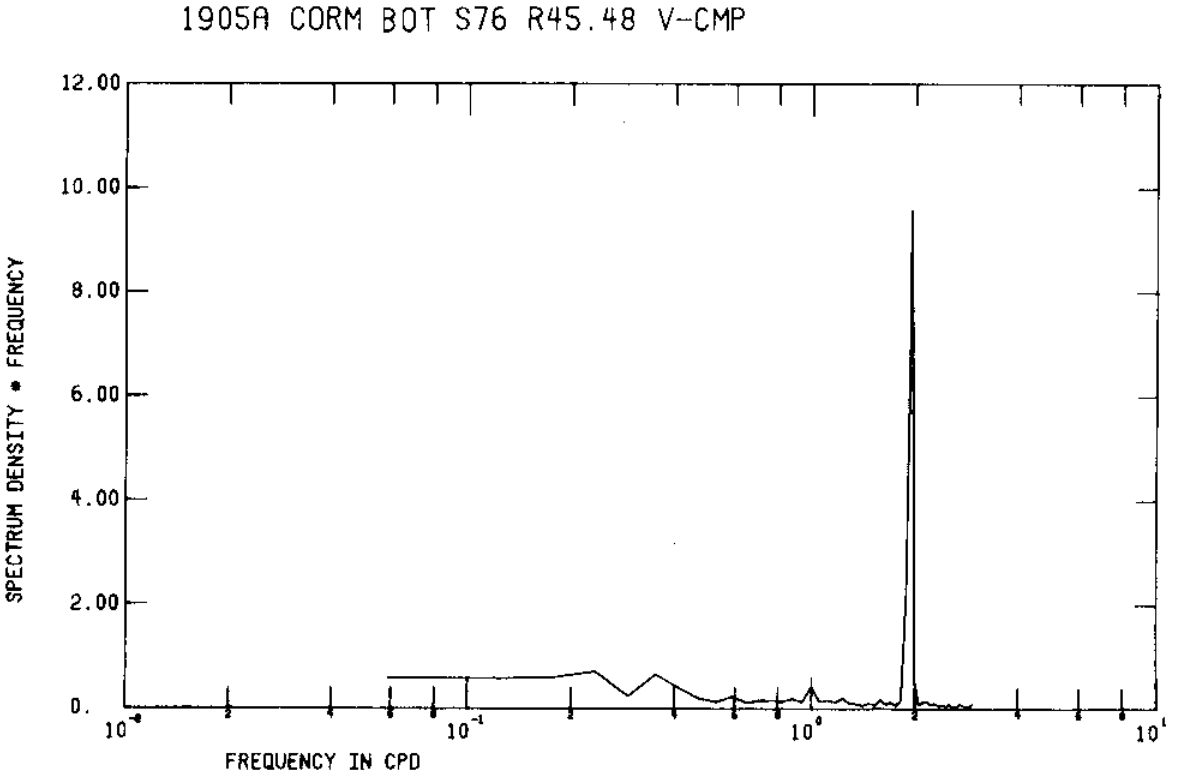

Figure 68 FFT of unfiltered current velocity components from meter C(Cormorant)$_{bot}$

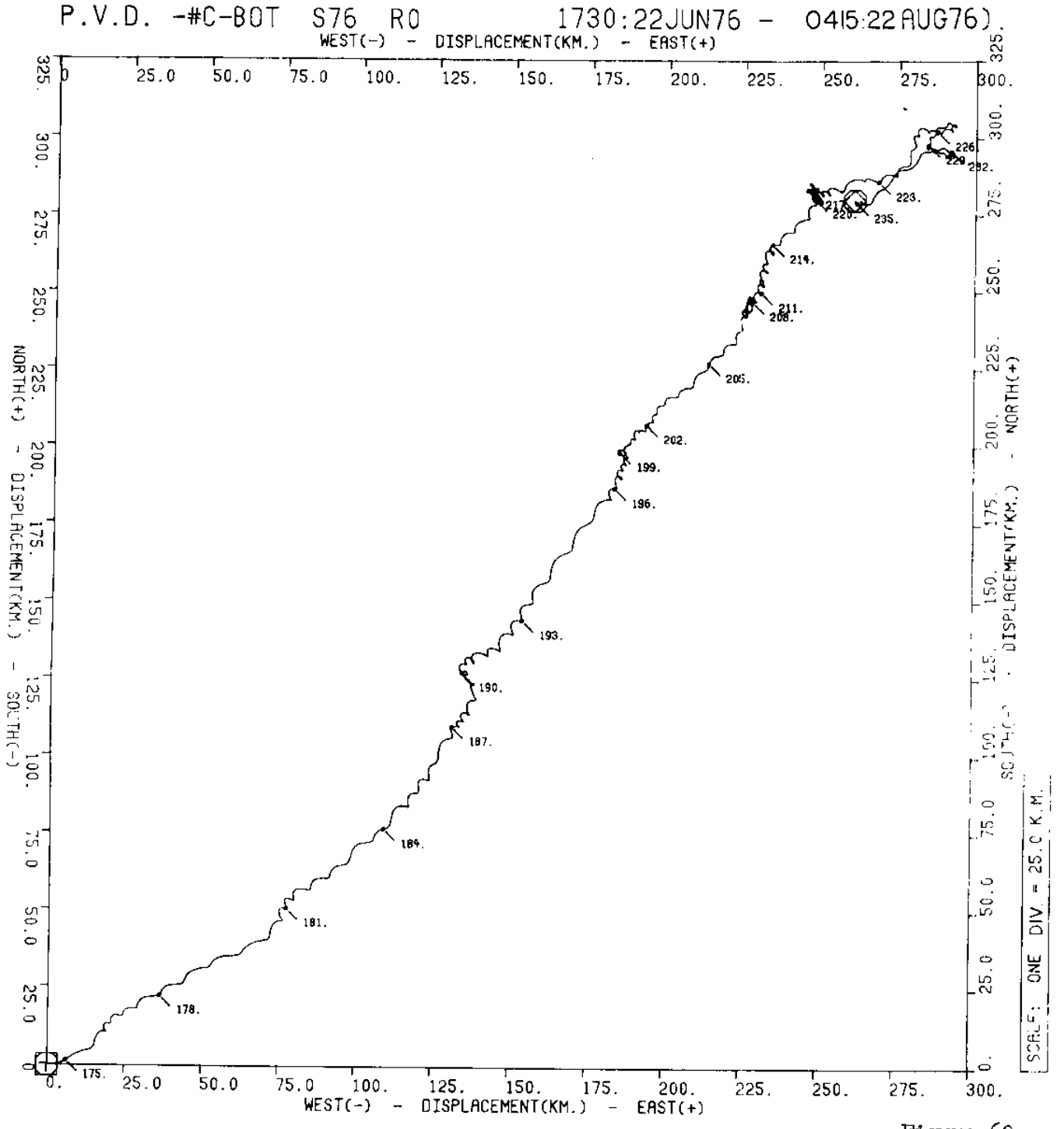

Figure 69 a

Figure 69 (a,b,c,d,e) Progressive vector diagrams of unfiltered current velocity from meter C(Cormorant)$_{bot}$

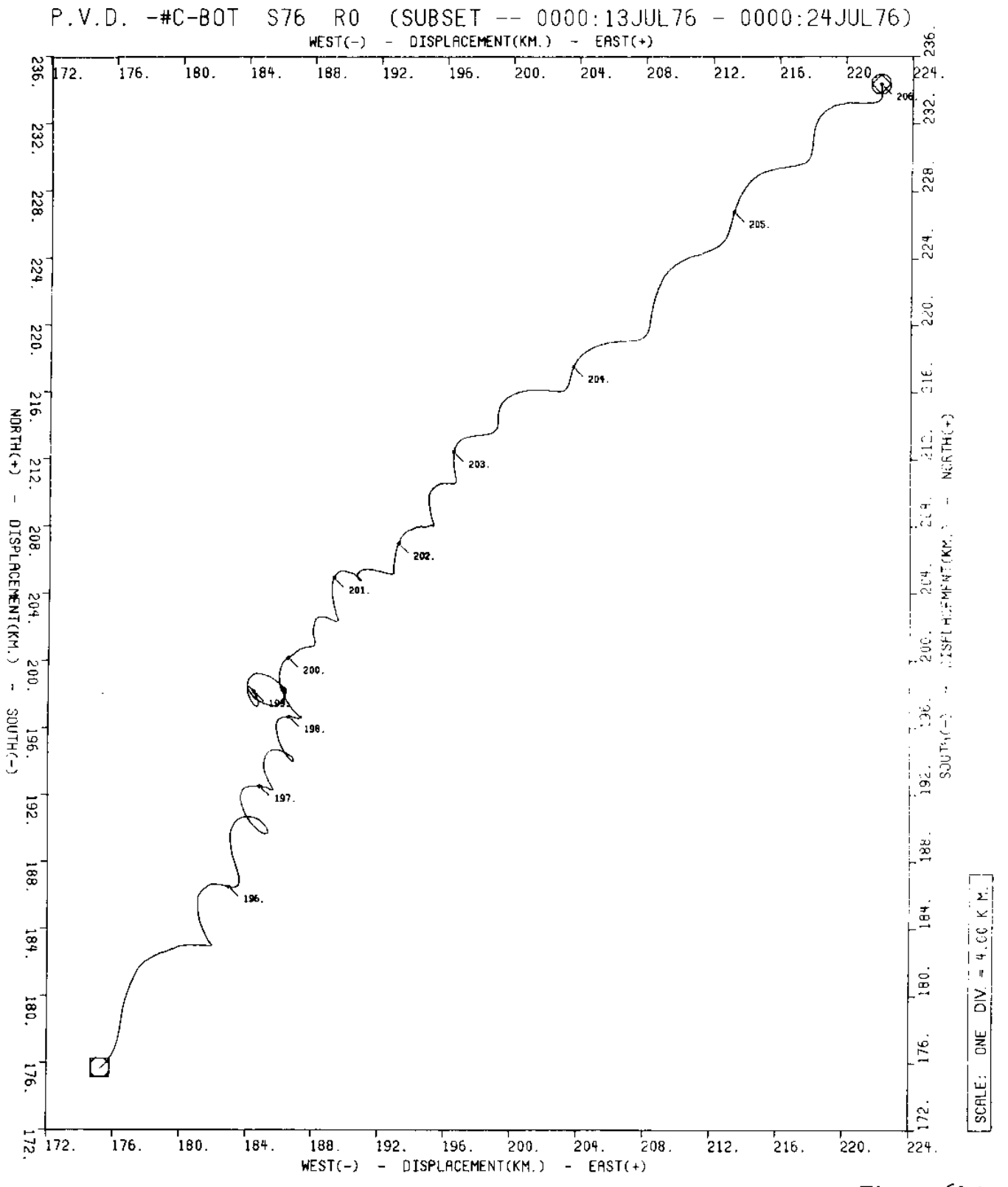
P.V.D. -#C-BOT S76 R0 (SUBSET -- 0000:13JUL76 - 0000:24JUL76)
WEST(-) - DISPLACEMENT(KM.) - EAST(+)
NORTH(+) - DISPLACEMENT(KM.) - SOUTH(-)
172. 176. 180. 184. 188. 192. 196. 200. 204. 208. 212. 216. 220. 224.
236. 232. 228. 224. 220. 216. 212. 208. 204. 200. 196. 192. 188. 184. 180. 176. 172.
206.
205.
204.
203.
202.
201.
200.
199.
198.
197.
196.
SCALE: ONE DIV. = 4.00 K.M.

Figure 69 b

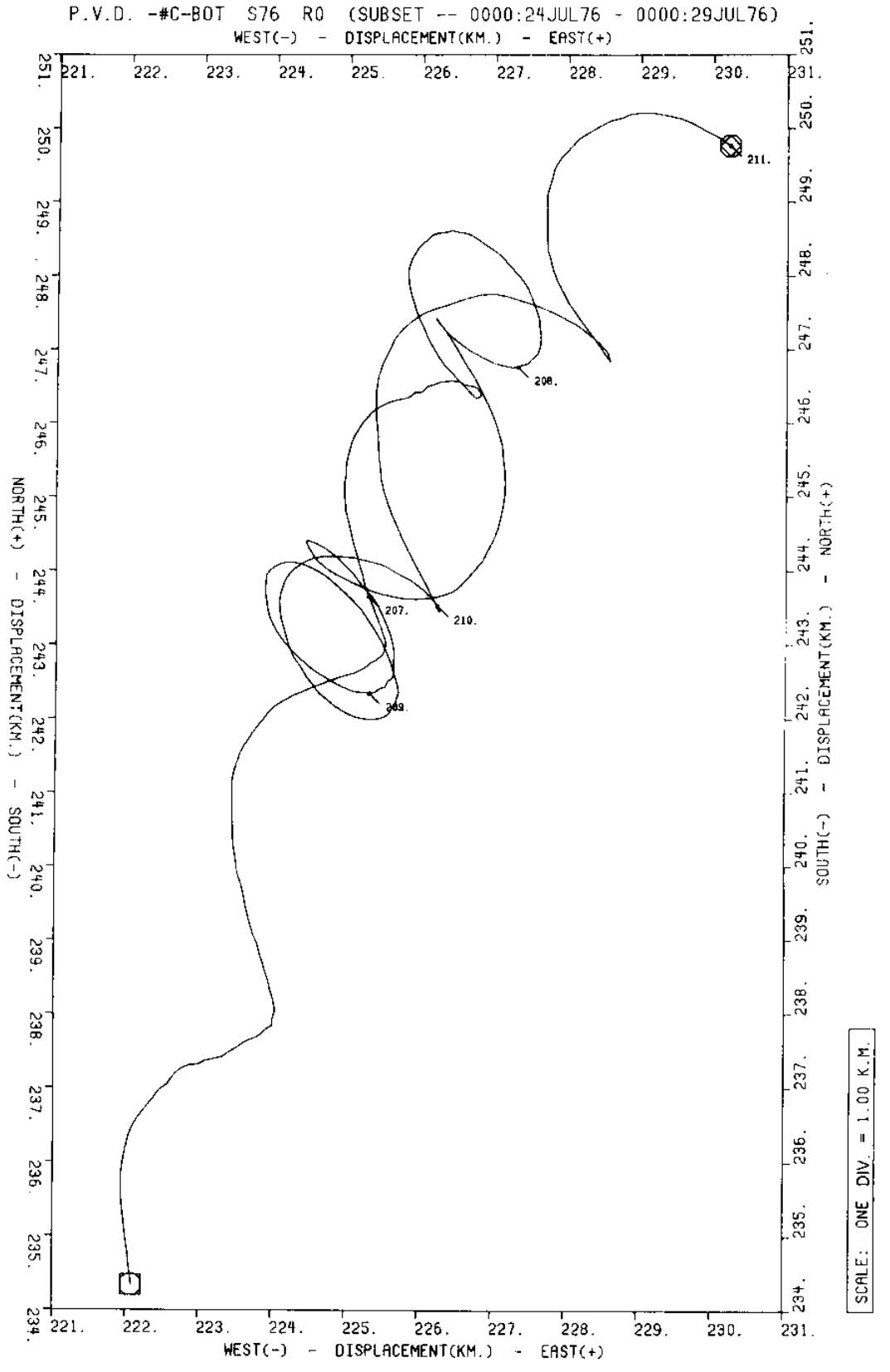
P.V.D. -#C-BOT S76 R0 (SUBSET -- 0000:24JUL76 - 0000:29JUL76)
WEST(-) - DISPLACEMENT(KM.) - EAST(+)
NORTH(+) - DISPLACEMENT(KM.) - SOUTH(-)
SOUTH(-) - DISPLACEMENT(KM.) - NORTH(+)
211.
208.
207.
210.
209.
SCALE: ONE DIV. = 1.00 K.M.

Figure 69 c

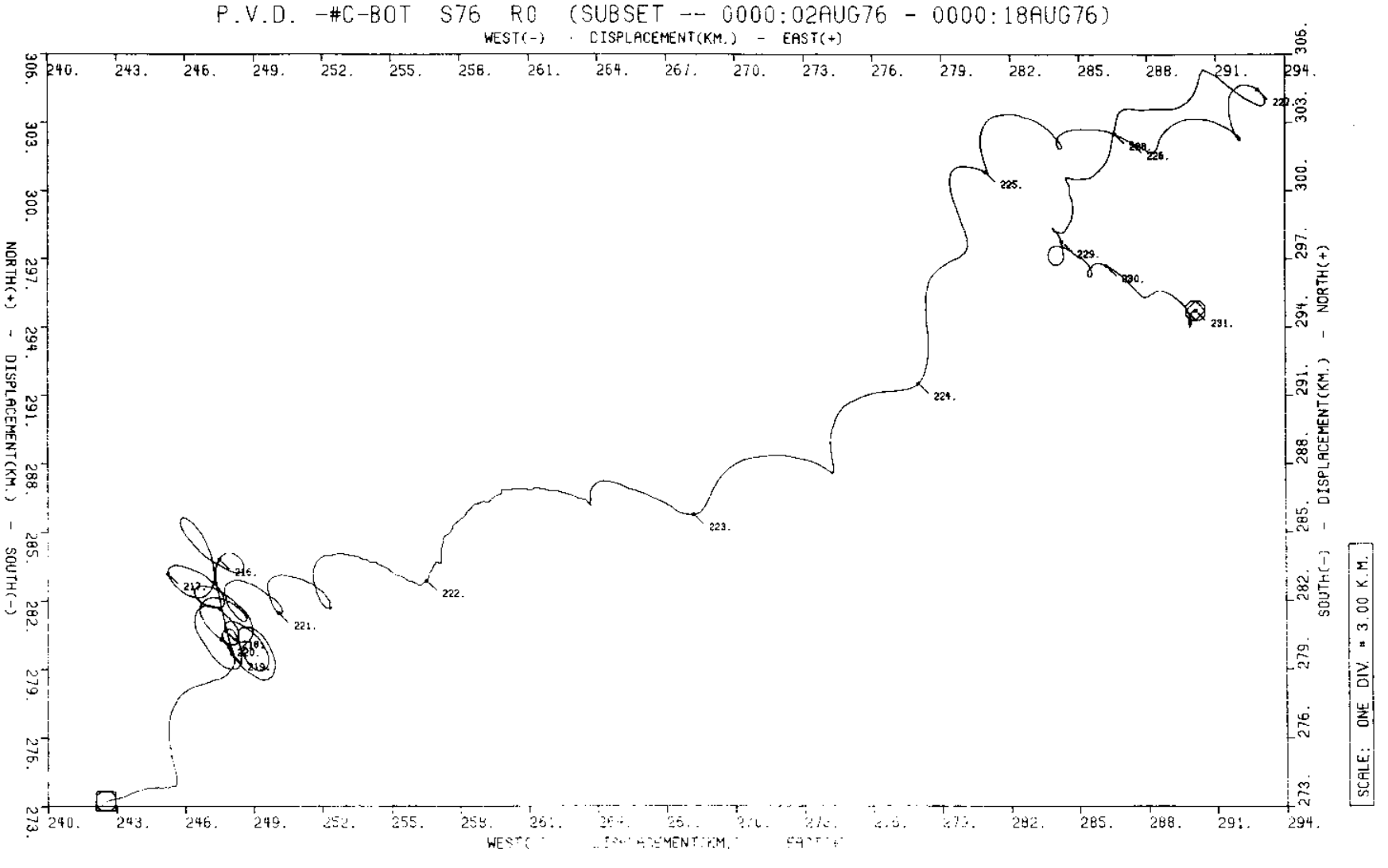
P.V.D. -#C-BOT S76 R0 (SUBSET -- 0000:02AUG76 - 0000:18AUG76)
WEST(-) - DISPLACEMENT(KM.) - EAST(+)
NORTH(+) - DISPLACEMENT(KM.) - SOUTH(-)
SOUTH(-) - DISPLACEMENT(KM.) - NORTH(+)
SCALE: ONE DIV. = 3.00 K.M.

Figure 69 d

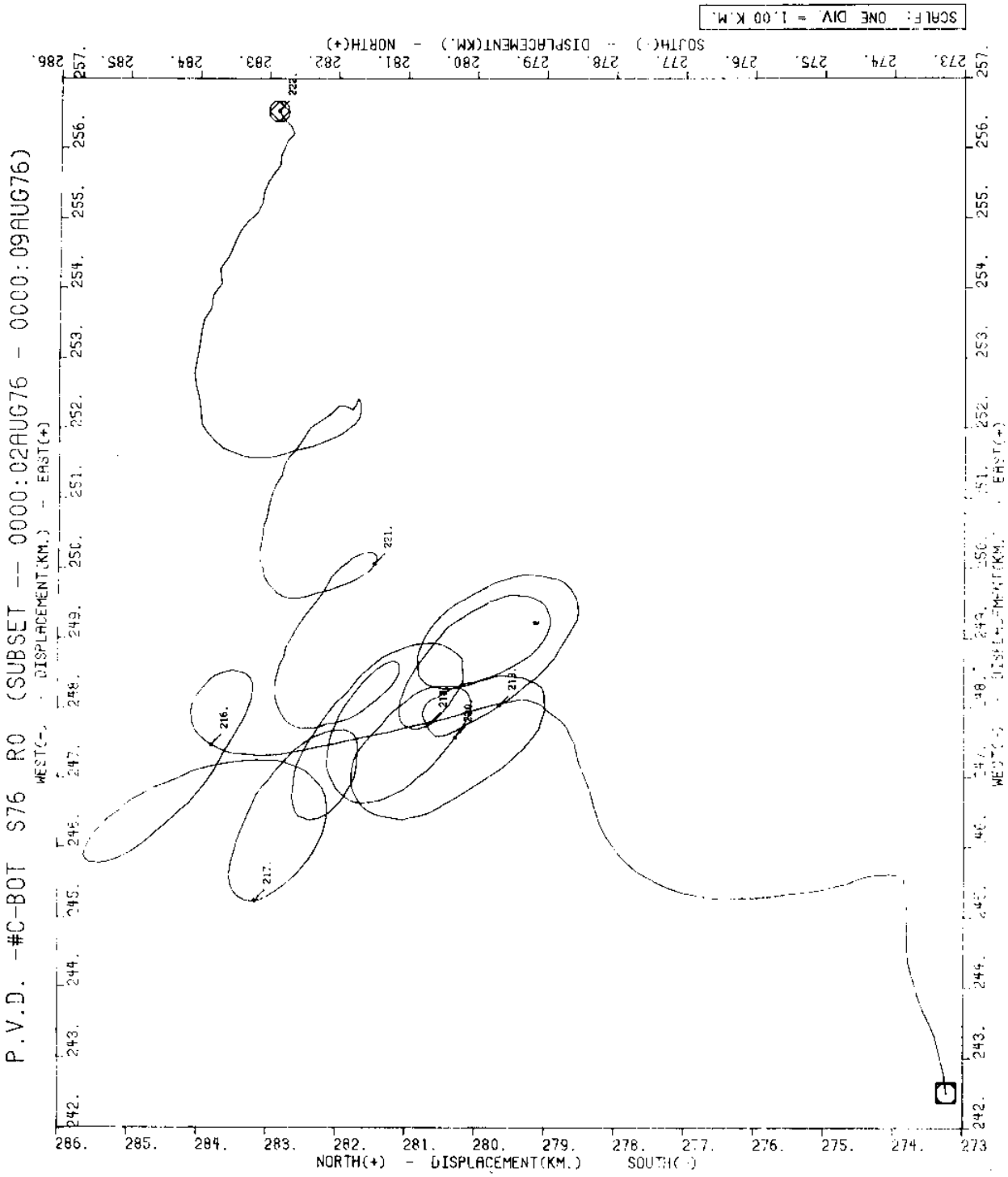
P.V.D. -#C-BOT S76 R0 (SUBSET -- 0000:02AUG76 - 0000:09AUG76)
SCALE: ONE DIV = 1.00 K.M.
NORTH(+) - DISPLACEMENT(KM.) SOUTH(-)
WEST(-) - DISPLACEMENT(KM.) - EAST(+)
222.
221.
216.
217.
218.
219.
220.

Figure 69 e

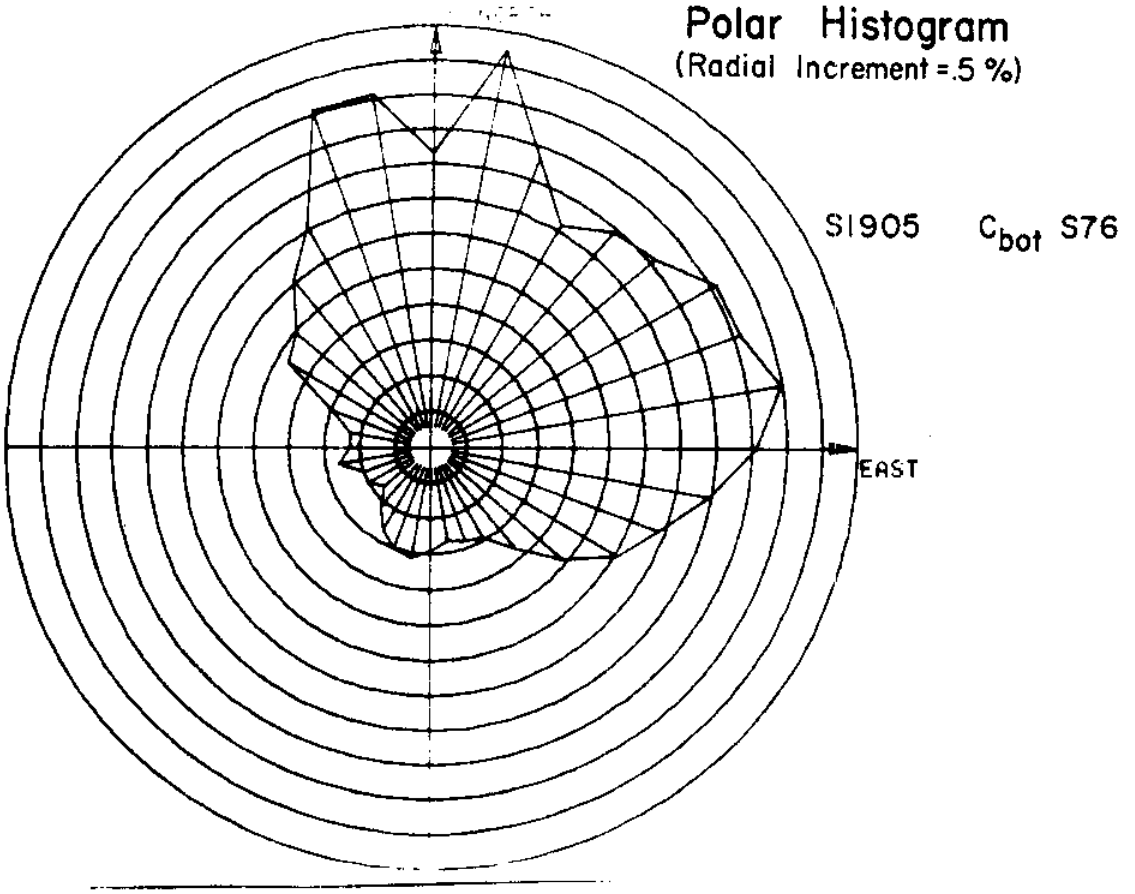

Figure 70 Histogram from meter C(Cormorant)$_{bot}$

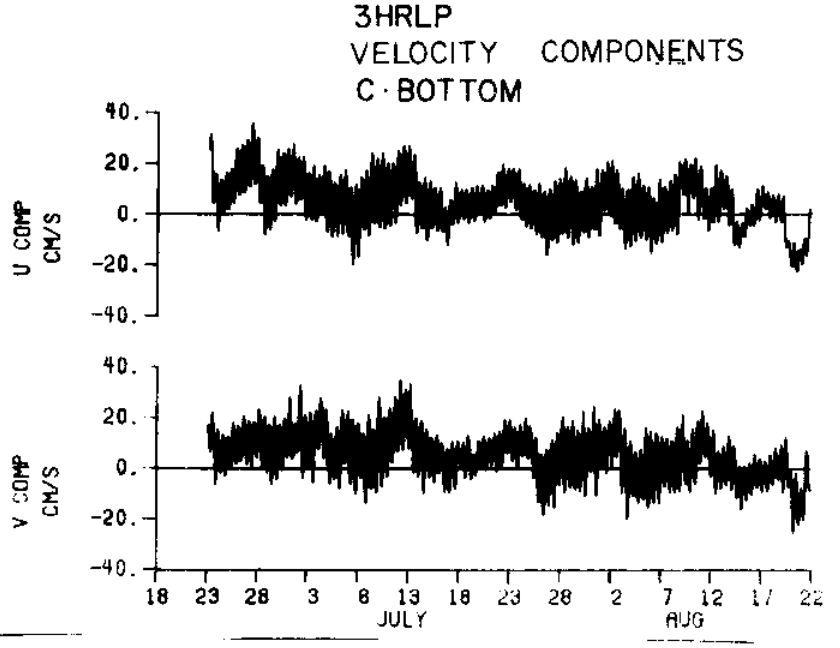

Figure 71 3HRLP velocity components for C_{bot}

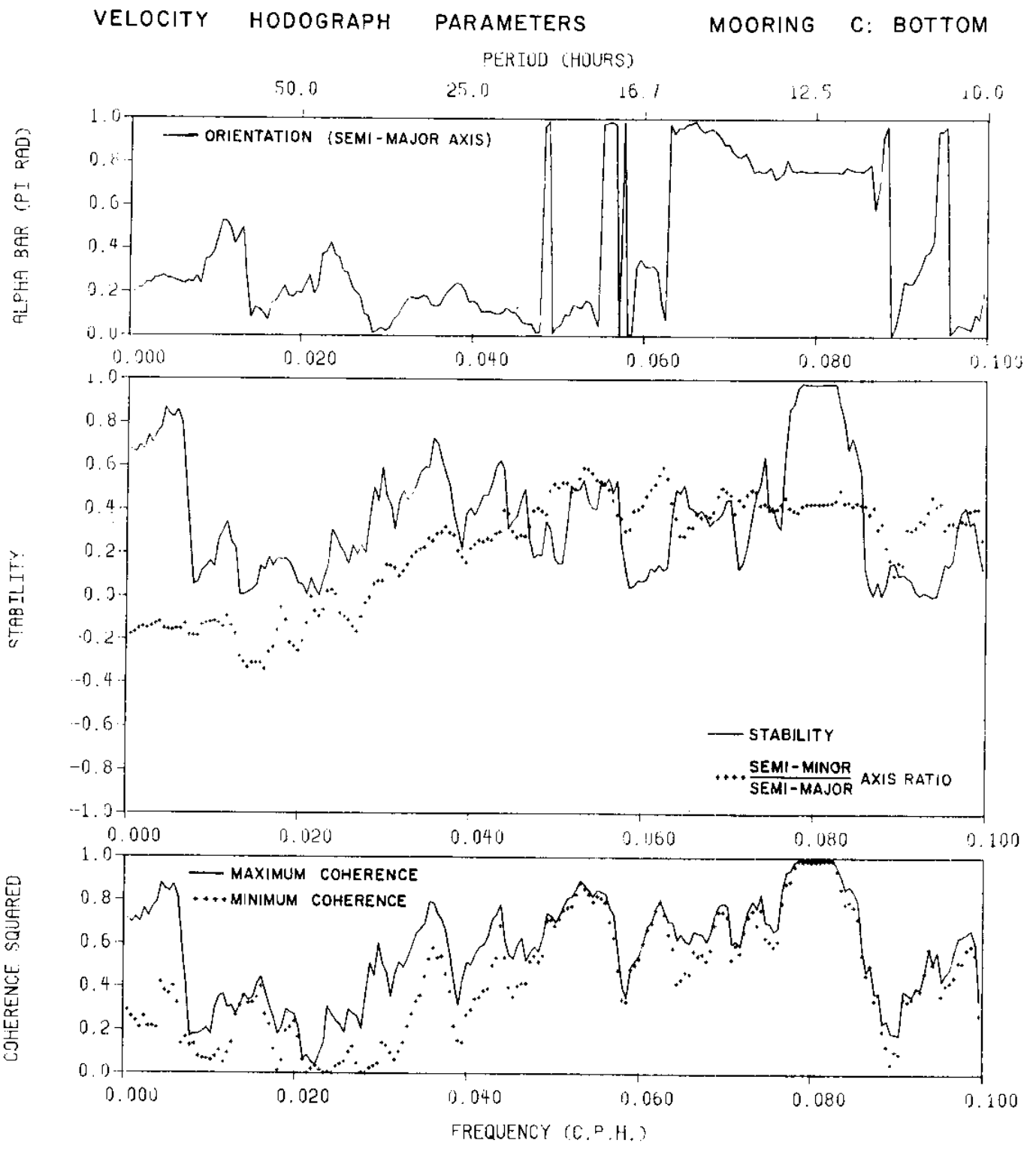

Figure 72 Hodograph parameters from meter C(Cormorant)$_{bot}$

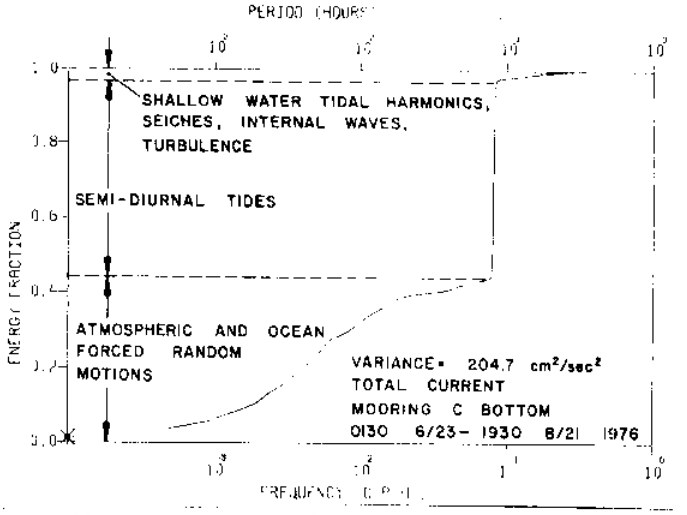

Figure 73 Energy fraction vs. frequency for C_{bot} total current

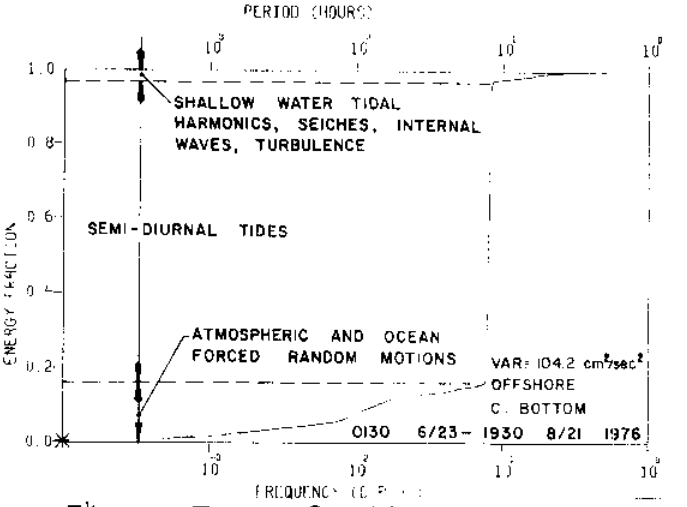

Figure 74 Energy fraction vs. frequency for C_{bot} offshore current

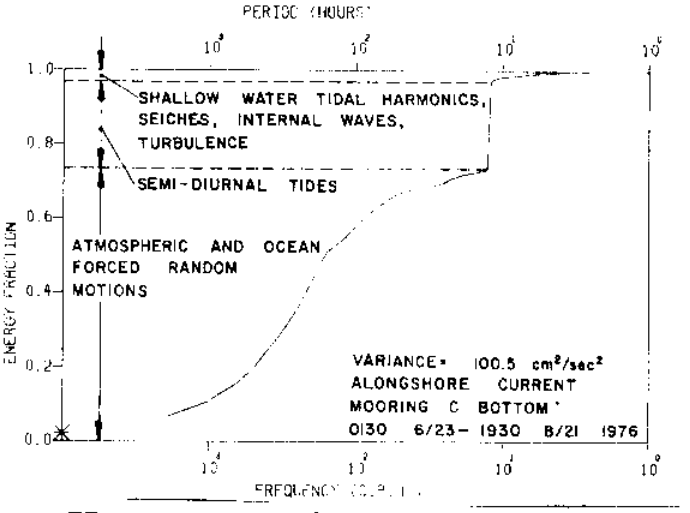

Figure 75 Energy fraction vs. frequency for C_{bot} alongshore current

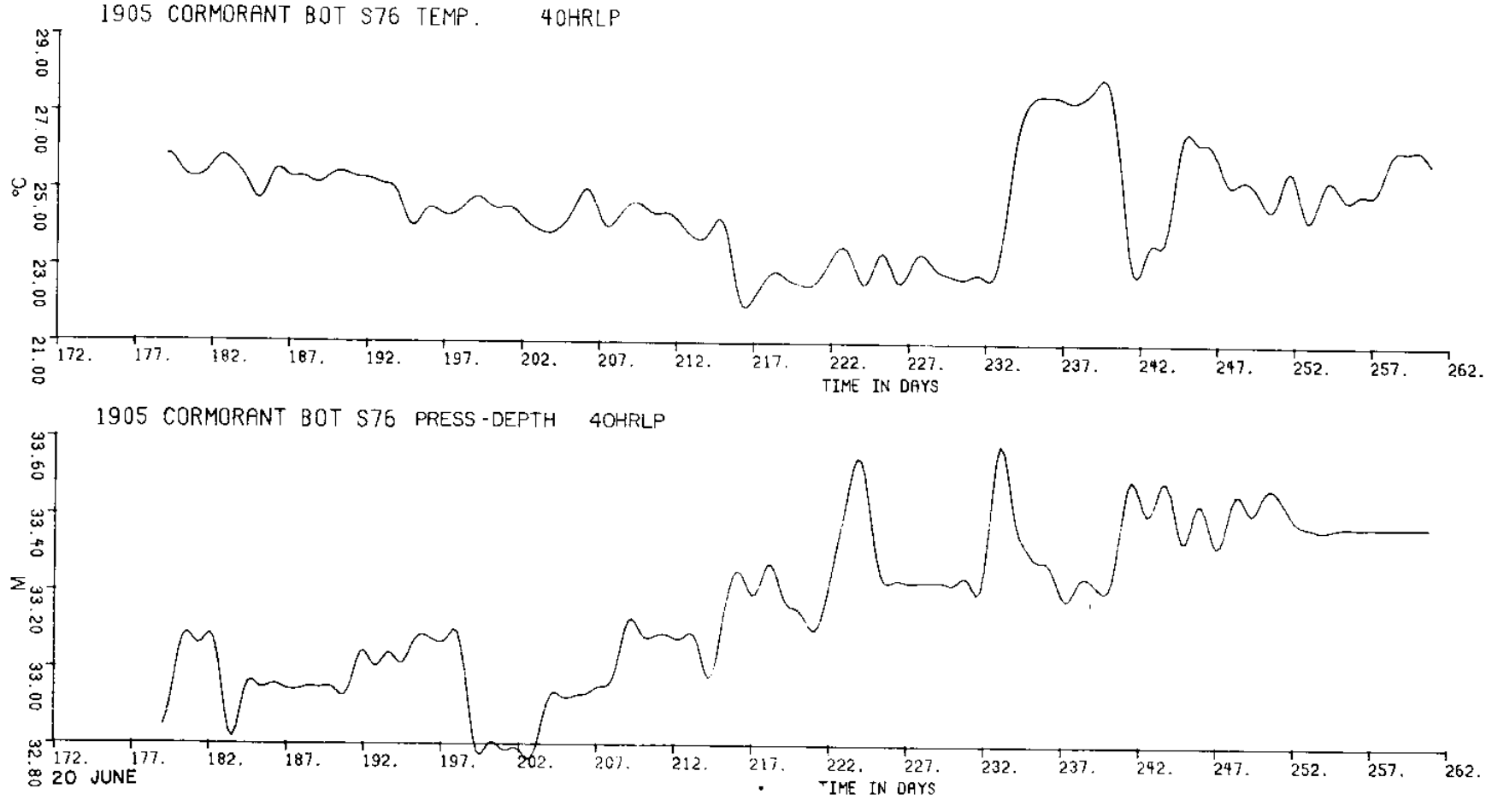

Figure 76 Low pass temperature and pressure from meter $C(\text{Cormorant})_{bot}$

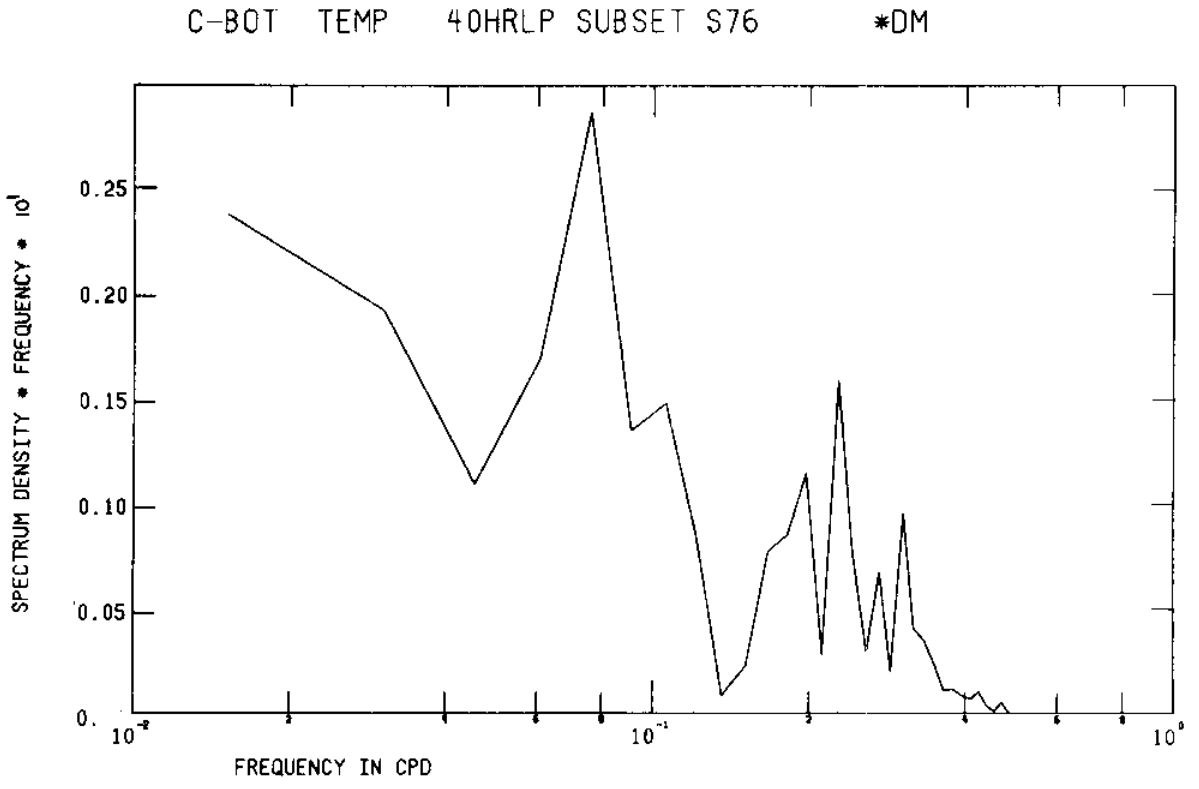

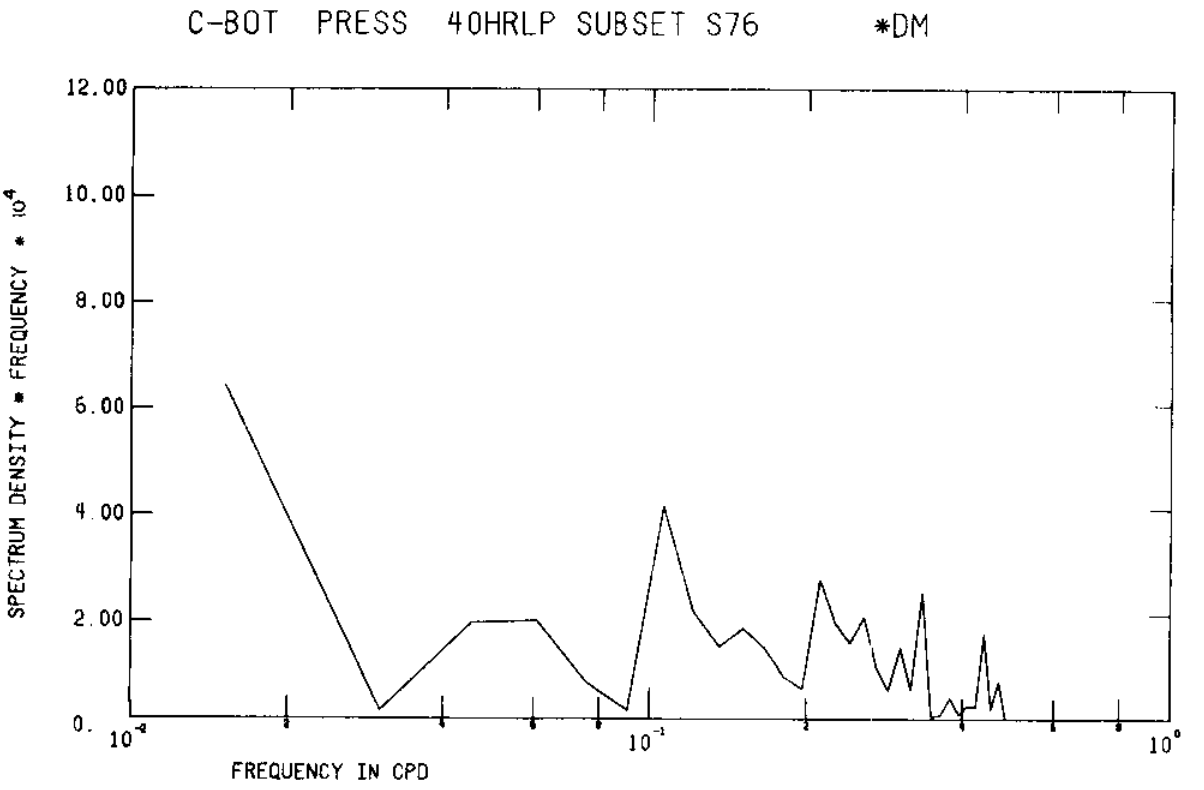

Figure 77 FFT of low pass temperature and pressure from meter $C(\text{Cormorant})_{bot}$

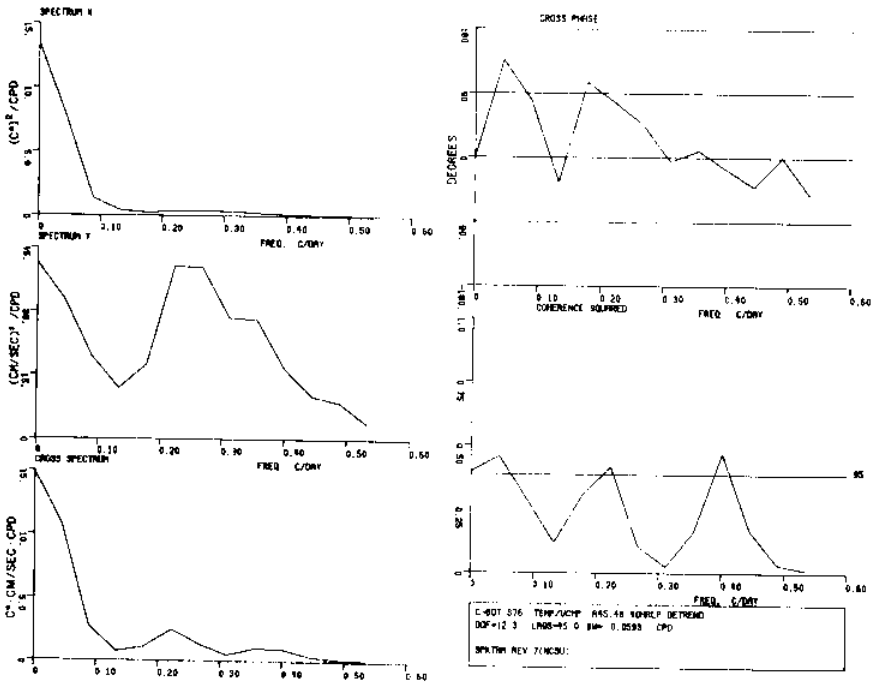

Figure 78 Spectra of temperature and the low pass current velocity u component, both from meter C(Cormorant)$_{bot}$

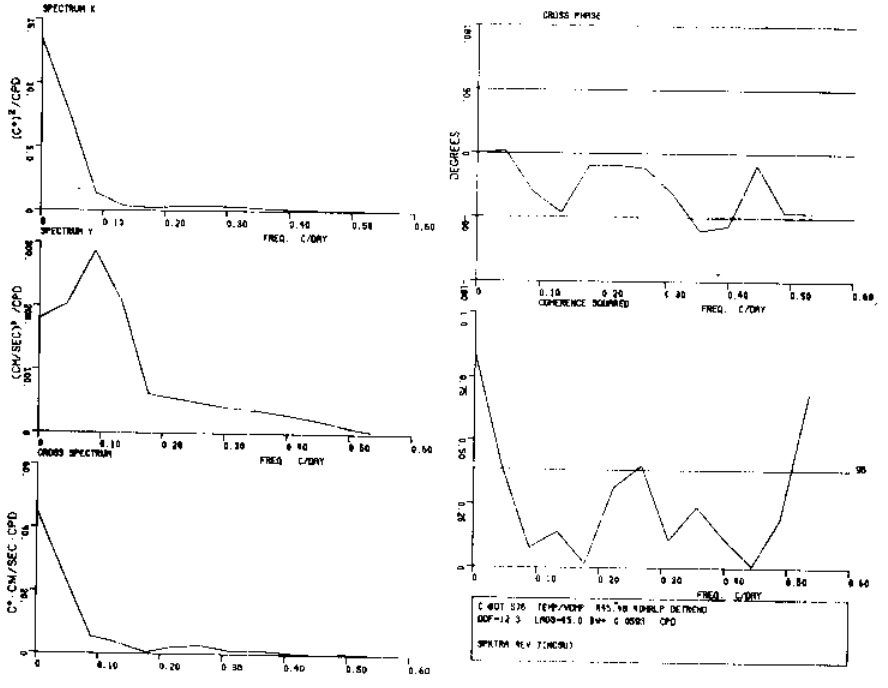

Figure 79 Spectra of temperature and the low pass current velocity v component, both from meter C(Cormorant)$_{bot}$

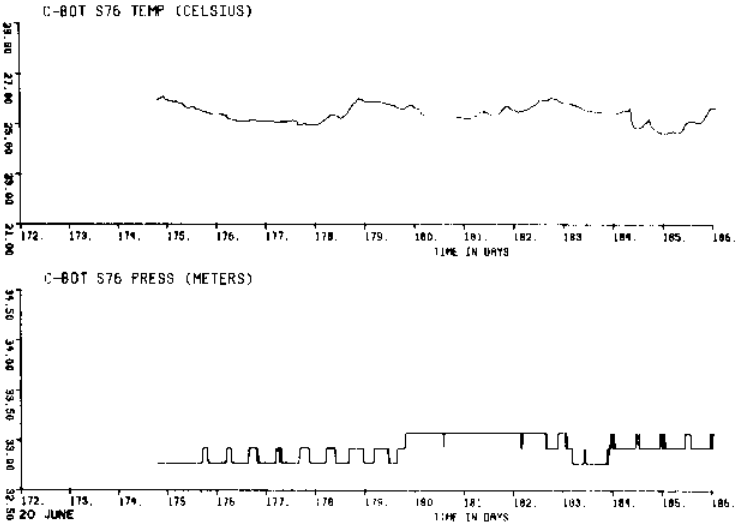

Figure 80 a

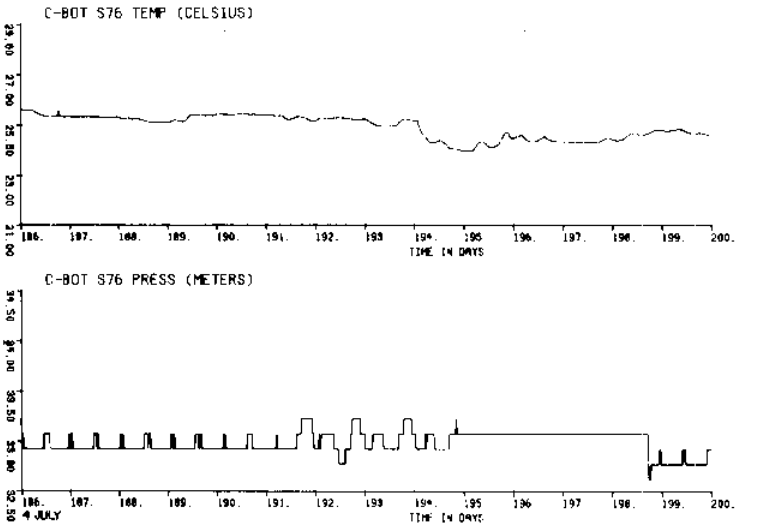

Figure 80 b

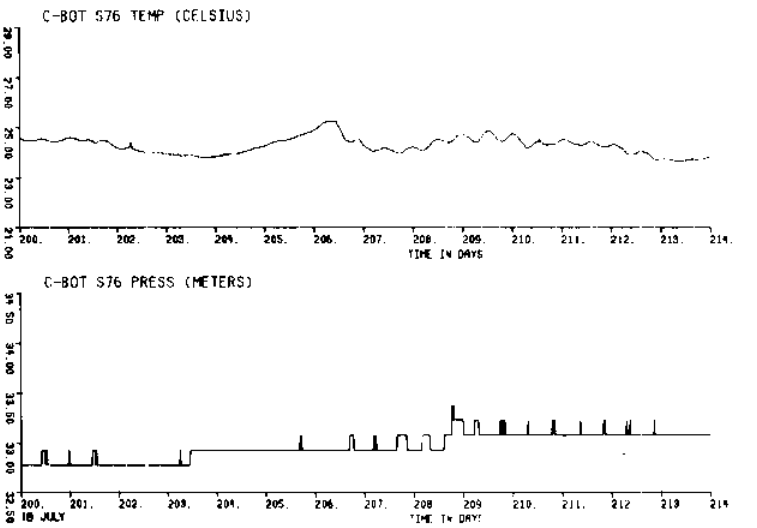

Figure 80 c

Figure 80 (a,b,c,d, e,f,g) Unfiltered temperature and pressure from meter C(Cormorant)$_{bot}$

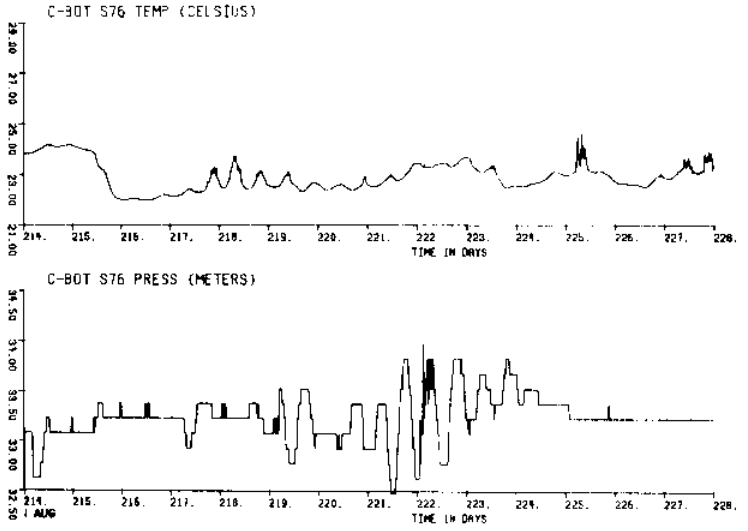

Figure 80 d

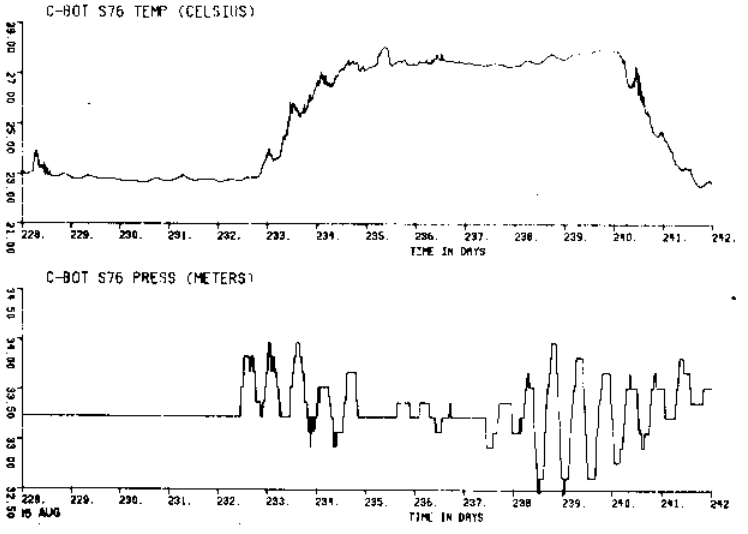

Figure 80 e

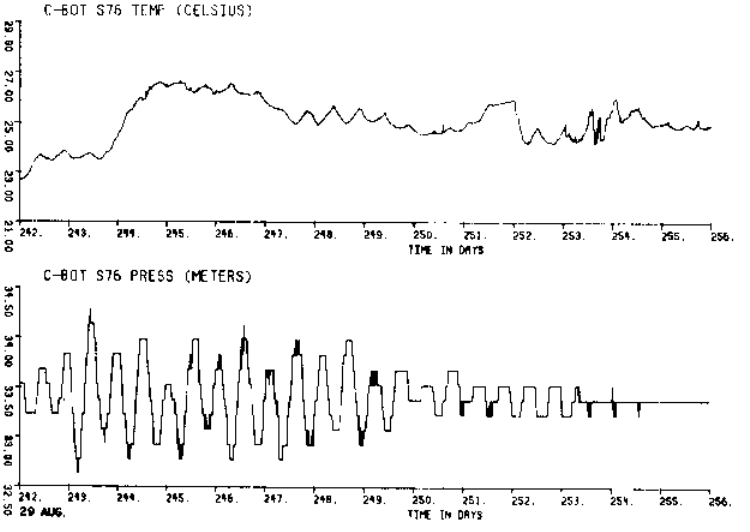

Figure 80 f

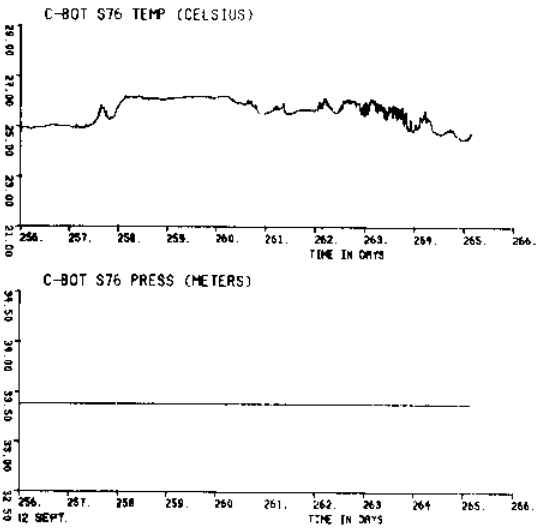
C-BOT S76 TEMP (CELSIUS)
29.00
27.00
25.00
23.00
21.00
256.
257.
258.
259.
260.
261.
262.
263.
264.
265.
266.
TIME IN DAYS
C-BOT S76 PRESS (METERS)
34.50
34.00
33.50
33.00
32.50
256.
257.
258
259.
260
261.
262.
263
264
265.
266.
12 SEPT.
TIME IN DAYS

Figure 80 g

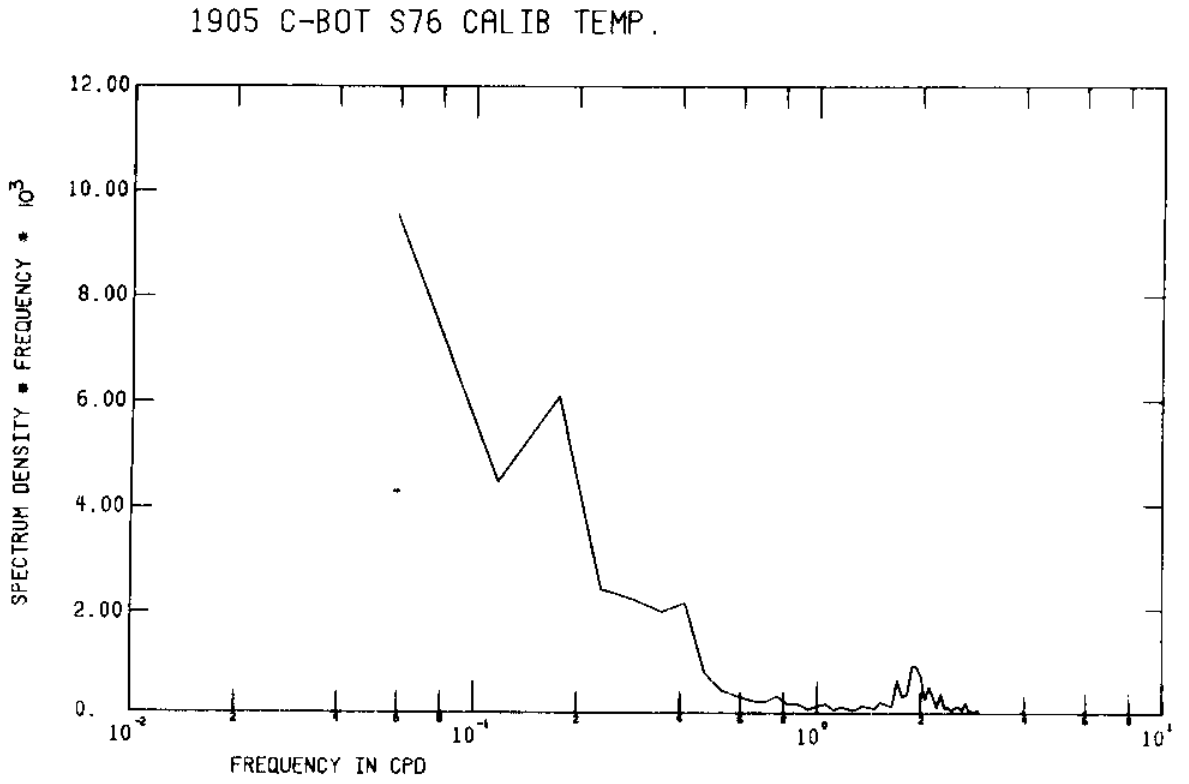

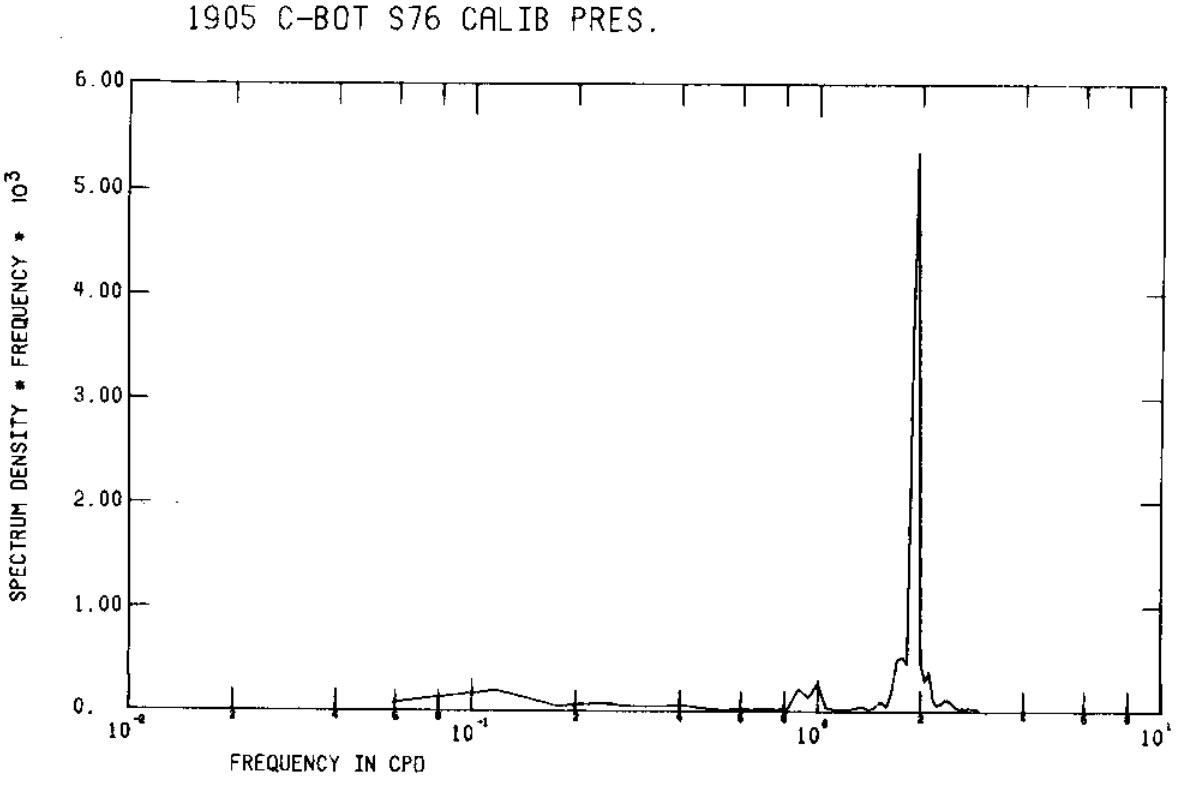

Figure 81 FFT of unfiltered temperature and pressure from meter C(Cormorant)$_{bot}$

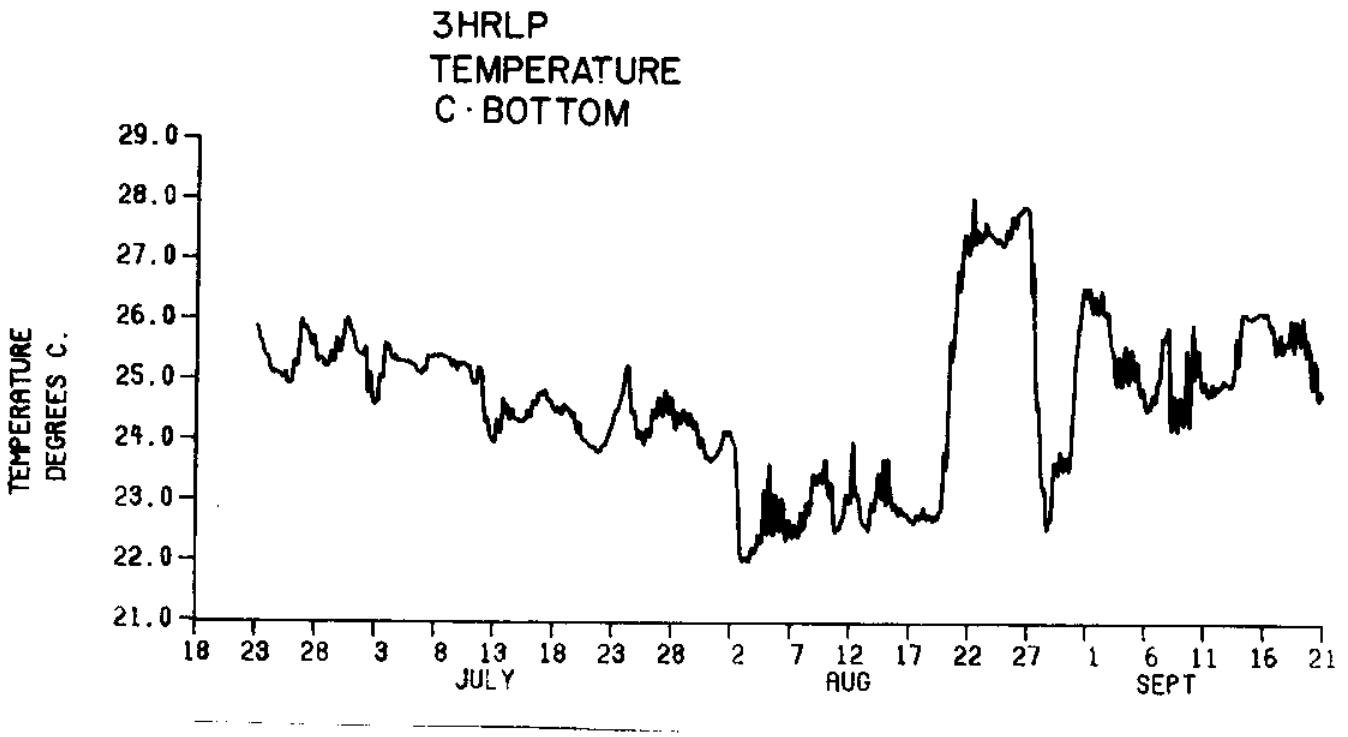

Figure 82 3HRLP temperature for C_{bot}

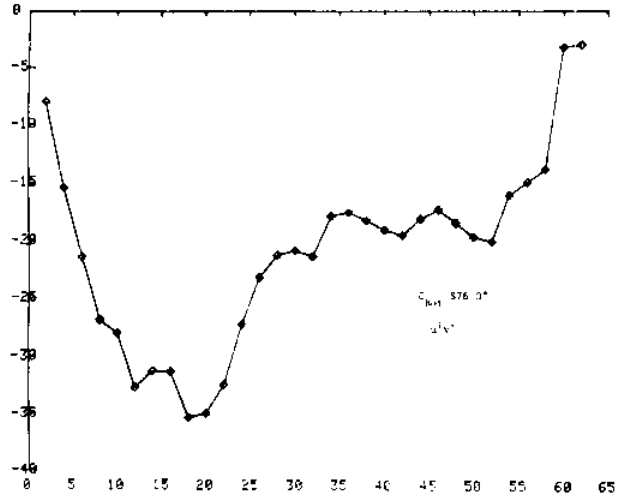

Figure 83 Momentum correlation variance in horizontal plane for C_{bot} Summer, 1976 (cumulative)

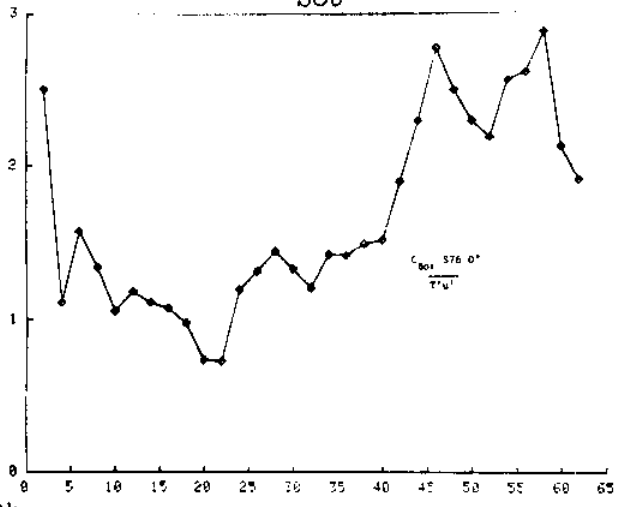

Figure 84 Heat correlation variance in x-direction for C_{bot} Summer, 1976 (cumulative)

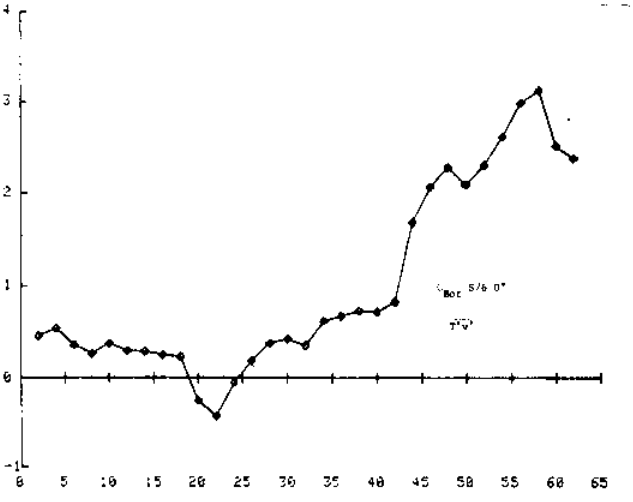

Figure 85 Heat correlation variance in y-direction for C_{bot} Summer, 1976 (cumulative)

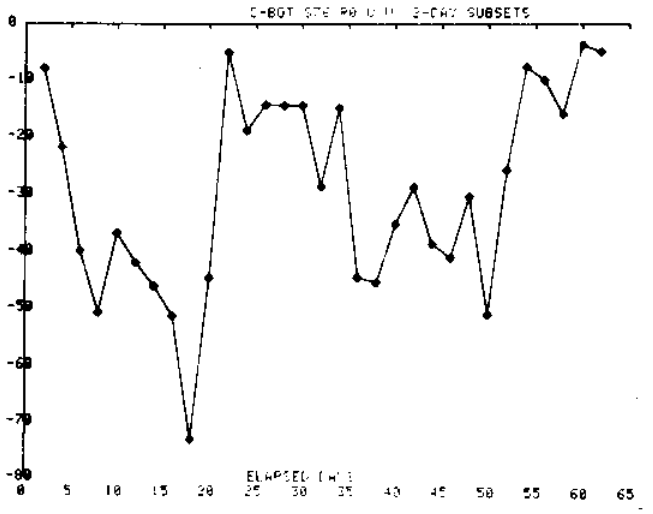

Figure 86 Momentum correlation variance in the horizontal plane for C_{bot} Summer, 1976 (2-day subset)

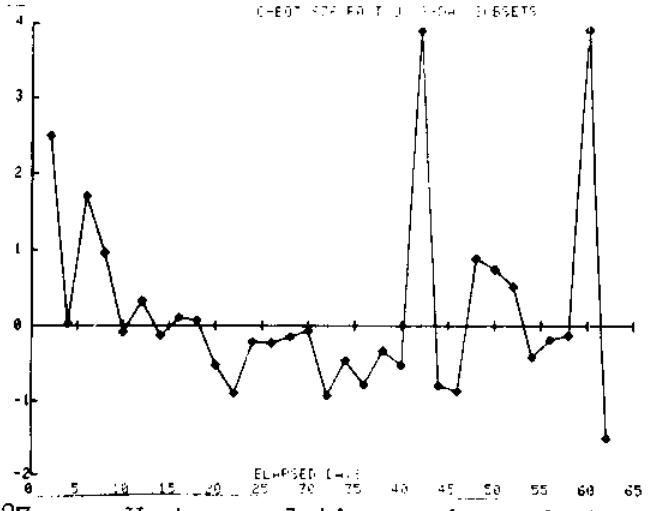

Figure 87 Heat correlation variance in the x-direction for C_{bot} Summer, 1976 (2-day subset)

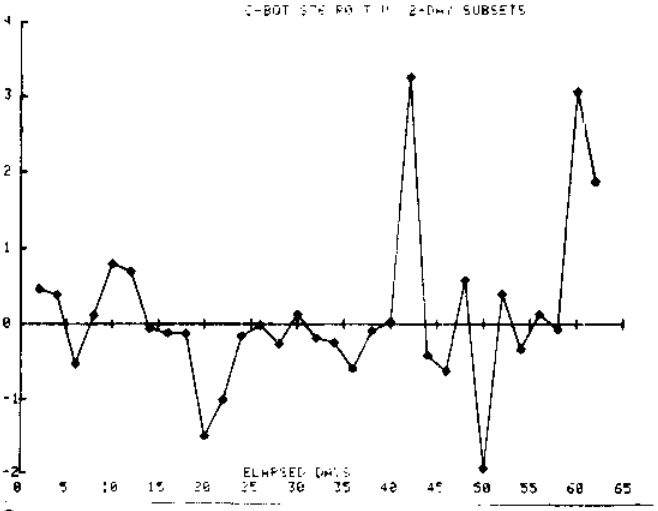

Figure 88 Heat correlation variance in the y-direction for C_{bot} Summer, 1976 (2-day subset)

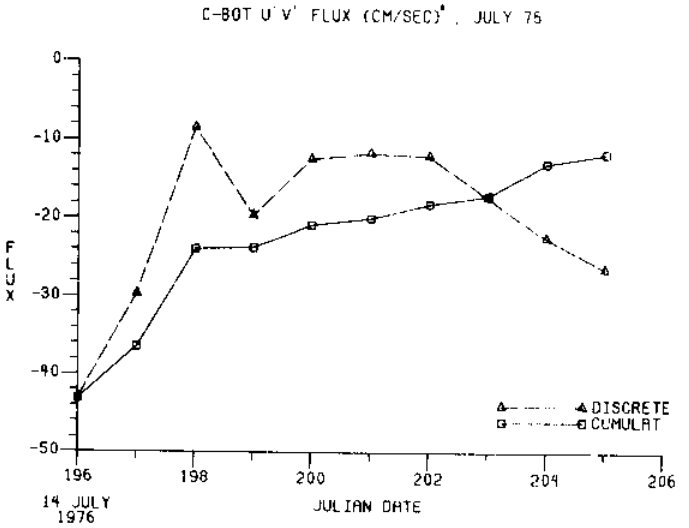

Figure 89 Momentum correlation variance in horizontal plane for C_{bot}, July 14-23, 1976

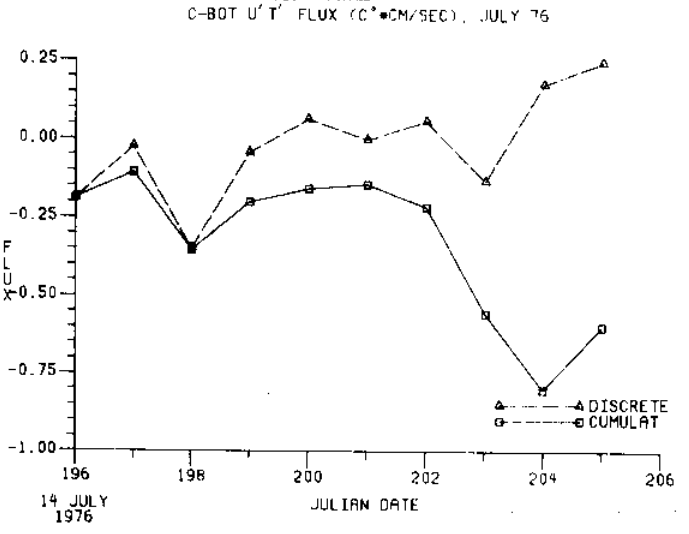

Figure 90 Heat correlation variance in x-direction for C_{bot}, July 14-23, 1976

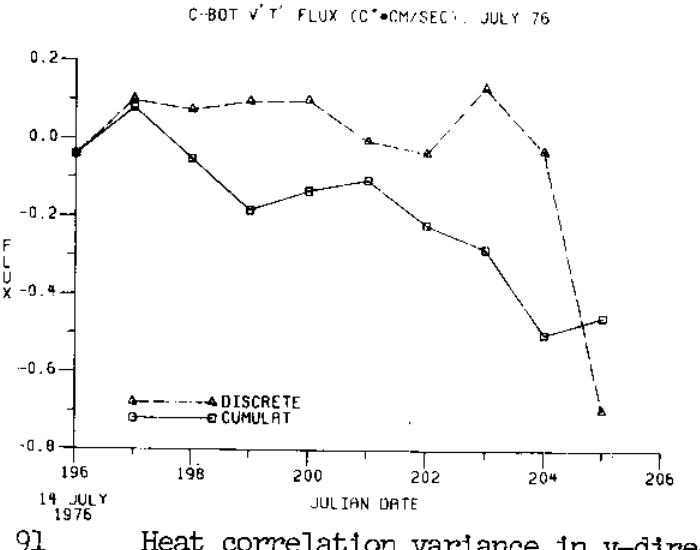

Figure 91 Heat correlation variance in y-direction for C_{bot}, July 14-23, 1976

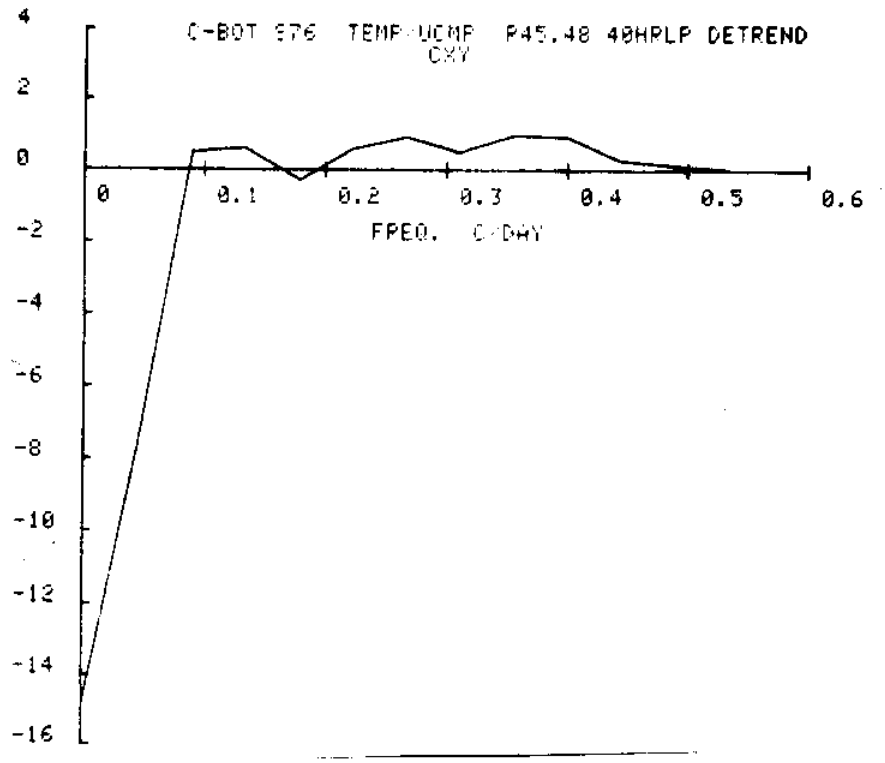

Figure 92 Cospectra of temperature vs. u-component for meter C_{bot}

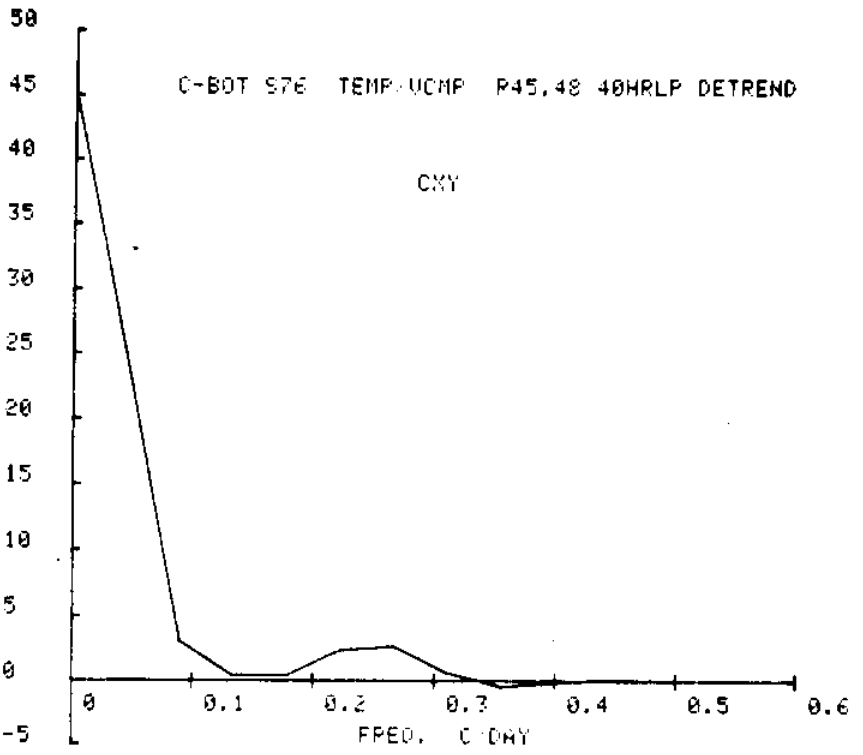

Figure 93 Cospectra of temperature vs. v-component for meter C_{bot}

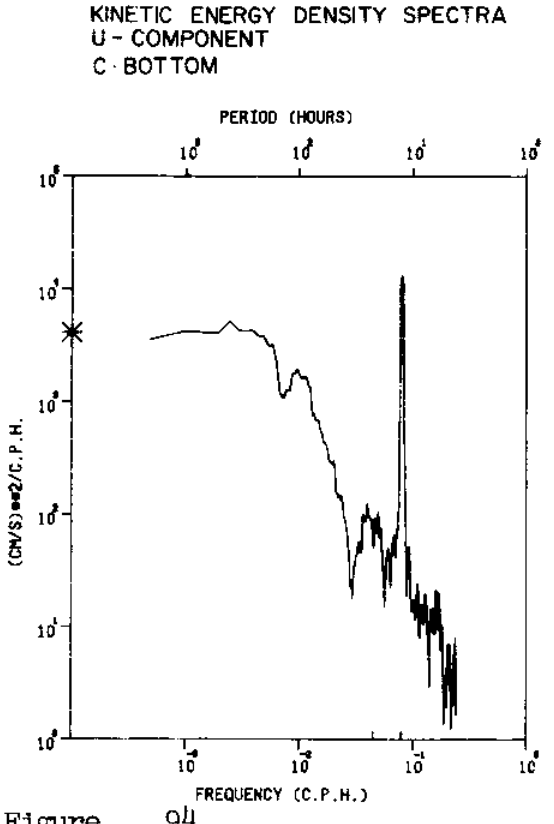

Figure 94
Kinetic energy density spectra for current velocity, u-component, C_{bot}

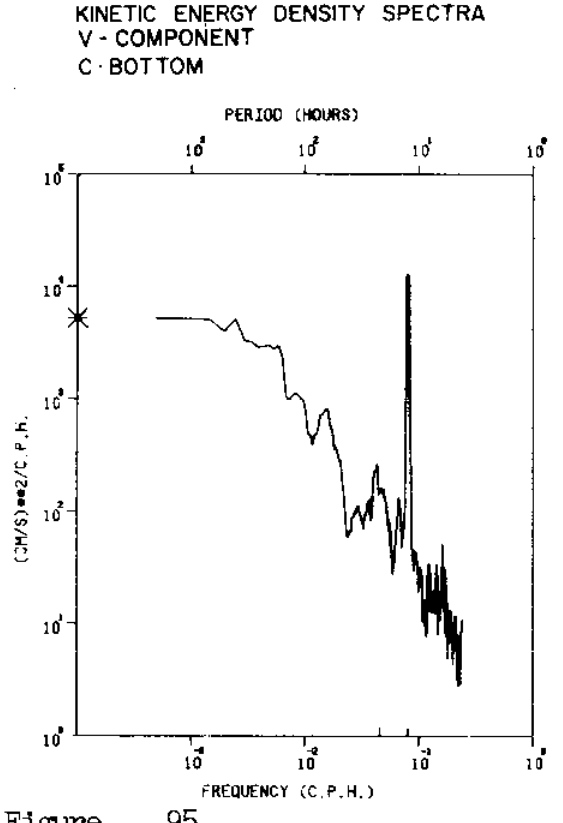

Figure 95
Kinetic energy density spectra for current velocity, v-component, C_{bot}

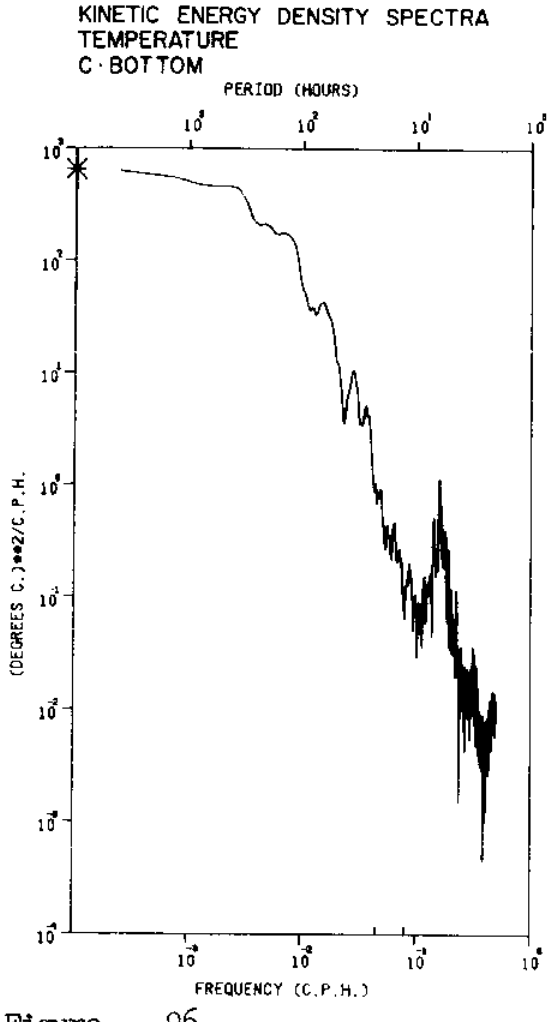

Figure 96
Kinetic energy density spectra for temperature at C_{bot}

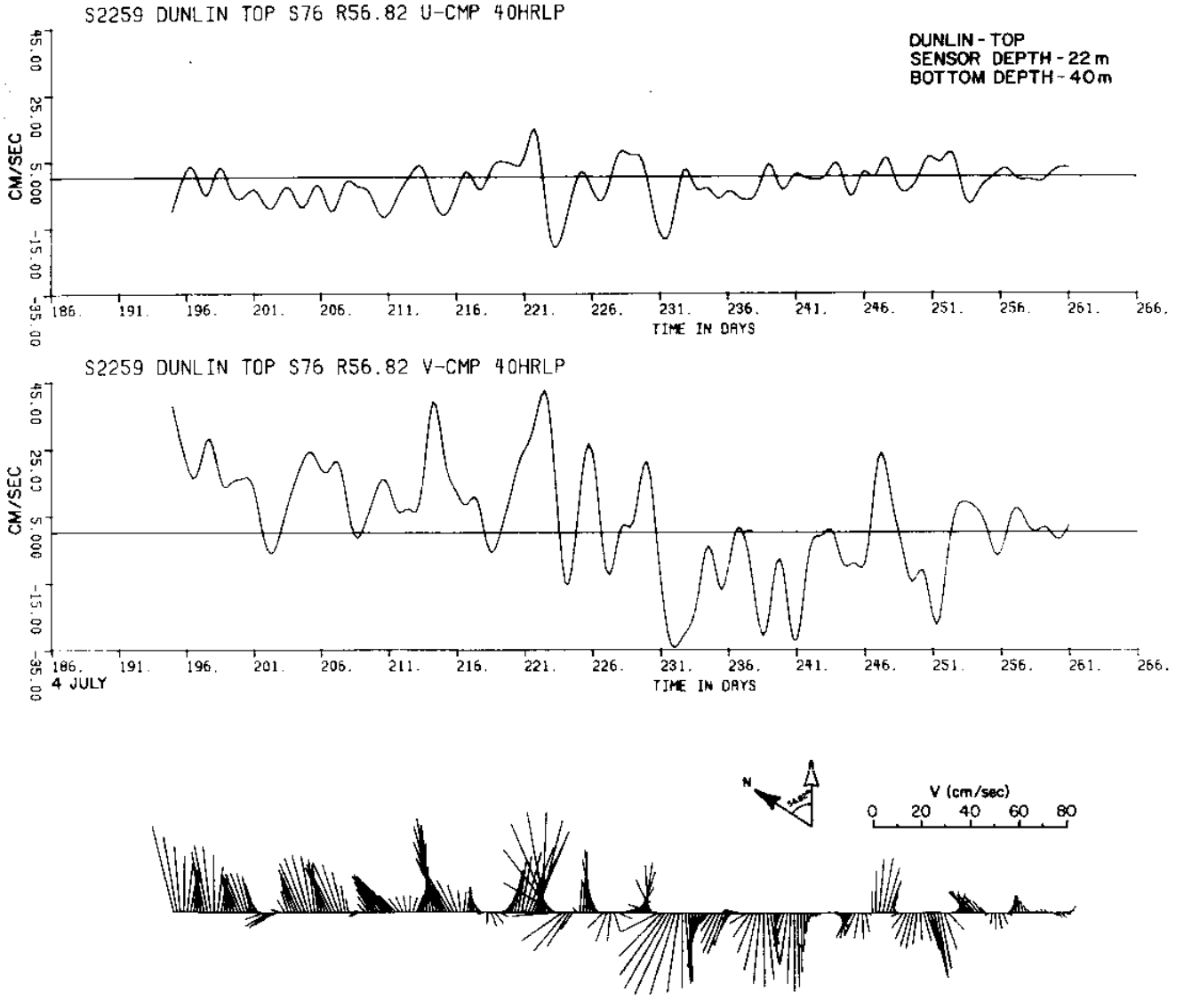

Figure 97 Low pass current velocity components and vectors from meter $D(Dunlin)_{top}$

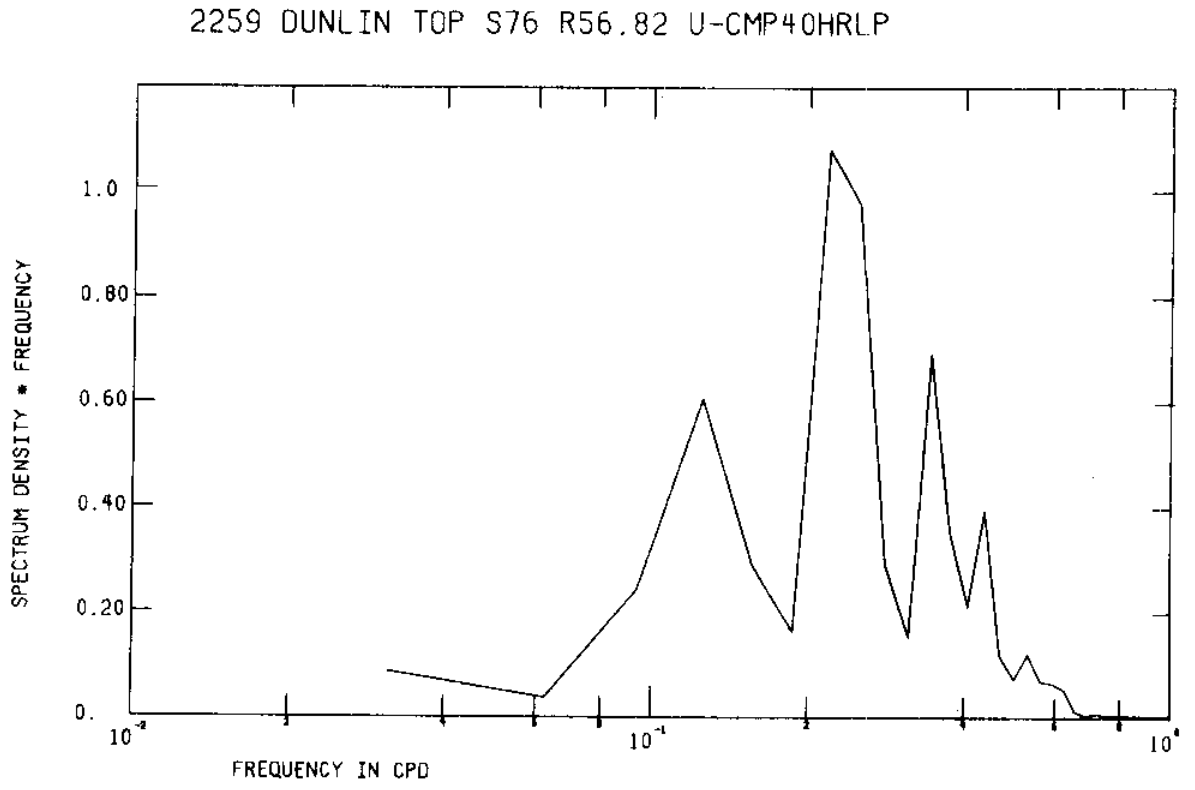

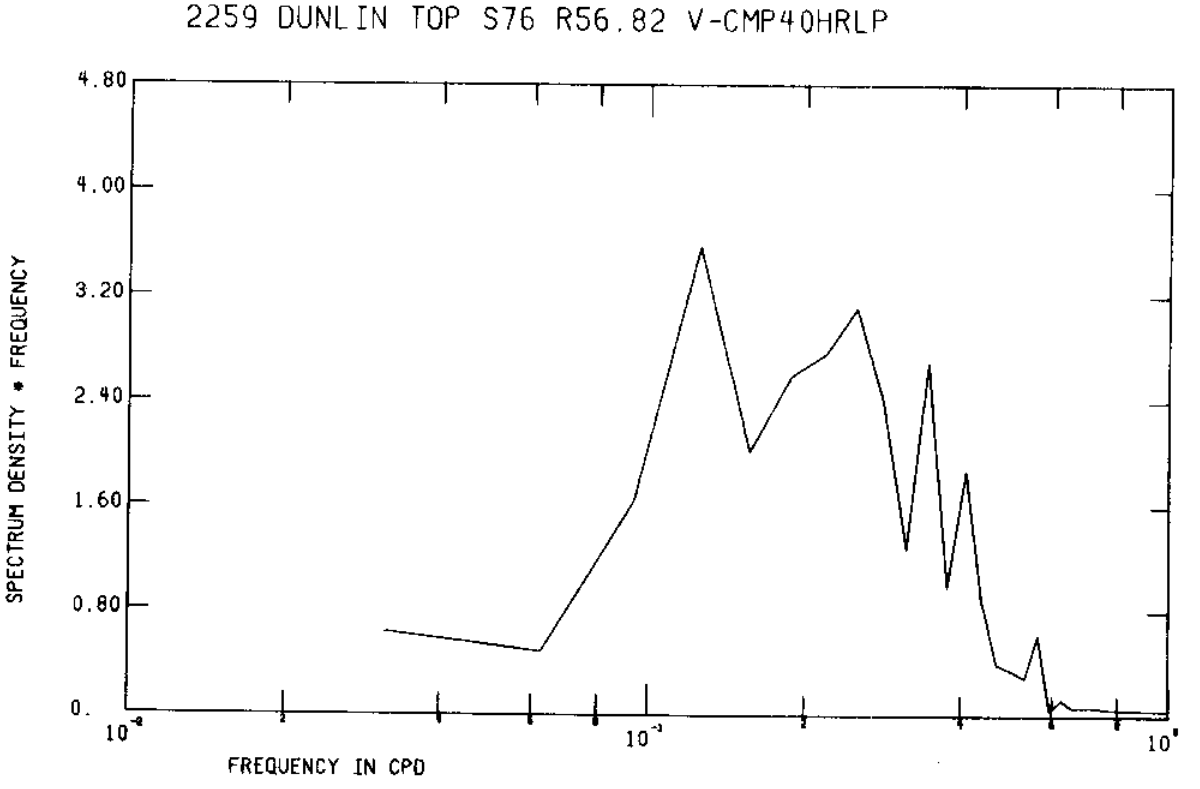

Figure 98 FFT of low pass current velocity components from meter D(Dunlin)$_{top}$

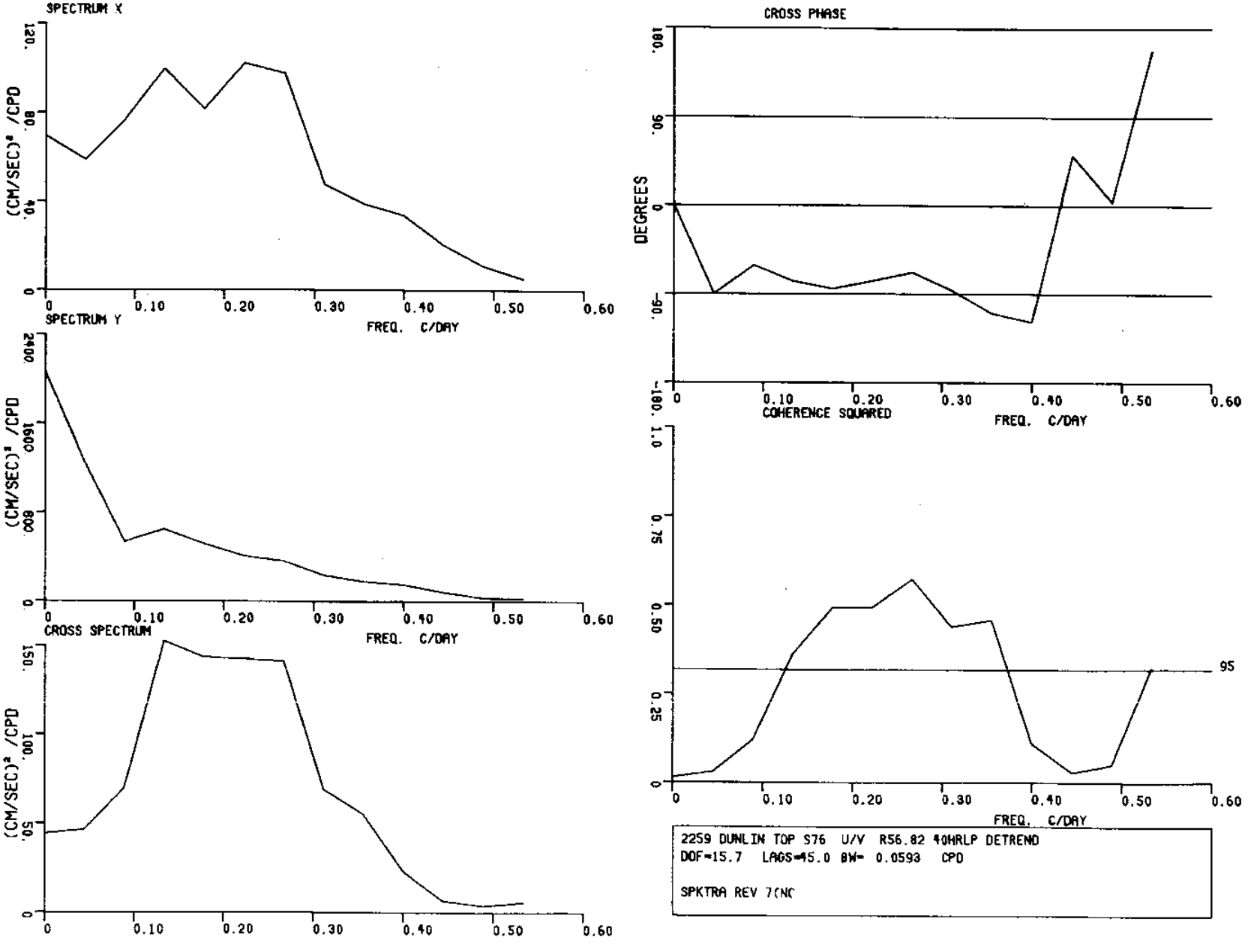

Figure 99 Spectra of low pass current velocity components from meter $D(Dunlin)_{top}$

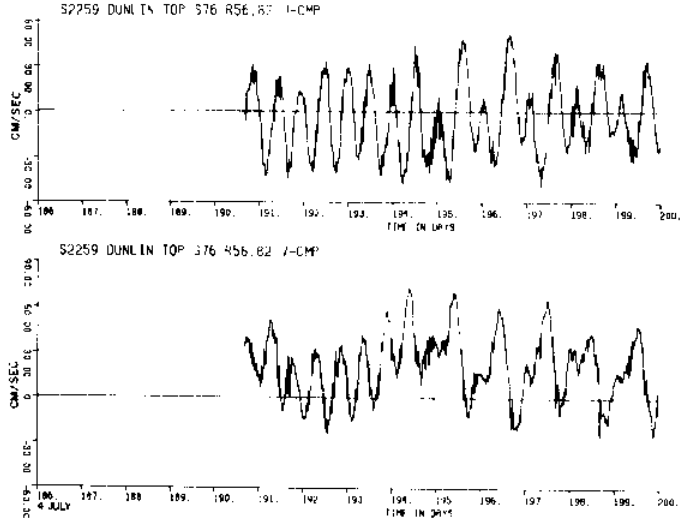

Figure 100 a

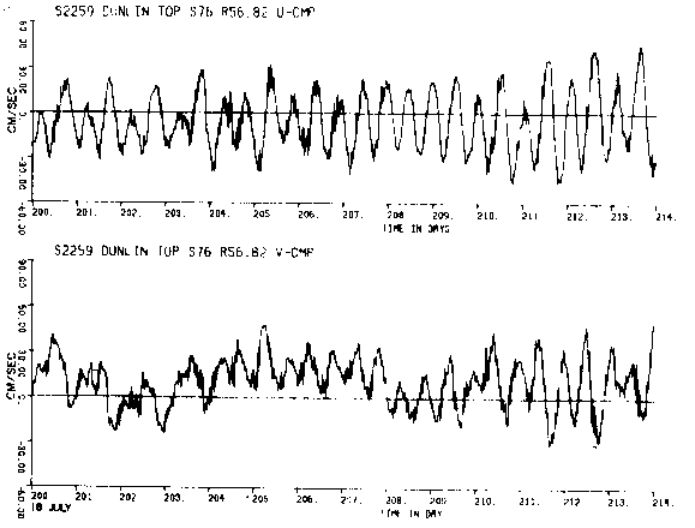

Figure 100 b

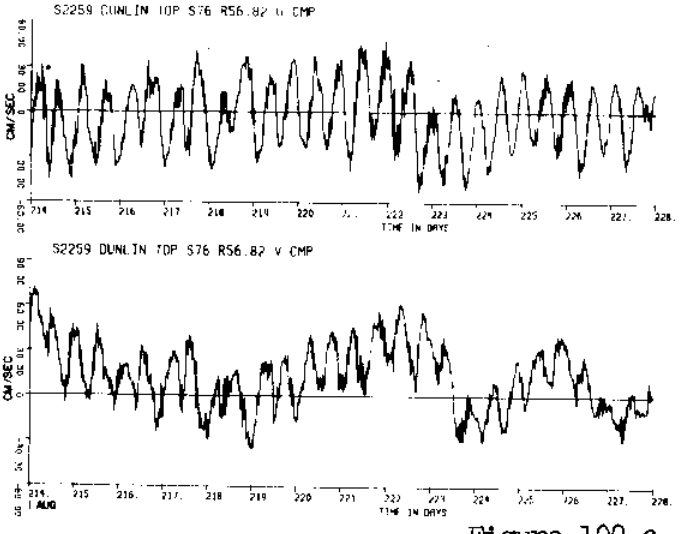

Figure 100 c

Figure 100 (a,b,c, d,e,f) Unfiltered current velocity components from meter D(Dunlin)$_{top}$

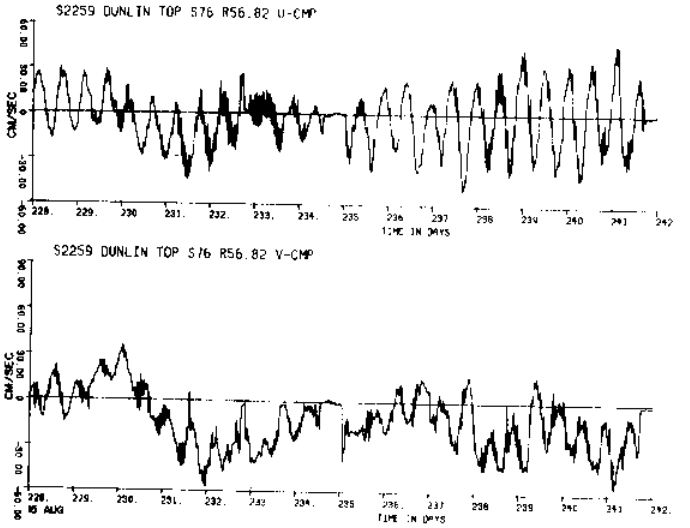

Figure 100 d

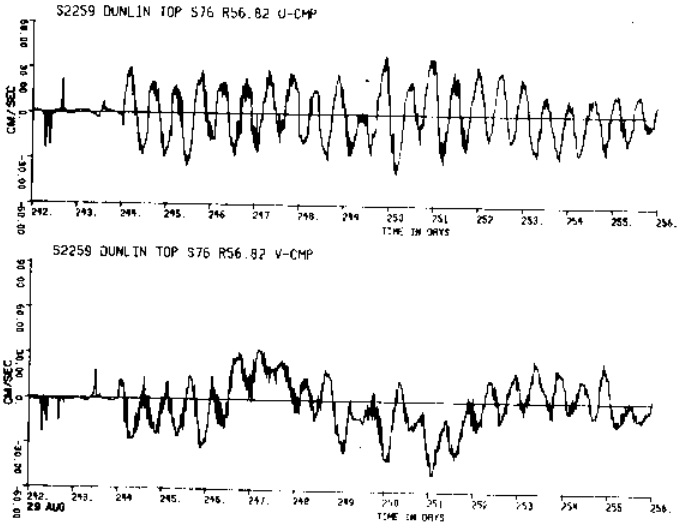

Figure 100 e

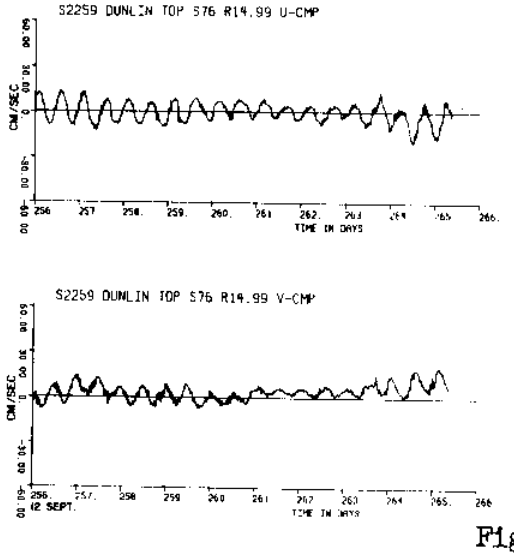

Figure 100 f

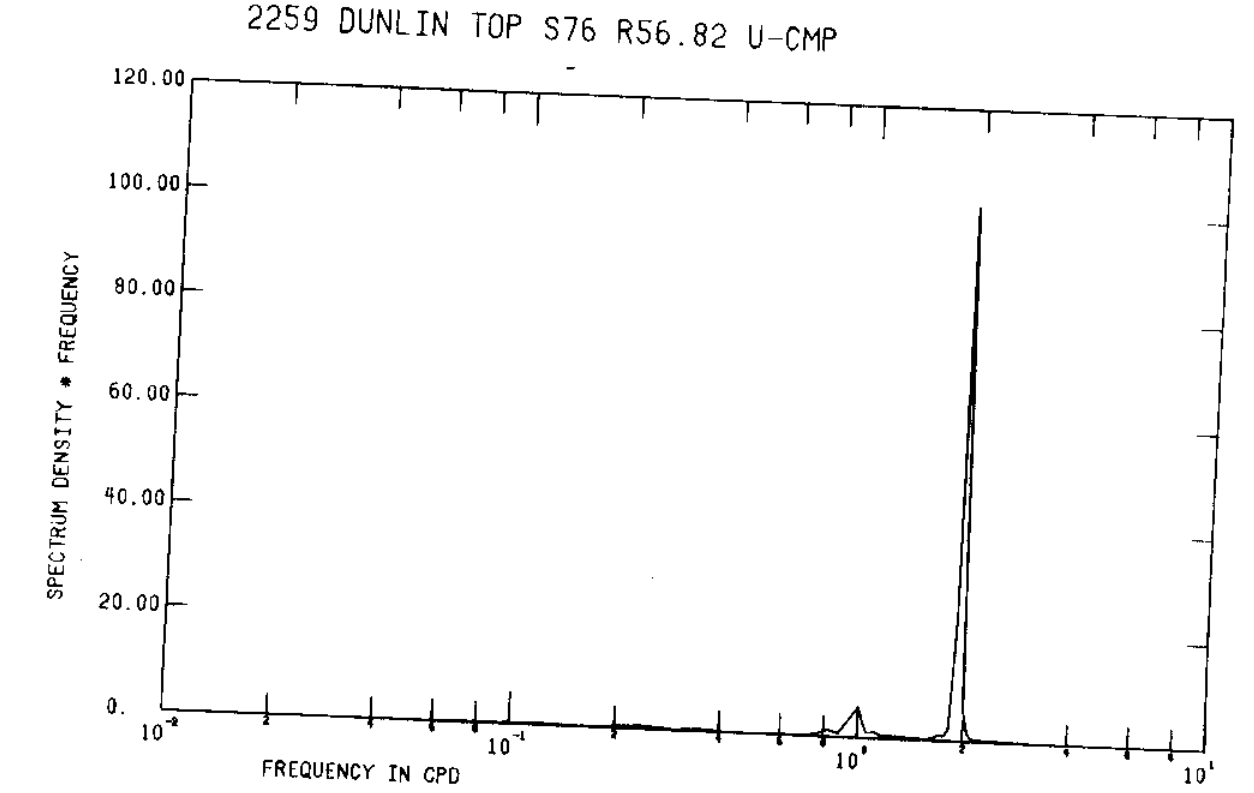

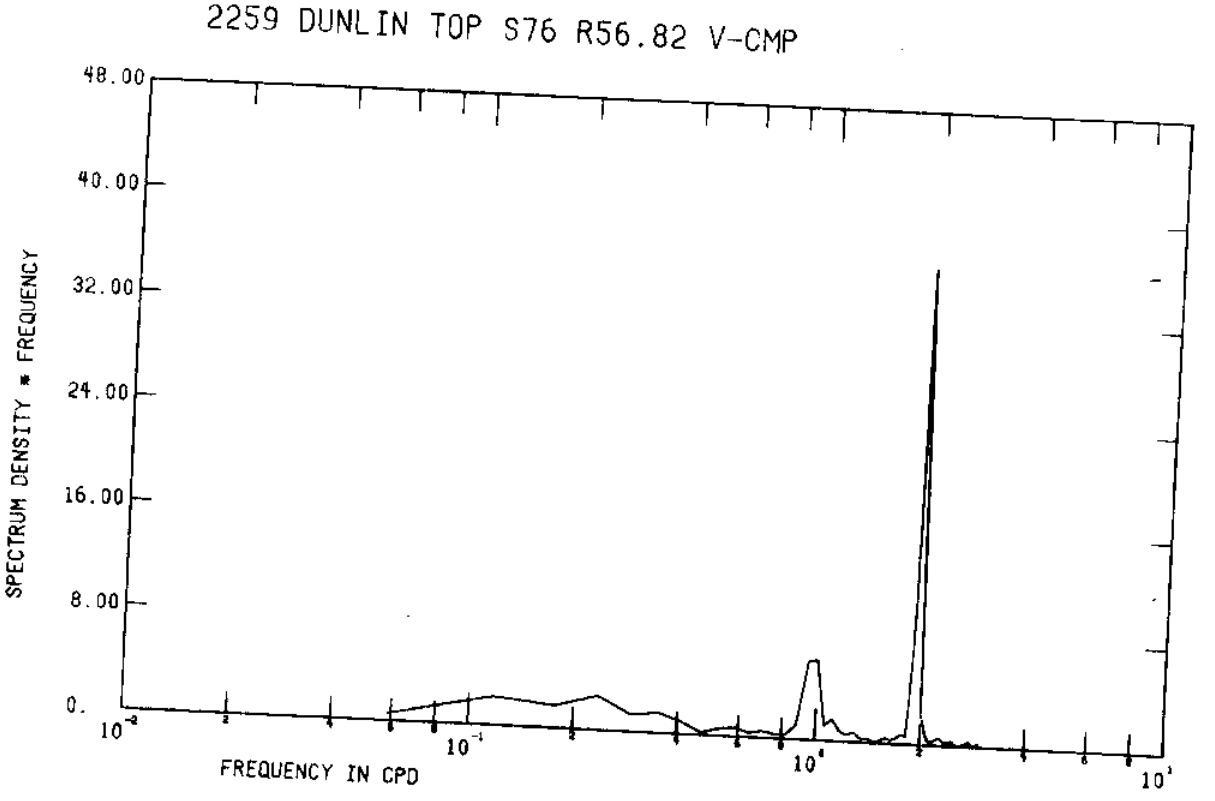

Figure 101 FFT of unfiltered current velocity components from meter D(Dunlin)$_{top}$

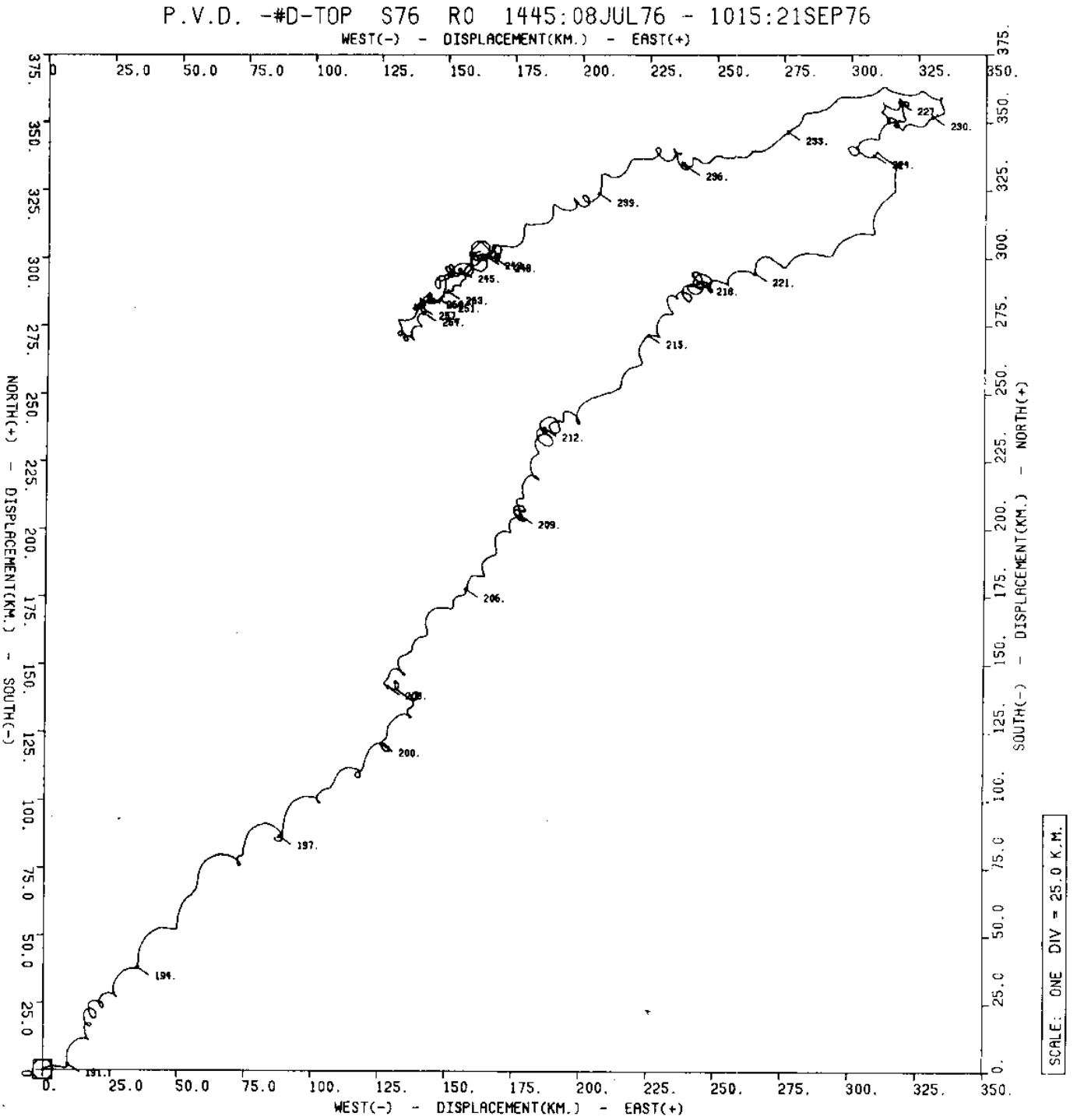

Figure 102 a

Figure 102 (a,b,c) Progressive vector diagrams of unfiltered current velocity from meter D(Dunlin)$_{top}$

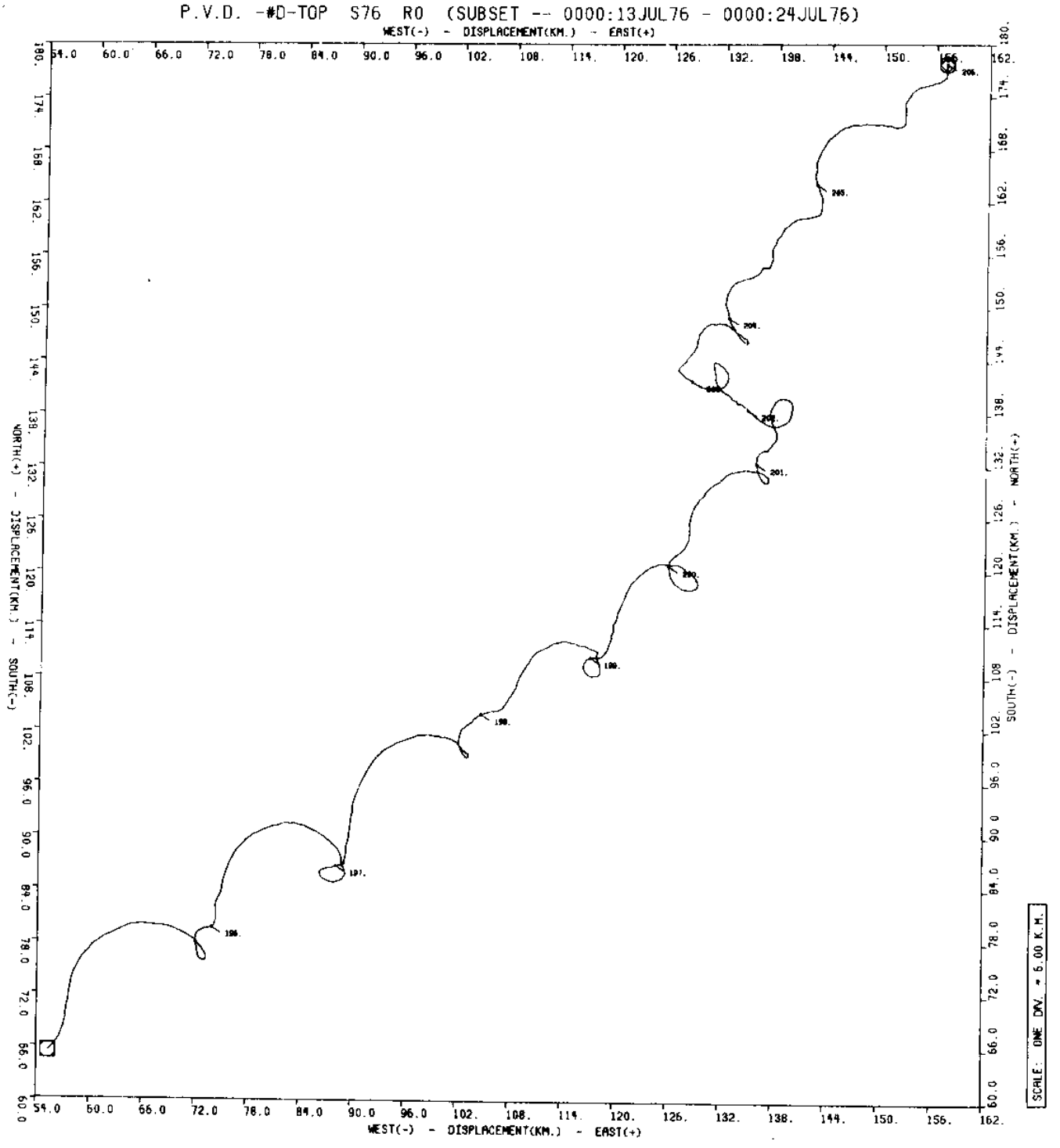
P.V.D. -#D-TOP S76 R0 (SUBSET -- 0000:13JUL76 - 0000:24JUL76)
WEST(-) - DISPLACEMENT(KM.) - EAST(+)
NORTH(+) - DISPLACEMENT(KM.) - SOUTH(-)
SCALE: ONE DIV. = 6.00 K.M.

Figure 102 b

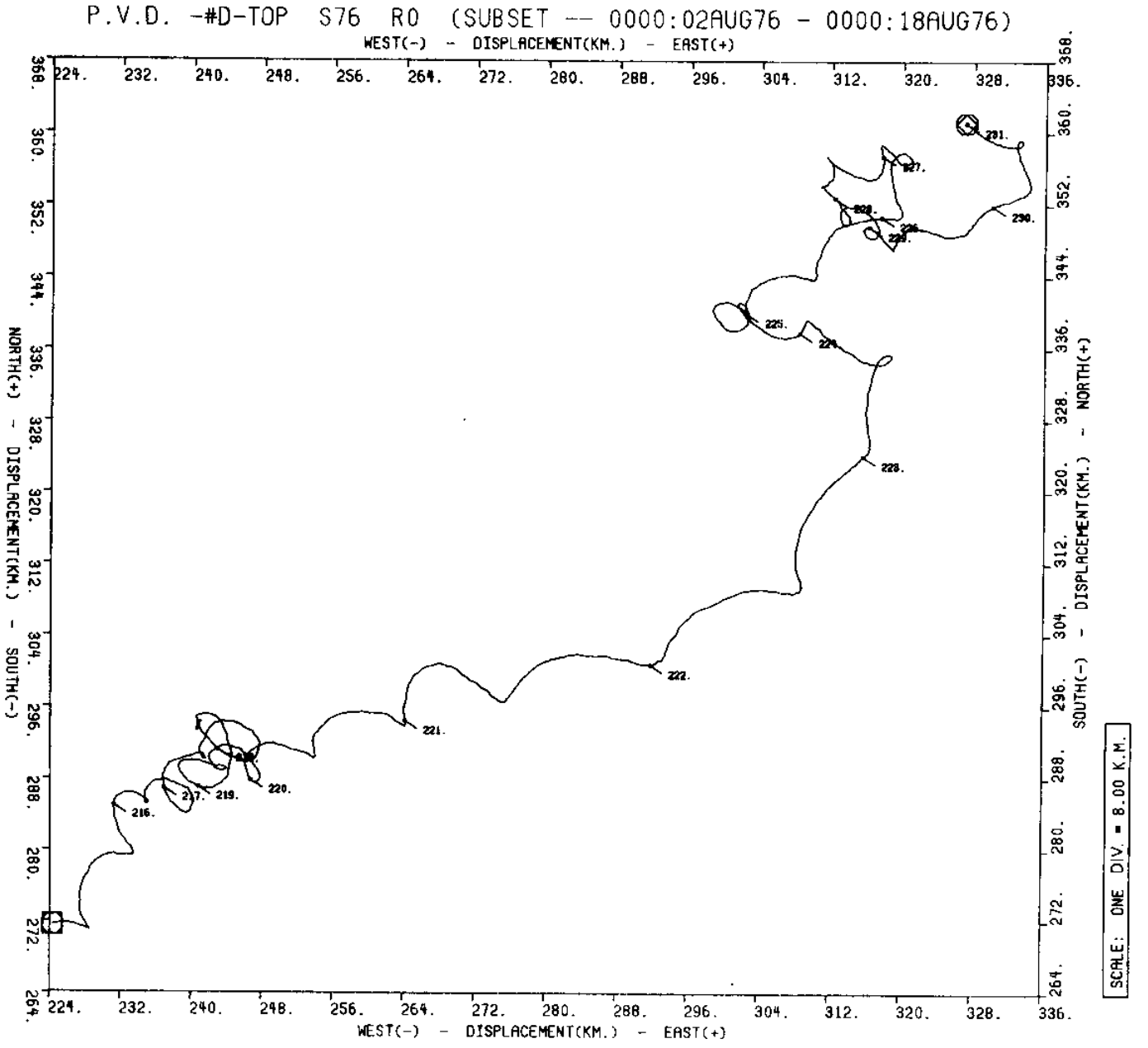
P.V.D. -#D-TOP S76 R0 (SUBSET -- 0000:02AUG76 - 0000:18AUG76)
WEST(-) - DISPLACEMENT(KM.) - EAST(+)
NORTH(+) - DISPLACEMENT(KM.) - SOUTH(-)
SCALE: ONE DIV. = 8.00 K.M.

Figure 102 c

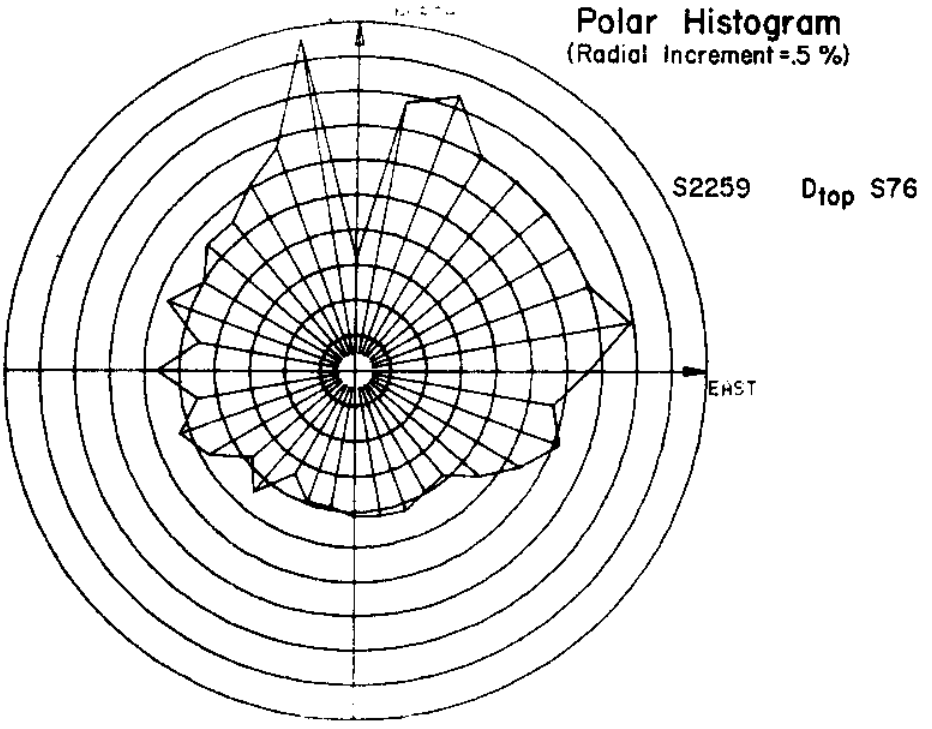

Figure 103 Histogram from meter D(Dunlin)$_{top}$

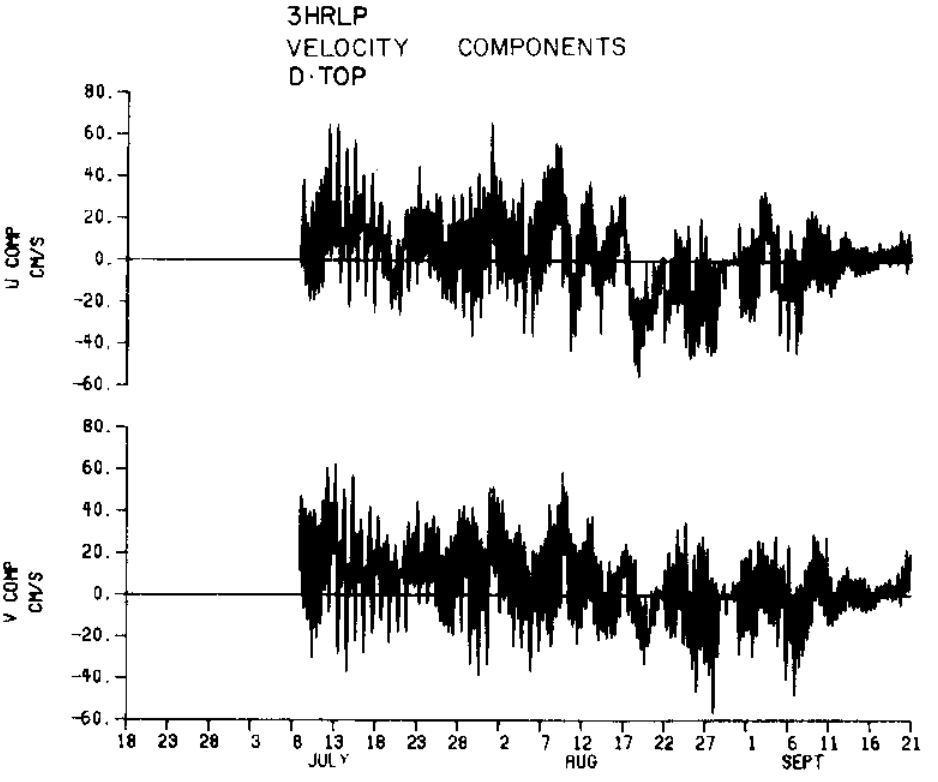

Figure 104 3HRLP velocity components for D$_{top}$

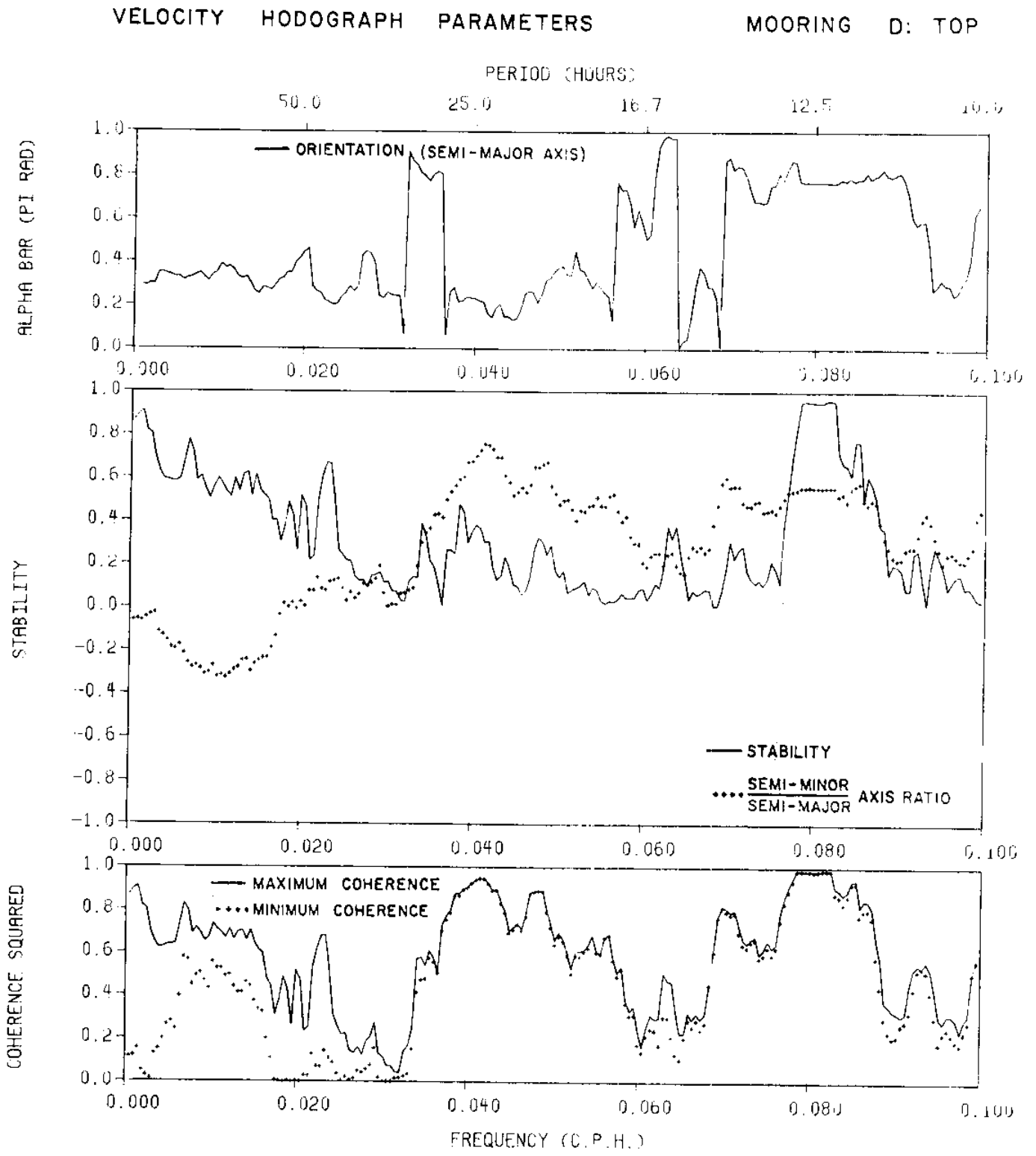

Figure 105 Hodograph parameters from meter D(Dunlin)$_{top}$

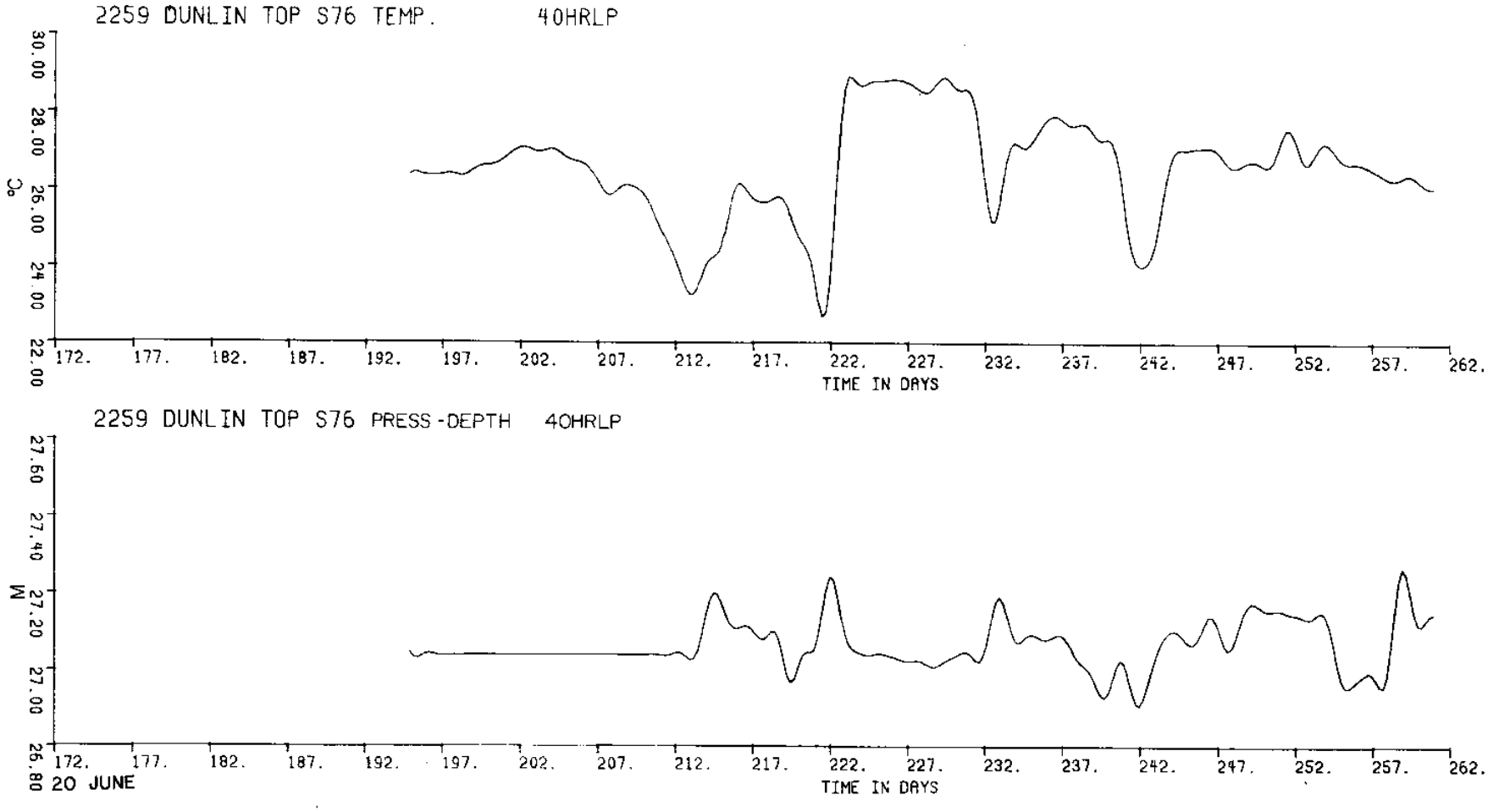

Figure 106 Low pass temperature and pressure from meter $D(Dunlin)_{top}$

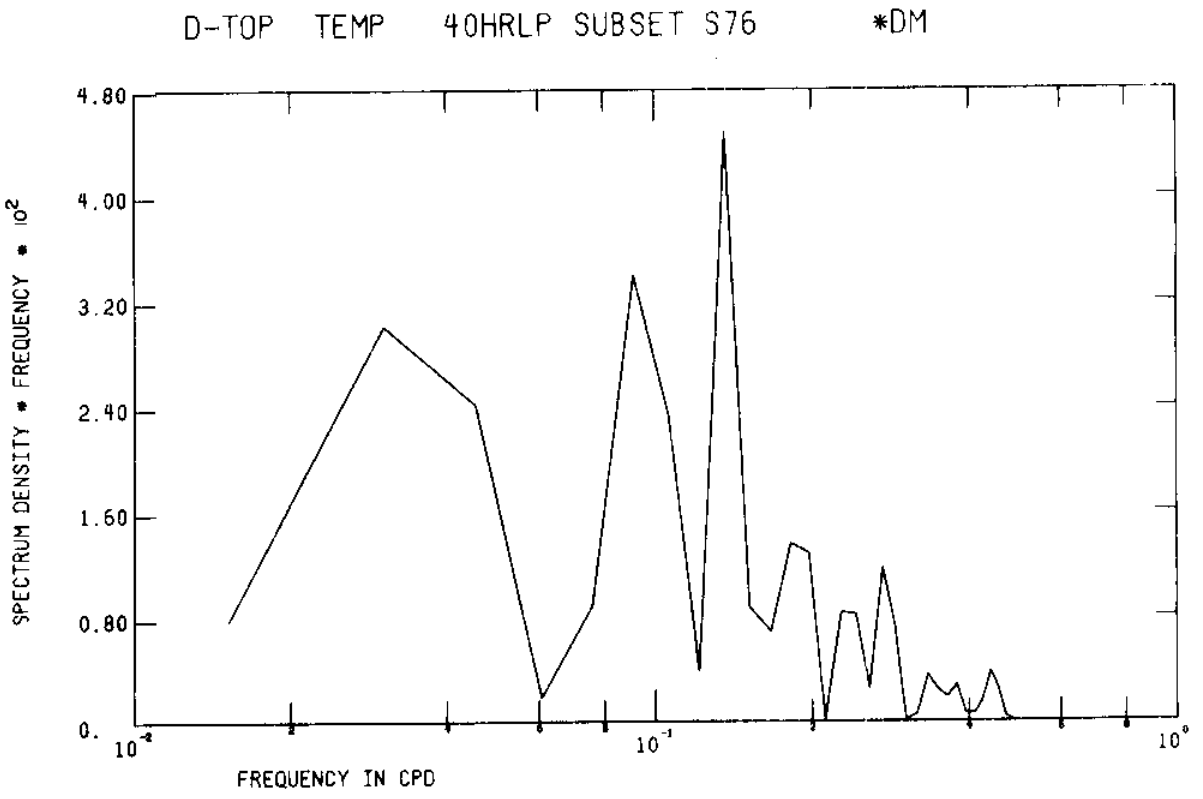

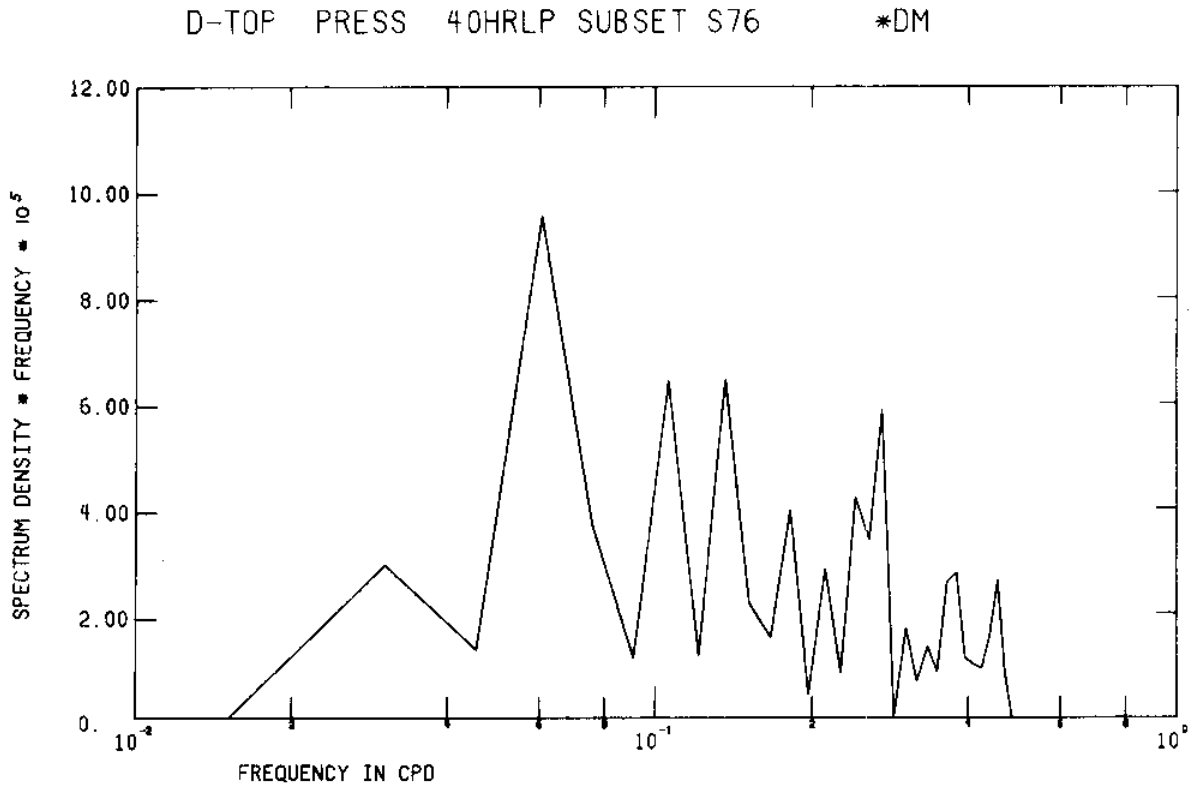

Figure 107 FFT of low pass temperature and pressure from meter $D(Dunlin)_{top}$

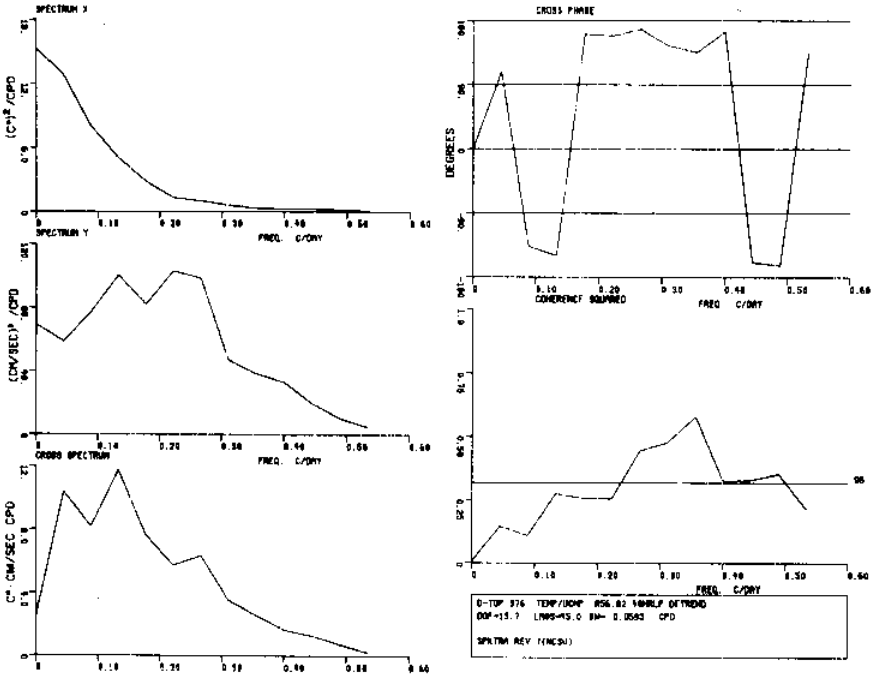

Figure 108 Spectra of temperature and the low pass current velocity u component, both from meter $D(Dunlin)_{top}$

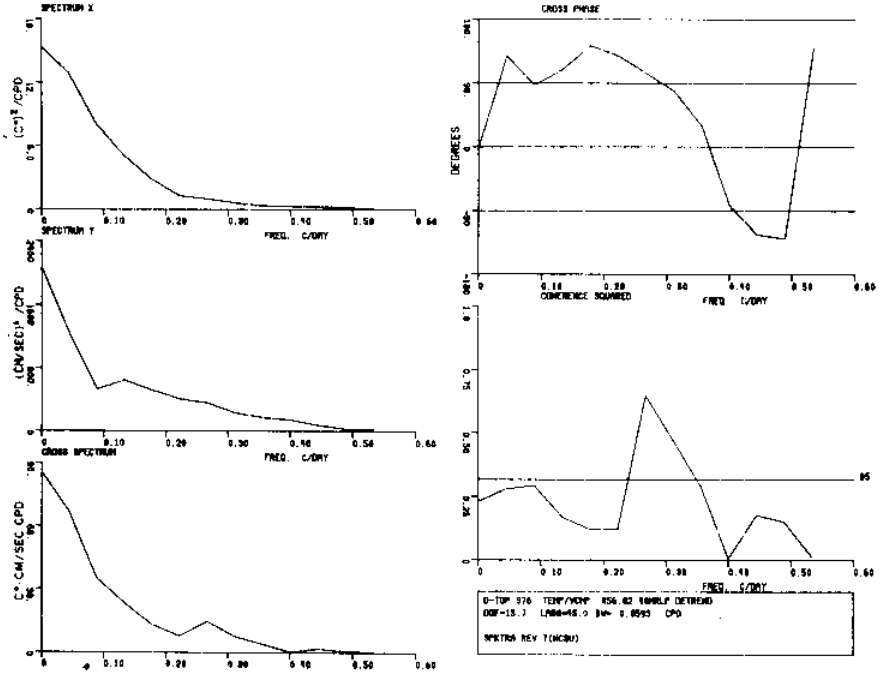

Figure 109 Spectra of temperature and the low pass current velocity v component, both from meter $D(Dunlin)_{top}$

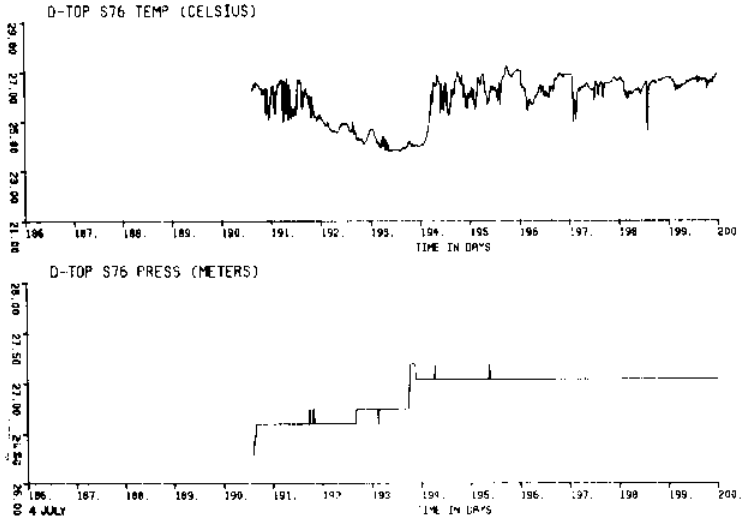

Figure 110 a

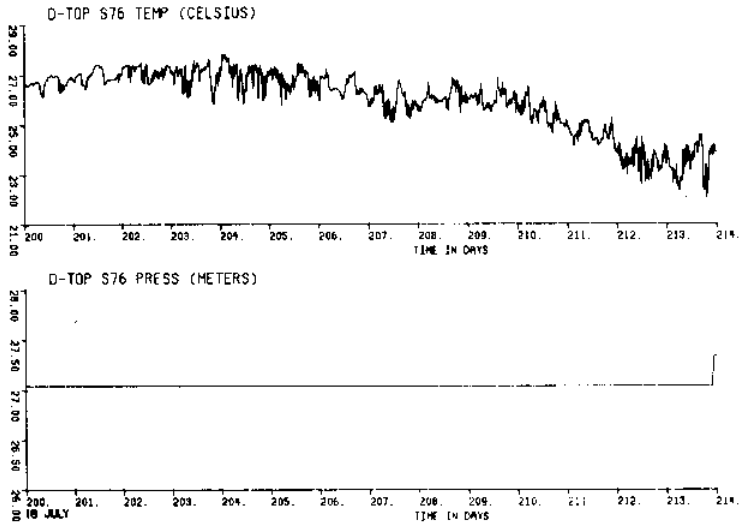

Figure 110 b

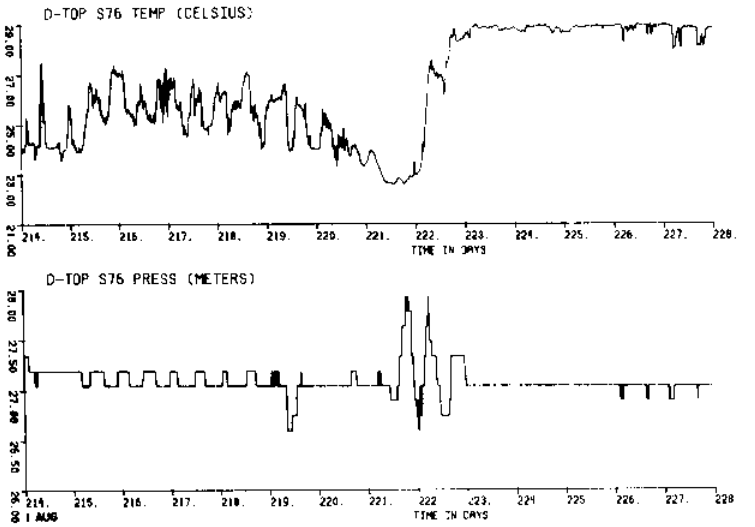

Figure 110 c

Figure 110 (a,b,c, d,e,f) Unfiltered temperature and pressure from meter $D(Dunlin)_{top}$

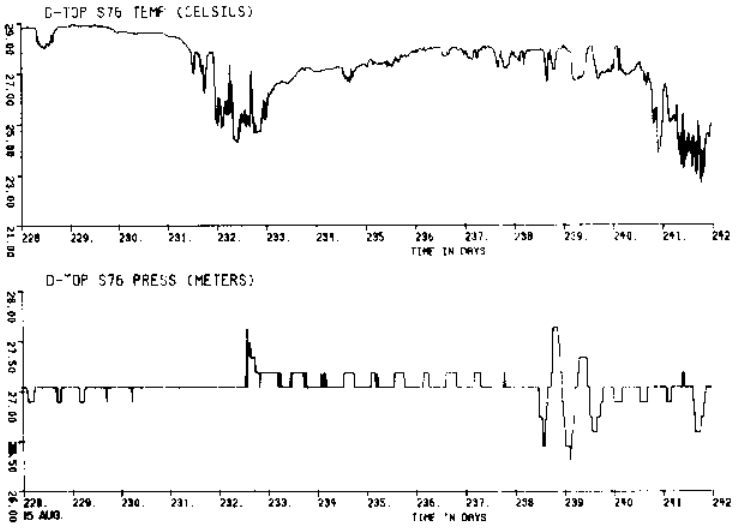

Figure 110 d

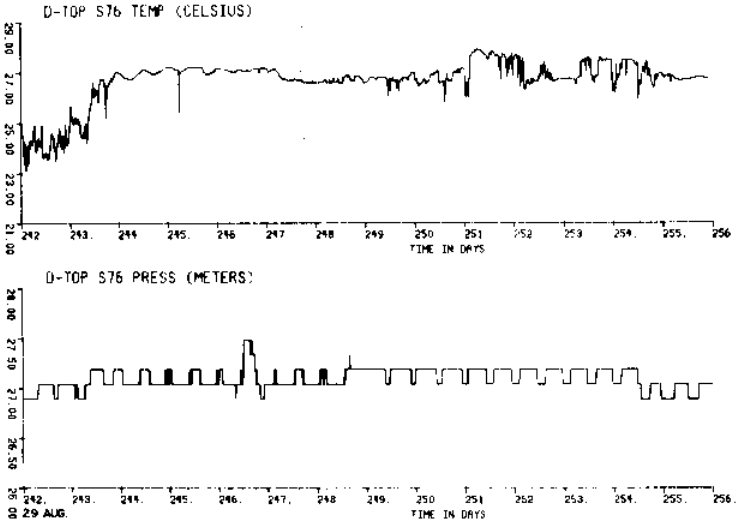

Figure 110 e

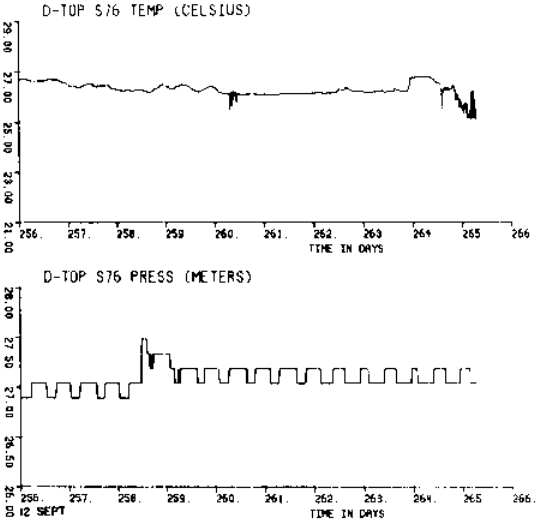

Figure 110 f

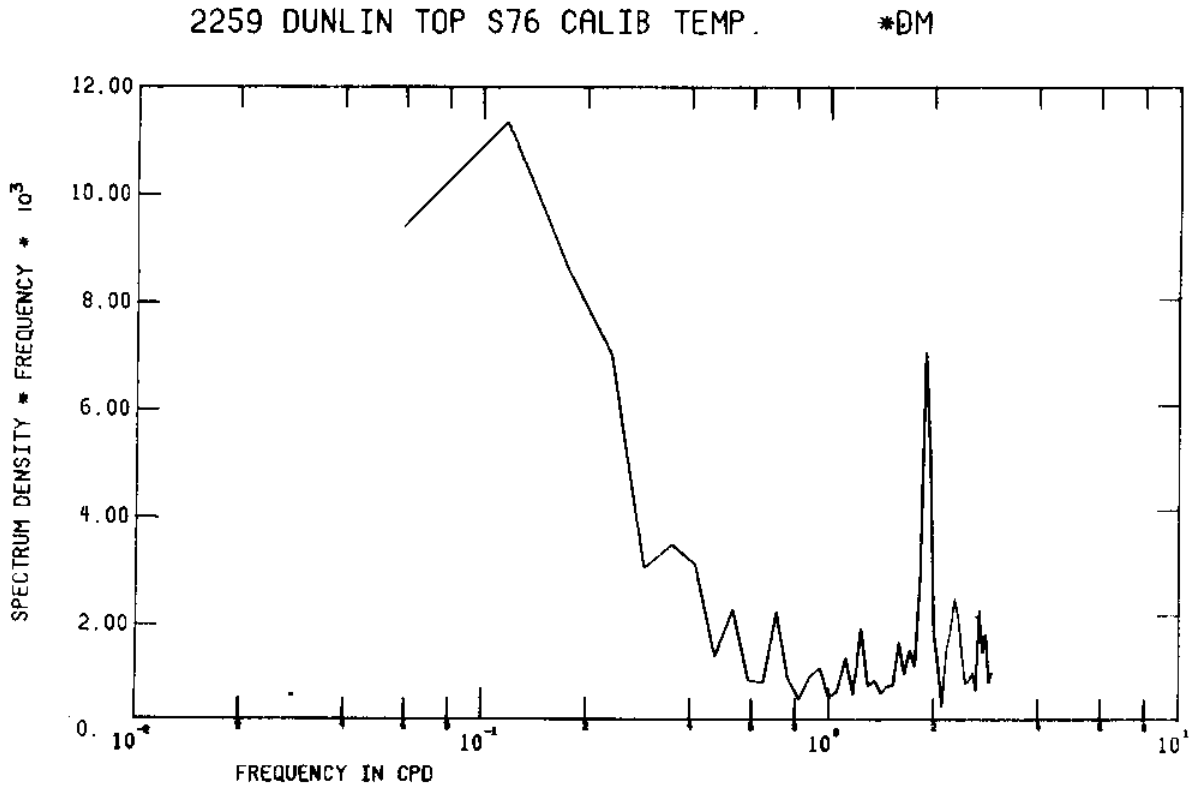

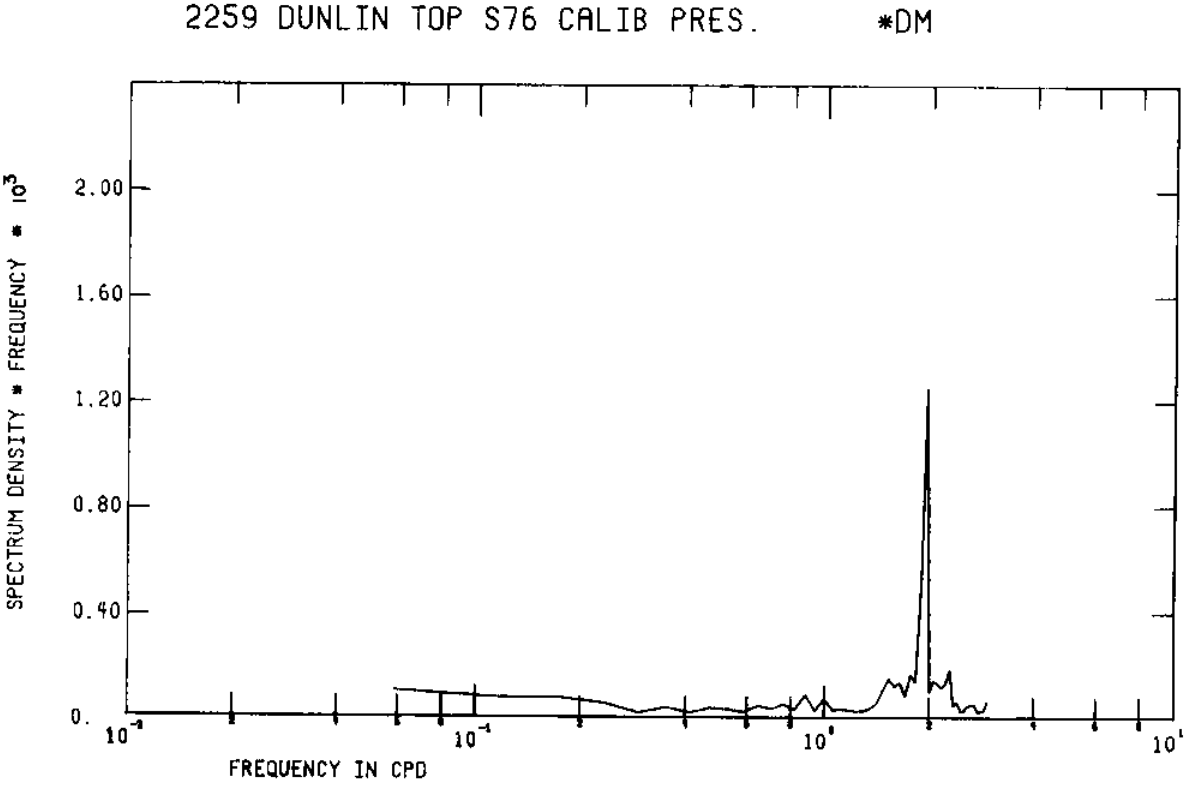

Figure 111 FFT of unfiltered temperature and pressure from meter $D(Dunlin)_{top}$

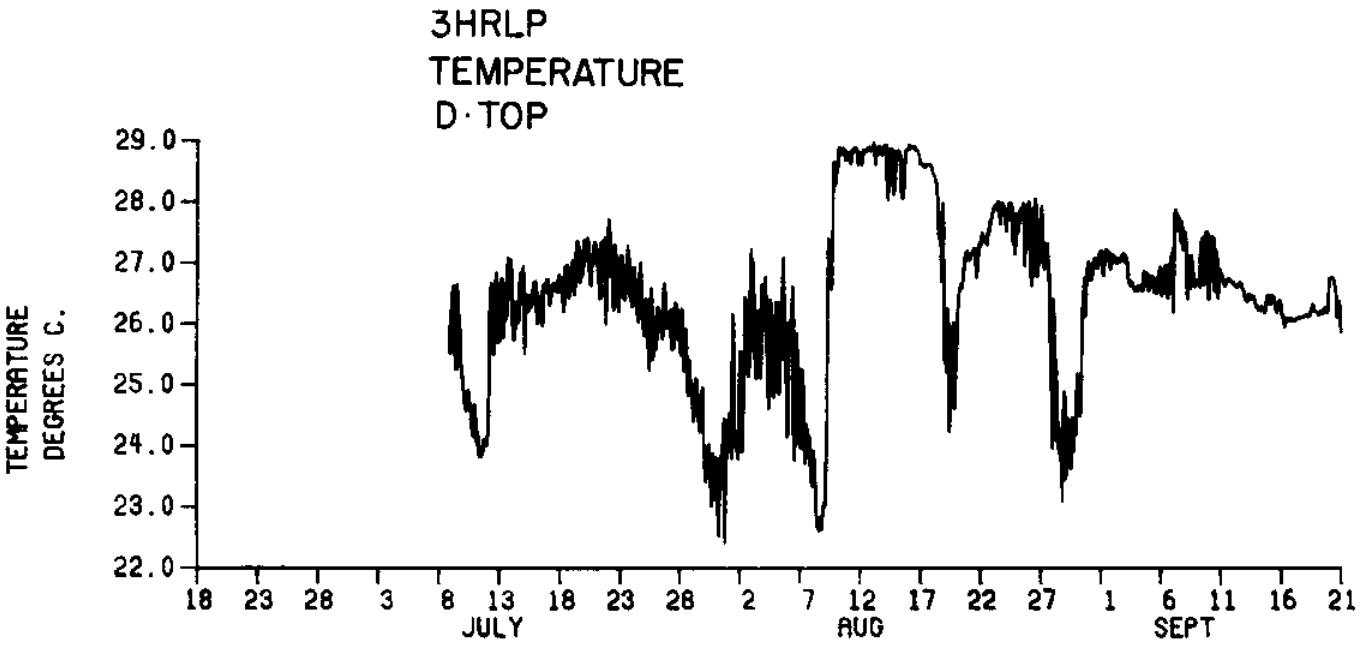

Figure 112 3HRLP temperature for D_{top}

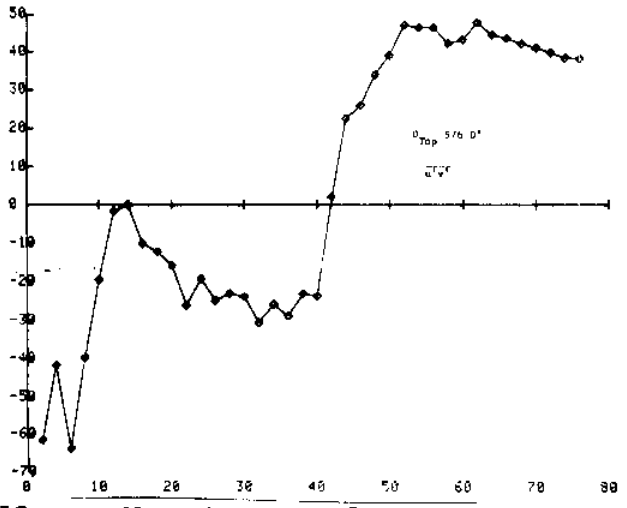

Figure 113 Momentum correlation variance in horizontal plane for D_{top} Summer, 1976 (cumulative)

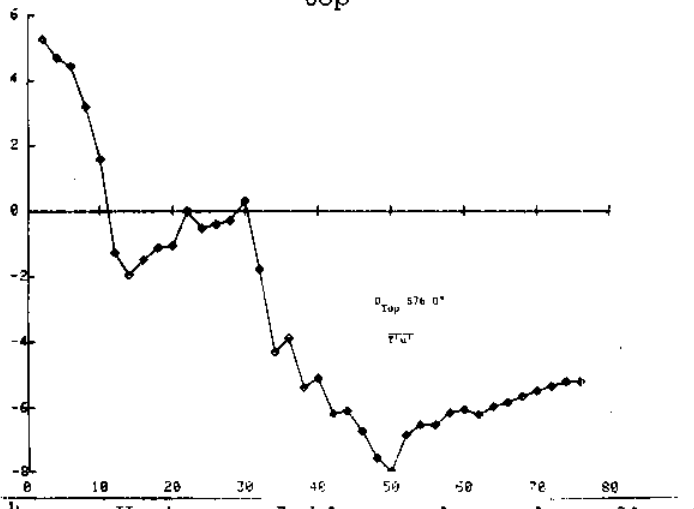

Figure 114 Heat correlation variance in x-direction for D_{top} Summer, 1976 (cumulative)

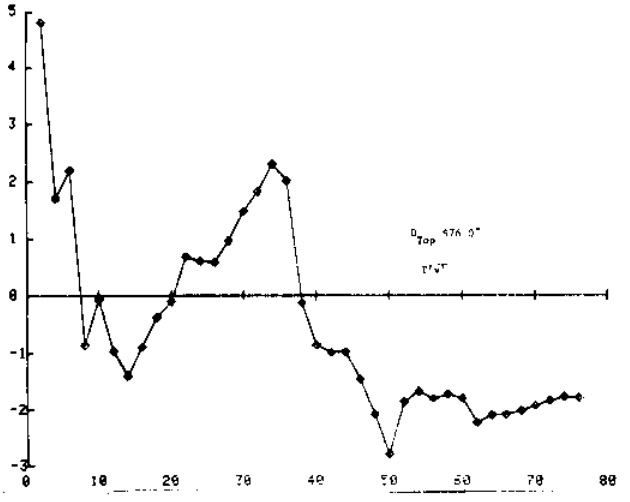

Figure 115 Heat correlation variance in y-direction for D_{top} Summer, 1976 (cumulative)

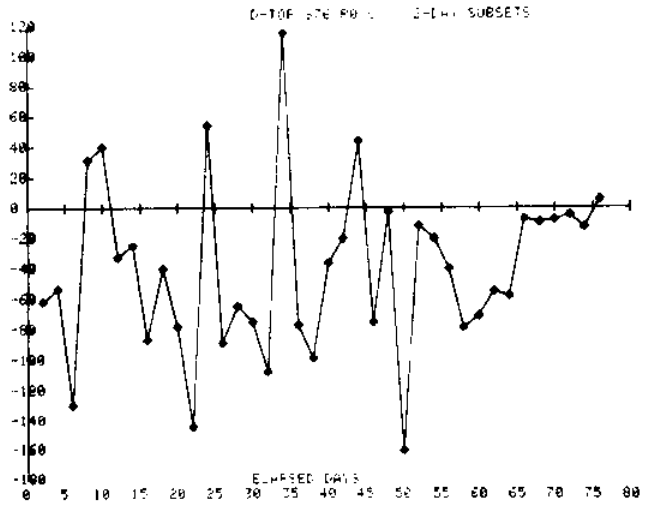

Figure 116 Momentum correlation variance in the horizontal plane for D_{top} Summer, 1976 (2-day subset)

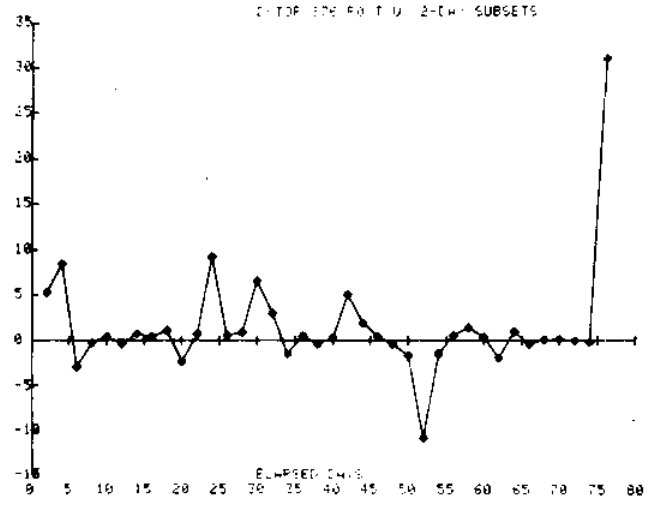

Figure 117 Heat correlation variance in the x-direction for D_{top} Summer, 1976 (2-day subset)

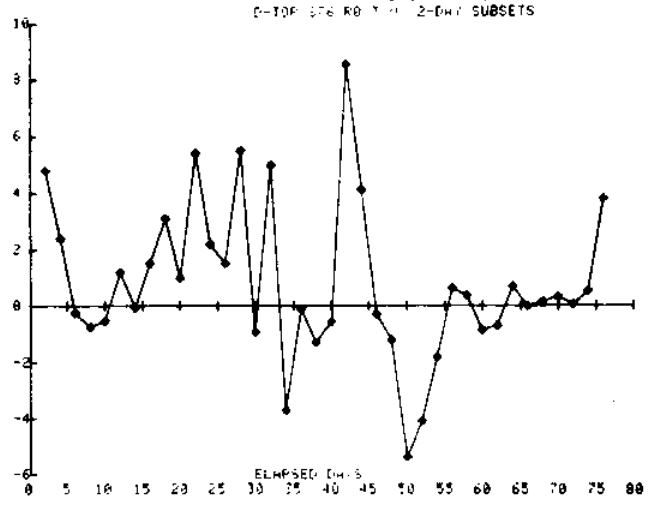

Figure 118 Heat correlation variance in the y-direction for D_{top} Summer, 1976 (2-day subset)

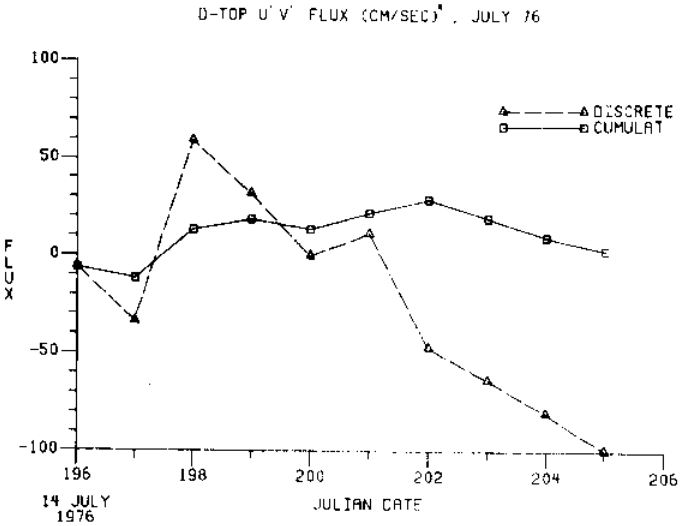

Figure 119 Momentum correlation variance in horizontal plane for D_{top}, July 14-23, 1976

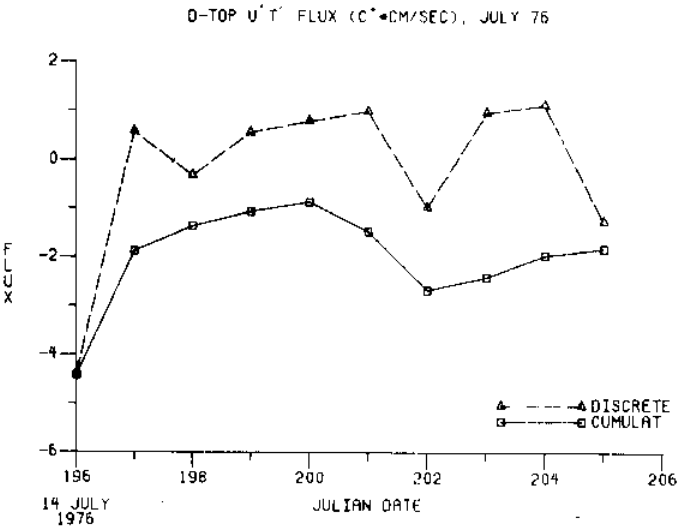

Figure 120 Heat correlation variance in x-direction for D_{top}, July 14-23, 1976

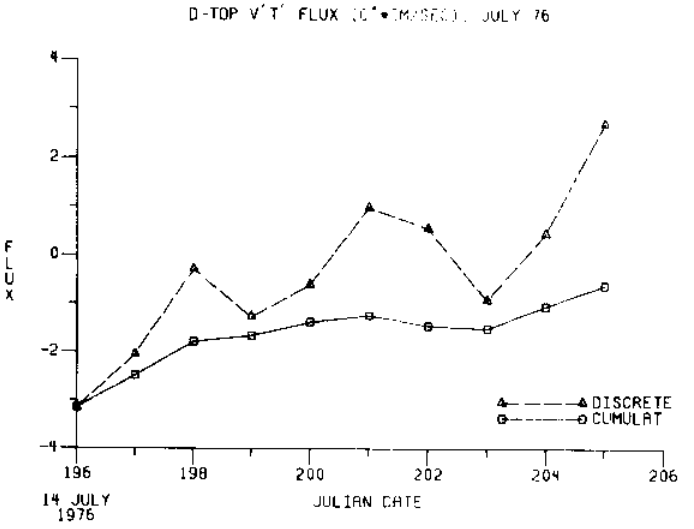

Figure 121 Heat correlation variance in y-direction for D_{top}, July 14-23, 1976

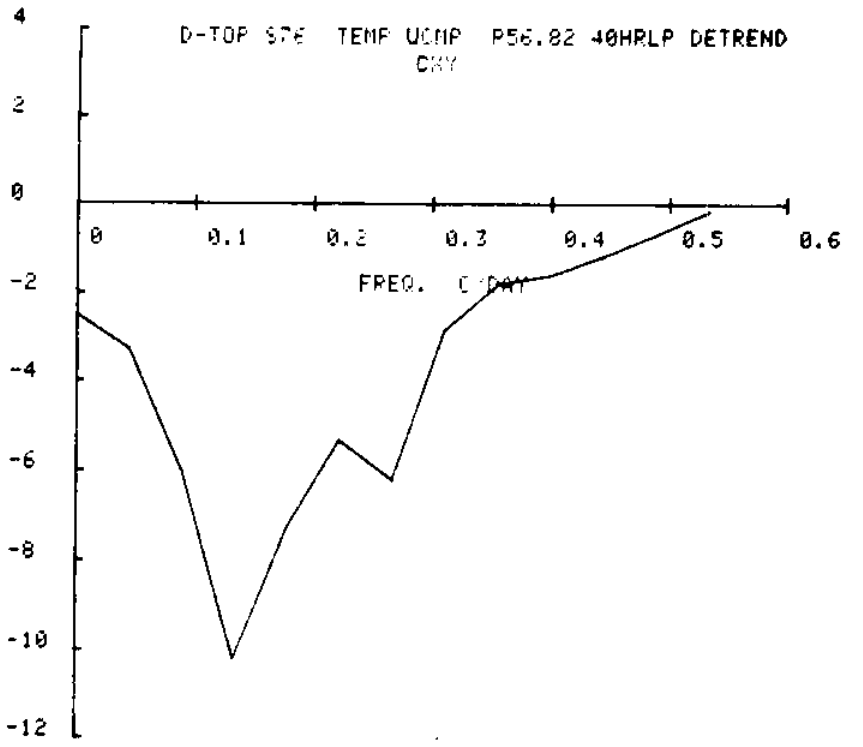

Figure 122 Cospectra of temperature vs. u-component for meter D_{top}

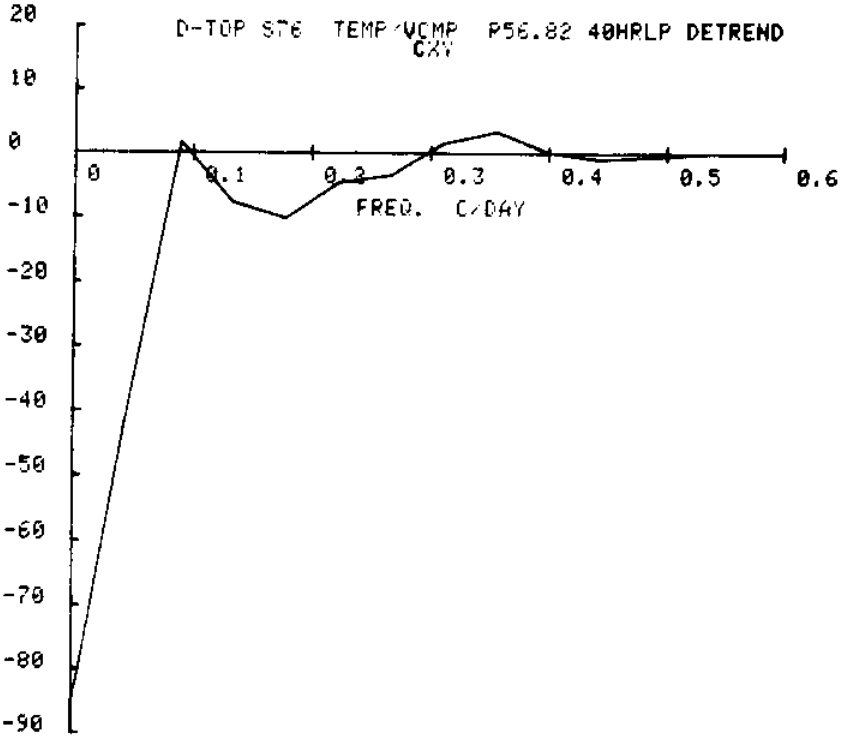

Figure 123 Cospectra of temperature vs. v-component for meter D_{top}

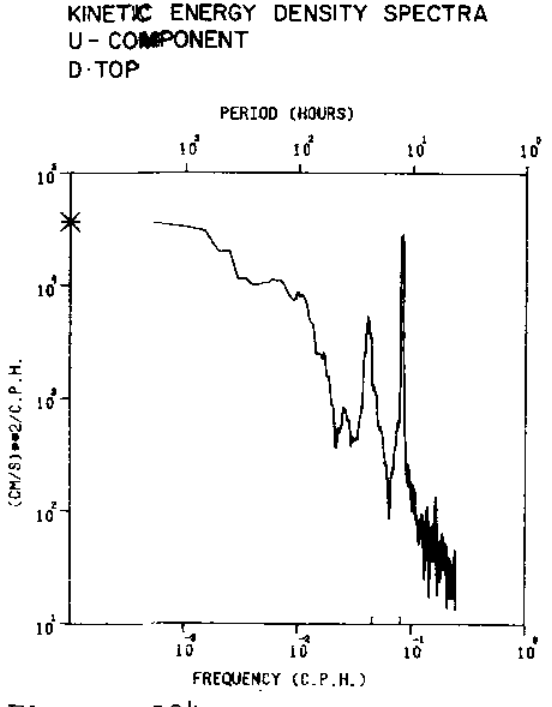

Figure 124
Kinetic energy density spectra for current velocity, u-component, D_{top}

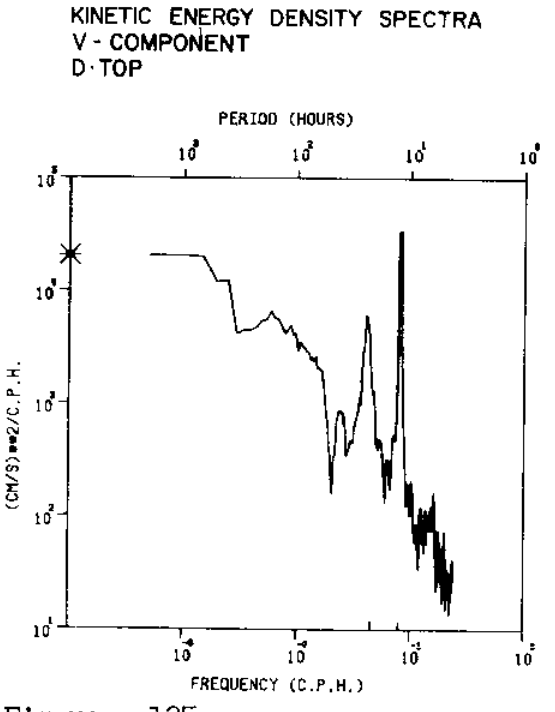

Figure 125
Kinetic energy density spectra for current velocity, v-component, D_{top}

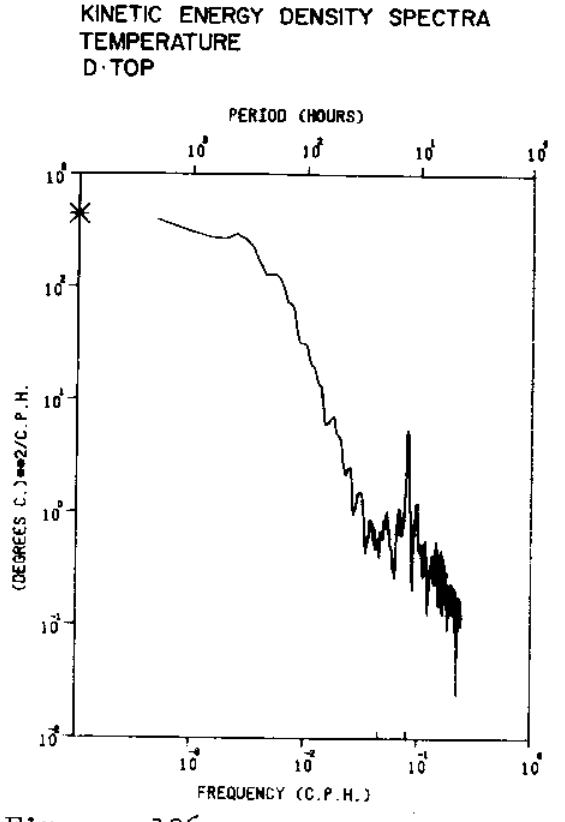

Figure 126
Kinetic energy density spectra for temperature at D_{top}

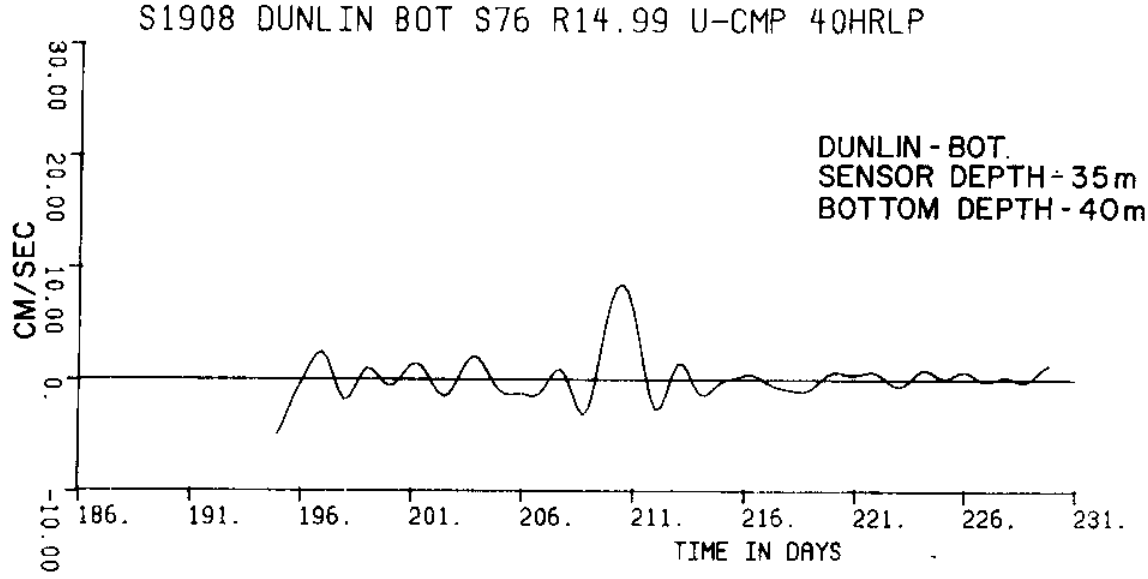

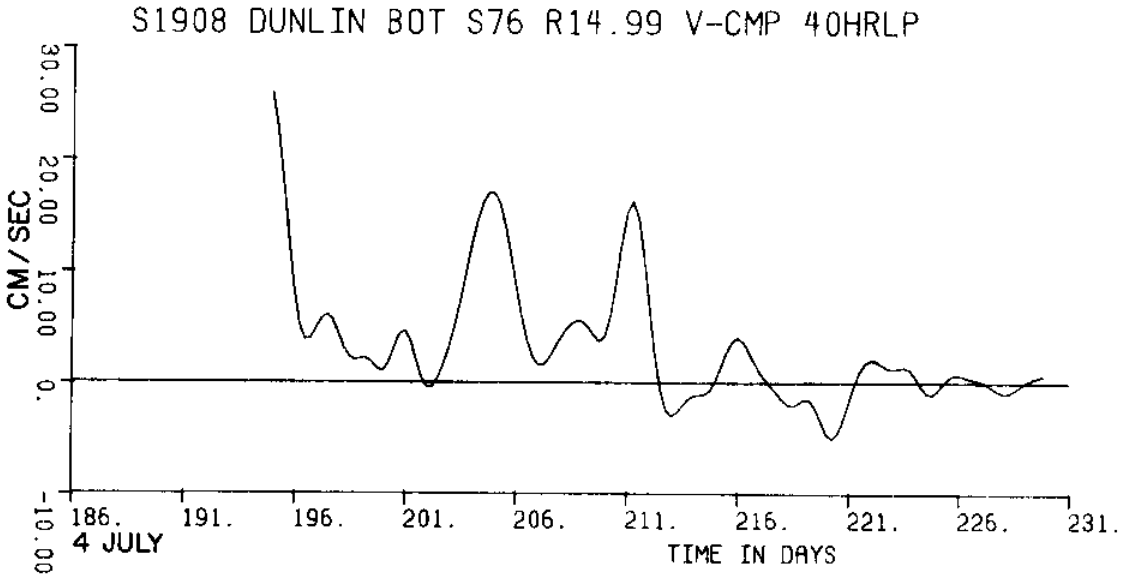

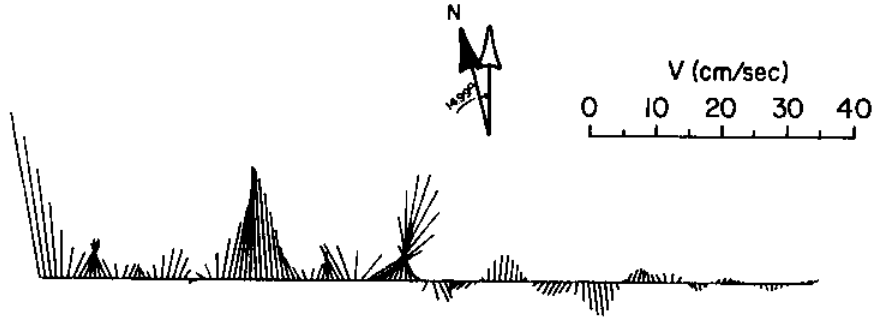

Figure 127 Low pass current velocity components and vectors from meter $D(Dunlin)_{bot}$

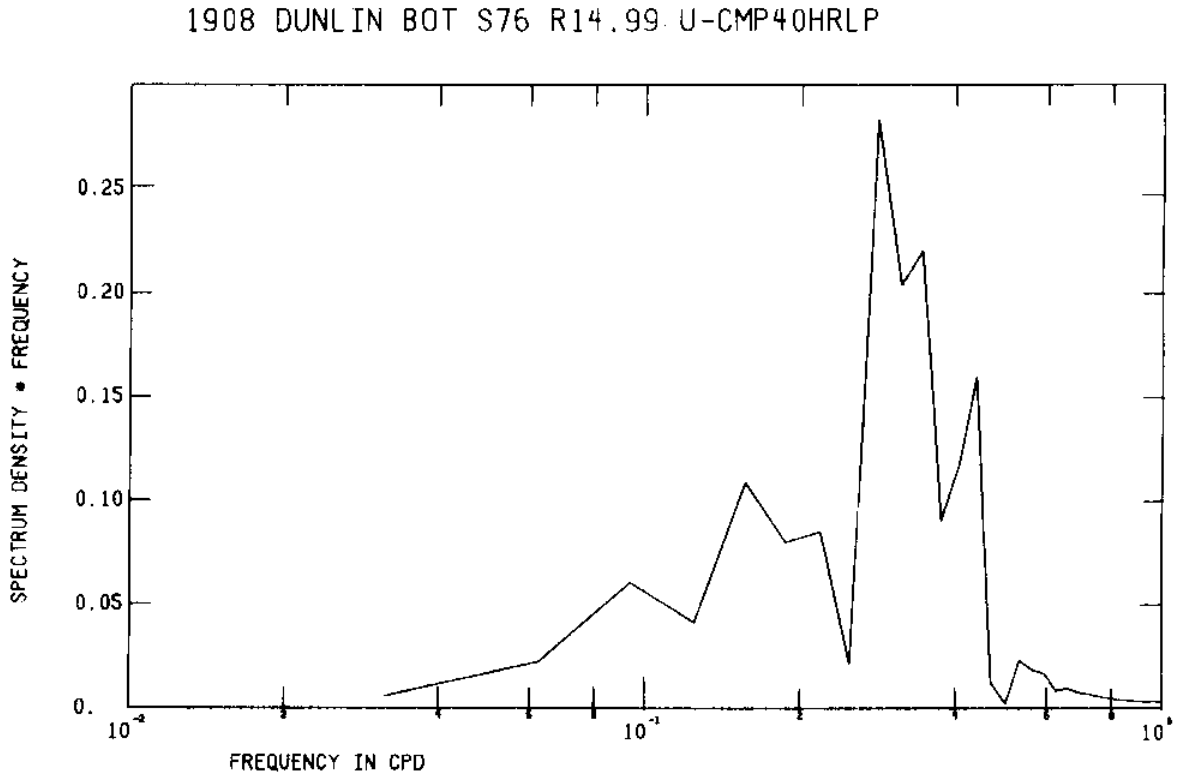

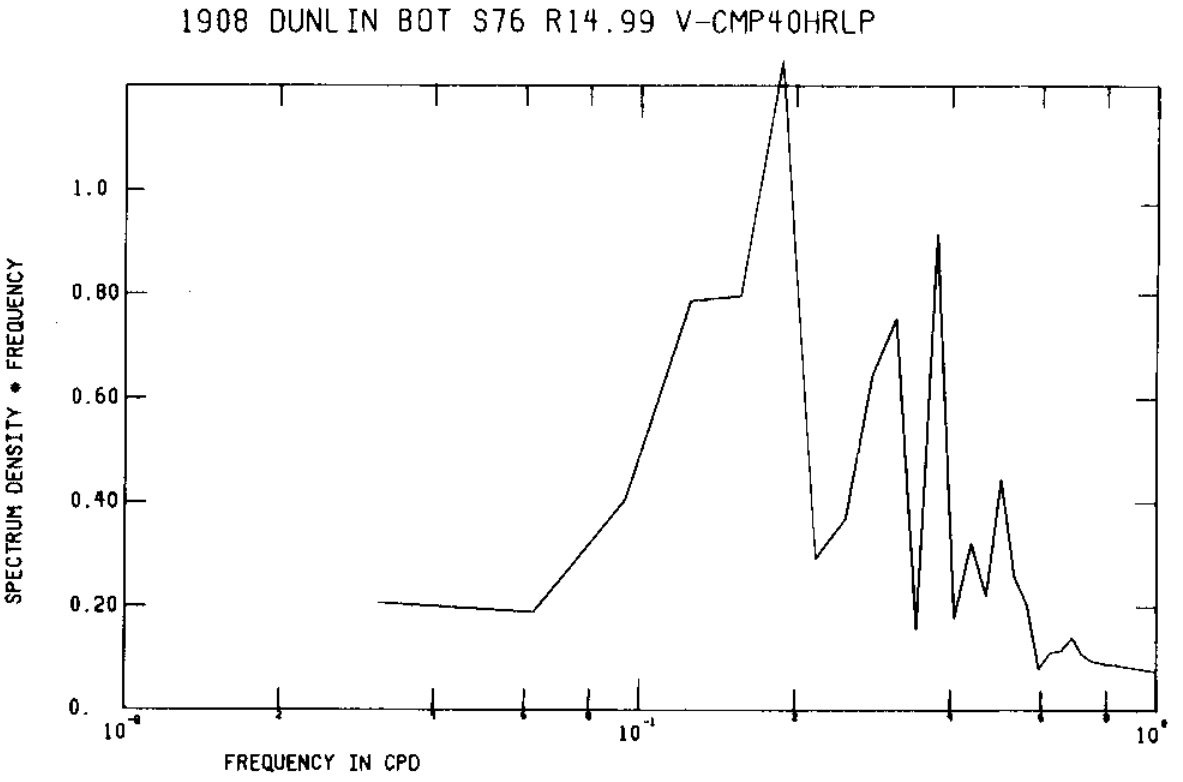

Figure 128 FFT of low pass current velocity components from meter $D(Dunlin)_{bot}$

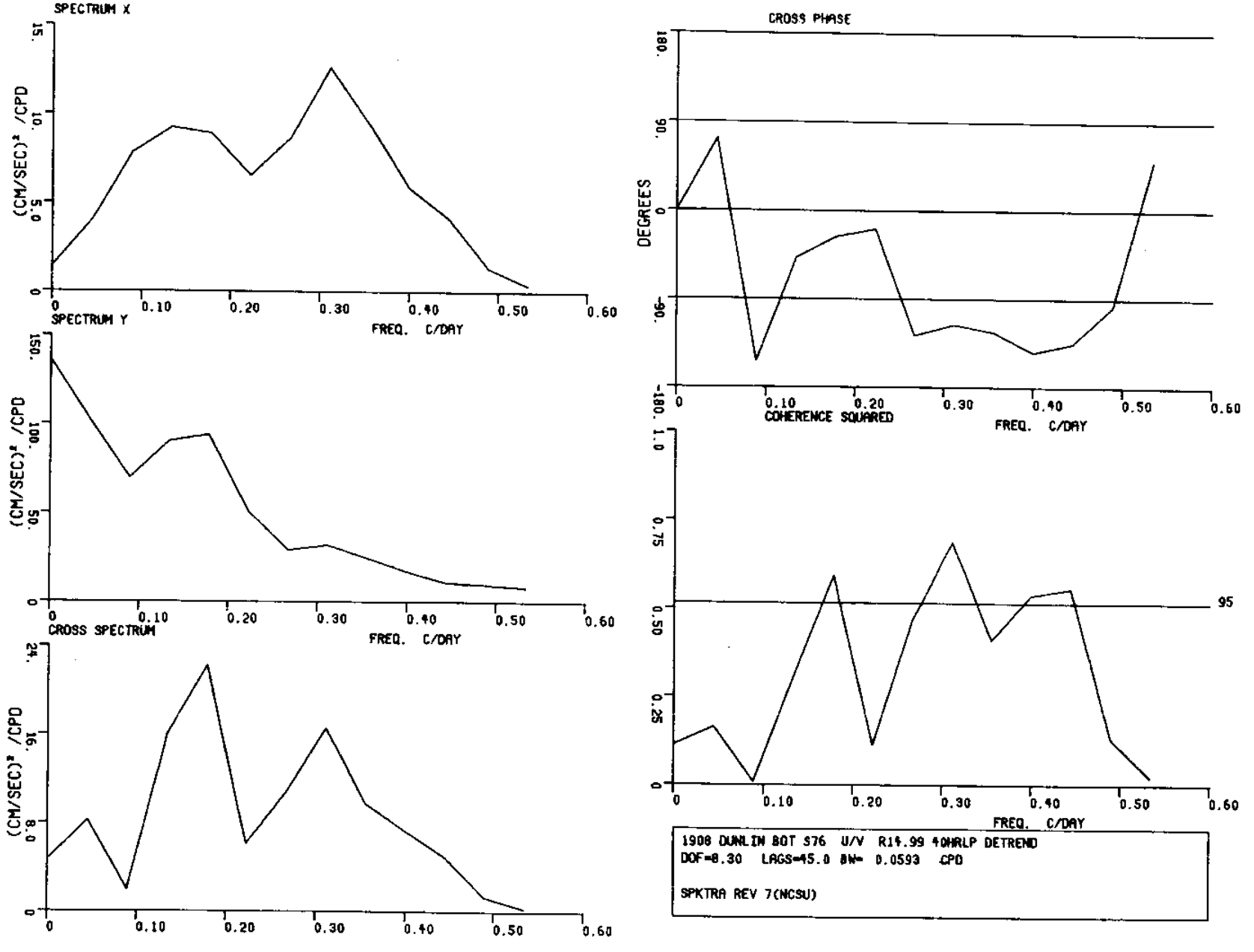

Figure 129 Spectra of low pass current velocity components from meter D(Dunlin)$_{bot}$

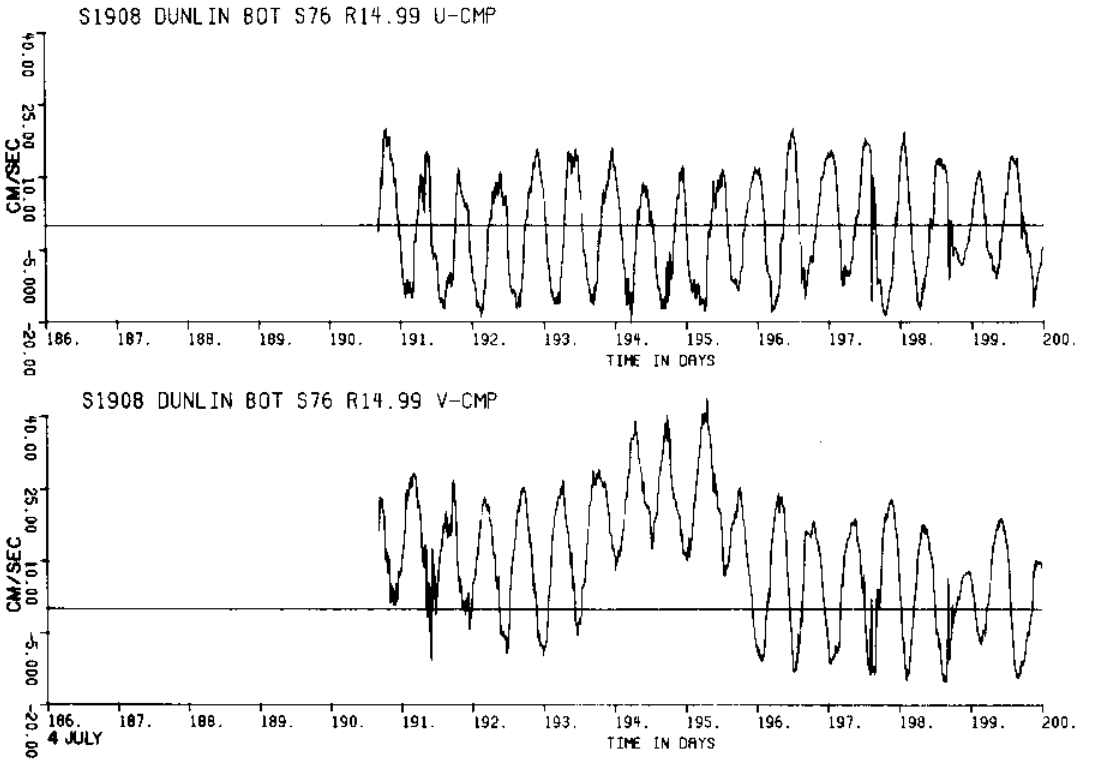

Figure 130 a

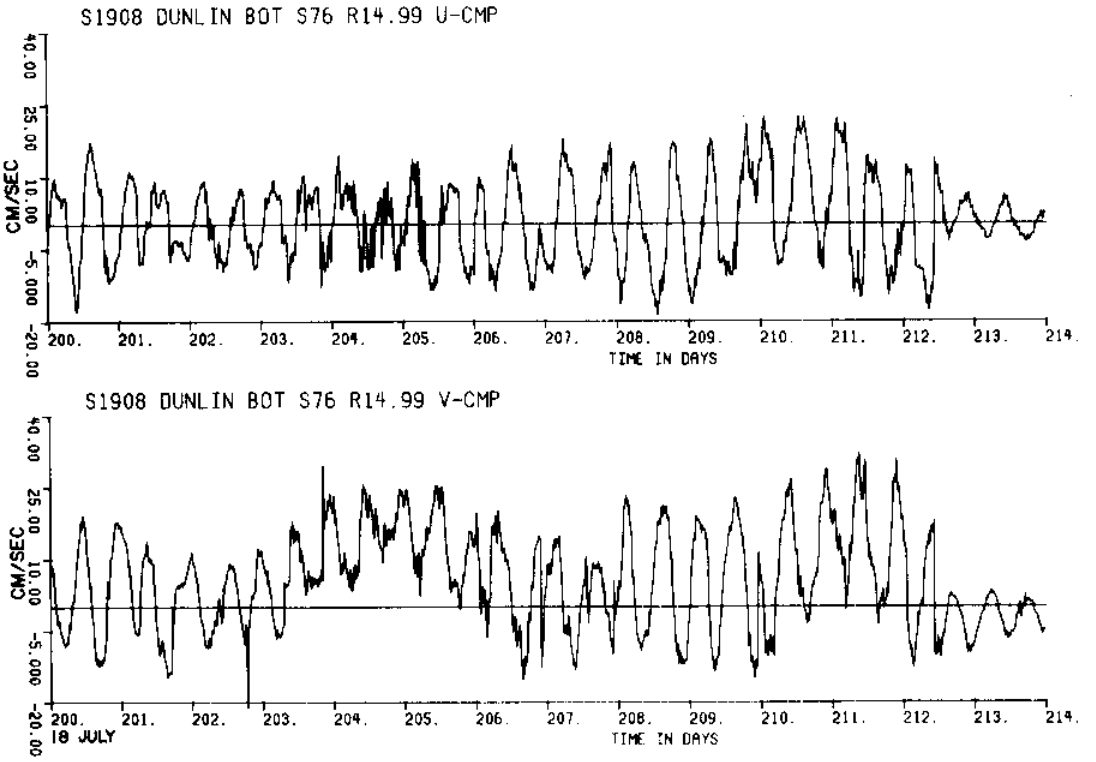

Figure 130 b

Figure 130 (a,b,c,d) Unfiltered current velocity components from meter $D(Dunlin)_{bot}$

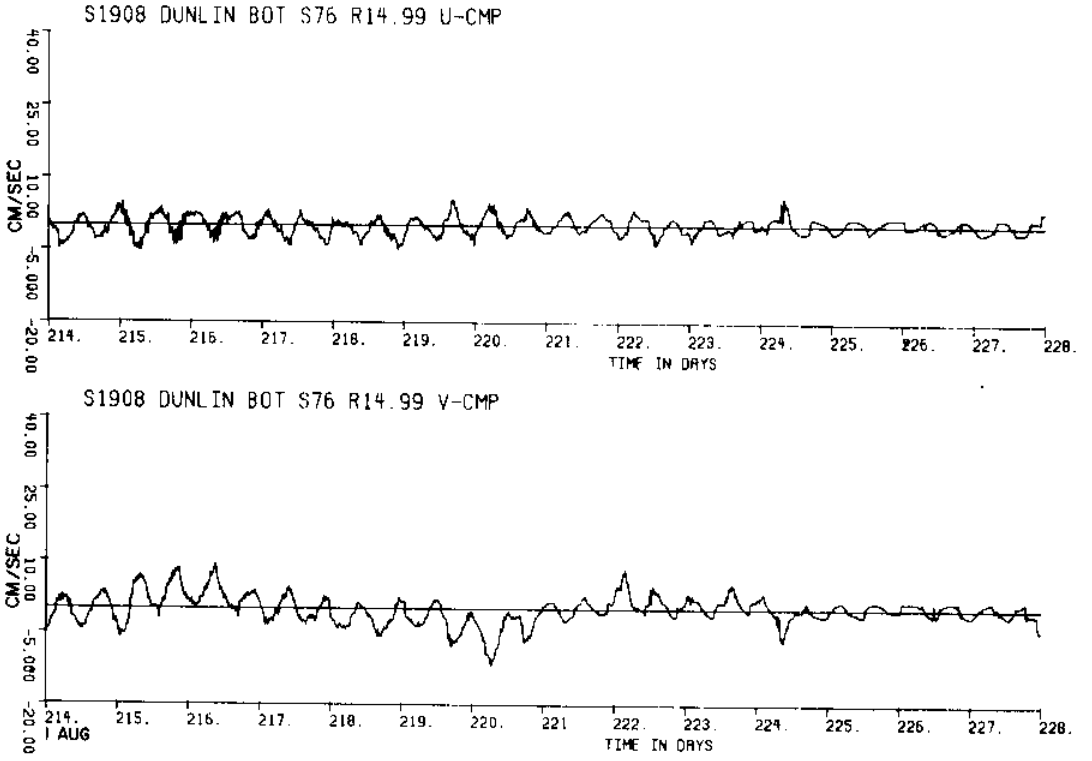

Figure 130 c

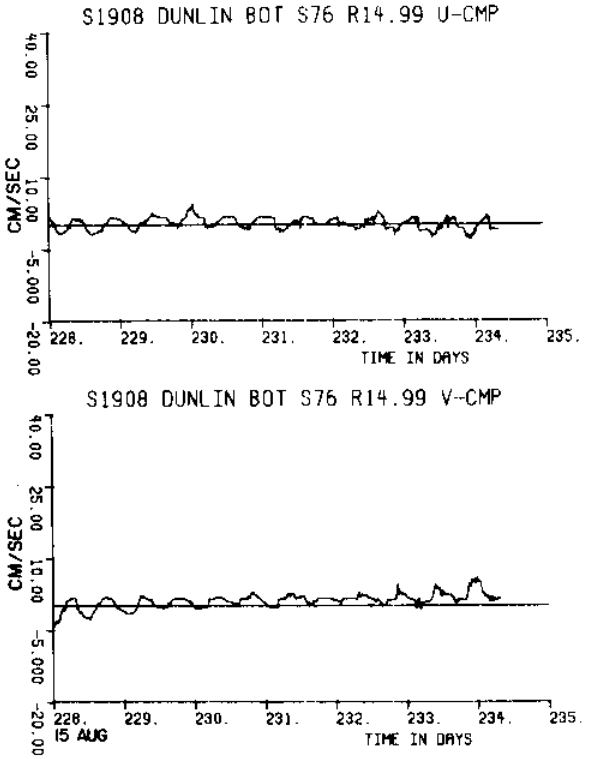

Figure 130 d

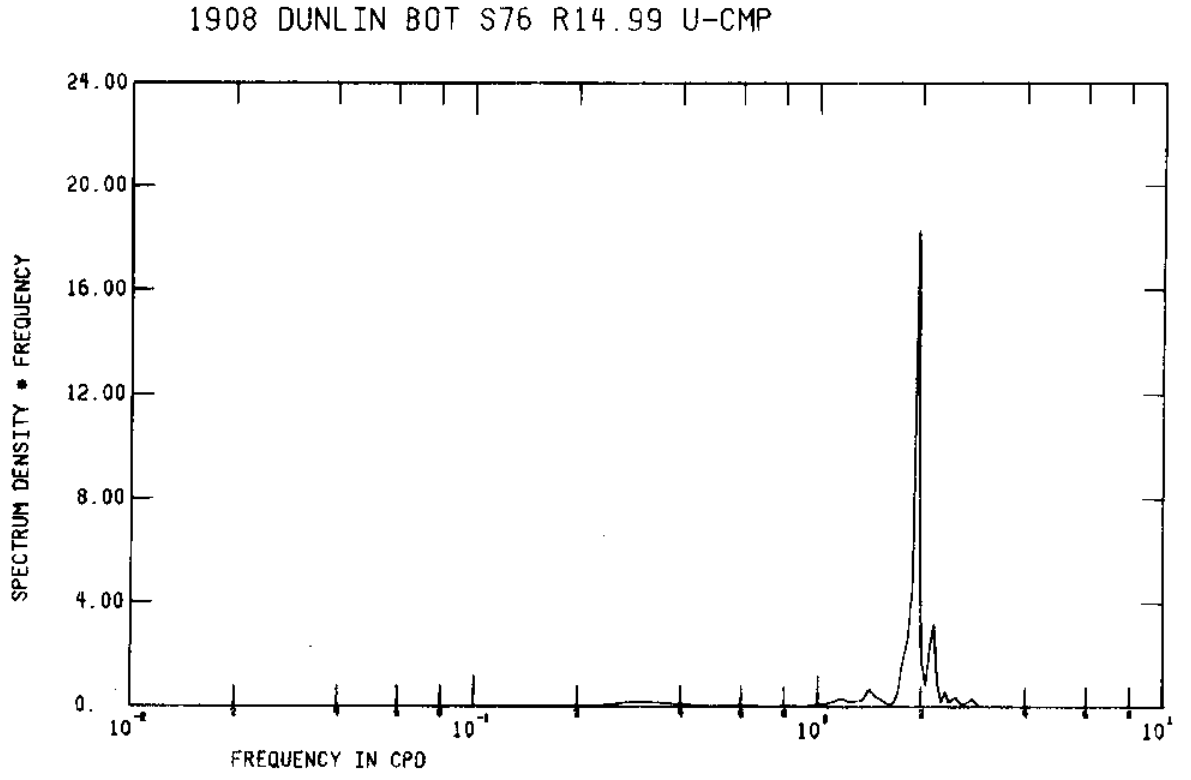

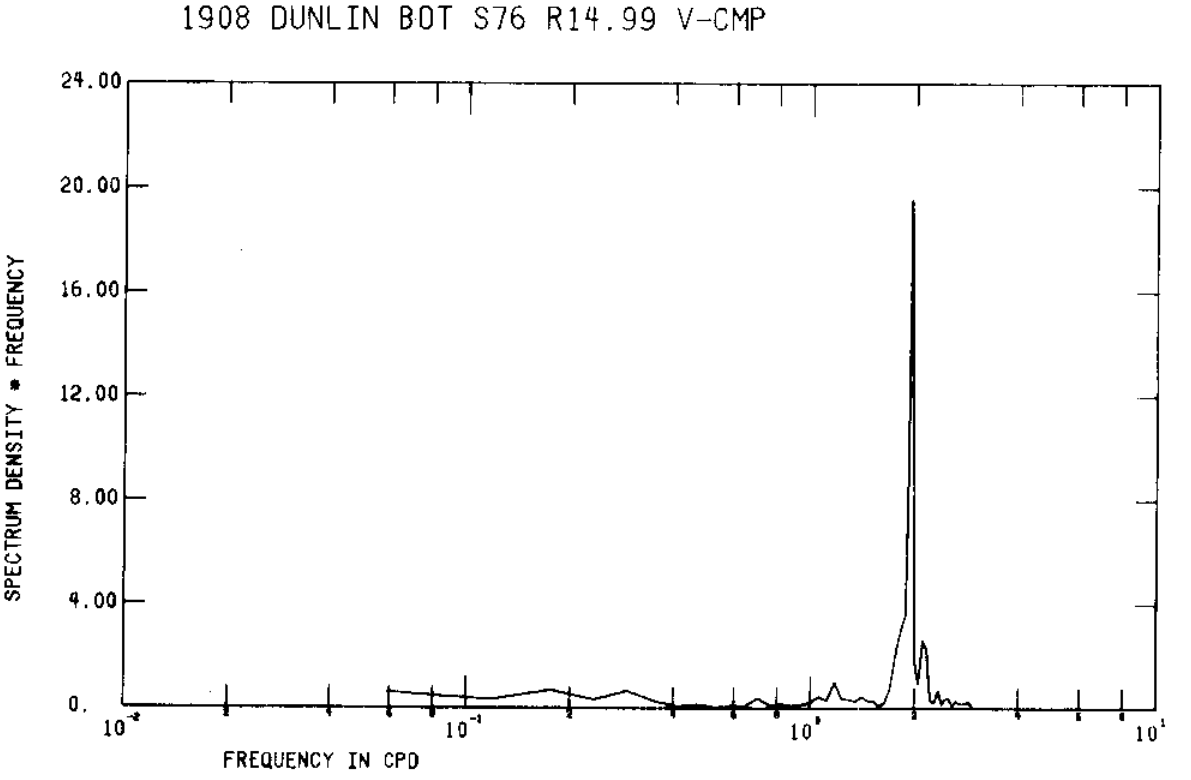

Figure 131 FFT of unfiltered current velocity components from meter $D(Dunlin)_{bot}$

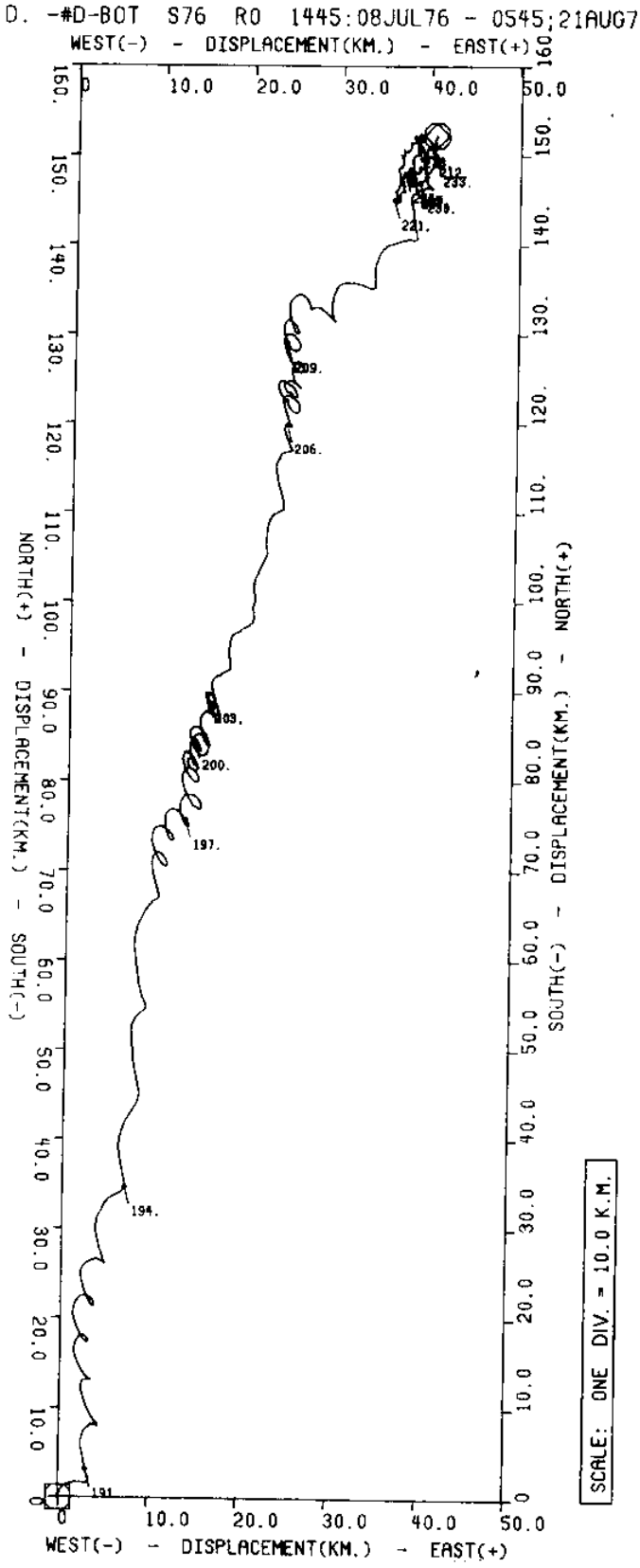

Figure 132 a

Figure 132 (a,b,c) Progressive vector diagrams of unfiltered current velocity from meter D(Dunlin)$_{bot}$

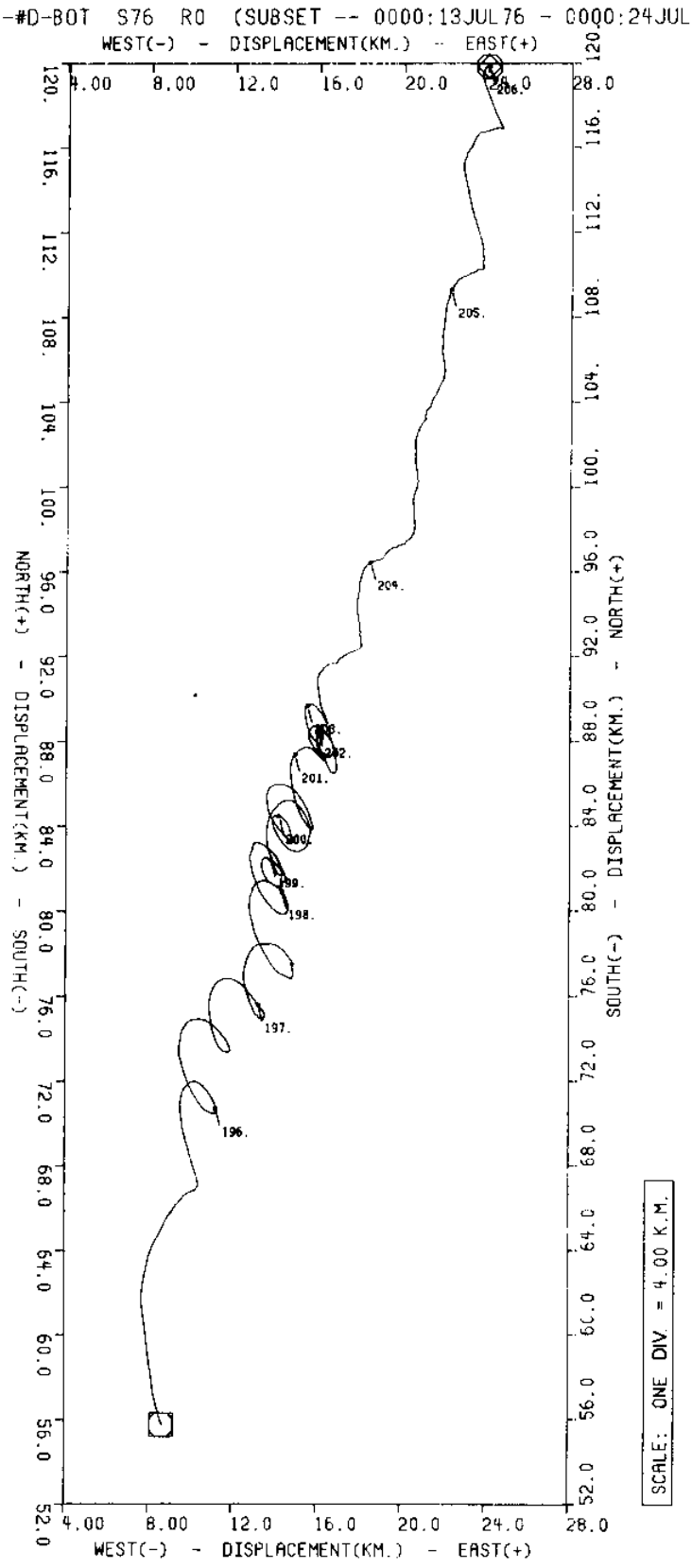
P.V.D. -#D-BOT S76 R0 (SUBSET -- 0000:13JUL76 - 0000:24JUL76)
WEST(-) - DISPLACEMENT(KM.) - EAST(+)
NORTH(+) - DISPLACEMENT(KM.) - SOUTH(-)
SOUTH(-) - DISPLACEMENT(KM.) - NORTH(+)
SCALE: ONE DIV. = 4.00 K.M.

Figure 132 b

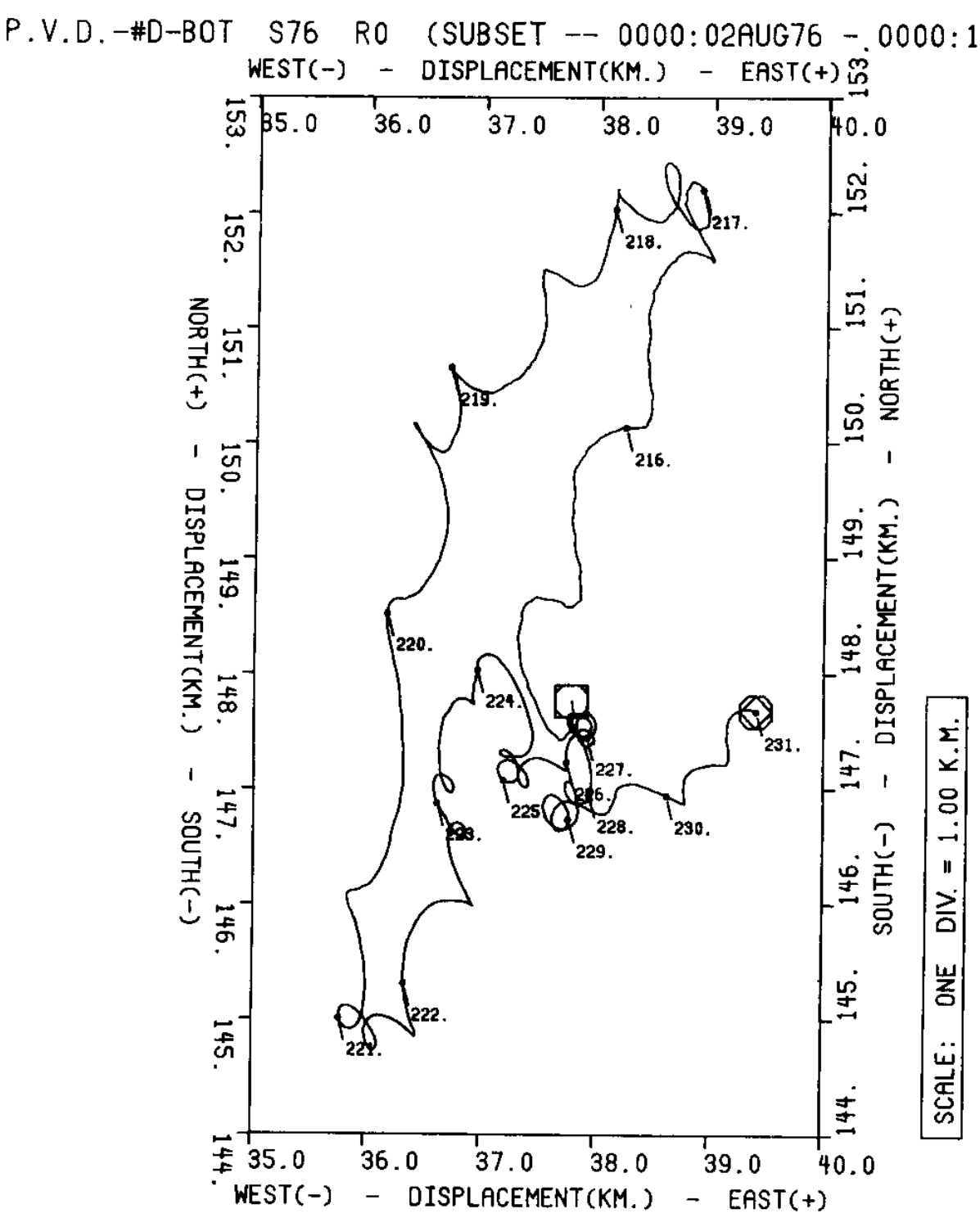
P.V.D.-#D-BOT S76 R0 (SUBSET -- 0000:02AUG76 - 0000:18AUG76)
WEST(-) - DISPLACEMENT(KM.) - EAST(+)
NORTH(+) - DISPLACEMENT(KM.) - SOUTH(-)
SOUTH(-) - DISPLACEMENT(KM.) - NORTH(+)
35.0
36.0
37.0
38.0
39.0
40.0
153.
152.
151.
150.
149.
148.
147.
146.
145.
144.
217.
218.
219.
216.
220.
224.
231.
227.
226.
225
228.
230.
229.
222.
221.
SCALE: ONE DIV. = 1.00 K.M.

Figure 132 c

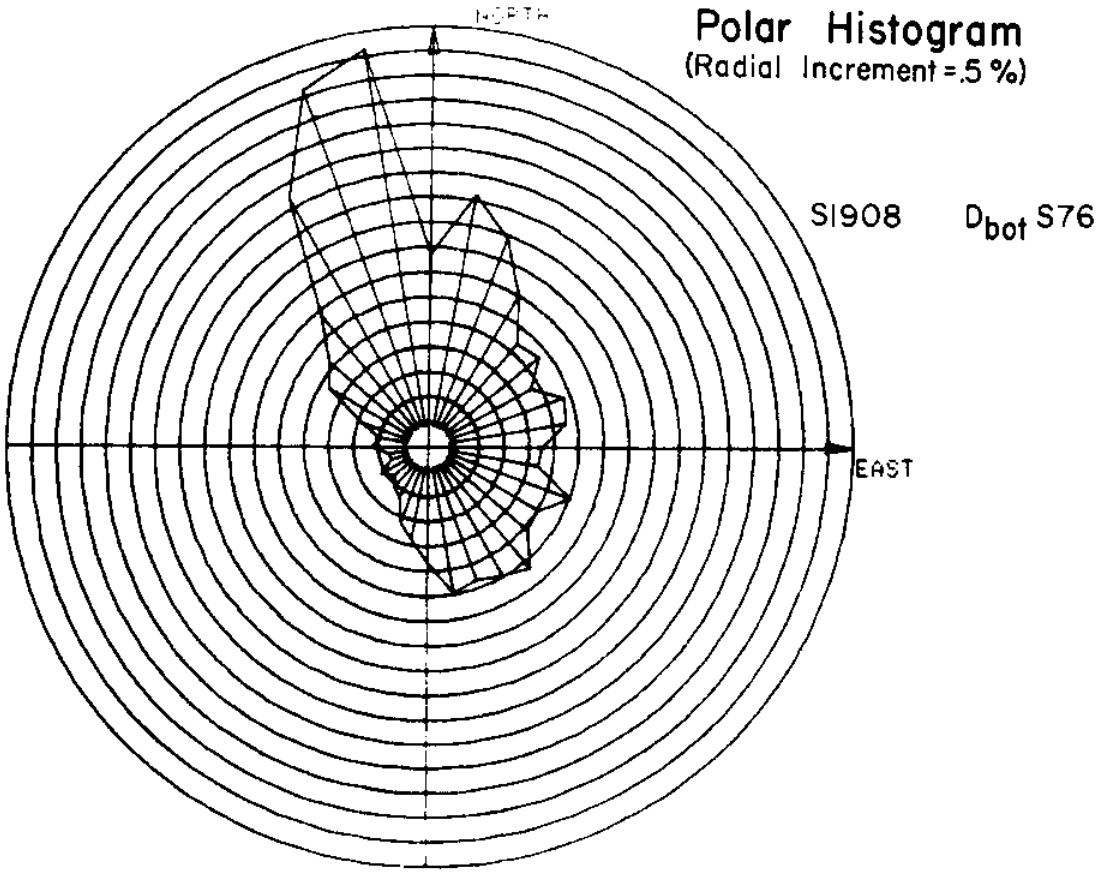

Figure 133 Histogram from meter $D(Dunlin)_{bot}$

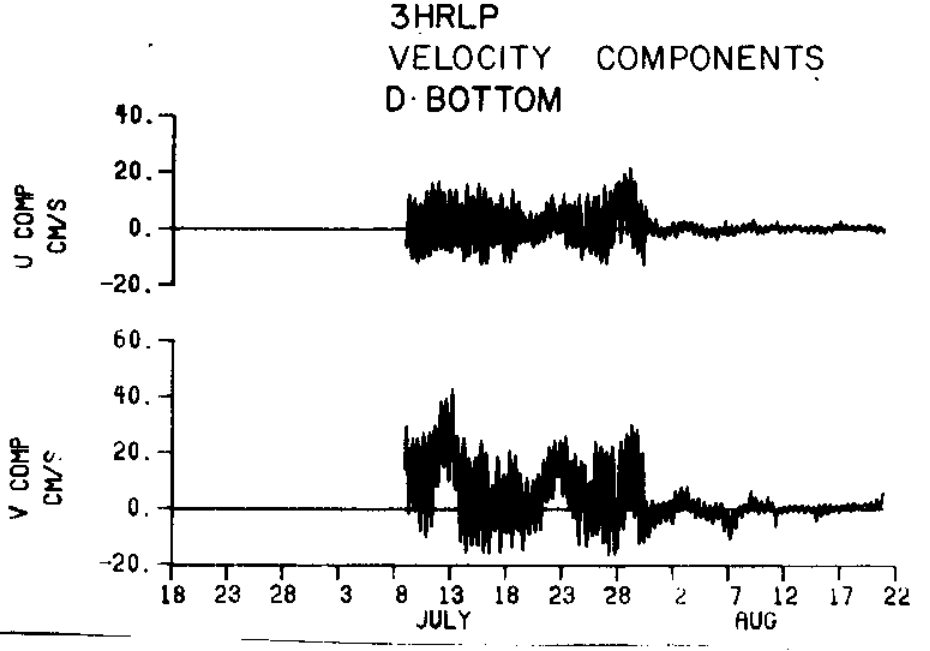

Figure 134 3HRLP velocity components for D_{bot}

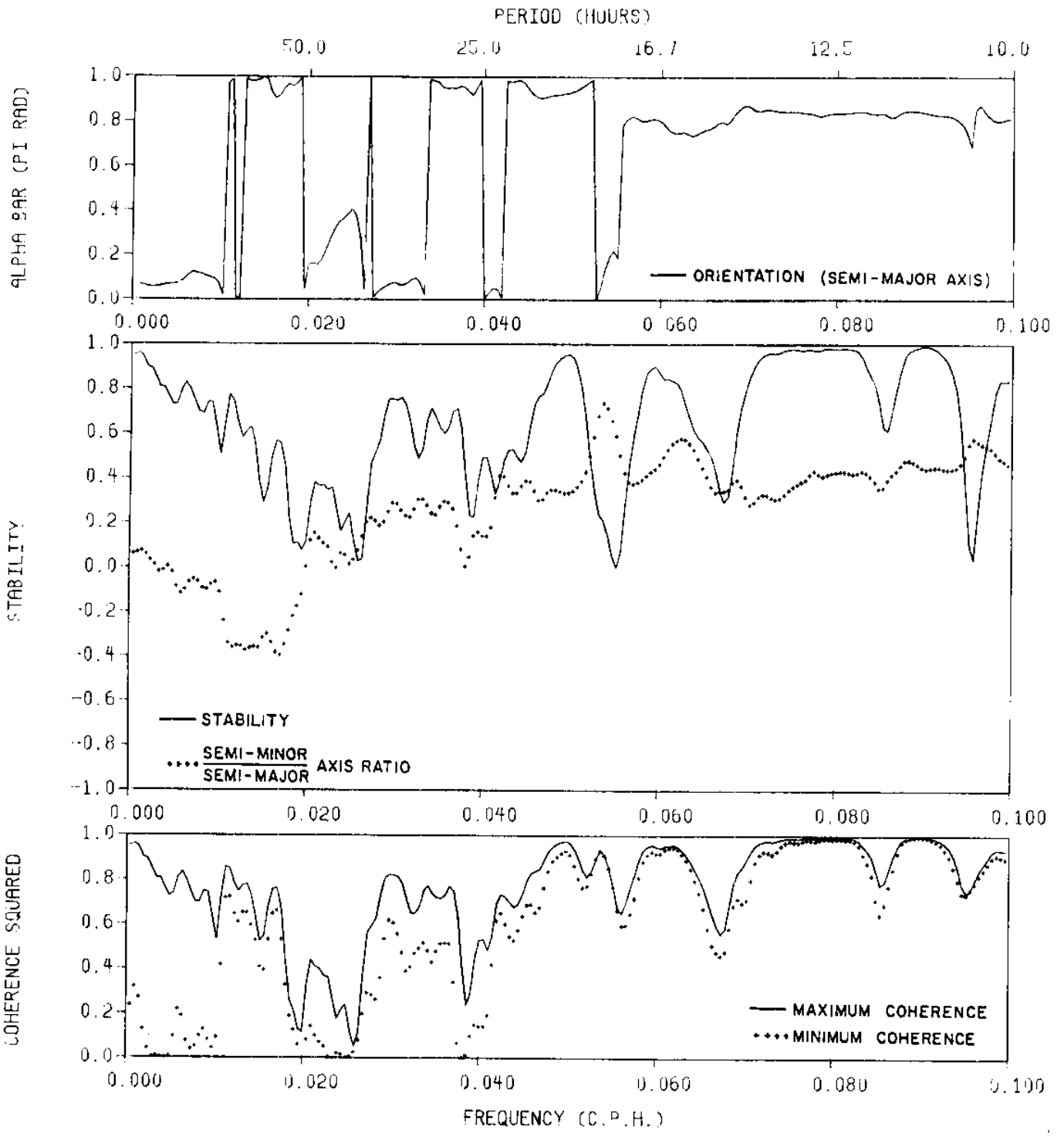

Figure 135 Hodograph parameters from meter D(Dunlin)$_{bot}$

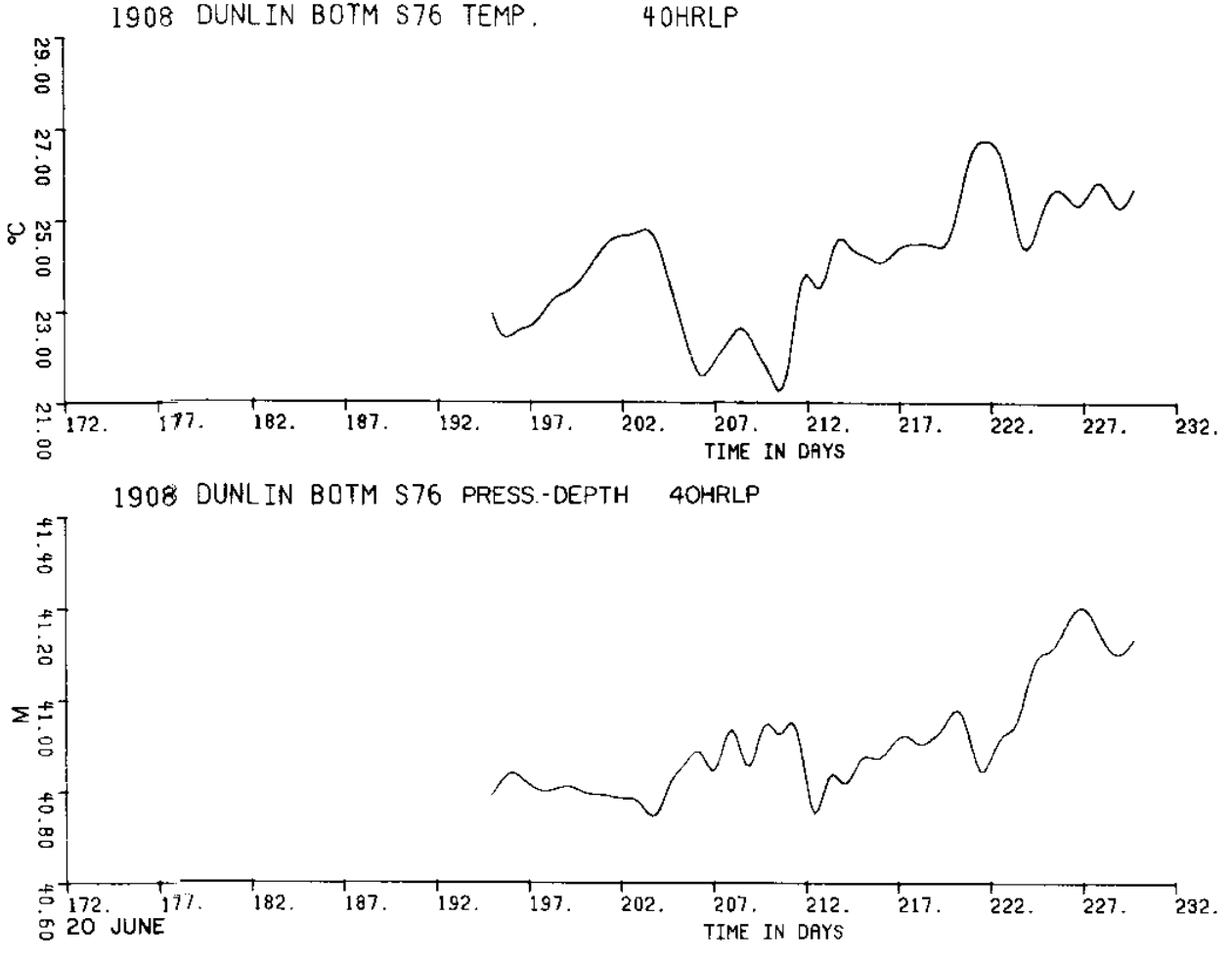

Figure 136 Low pass temperature and pressure from meter $D(Dunlin)_{bot}$

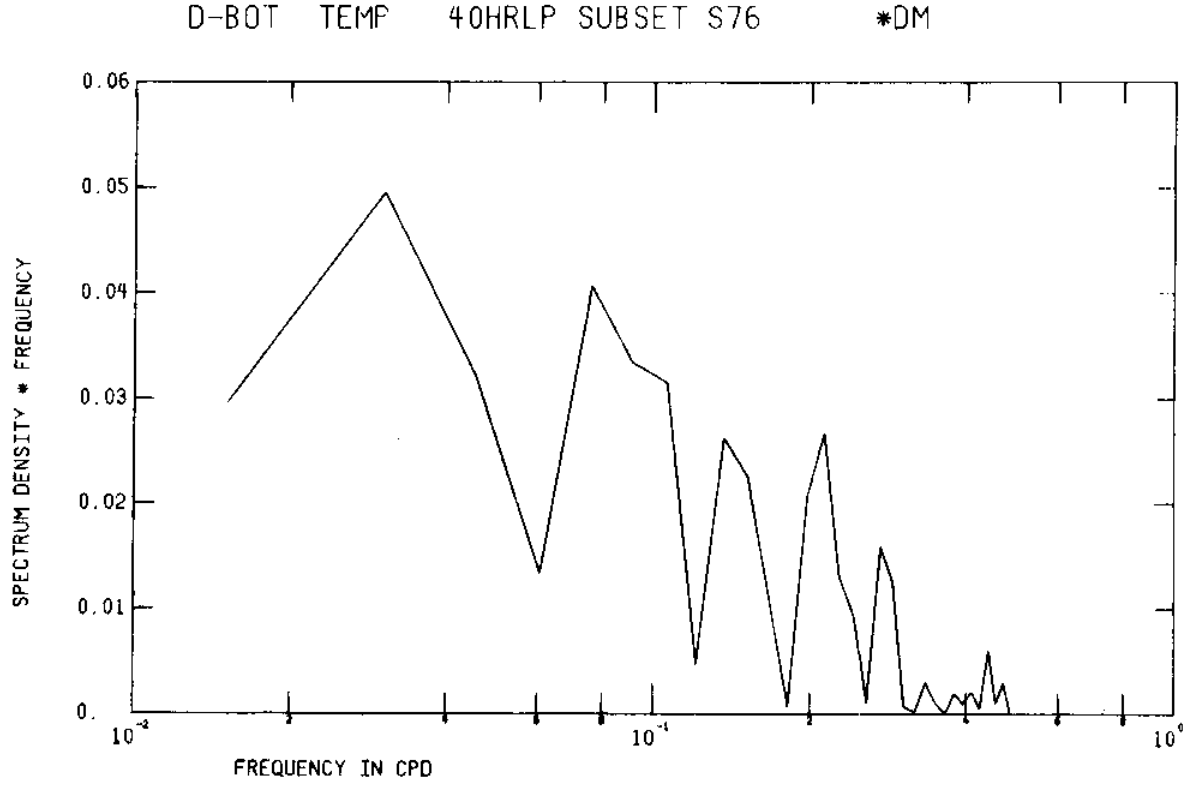

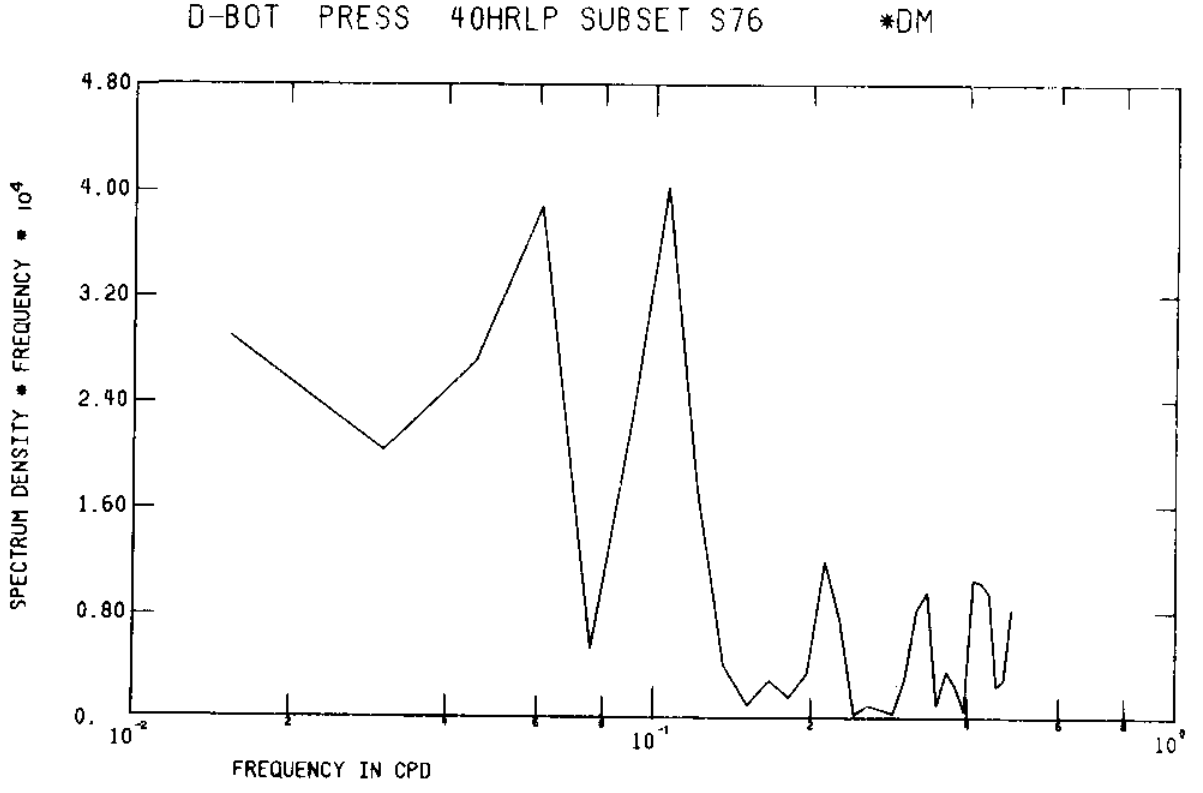

Figure 137 FFT of low pass temperature and pressure from meter $D(Dunlin)_{bot}$

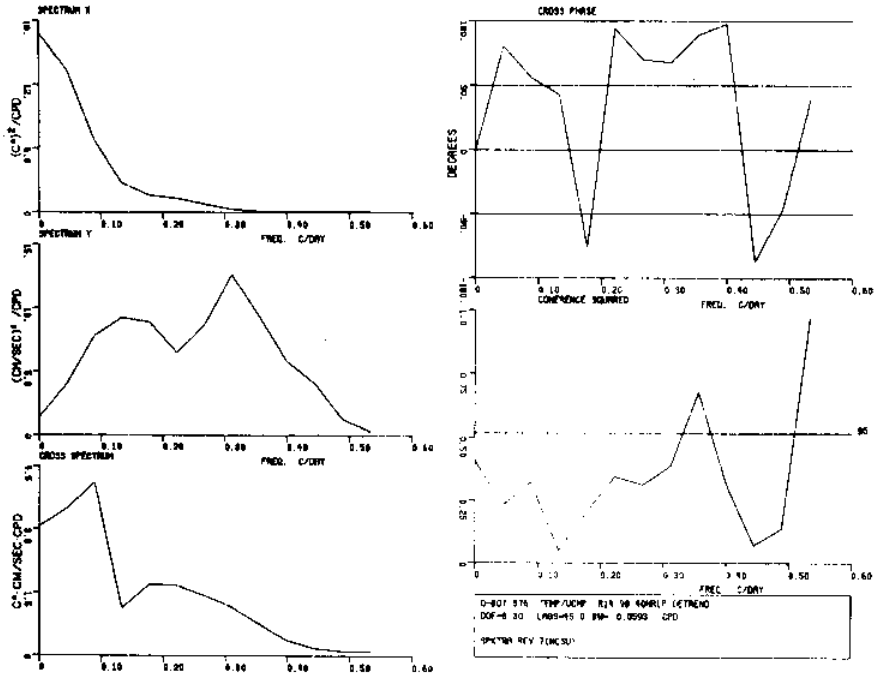

Figure 138 Spectra of temperature and the low pass current velocity u component, both from meter $D(Dunlin)_{bot}$

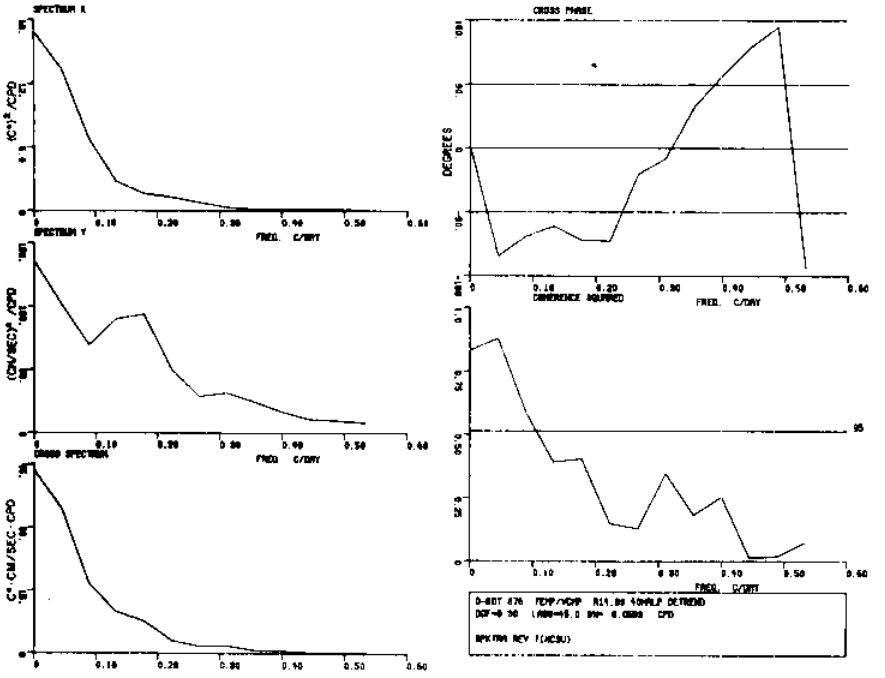

Figure 139 Spectra of temperature and the low pass current velocity v component, both from meter $D(Dunlin)_{bot}$

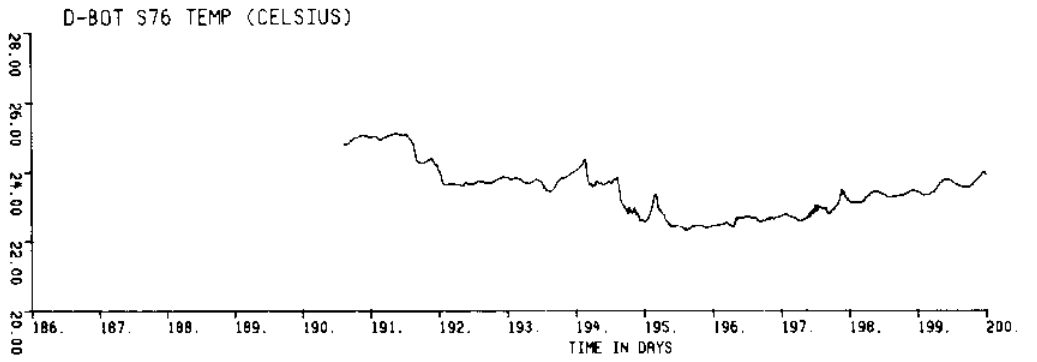

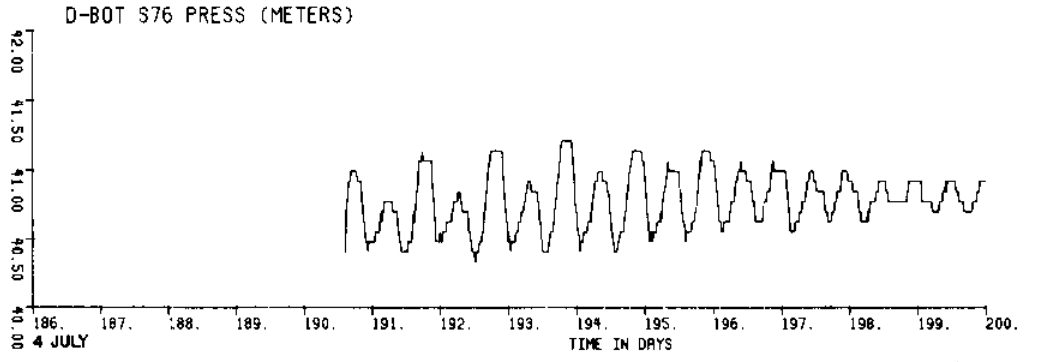

Figure 140 a

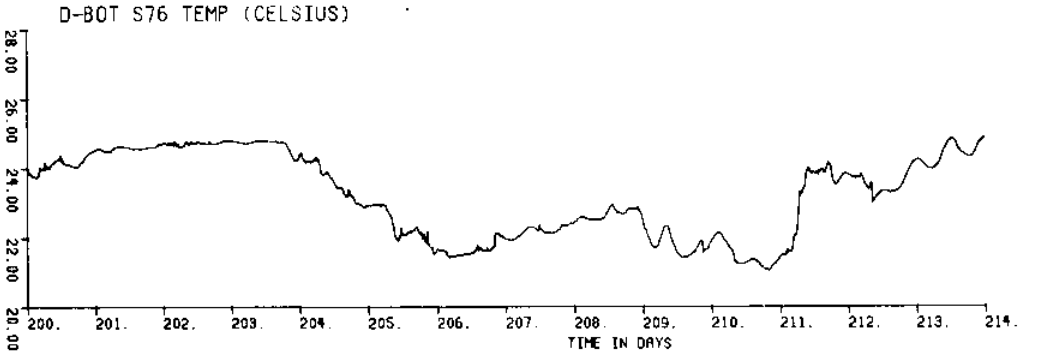

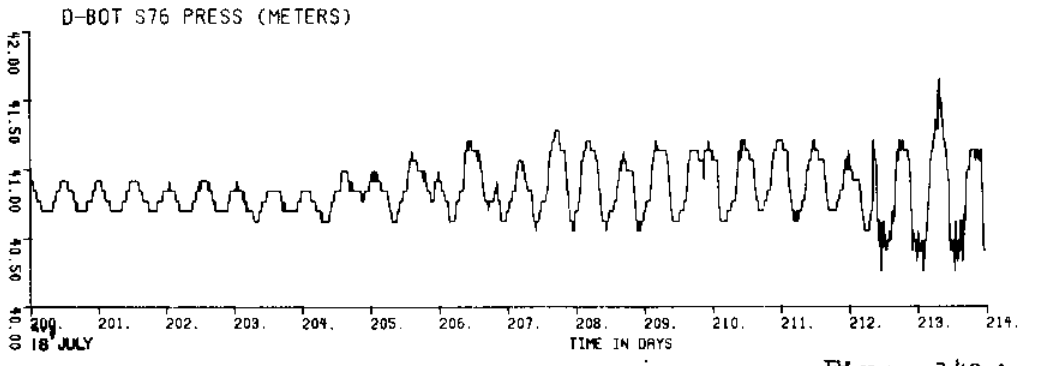

Figure 140 b

Figure 140 (a,b,c,d) Unfiltered temperature and pressure from meter D(Dunlin)$_{bot}$

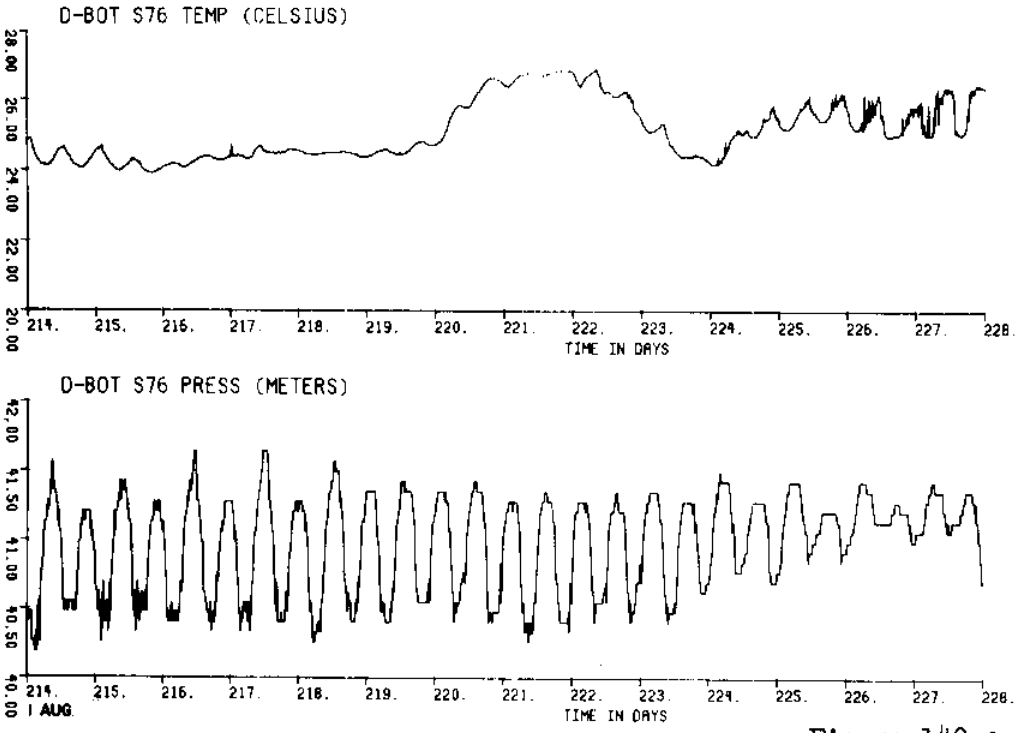

Figure 140 c

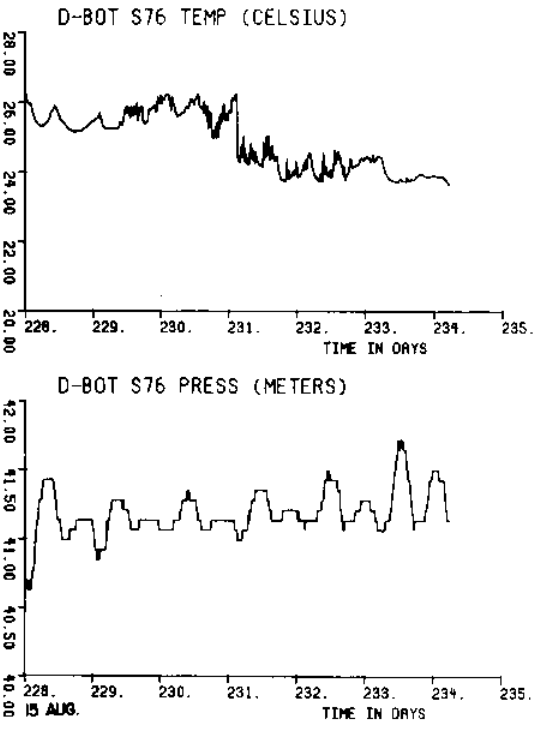

Figure 140 d

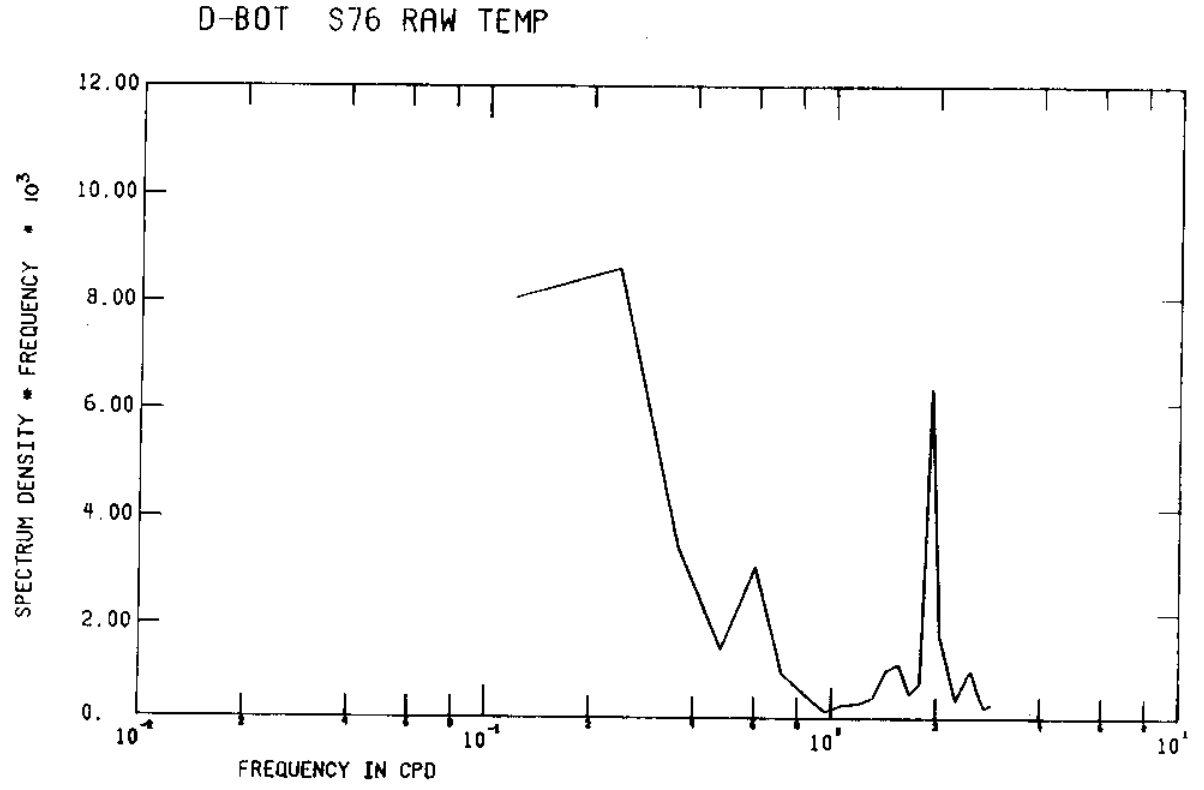

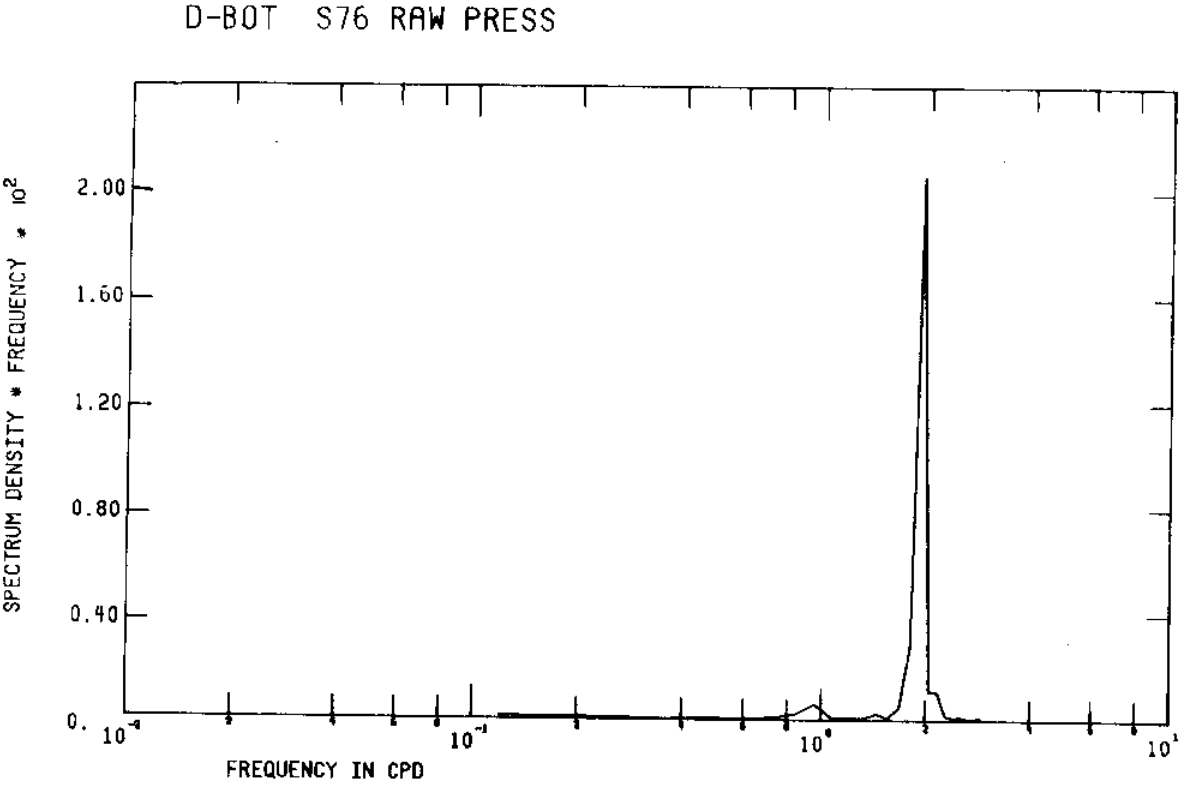

Figure 141 FFT of unfiltered temperature and pressure from meter $D(Dunlin)_{bot}$

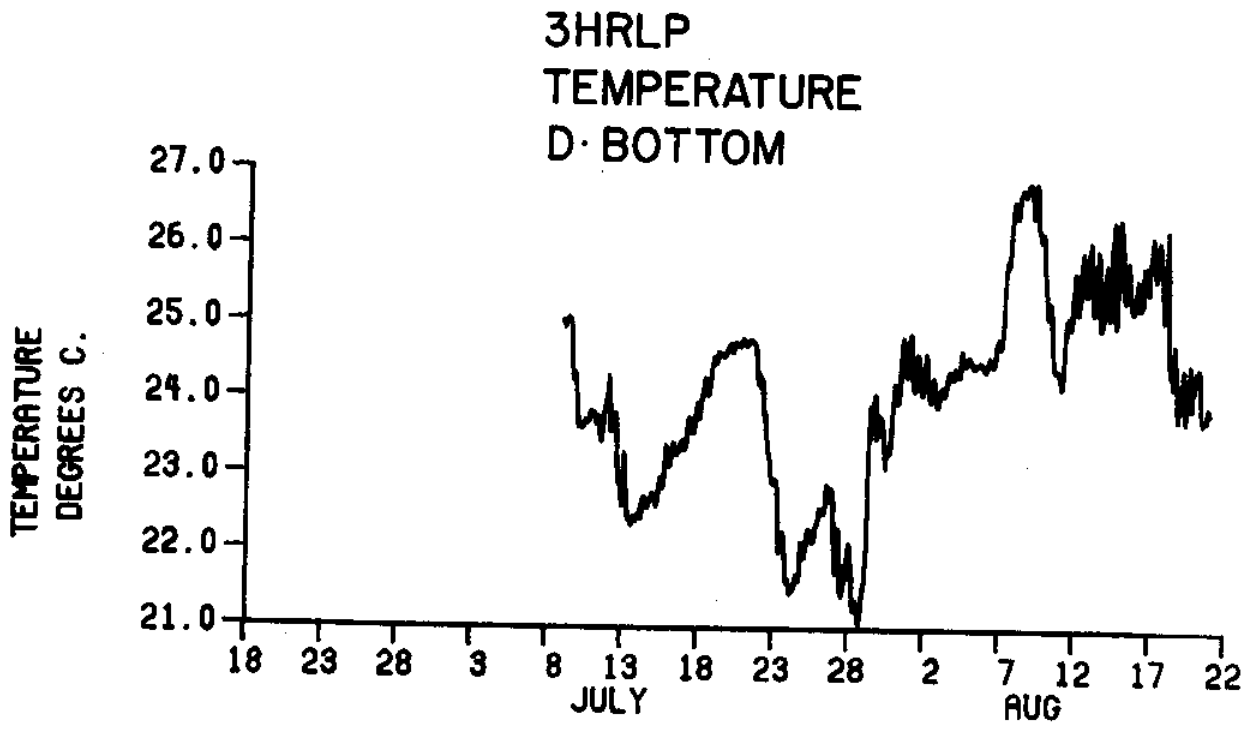

Figure 142 3HRLP temperature for D_{bot}

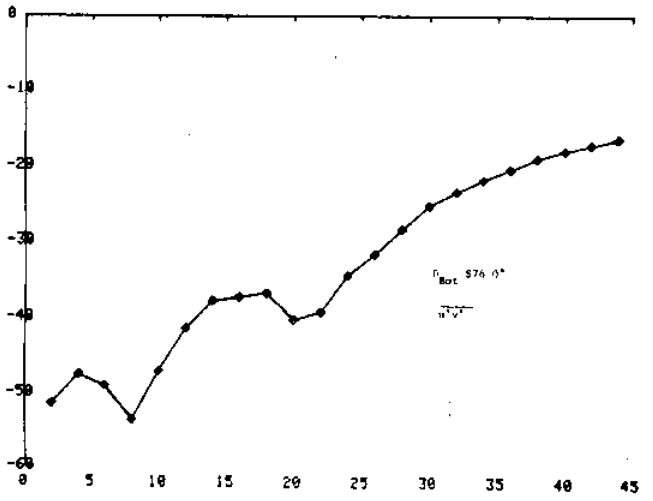

Figure 143 Momentum correlation variance in horizontal plane for D_{bot} Summer, 1976 (cumulative)

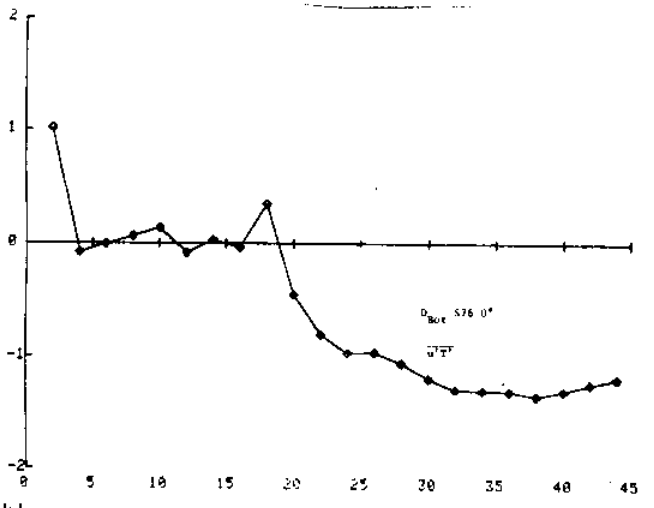

Figure 144 Heat correlation variance in x-direction for D_{bot} Summer, 1976 (cumulative)

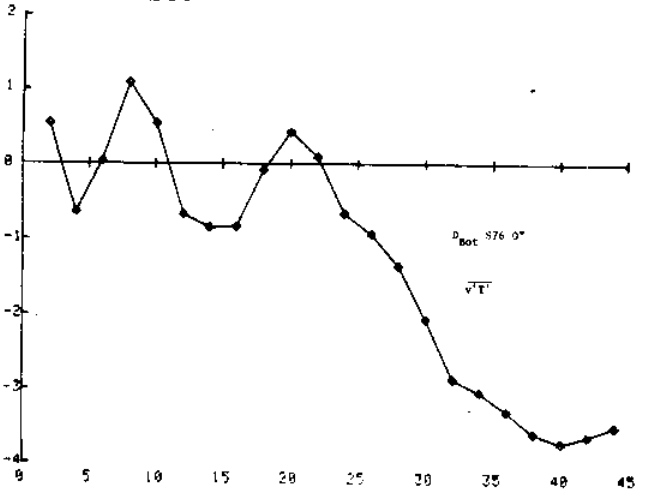

Figure 145 Heat correlation variance in y-direction for D_{bot} Summer, 1976 (cumulative)

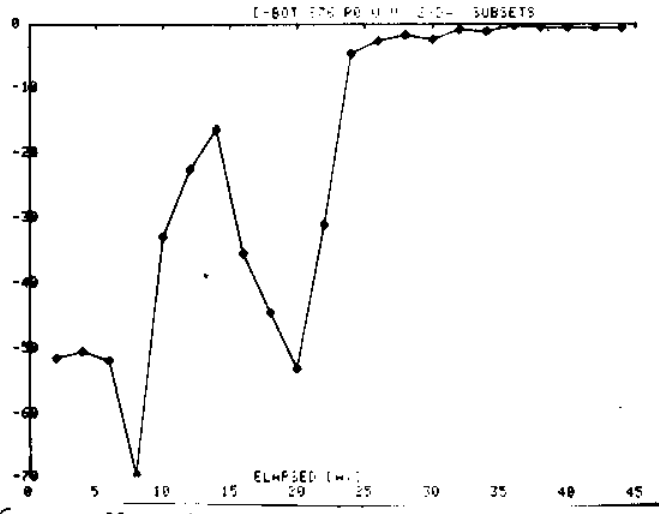

Figure 146 Momentum correlation variance in the horizontal plane for D_{bot} Summer, 1976 (2-day subset)

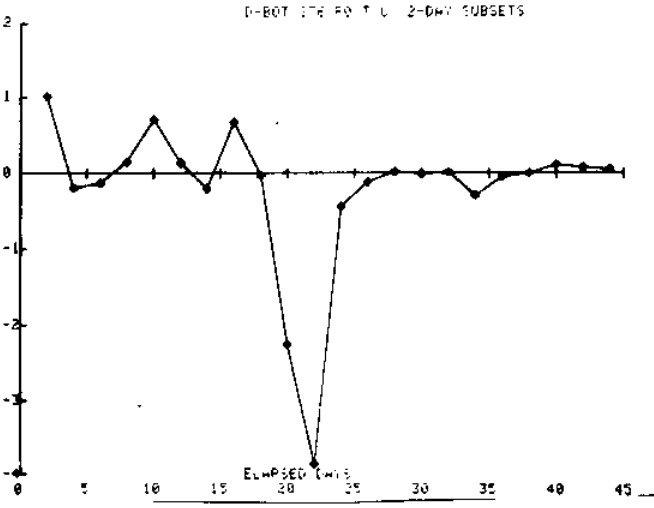

Figure 147 Heat correlation variance in the x-direction for D_{bot} Summer, 1976 (2-day subset)

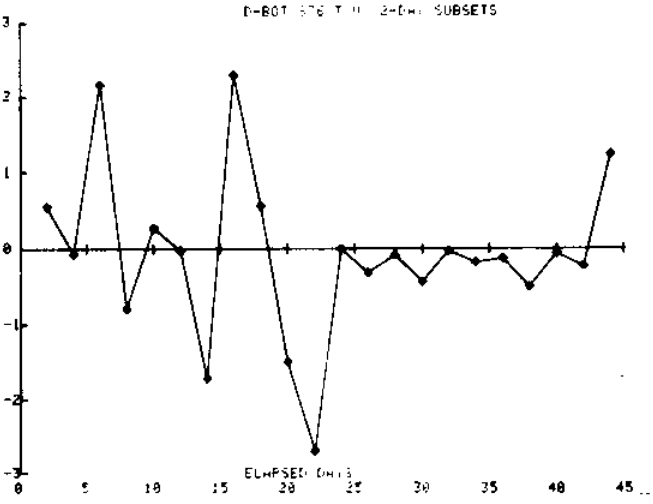

Figure 148 Heat correlation variance in the y-direction for D_{bot} Summer, 1976 (2-day subset)

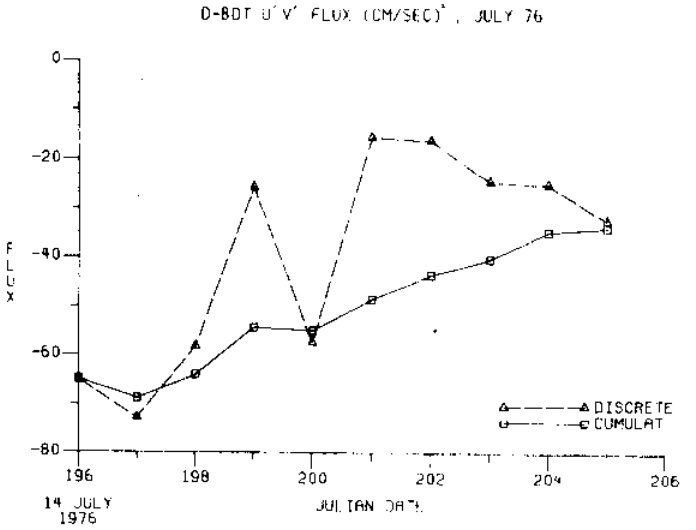

Figure 149 Momentum correlation variance in horizontal plane for D_{bot}, July 14-23, 1976

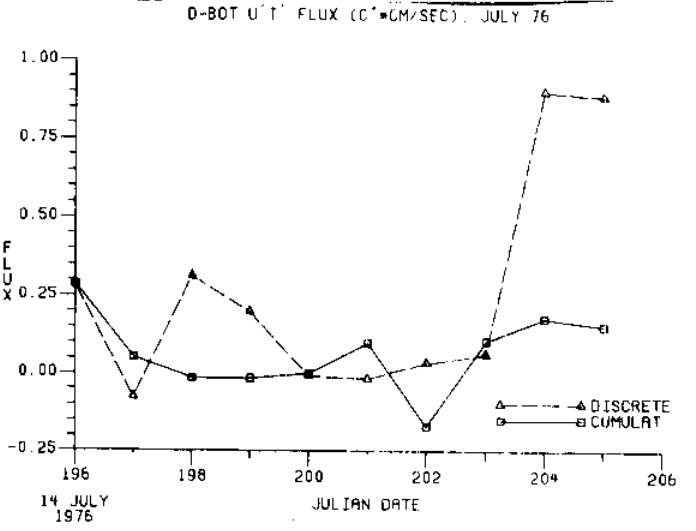

Figure 150 Heat correlation variance in x-direction for D_{bot}, July 14-23, 1976

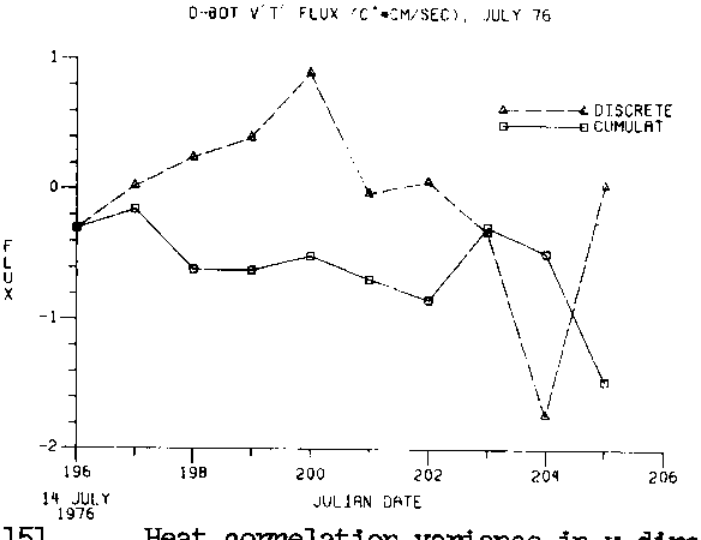

Figure 151 Heat correlation variance in y-direction for D_{bot}, July 14-23, 1976

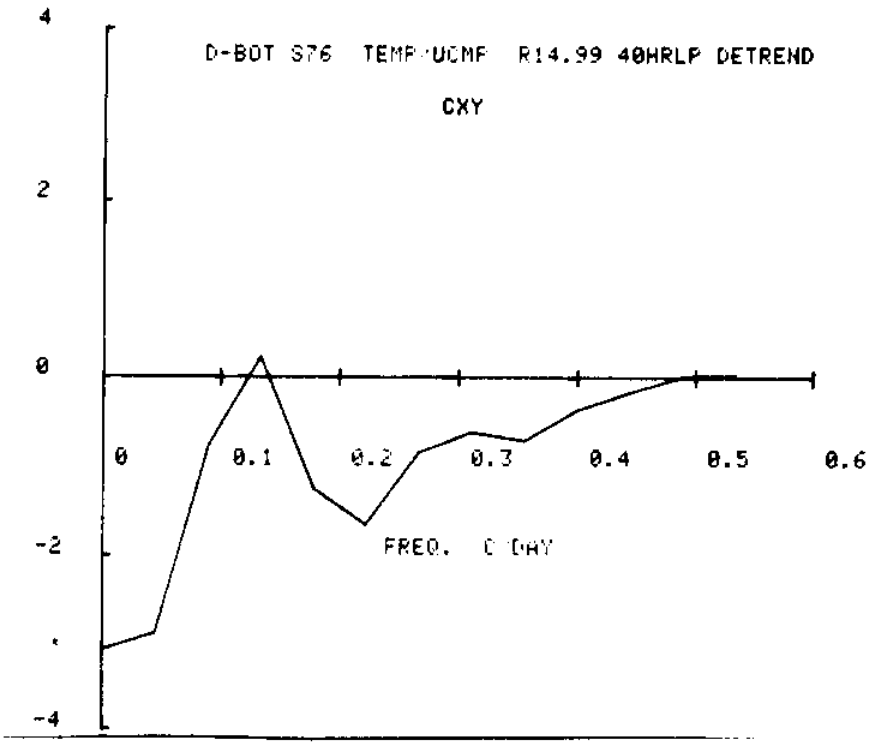

Figure 152 Cospectra of temperature vs. u-component for meter D_{bot}

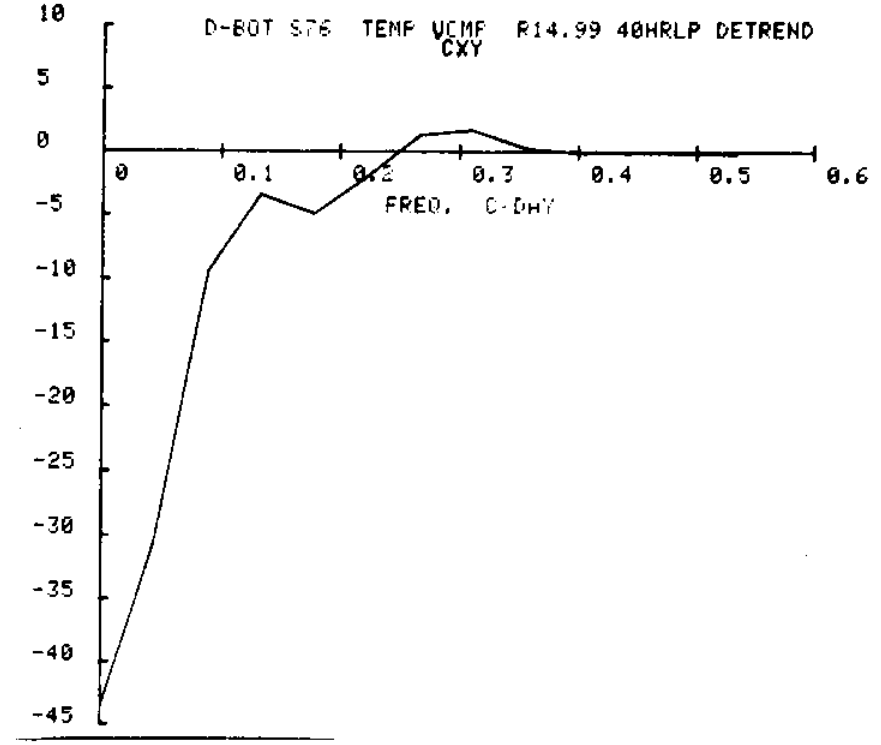

Figure 153 Cospectra of temperature vs. v-component for meter D_{bot}

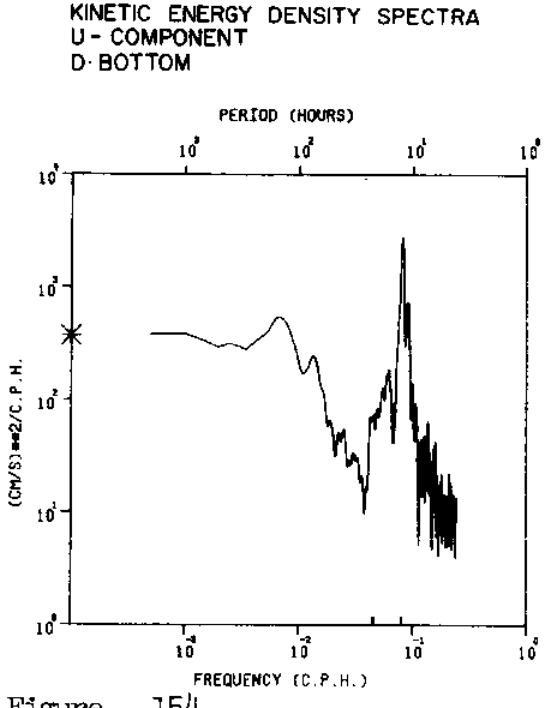

Figure 154
Kinetic energy density spectra for current velocity, u-component, D_{bot}

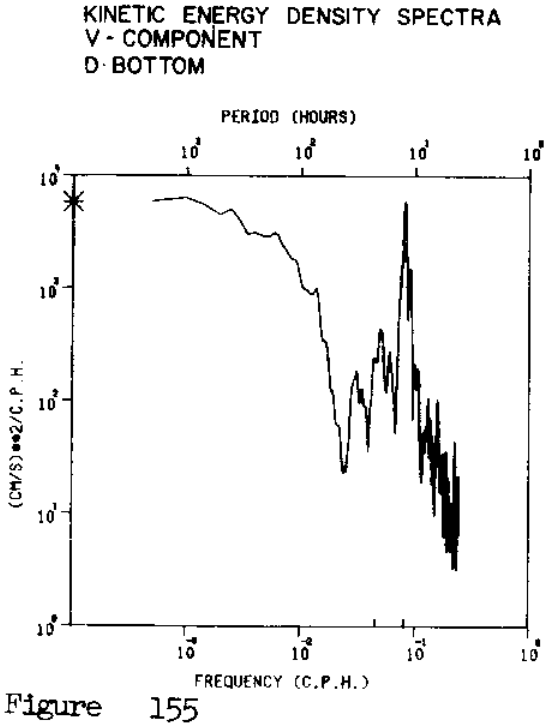

Figure 155
Kinetic energy density spectra for current velocity, v-component, D_{bot}

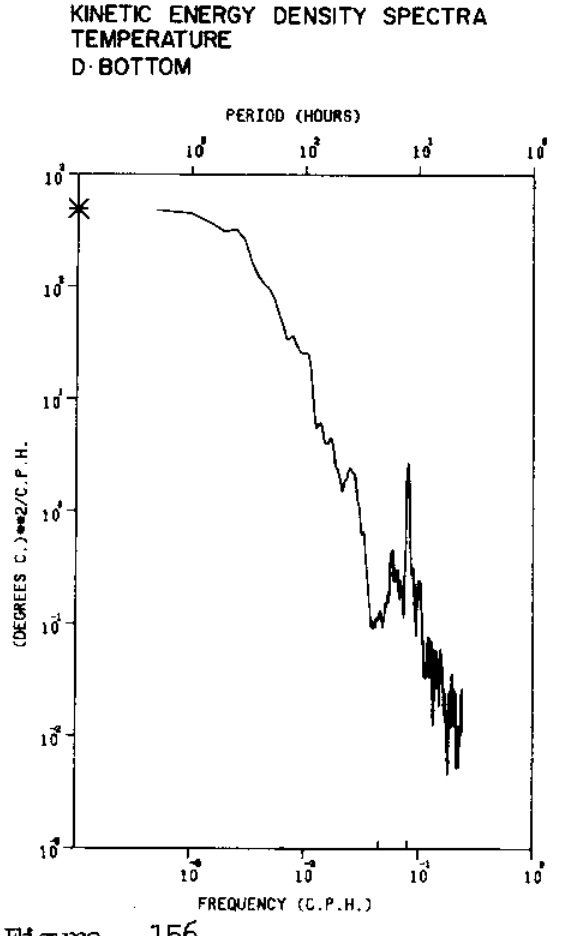

Figure 156
Kinetic energy density spectra for temperature at D_{bot}

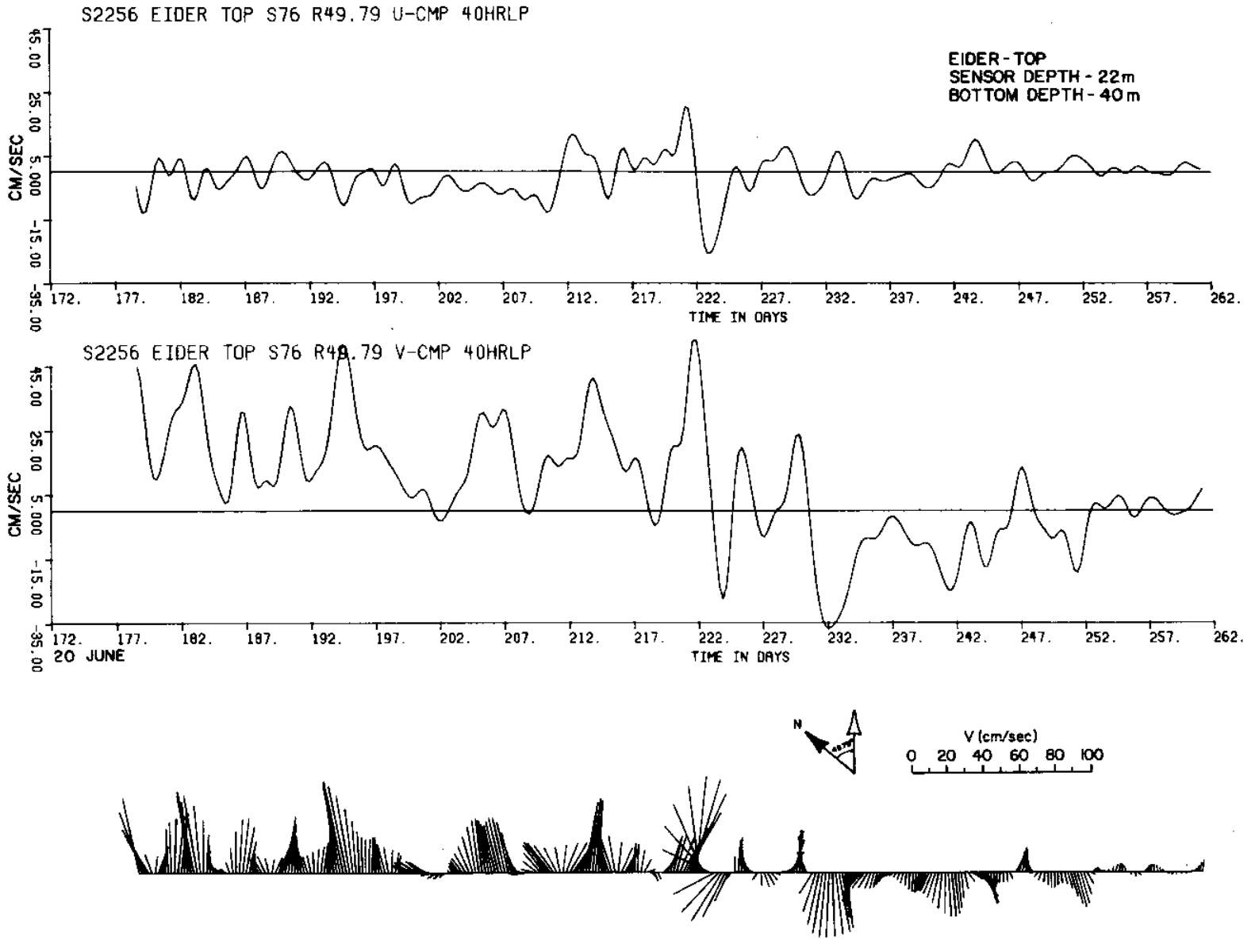

Figure 157 Low pass current velocity components and vectors from meter $E(Eider)_{top}$

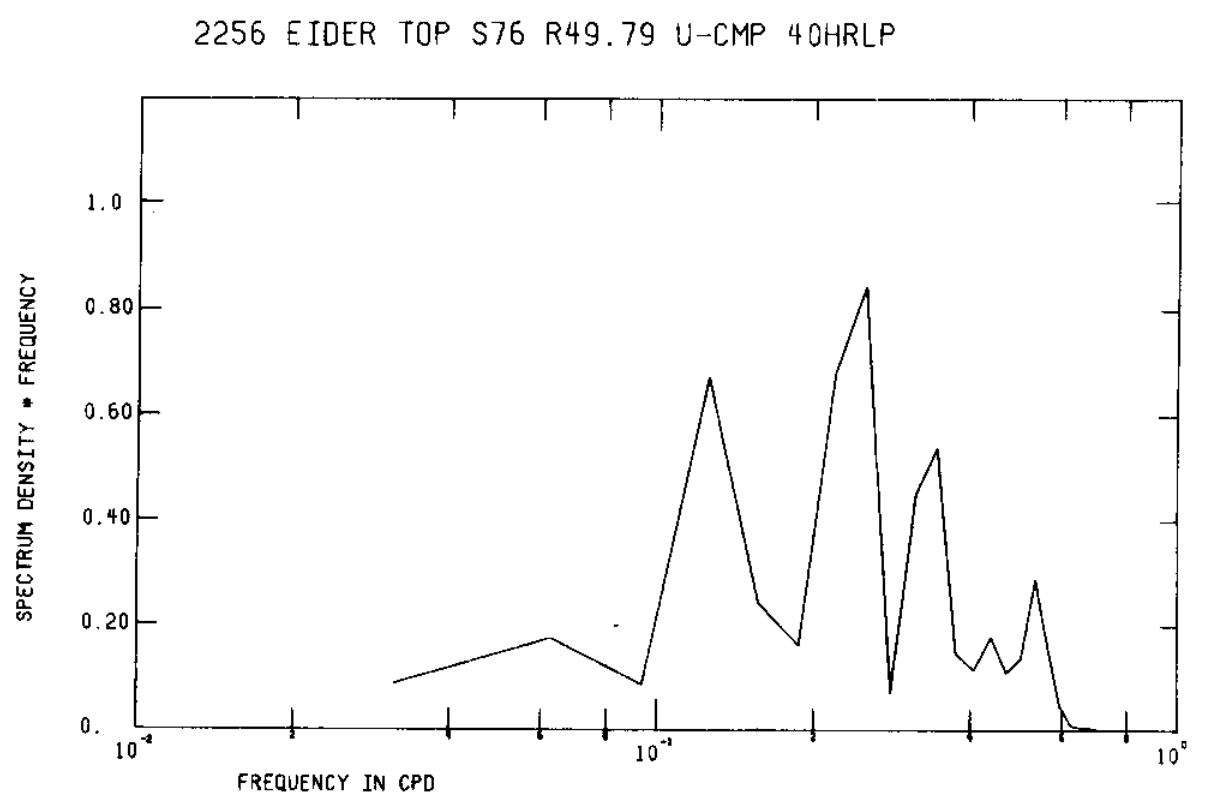

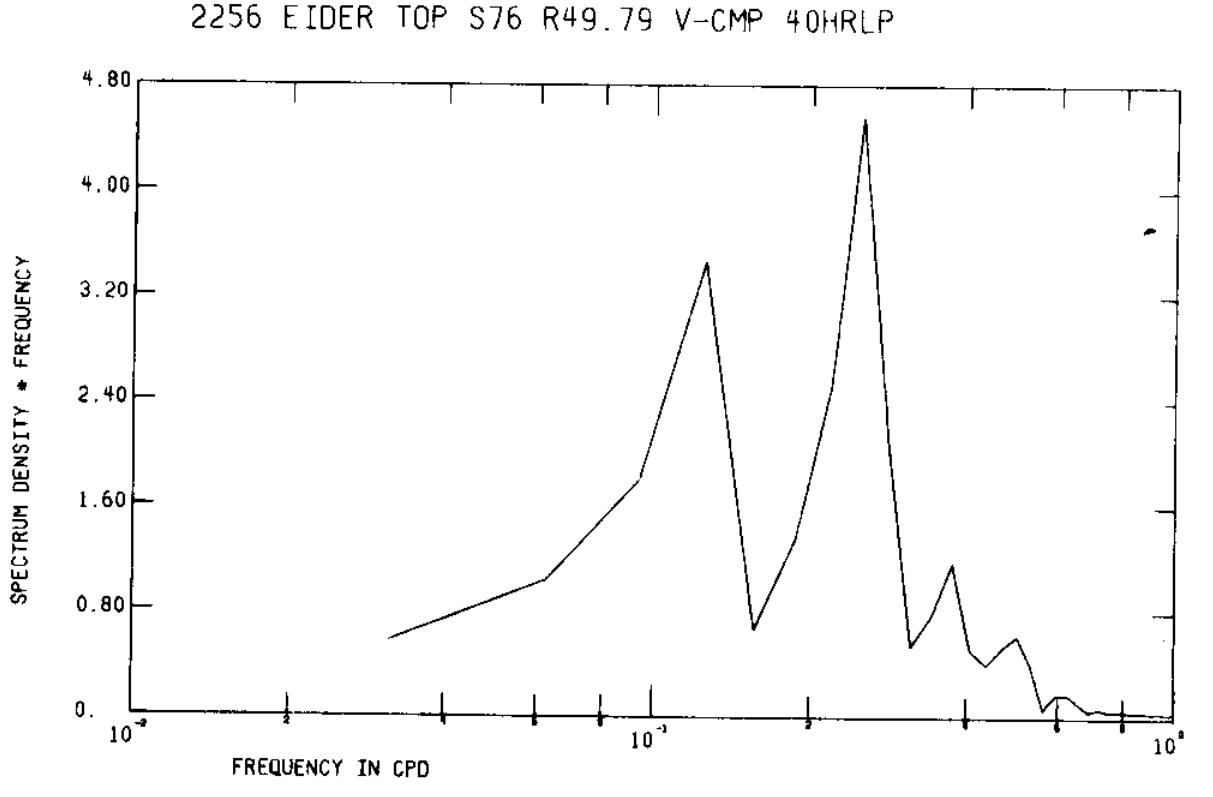

Figure 158 FFT of low pass current velocity components from meter $E(Eider)_{top}$

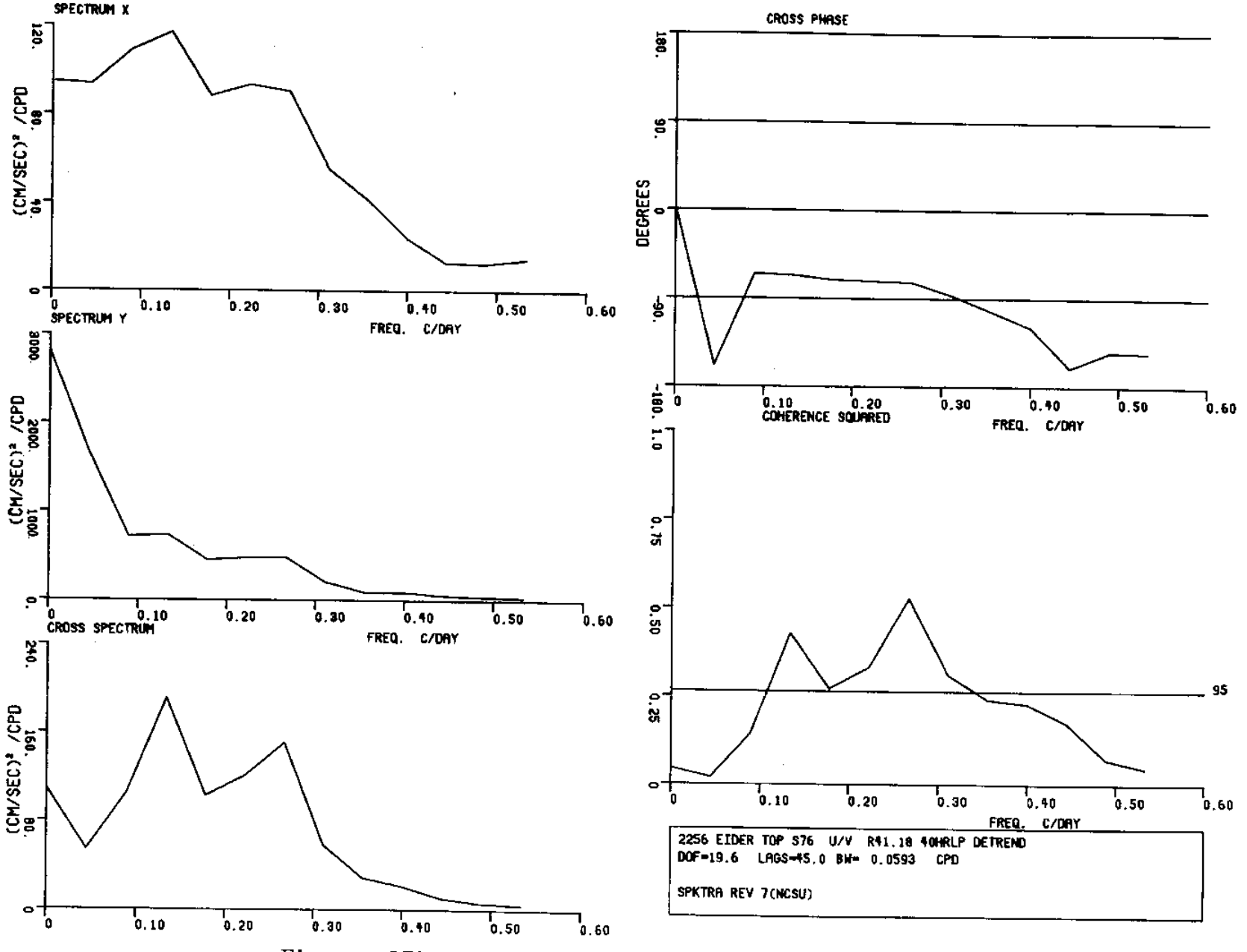

Figure 159 Spectra of low pass current velocity components from meter $E(Eider)_{top}$

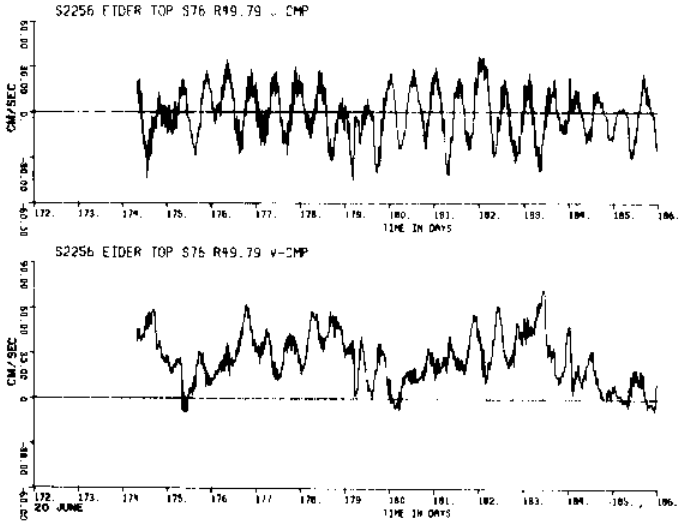

Figure 160 a

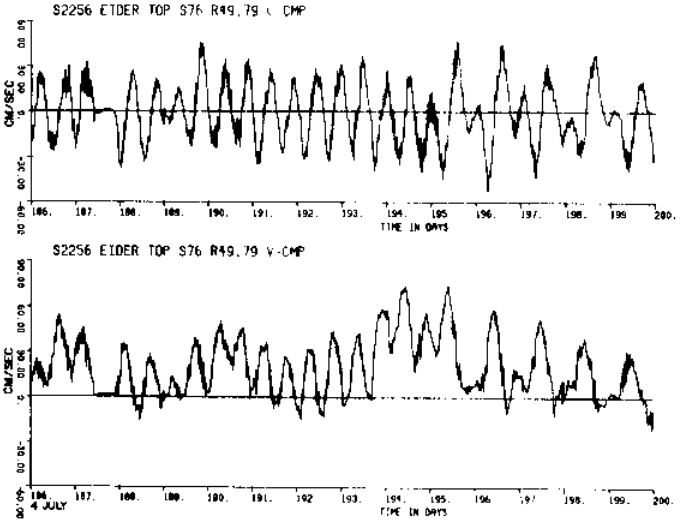

Figure 160 b

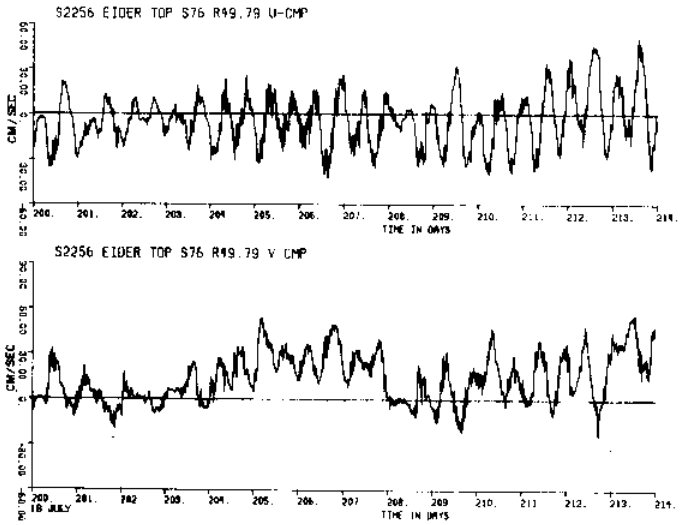

Figure 160 c

Figure 160 (a,b,c,d, e,f,g) Unfiltered current velocity components from meter E(Eider)$_{top}$

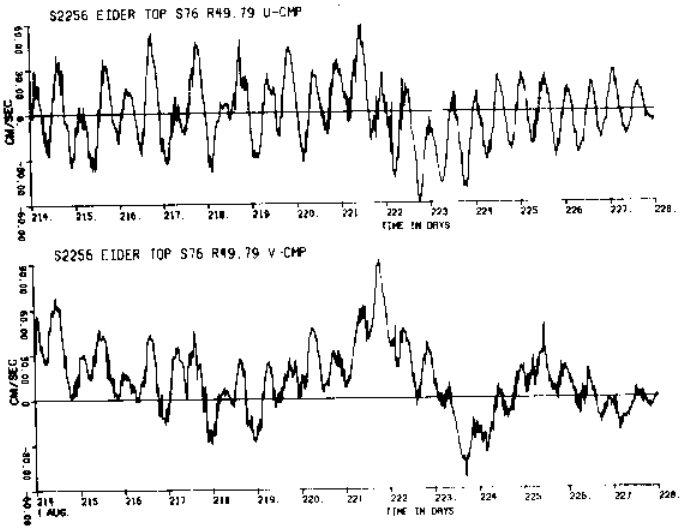

Figure 160 d

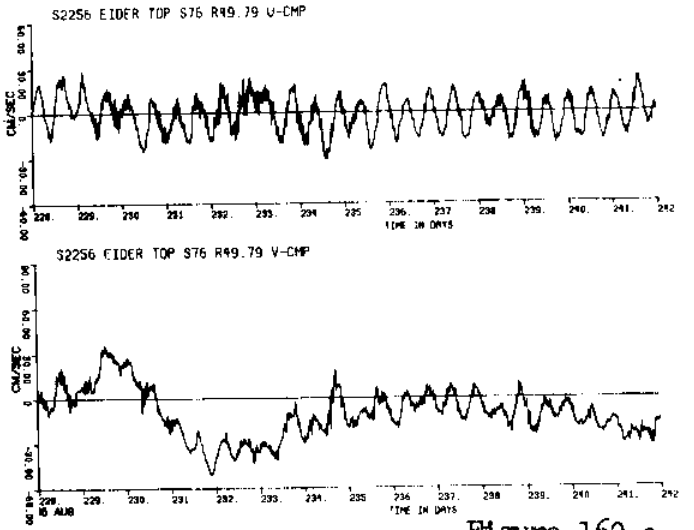

Figure 160 e

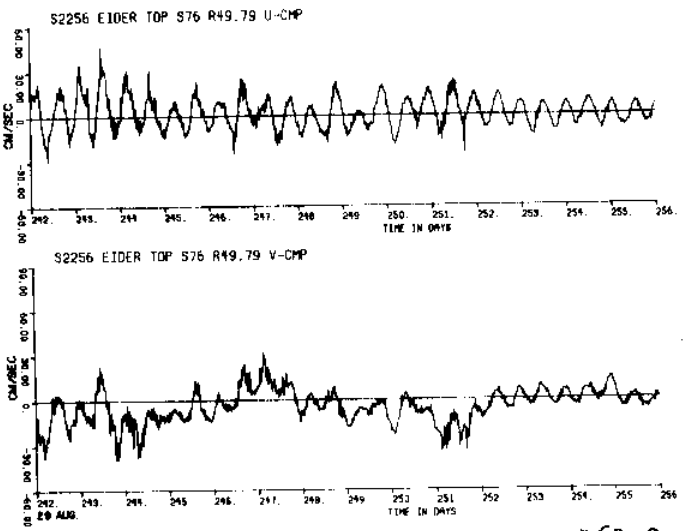

Figure 160 f

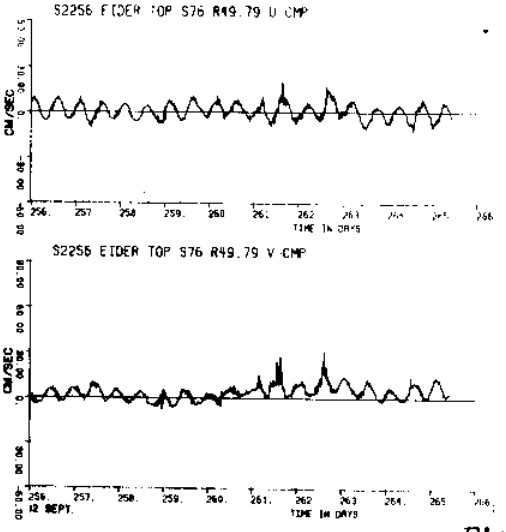
S2256 EIDER TOP S76 R49.79 U CMP
CM/SEC
TIME IN DAYS
S2256 EIDER TOP S76 R49.79 V CMP
CM/SEC
12 SEPT.
TIME IN DAYS

Figure 160 g

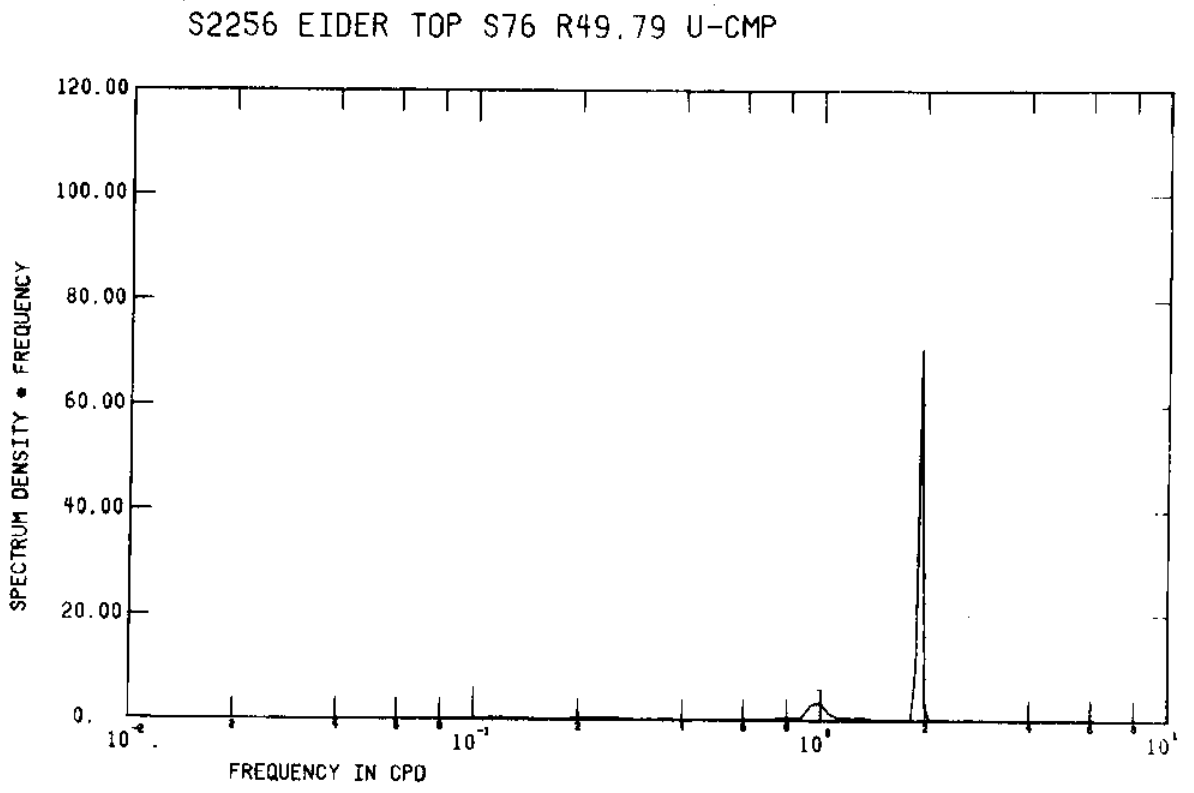

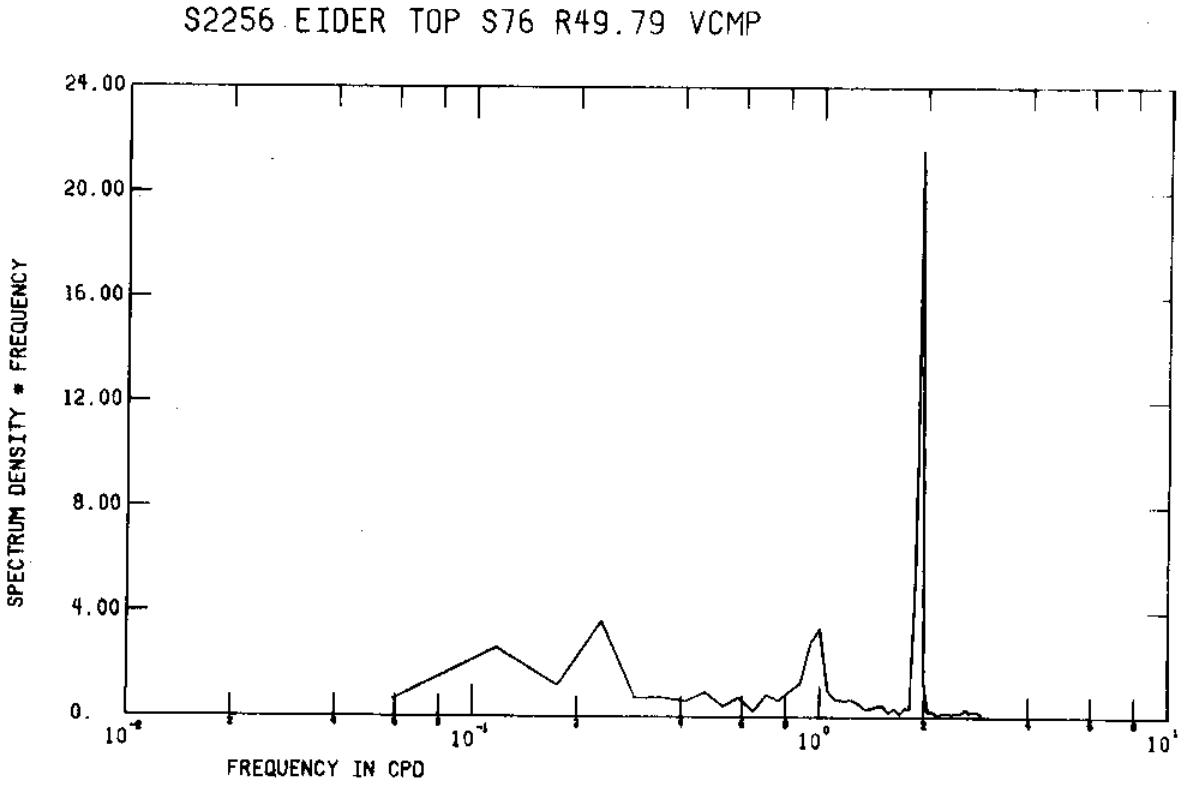

Figure 161 FFT of unfiltered current velocity components from meter $E(Eider)_{top}$

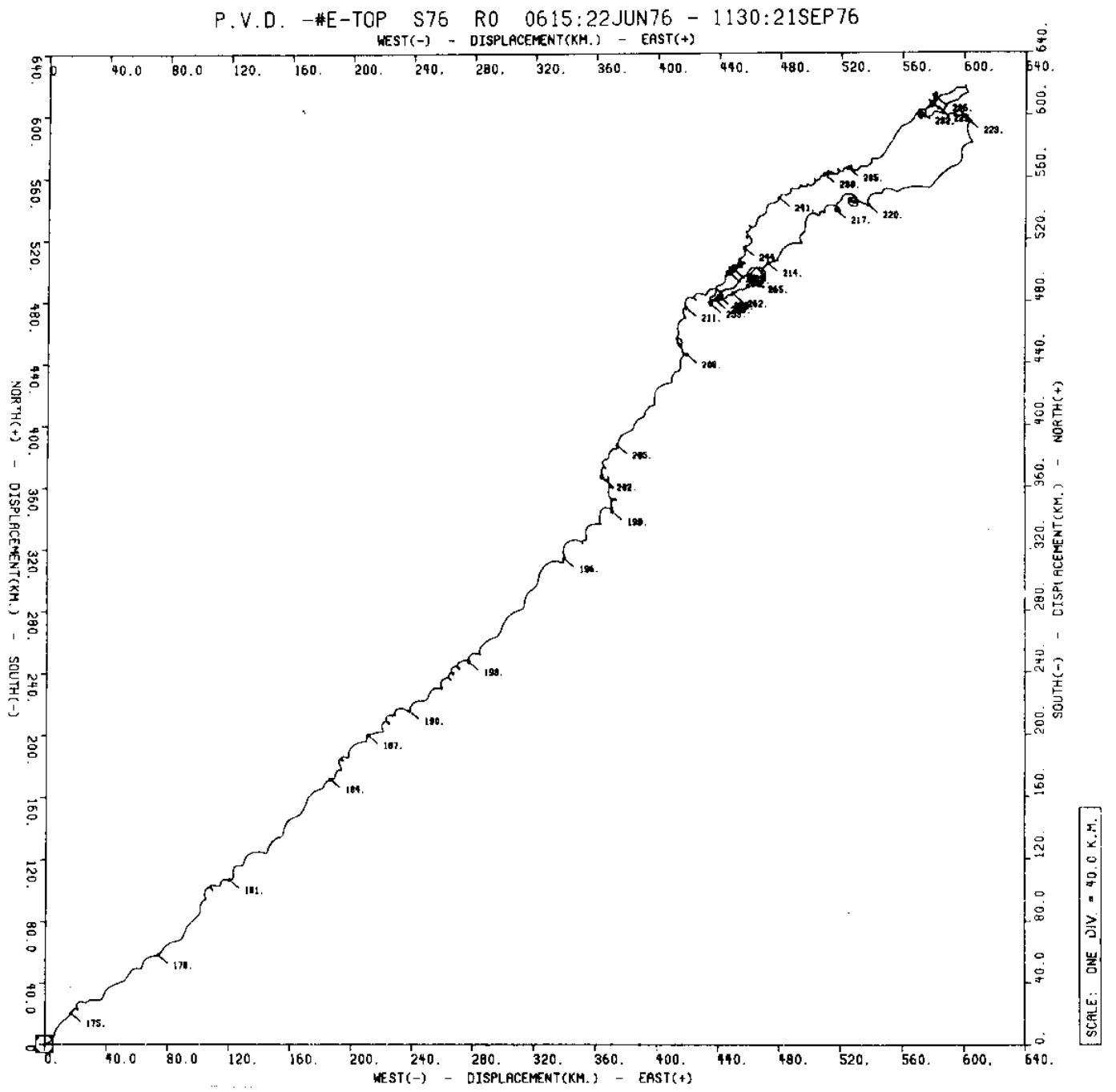

Figure 162 a

Figure 162 (a,b,c) Progressive vector diagrams of unfiltered current velocity from meter E(Eider)$_{top}$

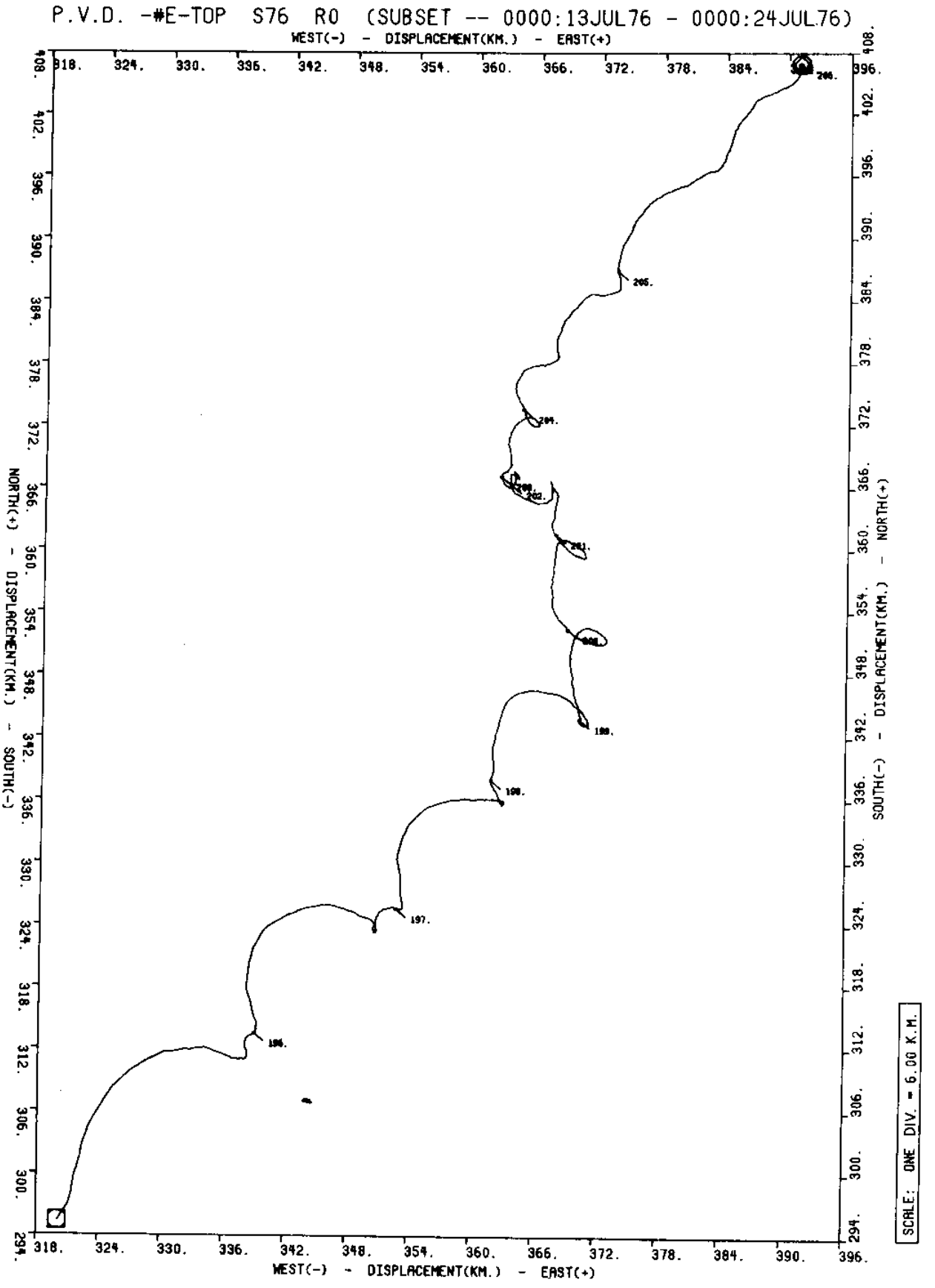
P.V.D. -#E-TOP S76 R0 (SUBSET -- 0000:13JUL76 - 0000:24JUL76)
WEST(-) - DISPLACEMENT(KM.) - EAST(+)
NORTH(+) - DISPLACEMENT(KM.) - SOUTH(-)
SOUTH(-) - DISPLACEMENT(KM.) - NORTH(+)
WEST(-) - DISPLACEMENT(KM.) - EAST(+)
SCALE: ONE DIV. = 6.00 K.M.

Figure 162 b

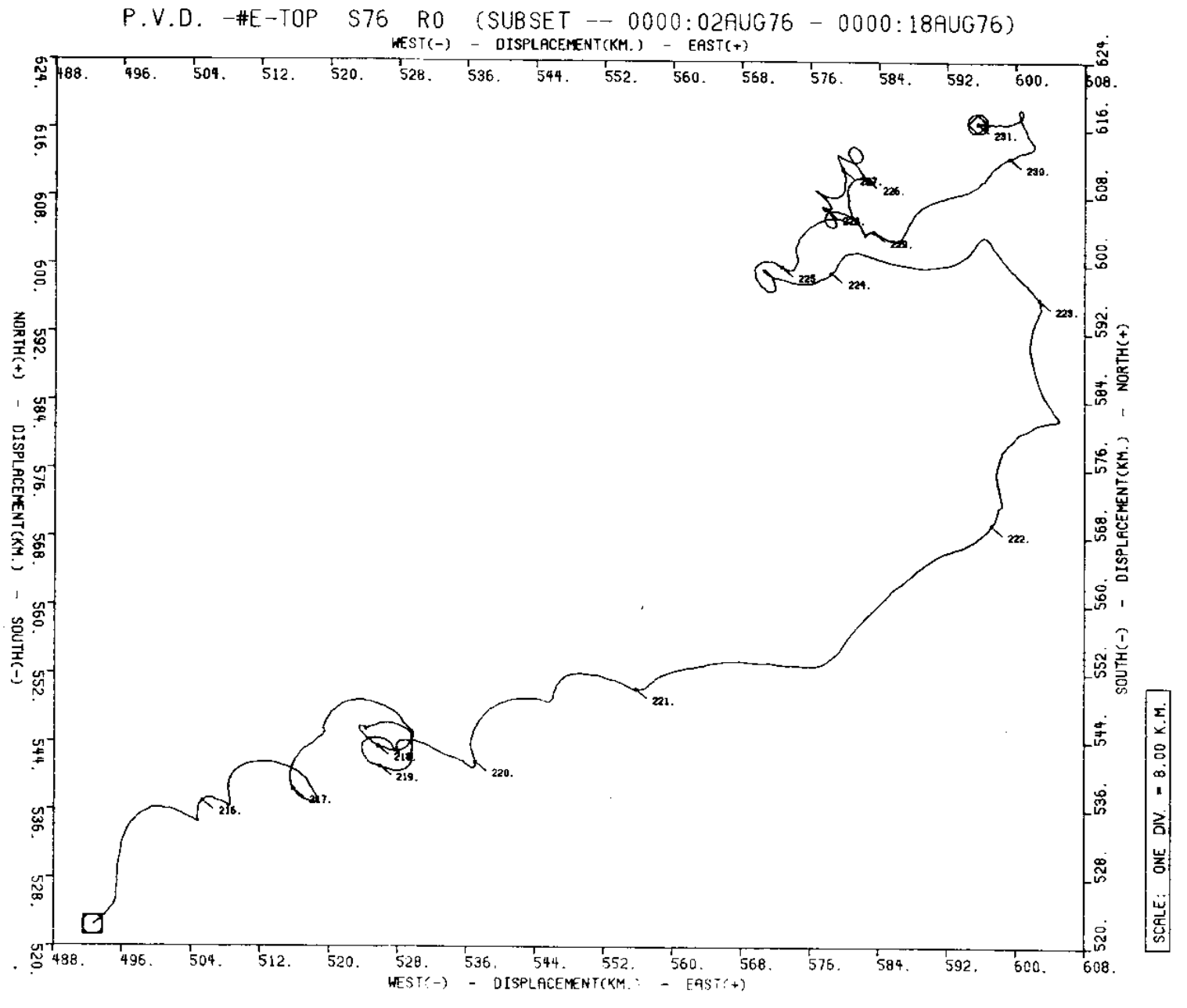
P.V.D. -#E-TOP S76 R0 (SUBSET -- 0000:02AUG76 - 0000:18AUG76)
WEST(-) - DISPLACEMENT(KM.) - EAST(+)
NORTH(+) - DISPLACEMENT(KM.) - SOUTH(-)
SOUTH(-) - DISPLACEMENT(KM.) - NORTH(+)
SCALE: ONE DIV. = 8.00 K.M.
488. 496. 504. 512. 520. 528. 536. 544. 552. 560. 568. 576. 584. 592. 600. 608.
624. 616. 608. 600. 592. 584. 576. 568. 560. 552. 544. 536. 528. 520.
231.
230.
226.
225.
224.
223.
222.
221.
220.
219.
218.
217.
216.

Figure 162 c

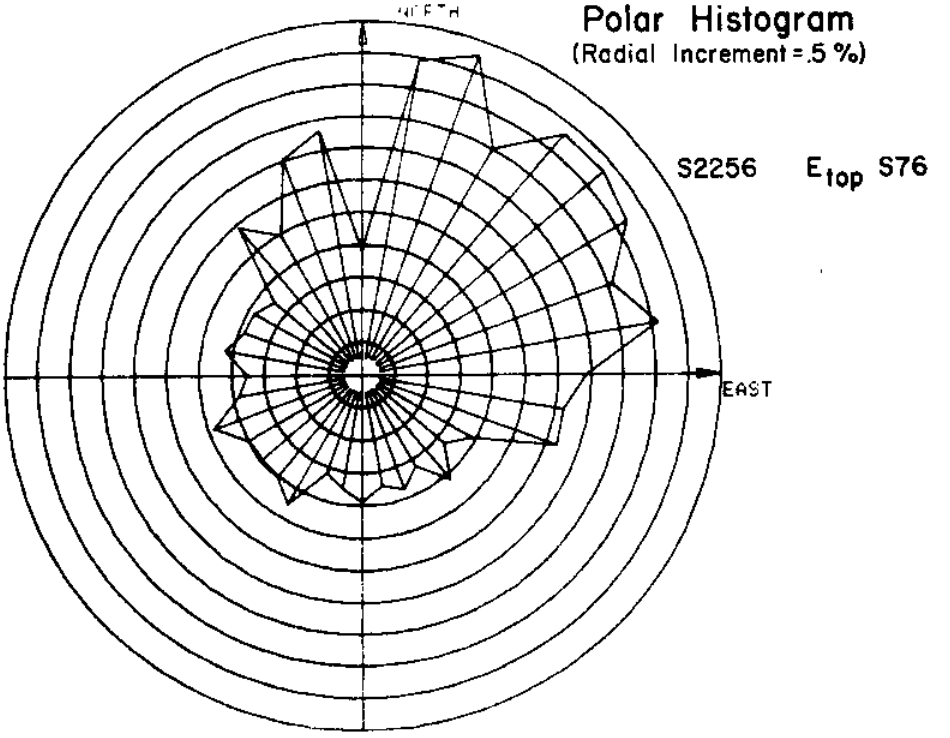

Figure 163 Histogram from meter $E(Eider)_{top}$

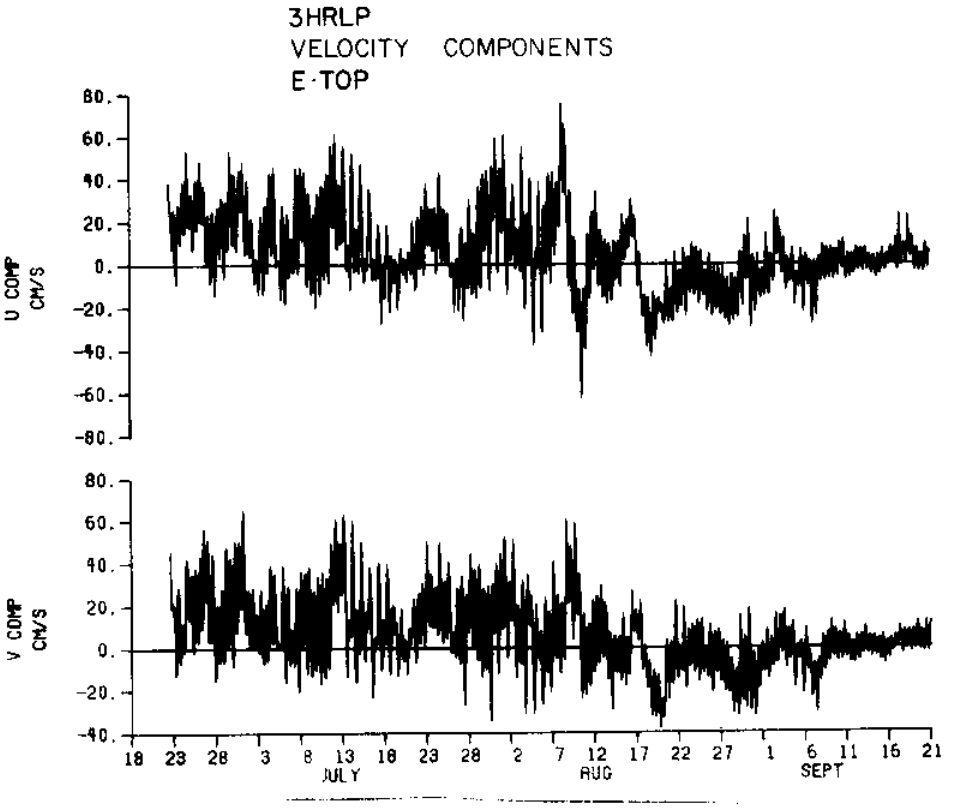

Figure 164 3HRLP velocity components for E_{top}

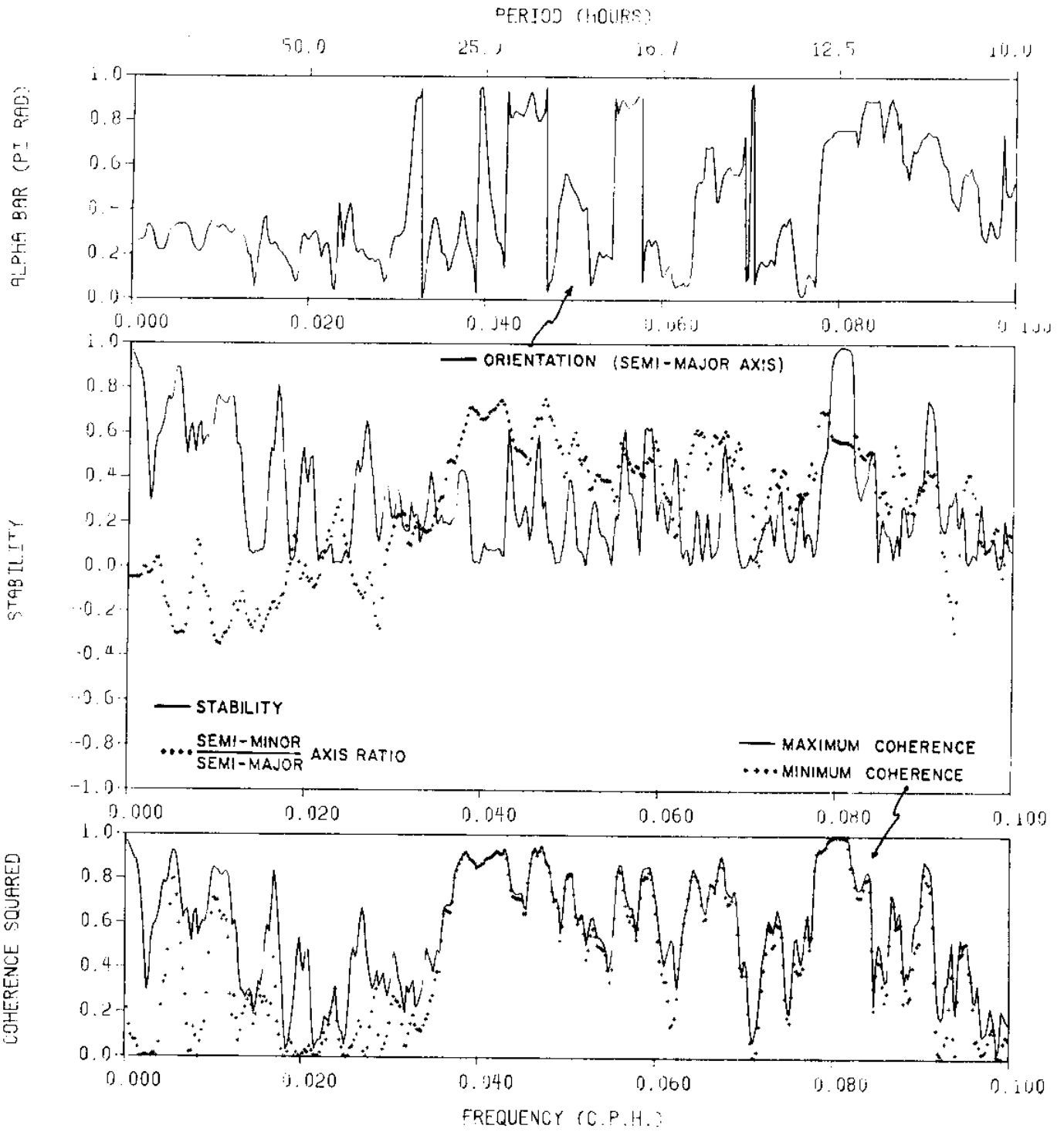

Figure 165 Hodograph parameters from meter E(Eider)$_{top}$

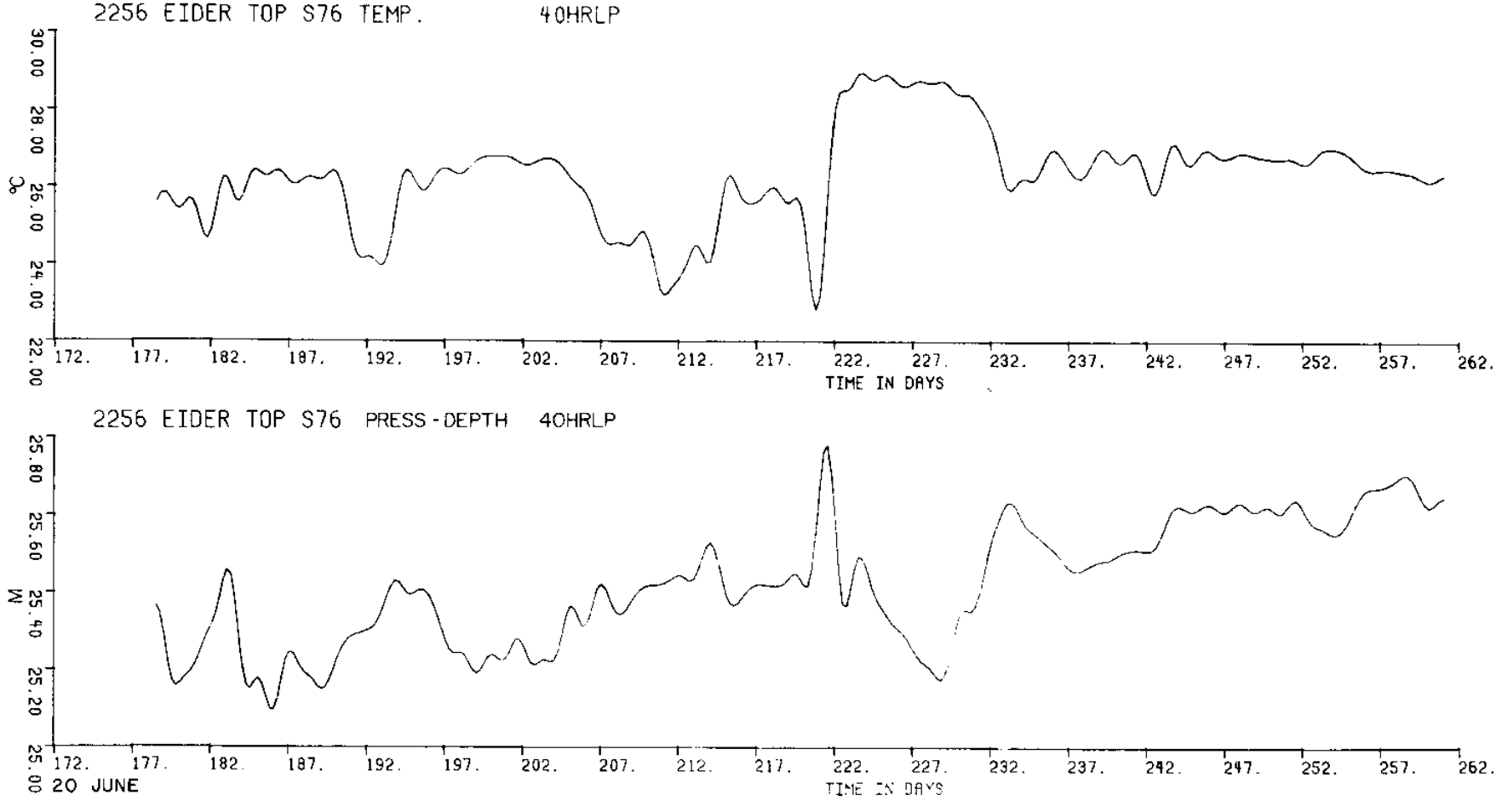

Figure 166 Low pass temperature and pressure from meter $E(Eider)_{top}$

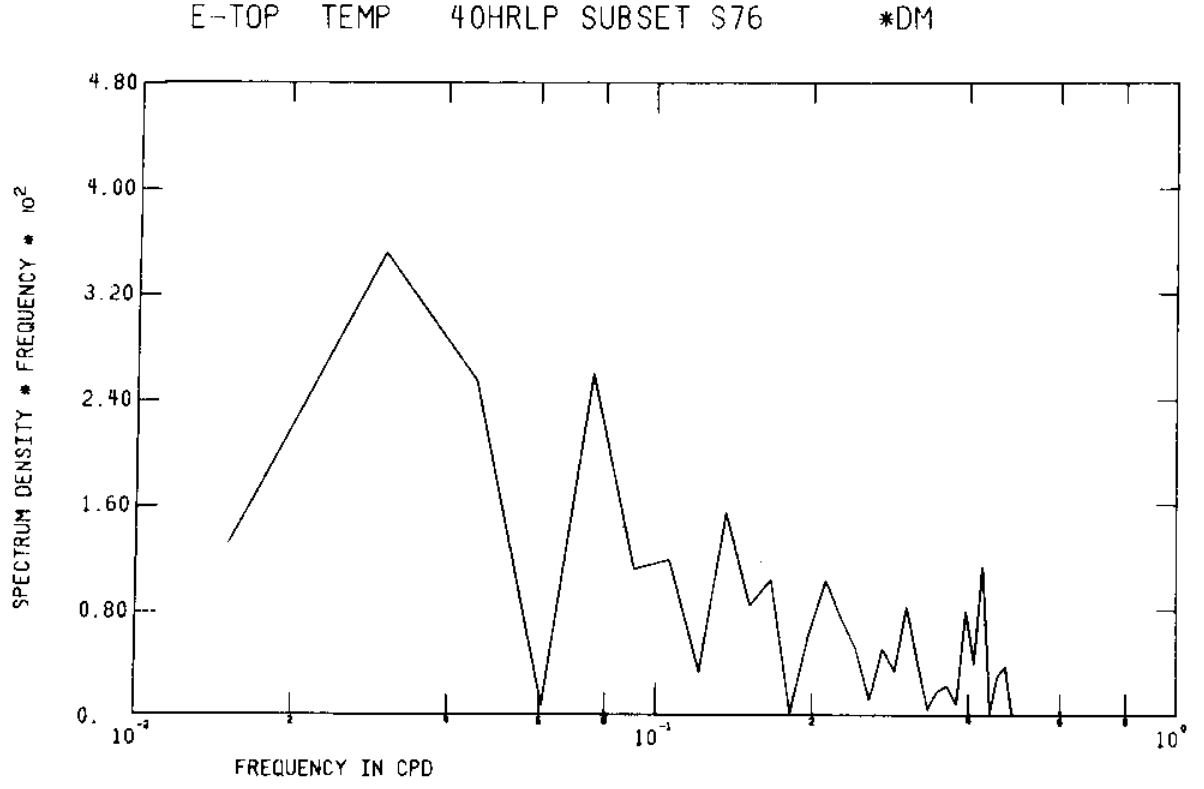

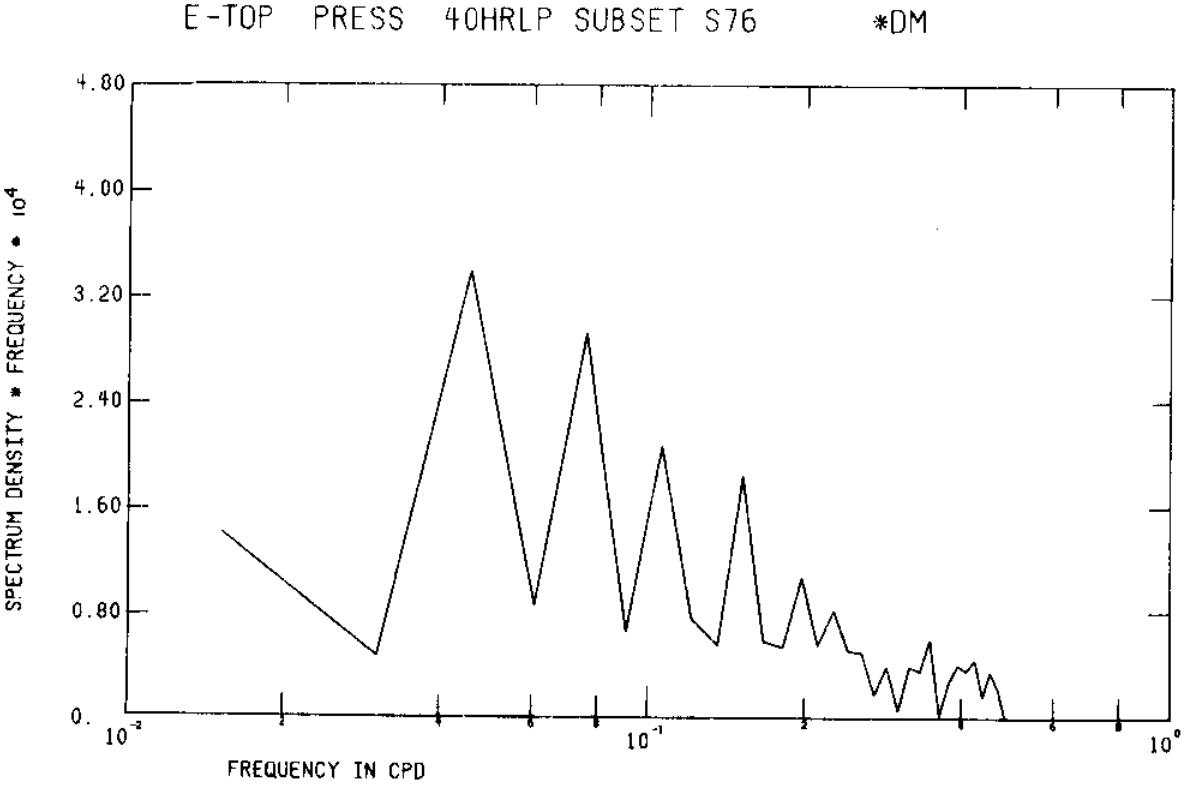

Figure 167 FFT of low pass temperature and pressure from meter E(Elder)$_{top}$

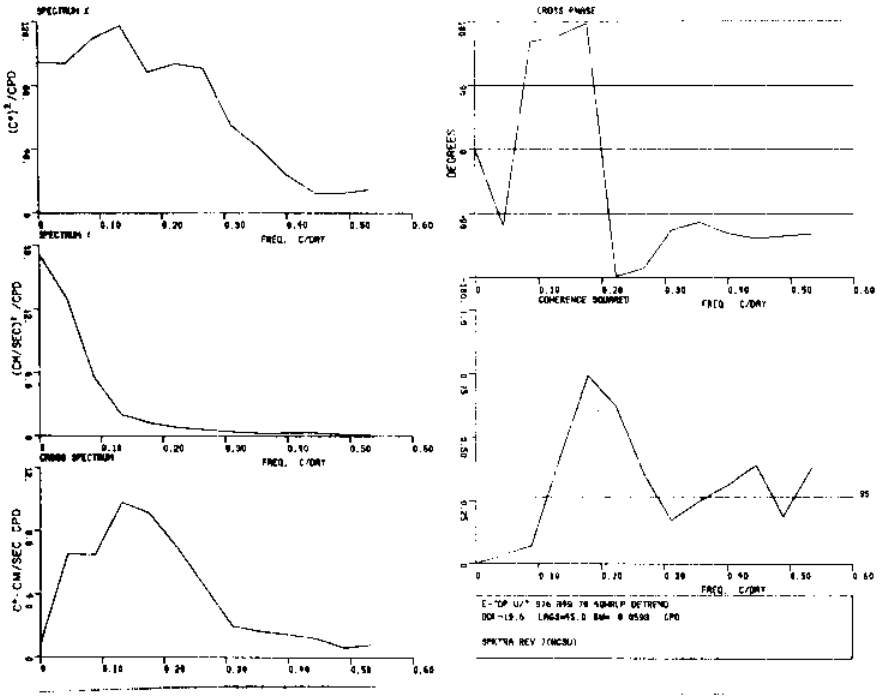

Figure 168 Spectra of temperature and the low pass current velocity u component, both from meter $E(Eider)_{top}$

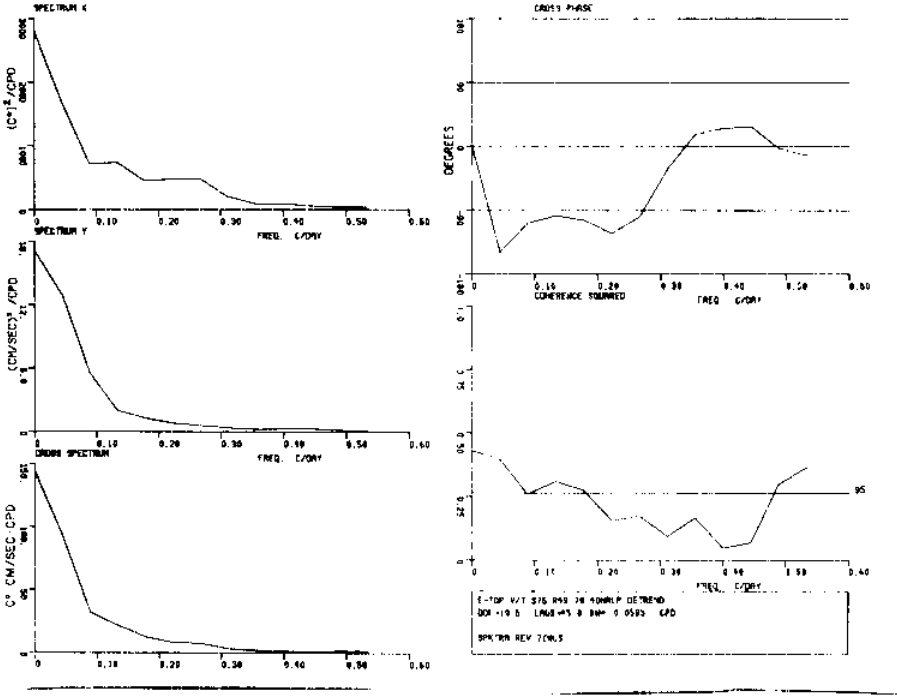

Figure 169 Spectra of temperature and the low pass current velocity v component, both from meter $E(Eider)_{top}$

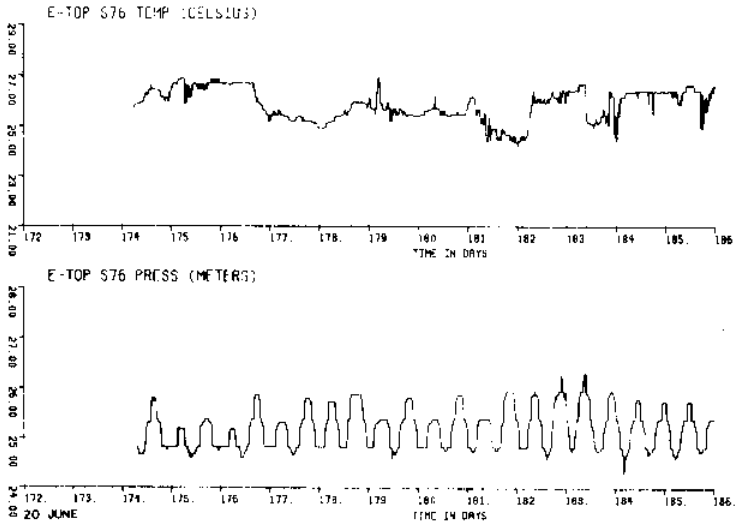

Figure 170 a

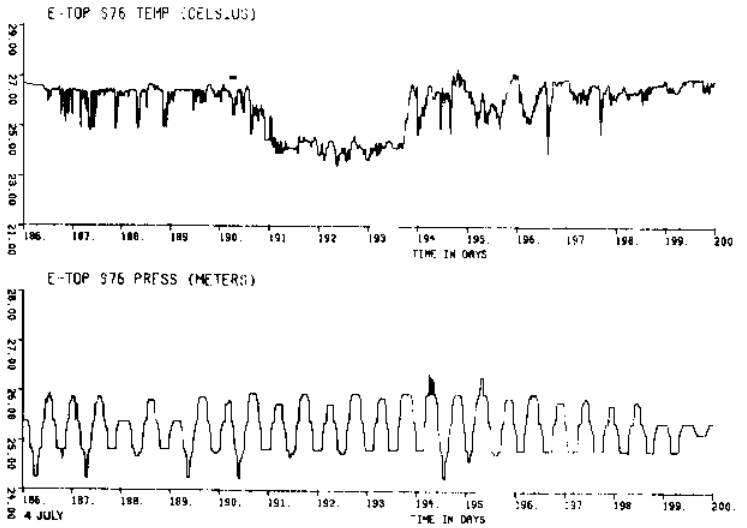

Figure 170 b

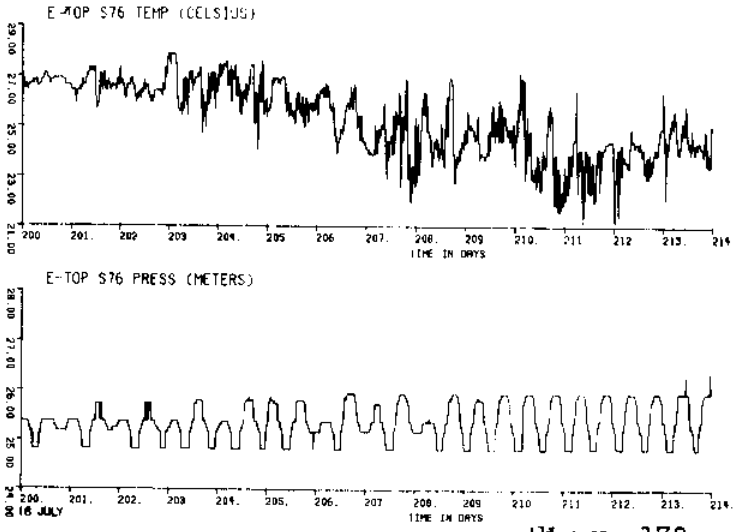

Figure 170 c

Figure 170 (a,b,c,d, e,f,g) Unfiltered temperature and pressure from meter E(Eider)$_{top}$

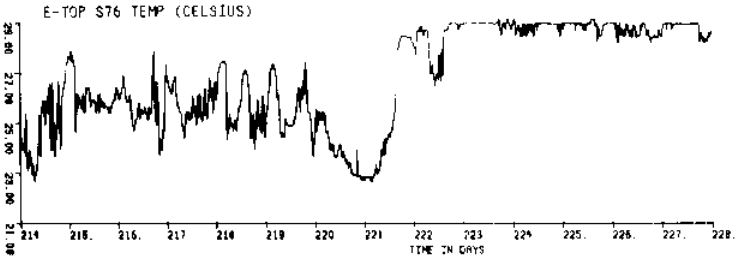

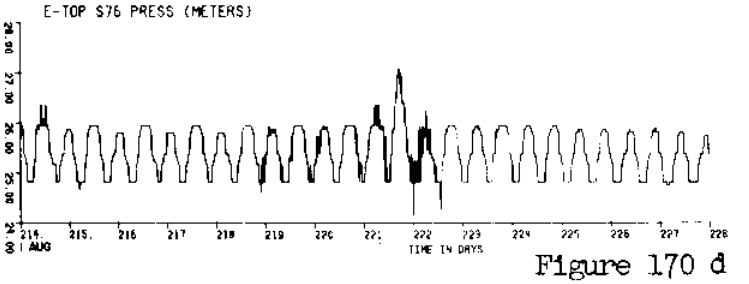

Figure 170 d

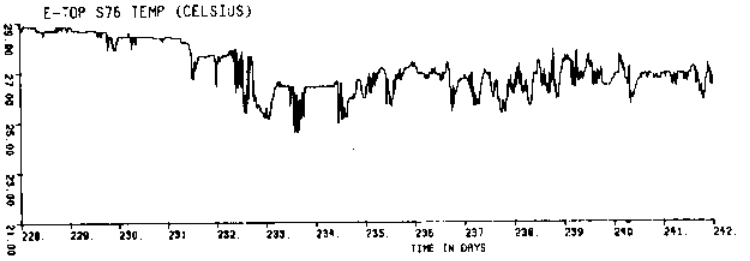

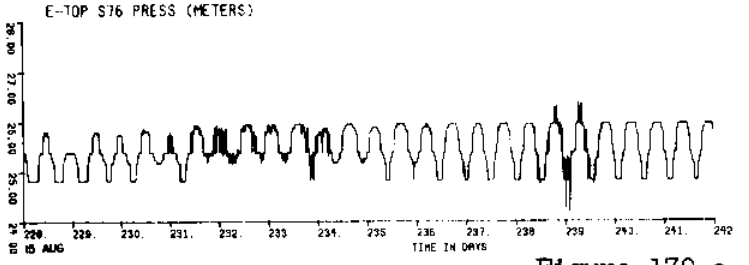

Figure 170 e

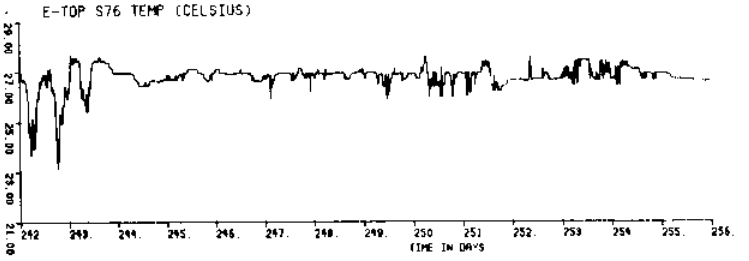

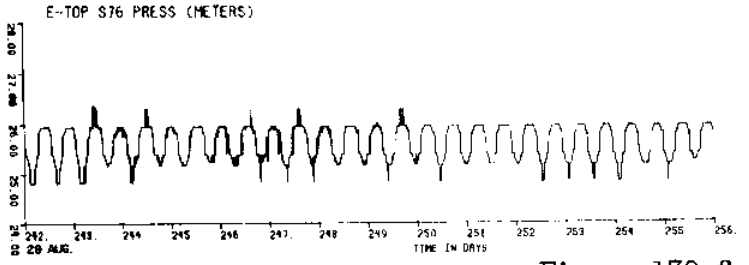

Figure 170 f

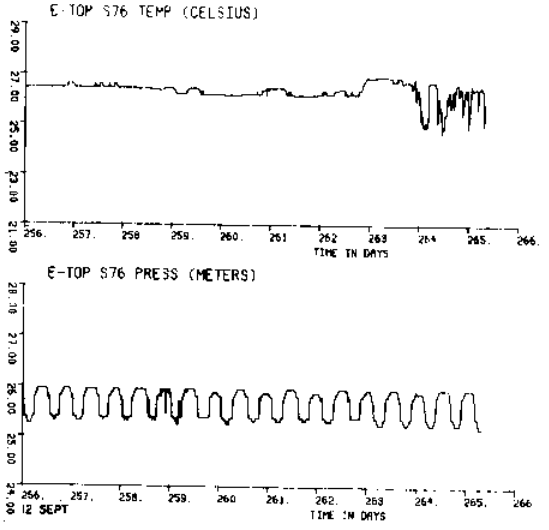
E-TOP S76 TEMP (CELSIUS)
29.00
27.00
25.00
23.00
21.00
256.
257.
258.
259.
260.
261.
262.
263.
264.
265.
266.
TIME IN DAYS
E-TOP S76 PRESS (METERS)
28.00
27.00
26.00
25.00
24.00
256.
257.
258.
259.
260.
261.
262.
263.
264.
265.
266
12 SEPT
TIME IN DAYS

Figure 170 g

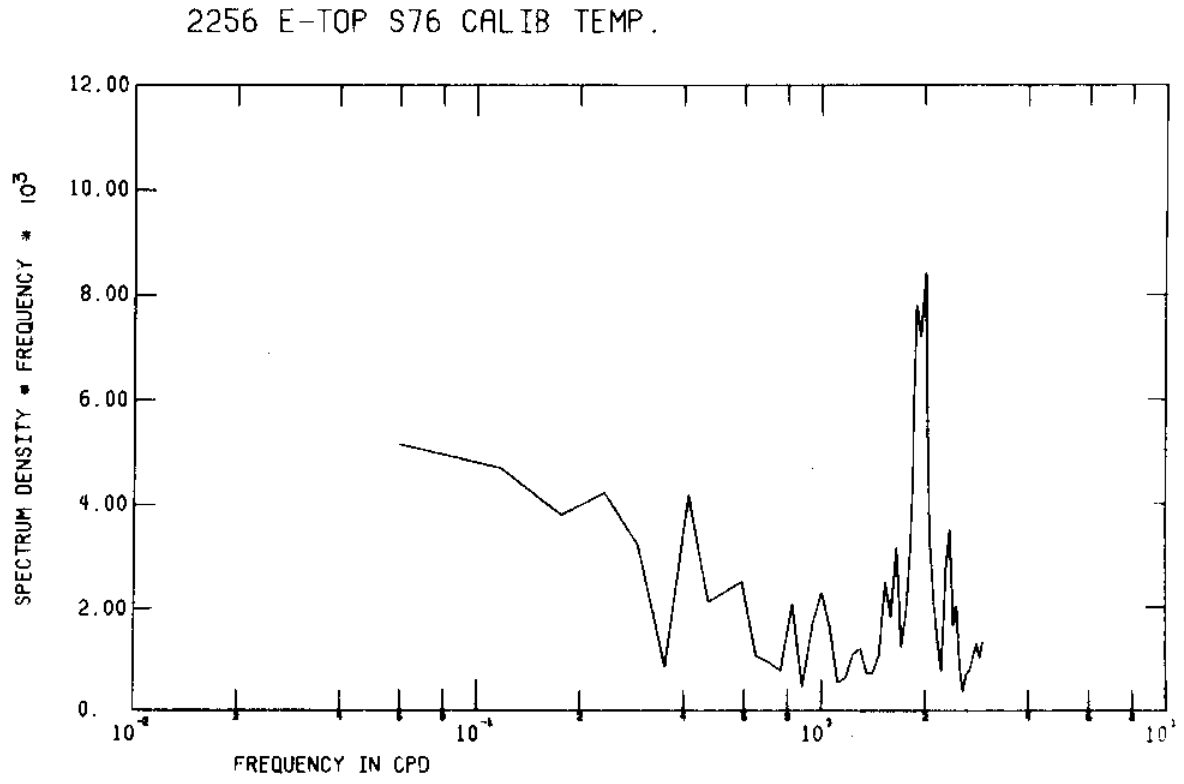

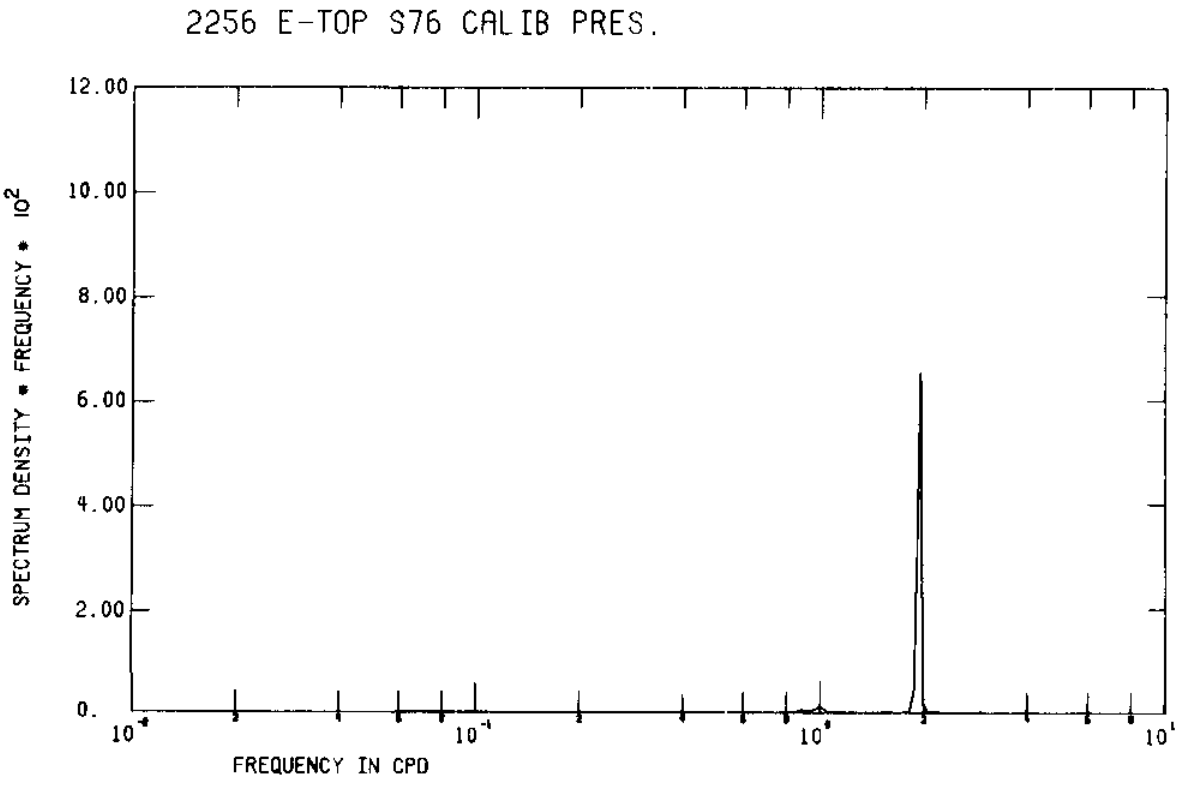

Figure 171 FFT of unfiltered temperature and pressure from meter $E(Eider)_{top}$

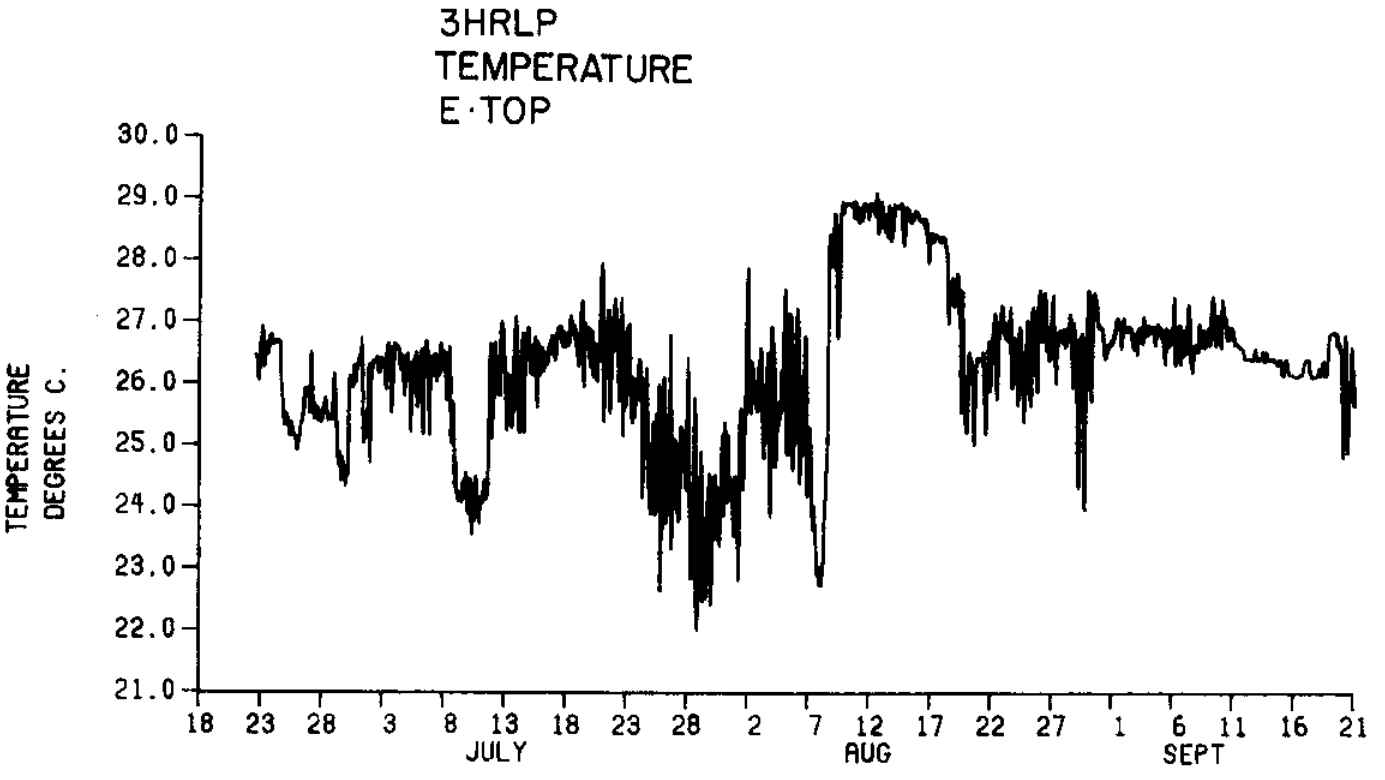

Figure 172 3HRLP temperature for E_{top}

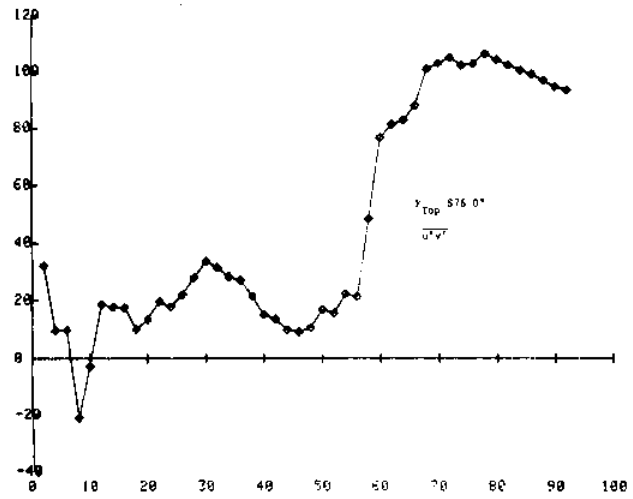

Figure 173 Momentum correlation variance in horizontal plane for E_{top} Summer, 1976 (cumulative)

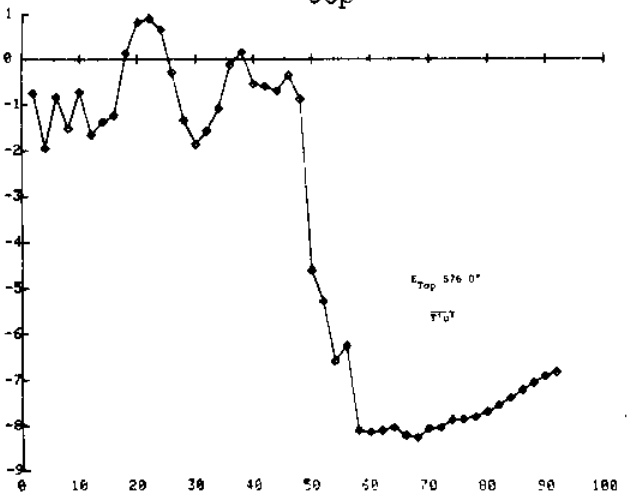

Figure 174 Heat correlation variance in x-direction for E_{top} Summer, 1976 (cumulative)

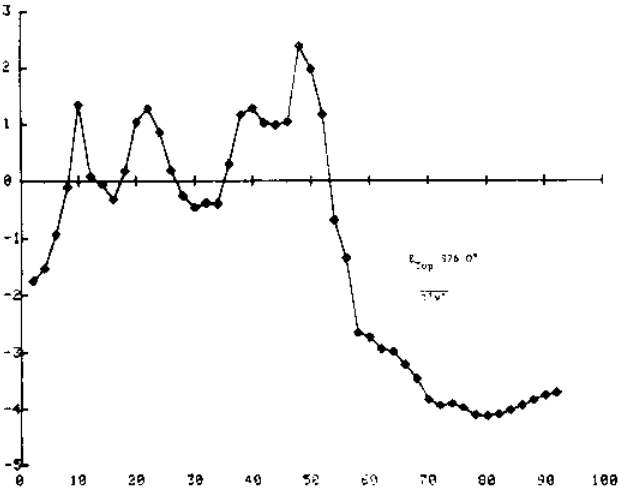

Figure 175 Heat correlation variance in y-direction for E_{top} Summer, 1976 (cumulative)

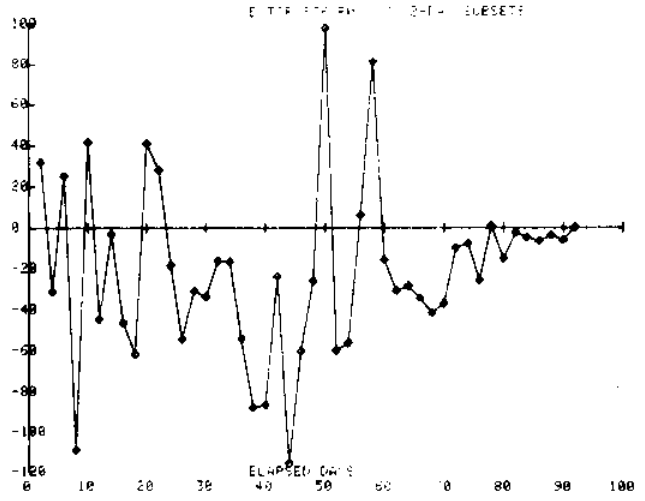

Figure 176 Momentum correlation variance in the horizontal plane for E_{top} Summer, 1976 (2-day subset)

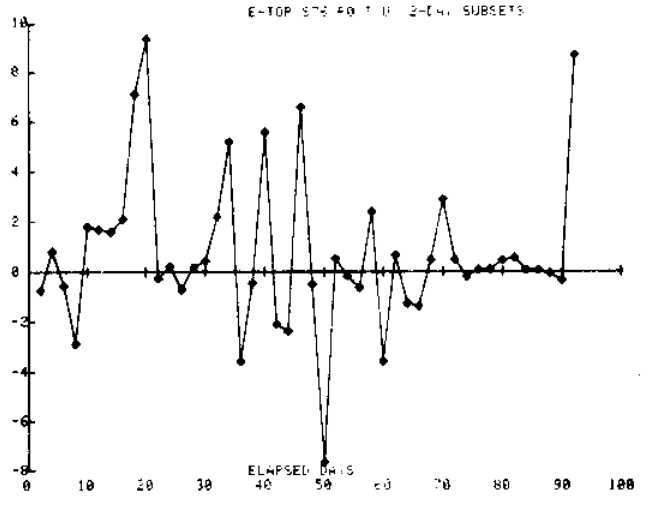

Figure 177 Heat correlation variance in the x-direction for E_{top} Summer, 1976 (2-day subset)

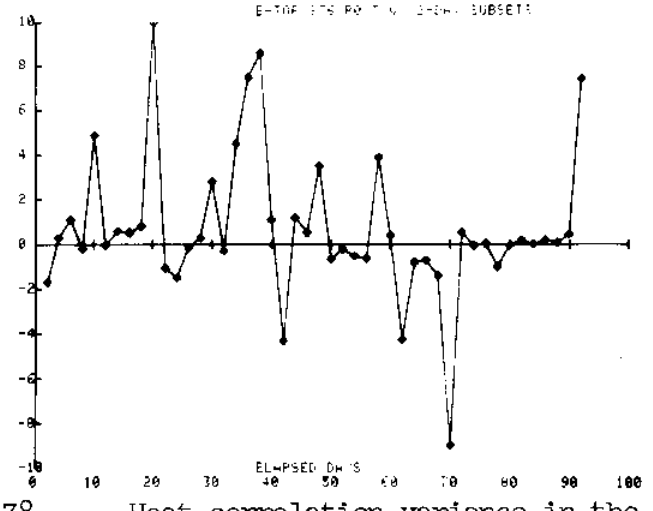

Figure 178 Heat correlation variance in the y-direction for E_{top} Summer, 1976 (2-day subset)

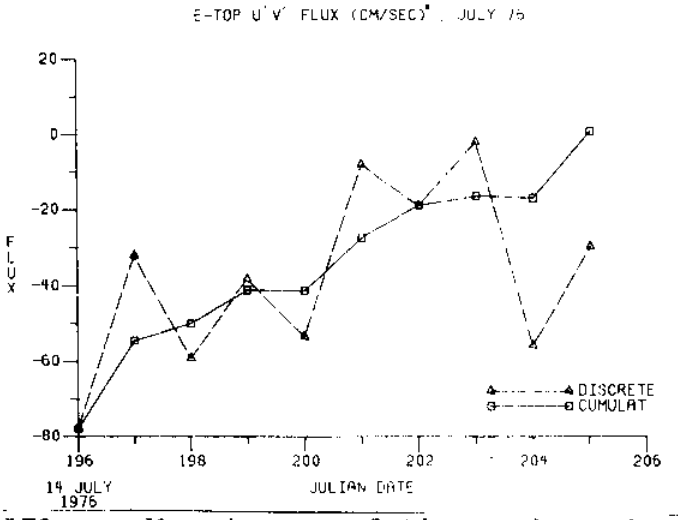

Figure 179 Momentum correlation variance in horizontal plane for E_{top} July 14-23, 1976

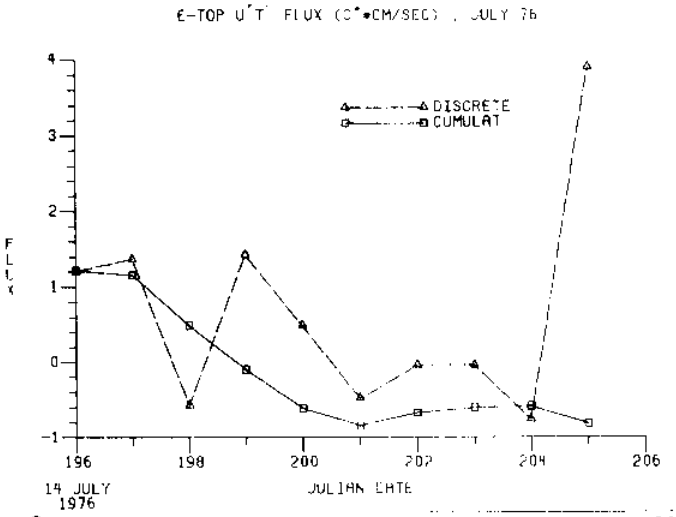

Figure 180 Heat correlation variance in x-direction for E_{top} July 14-23, 1976

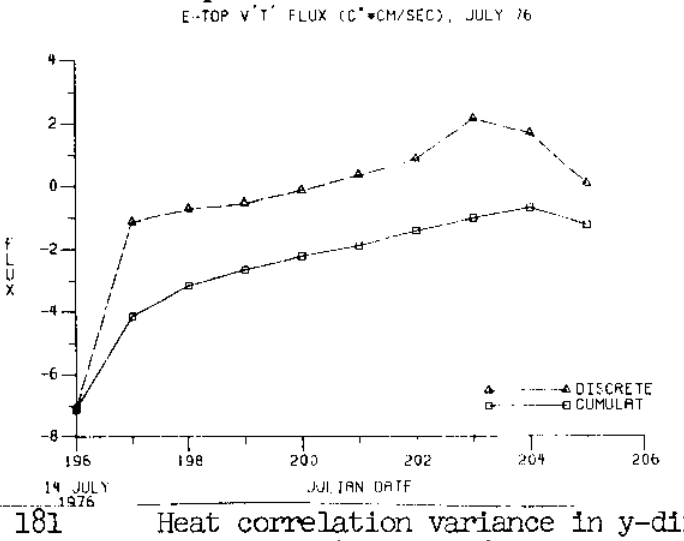

Figure 181 Heat correlation variance in y-direction for E_{top} July 14-23, 1976

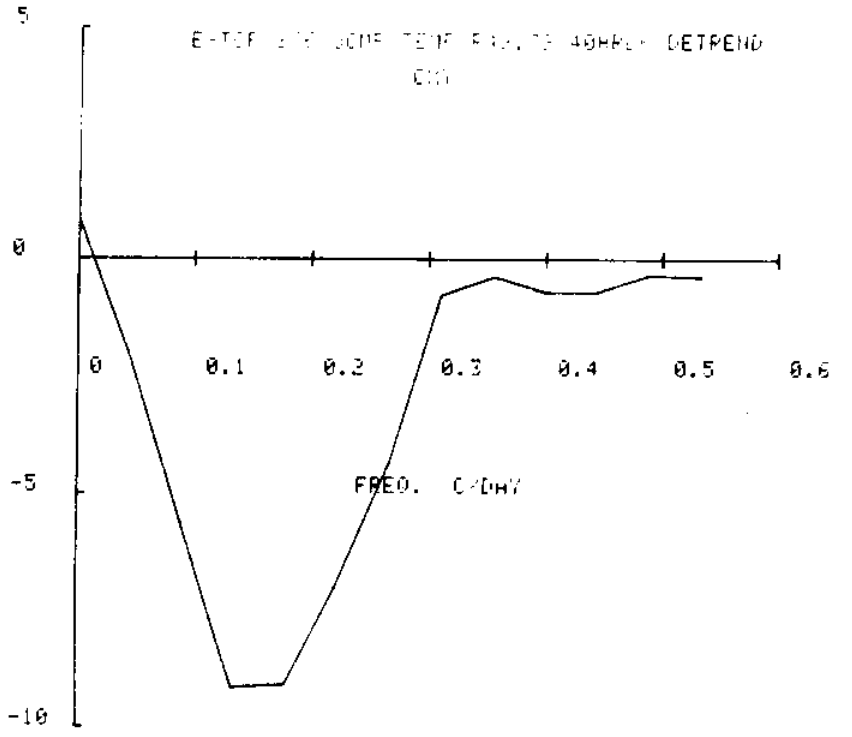

Figure 182 Cospectra of temperature vs. u-component for meter E_{top}

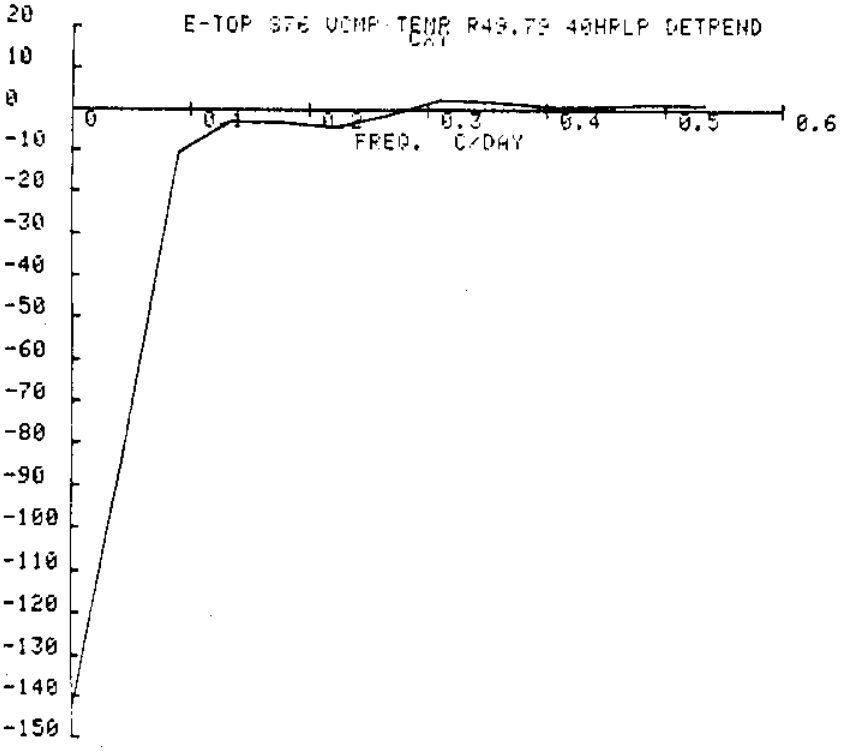

Figure 183 Cospectra of temperature vs. v-component for meter E_{top}

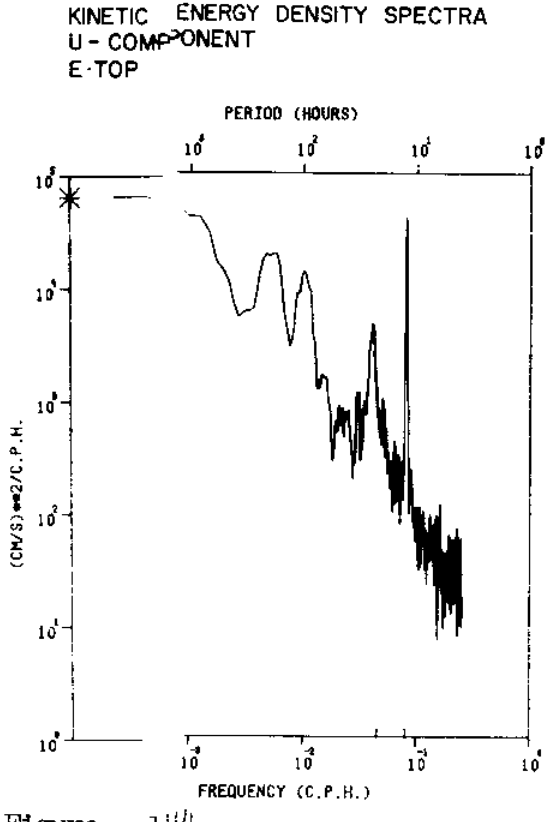

Figure 184
Kinetic energy density spectra for current velocity, u-component, E_{top}

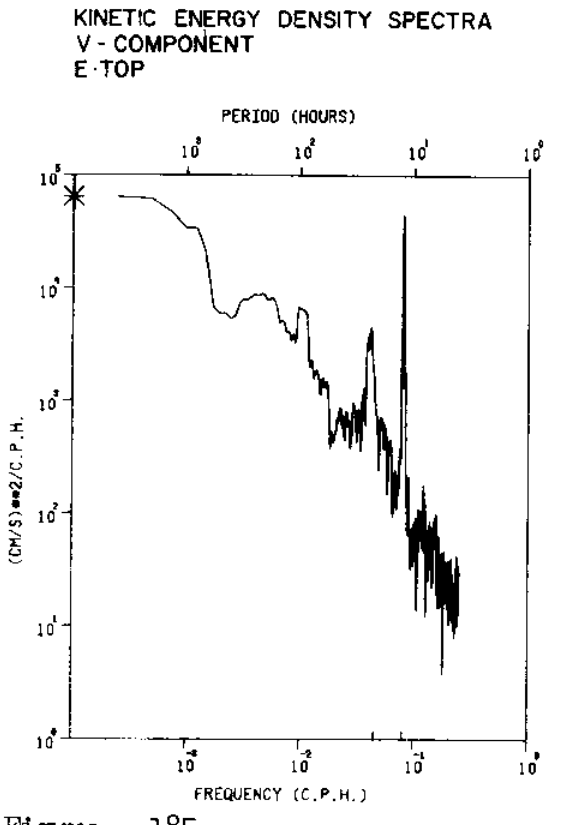

Figure 185
Kinetic energy density spectra for current velocity, v-component, E_{top}

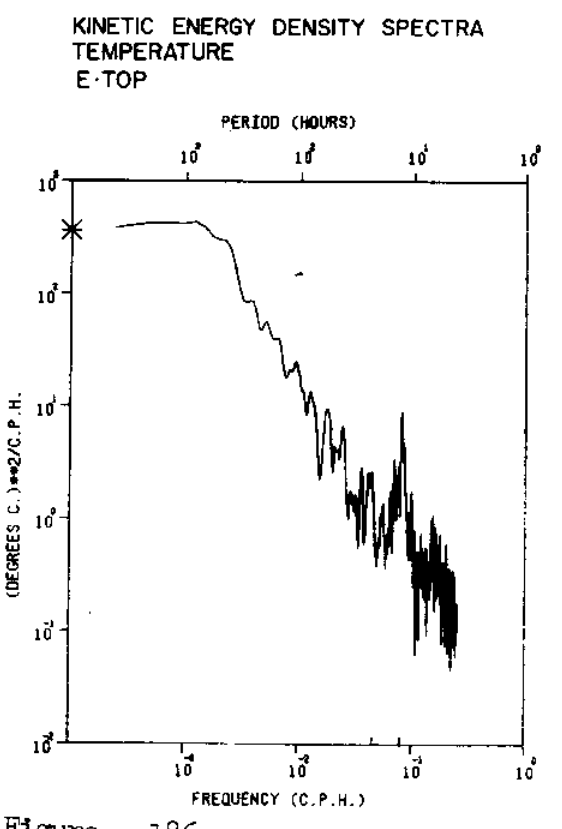

Figure 186
Kinetic energy density spectra for temperature at E_{top}

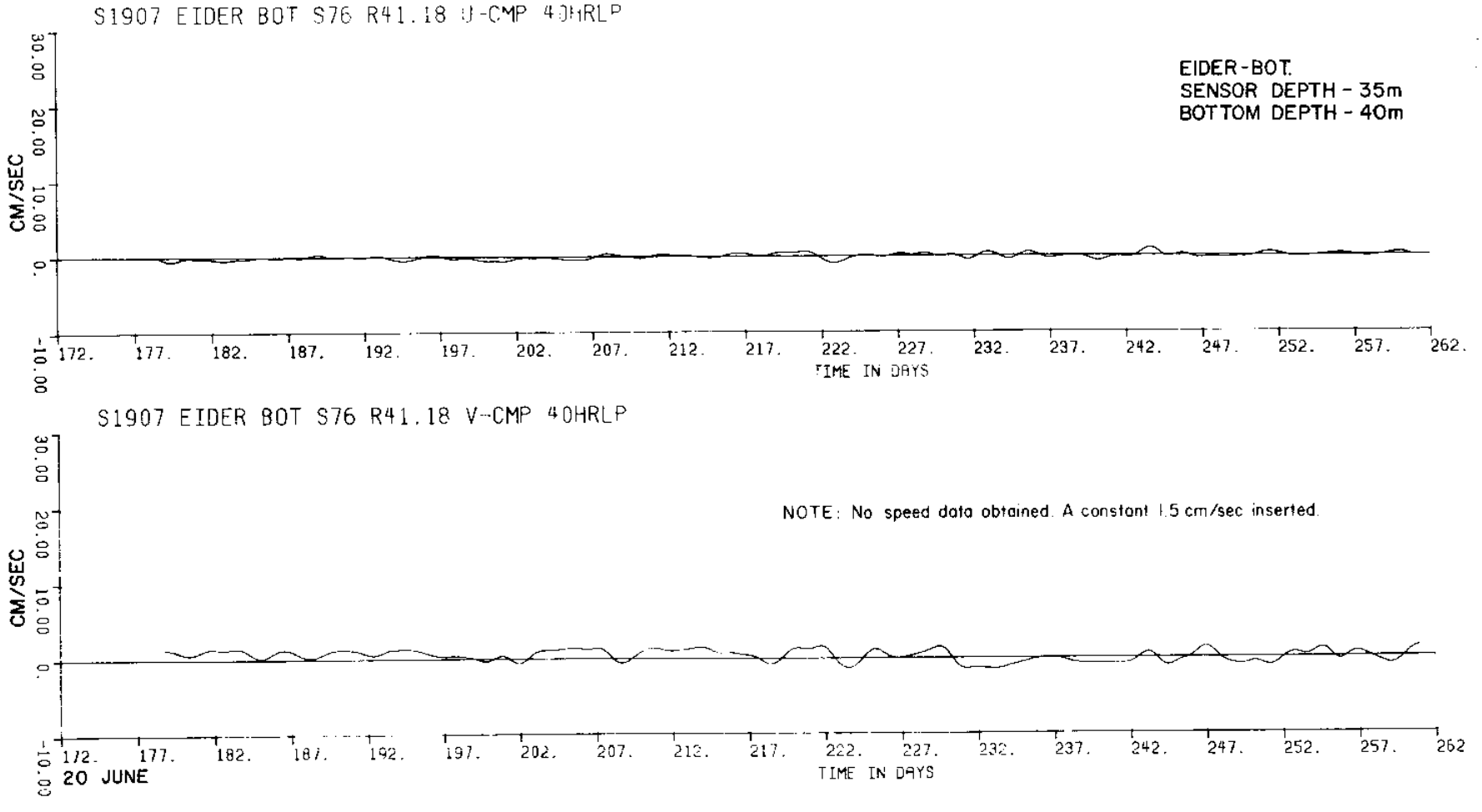

Figure 187 Low pass current velocity components from meter $E(Eider)_{bot}$

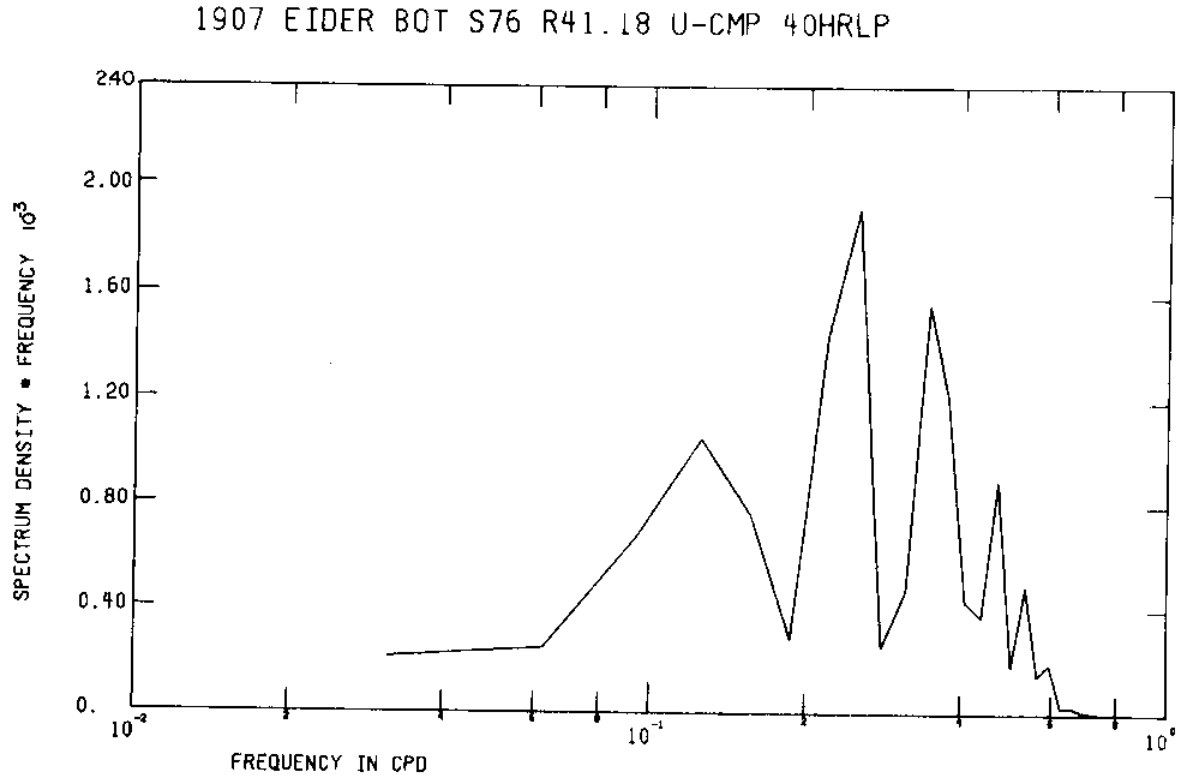

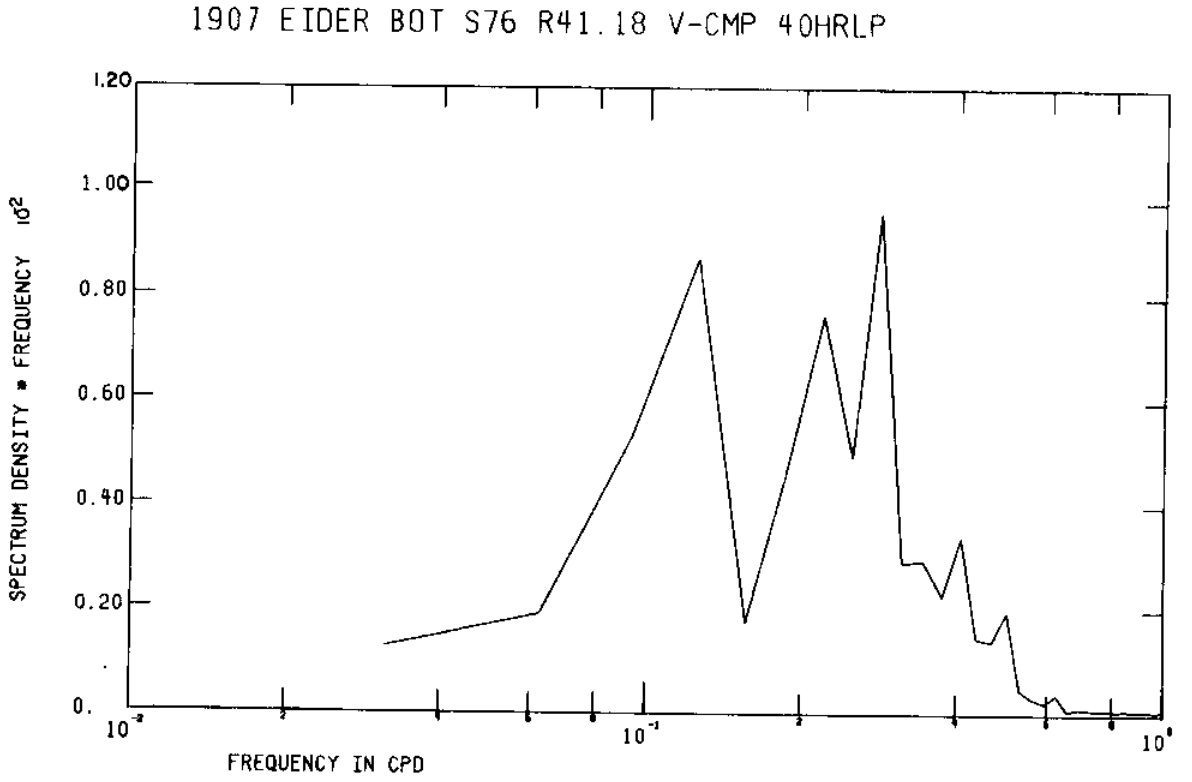

Figure 188 FFT of low pass current velocity components from meter $E(Eider)_{bot}$

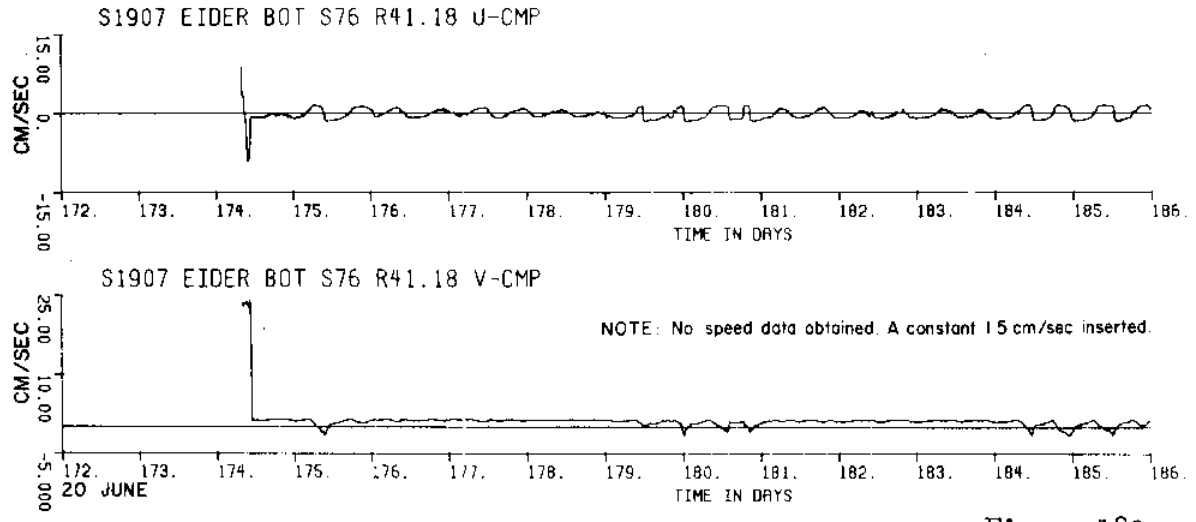

Figure 189 a

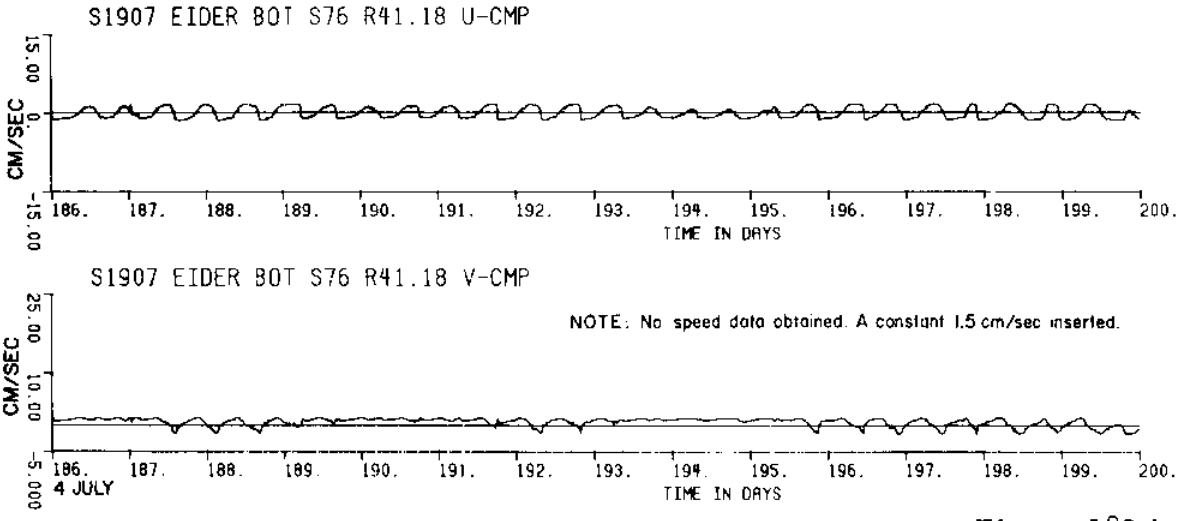

Figure 189 b

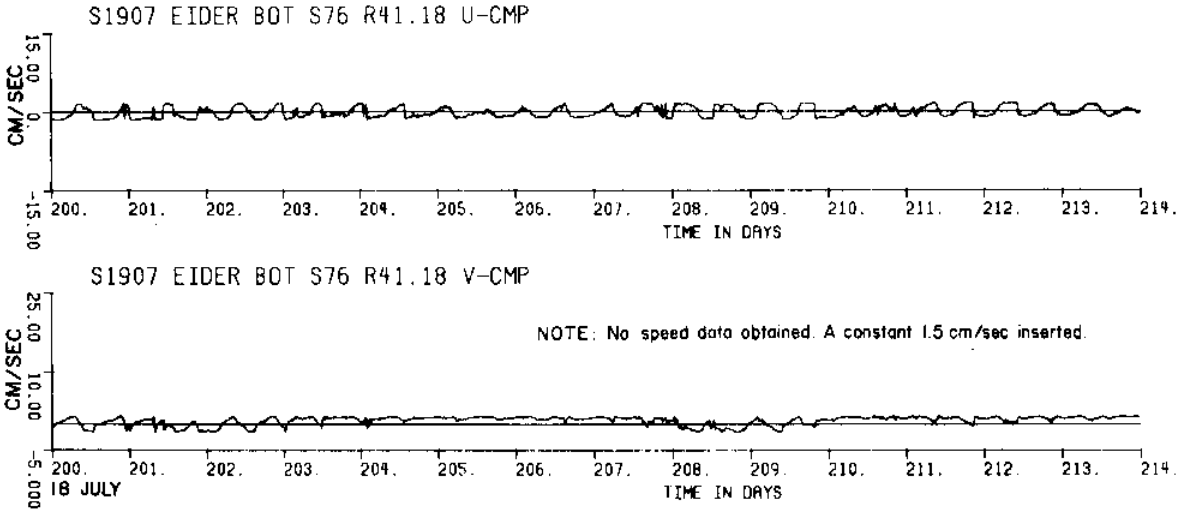

Figure 189 c

Figure 189 (a,b,c,d, e,f,g) Unfiltered current velocity components from meter $E(Eider)_{bot}$

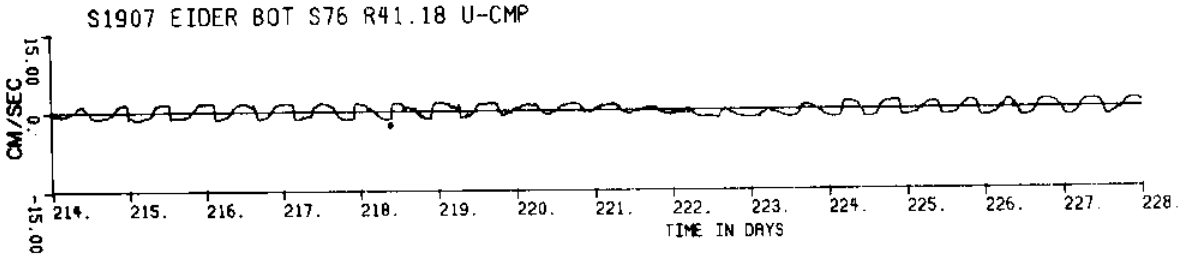

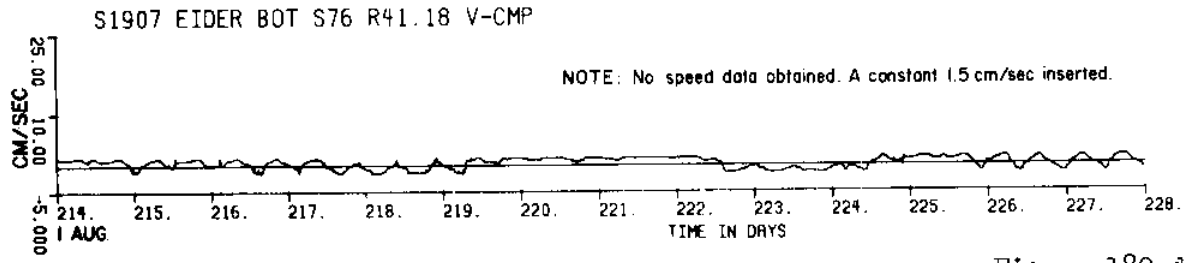

Figure 189 d

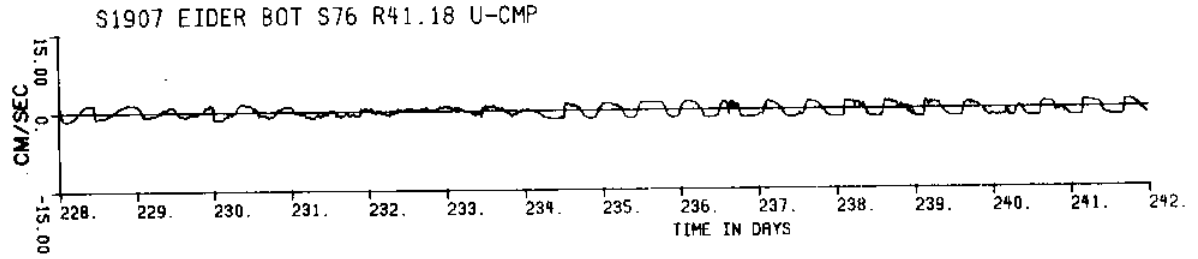

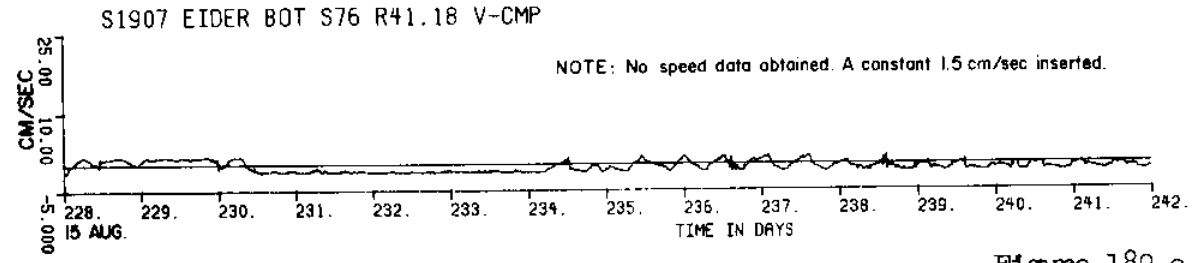

Figure 189 e

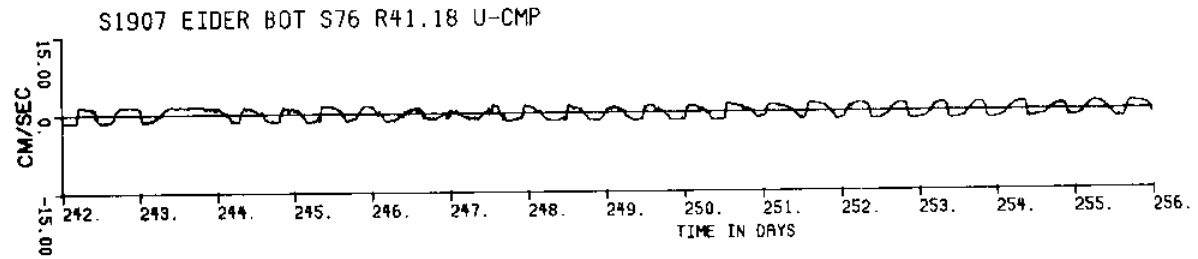

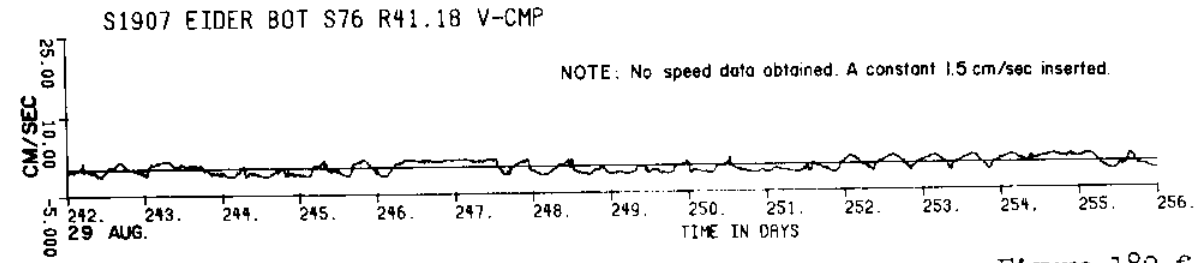

Figure 189 f

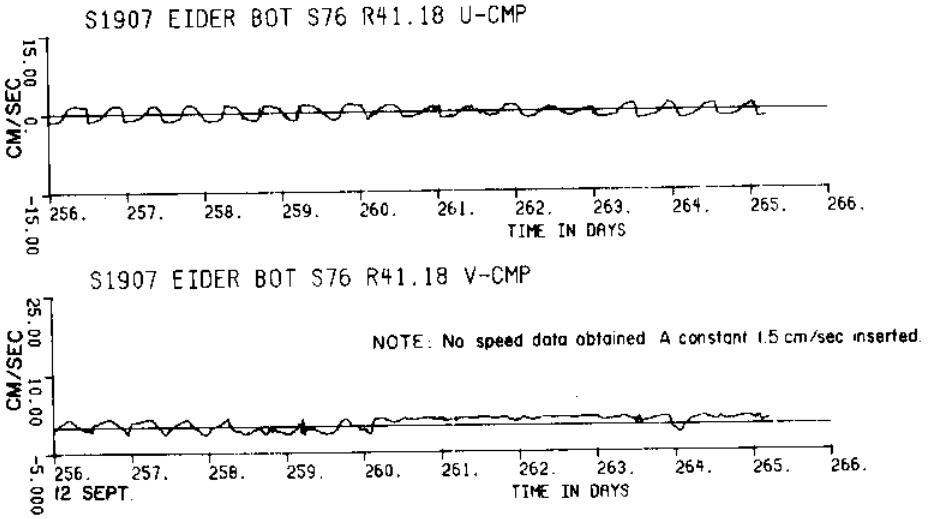
S1907 EIDER BOT S76 R41.18 U-CMP
CM/SEC
15.00
0
-15.00
256.
257.
258.
259.
260.
261.
262.
263.
264.
265.
266.
TIME IN DAYS
S1907 EIDER BOT S76 R41.18 V-CMP
NOTE: No speed data obtained A constant 1.5 cm/sec inserted.
CM/SEC
25.00
10.00
-5.000
256.
257.
258.
259.
260.
261.
262.
263.
264.
265.
266.
12 SEPT.
TIME IN DAYS

Figure 189 g

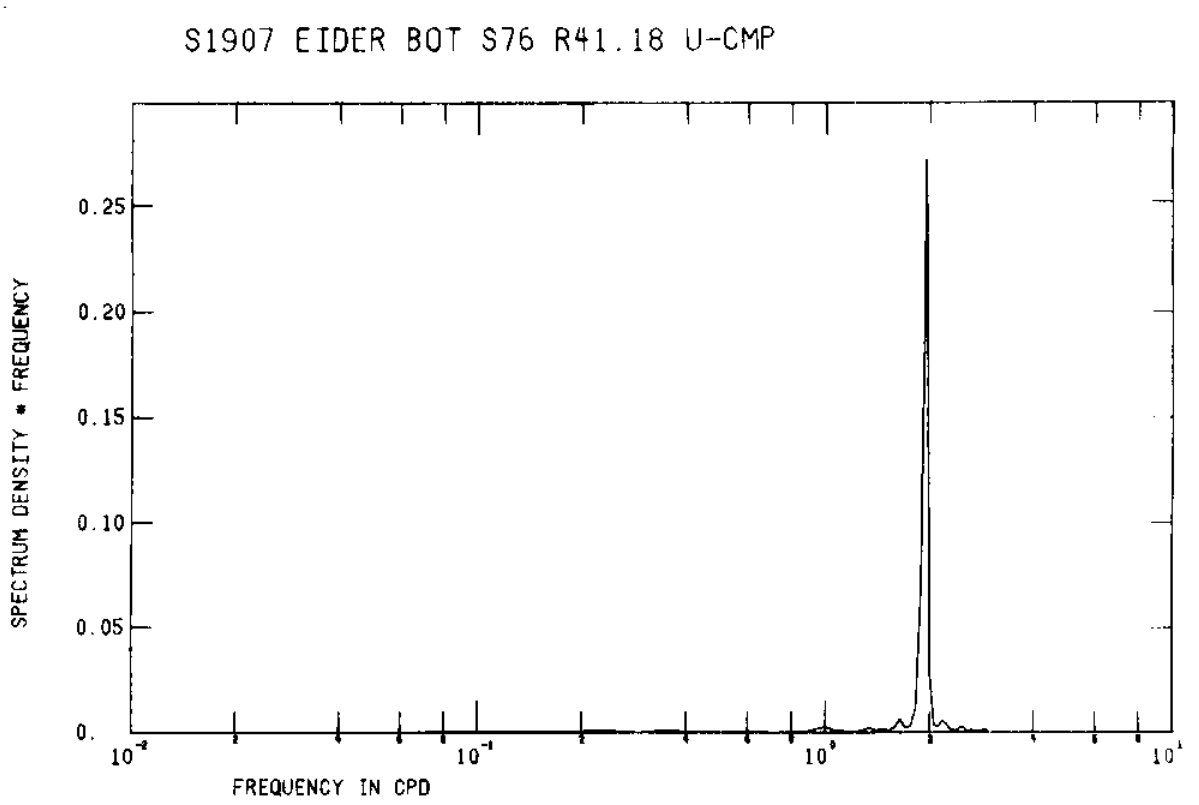

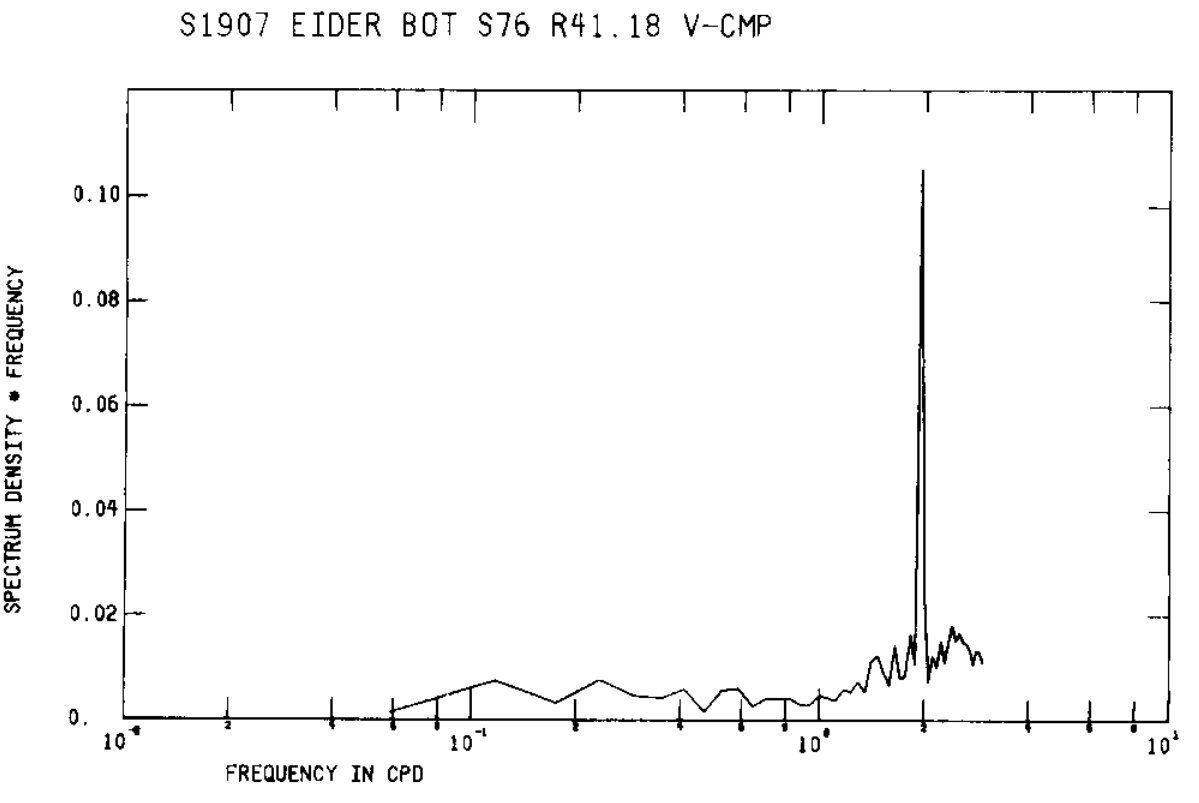

Figure 190 FFT of unfiltered current velocity components from meter $E(Eider)_{bot}$

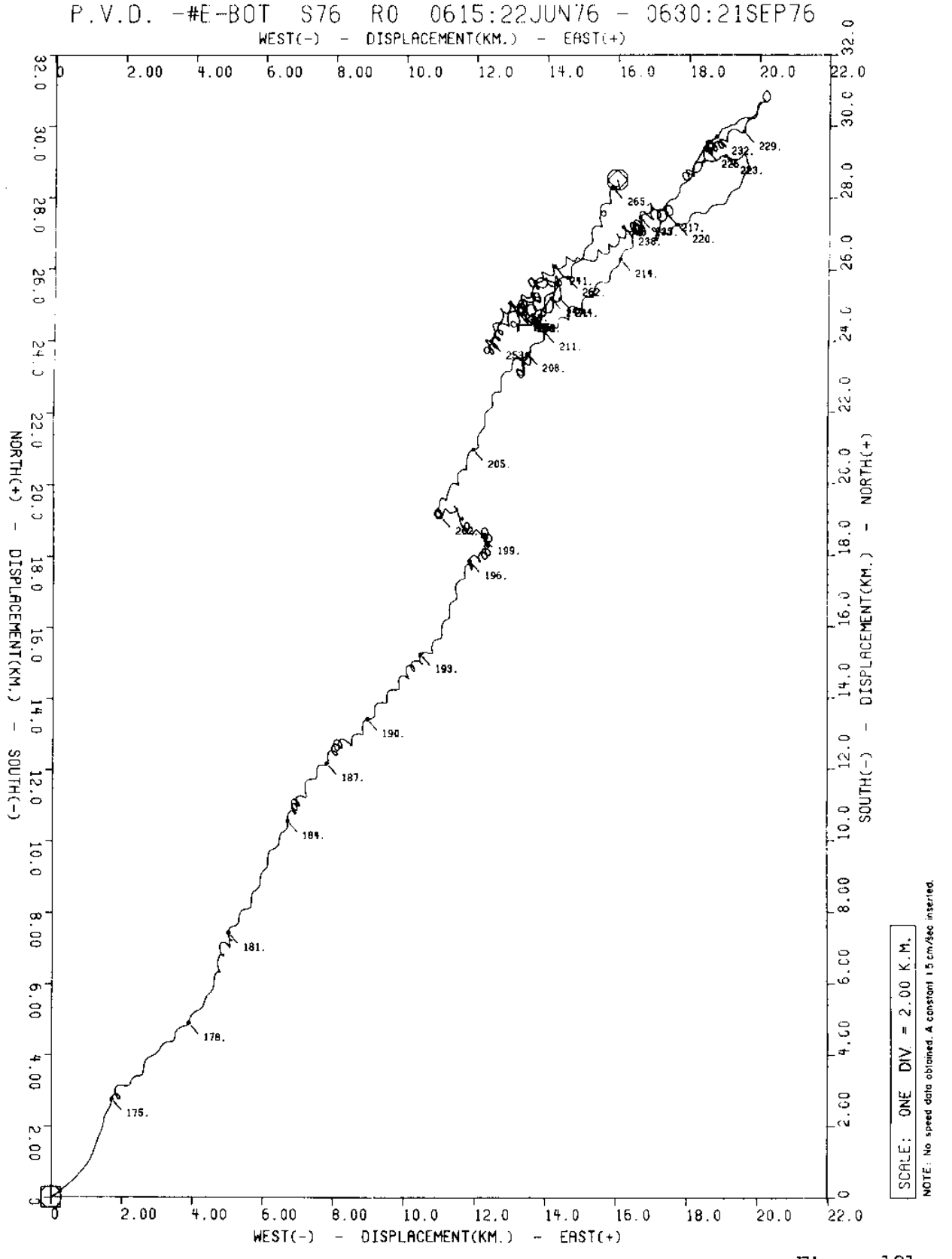

Figure 191 a

Figure 191 (a,b,c) Progressive vector diagrams of unfiltered current velocity from meter E(Eider)$_{bot}$

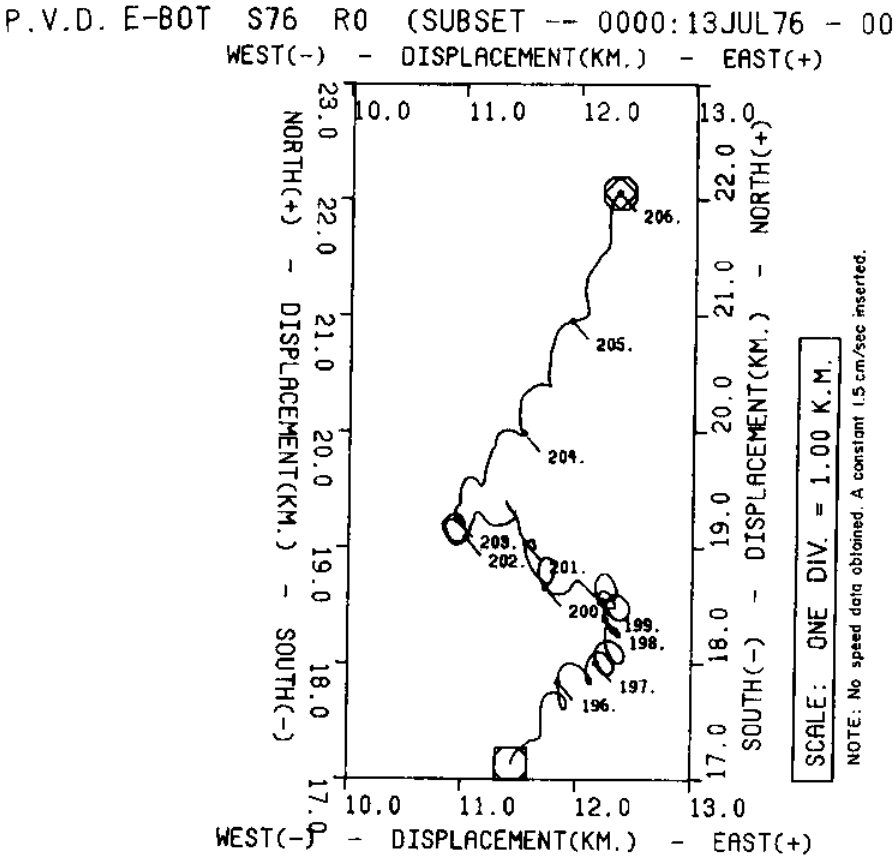

Figure 191 b

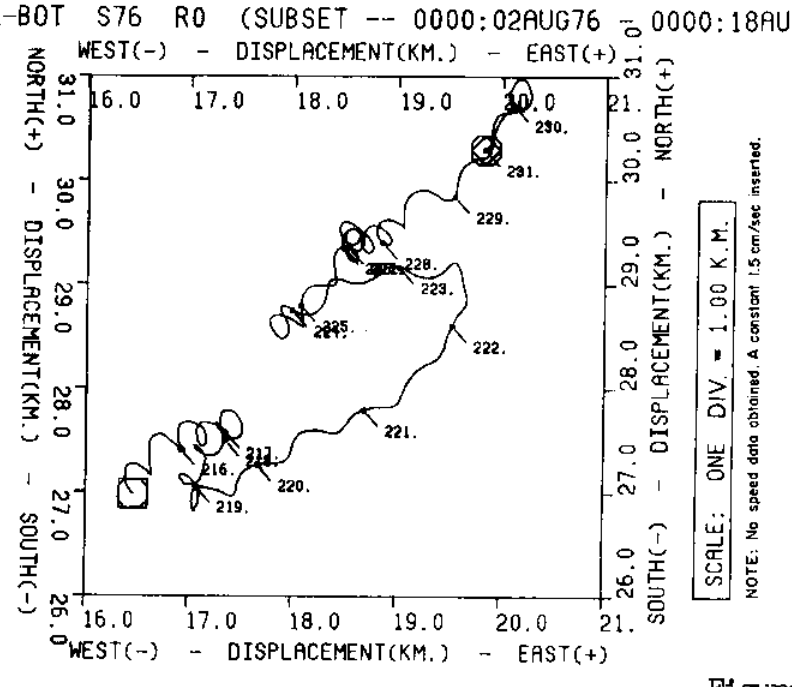

Figure 191 c

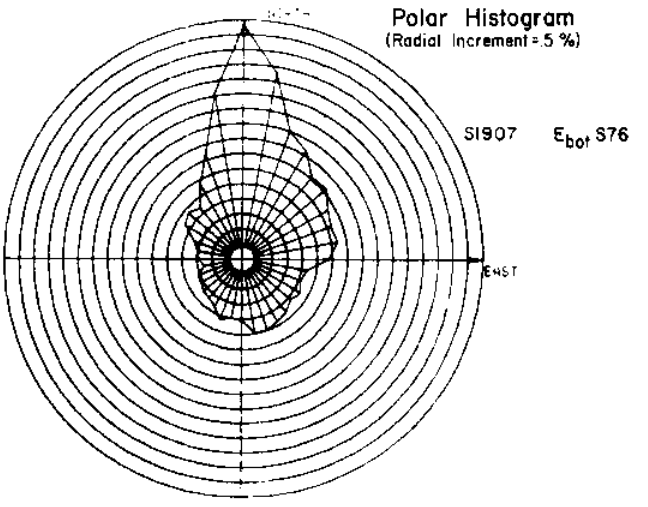

Figure 192 Histogram from meter E(Eider)$_{bot}$

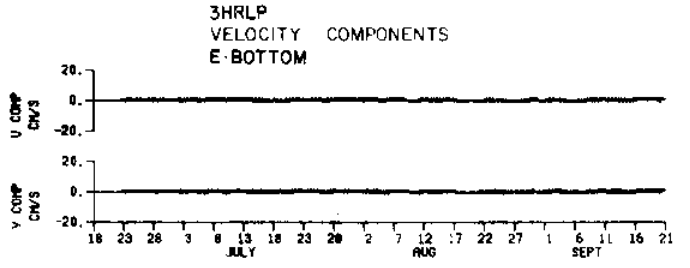

Figure 193 3HRLP velocity components for E_{bot}

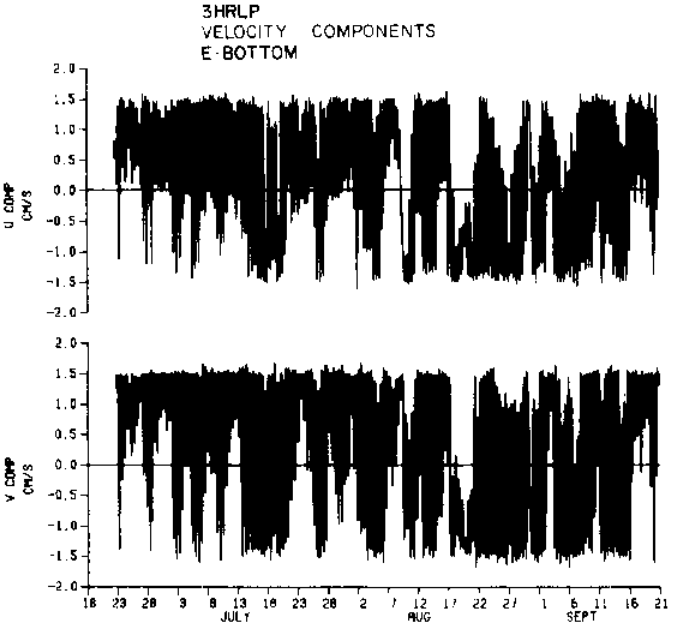

Figure 194 3HRLP velocity components for E_{bot}, (expanded scale)

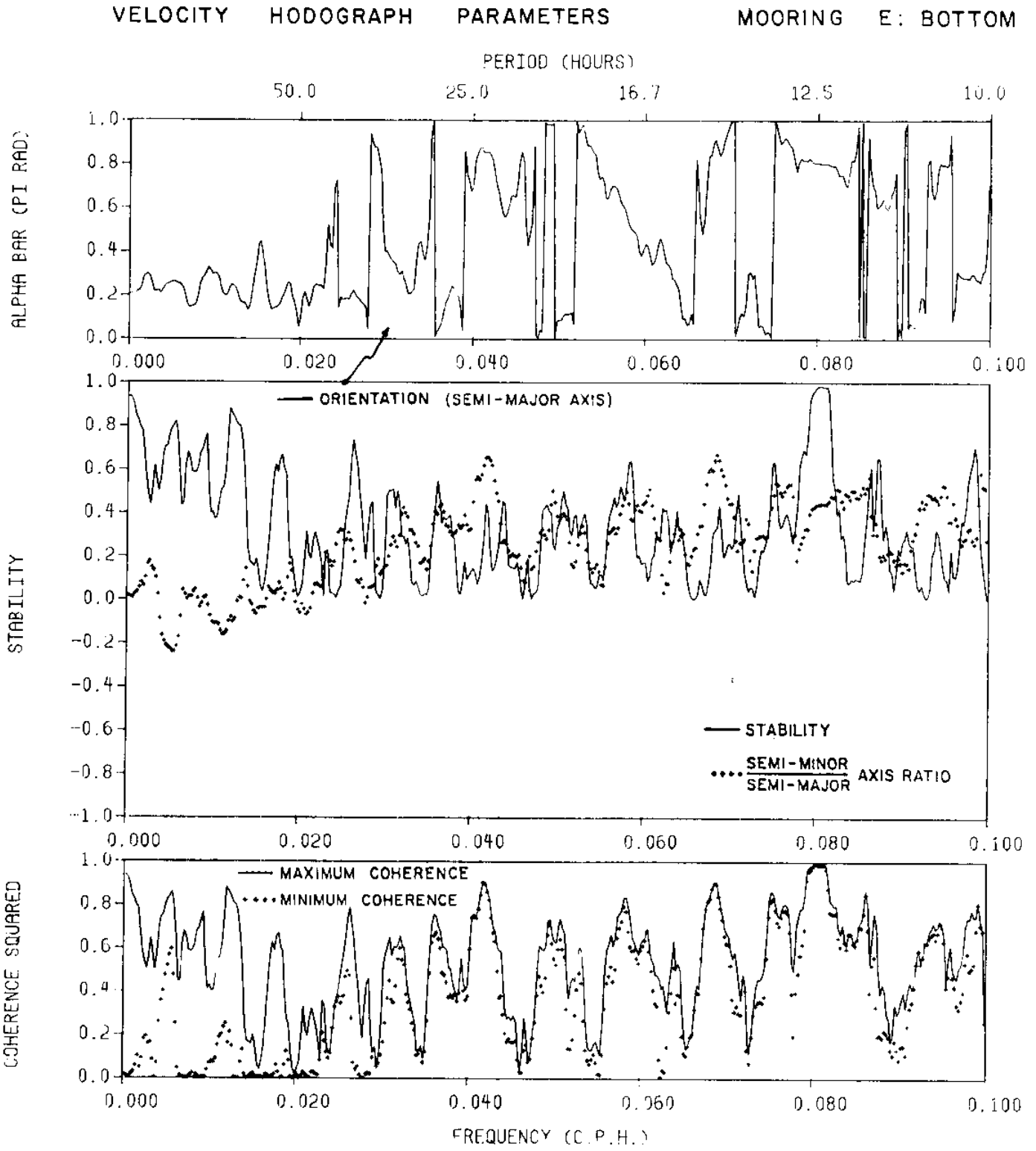

Figure 195 Hodograph parameters from meter E(Eider)$_{bot}$

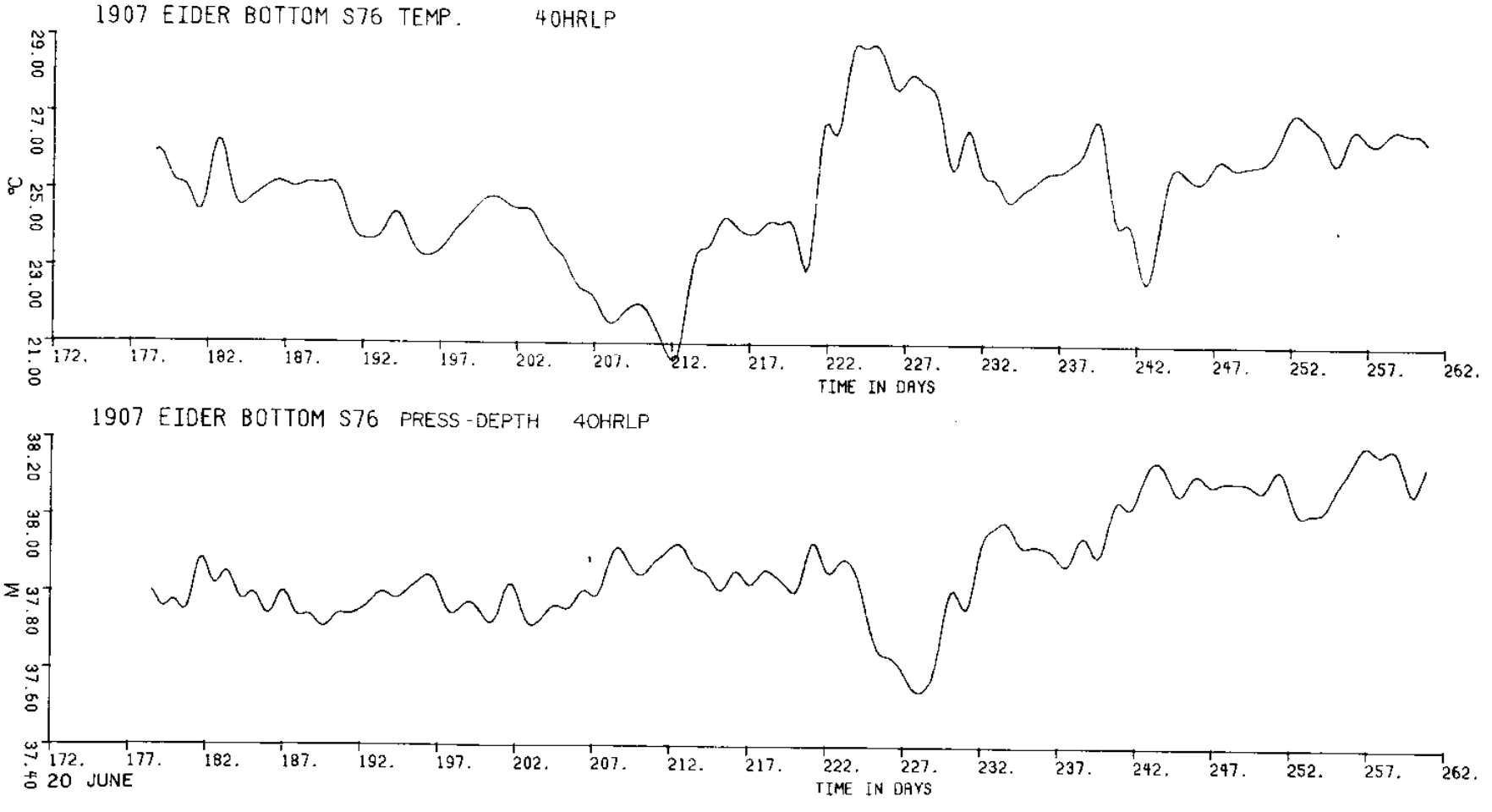

Figure 196 Low pass temperature and pressure from meter $E(Eider)_{bot}$

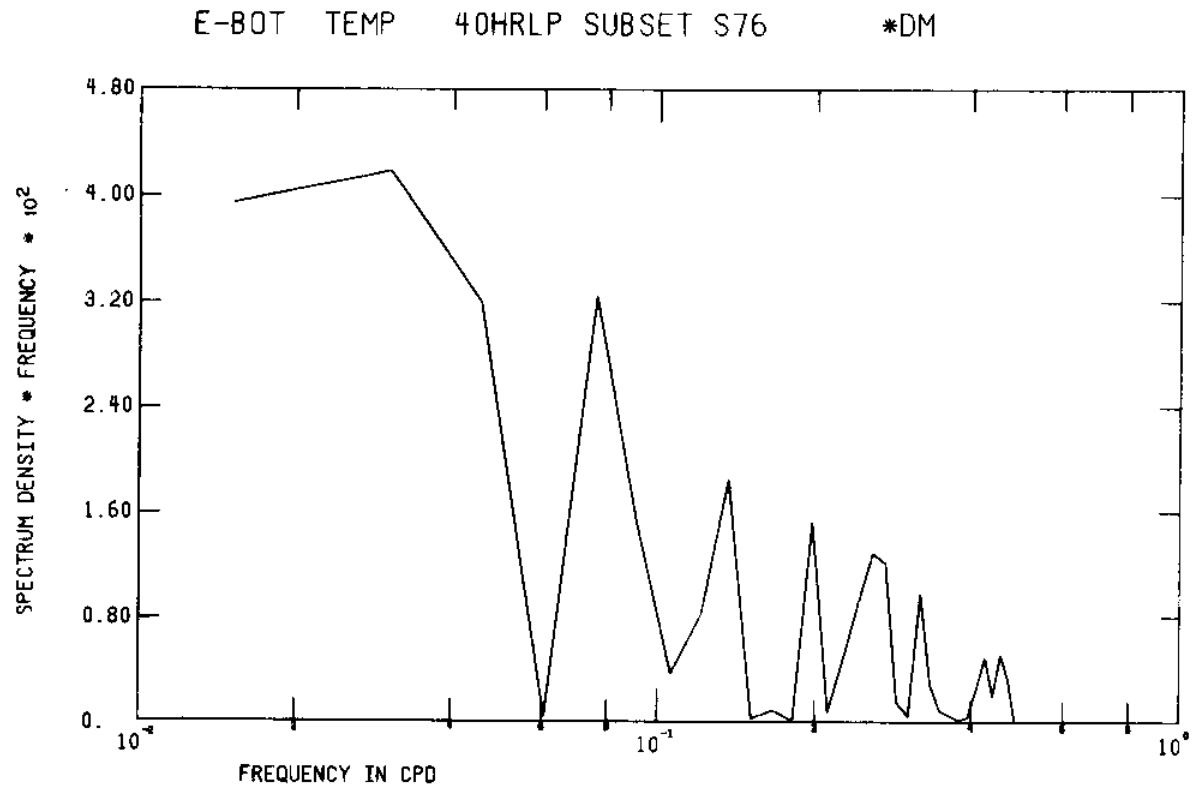

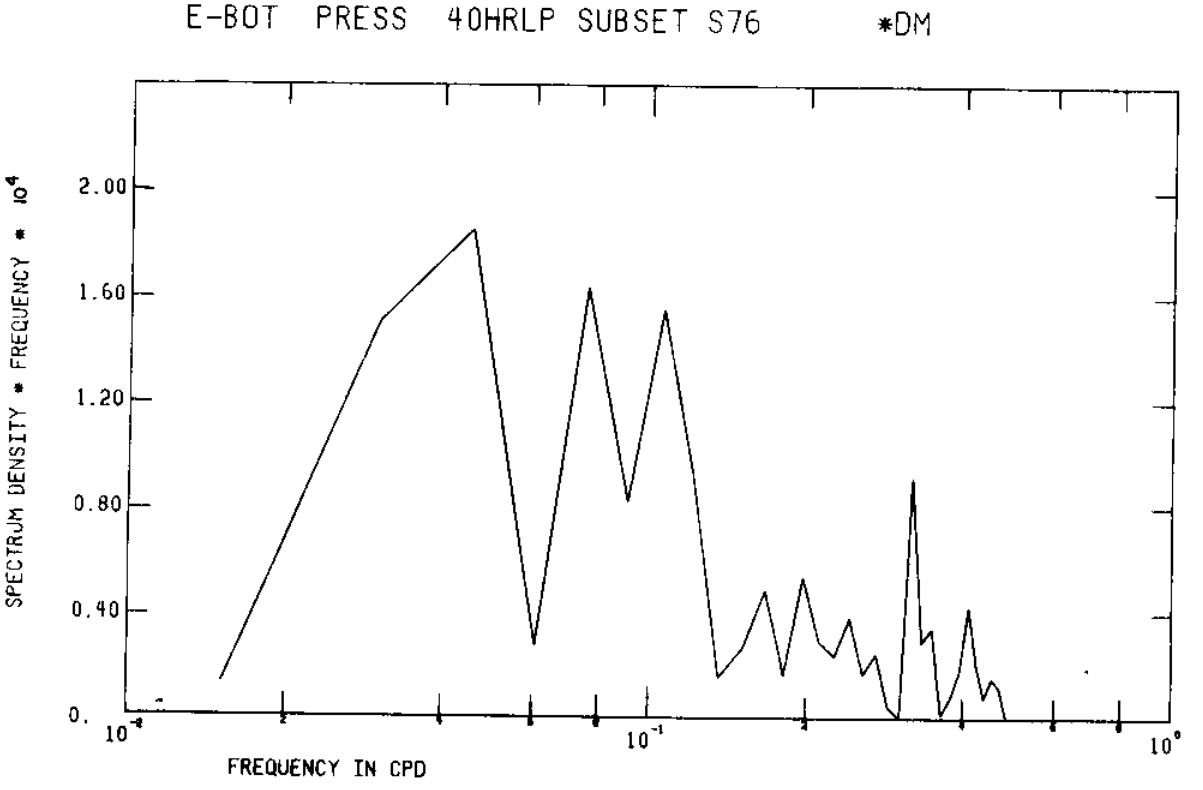

Figure 197 FFT of low pass temperature and pressure from meter $E(Eider)_{bot}$

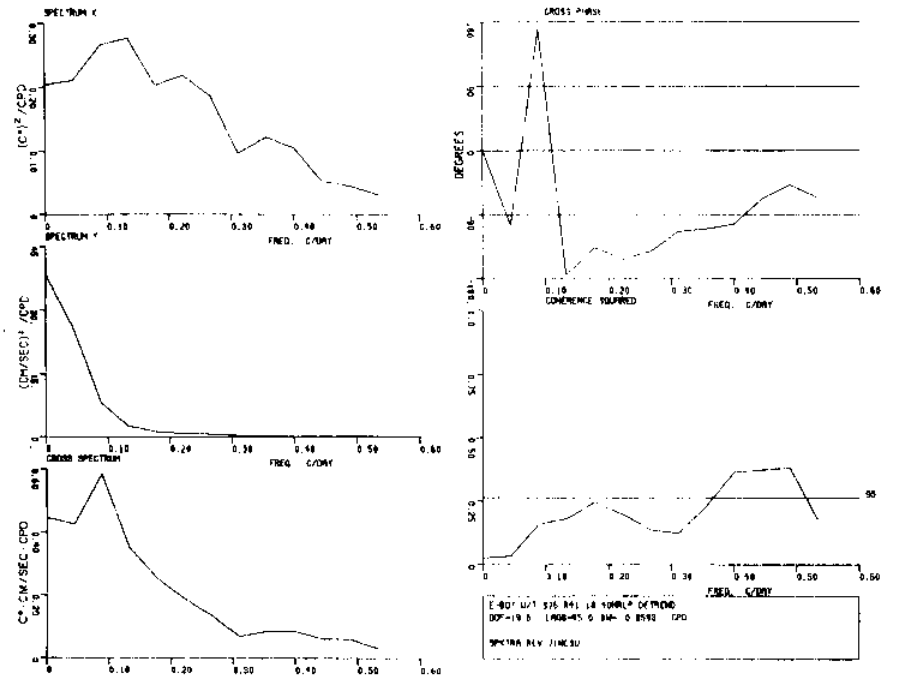

Figure 198 Spectra of temperature and low pass current velocity u component, both from meter $E(Eider)_{bot}$

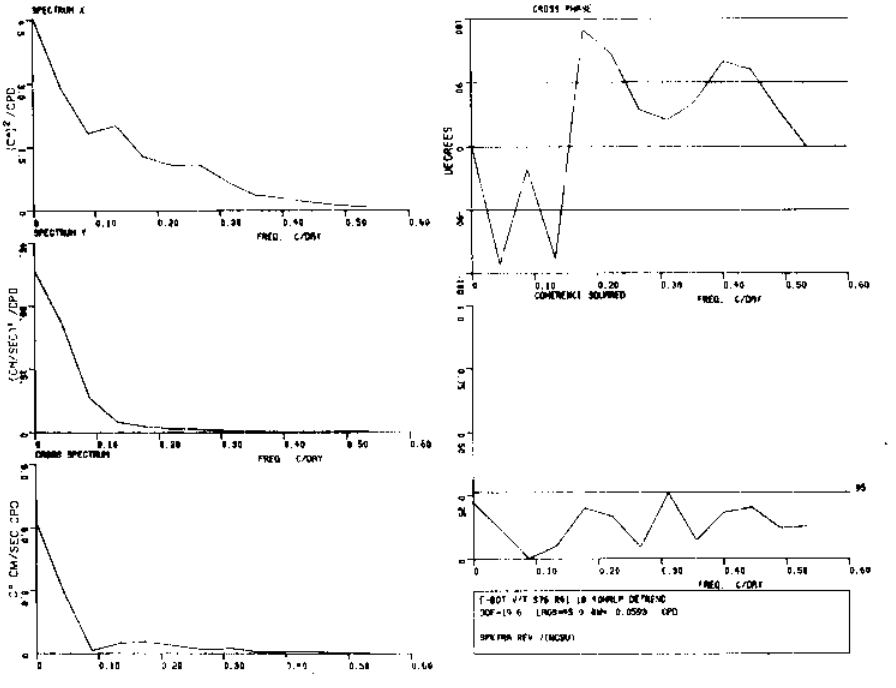

Figure 199 Spectra of temperature and low pass current velocity v component, both from meter $E(Eider)_{bot}$

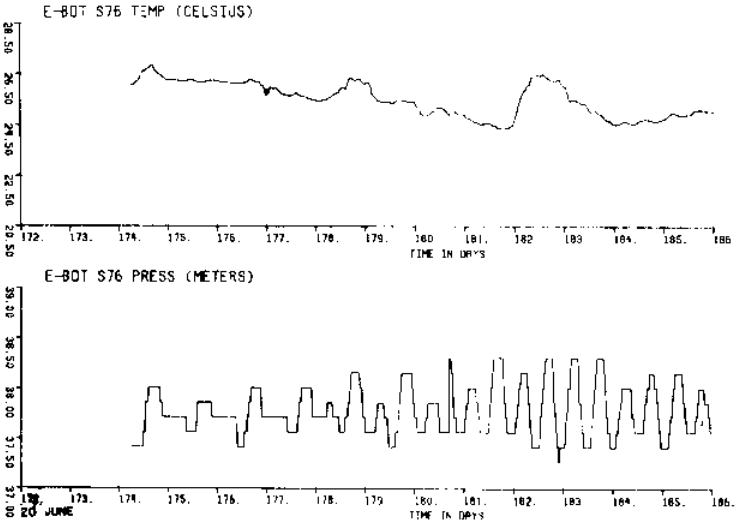

Figure 200 a

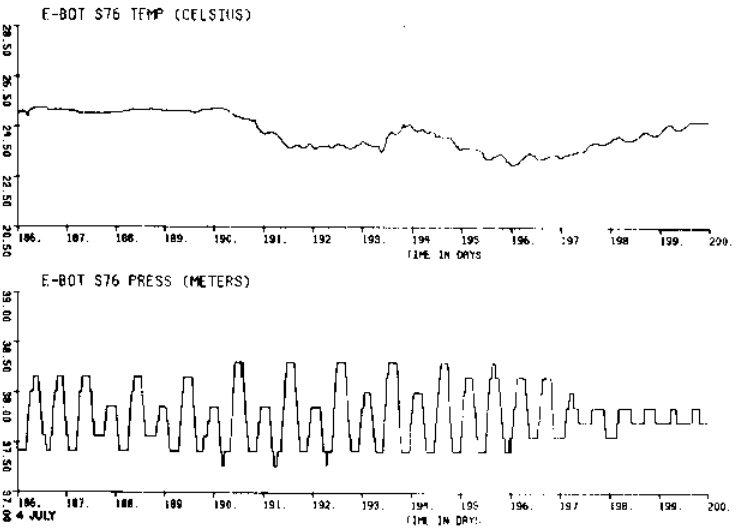

Figure 200 b

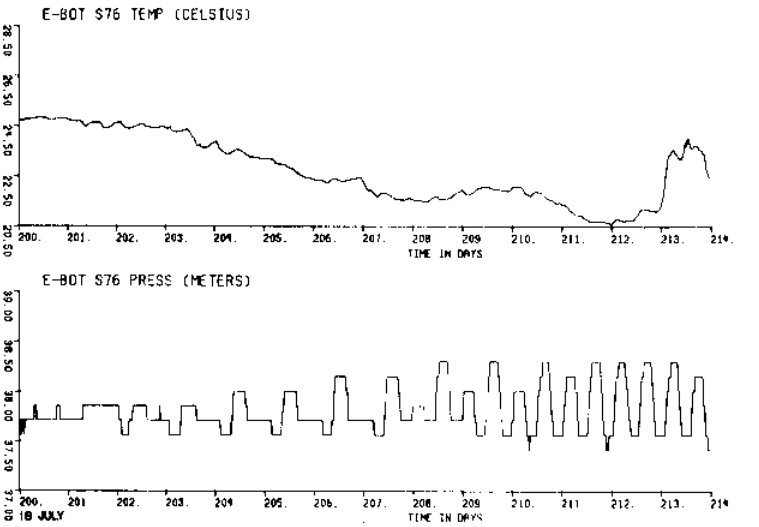

Figure 200 c

Figure 200 (a,b,c,d, e,f,g) Unfiltered temperature and pressure from meter E(Eider)$_{bot}$

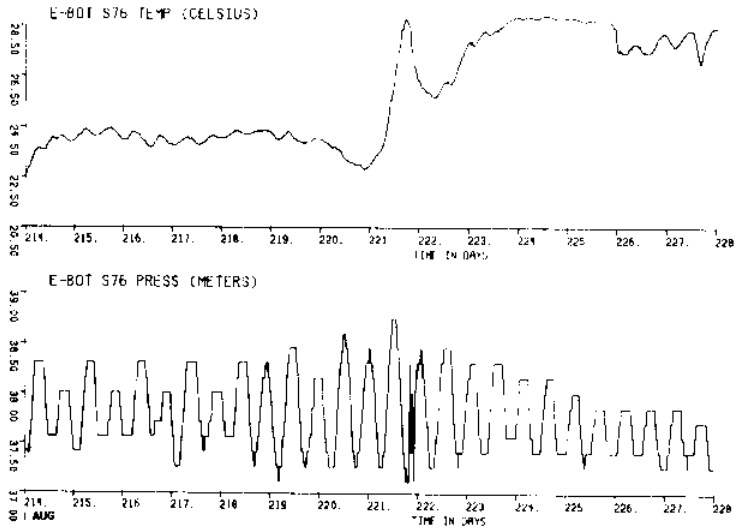

Figure 200 d

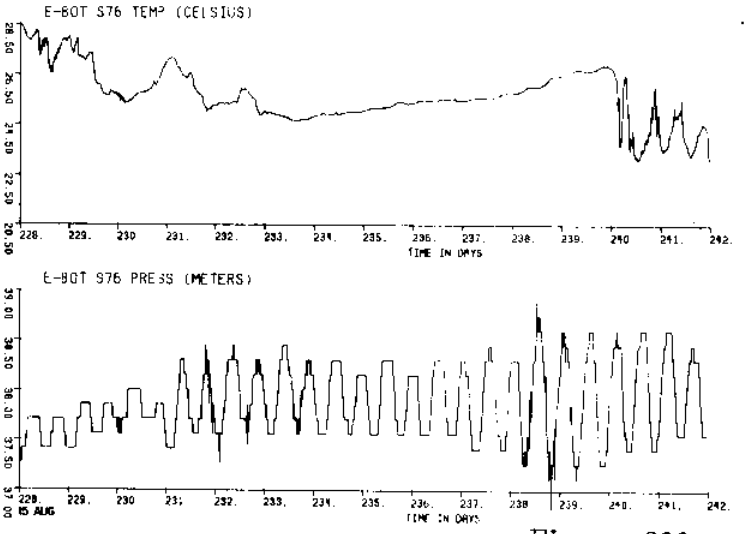

Figure 200 e

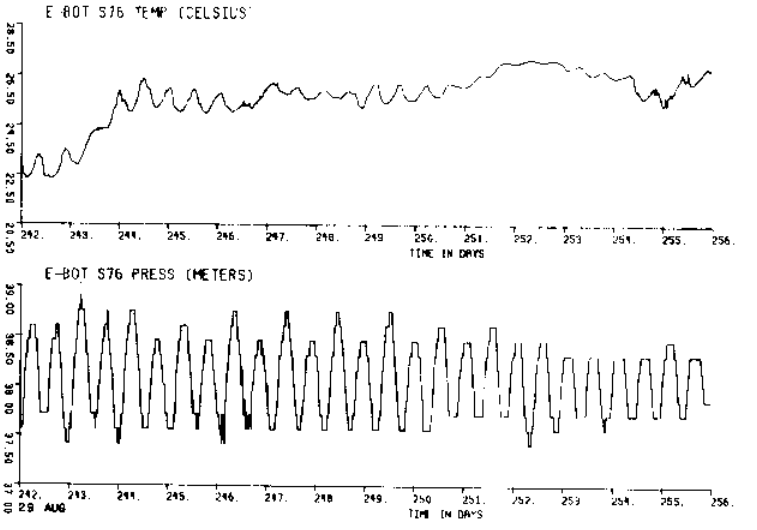

Figure 200 f

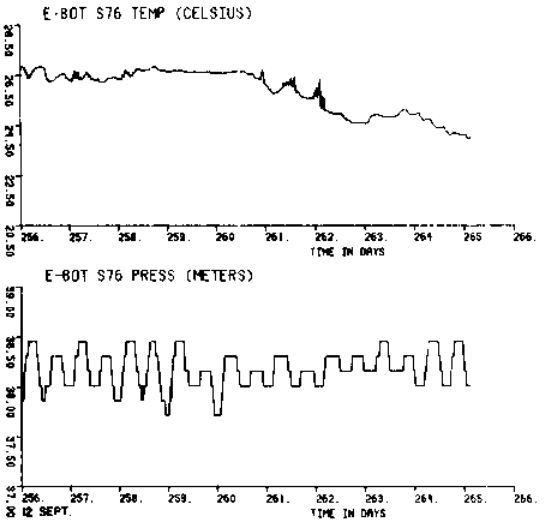
E-BOT S76 TEMP (CELSIUS)
256. 257. 258. 259. 260 261. 262. 263. 264 265 266.
TIME IN DAYS
E-BOT S76 PRESS (METERS)
256. 257. 258. 259. 260 261. 262. 263. 264. 265. 266.
02 SEPT.
TIME IN DAYS

Figure 200 g

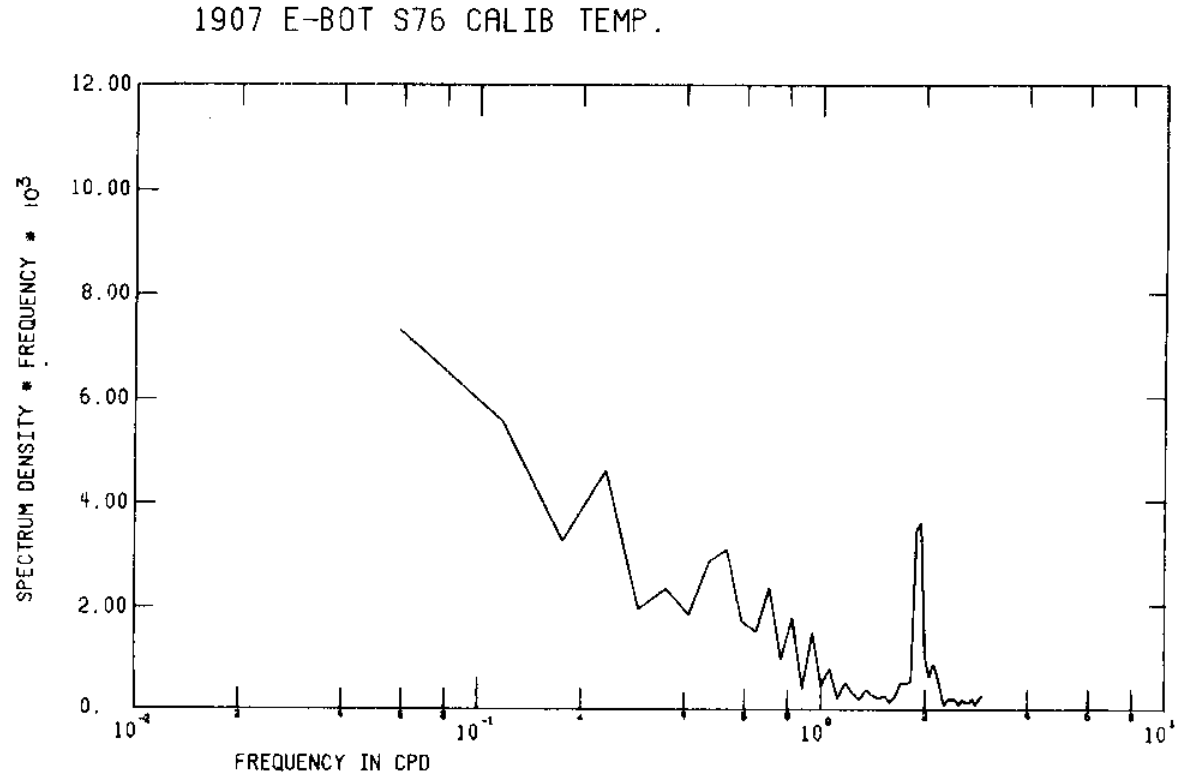

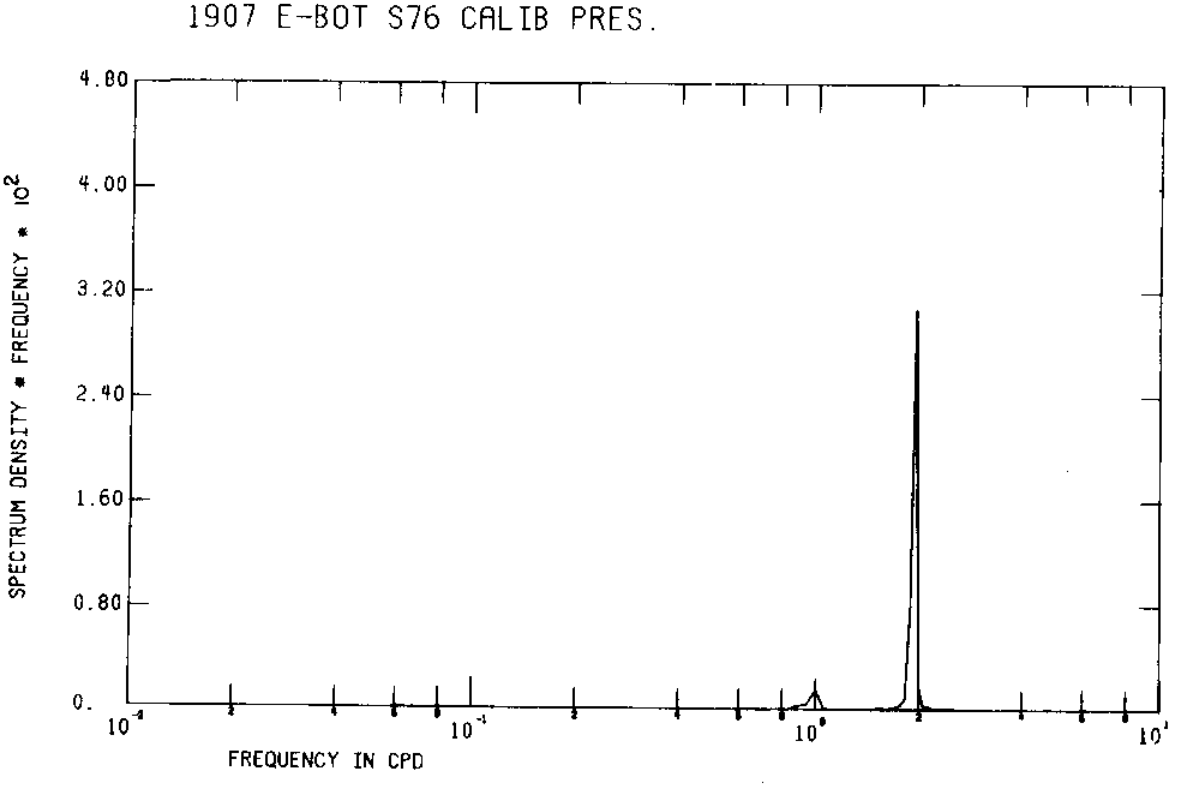

Figure 201 FFT of unfiltered temperature and pressure from meter $E(Eider)_{bot}$

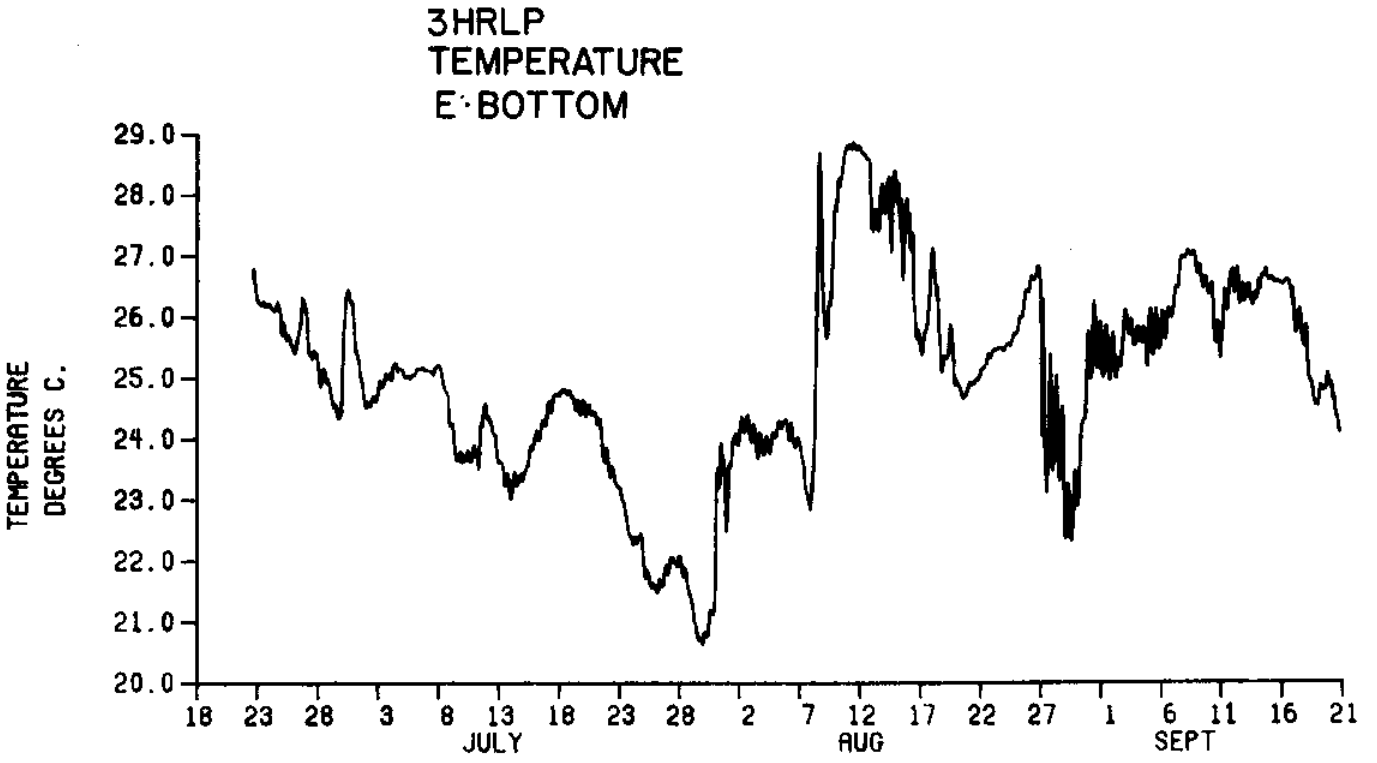

Figure 202 3HRLP temperature for E_{bot}

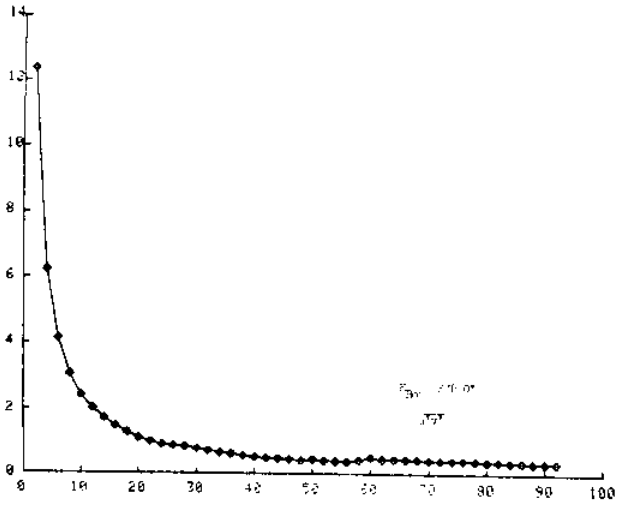

Figure 203 Momentum correlation variance in horizontal plane for E_{bot} Summer, 1976 (cumulative)

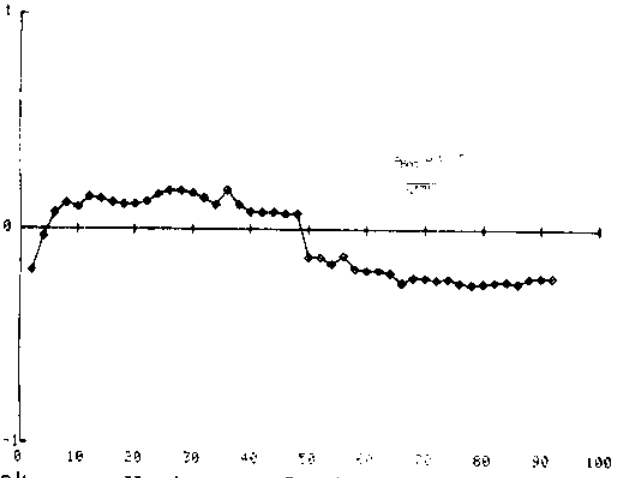

Figure 204 Heat correlation variance in x-direction for E_{bot} Summer, 1976 (cumulative)

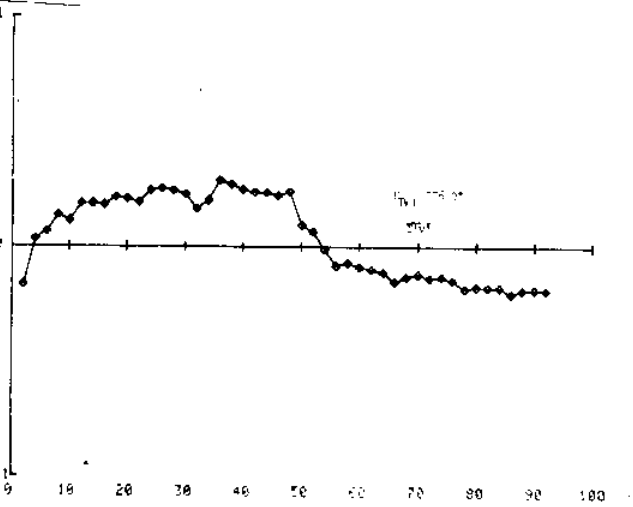

Figure 205 Heat correlation variance in y-direction for E_{bot} Summer, 1976 (cumulative)

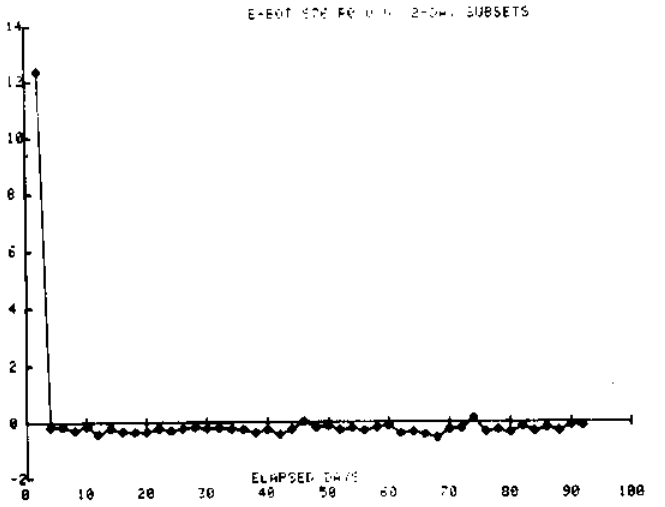

Figure 206 Momentum correlation variance in the horizontal plane for E_{bot} Summer, 1976 (2-day subset)

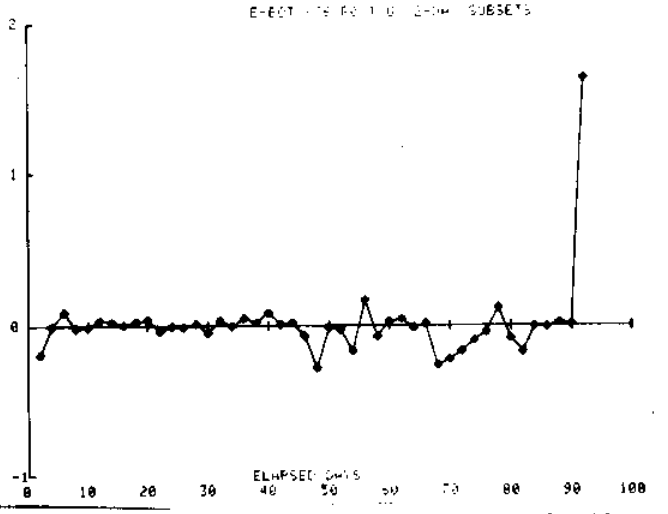

Figure 207 Heat correlation variance in the x-direction for E_{bot} Summer, 1976 (2-day subset)

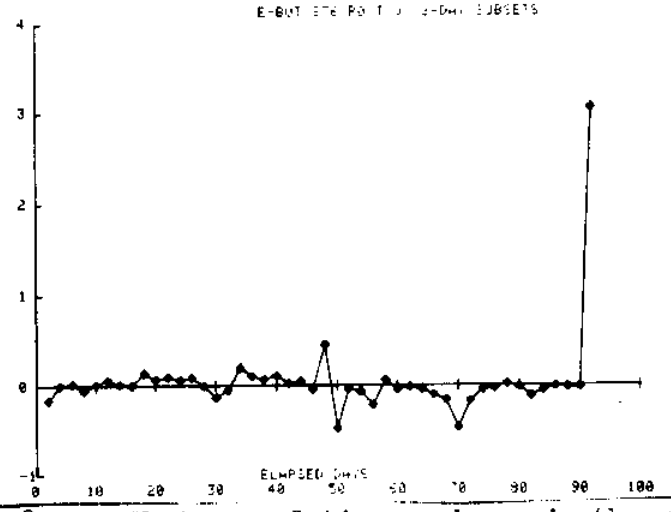

Figure 208 Heat correlation variance in the y-direction for E_{bot} Summer, 1976 (2-day subset)

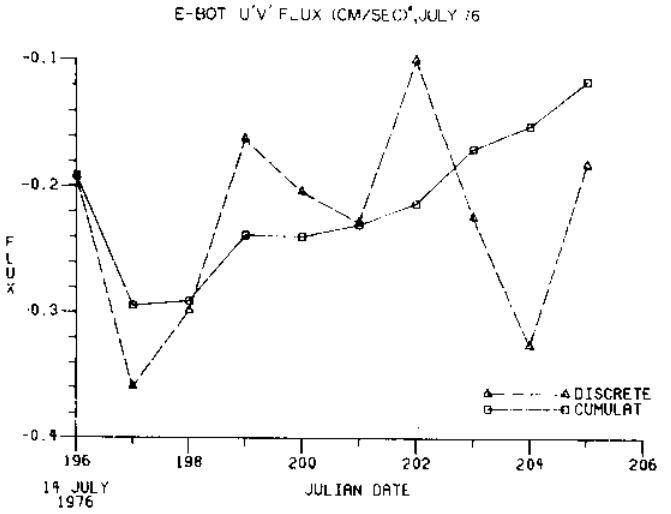

Figure 209 Momentum correlation variance in horizontal plane for E_{bot} July 14-23, 1976

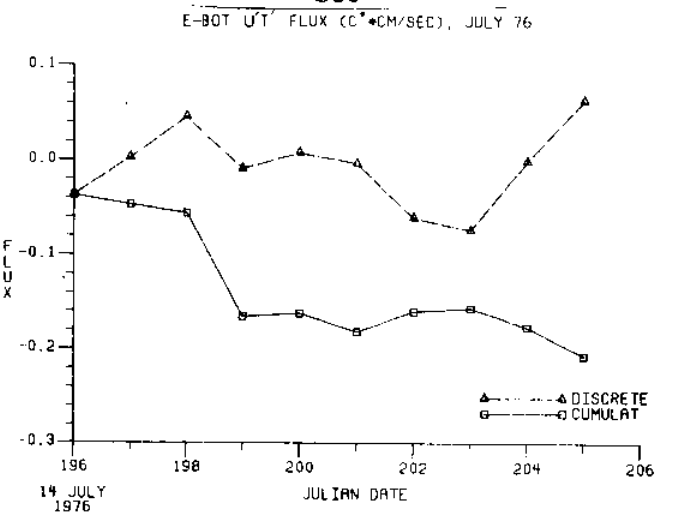

Figure 210 Heat correlation variance in x-direction for E_{bot} July 14-23, 1976

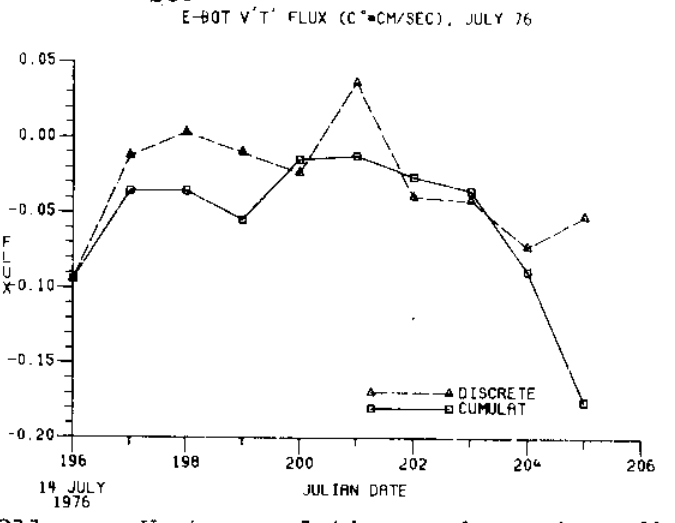

Figure 211 Heat correlation variance in y-direction for E_{bot} July 14-23, 1976

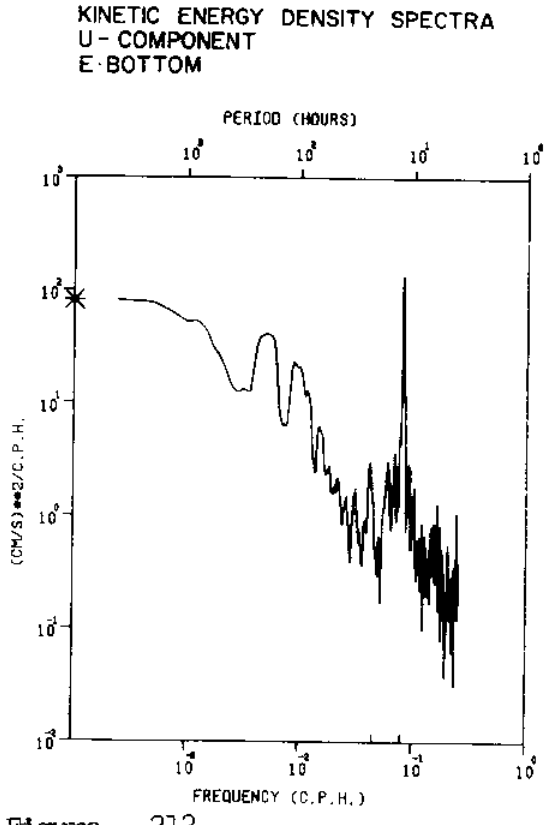

Figure 212
Kinetic energy density spectra for current velocity, u-component, E_{bot}

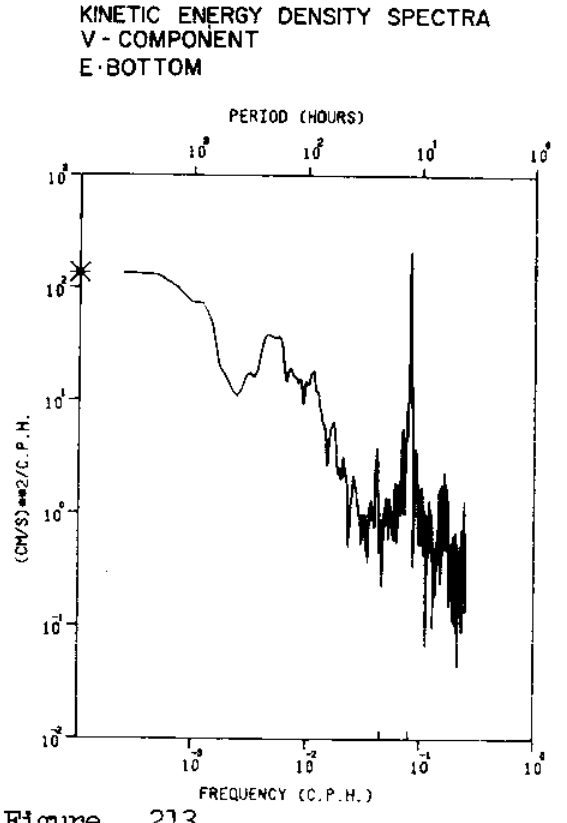

Figure 213
Kinetic energy density spectra for current velocity, v-component, E_{bot}

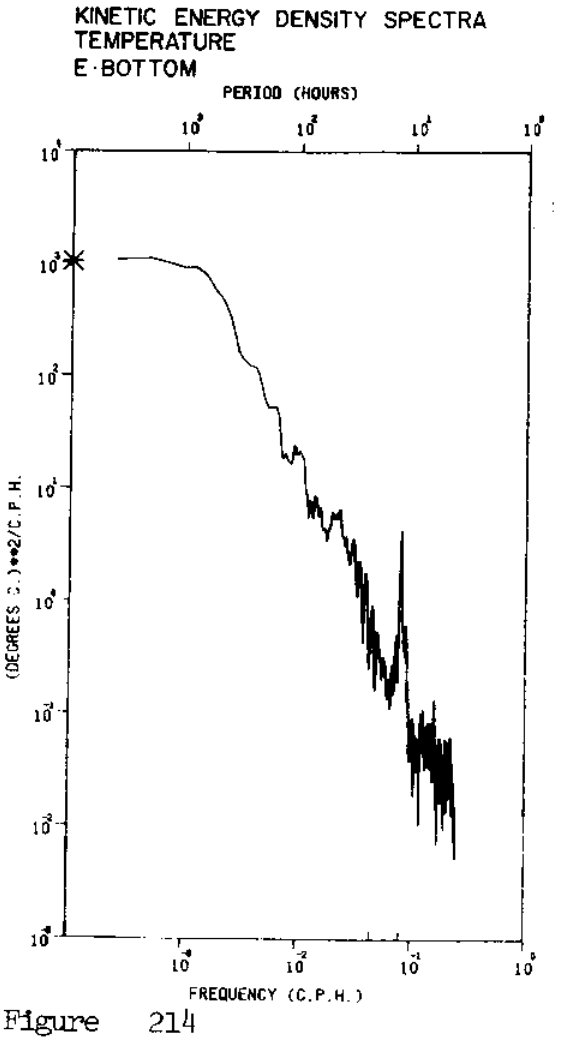

Figure 214
Kinetic energy density spectra for temperature at E_{bot}

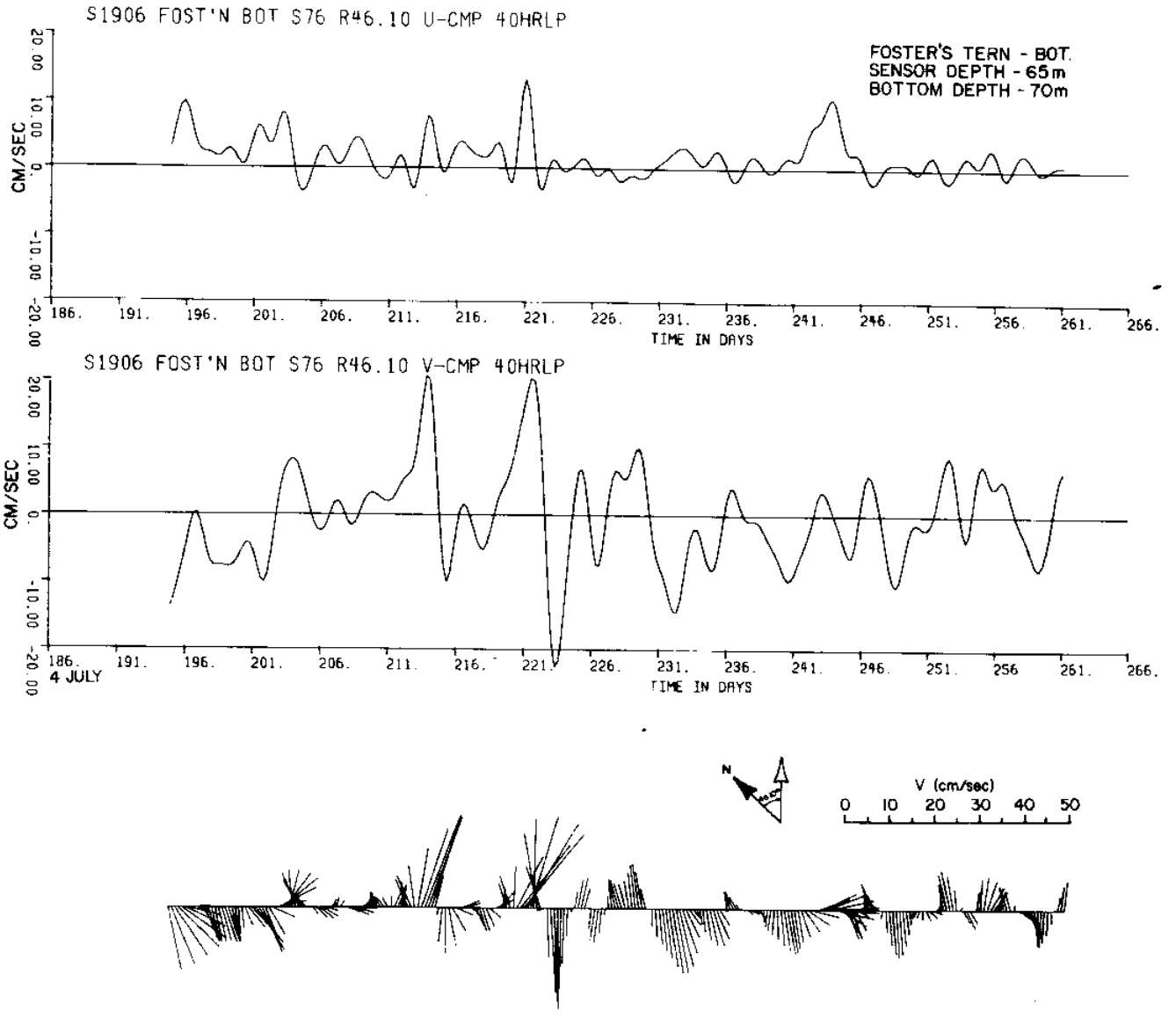

Figure 215 Low pass current velocity components and vectors from meter F(Foster's Tern)$_{bot}$

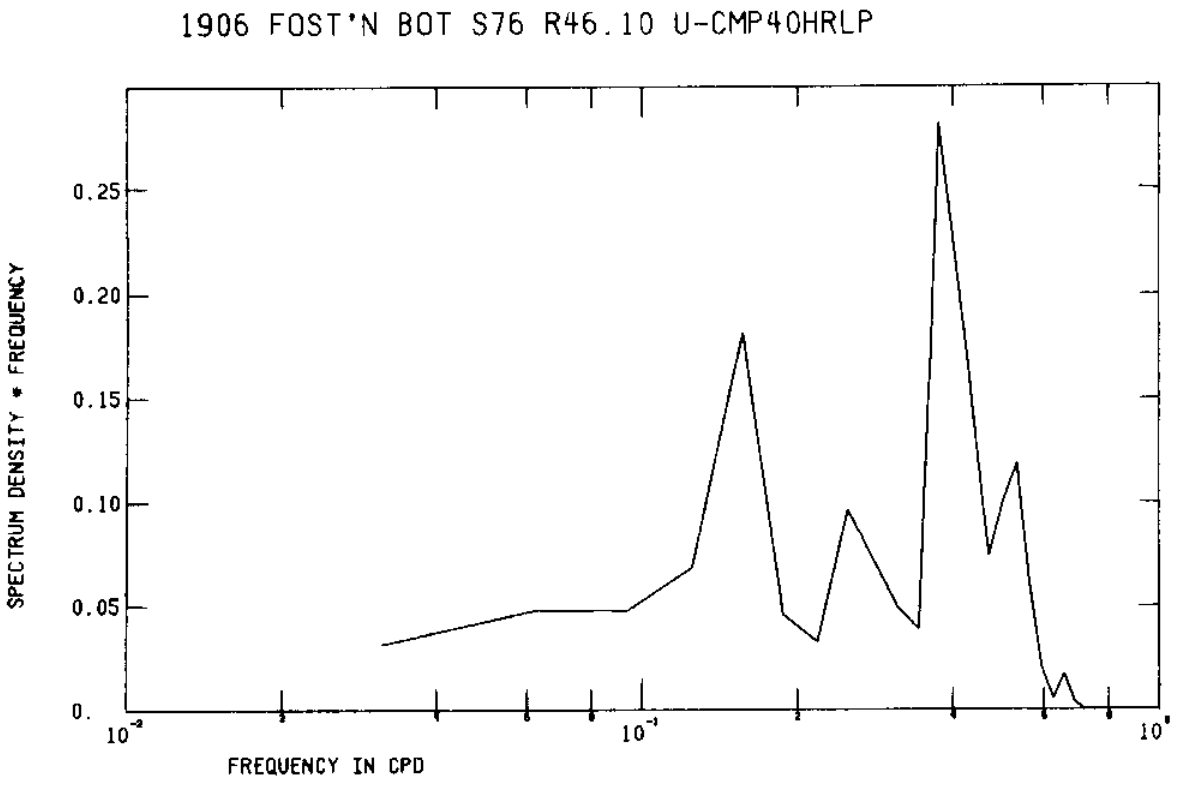

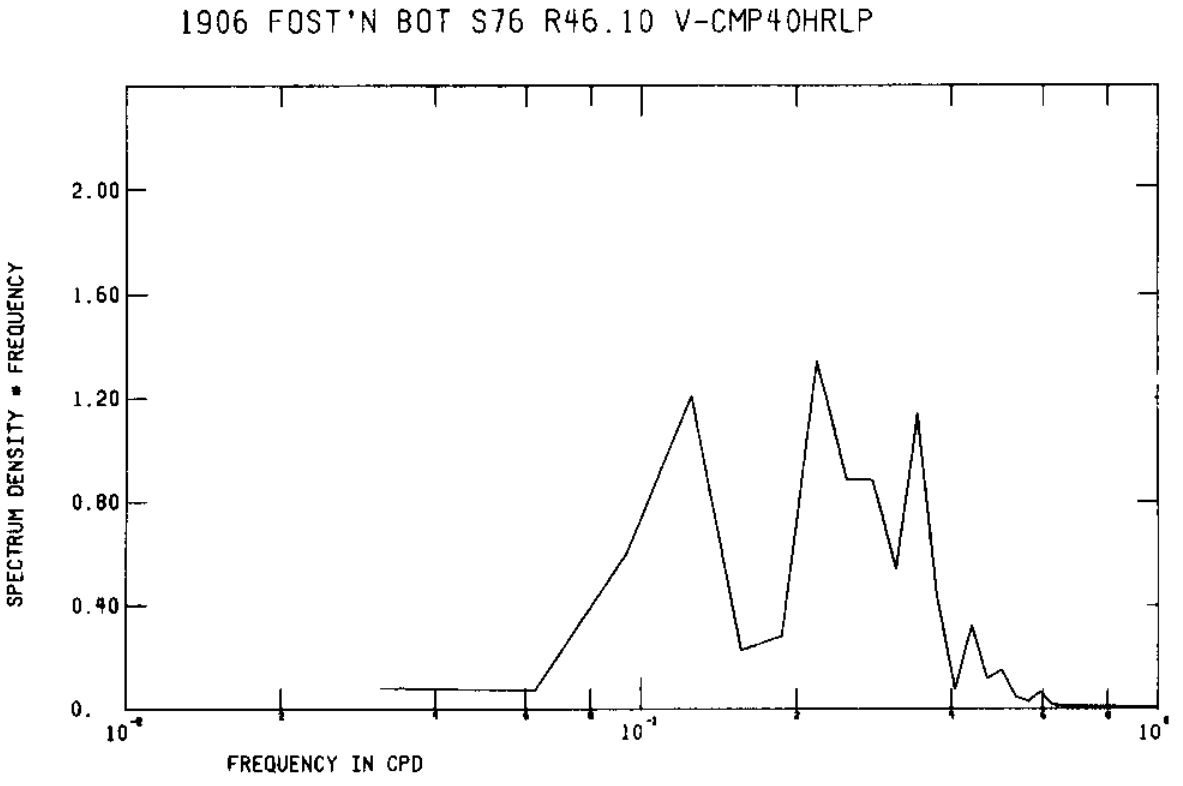

Figure 216 FFT of low pass current velocity components from meter F(Foster's Tern)$_{bot}$

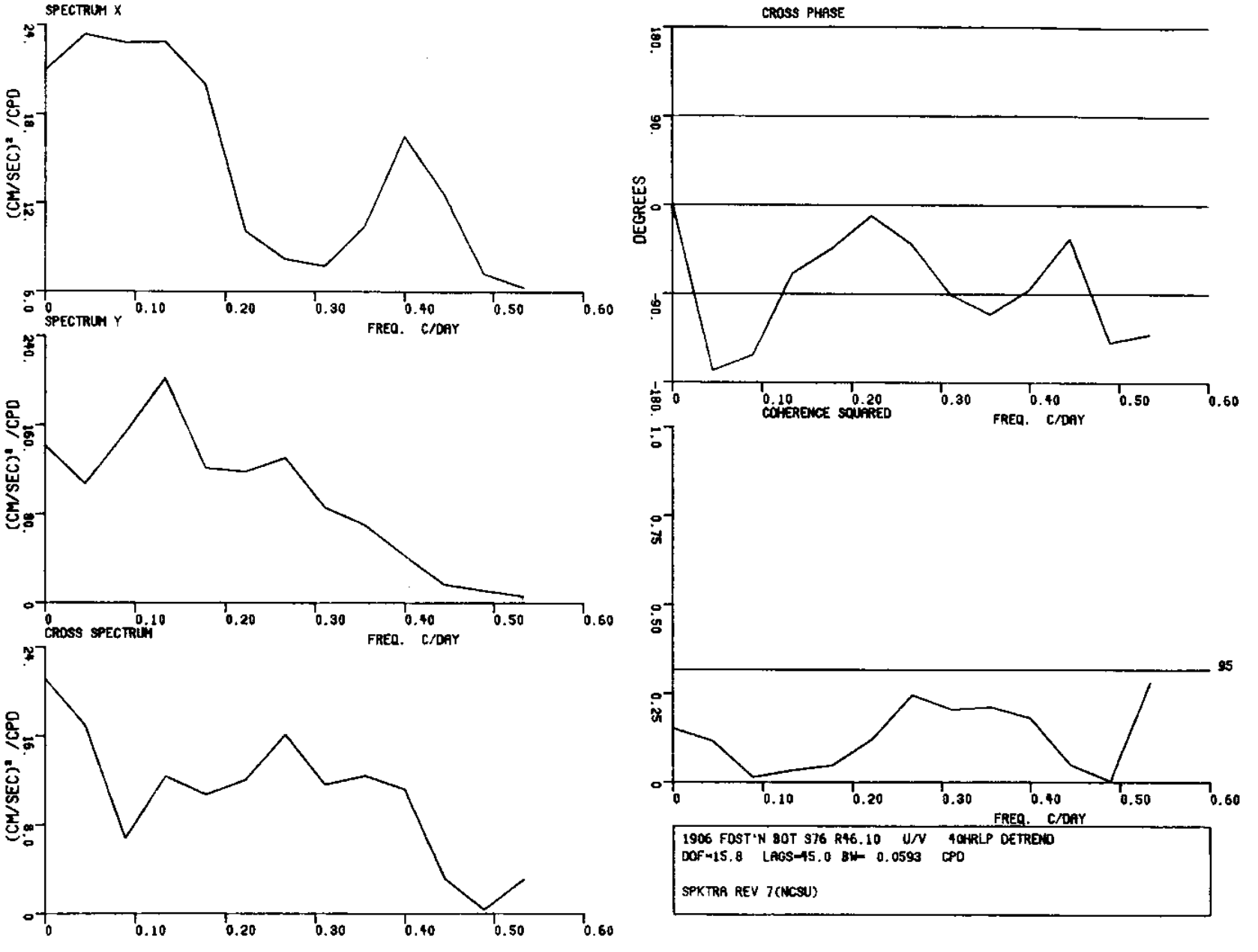

Figure 217 Spectra of low pass current velocity components from meter F(Foster's Tern)$_{bot}$

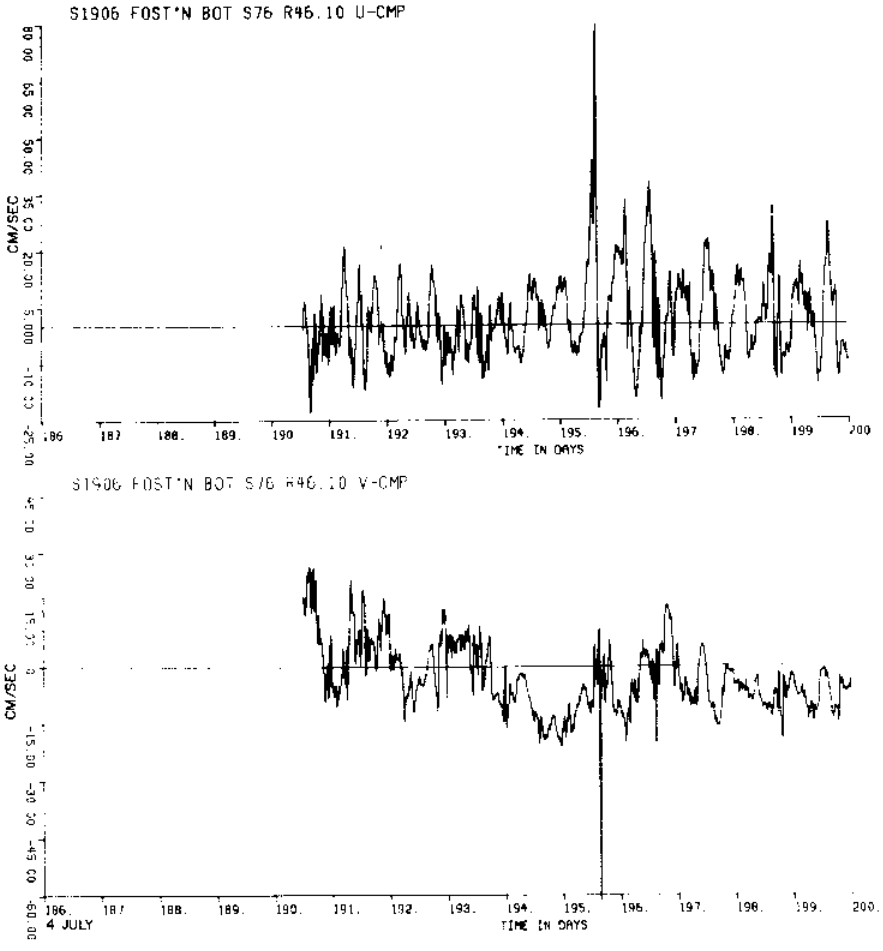

Figure 218 a

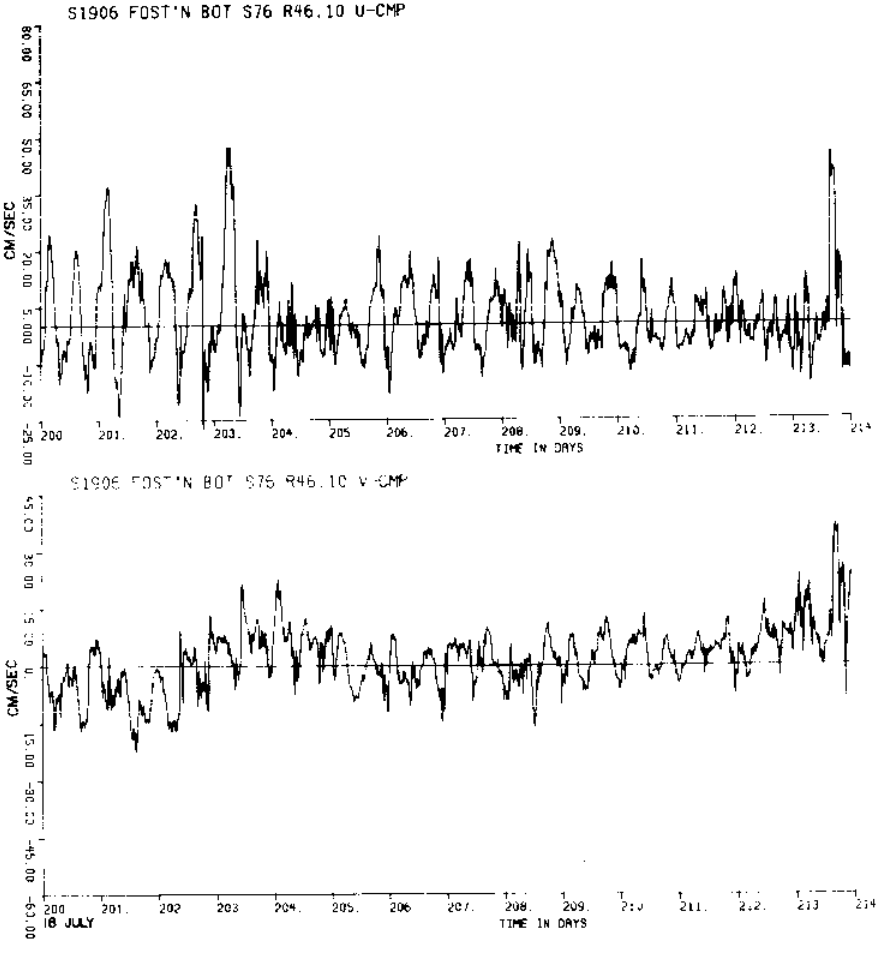

Figure 218 b

Figure 218 (a,b,c, d,e,f) Unfiltered current velocity components from meter F(Foster's Tern)$_{bot}$

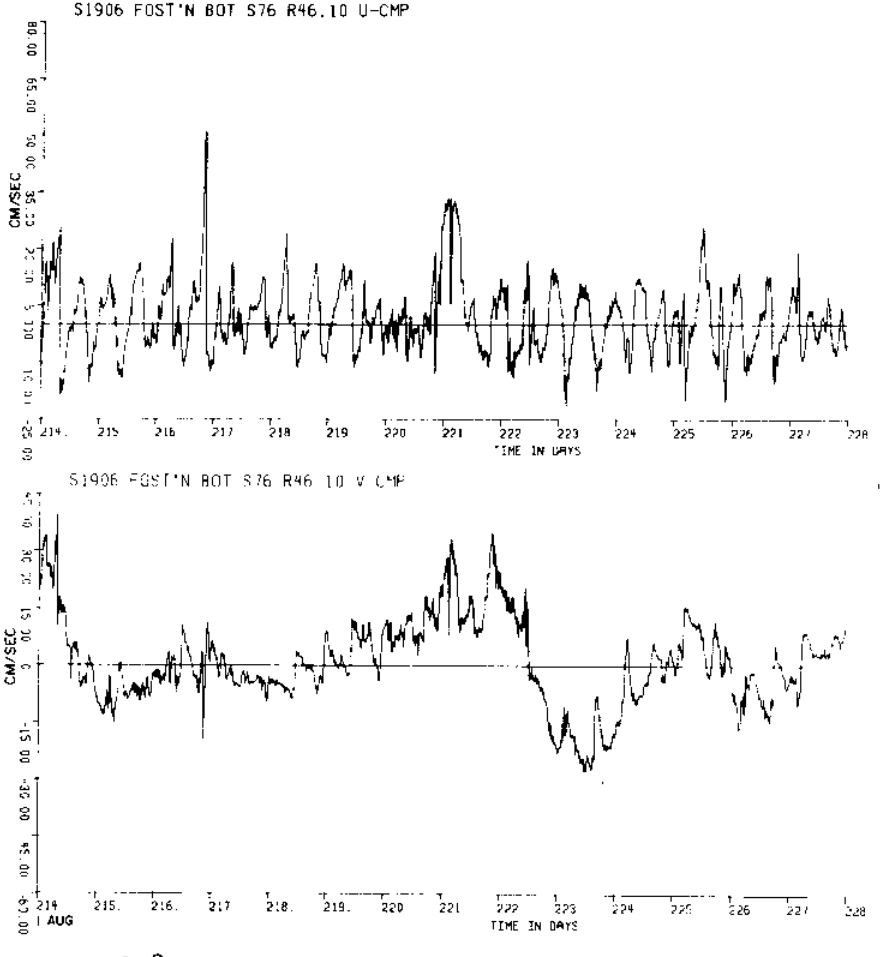

Figure 218 c

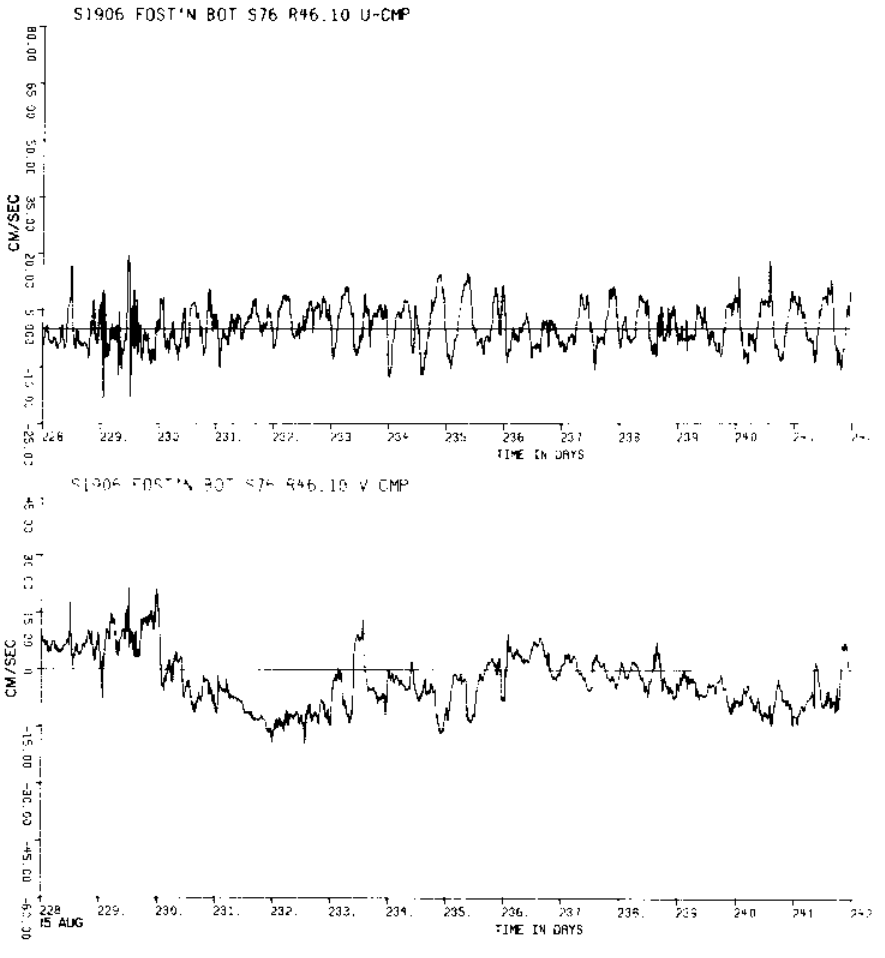

Figure 218 d

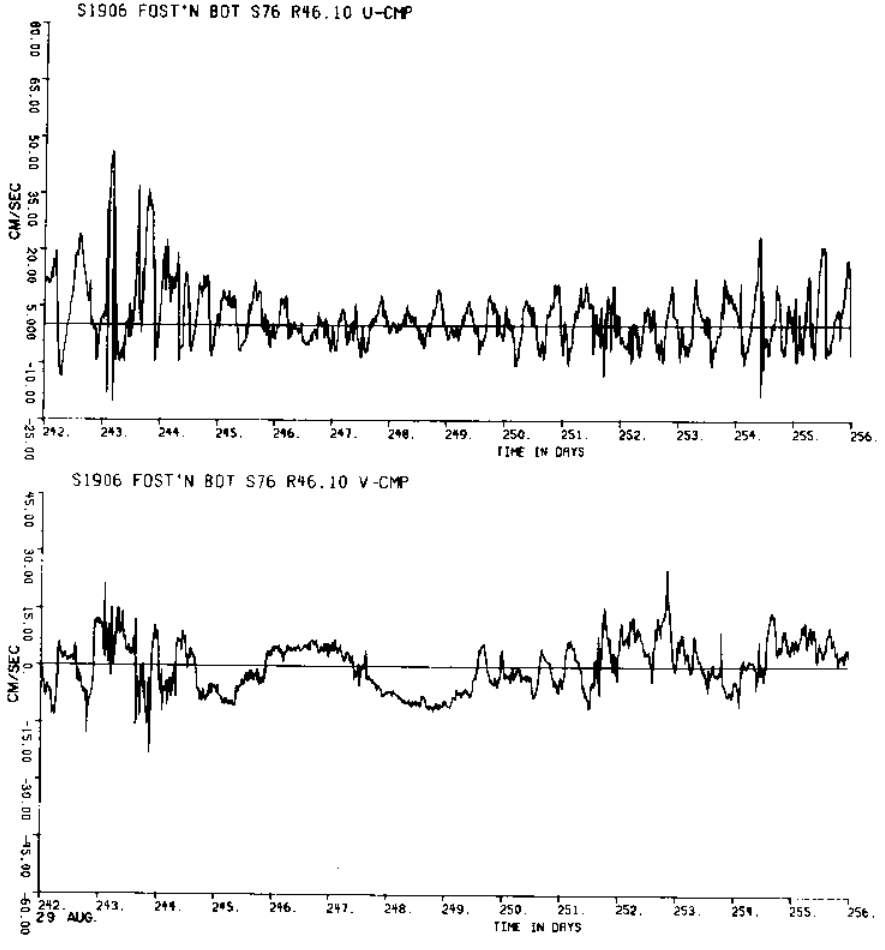

Figure 218 e

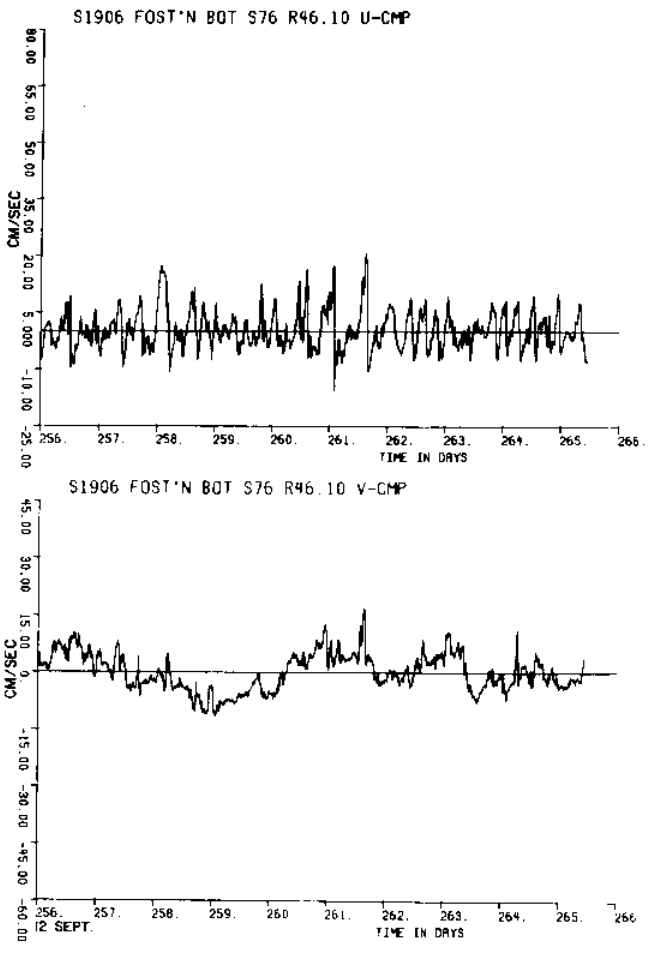

Figure 218 f

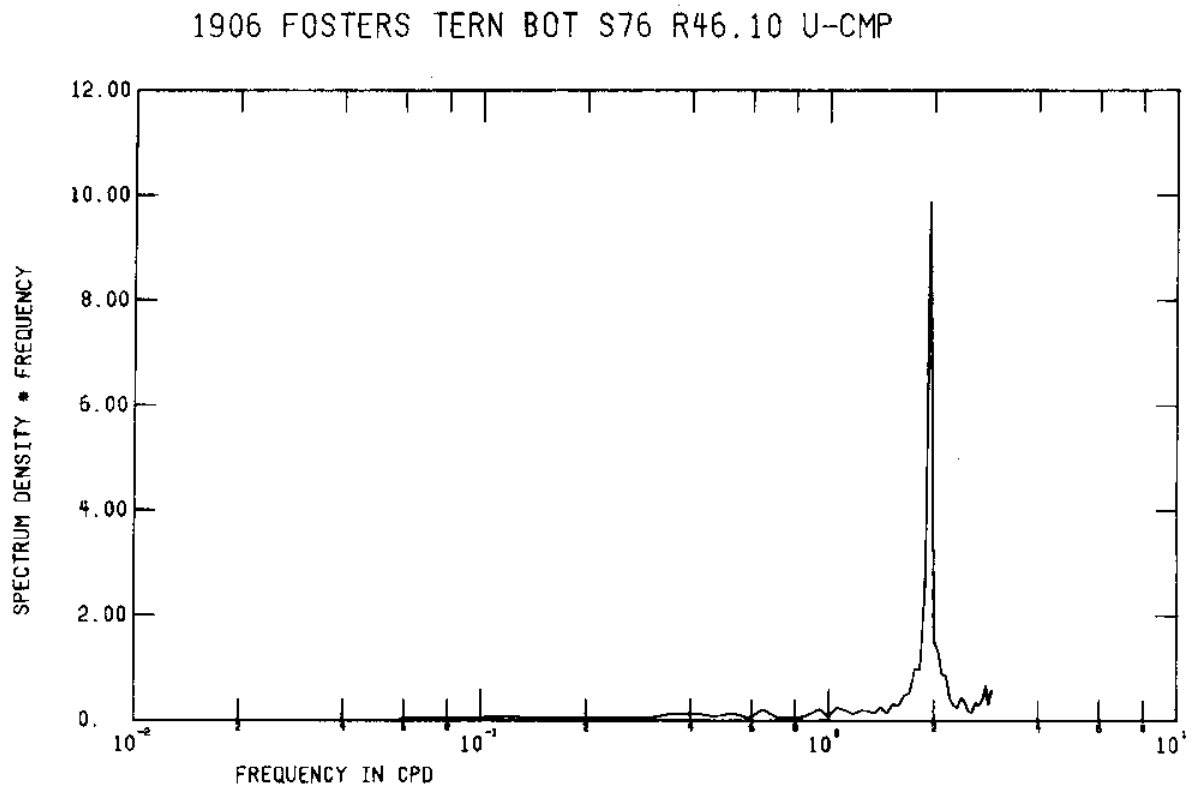

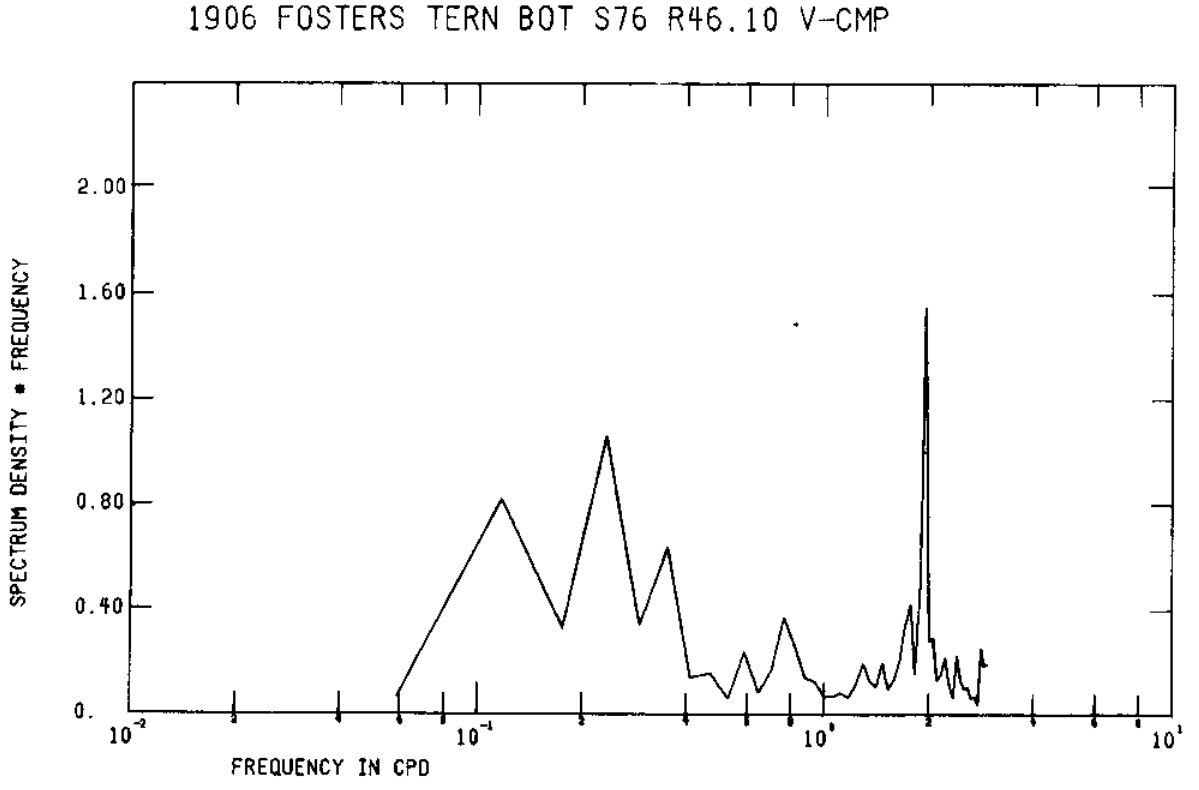

Figure 219 FFT of unfiltered current velocity components from meter F(Foster's Tern)$_{bot}$

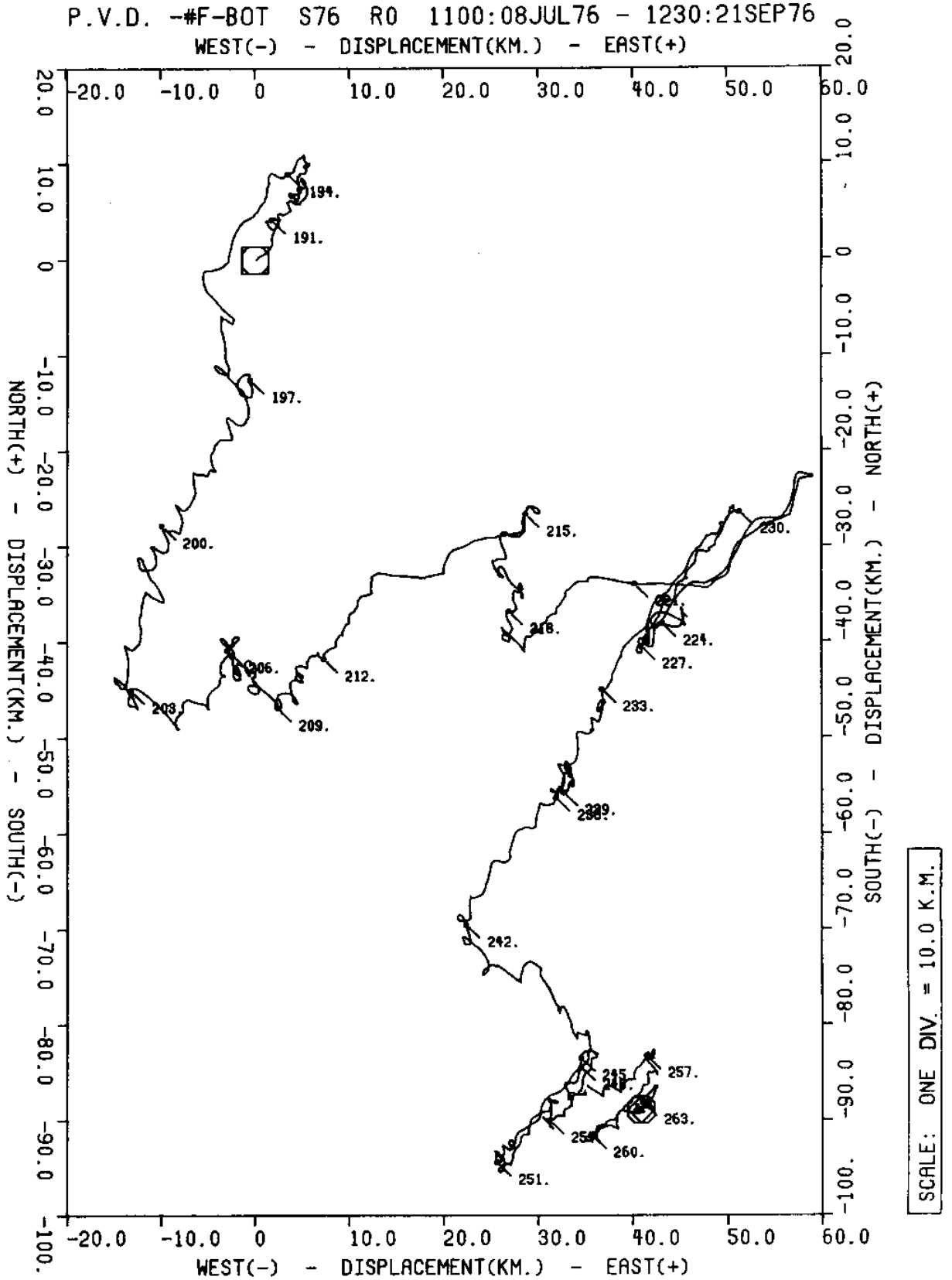

Figure 220 a

Figure 220 (a,b,c) Progressive vector diagrams of unfiltered current velocity from meter F(Foster's Tern)$_{bot}$

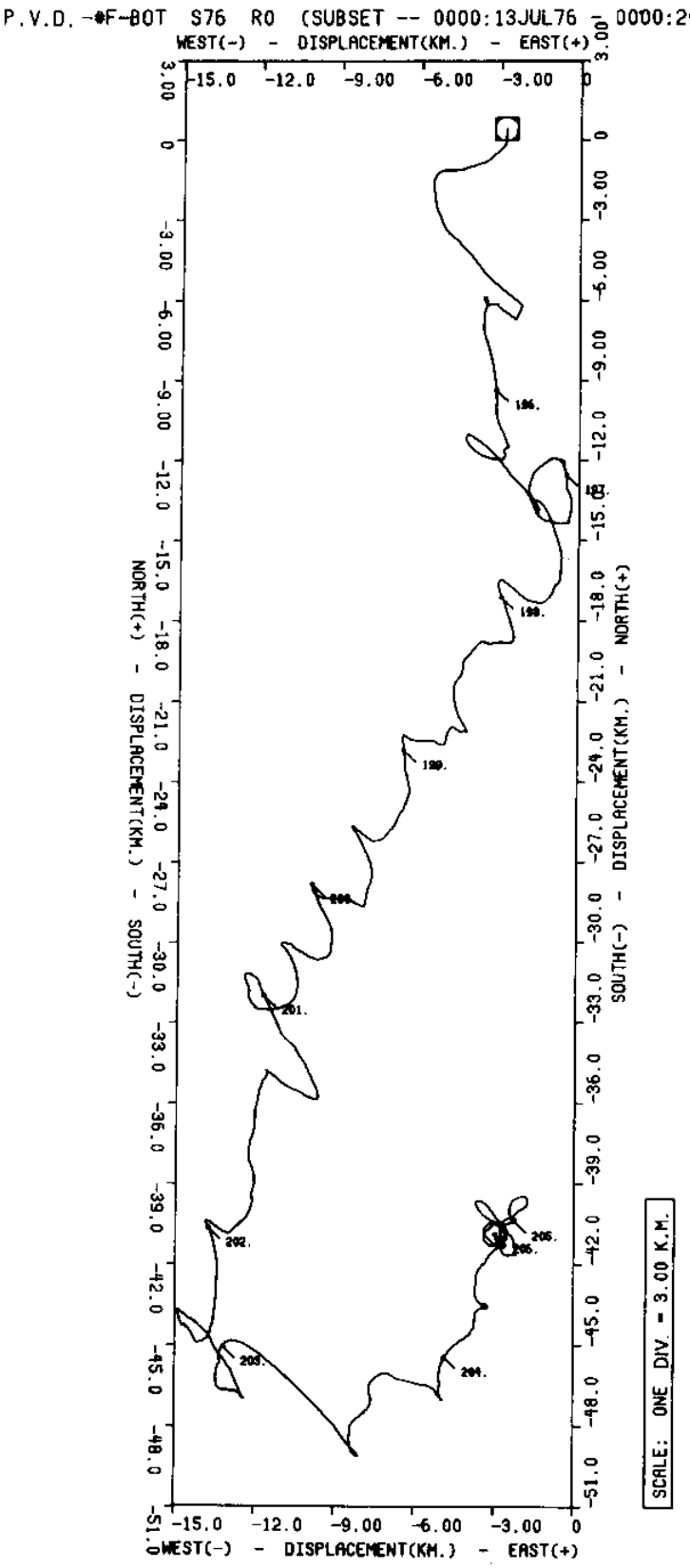
P.V.D. -#F-BOT S76 R0 (SUBSET -- 0000:13JUL76 - 0000:24JUL76)
WEST(-) - DISPLACEMENT(KM.) - EAST(+)
NORTH(+) - DISPLACEMENT(KM.) - SOUTH(-)
SOUTH(-) - DISPLACEMENT(KM.) - NORTH(+)
SCALE: ONE DIV = 3.00 K.M.

Figure 220 b

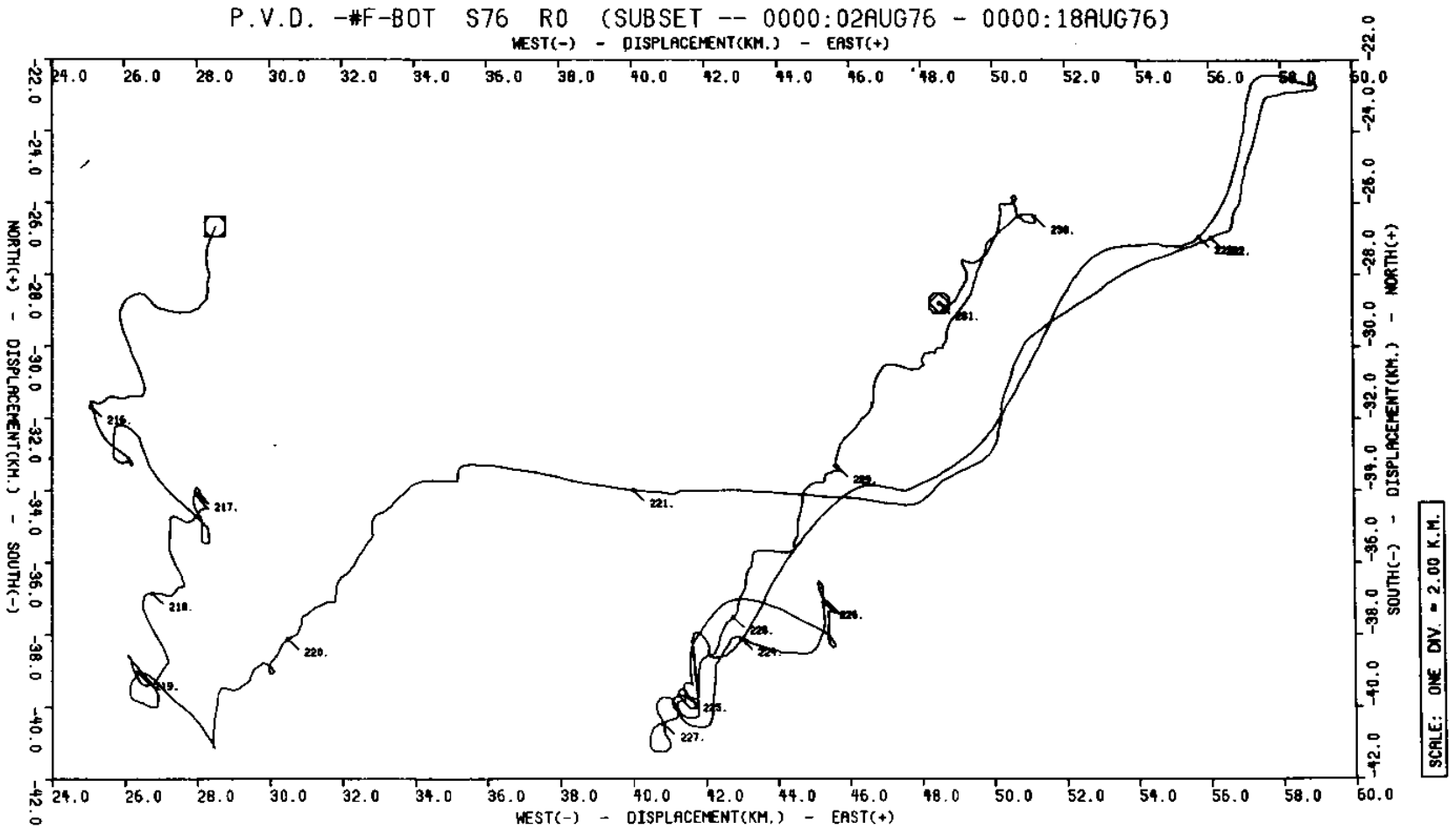
P.V.D. -#F-BOT S76 R0 (SUBSET -- 0000:02AUG76 - 0000:18AUG76)
WEST(-) - DISPLACEMENT(KM.) - EAST(+)
NORTH(+) - DISPLACEMENT(KM.) - SOUTH(-)
SCALE: ONE DIV. = 2.00 K.M.

Figure 220 c

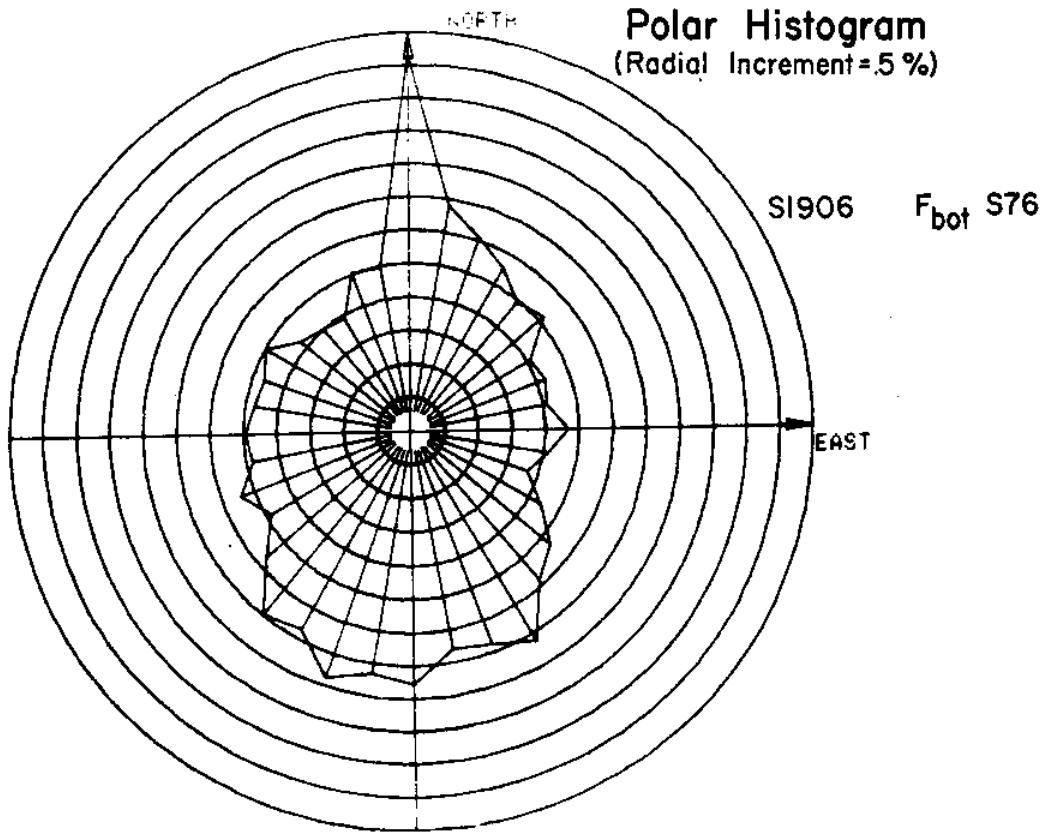

Figure 221 Histogram from meter F(Foster's Tern)$_{bot}$

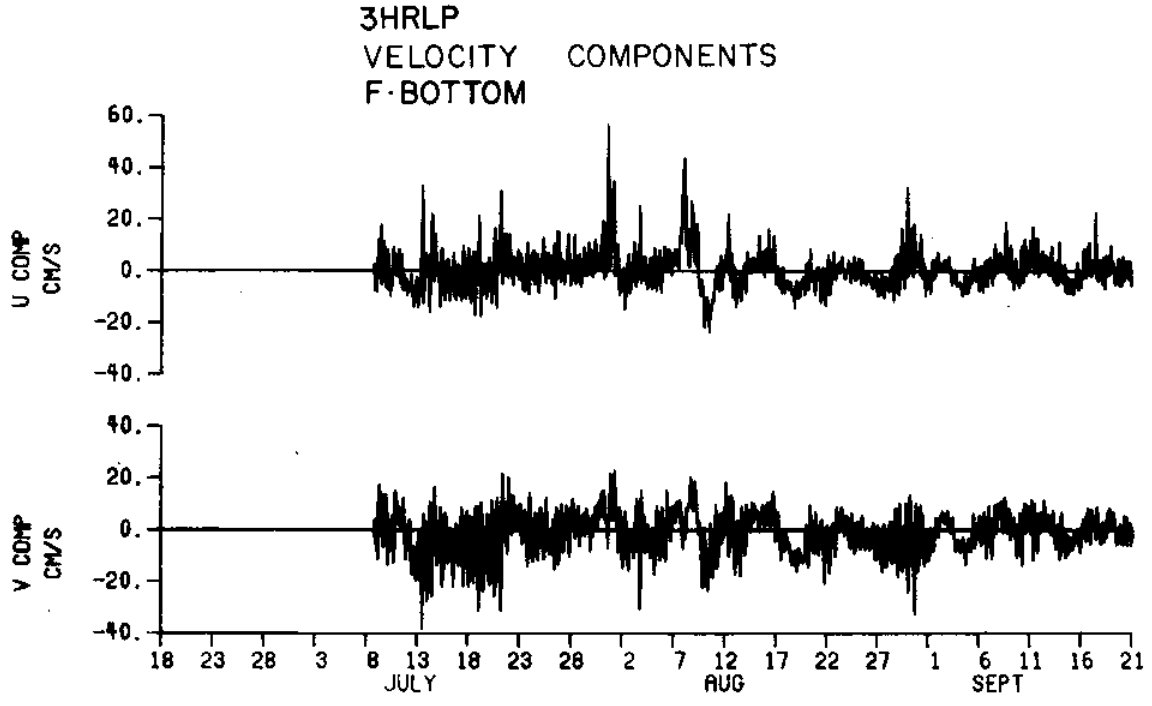

Figure 222 3HRLP velocity components for F_{bot}

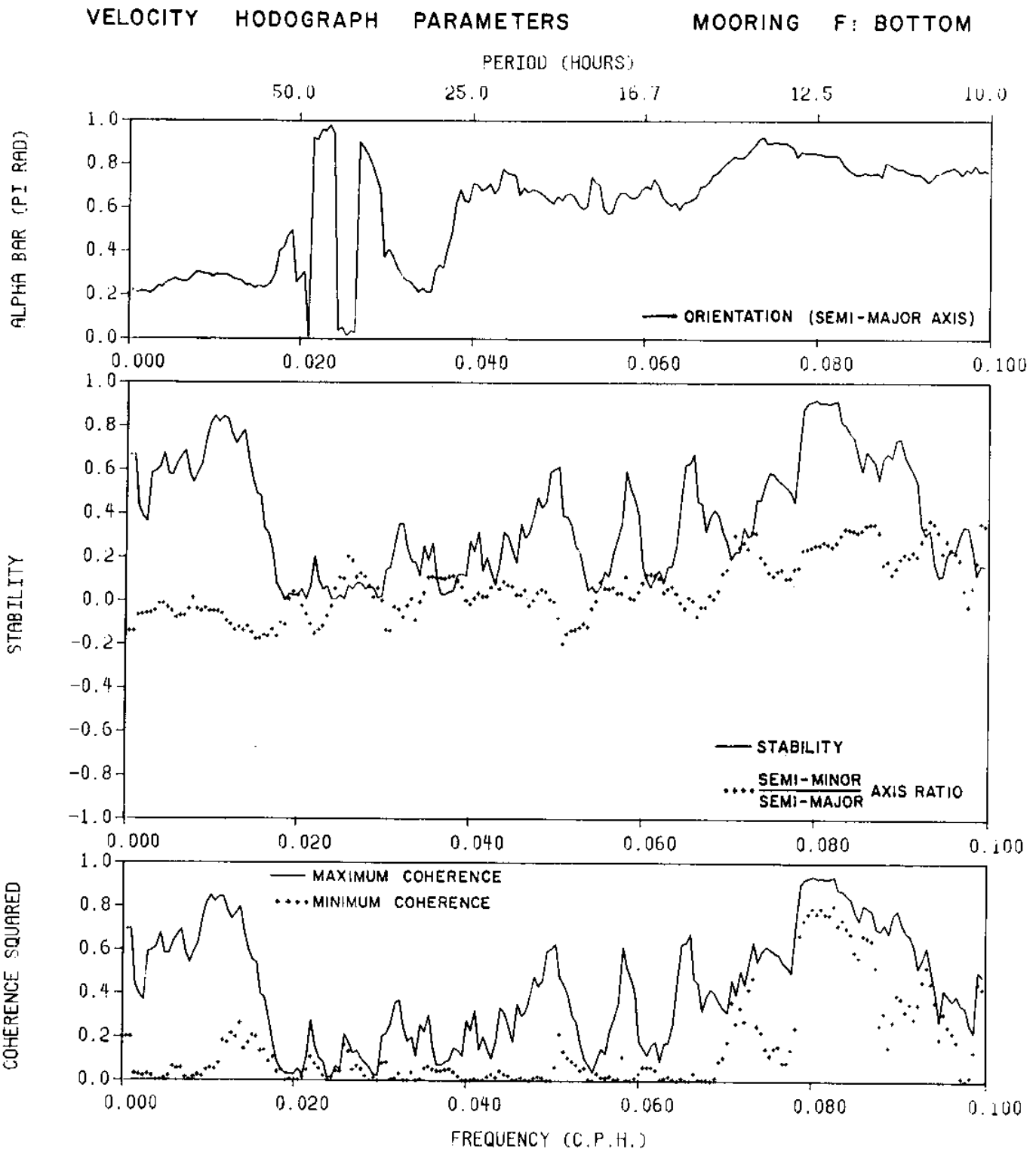

Figure 223 Hodograph parameters from meter F(Foster's Tern)$_{bot}$

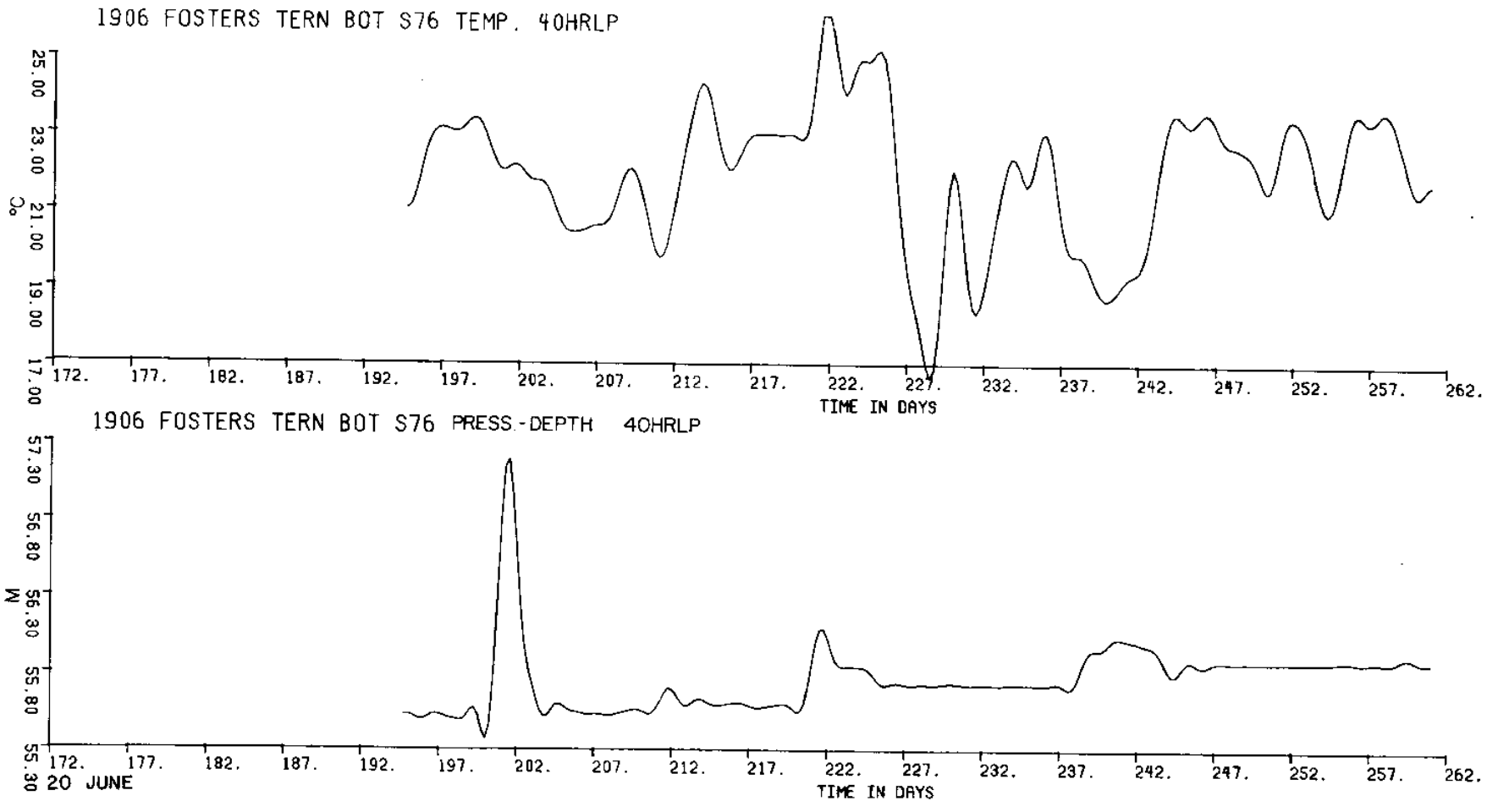

Figure 224 Low pass temperature and pressure from meter $F(\text{Foster's Tern})_{bot}$

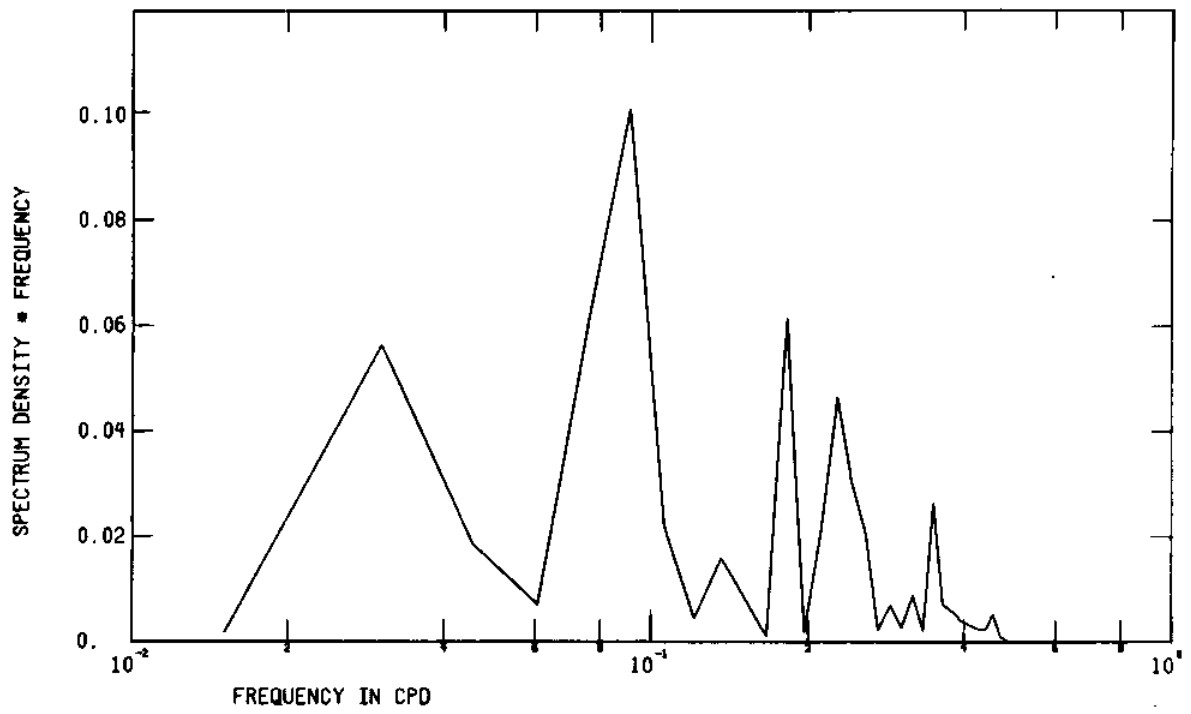

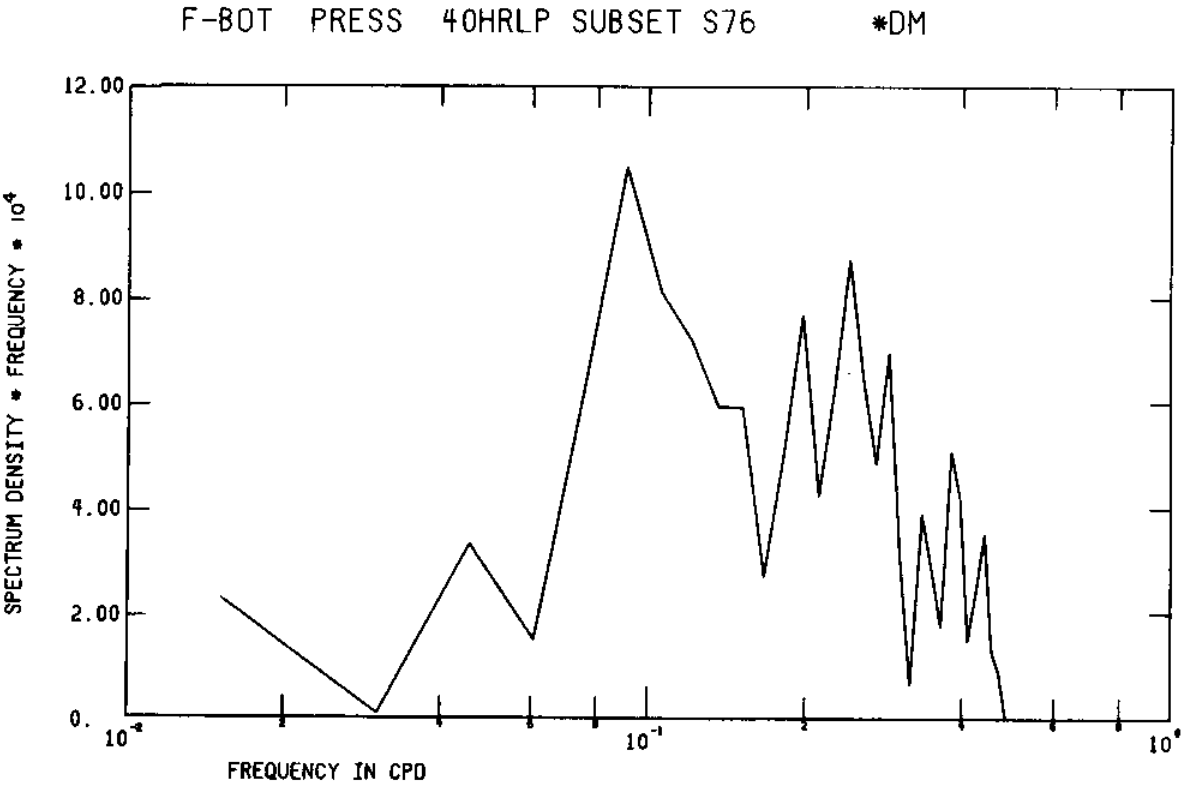

Figure 225 FFT of low pass temperature and pressure from meter F(Foster's Tern)$_{bot}$

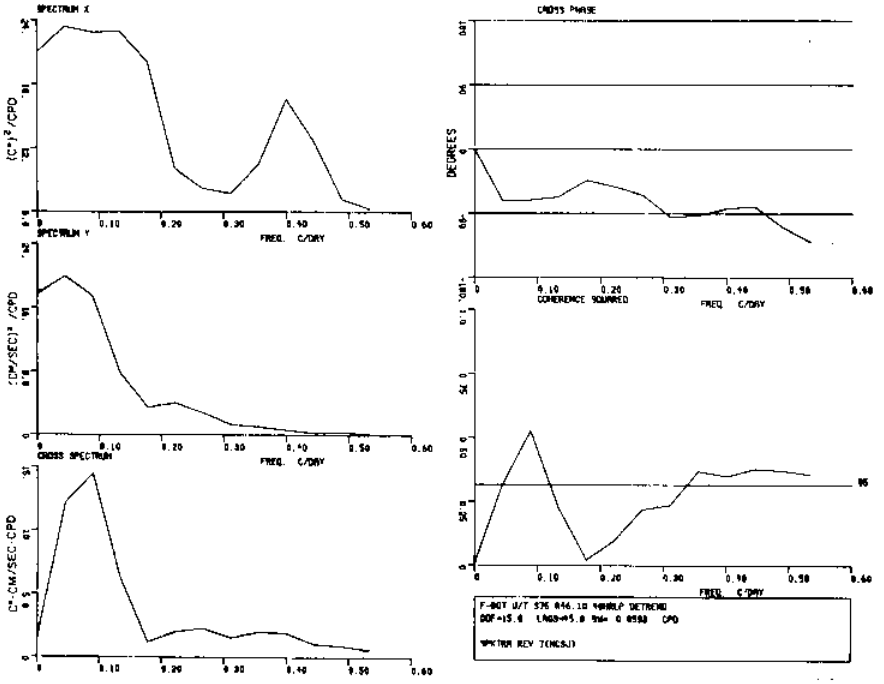

Figure 226 Spectra of temperature and the low pass current velocity u component, both from meter F(Foster's Tern)$_{bot}$

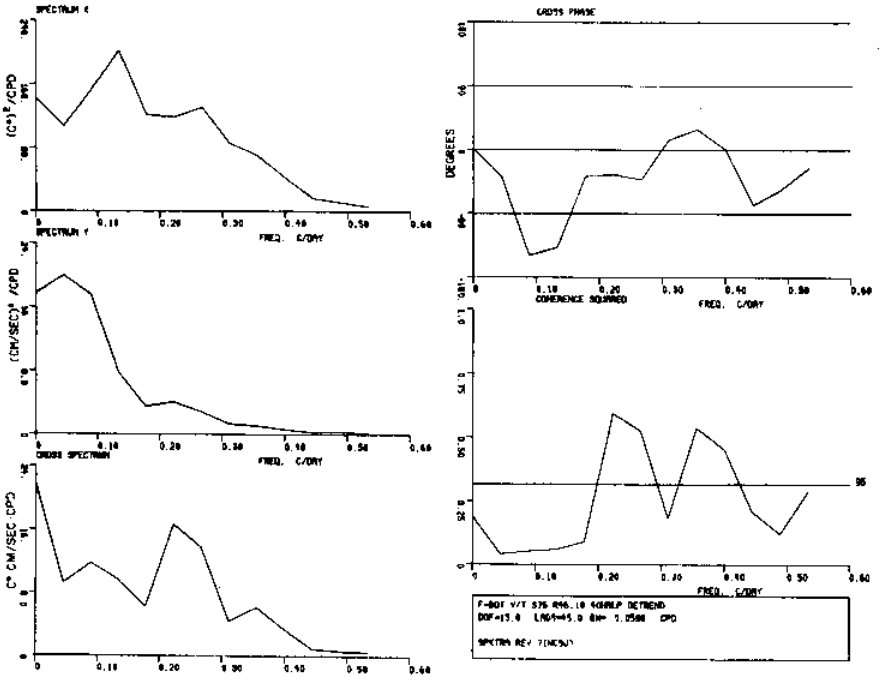

Figure 227 Spectra of temperature and the low pass current velocity v component, both from meter F(Foster's Tern)$_{bot}$

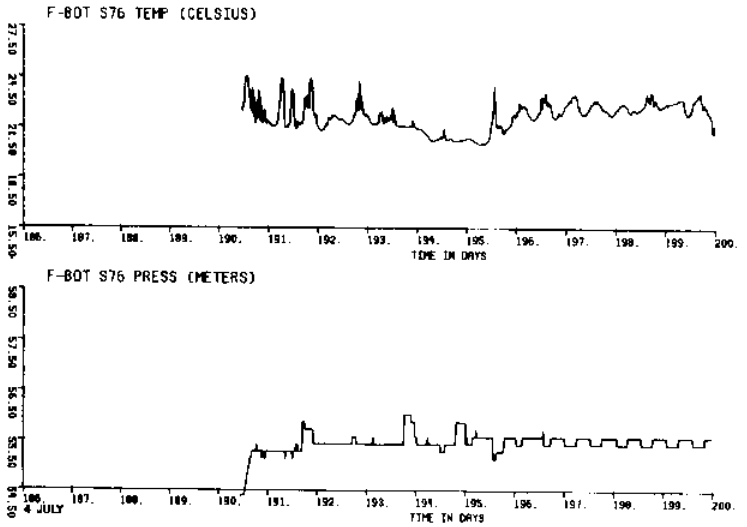

Figure 228 a

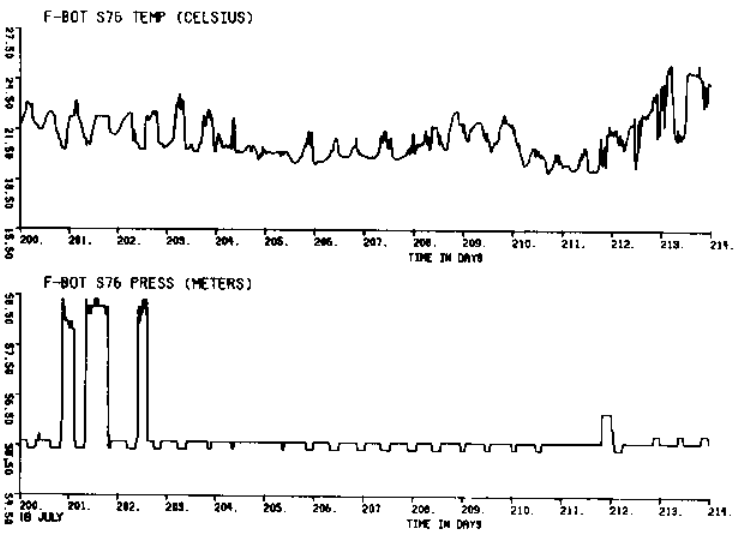

Figure 228 b

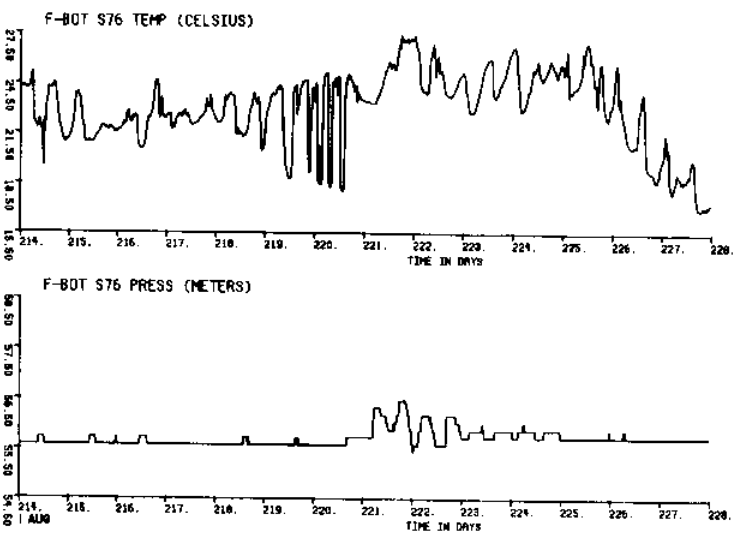

Figure 228 c

Figure 228 (a,b,c, d,e,f) Unfiltered temperature and pressure from meter F(Foster's Tern)$_{bot}$

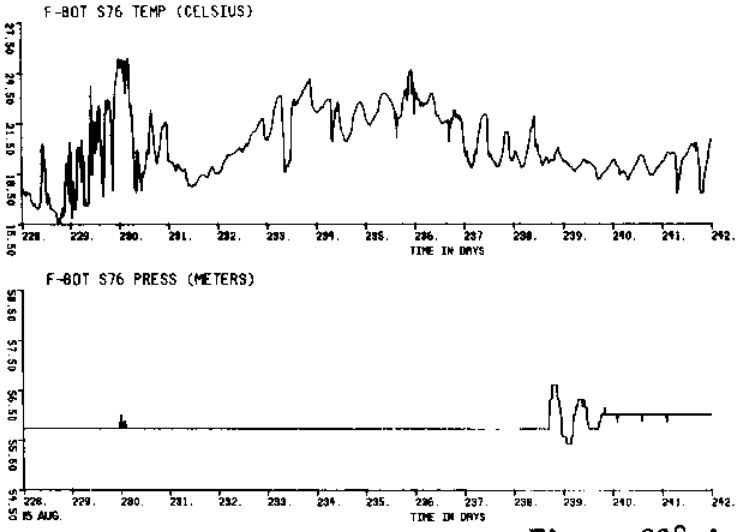

Figure 228 d

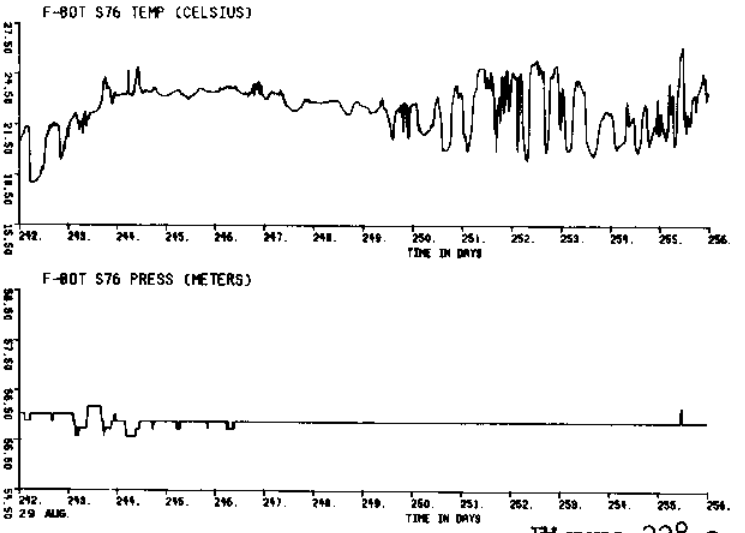

Figure 228 e

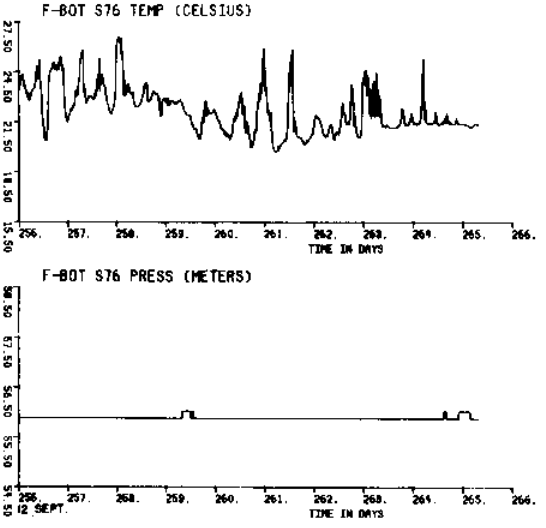

Figure 228 f

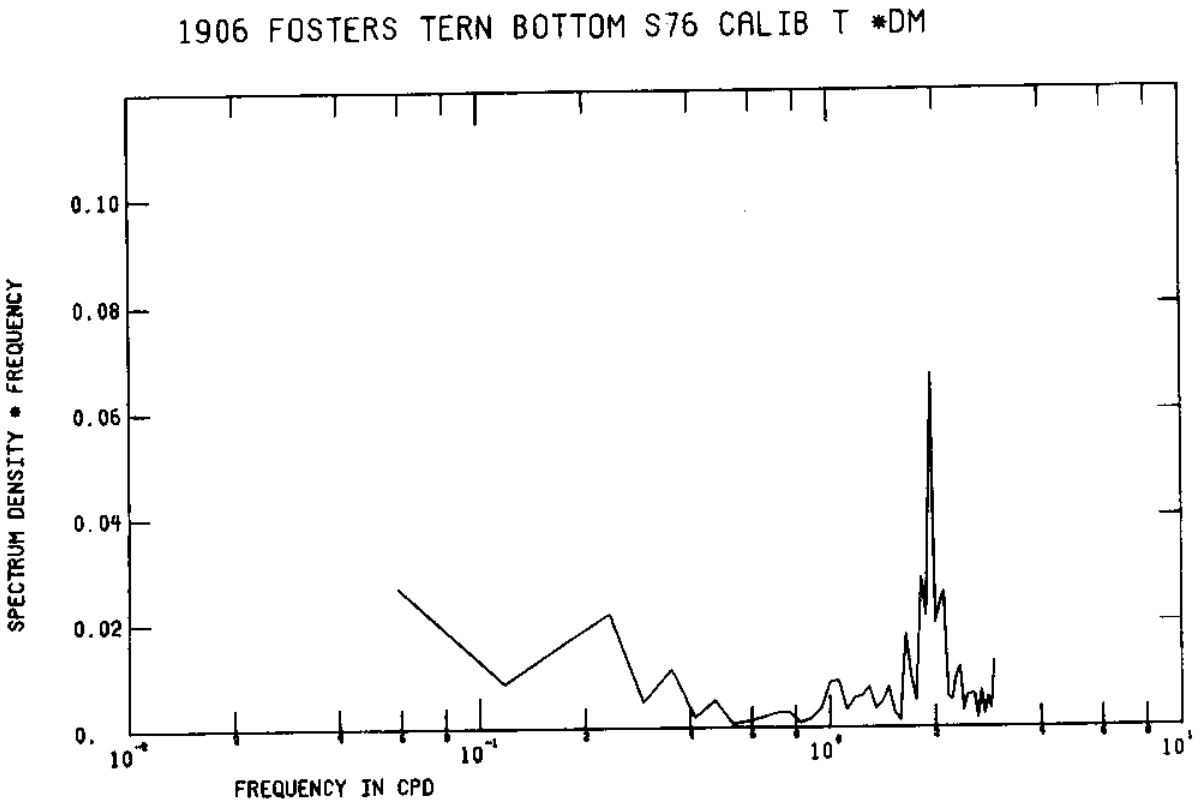

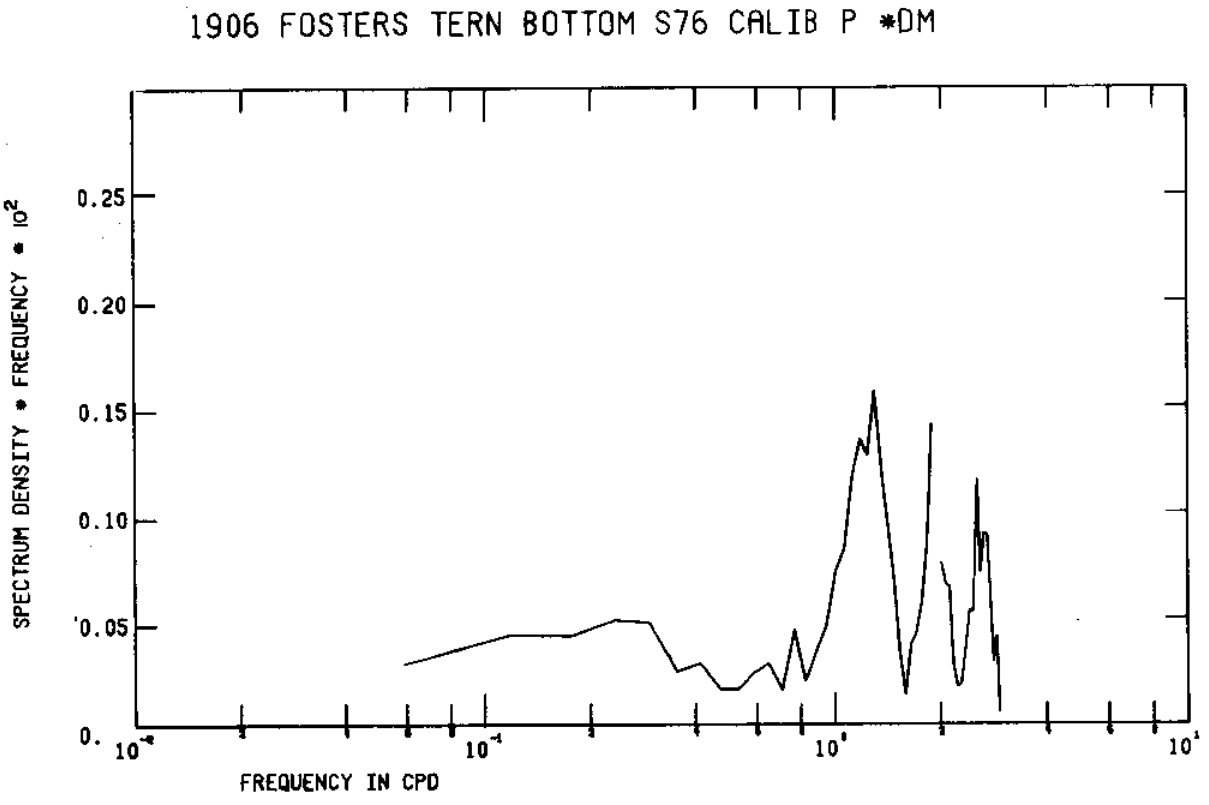

Figure 229 FFT of unfiltered temperature and pressure from meter F(Foster's Tern)$_{bot}$

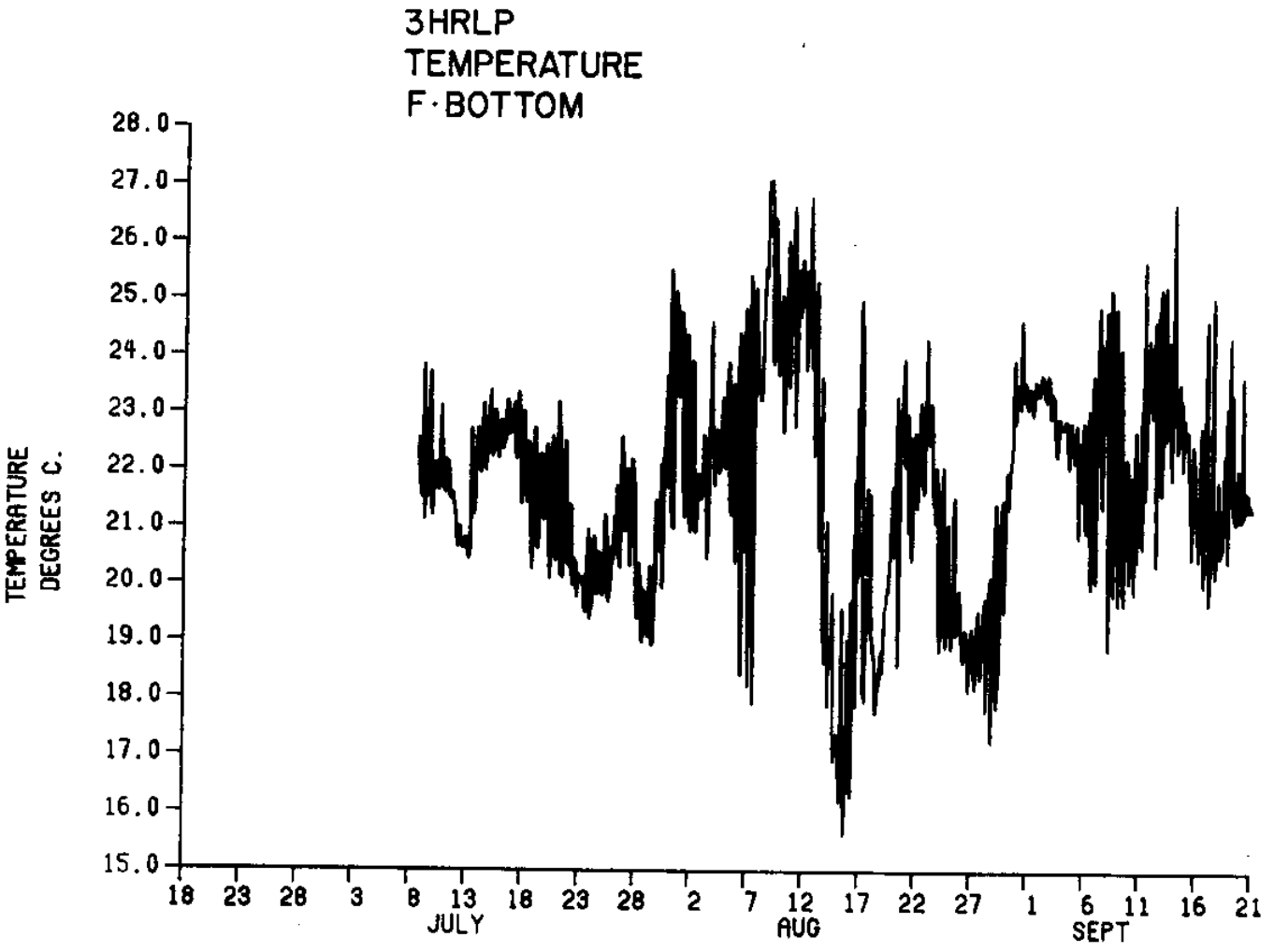

Figure 230 3HRLP temperature for F_{bot}

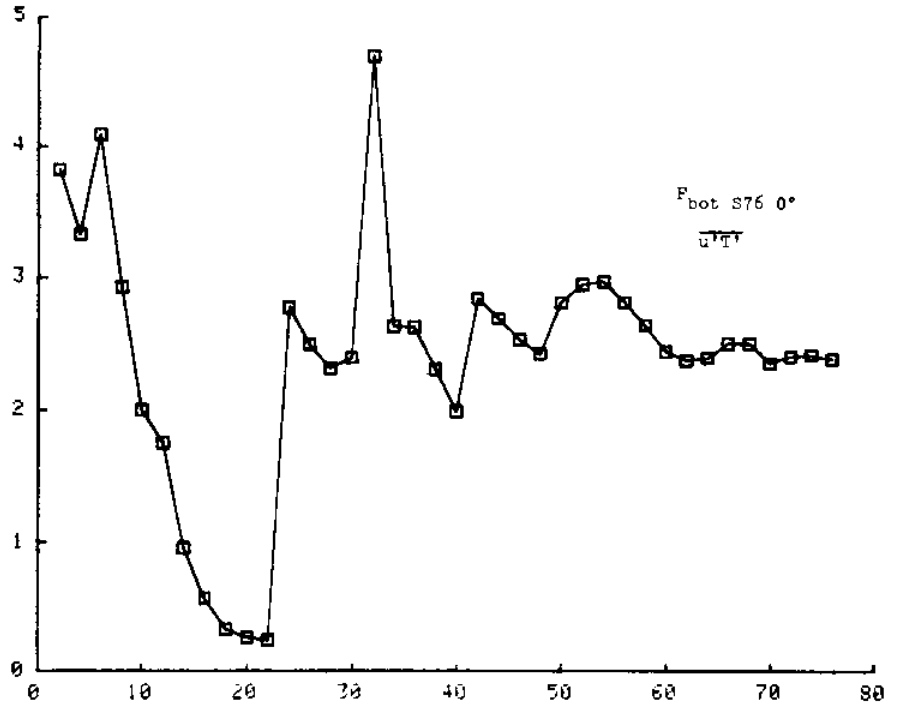

Figure 231 Heat correlation variance in x-direction for F_{bot} Summer, 1976 (cumulative)

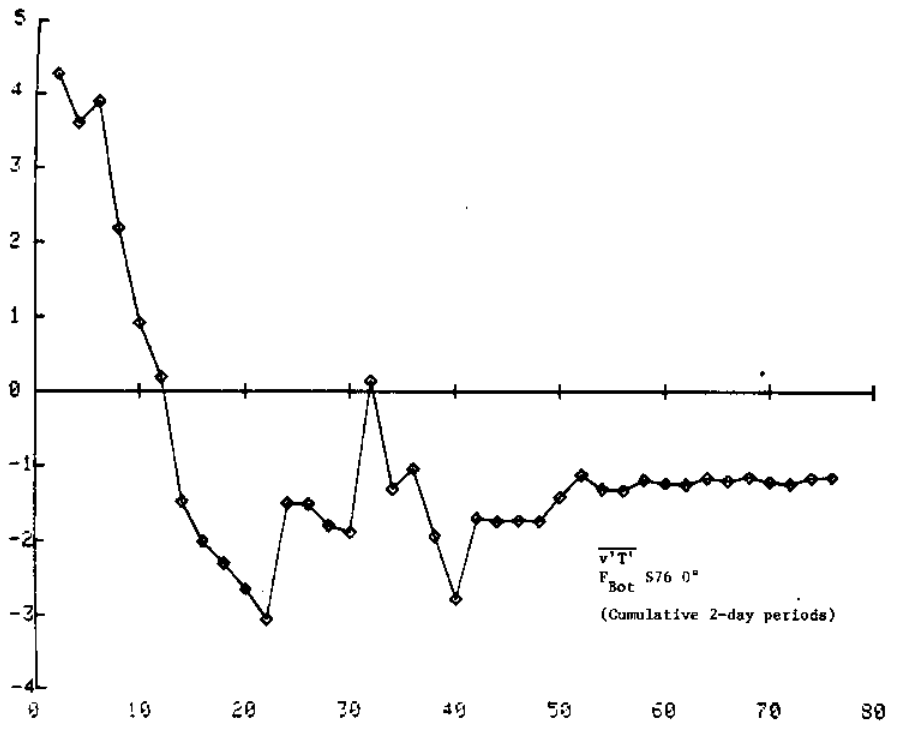

Figure 232 Heat correlation variance in y-direction for F_{bot} Summer, 1976 (cumulative

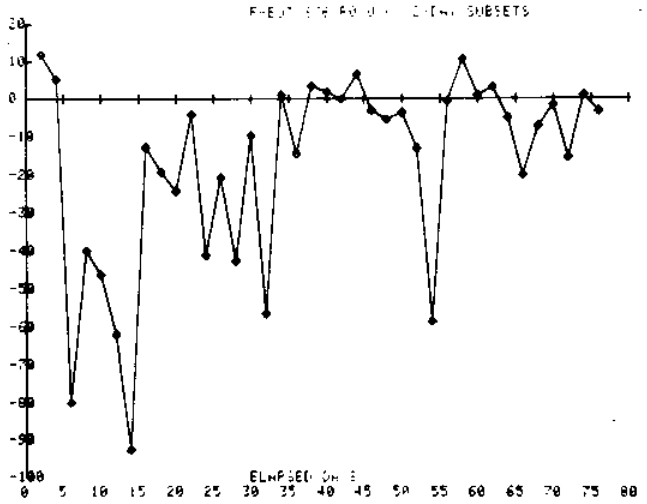

Figure 233 Momentum correlation variance in the horizontal plane for F_{bot} Summer, 1976 (2-day subset)

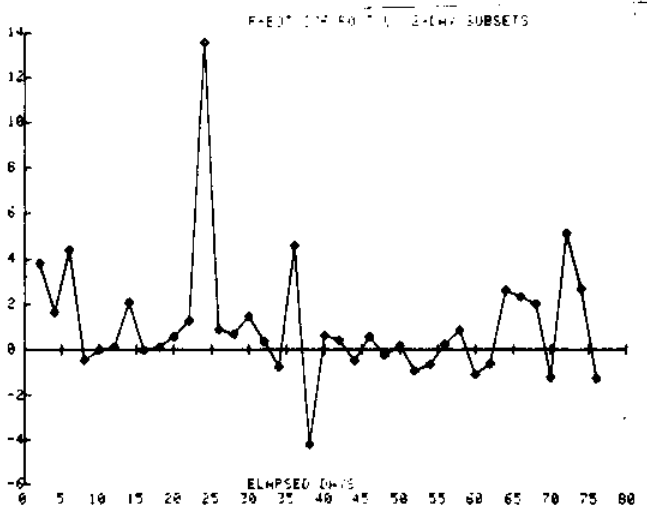

Figure 234 Heat correlation variance in the x-direction for F_{bot} Summer, 1976 (2-day subset)

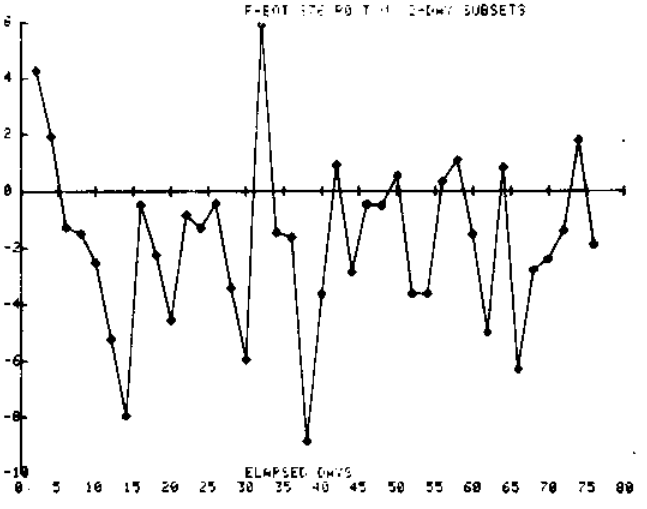

Figure 235 Heat correlation variance in the y-direction for F_{bot} Summer, 1976 (2-day subset)

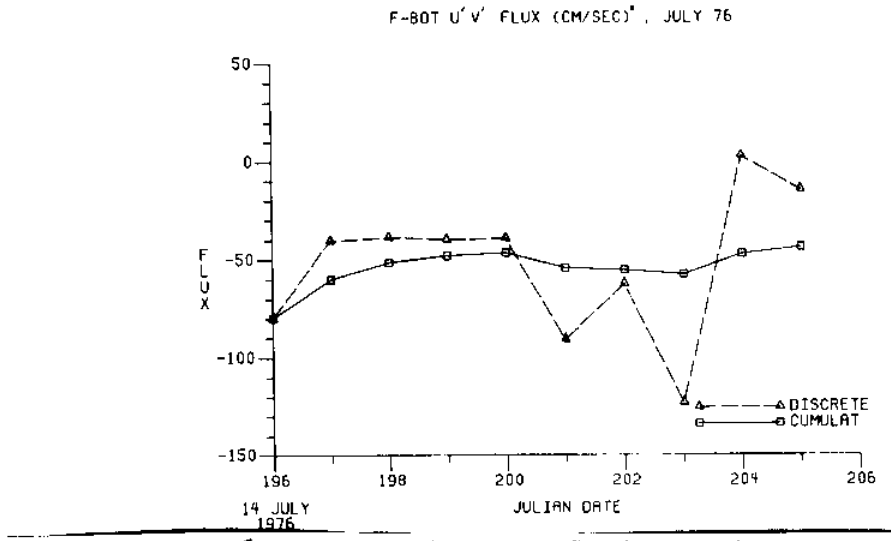

Figure 236 Momentum correlation variance in horizontal plane for F_{bot} July 14-23, 1976

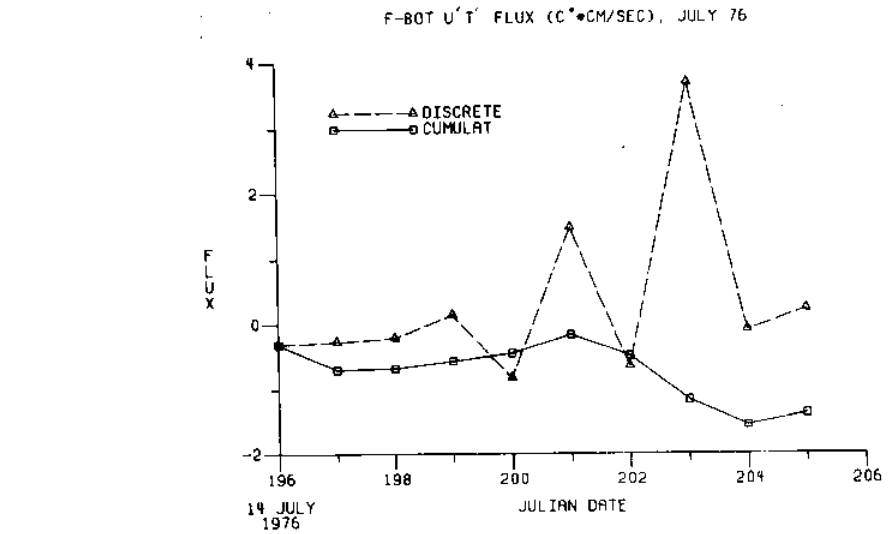

Figure 237 Heat correlation variance in x-direction for F_{bot} July 14-23, 1976

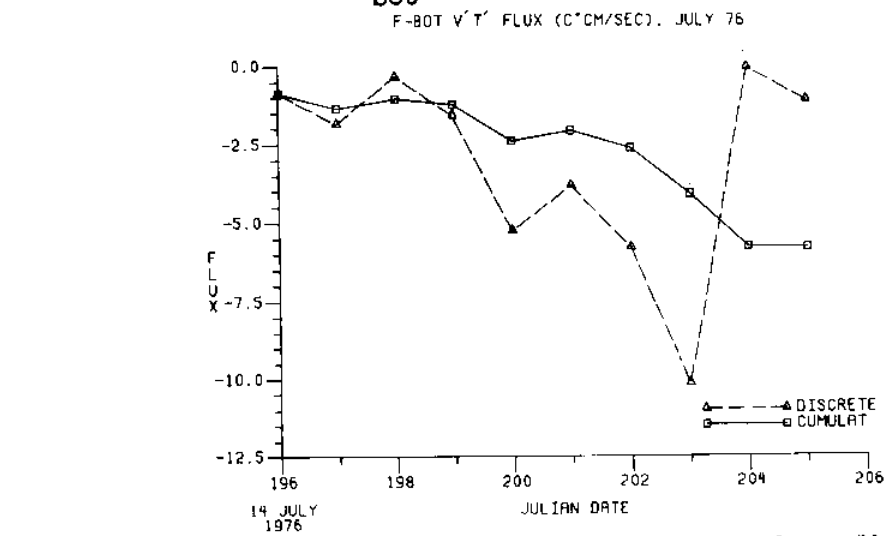

Figure 238 Heat correlation variance in y-direction for F_{bot} July 14-23, 1976

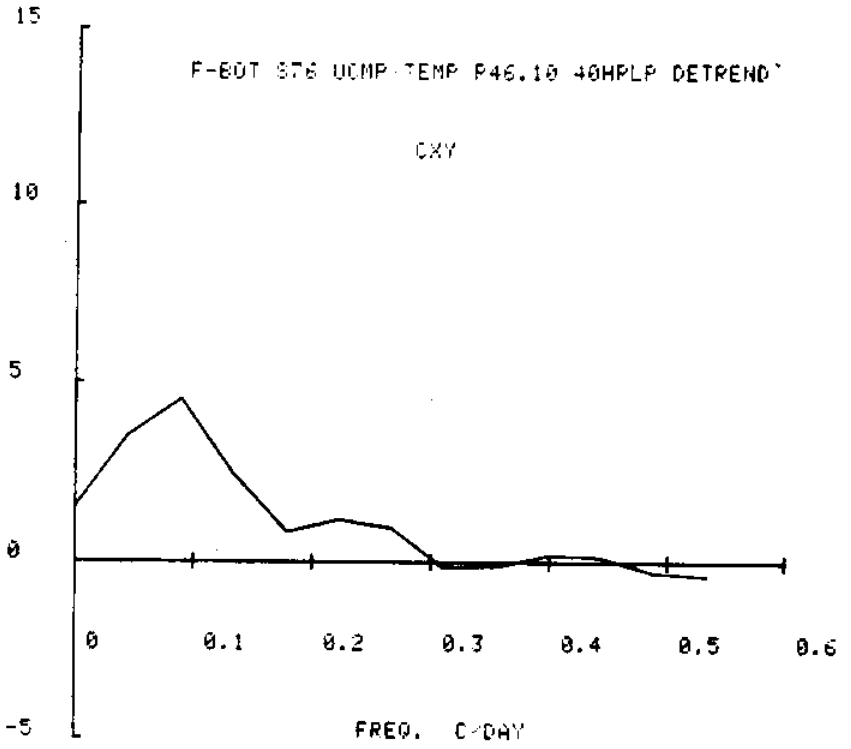

Figure 239 Cospectra of temperature vs. u-component for meter F_{bot}

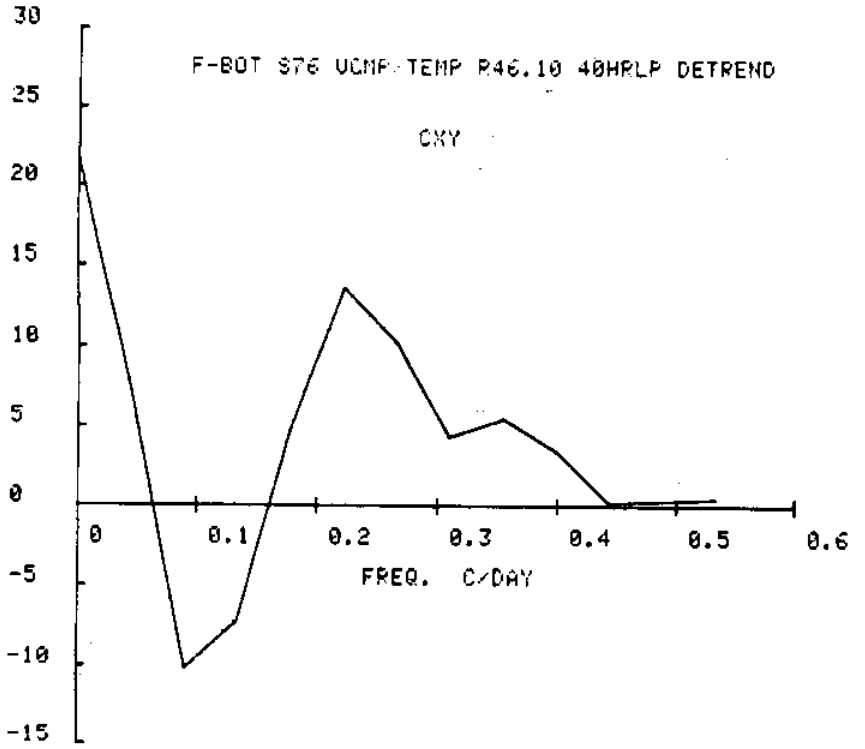

Figure 240 Cospectra of temperature vs. v-component for meter F_{bot}

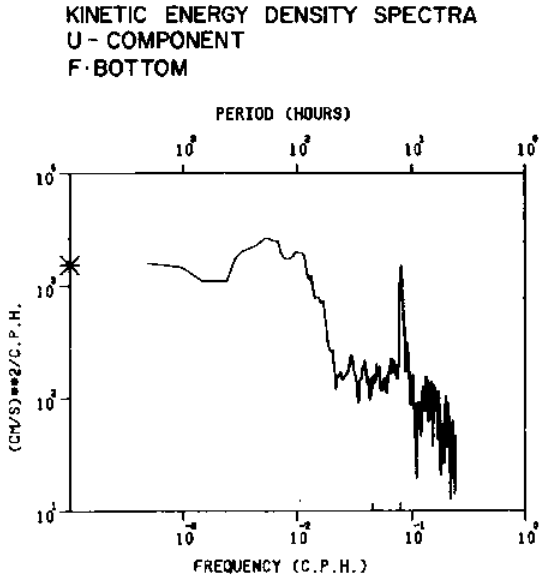

Figure 241
Kinetic energy density spectra for current velocity, u-component, F_{bot}

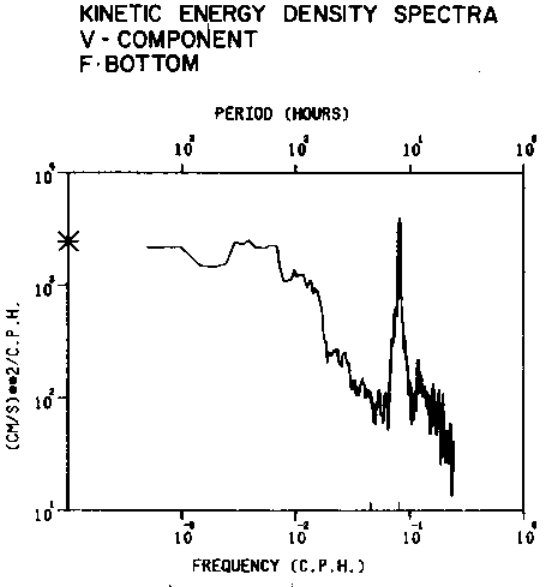

Figure 242
Kinetic energy density spectra for current velocity, v-component, F_{bot}

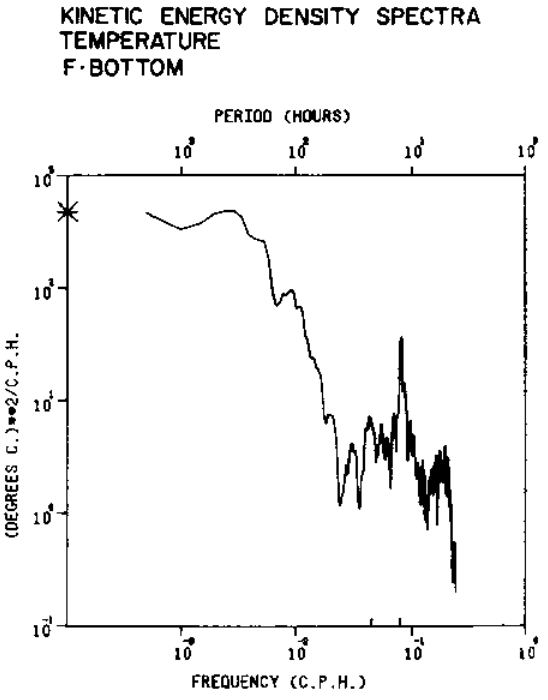

Figure 243
Kinetic energy density spectra for temperature at F_{bot}

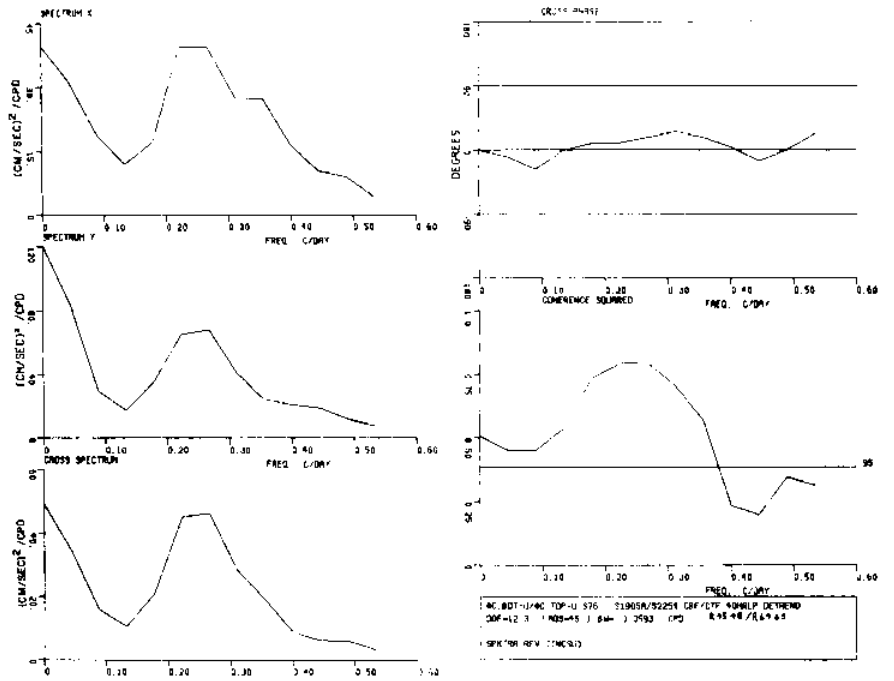

Figure 244 Spectra of low pass current velocity components from meter C_{bot} (u component and meter C_{top} (u component)

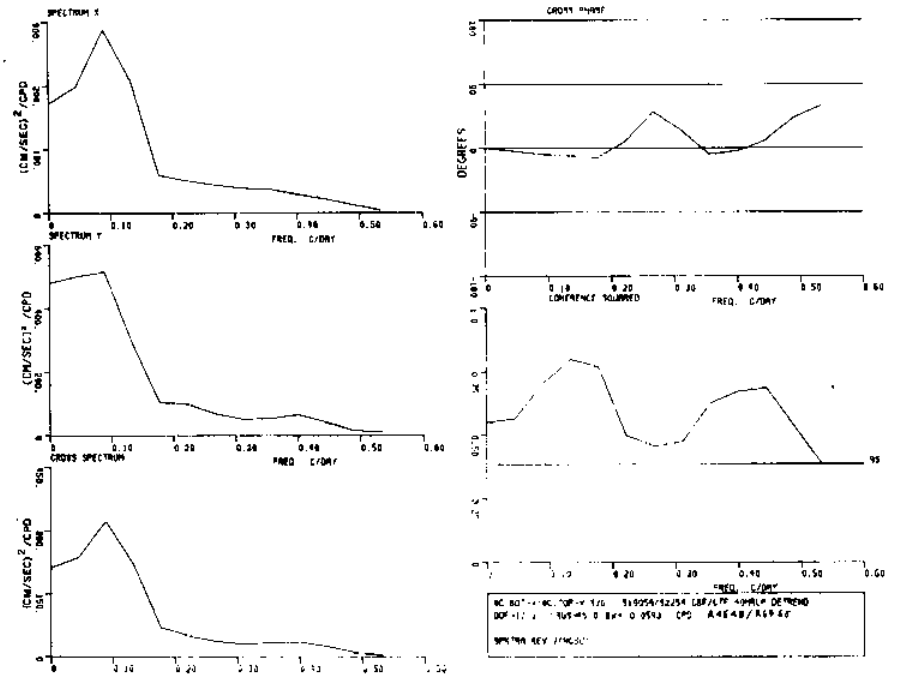

Figure 245 Spectra of low pass current velocity components from meter C_{bot} (v component) and meter C_{top} (v component)

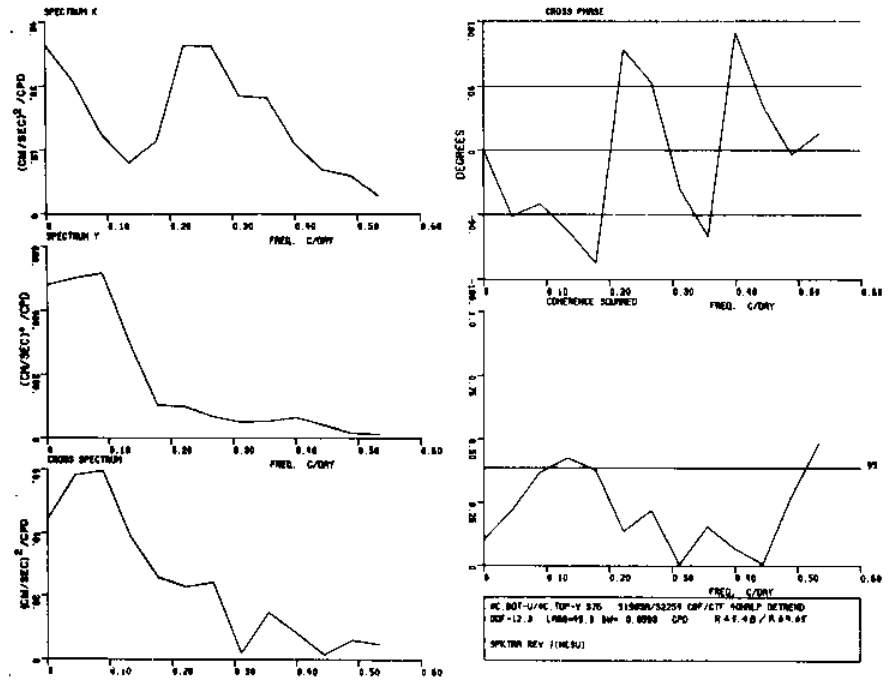

Figure 246 Spectra of low pass current velocity components from meter C_{bot} (u component) and meter C_{top} (v component)

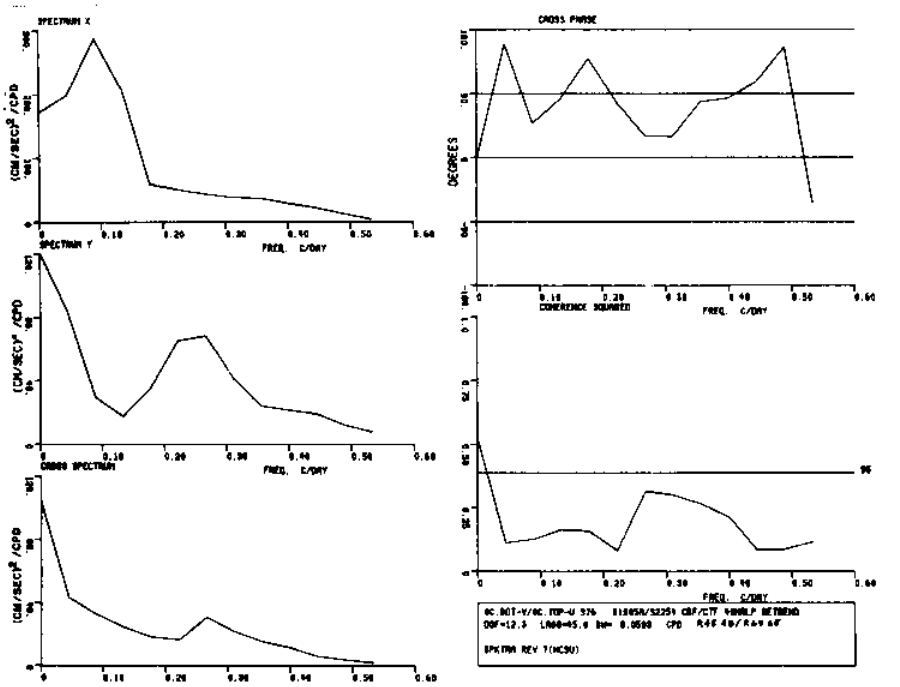

Figure 247 Spectra of low pass current velocity components from meter C_{bot} (v component) and meter C_{top} (u component)

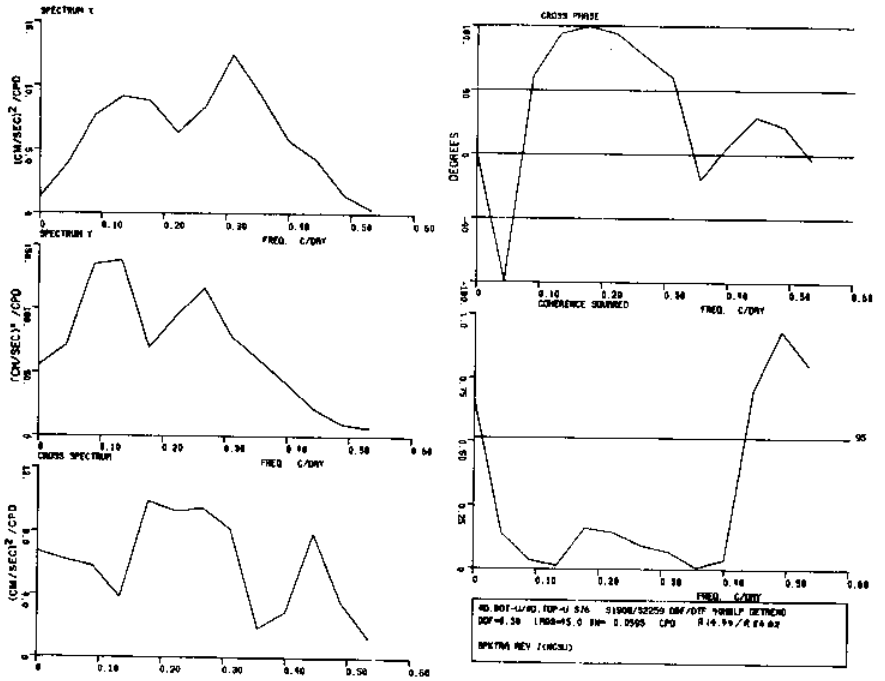

Figure 248 Spectra of low pass current velocity components from meter D_{bot} (u component) and meter D_{top} (u component)

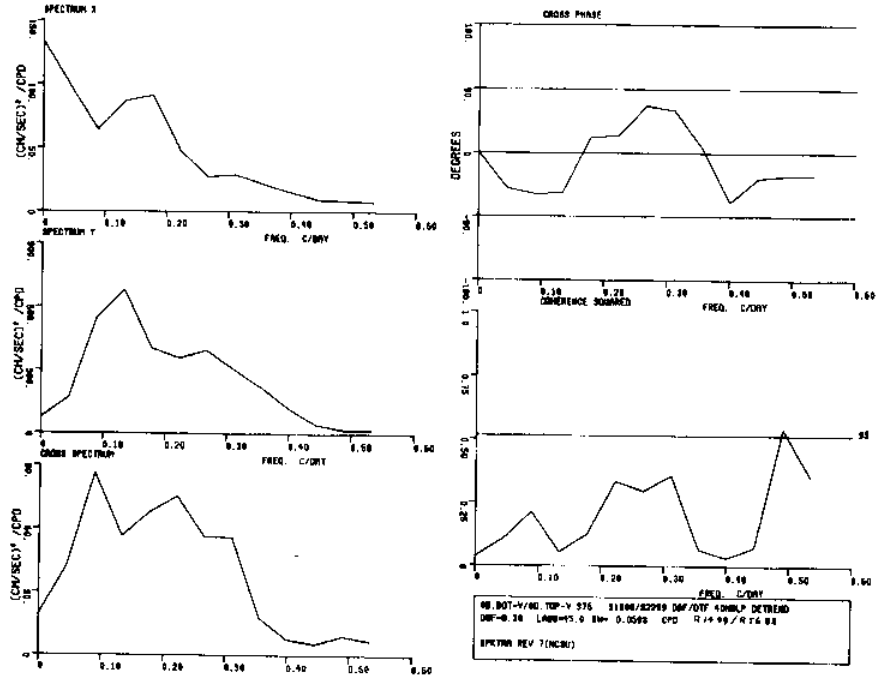

Figure 249 Spectra of low pass current velocity components from meter D_{bot} (v component) and meter D_{top} (v component)

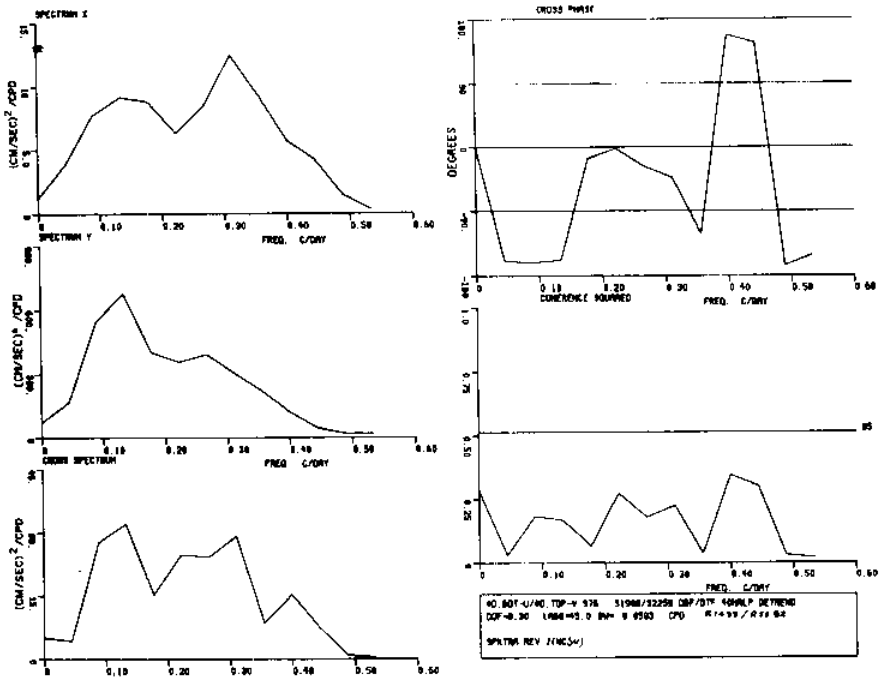

Figure 250 Spectra of low pass current velocity components from meter D_{bot} (u component) and meter D_{top} (v component)

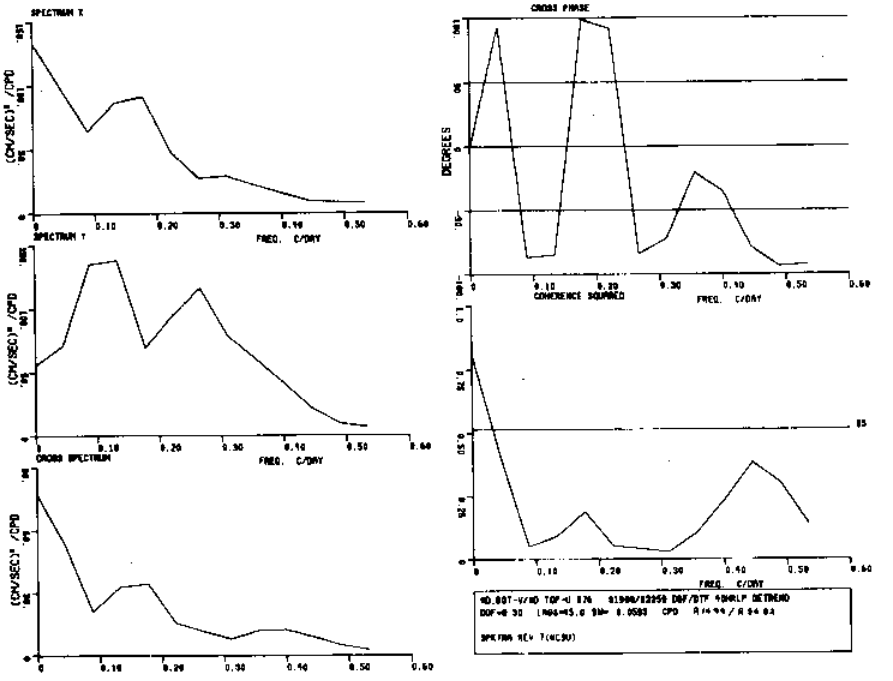

Figure 251 Spectra of low pass current velocity components from meter D_{bot} (v component) and meter D_{top} (u component)

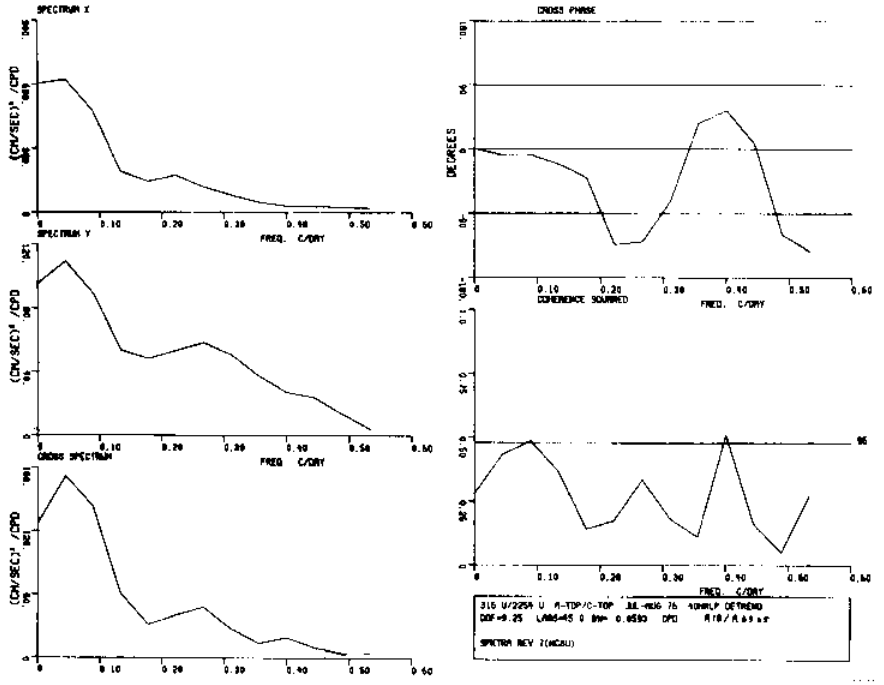

Figure 252 Spectra of low pass current velocity components from meter A_{top} (u component) and meter C_{top} (u component)

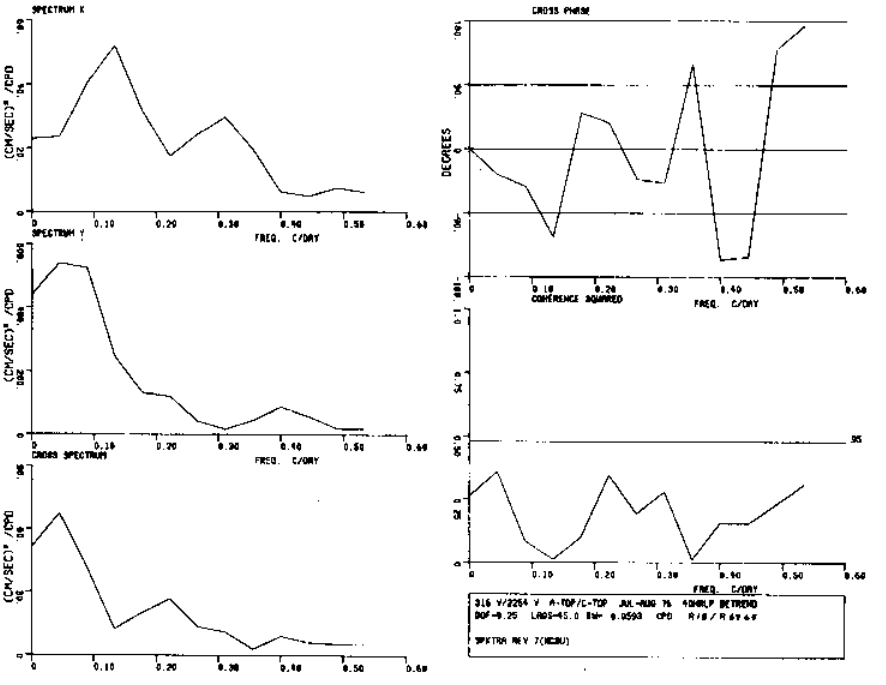

Figure 253 Spectra of low pass current velocity components from meter A_{top} (v component) and meter C_{top} (v component)

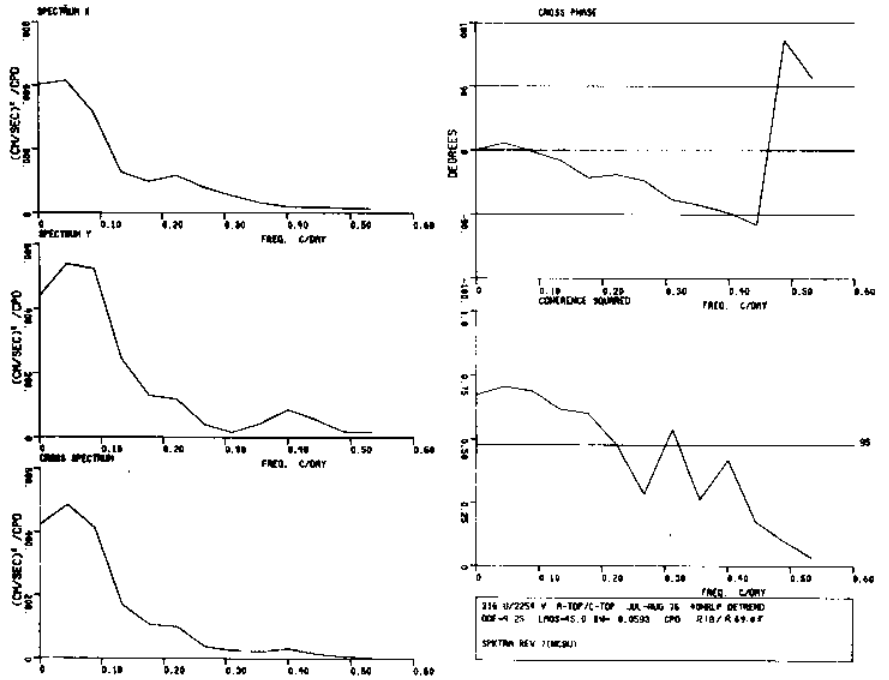

Figure 254 Spectra of low pass current velocity components from meter A_{top} (u component) and meter C_{top} (v component)

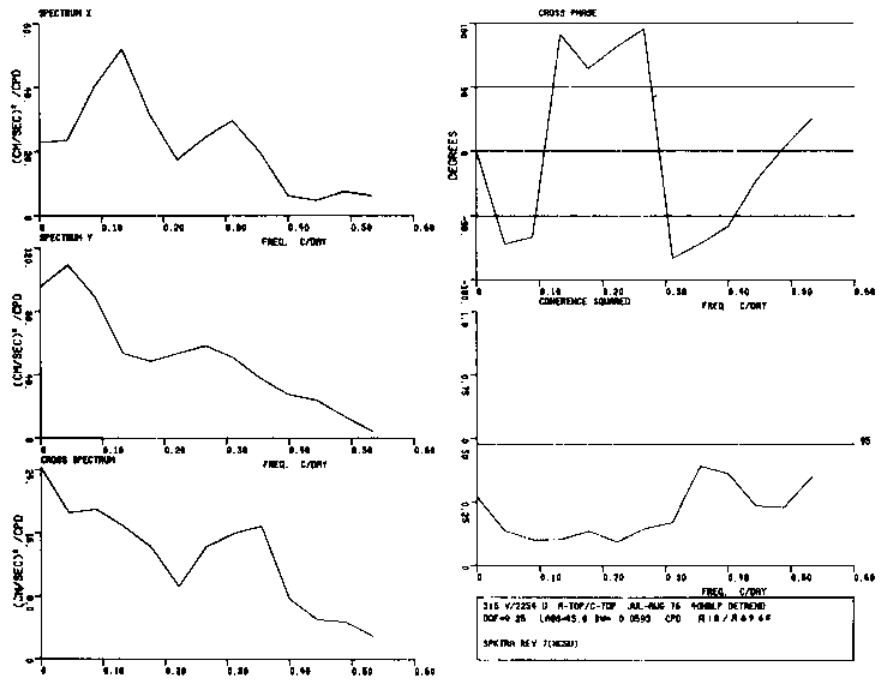

Figure 255 Spectra of low pass current velocity components from meter A_{top} (v component) and meter C_{top} (u component)

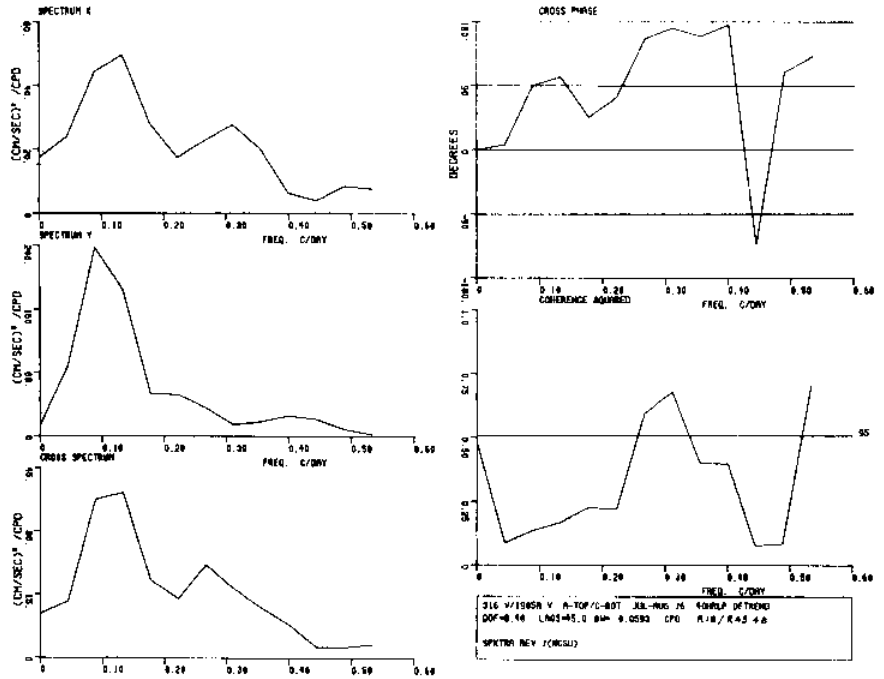

Figure 256 Spectra of low pass current velocity components from meter A_{top} (u component) and meter C_{bot} (u component)

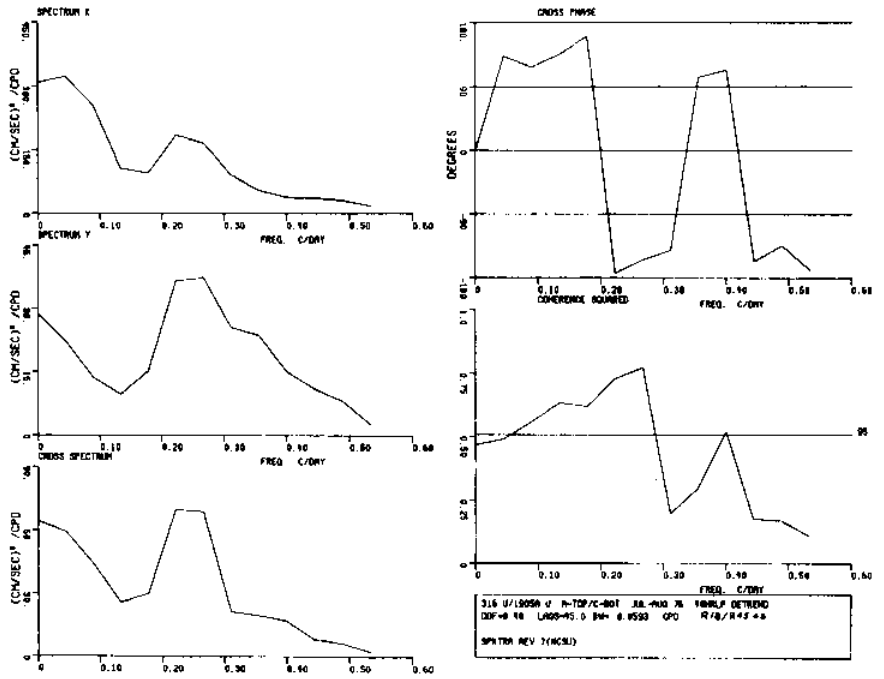

Figure 257 Spectra of low pass current velocity components from meter A_{top} (v component) and meter C_{bot} (v component)

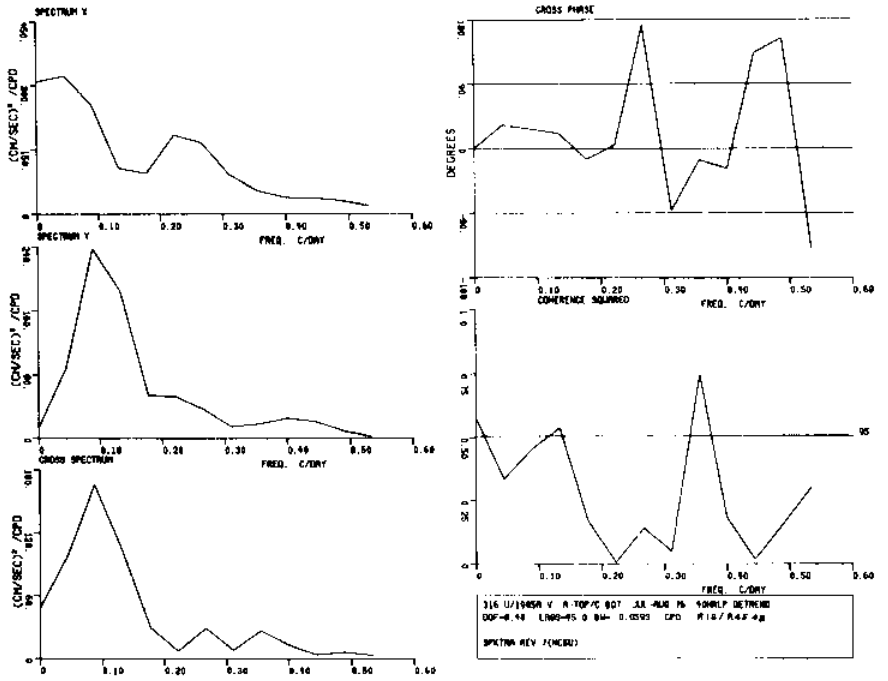

Figure 258 Spectra of low pass current velocity components from meter A_{top} (u component) and meter C_{bot} (v component)

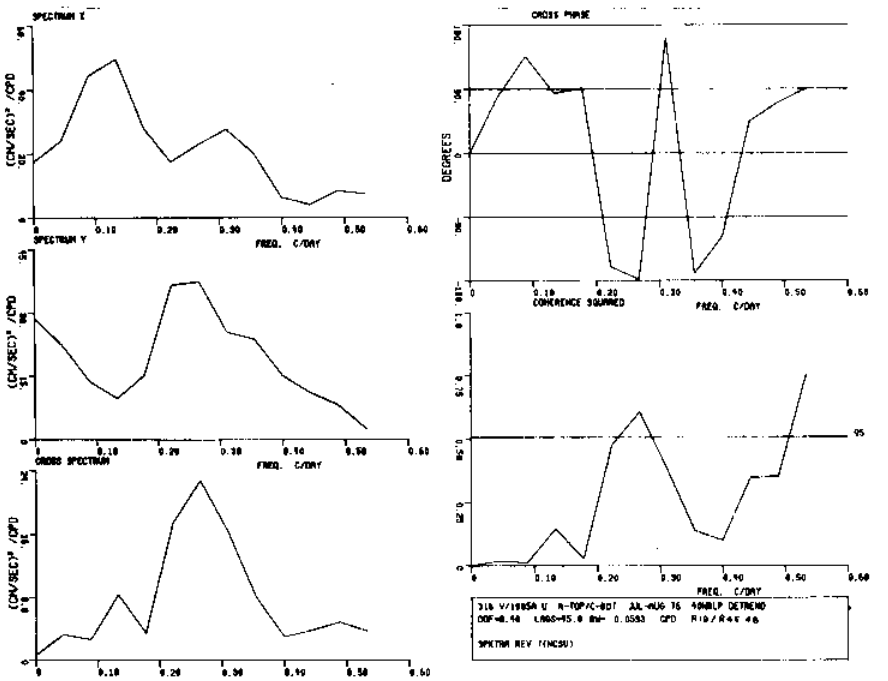

Figure 259 Spectra of low pass current velocity components from meter A_{top} (v component) and meter C_{bot} (u component)

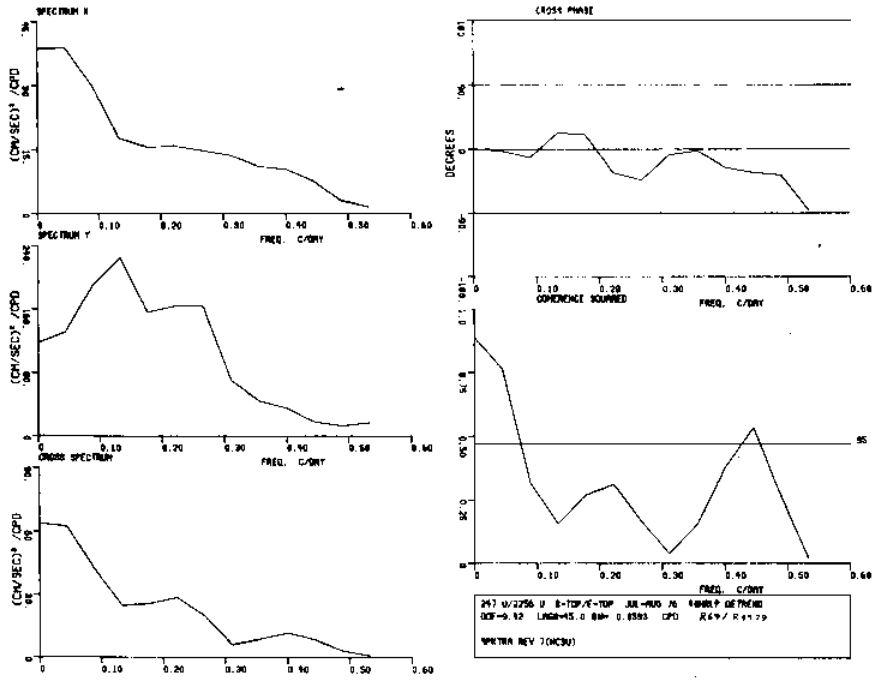

Figure 260 Spectra of low pass current velocity components from meter B_{top} (u component) and meter E_{top} (u component)

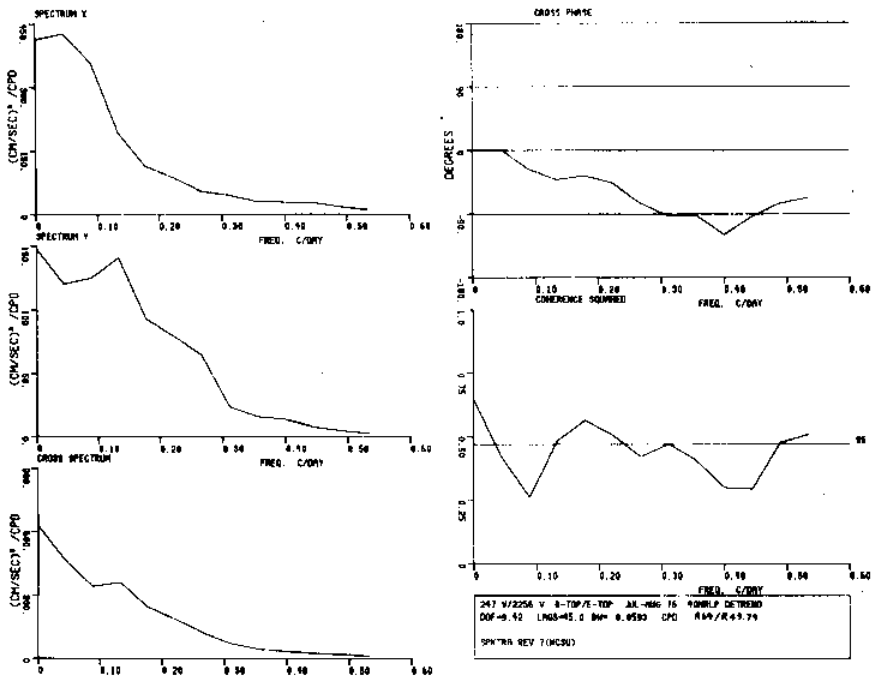

Figure 261 Spectra of low pass current velocity components from meter B_{top} (v component) and meter E_{top} (v component)

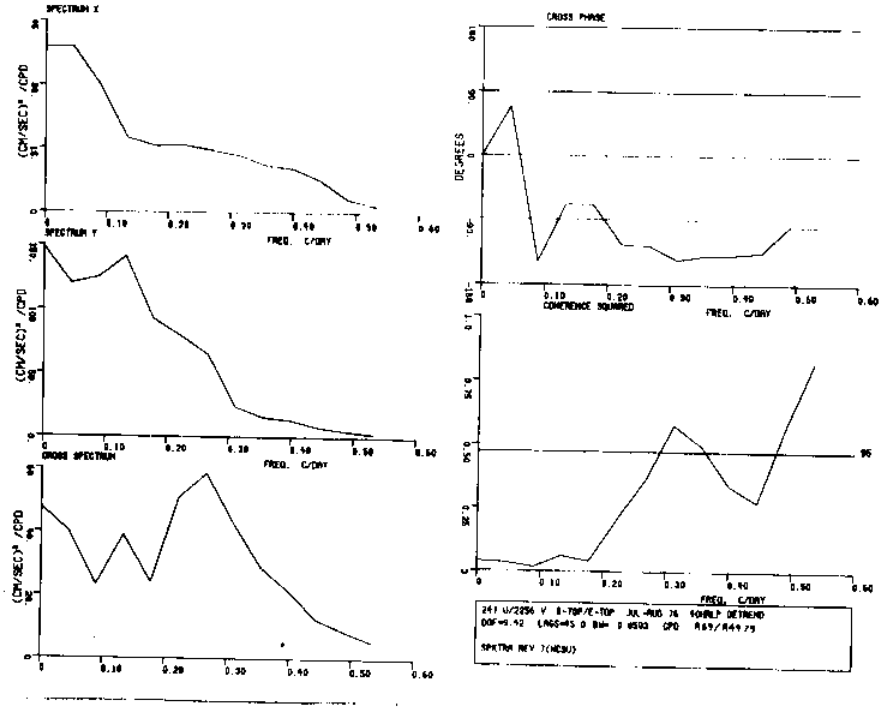

Figure 262 Spectra of low pass current velocity components from meter B_{top} (u component) and meter E_{top} (v component)

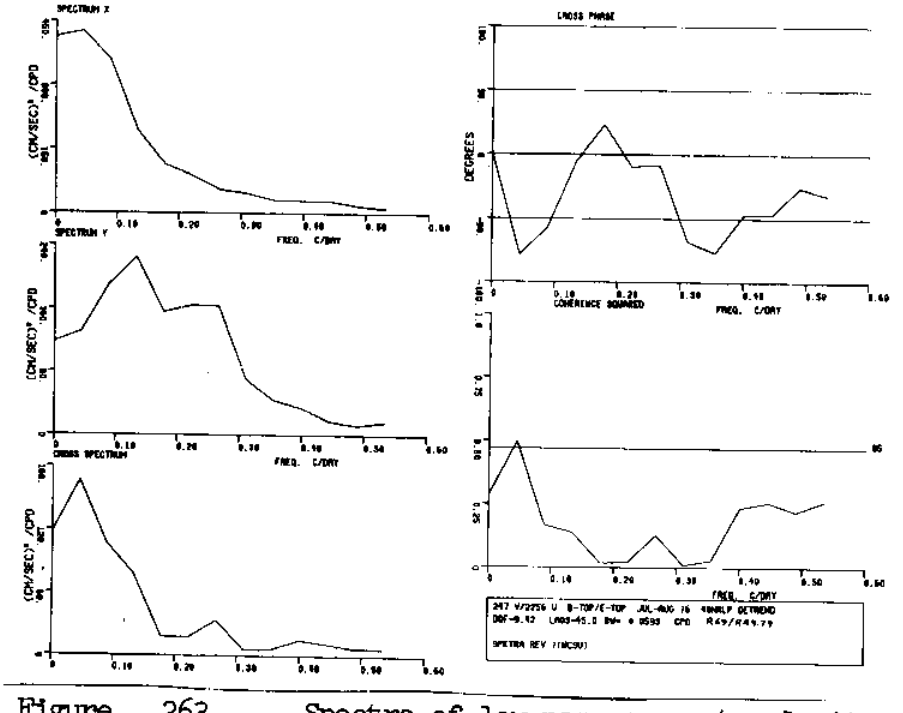

Figure 263 Spectra of low pass current velocity components from meter B_{top} (v component) and meter E_{top} (u component)

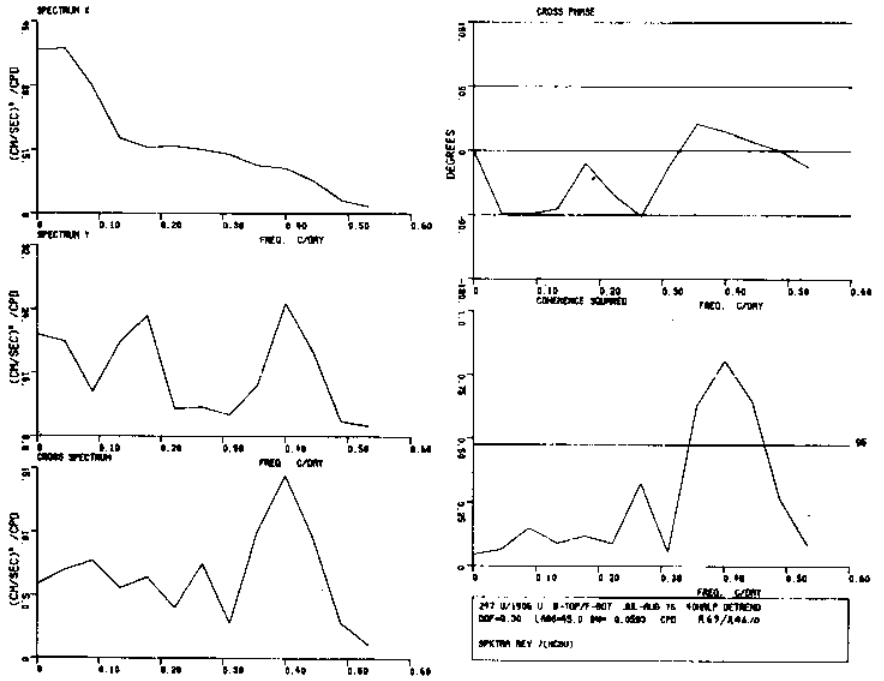

Figure 264 Spectra of low pass current velocity components from meter B_{top} (u component) and meter F_{bot} (u component)

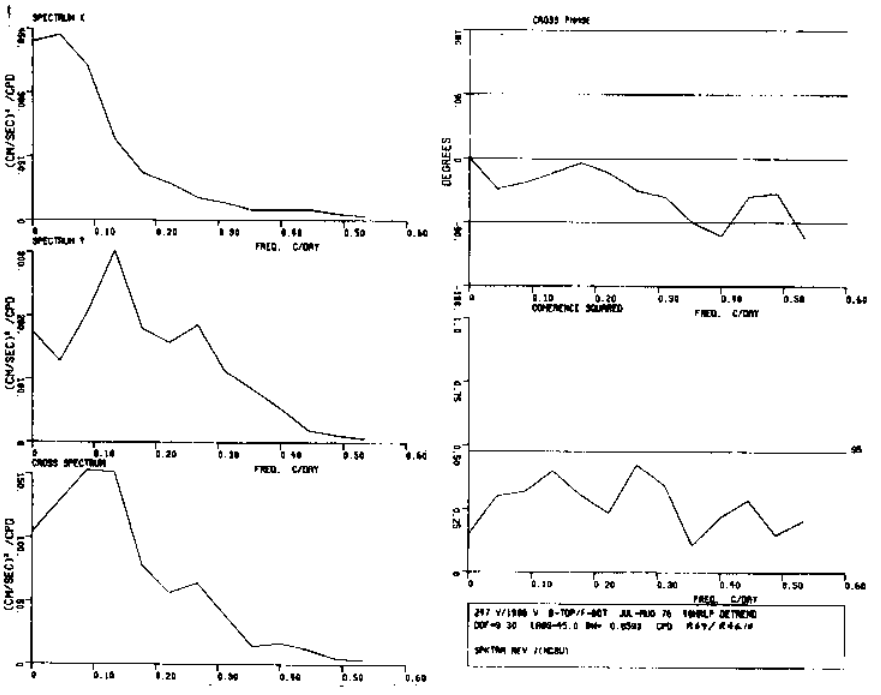

Figure 265 Spectra of low pass current velocity components from meter B_{top} (v component) and meter F_{bot} (v component)

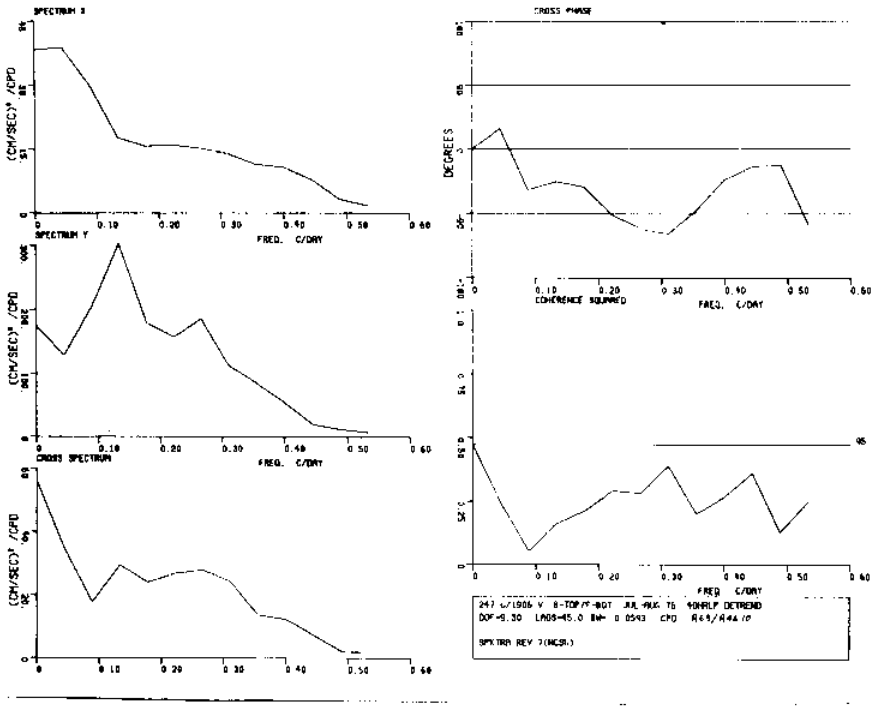

Figure 266 Spectra of low pass current velocity components from meter B_{top} (u component) and meter F_{bot} (v component)

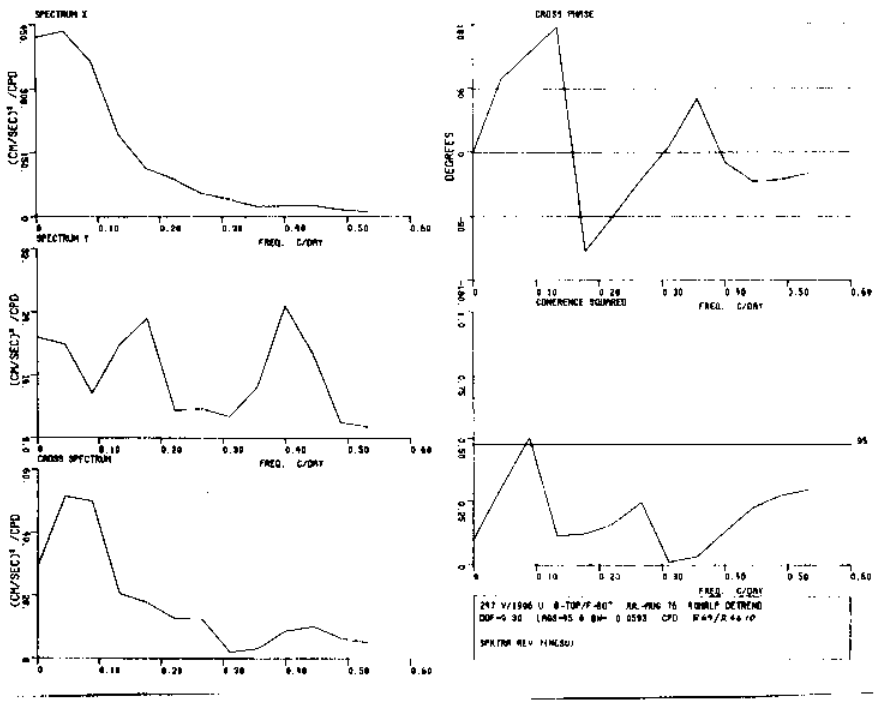

Figure 267 Spectra of low pass current velocity components from meter B_{top} (v component) and meter F_{bot} (u component)

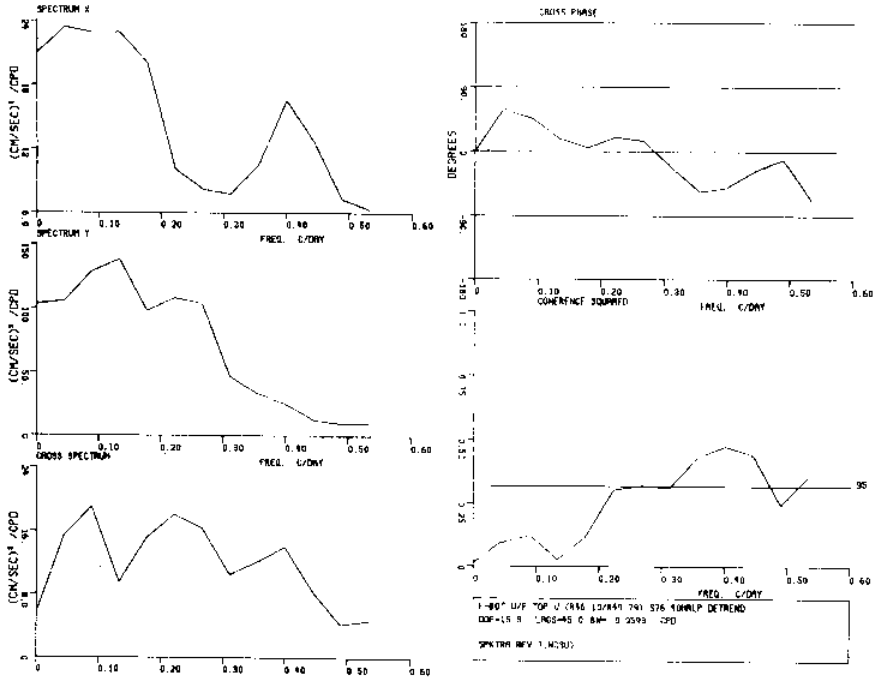

Figure 268 Spectra of low pass current velocity components from meter F_{bot} (u component) and meter E_{top} (u component)

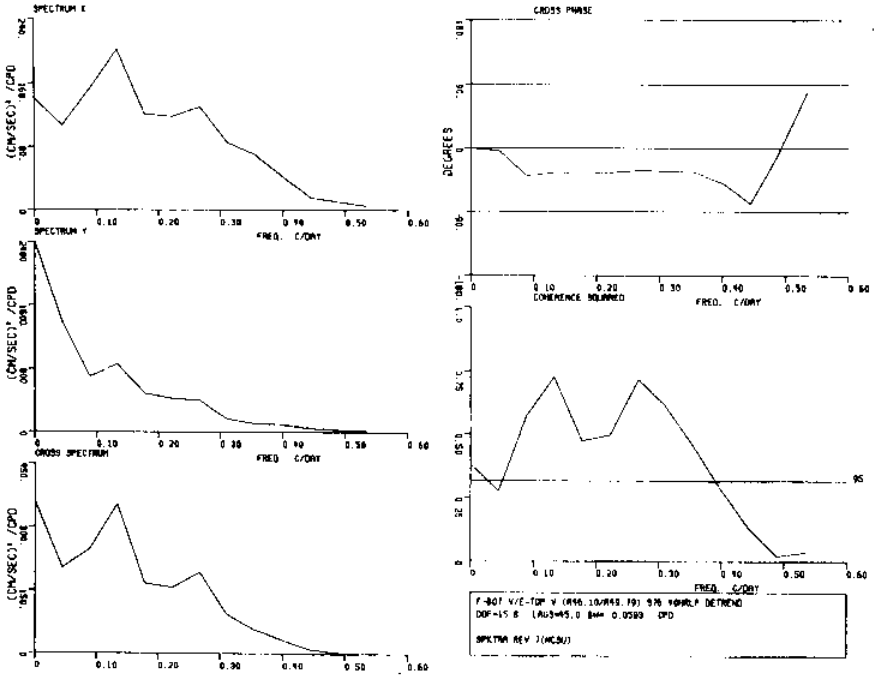

Figure 269 Spectra of low pass current velocity components from meter F_{bot} (v component) and meter E_{top} (v component)

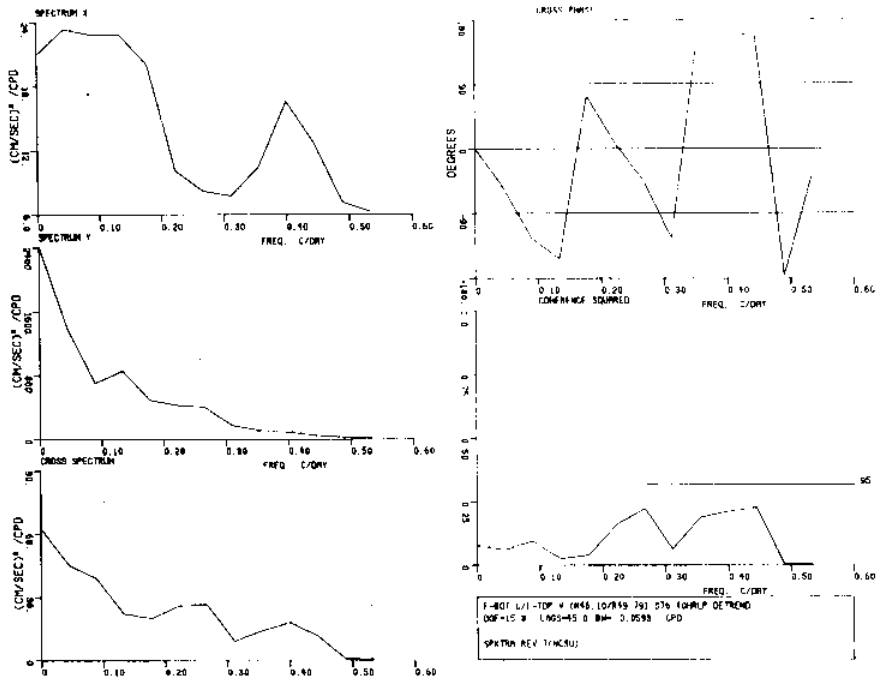

Figure 270 Spectra of low pass current velocity components from meter F_{bot} (u component) and meter E_{top} (v component)

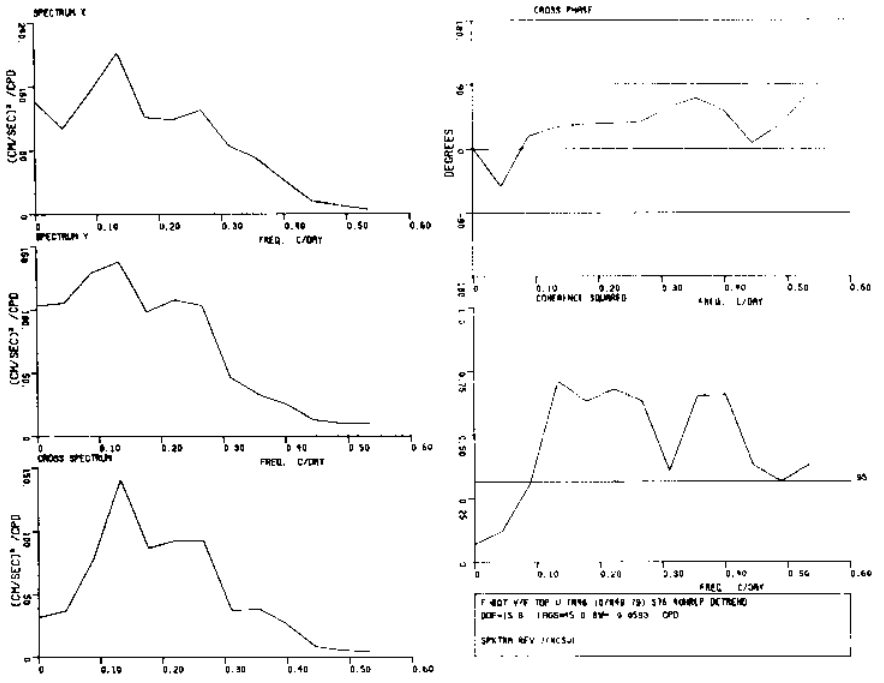

Figure 271 Spectra of low pass current velocity components from meter F_{bot} (v component) and meter E_{top} (u component)

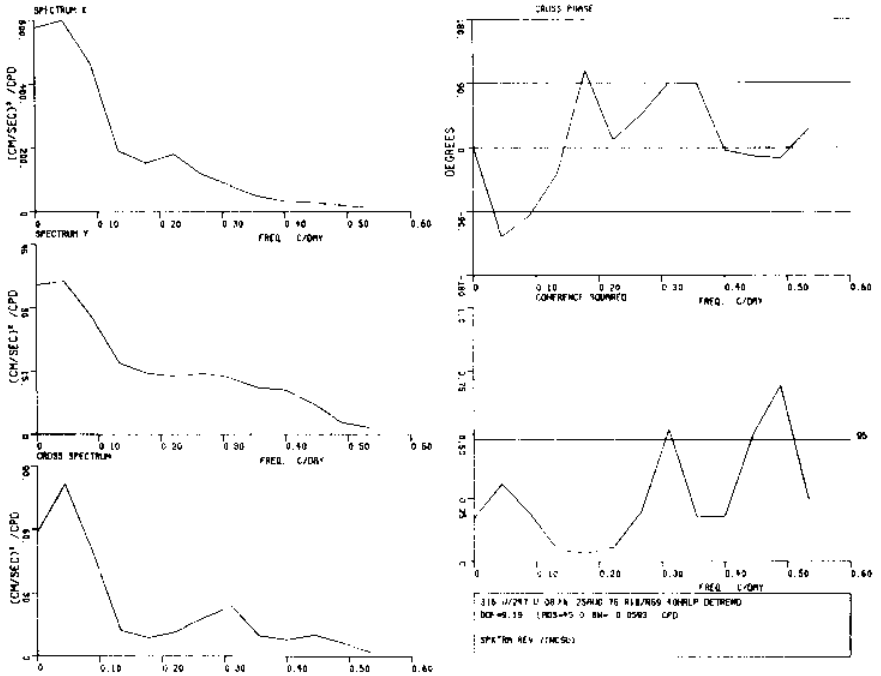

Figure 272 Spectra of low pass current velocity components from meter A_{top} (u component) and meter B_{top} (u component)

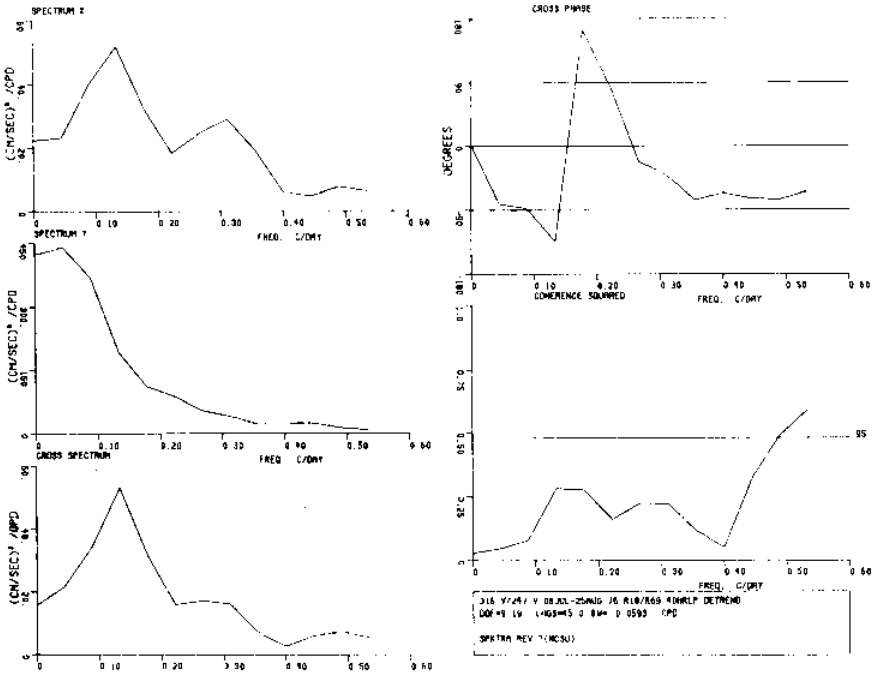

Figure 273 Spectra of low pass current velocity components from meter A_{top} (v component) and meter B_{top} (v component)

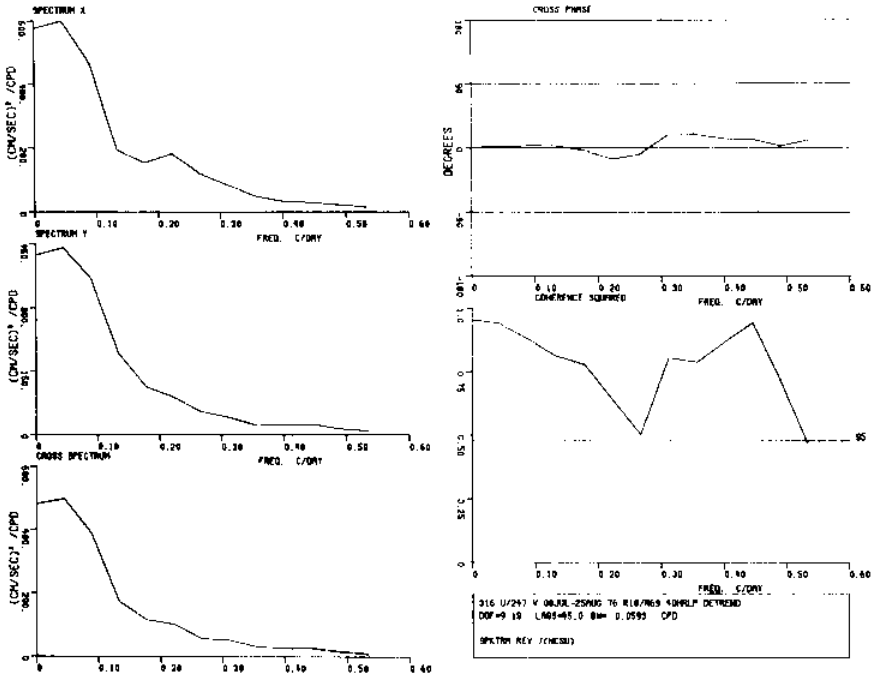

Figure 274 Spectra of low pass current velocity components from meter A_{top} (u component) and meter B_{top} (v component)

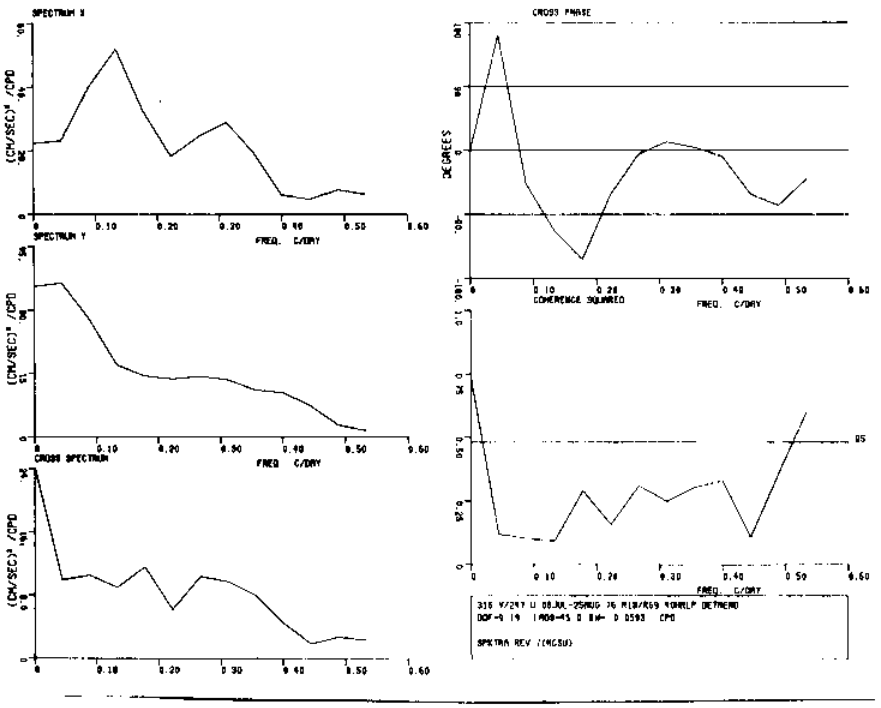

Figure 275 Spectra of low pass current velocity components from meter A_{top} (v component) and meter B_{top} (u component)

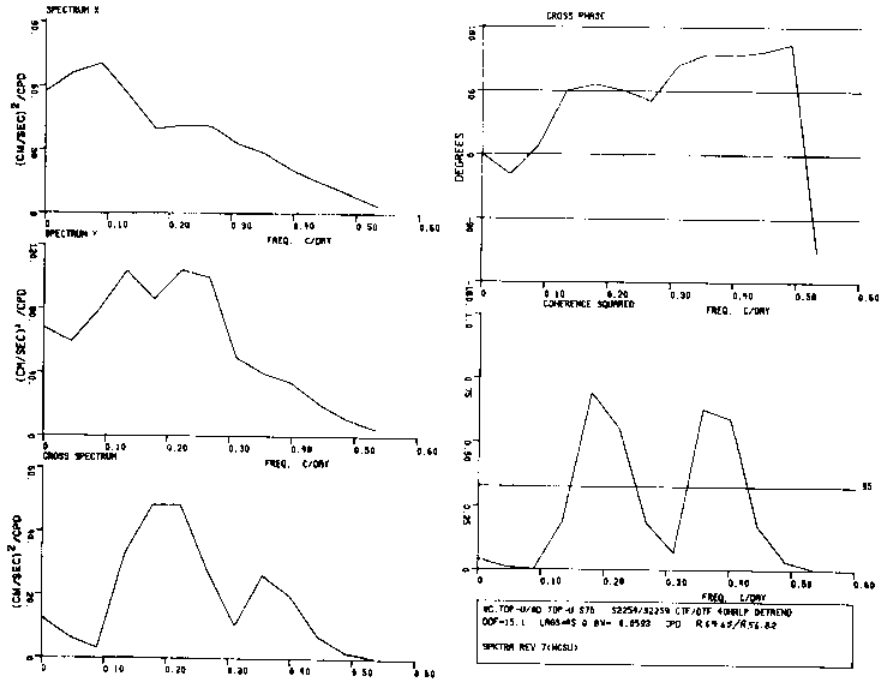

Figure 276 Spectra of low pass current velocity components from meter C_{top} (u component) and meter D_{top} (u component)

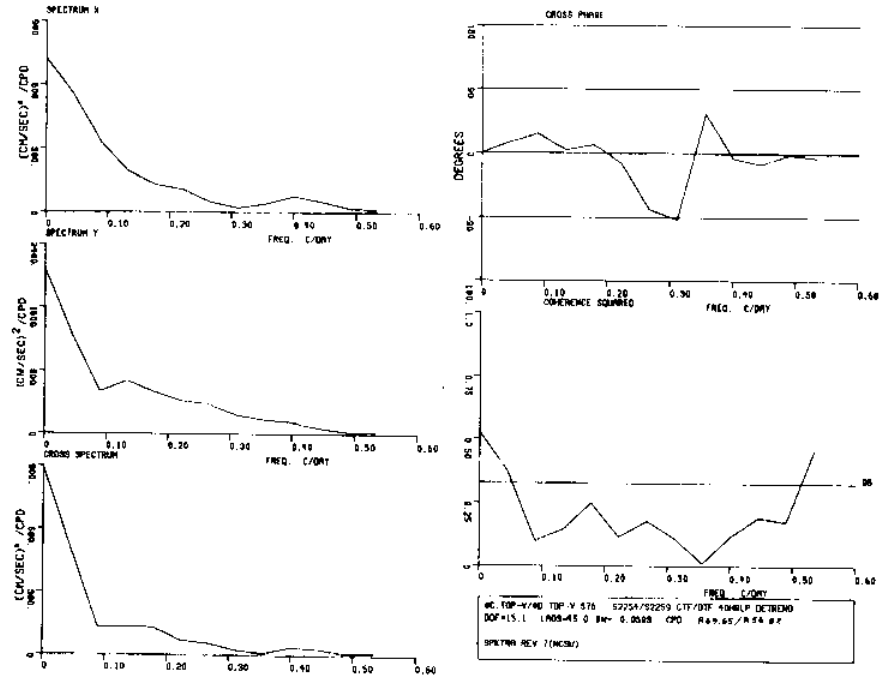

Figure 277 Spectra of low pass current velocity components from meter C_{top} (v component) and meter D_{top} (v component)

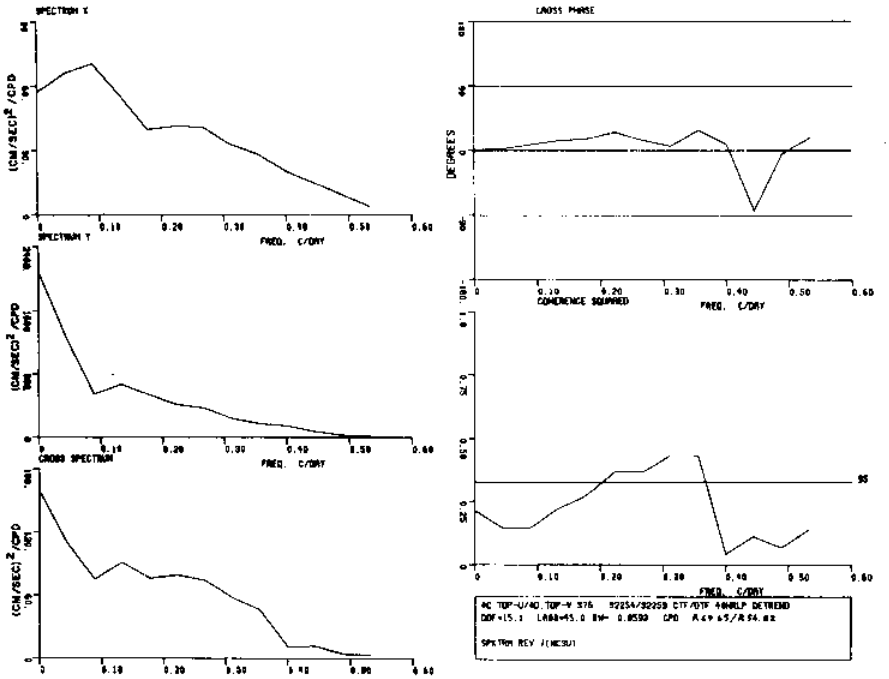

Figure 278 Spectra of low pass current velocity components from meter C_{top} (u component) and meter D_{top} (v component)

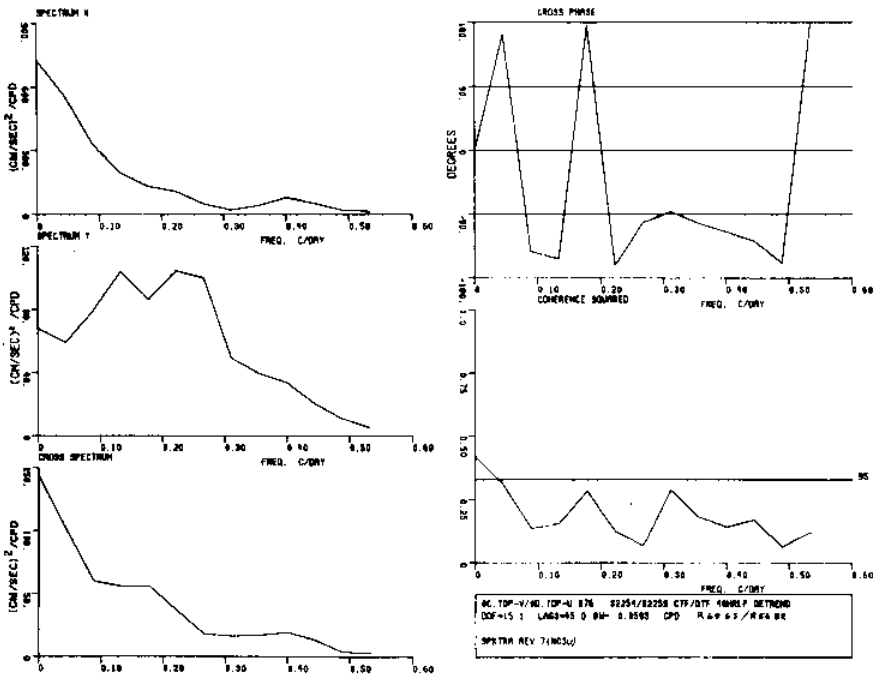

Figure 279 Spectra of low pass current velocity components from meter C_{top} (v component) and meter D_{top} (u component)

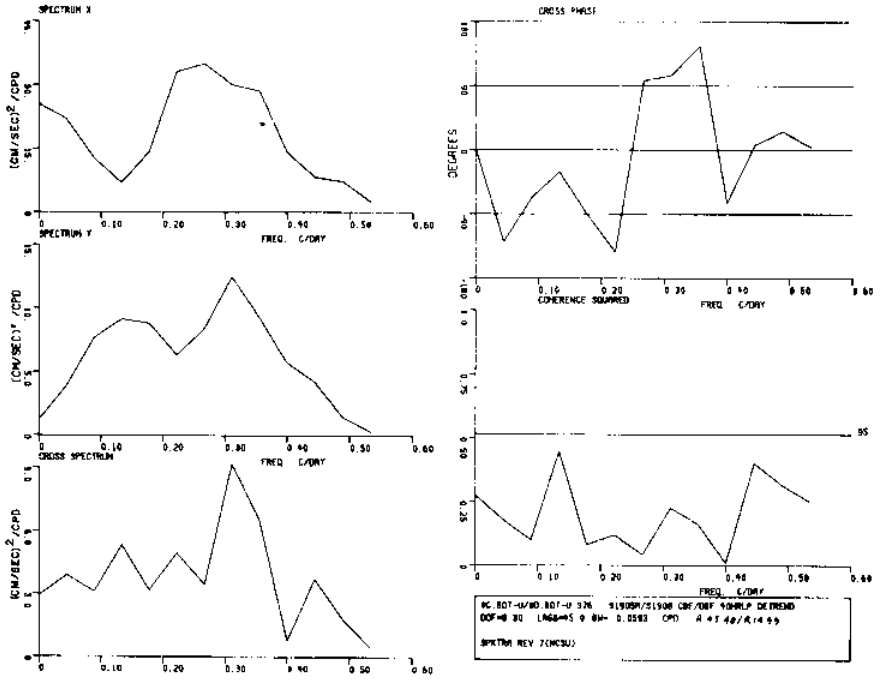

Figure 280 Spectra of low pass current velocity components from meter C_{bot} (u component) and meter D_{bot} (u component)

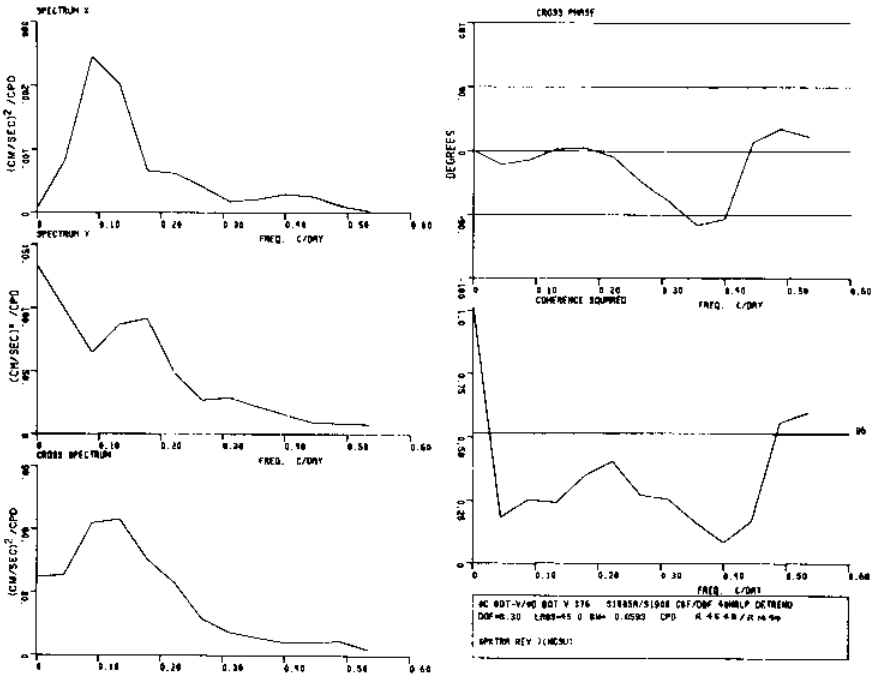

Figure 281 Spectra of low pass current velocity components from meter C_{bot} (v component) and meter D_{bot} (v component)

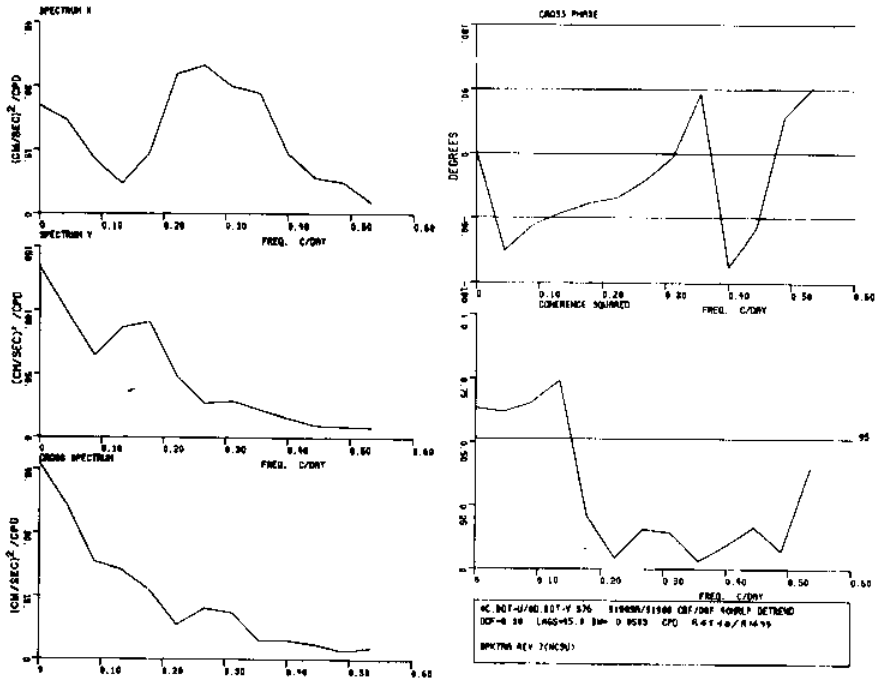

Figure 282 Spectra of low pass current velocity components from meter C_{bot} (u component) and met and meter D_{bot} (v component)

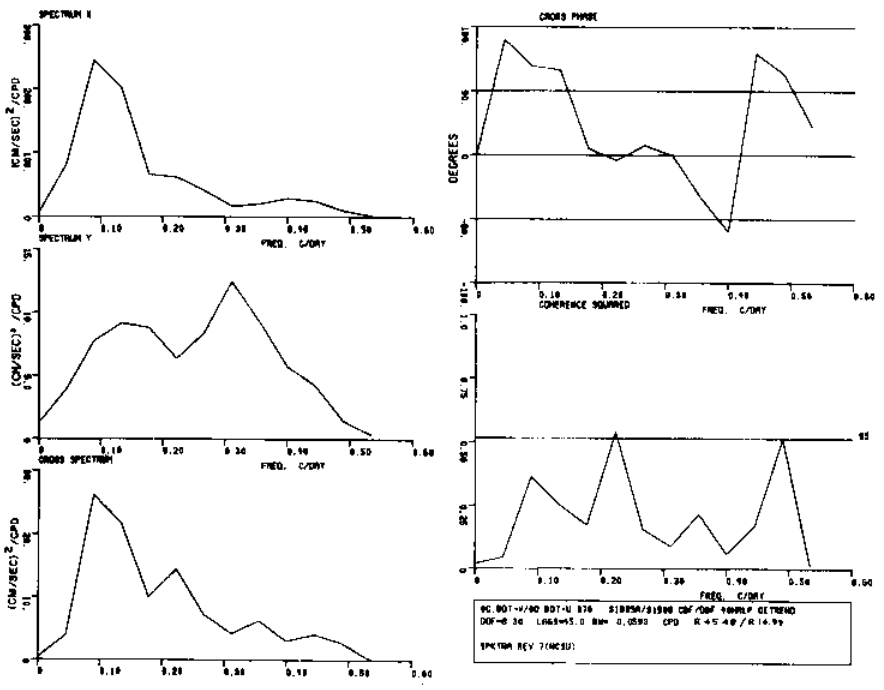

Figure 283 Spectra of low pass current velocity components from meter C_{bot} (v component) and meter D_{bot} (u component)

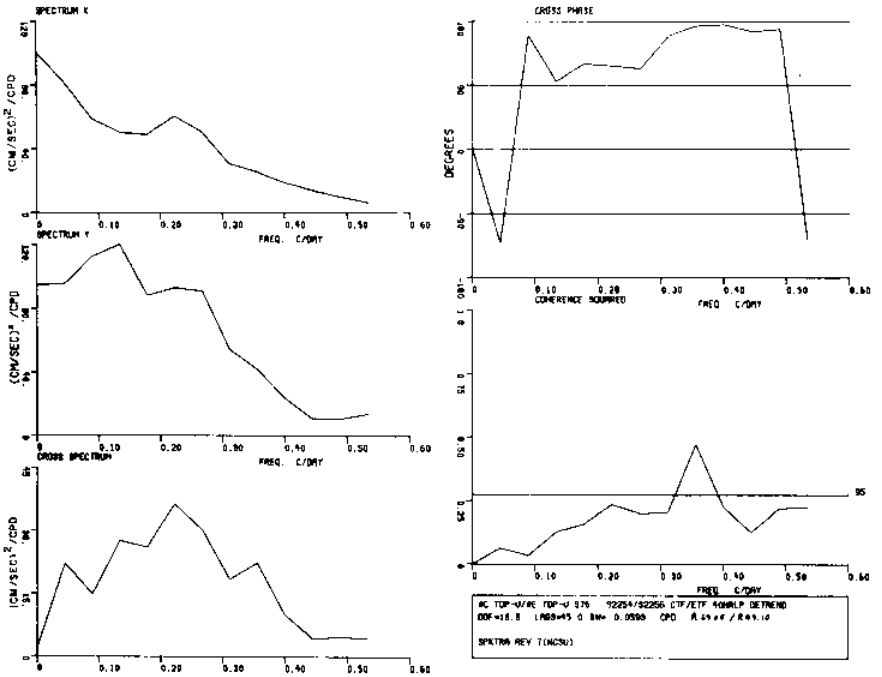

Figure 284 Spectra of low pass current velocity components from meter C_{top} (u component) and meter E_{top} (u component)

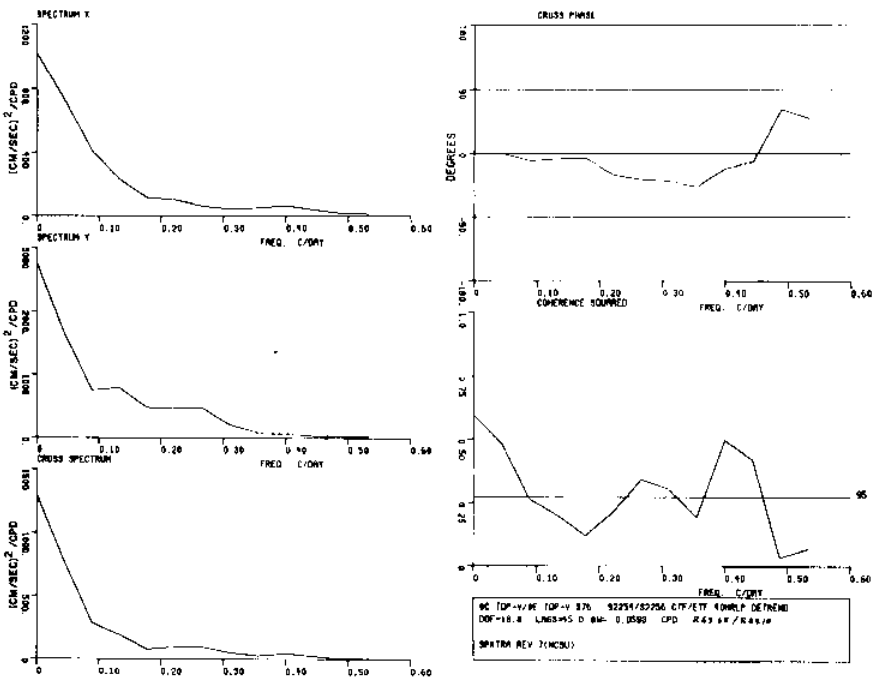

Figure 285 Spectra of low pass current velocity components from meter C_{top} (v component) and meter E_{top} (v component)

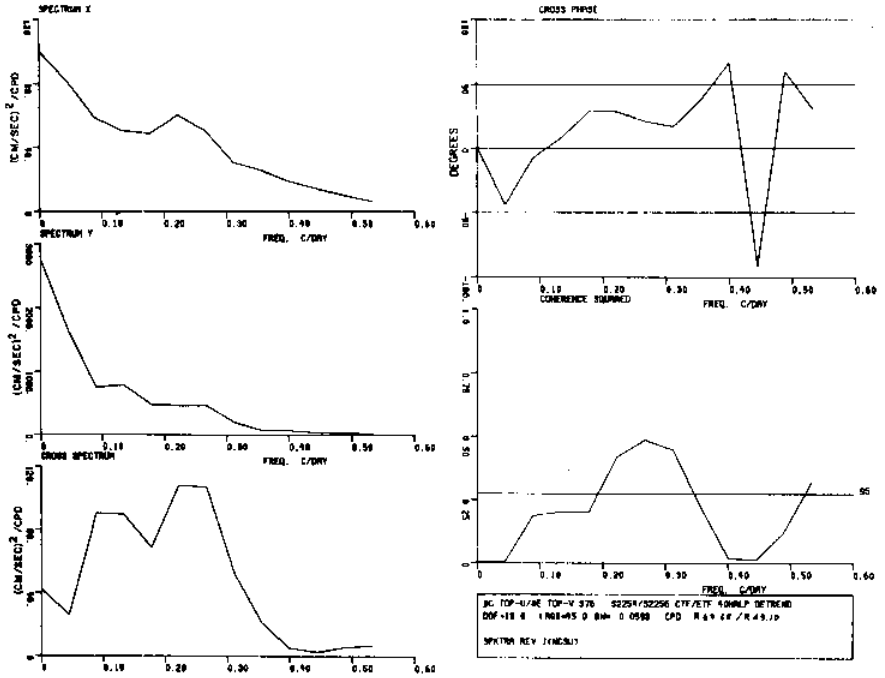

Figure 286 Spectra of low pass current velocity components from meter C_{top} (u component) and meter E_{top} (v component)

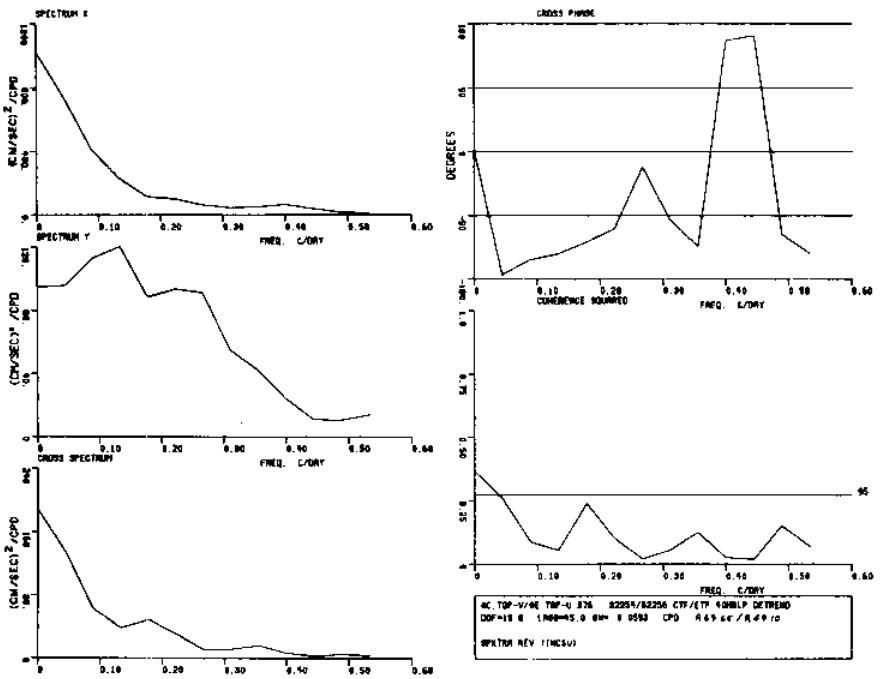

Figure 287 Spectra of low pass current velocity components from meter C_{top} (v component) and meter E_{top} (u component)

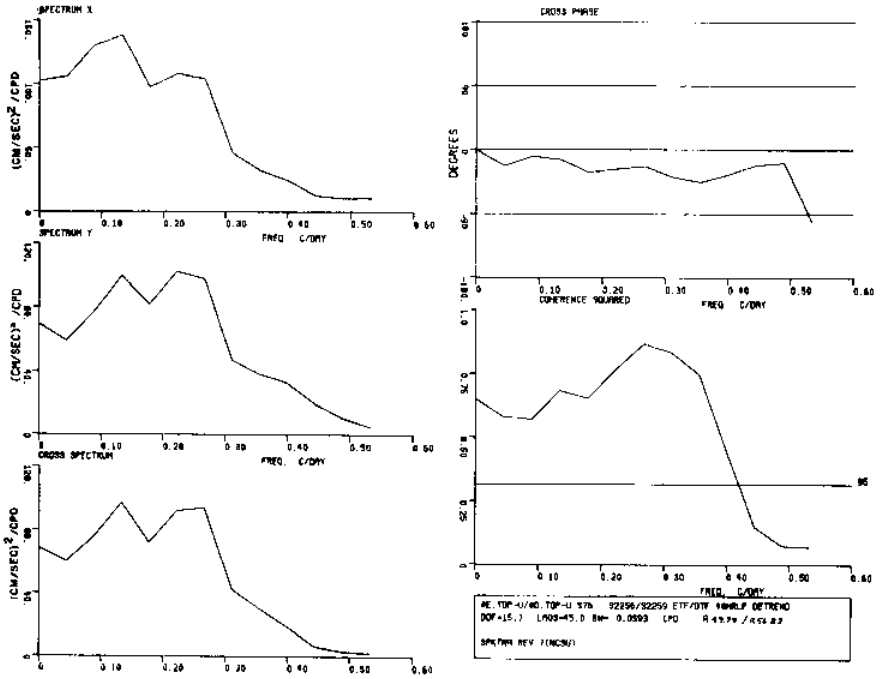

Figure 288 Spectra of low pass current velocity components from meter E_{top} (u component) and meter D_{top} (u component)

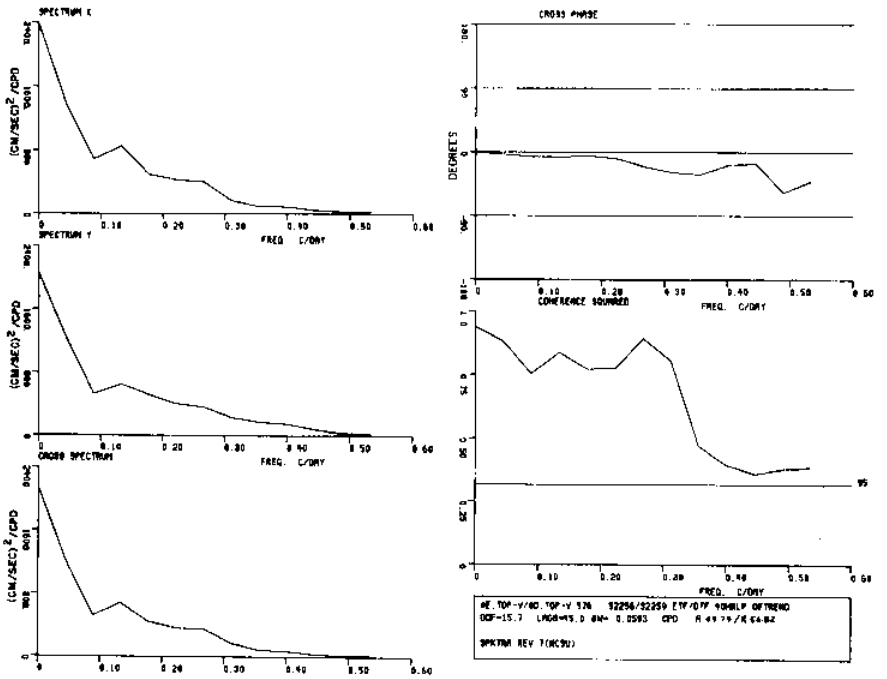

Figure 289 Spectra of low pass current velocity components from meter E_{top} (v component) and meter D_{top} (v component)

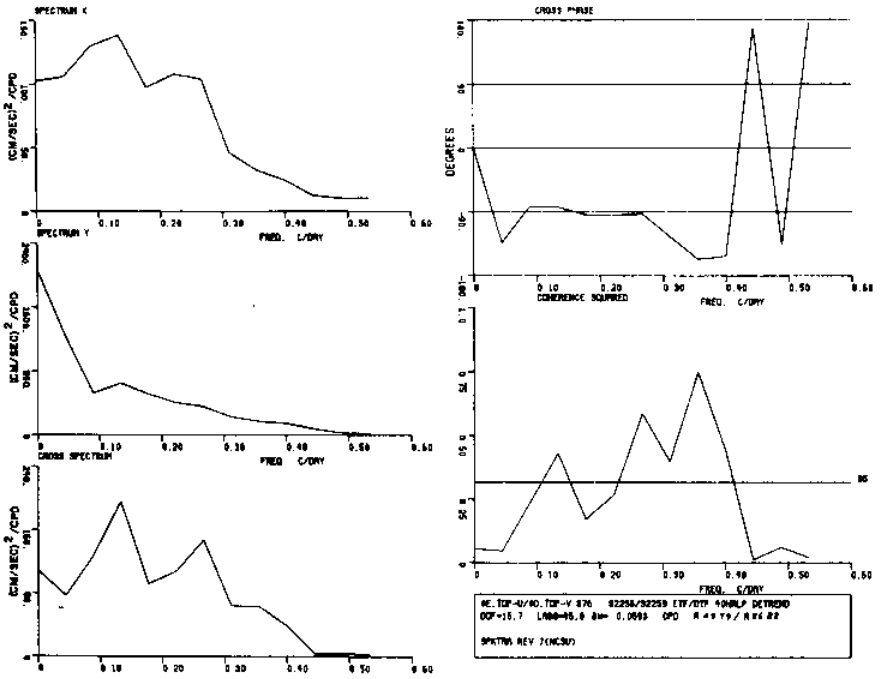

Figure 290 Spectra of low pass current velocity components from meter E_{top} (u component) and meter D_{top} (v component)

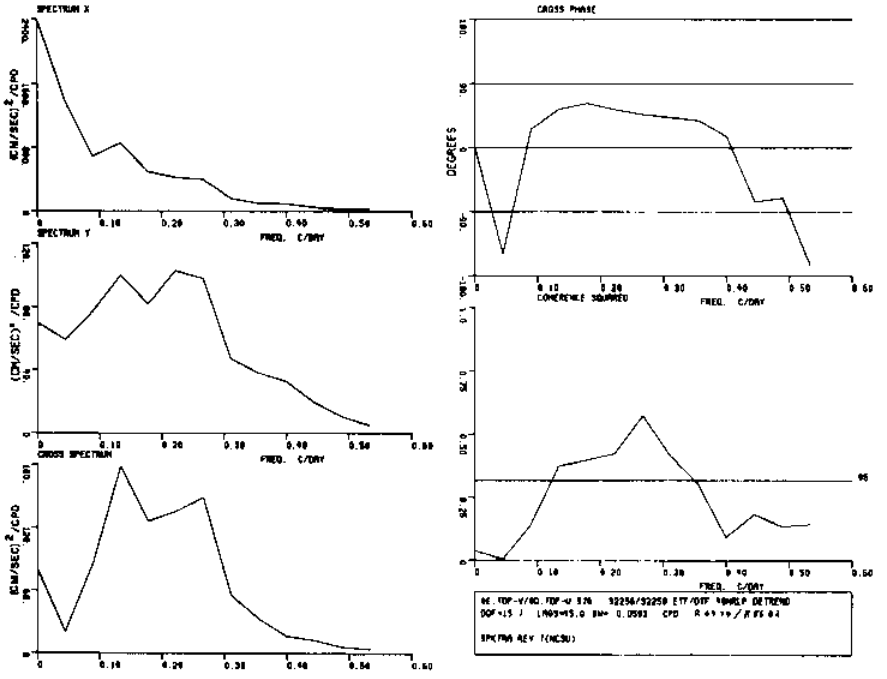

Figure 291 Spectra of low pass current velocity components from meter E_{top} (v component) and meter D_{top} (u component)

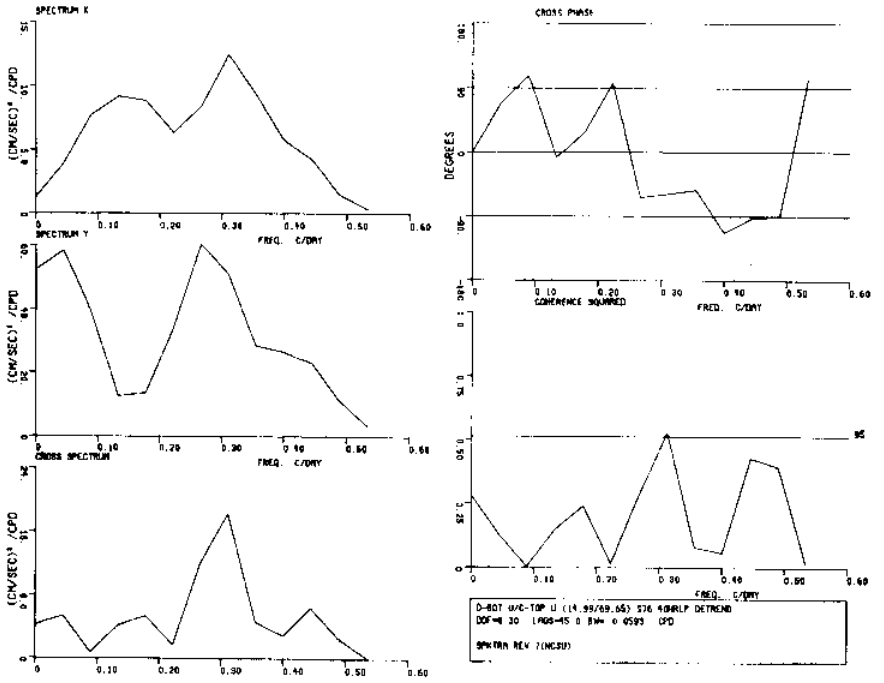

Figure 292 Spectra of low pass current velocity components from meter D_{bot} (u component) and meter C_{top} (u component)

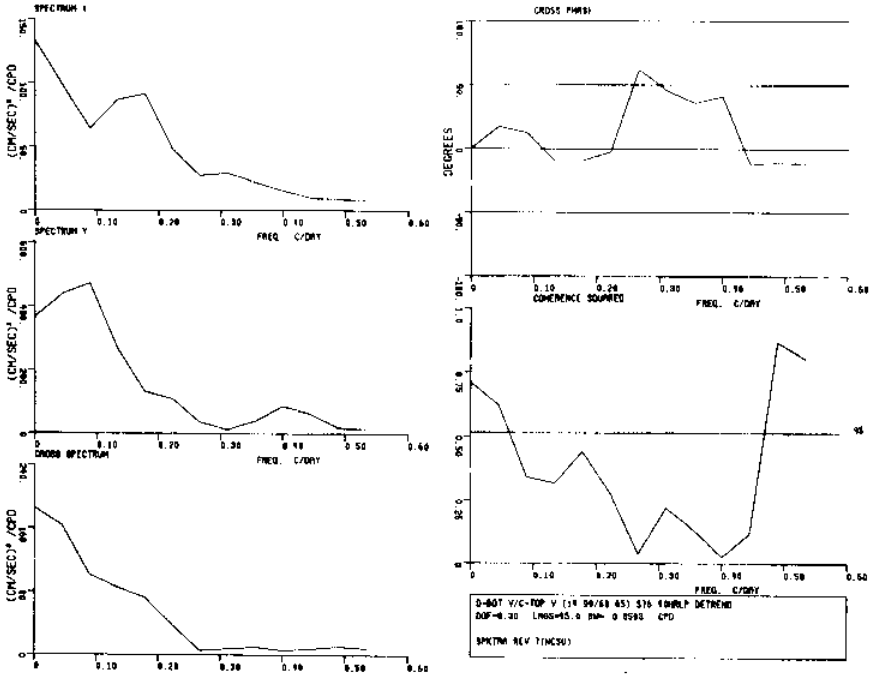

Figure 293 Spectra of low pass current velocity components from meter D_{bot} (v component) and meter C_{top} (v component)

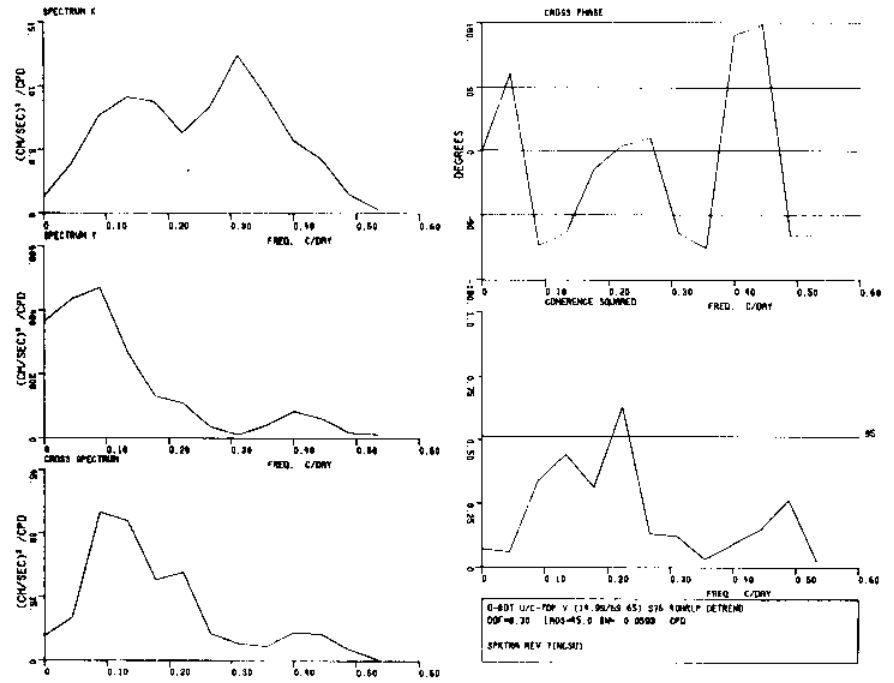

Figure 294 Spectra of low pass current velocity components from meter D_{bot} (u component) and meter C_{top} (v component)

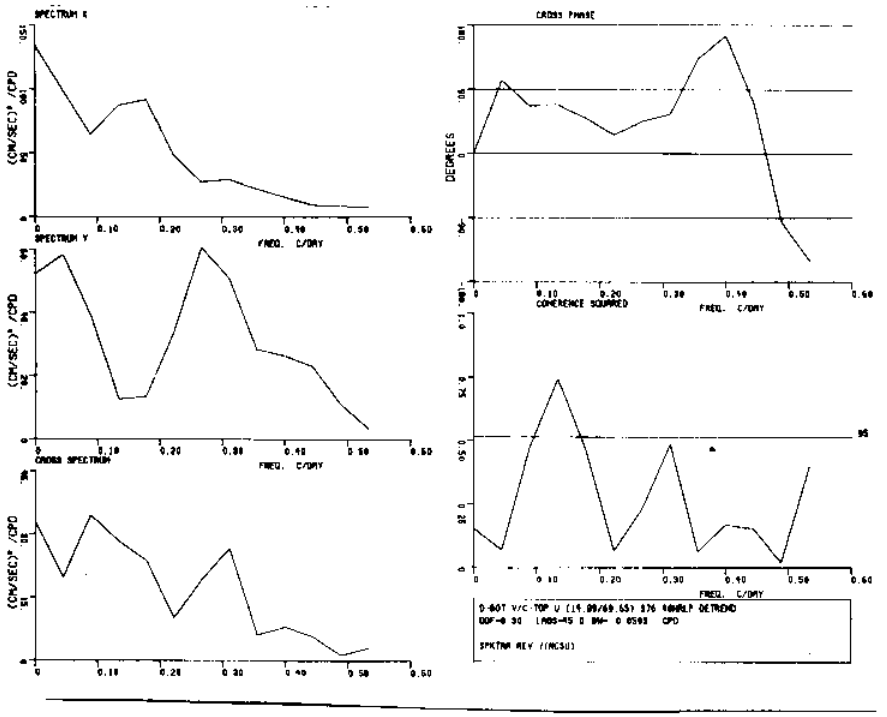

Figure 295 Spectra of low pass current velocity components from meter D_{bot} (v component) and meter C_{top} (u component)

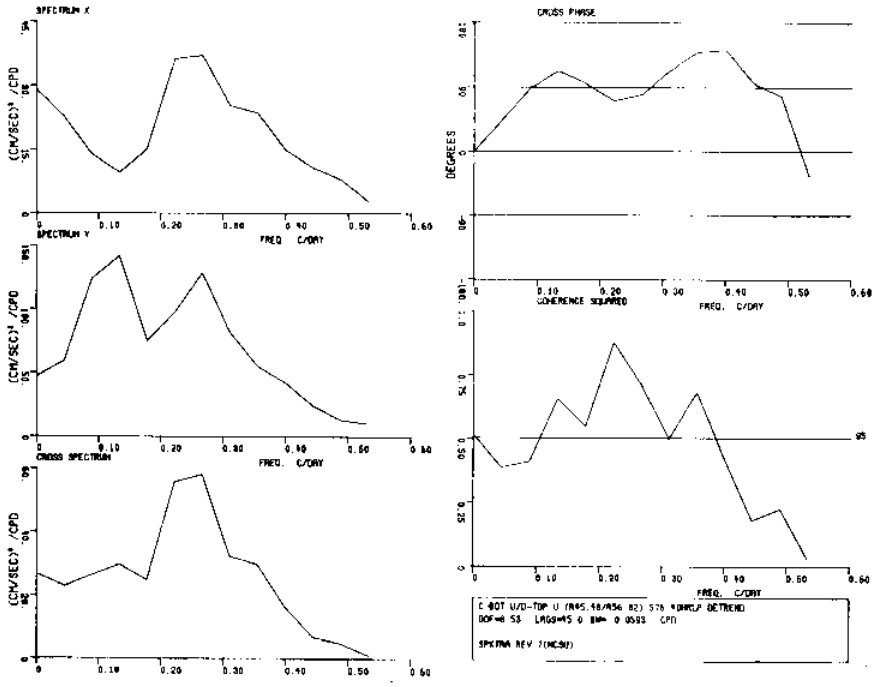

Figure 296 Spectra of low pass current velocity components from meter C_{bot} (u component) and meter D_{top} (u component)

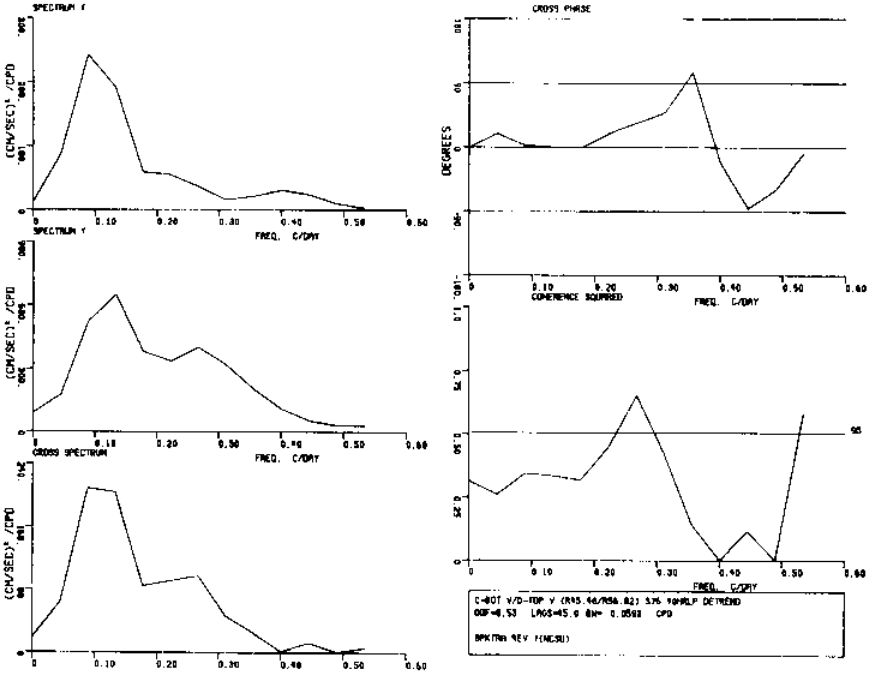

Figure 297 Spectra of low pass current velocity components from meter C_{bot} (v component) and meter D_{top} (v component)

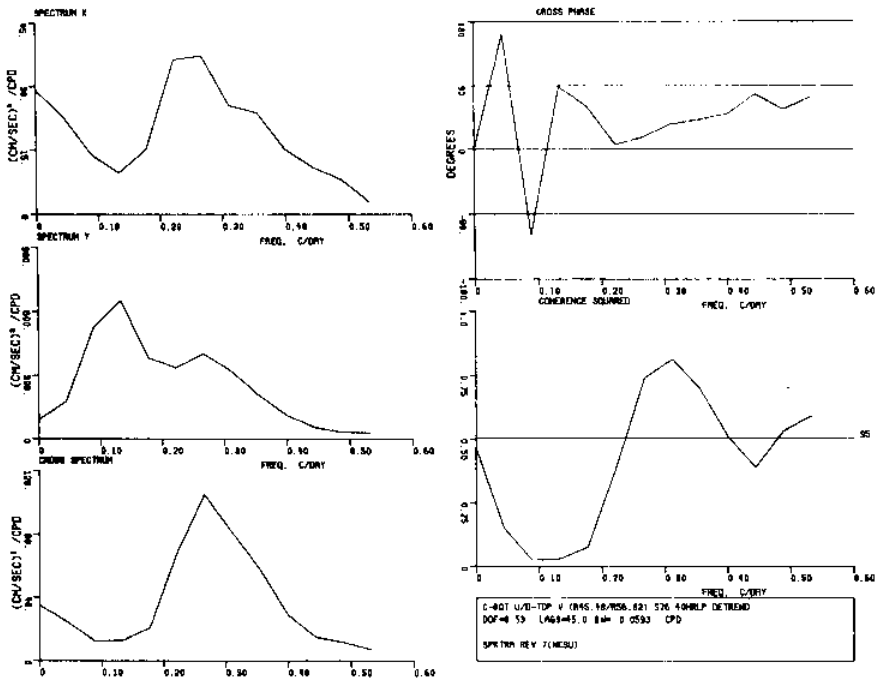

Figure 298 Spectra of low pass current velocity components from meter C_{bot} (u component) and meter D_{top} (v component)

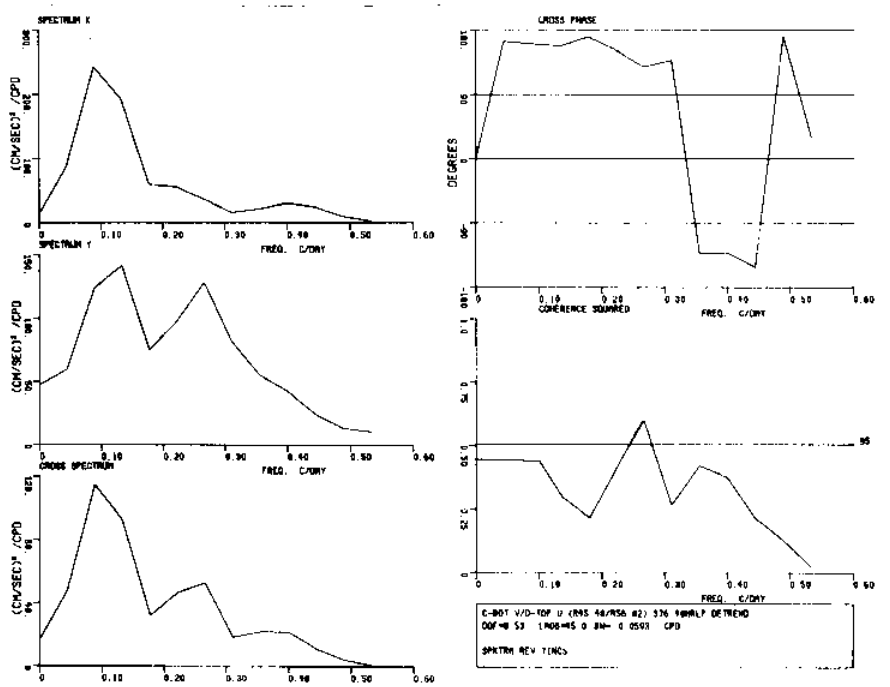

Figure 299 Spectra of low pass current velocity components from meter C_{bot} (v component) and meter D_{top} (u component)

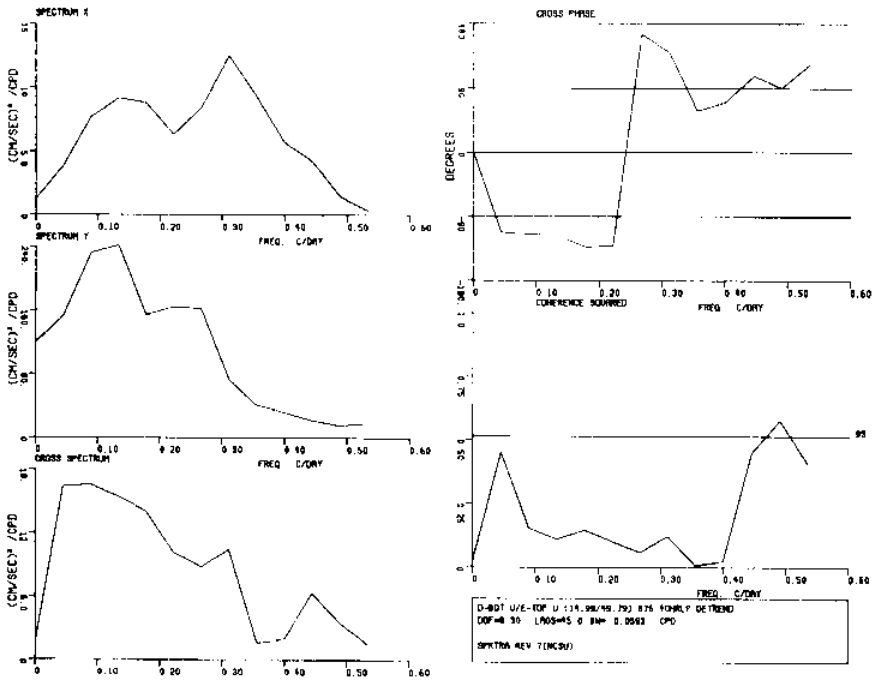

Figure 300 Spectra of low pass current velocity components from meter D_{bot} (u component) and meter E_{top} (u component)

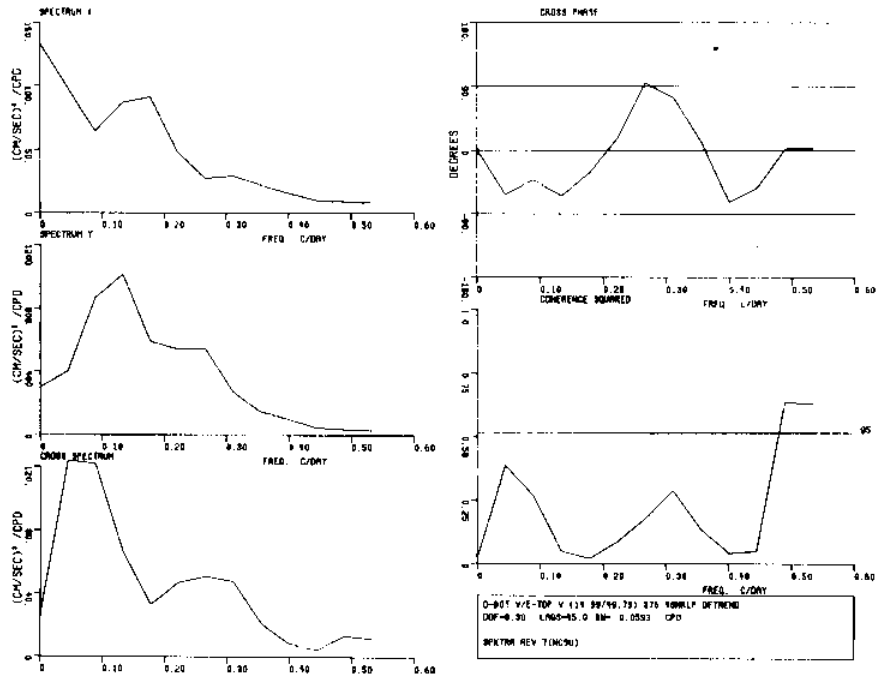

Figure 301 Spectra of low pass current velocity components from meter D_{bot} (v component) and meter E_{top} (v component)

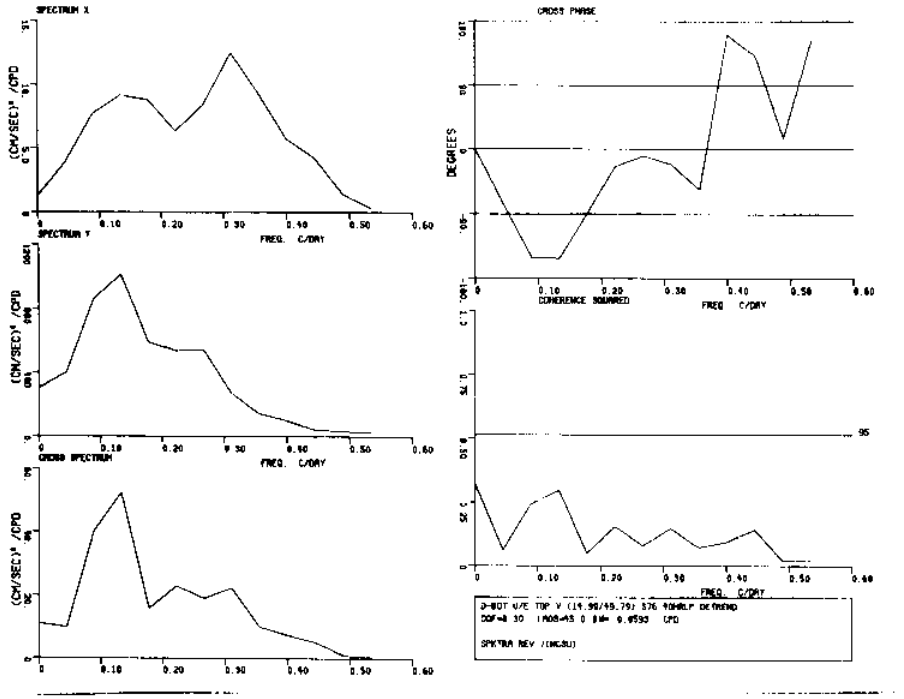

Figure 302 Spectra of low pass current velocity components from meter D_{bot} (u component) and meter E_{top} (v component)

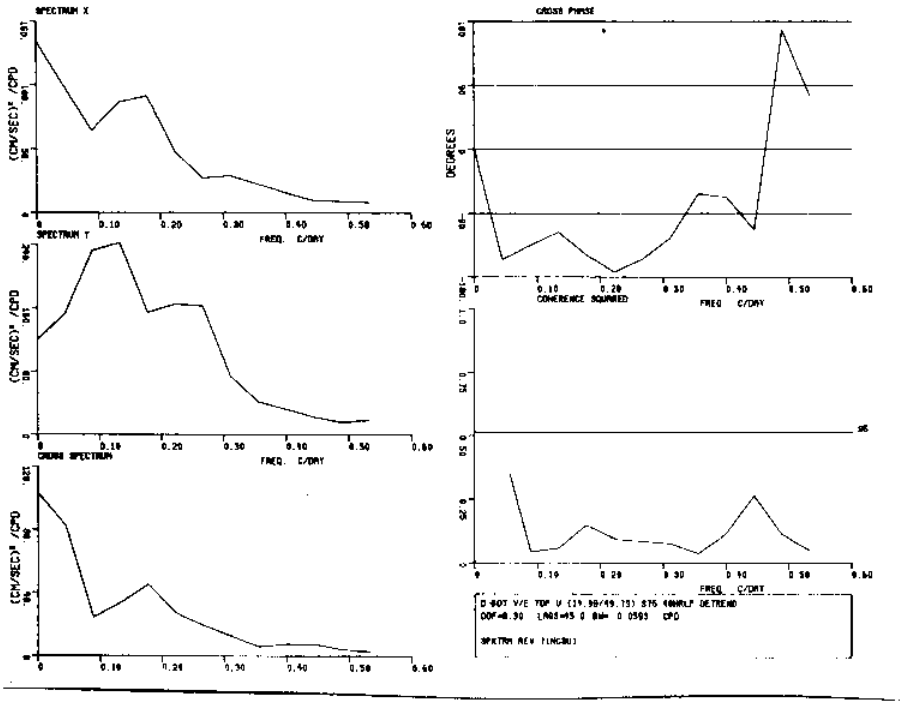

Figure 303 Spectra of low pass current velocity components from meter D_{bot} (v component) and meter E_{top} (u component)

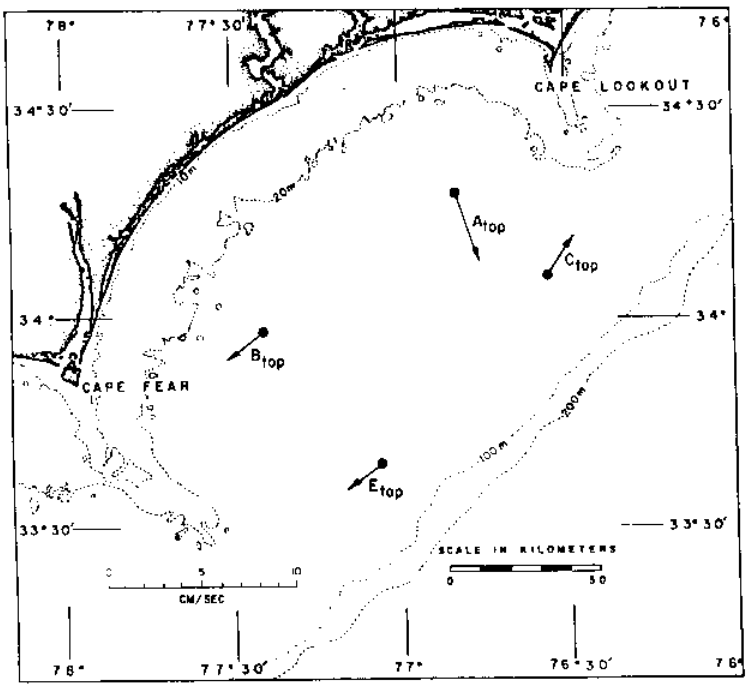

Figure 304 Mean velocity for July 23-Aug. 22, 1976 (top meters)

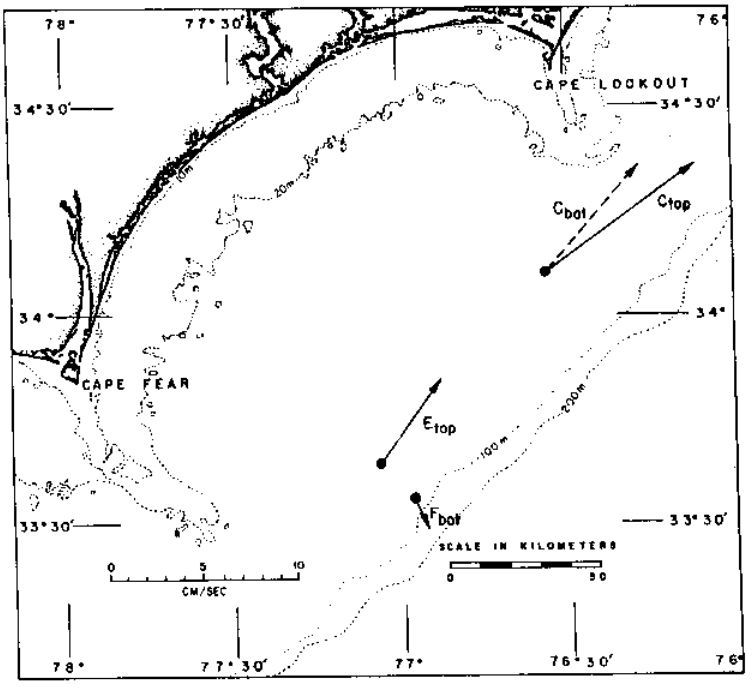

Figure 305 Mean velocity for Summer 1976

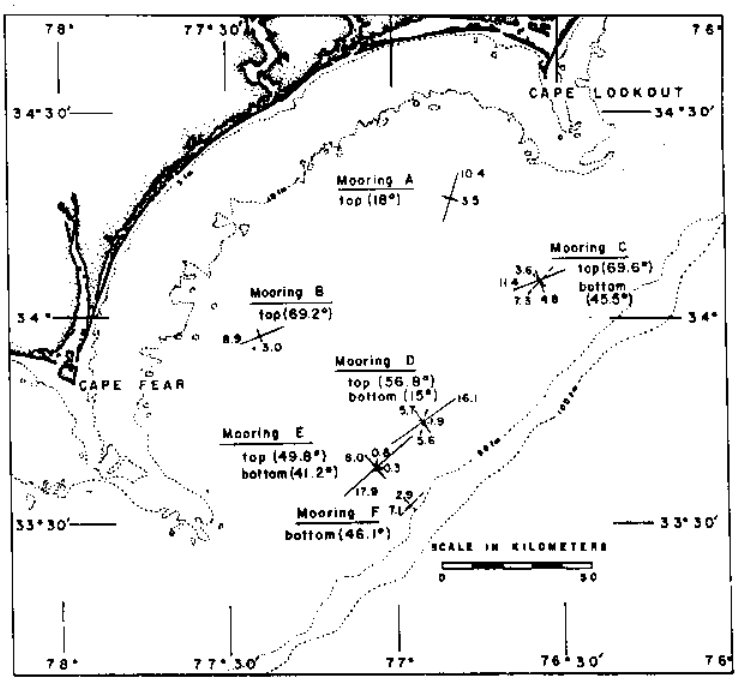

Figure 306 Principal axes and root mean square velocities for Moorings A-F

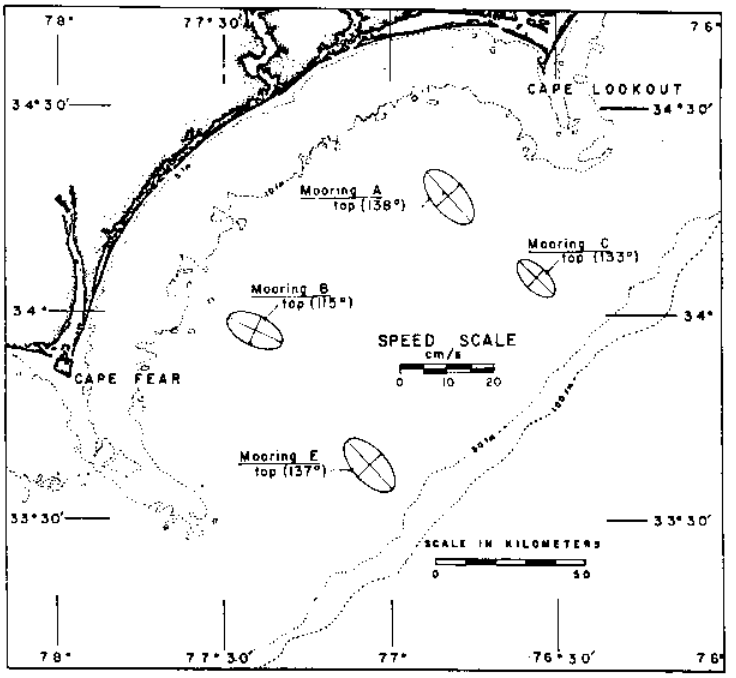

Figure 307 Tidal elipses for July 23-Aug. 22, 1976 (top meters)

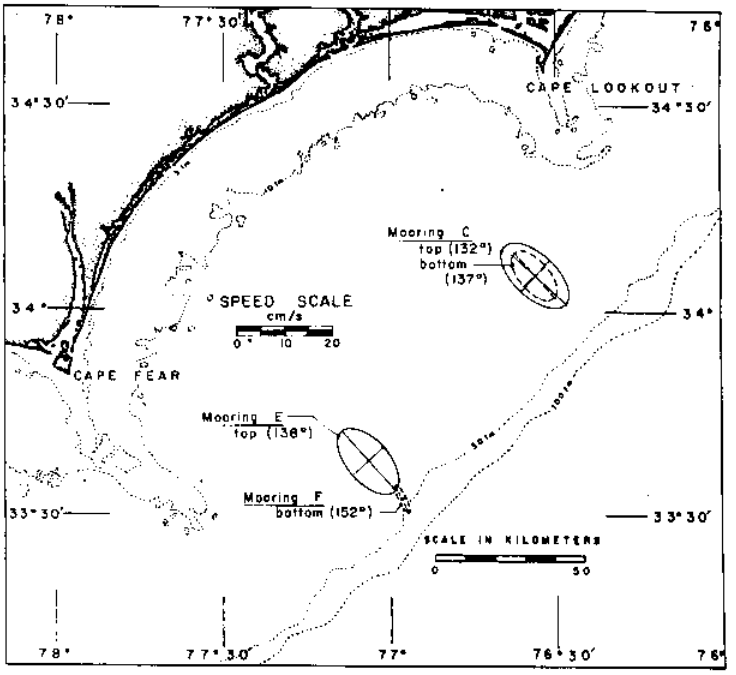

Figure 308 Tidal elipses for Summer 1976

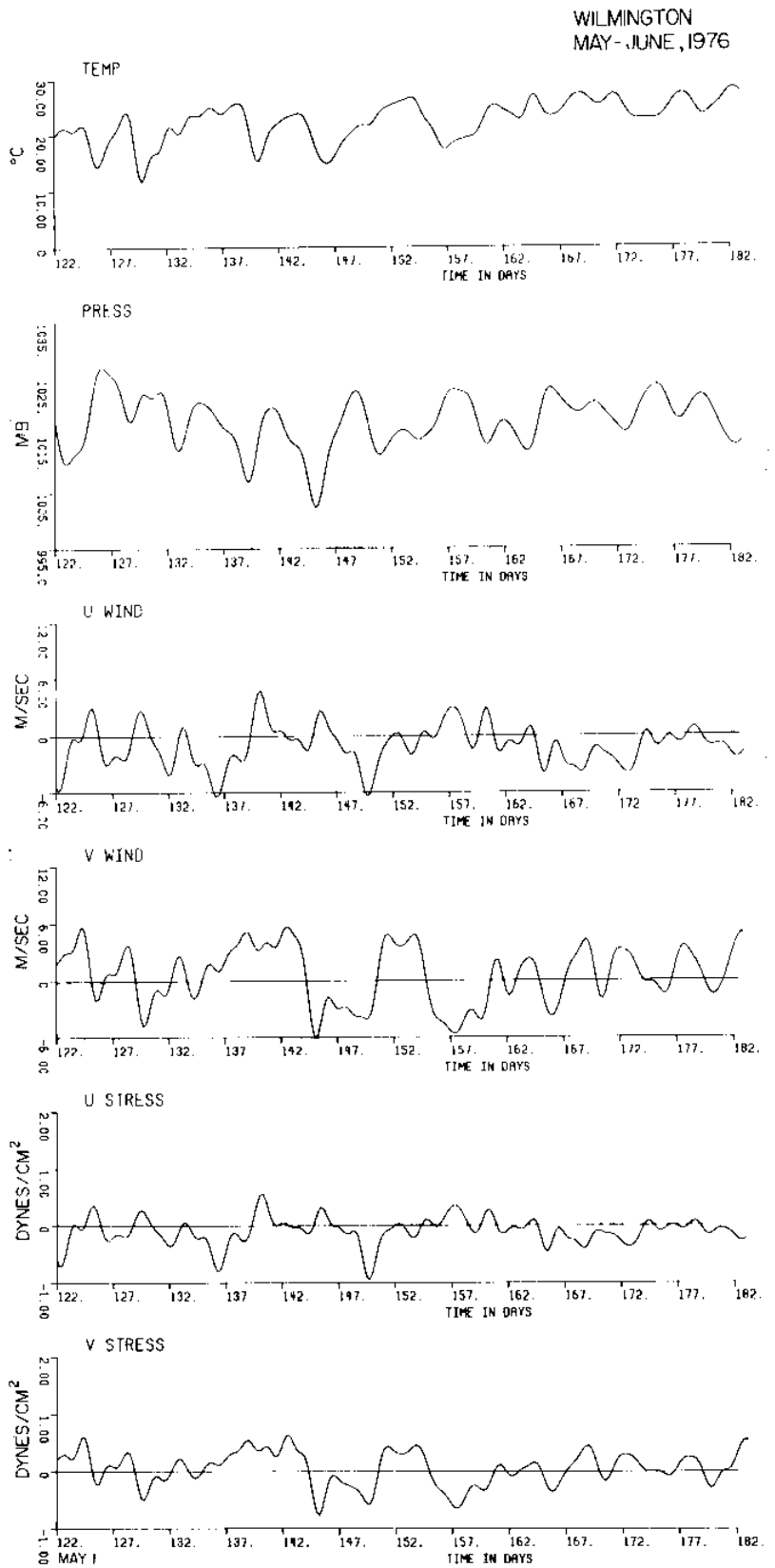

Figure 309 Low pass temperature, pressure, wind velocity components, and wind stress components at Wilmington, N. C. May-June, 1976

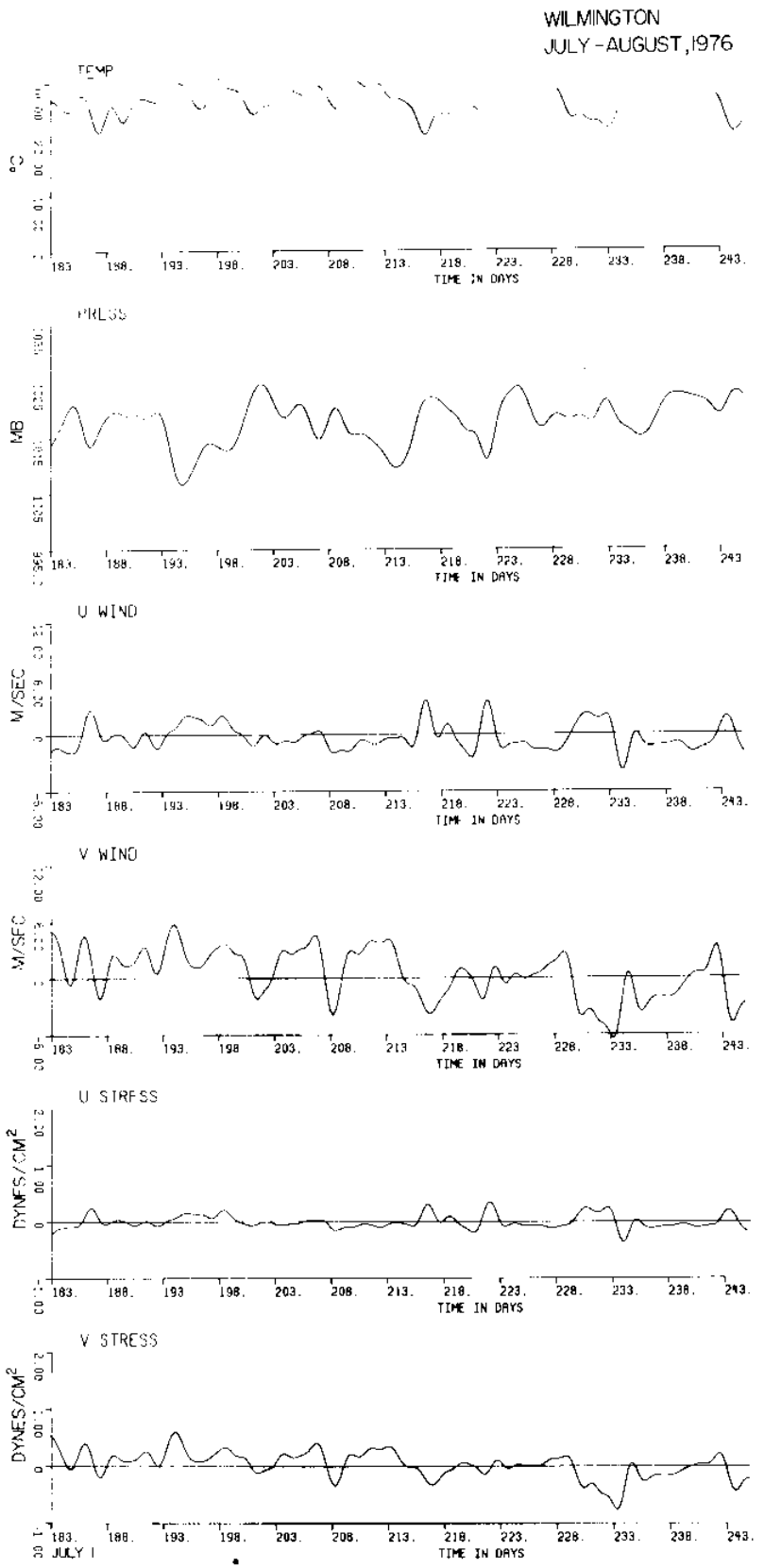

Figure 310 Low pass temperature, pressure, wind velocity components, and wind stress components at Wilmington, N. C. July-August, 1976

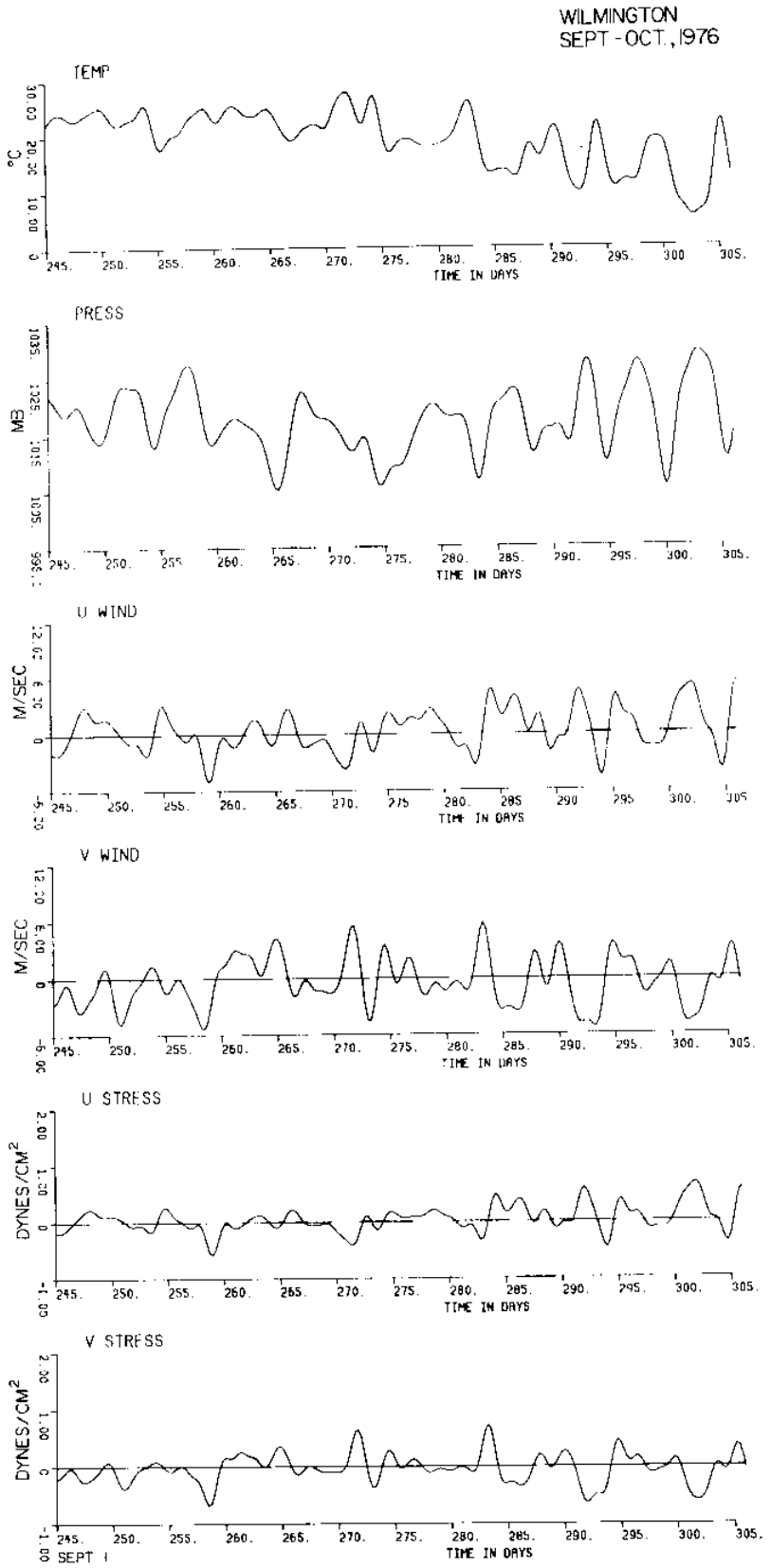

Figure 311 Low pass temperature, pressure, wind velocity components, and wind stress components at Wilminton, N. C. September-October, 1976

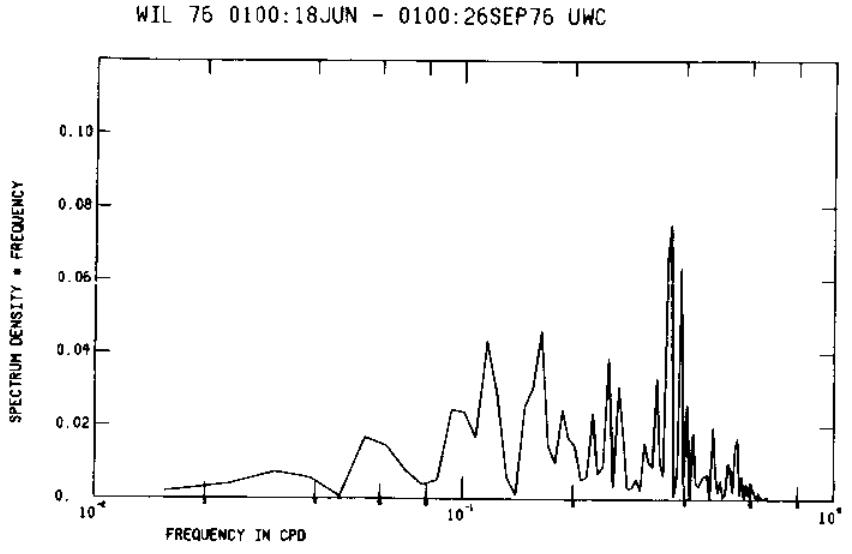

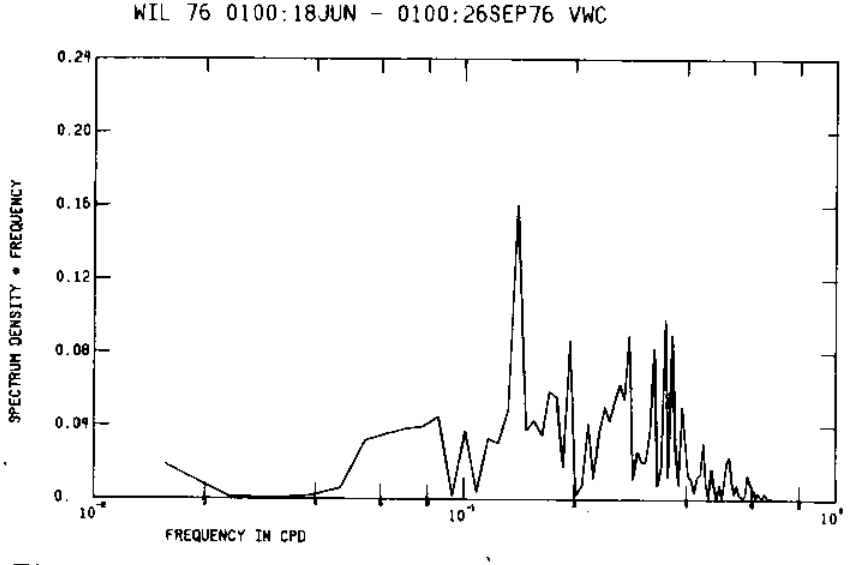

Figure 312

FFT of low pass wind velocity components at Wilmington, N. C. 18 June-26 September, 1976

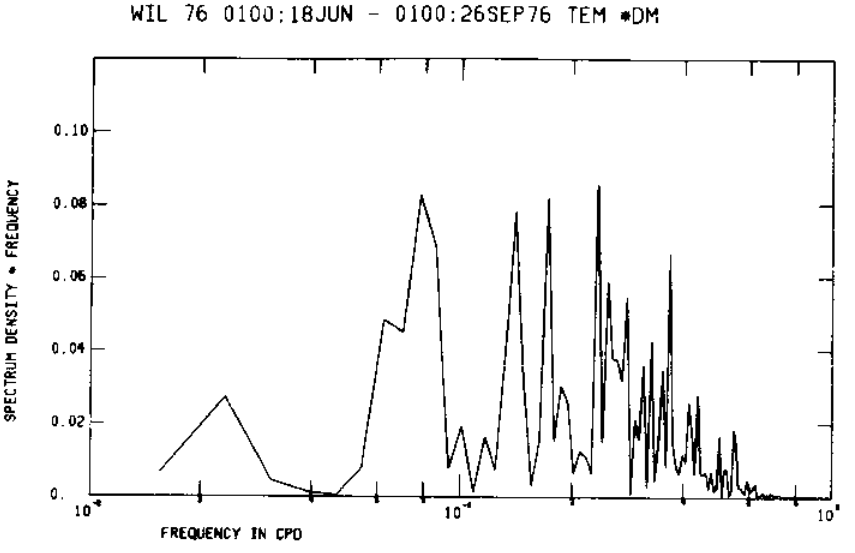

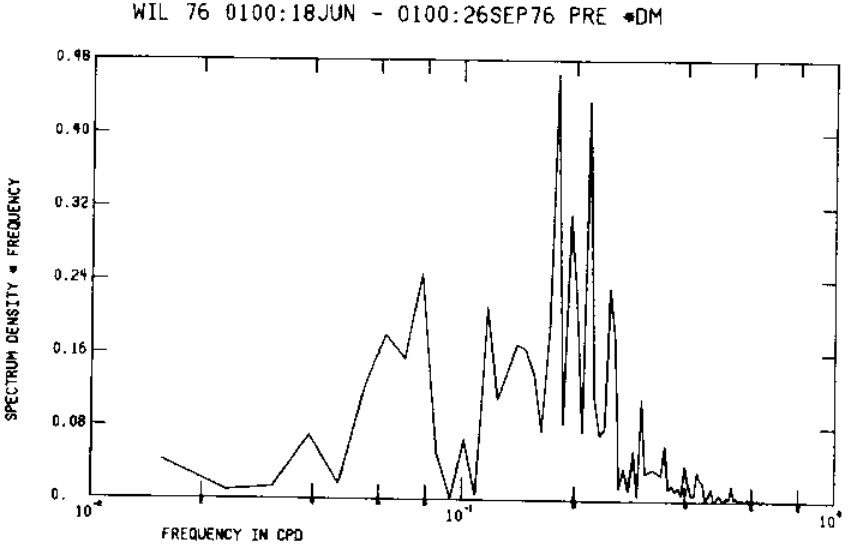

Figure 313

FFT of low pass temperature and pressure at Wilmington, N. C. 18 June-26 September, 1976

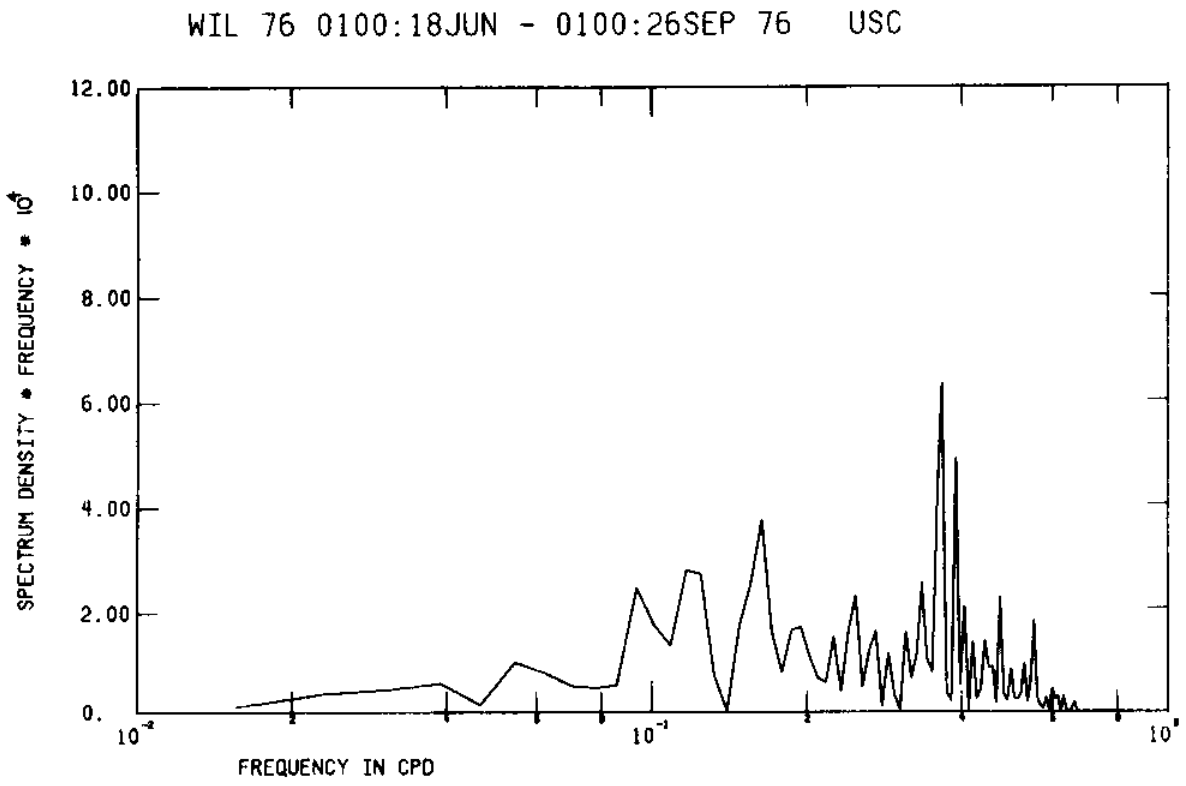

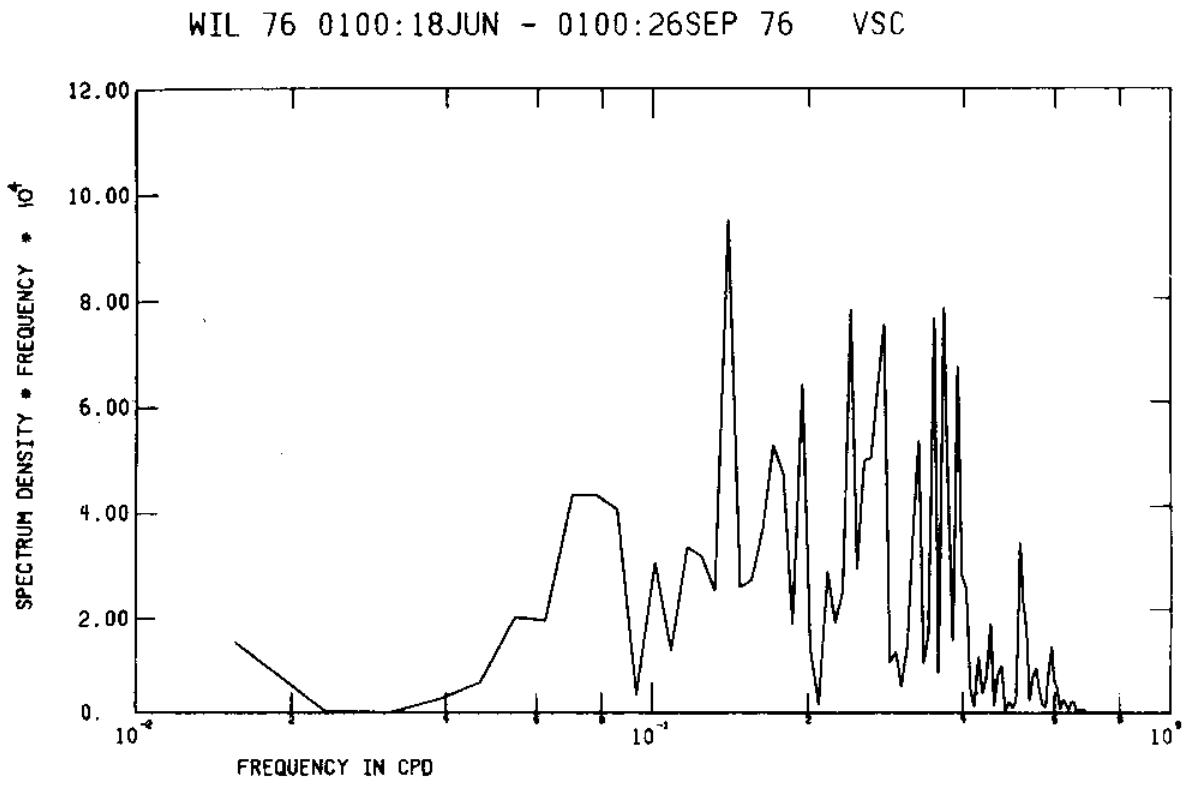

Figure 314 FFT of low pass wind stress components at Wilmington, N. C. 18 June-26 September, 1976

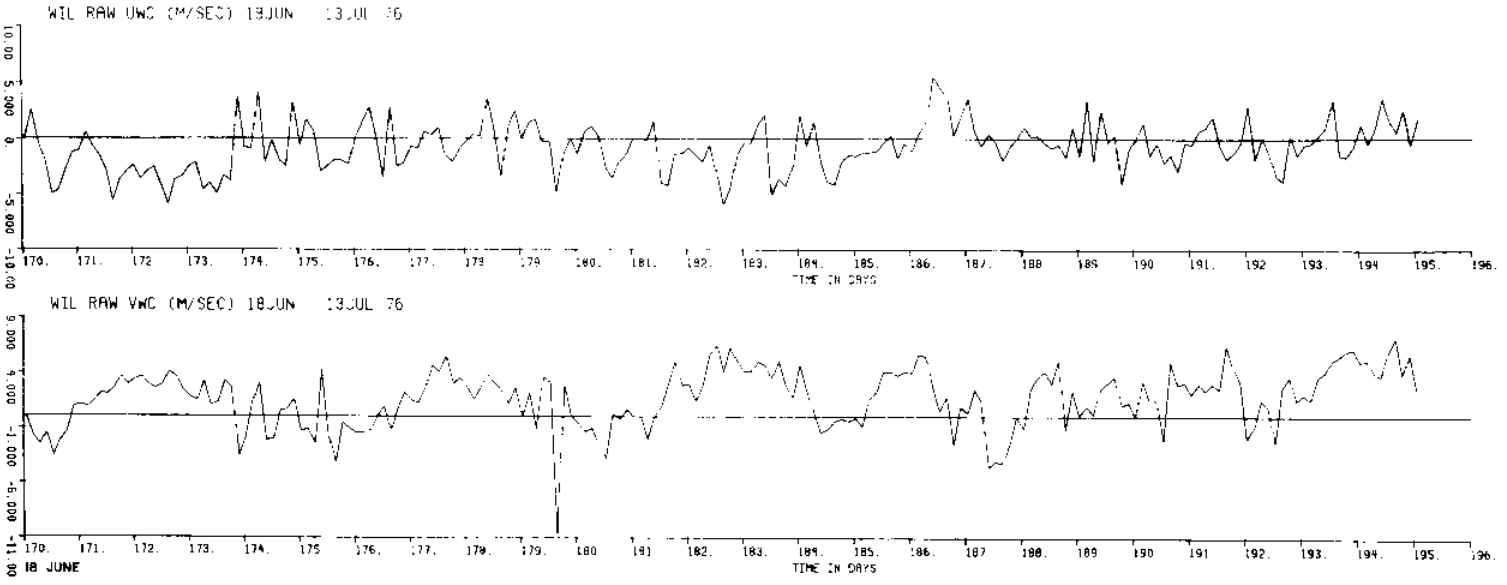

Figure 315 a

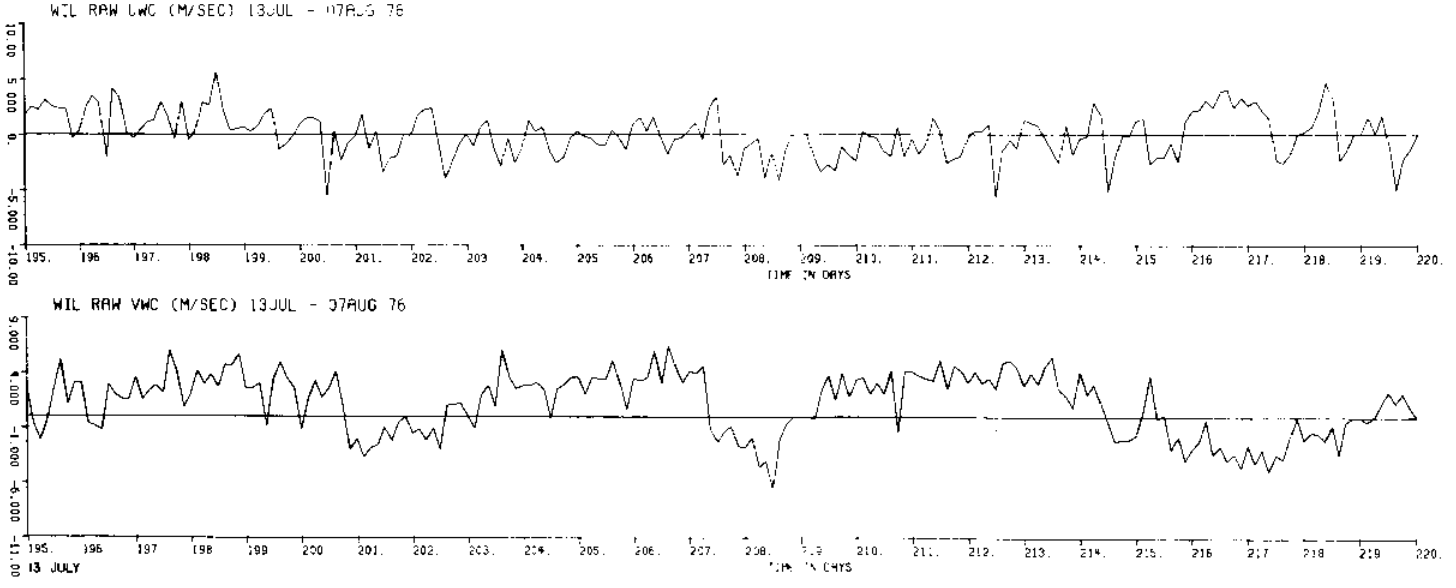

Figure 315 b

Figure 315 (a,b,c,d) Unfiltered wind velocity components at Wilmington, N. C. 18 June-26 September, 1976

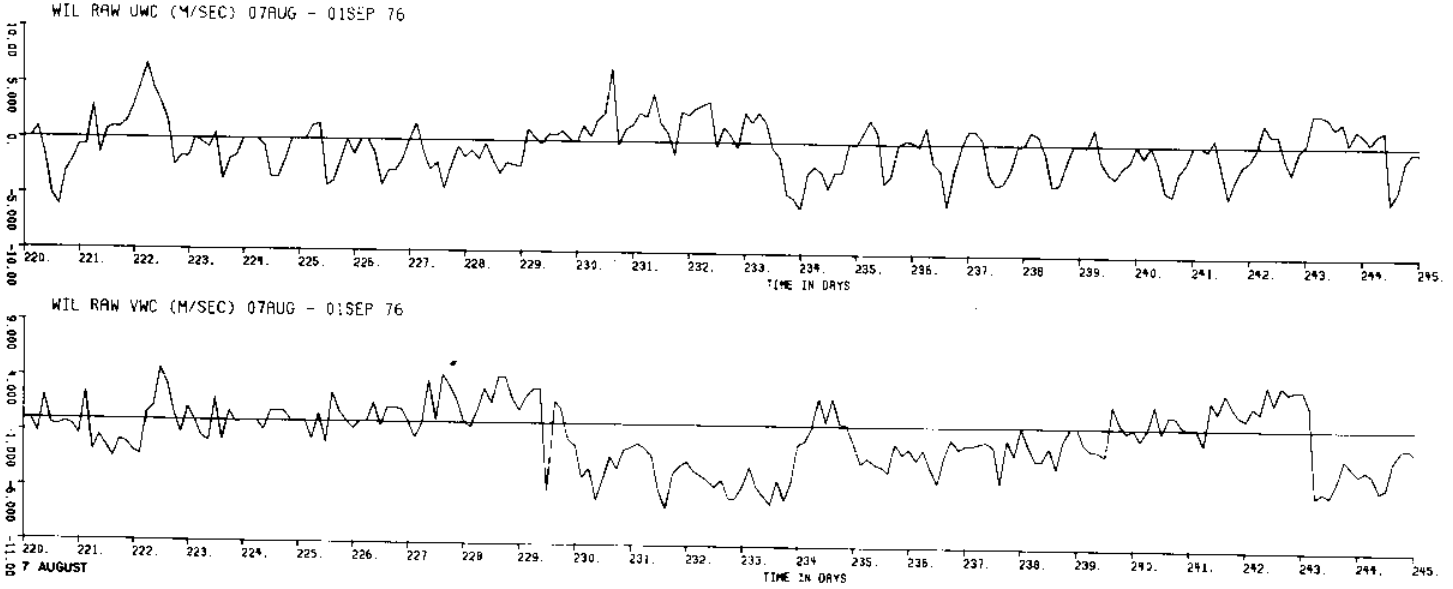

Figure 315 c

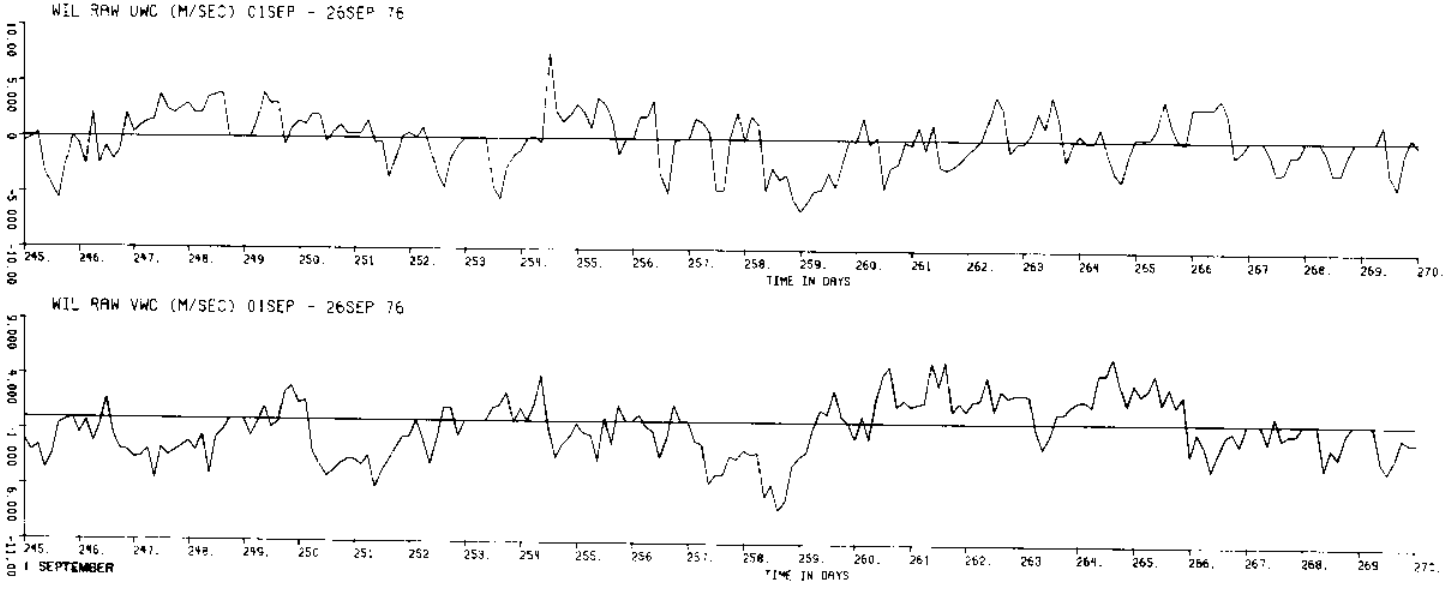

Figure 315 d

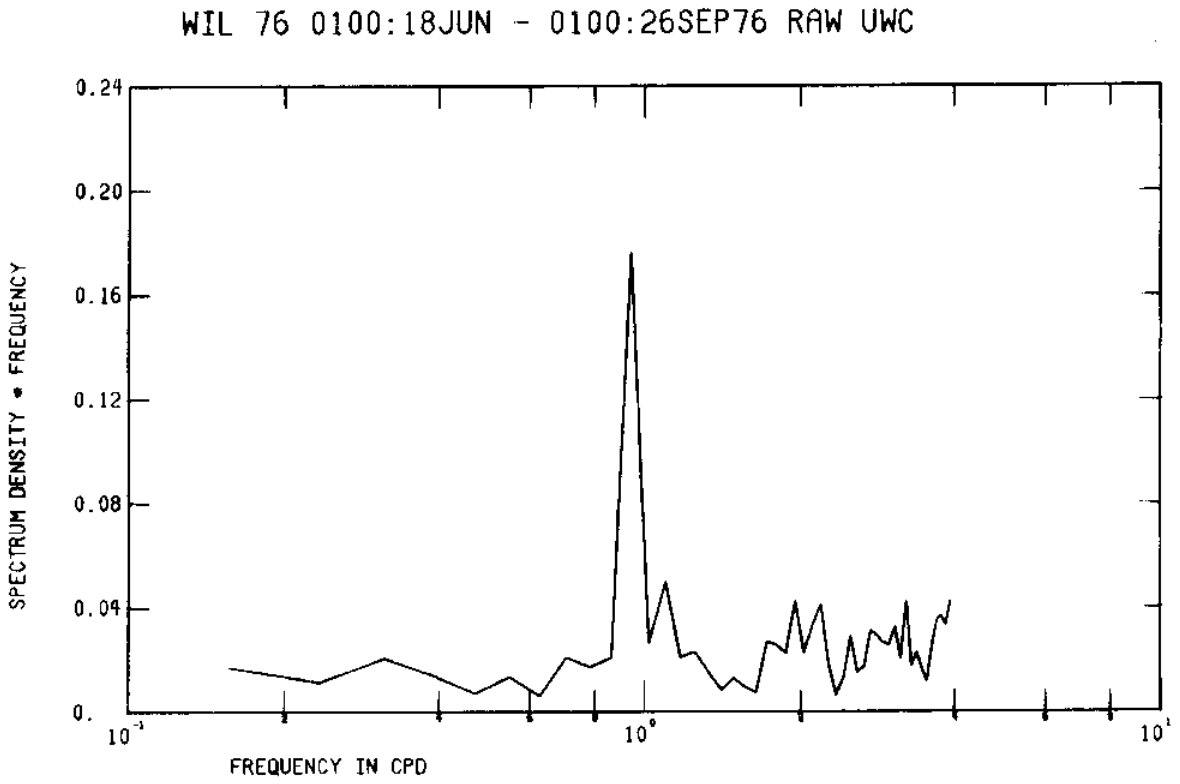

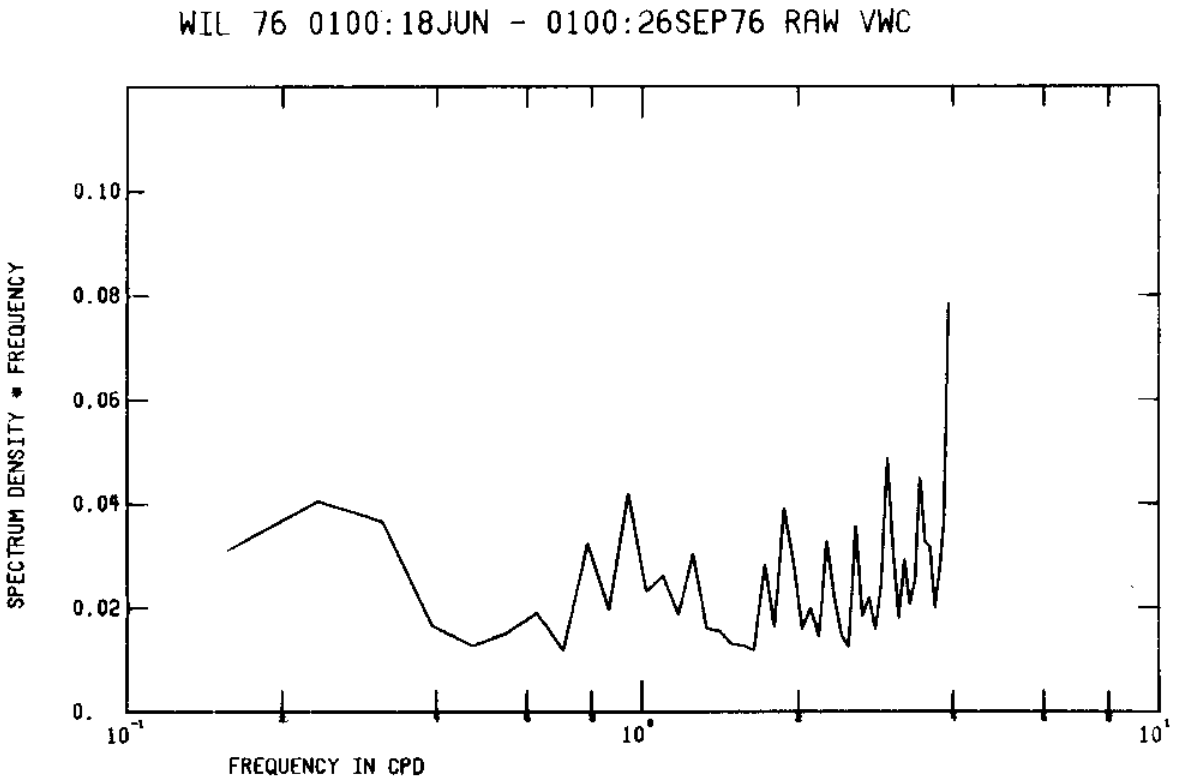

Figure 316 FFT of unfiltered wind velocity components at Wilmington, N. C. 18 June–26 September, 1976

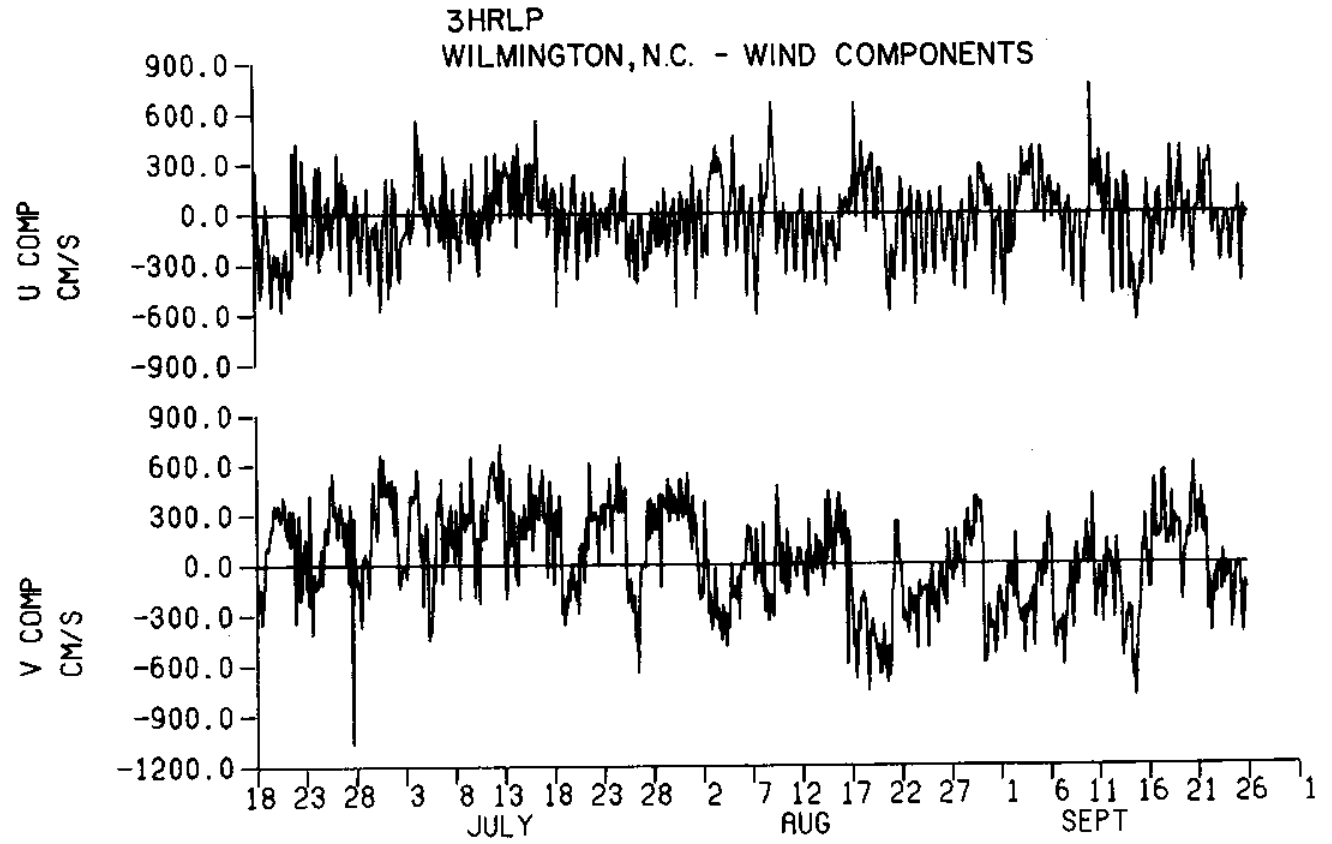

Figure 317 3HRLP wind velocity components for Wilmington, N. C.

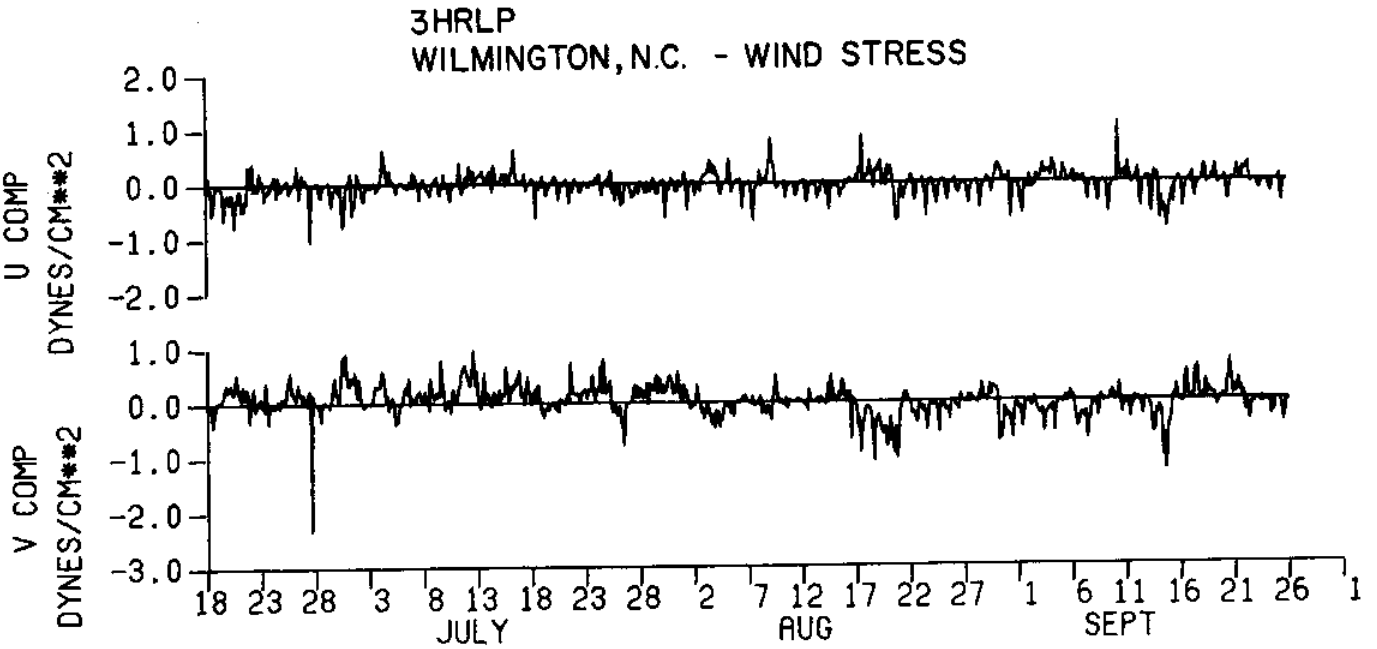

Figure 318 3HRLP wind stress components for Wilmington, N. C.

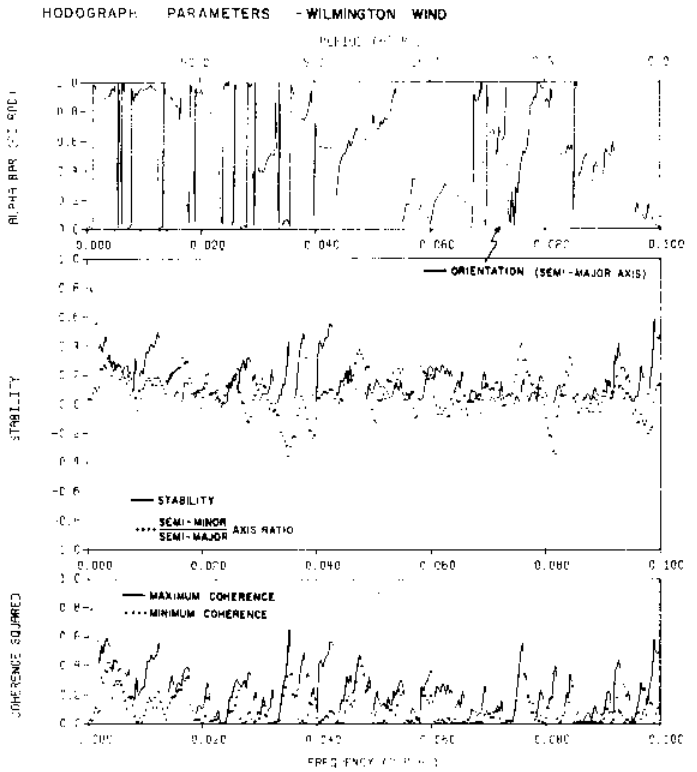

Figure 319 Hodograph parameters of Wilmington, N. C. wind velocity

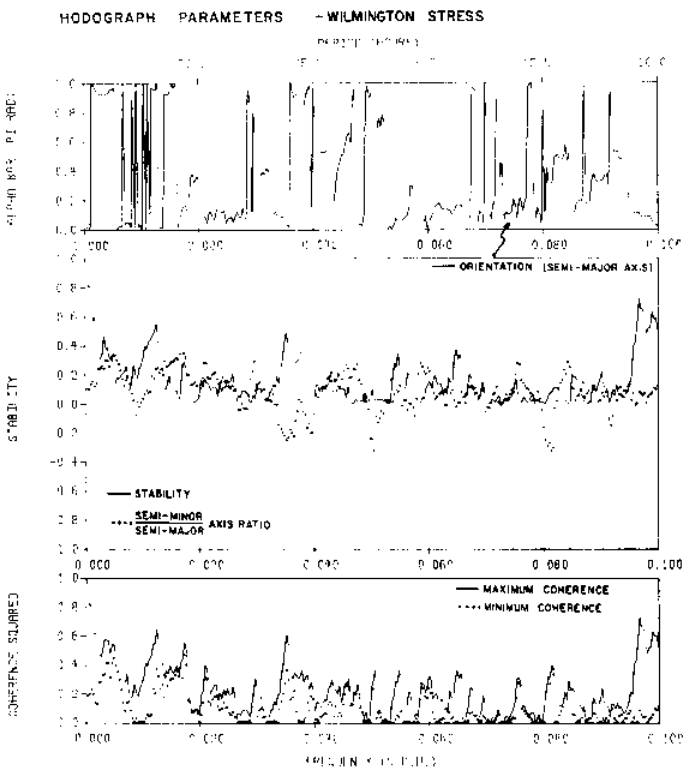

Figure 320 Hodograph parameters of Wilmington, N. C. wind stress

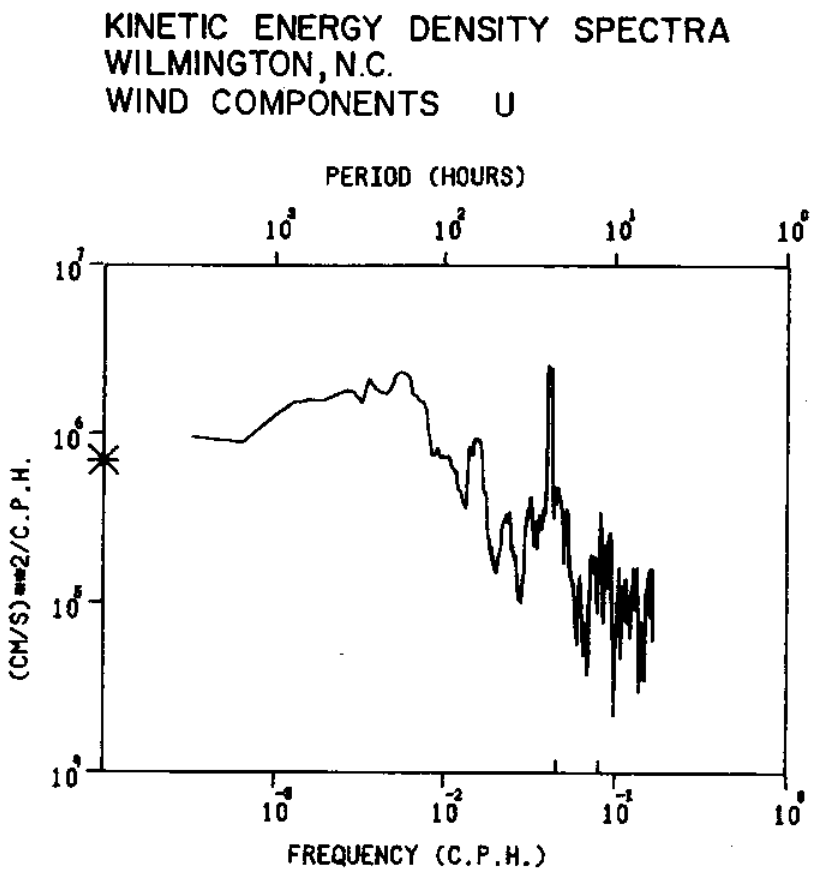

Figure 321
Kinetic energy density spectra for u-component of wind velocity at Wilmington, N. C.

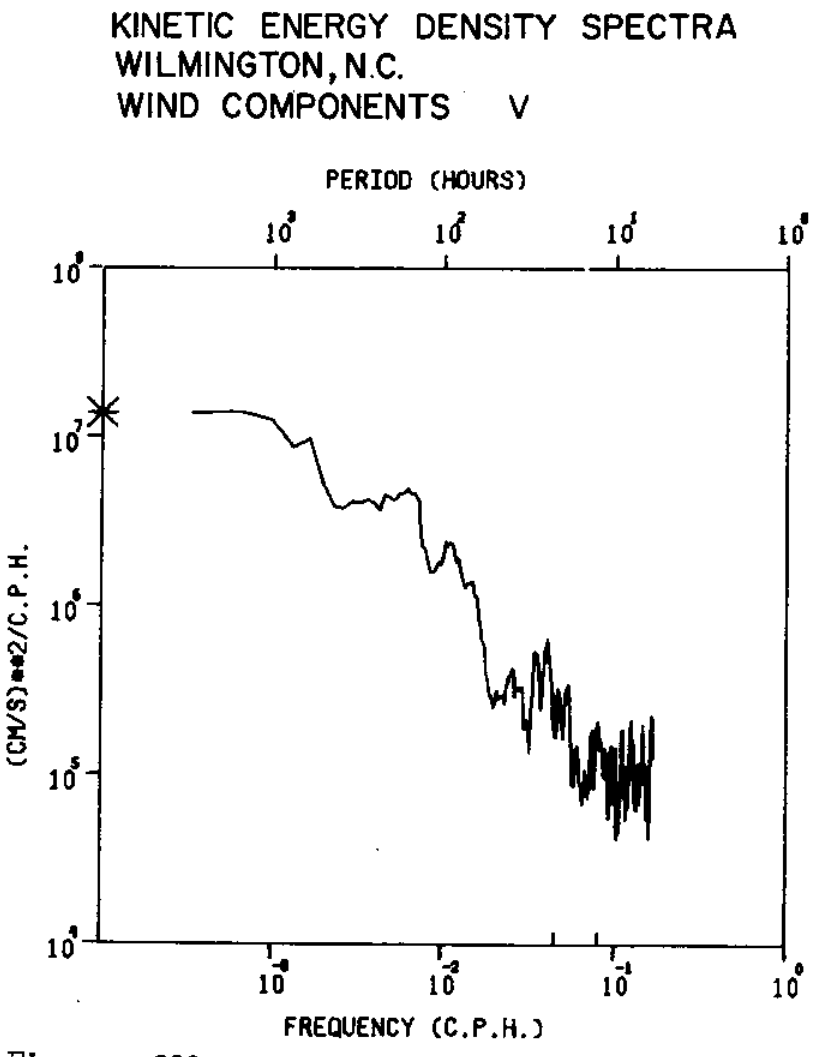

Figure 322
Kinetic energy density spectra for v-component of wind stress at Wilmington, N. C.

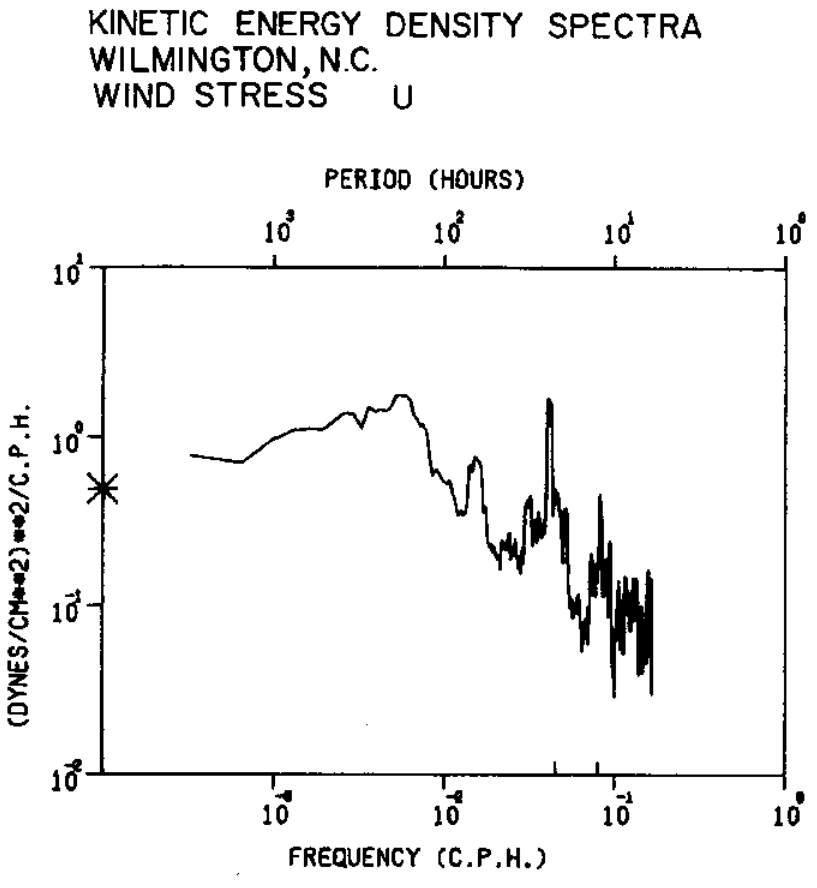

Figure 323

Kinetic energy density spectra for u-component of wind stress at Wilmington, N. C.

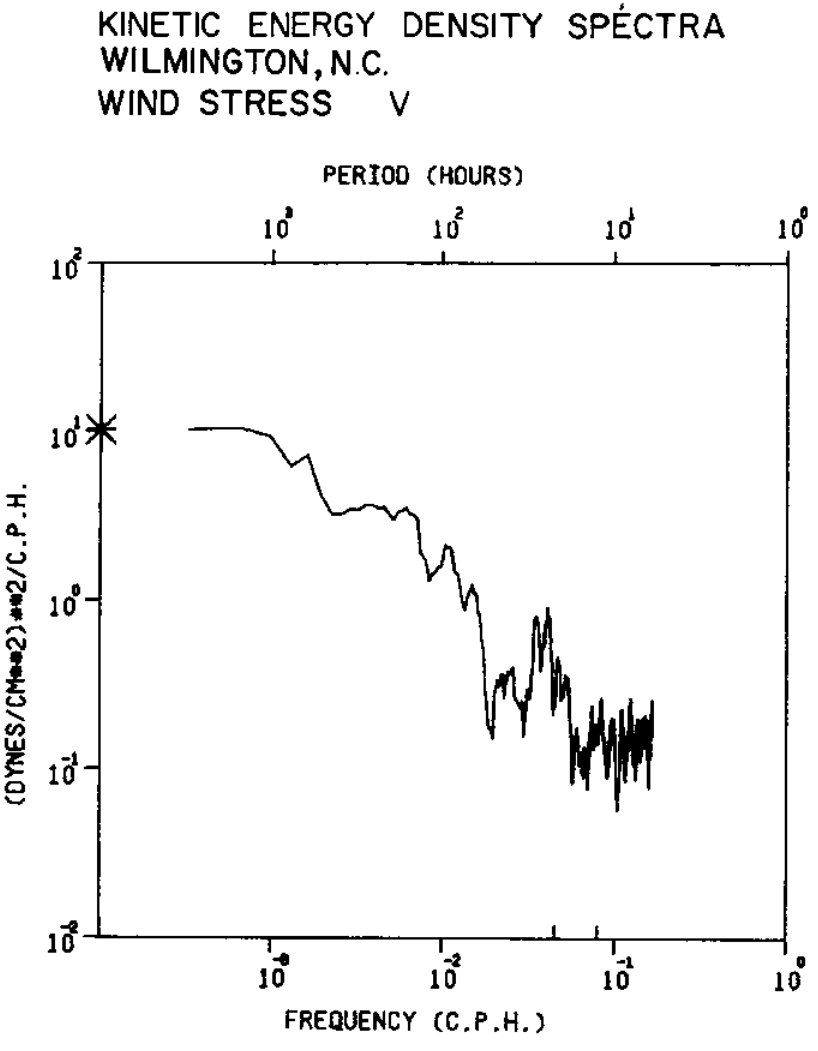

Figure 324

Kinetic energy density spectra for v-component of wind stress at Wilmington, N.C.

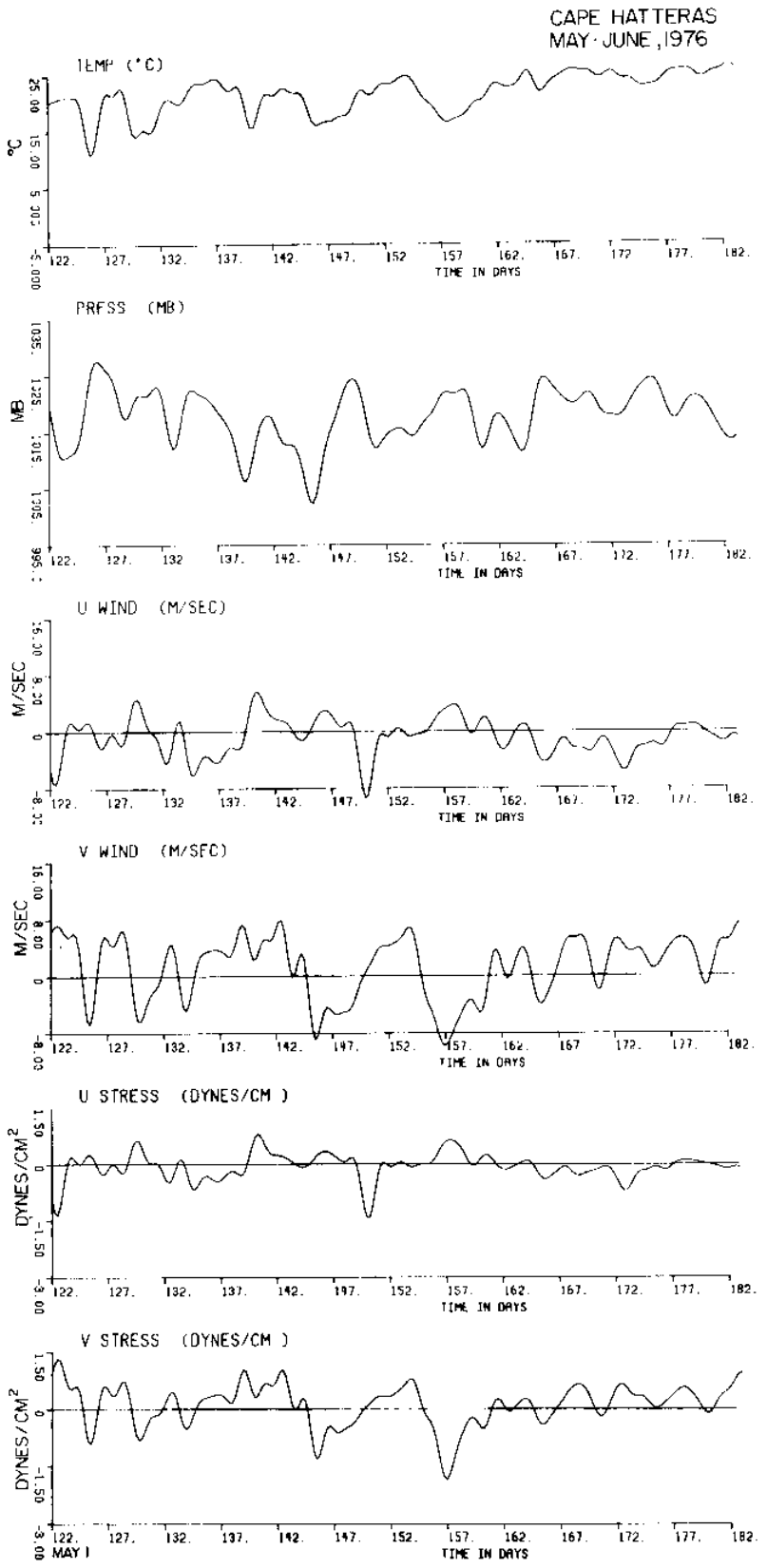

Figure 325 Low pass temperature, pressure, wind velocity components, and wind stress components at Cape Hatteras, N. C. May-June, 1976

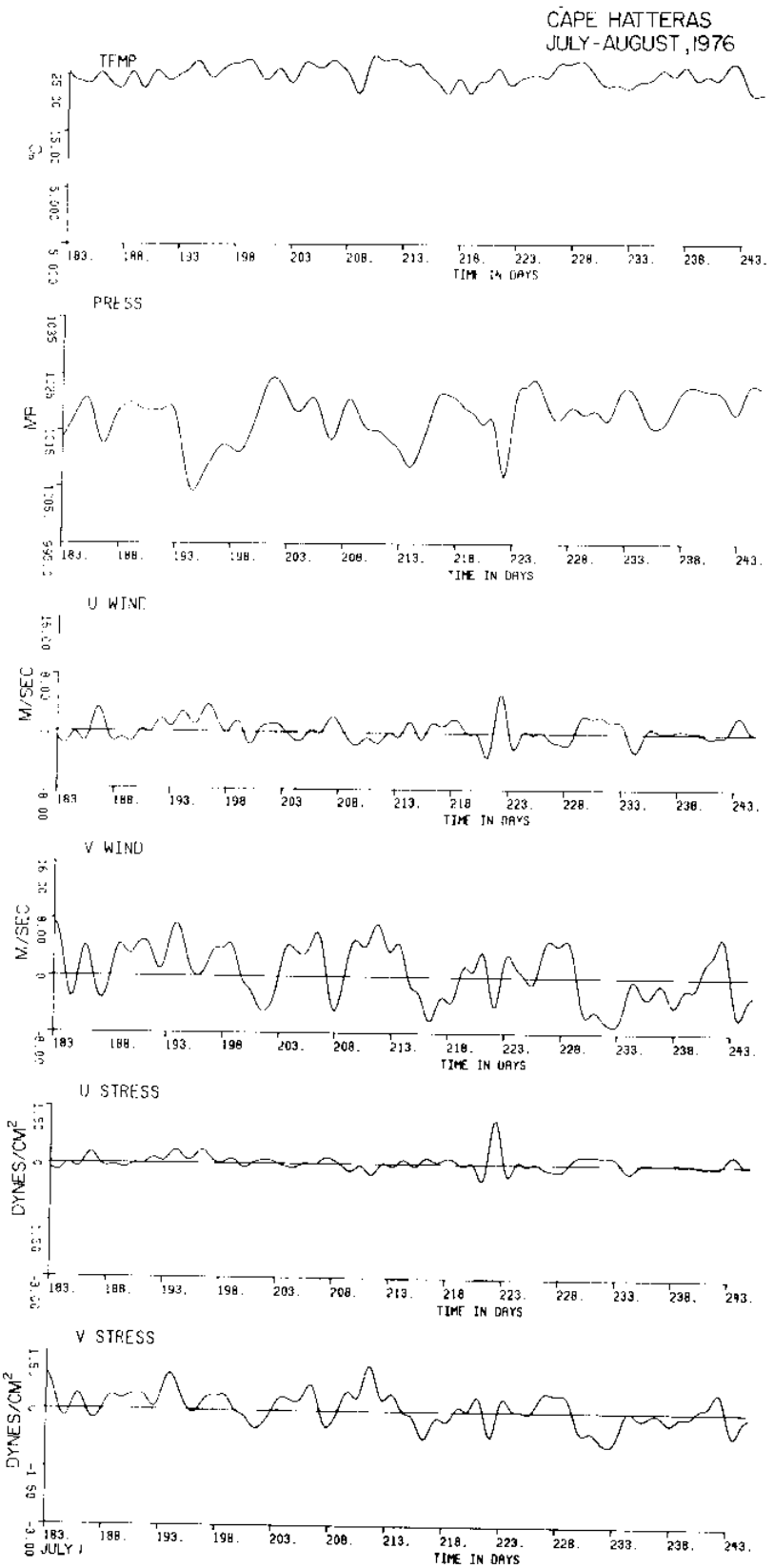

Figure 326 Low pass temperature, pressure, wind velocity components, and wind stress components at Cape Hatteras, N. C. July-August, 1976

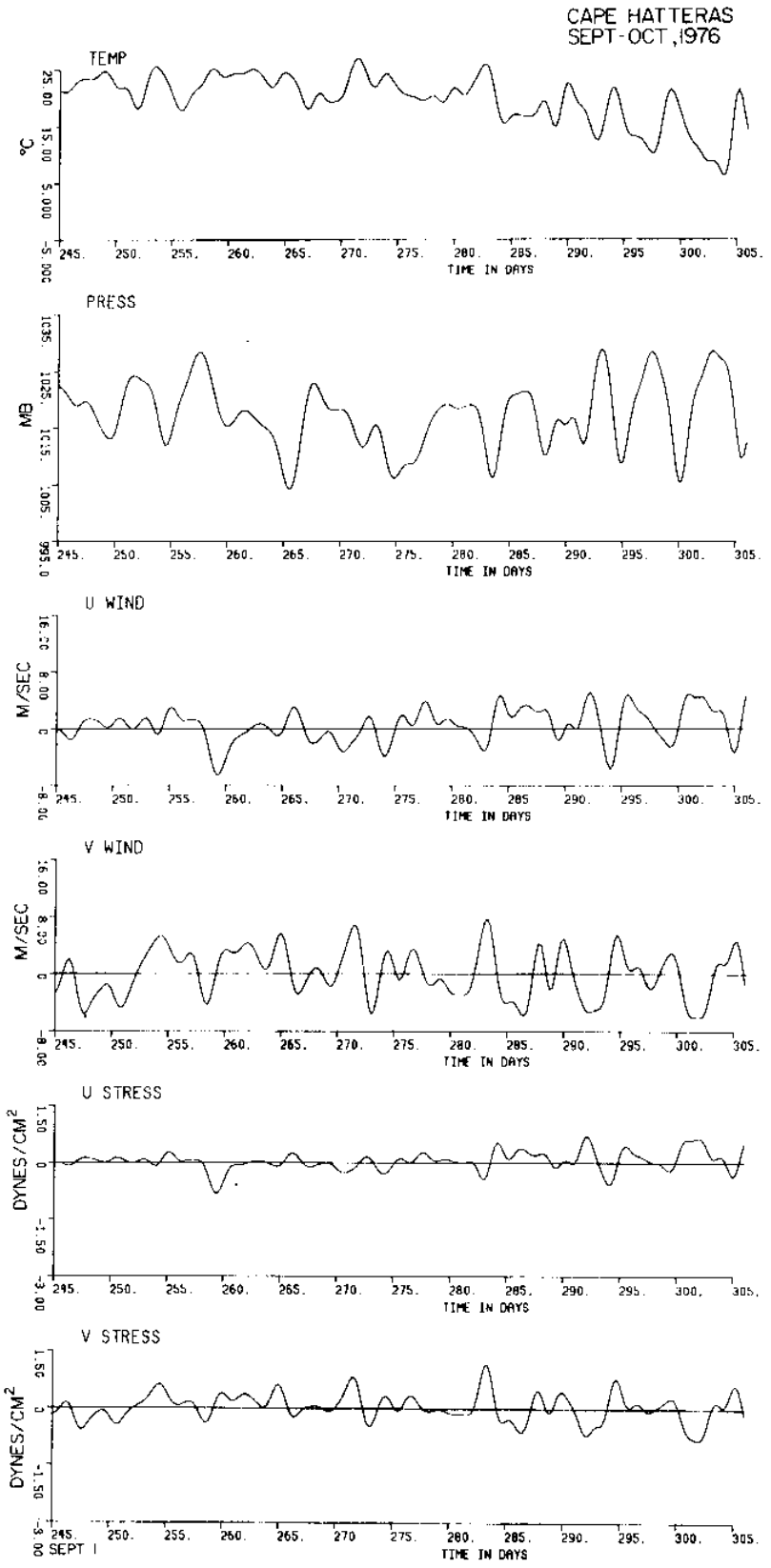

Figure 327 Low pass temperature, pressure, wind velocity components, and wind stress components at Cape Hatteras, N. C. September-October, 1976

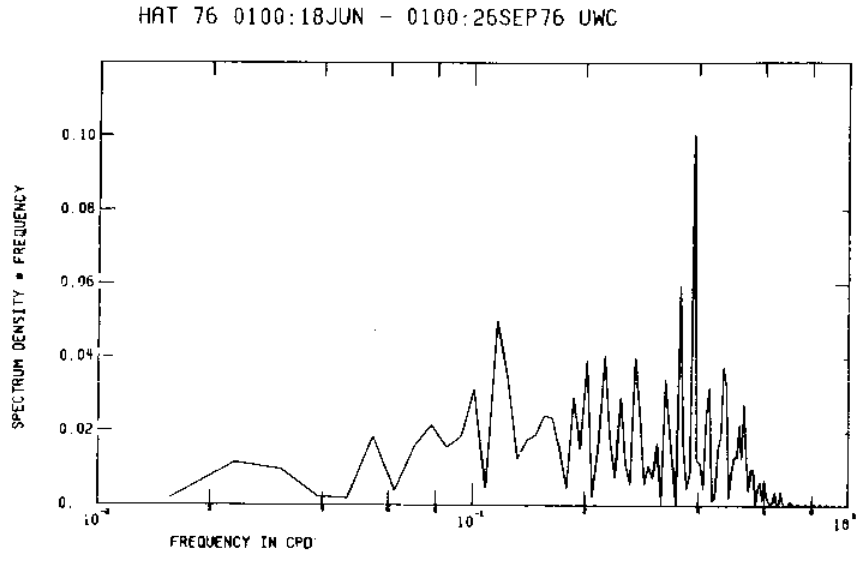

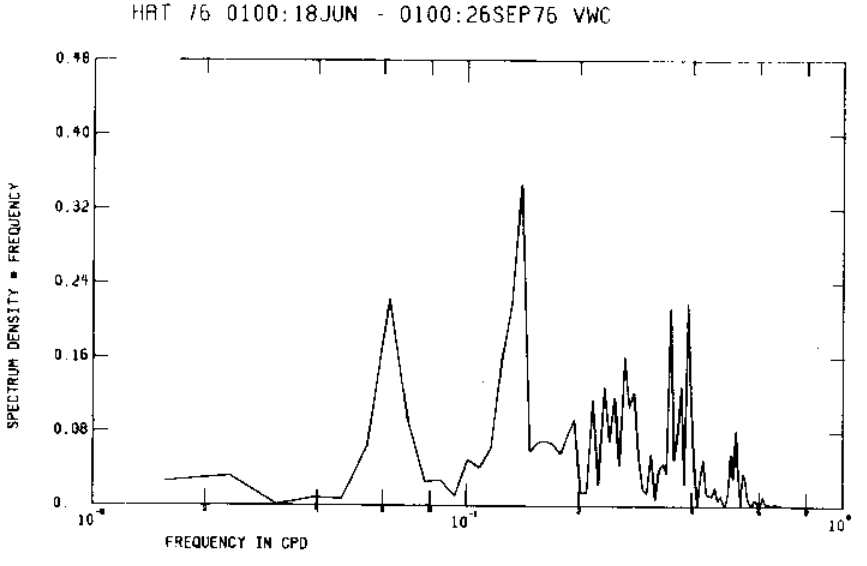

Figure 328

FFT of low pass wind velocity components at Cape Hatteras, N. C. 18 June-26 September, 1976

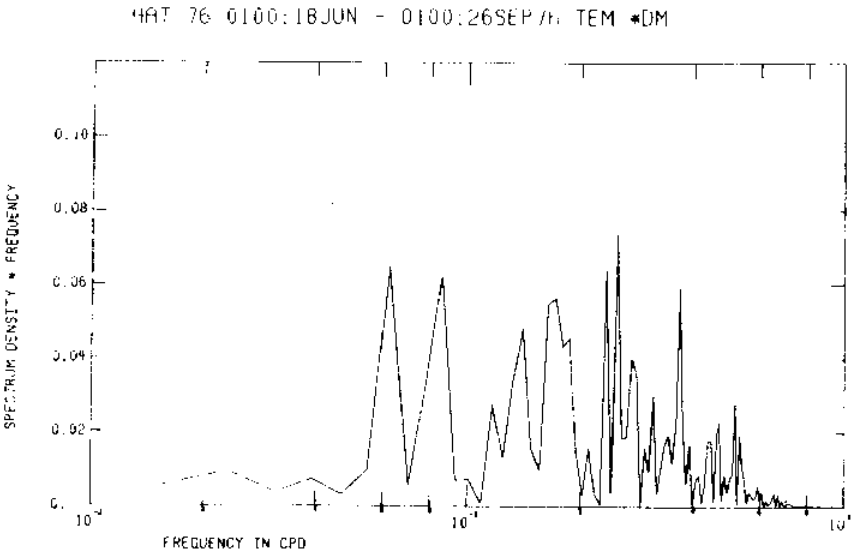

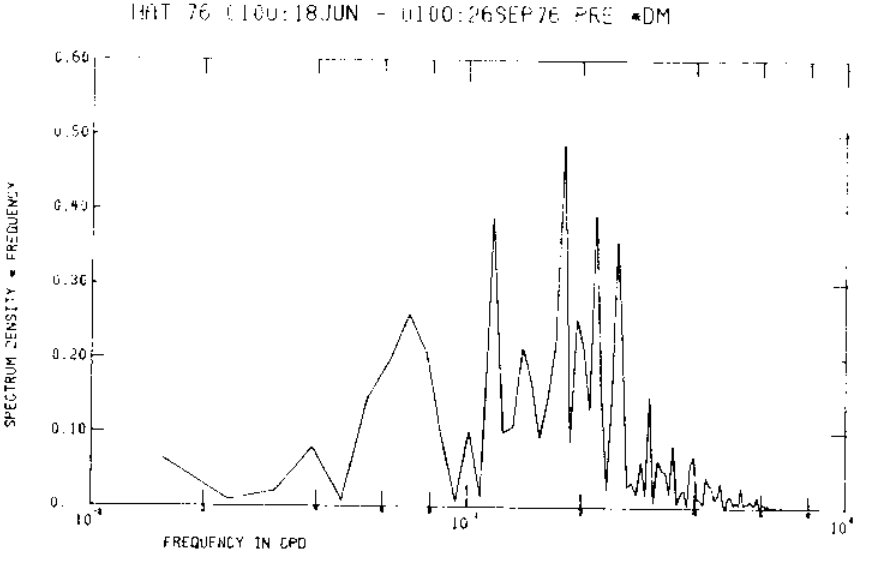

Figure 329

FFT of low pass temperature and pressure at Cape Hatteras, N. C. 18 June-26 September, 1976

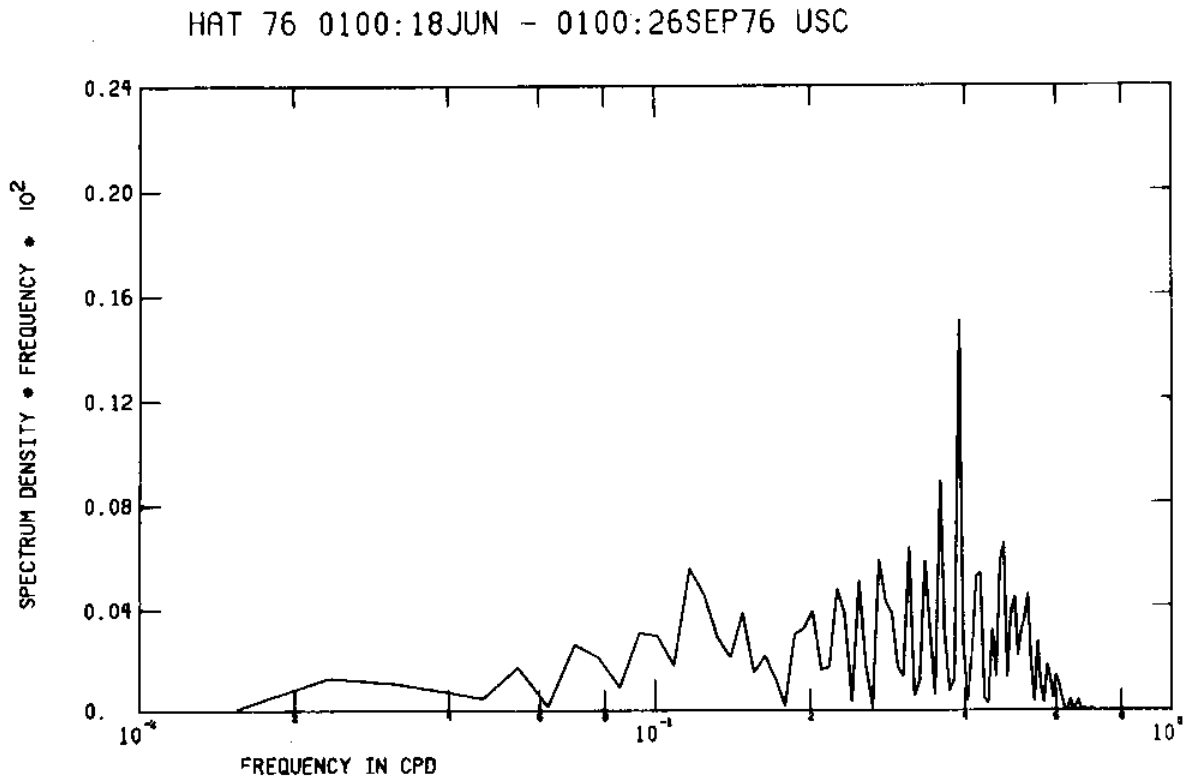

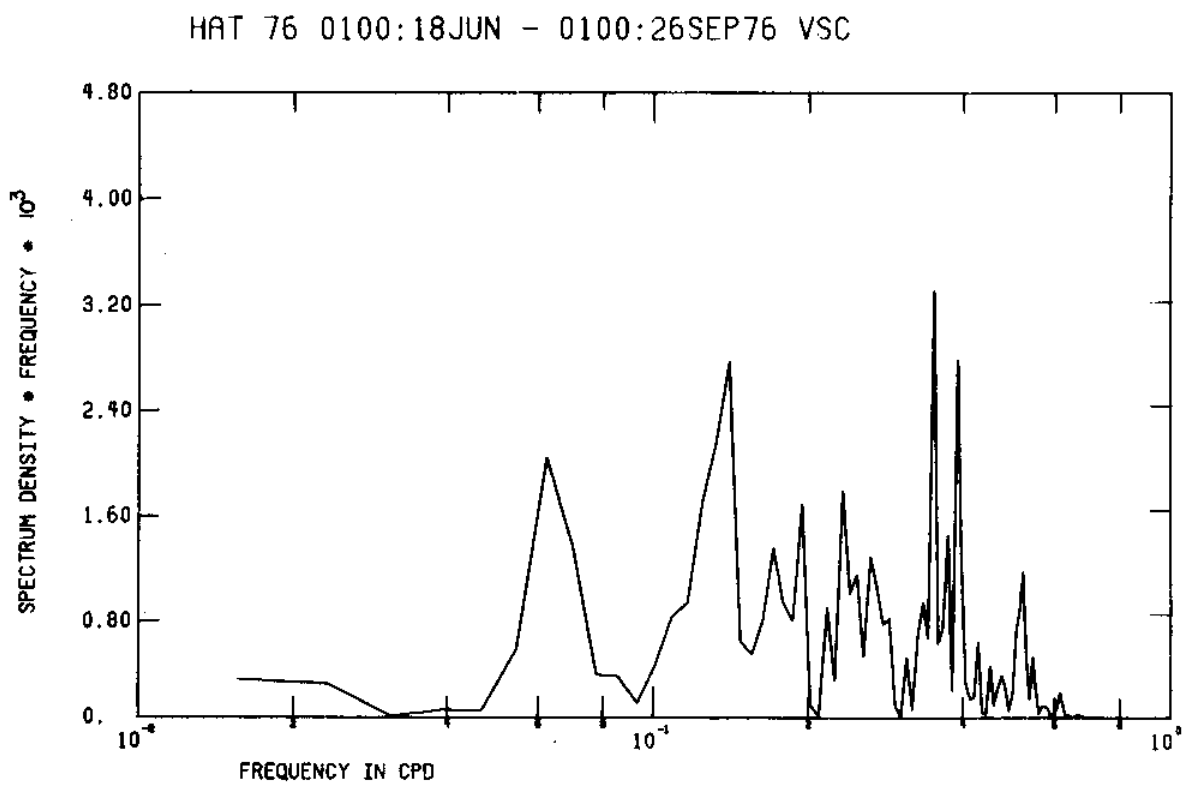

Figure 330 FFT of low pass wind stress components at Cape Hatteras, N. C. 18 June-26 September, 1976

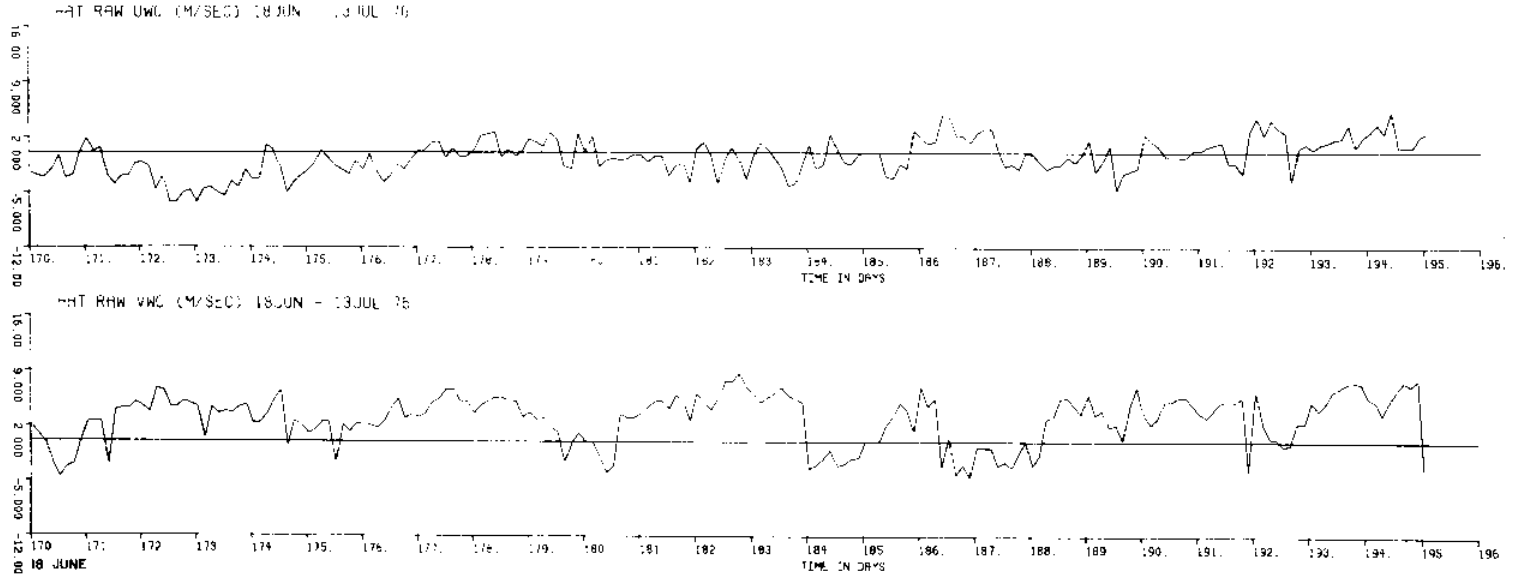

Figure 331 a

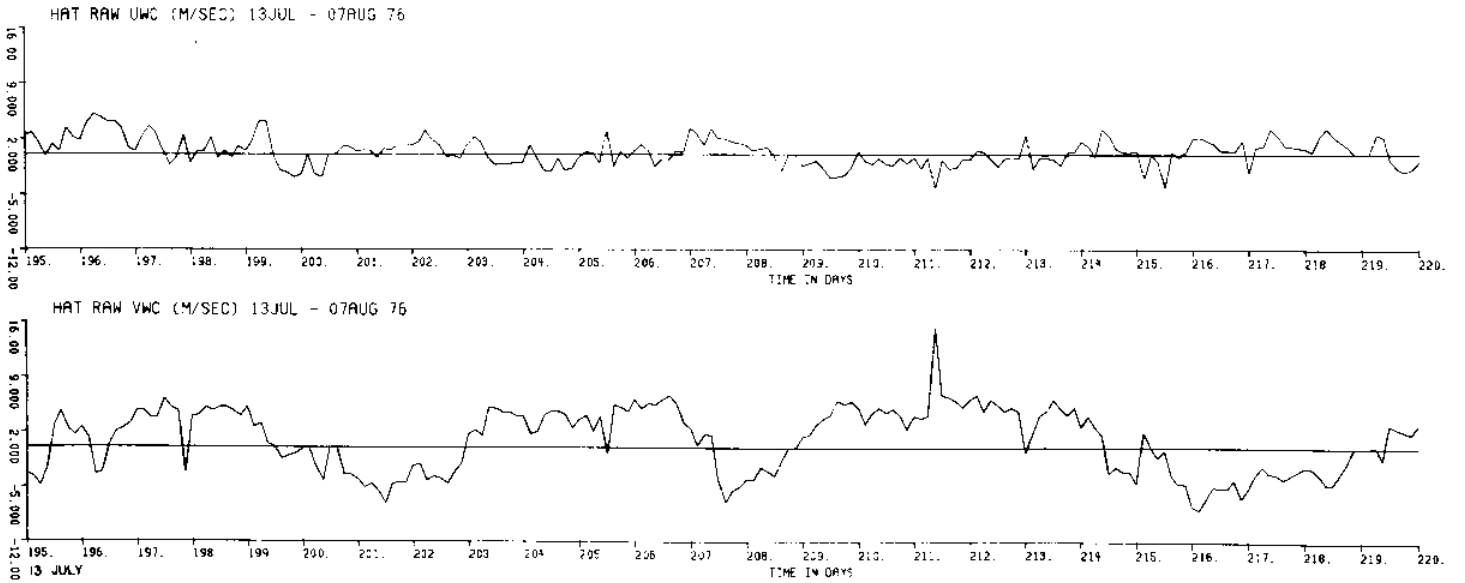

Figure 331 b

Figure 331 (a,b,c,d) Unfiltered wind velocity components at Cape Hatteras, N. C. 18 June-26 September, 1976

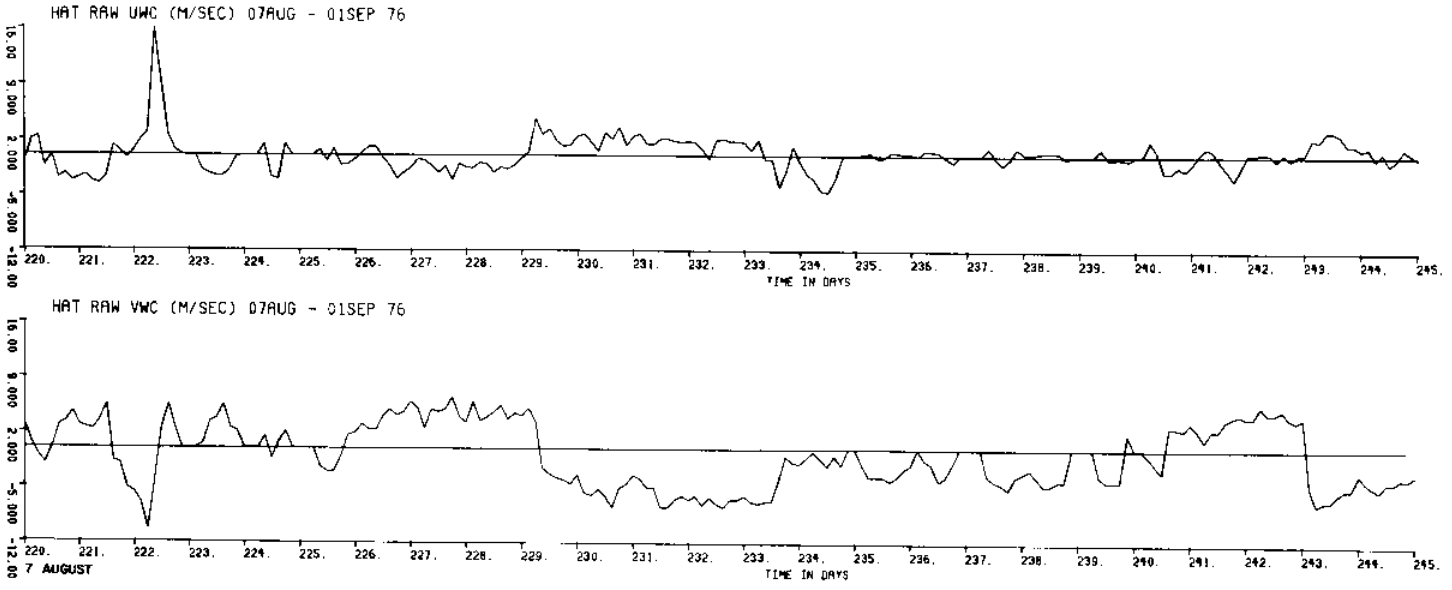

Figure 331 c

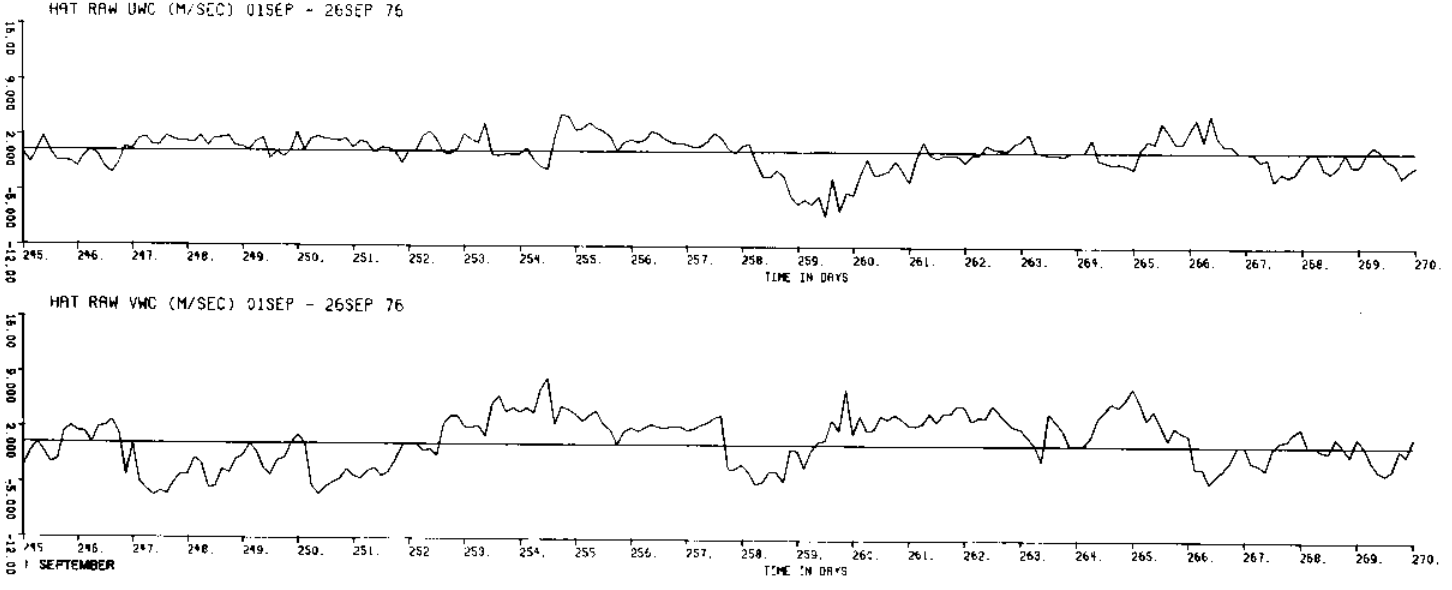

Figure 331 d

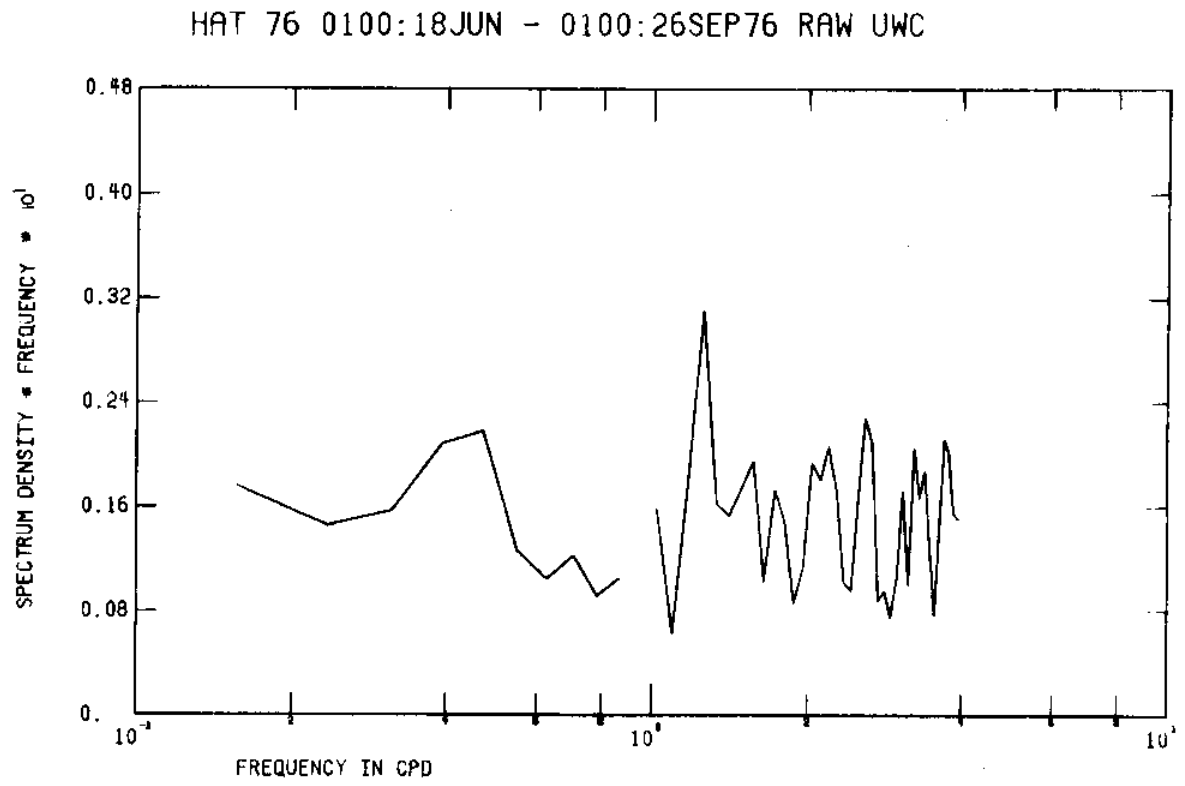

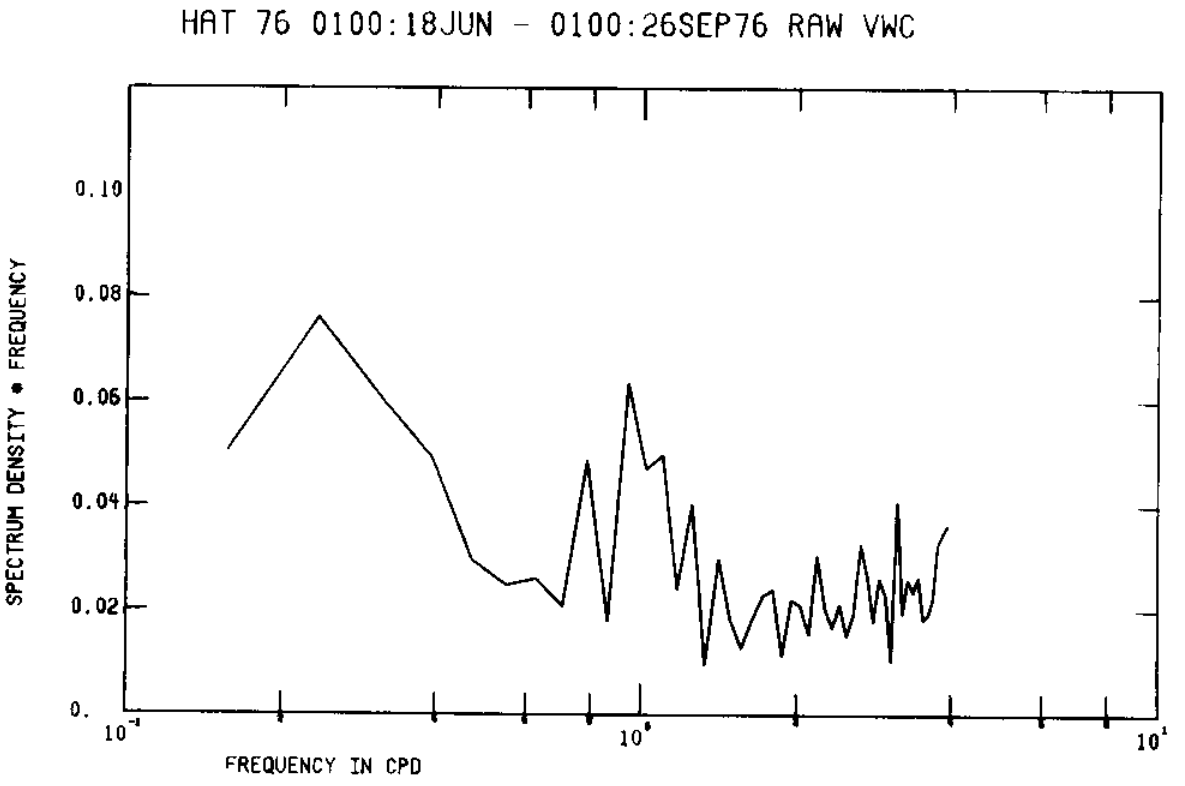

Figure 332 FFT of unfiltered wind velocity components at Cape Hatteras, N. C. June-September, 1976

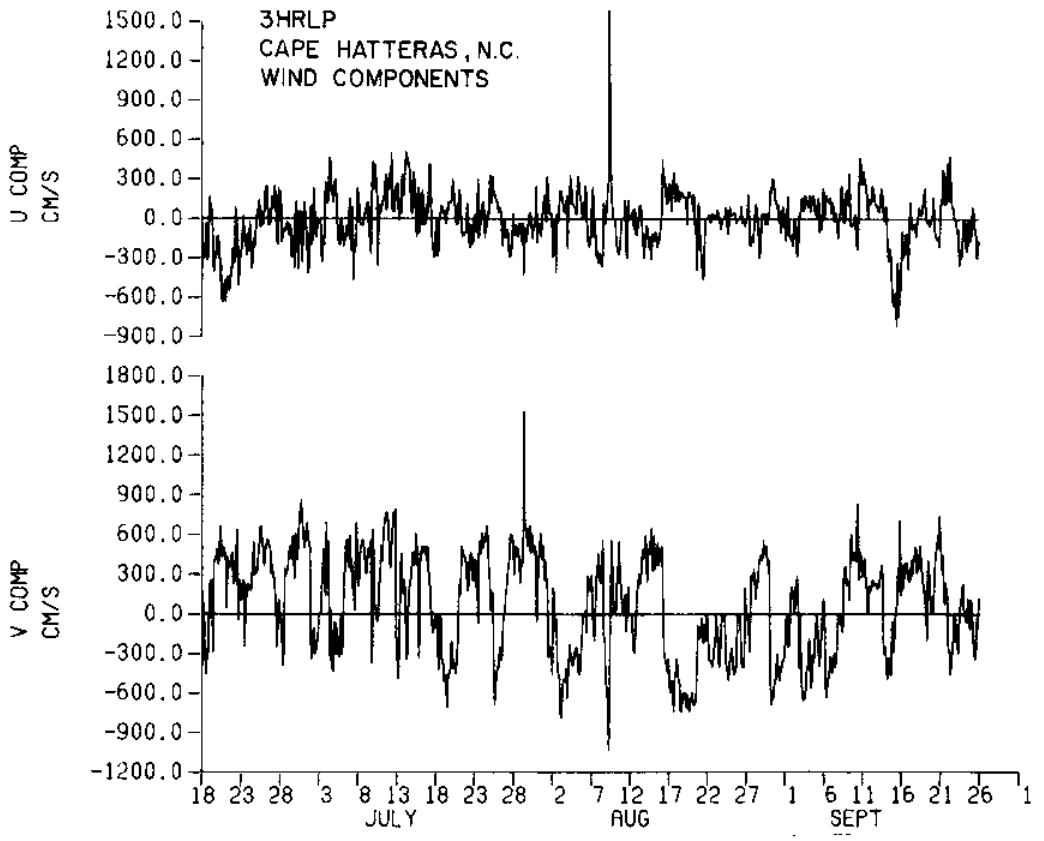

Figure 333 3HRLP wind velocity components for Cape Hatteras, N. C.

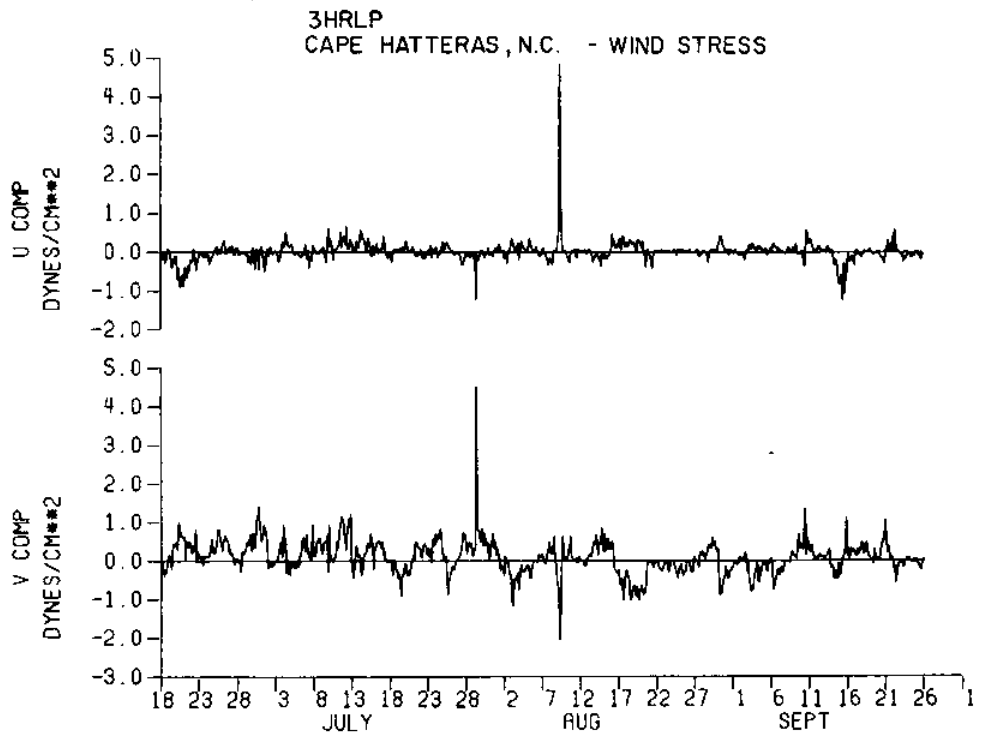

Figure 334 3HRLP wind stress components for Cape Hatteras, N. C.

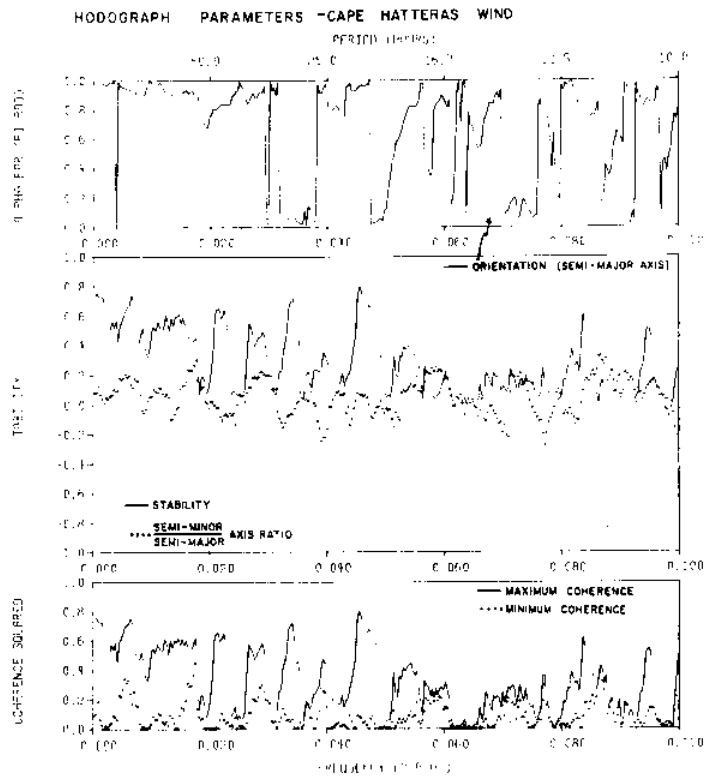

Figure 335 Hodograph parameters of Cape Hatteras, N. C. wind velocity

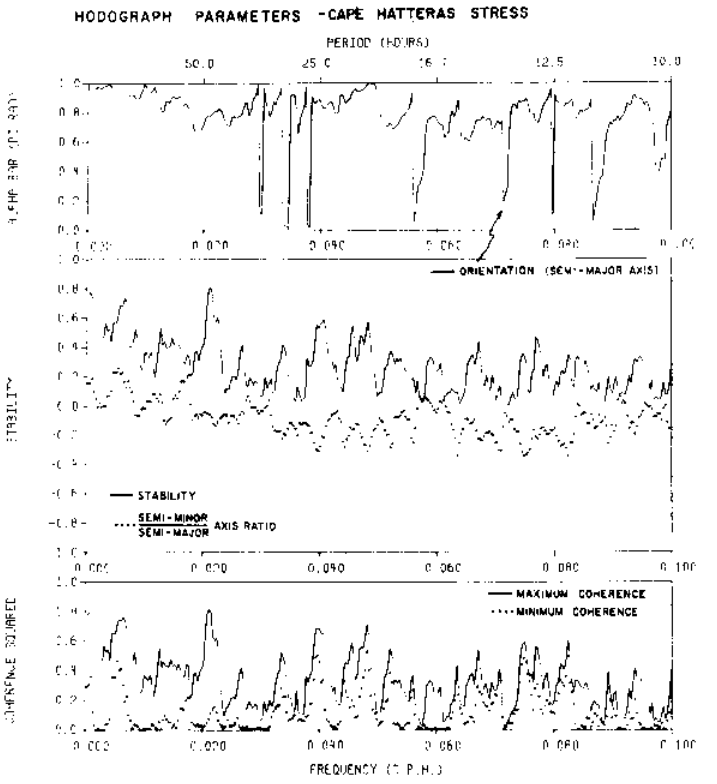

Figure 336 Hodograph parameters of Cape Hatteras, N. C. wind stress

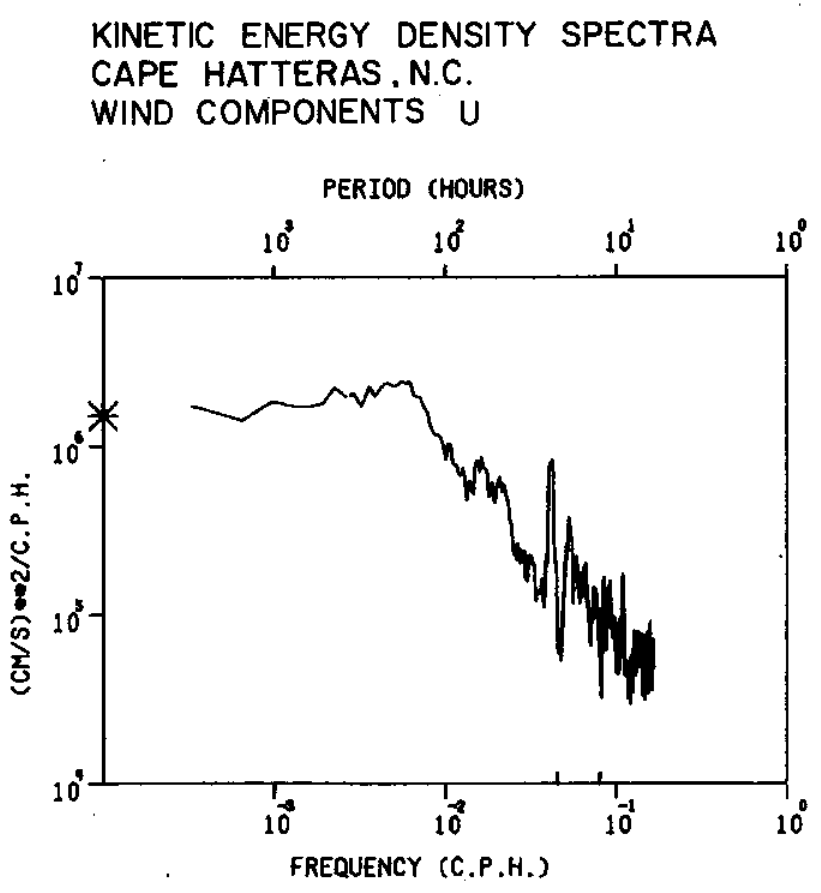

Figure 337

Kinetic energy density spectra for u-component of wind velocity at Cape Hatteras, N. C.

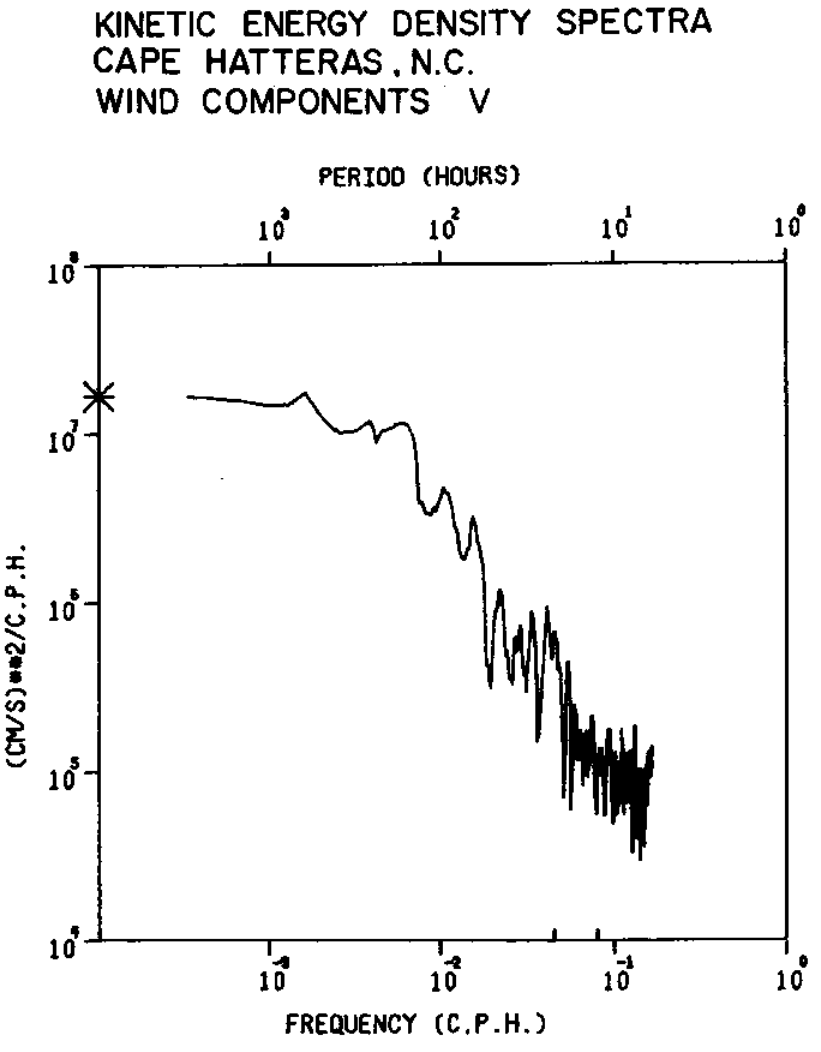

Figure 338

Kinetic energy density spectra for v-component of wind velocity at Cape Hatteras, N. C.

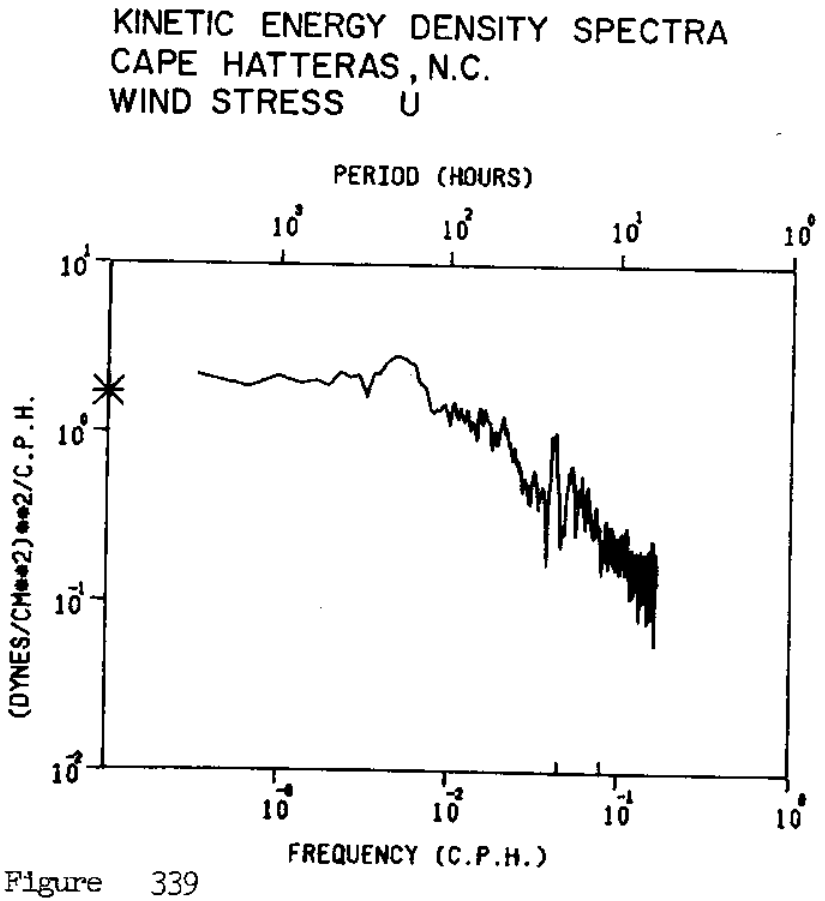

Figure 339
Kinetic energy density spectra for u-component of wind stress at Cape Hatteras, N. C.

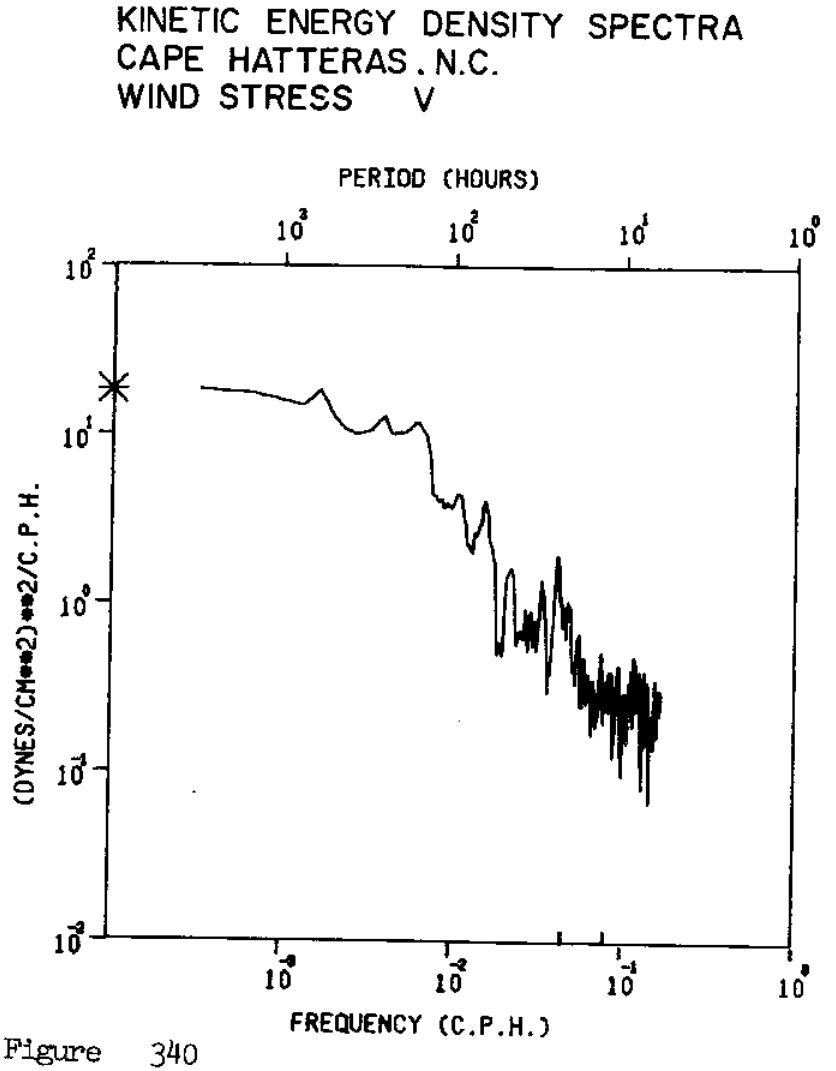

Figure 340
Kinetic energy density spectra for v-component of wind stress at Cape Hatteras, N.C.

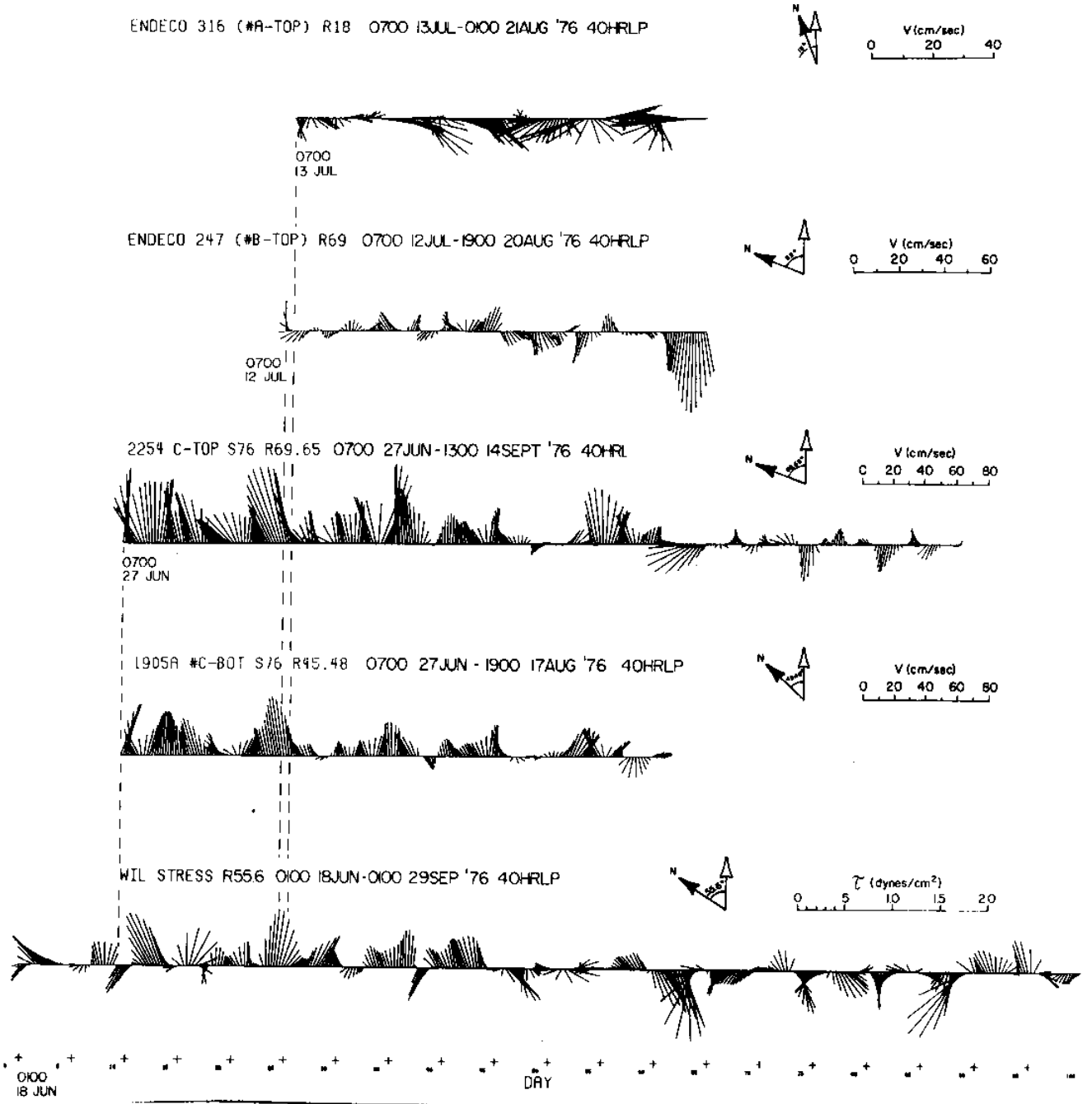

Figure 341 Comparison of low pass current vectors, from meters A_{top}, B_{top}, C_{top}, C_{bot} and low pass wind stress vector at Wilmington, 18 June-26 September, 1976

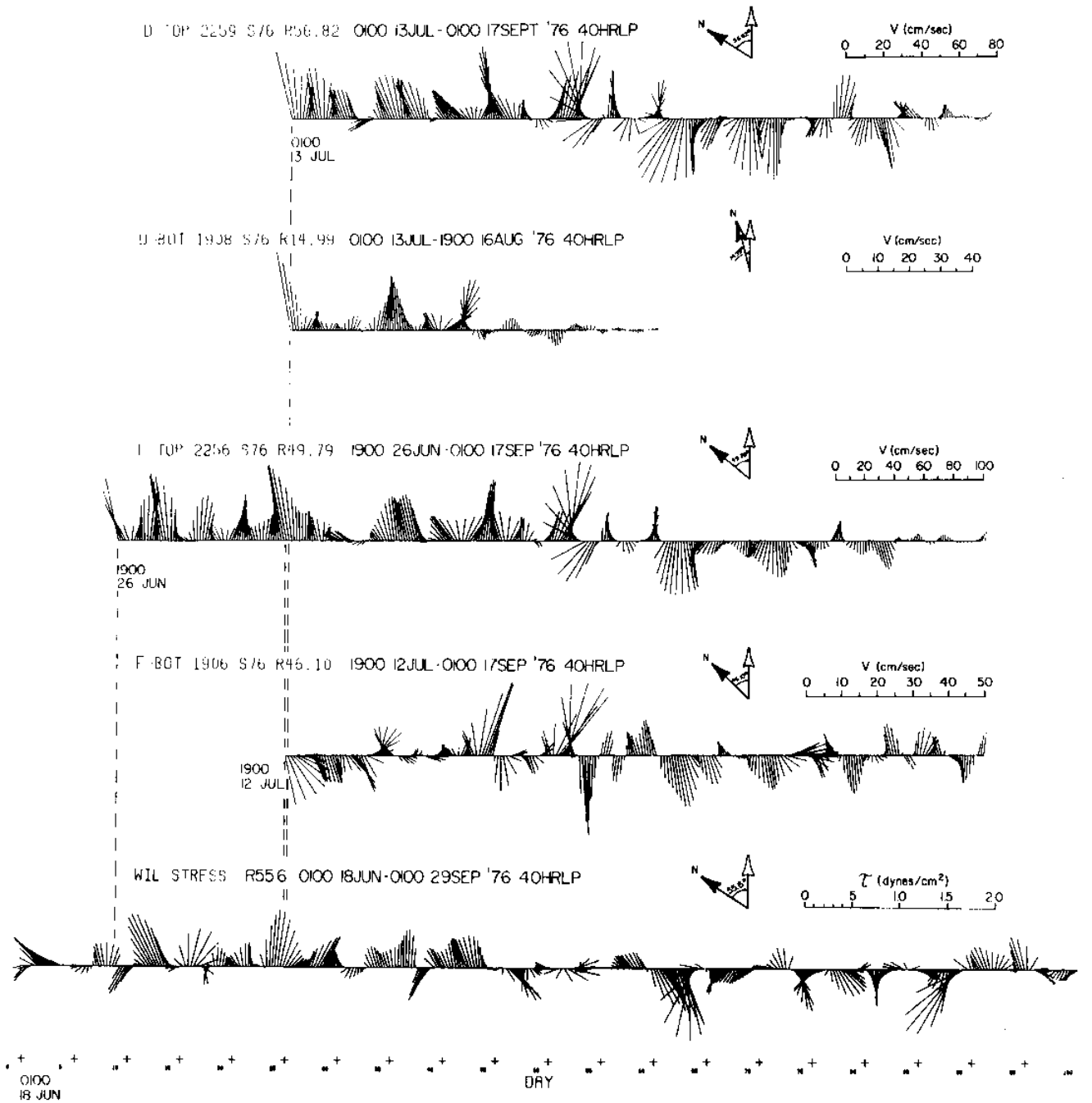

Figure 342 Comparison of low pass current vectors from meters D_{top}, D_{bot}, E_{top}, F_{bot}, and low pass wind stress vector at Wilmington, 18 June–26 September, 1976

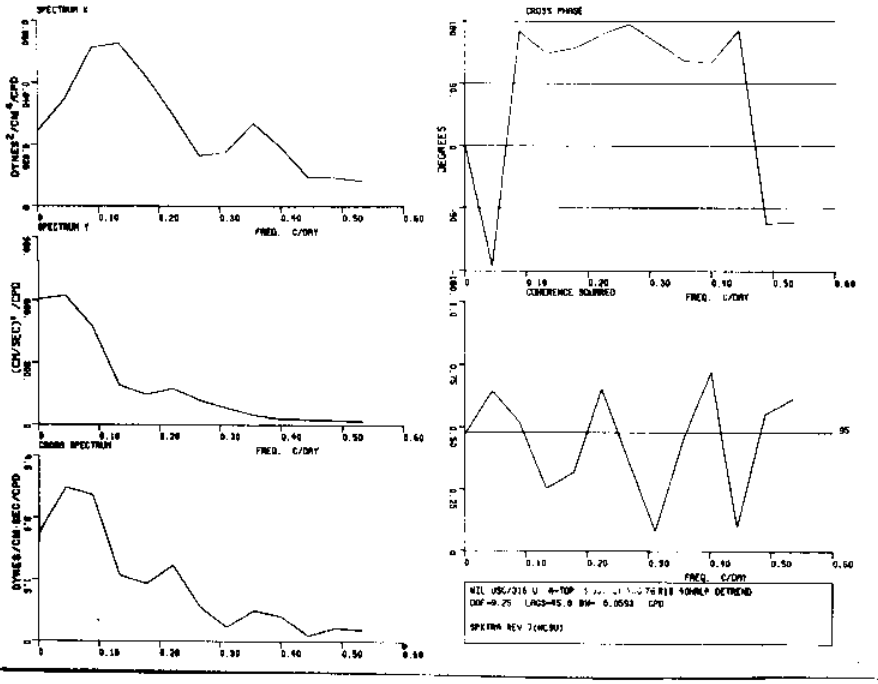

Figure 343 Spectra of the low pass wind stress u component at Wilmington, 13 July-21 August, 1976 and low pass current velocity u component from meter A_{top}

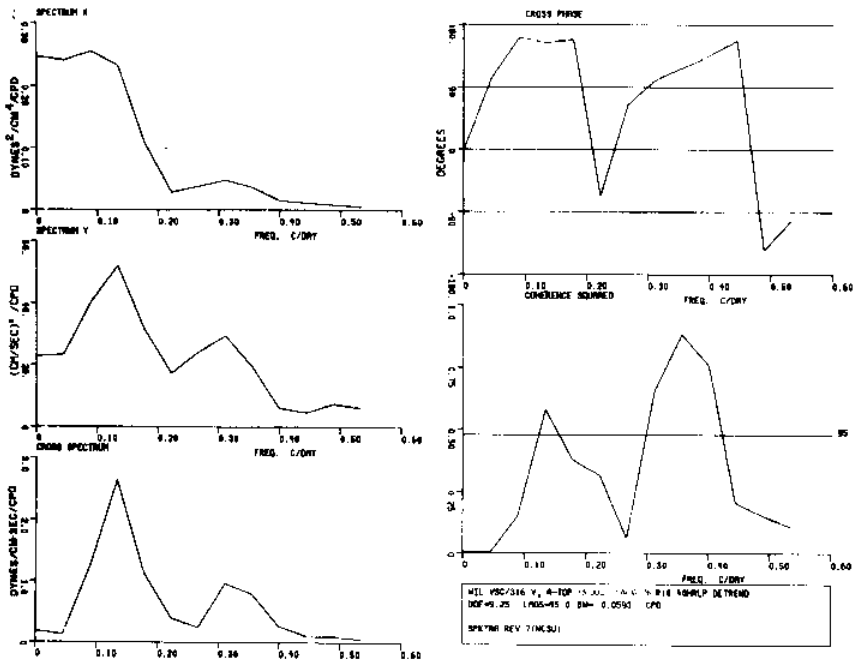

Figure 344 Spectra of the low pass wind stress v component at Wilmington, 13 July-21 August, 1976 and low pass current velocity v component from meter A_{top}

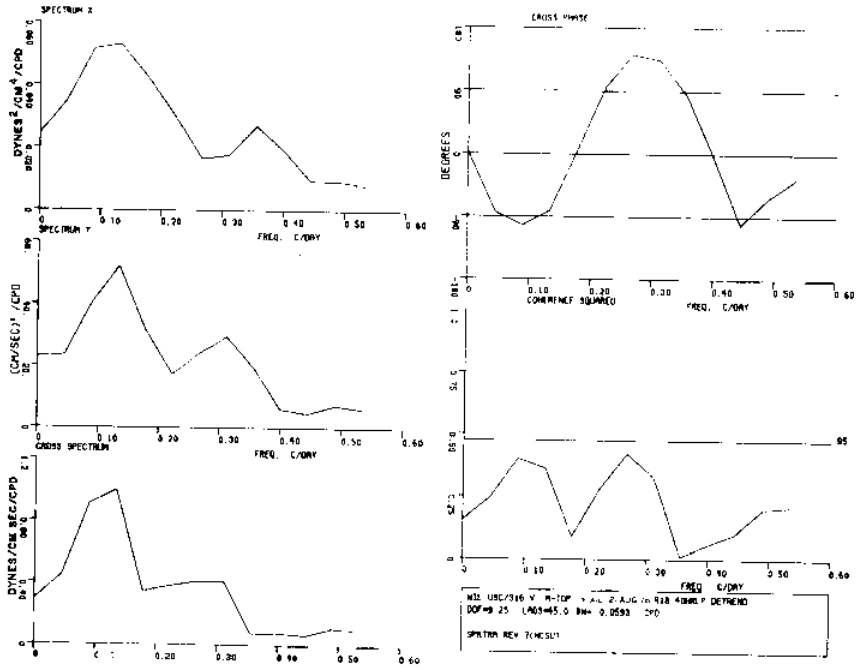

Figure 345 Spectra of the low pass wind stress u component at Wilmington, 13 July-21 August, 1976 and low pass current velocity v component from meter A_{top}

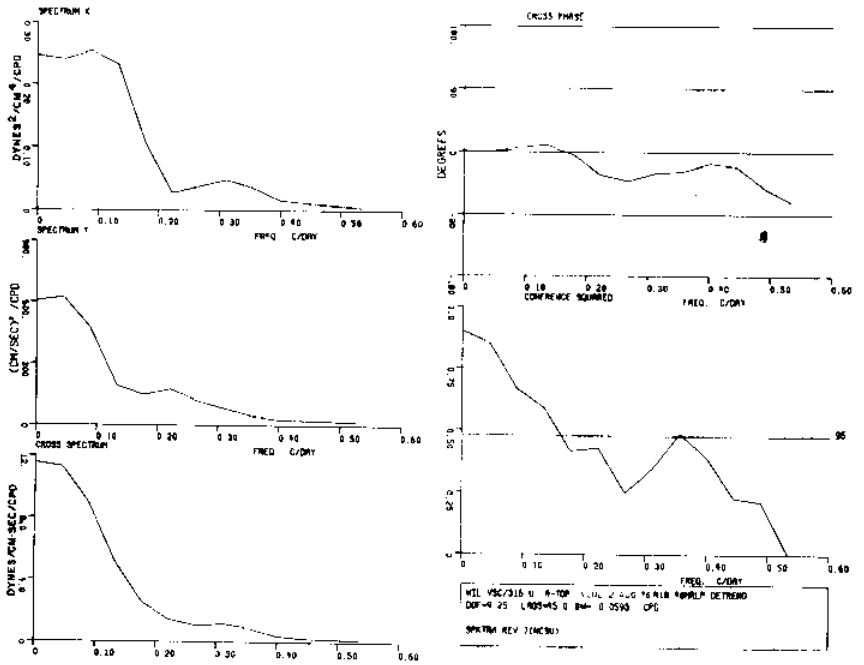

Figure 346 Spectra of the low pass wind stress v component at Wilmington, 13 July-21 August, 1976 and low pass current velocity u component from meter A_{top}

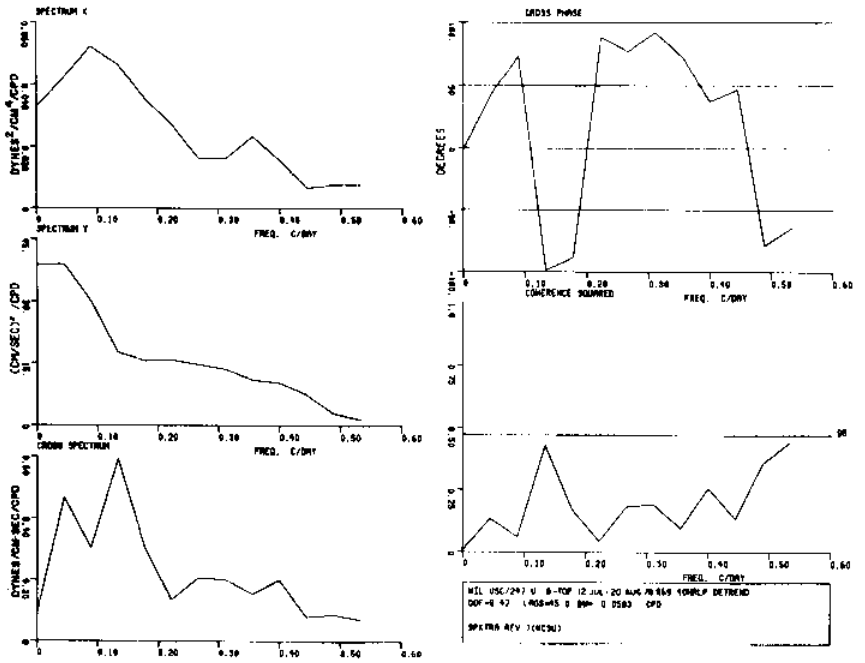

Figure 347 Spectra of the low pass wind stress u component at Wilmington, 12 July-20 August, 1976 and low pass current velocity u component from meter B_{top}

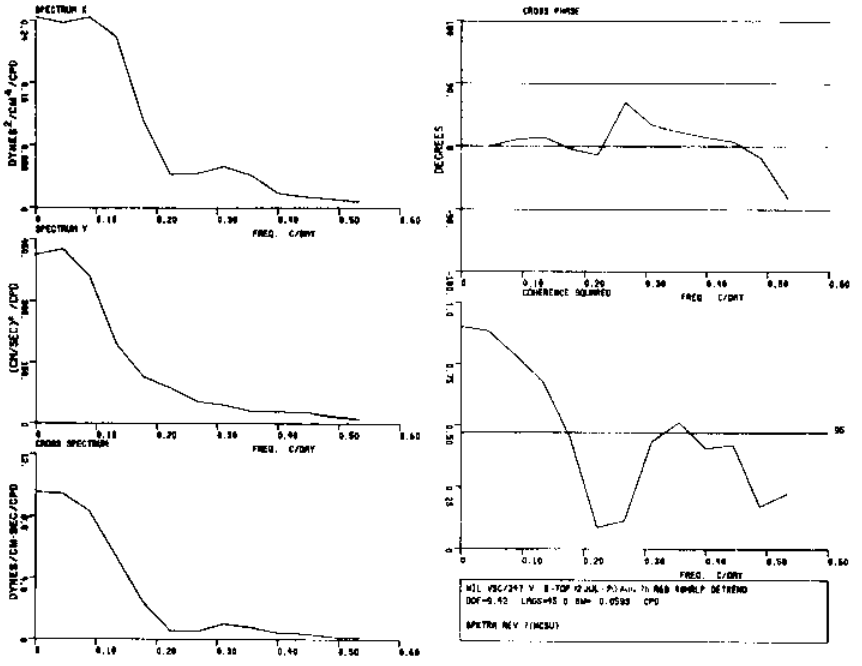

Figure 348 Spectra of the low pass wind stress v component at Wilmington, 12 July-August, 1976 and low pass current velocity v component from meter B_{top}

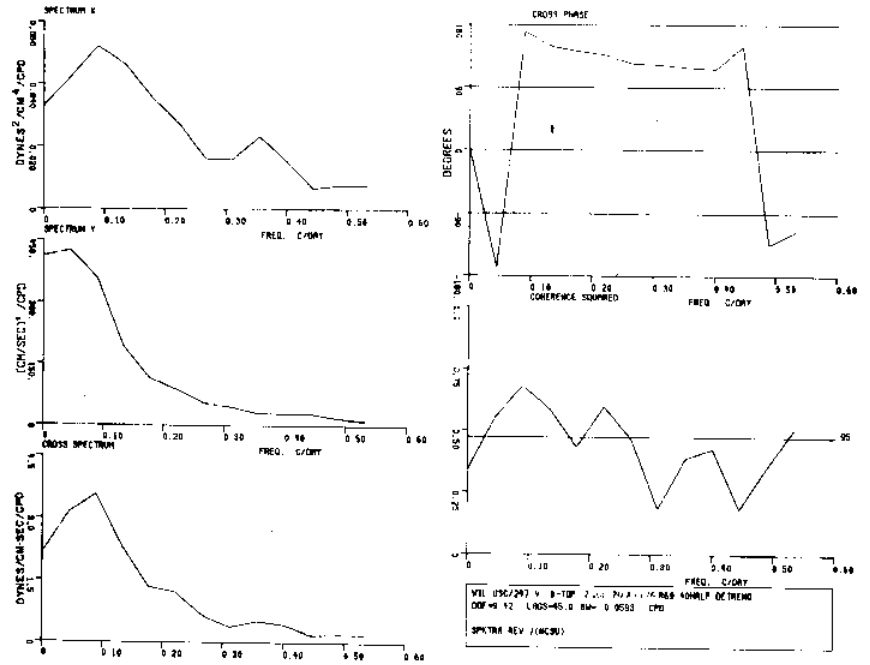

Figure 349 Spectra of the low pass wind stress u component at Wilmington, 12 July-20 August, 1976 and low pass current velocity v component from meter B_{top}

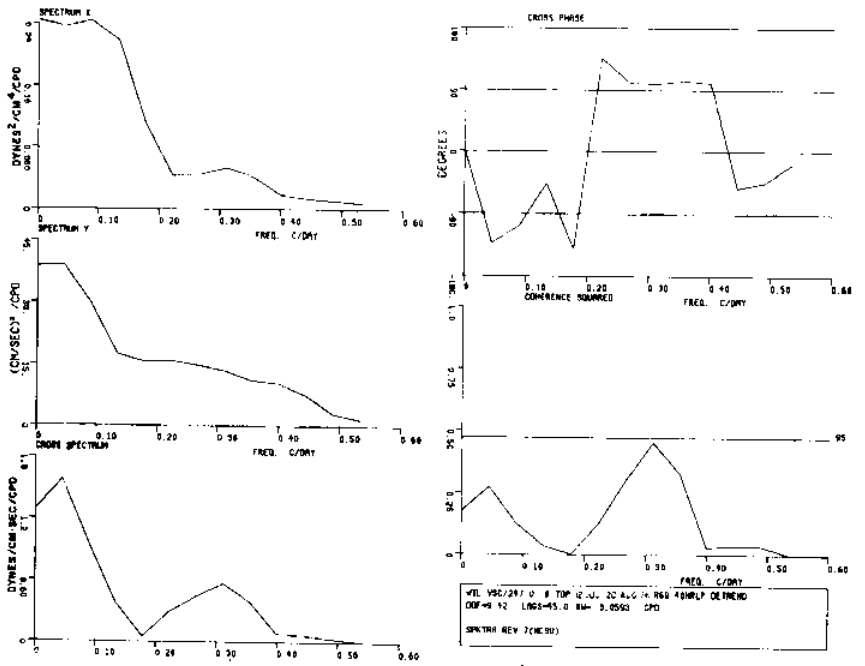

Figure 350 Spectra of the low pass wind stress v component at Wilmington, 12 July-20 August, 1976 and low pass current velocity u component from meter B_{top}

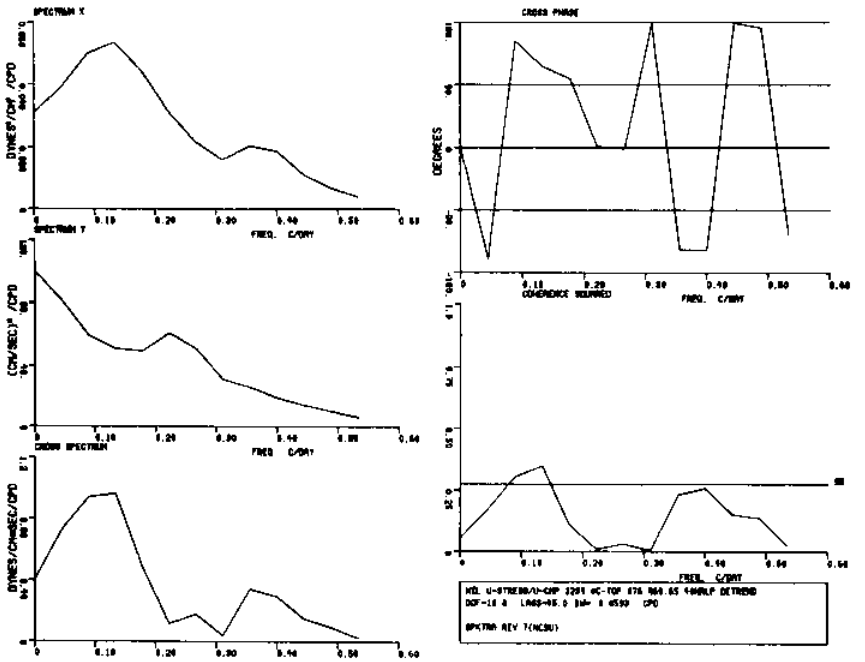

Figure 351 Spectra of the low pass wind stress u component at Wilmington, 18 June–26 September, and low pass current velocity u component from meter C_{top}

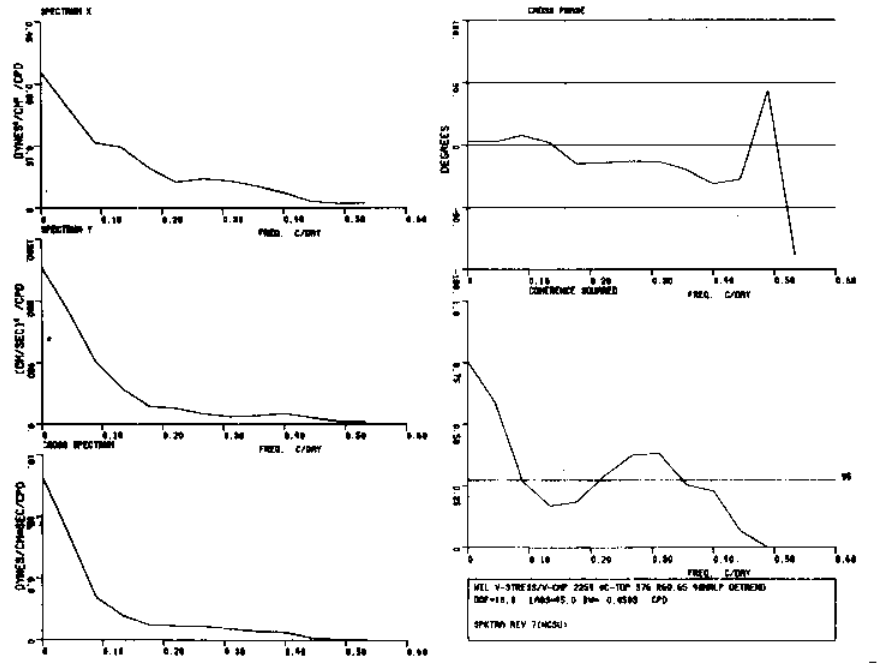

Figure 352 Spectra of the low pass wind stress v component at Wilmington, 18 June–26 September, and low pass current velocity v component from meter C_{top}

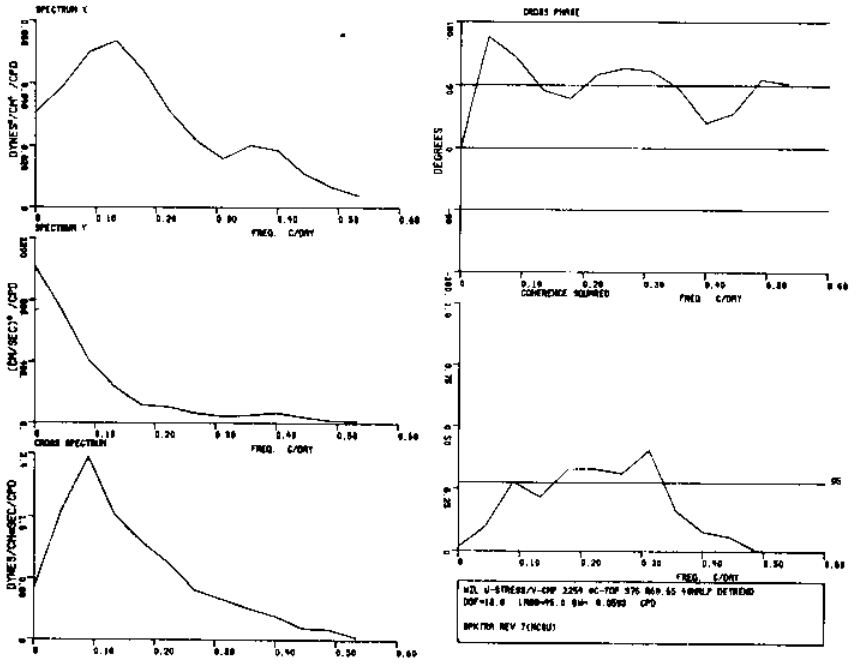

Figure 353 Spectra of the low pass wind stress u component at Wilmington, 18 June–26 September, and low pass current velocity v component from meter C_{top}

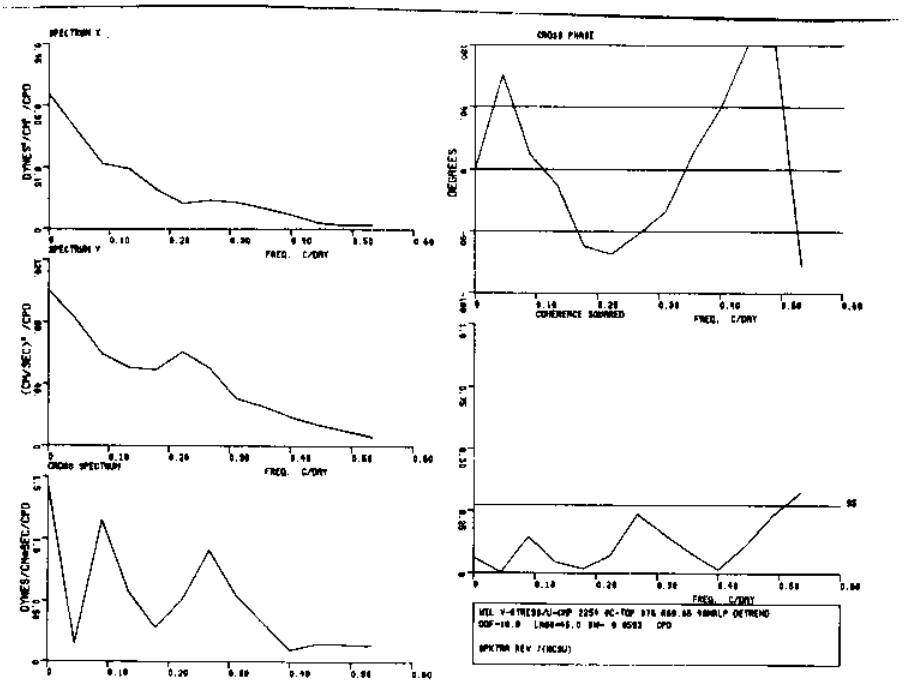

Figure 354 Spectra of the low pass wind stress v component at Wilmington, 18 June–26 September, and low pass current velocity u component from meter C_{top}

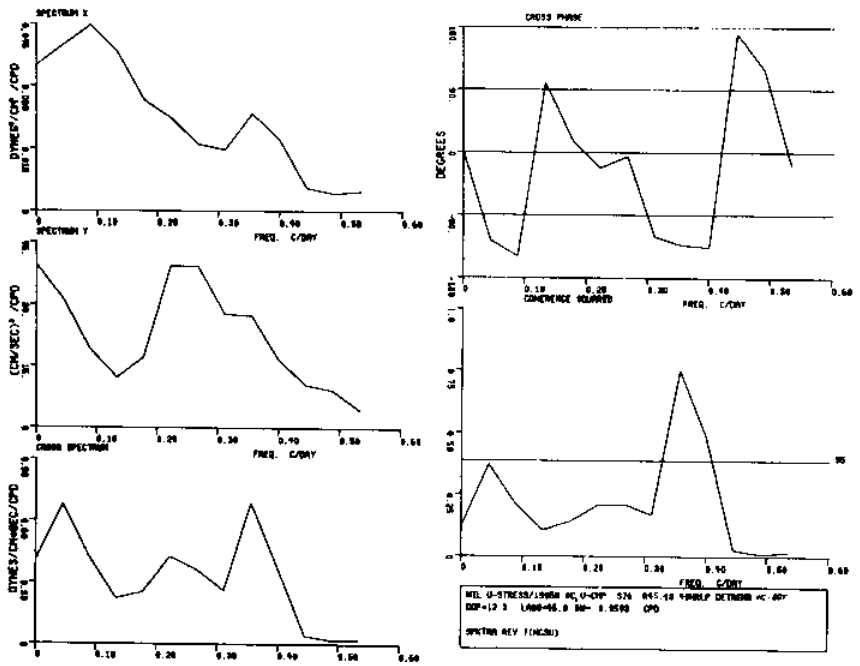

Figure 355 Spectra of the low pass wind stress u component at Wilmington, 18 June–26 September, and low pass current velocity u component from meter C_{bot}

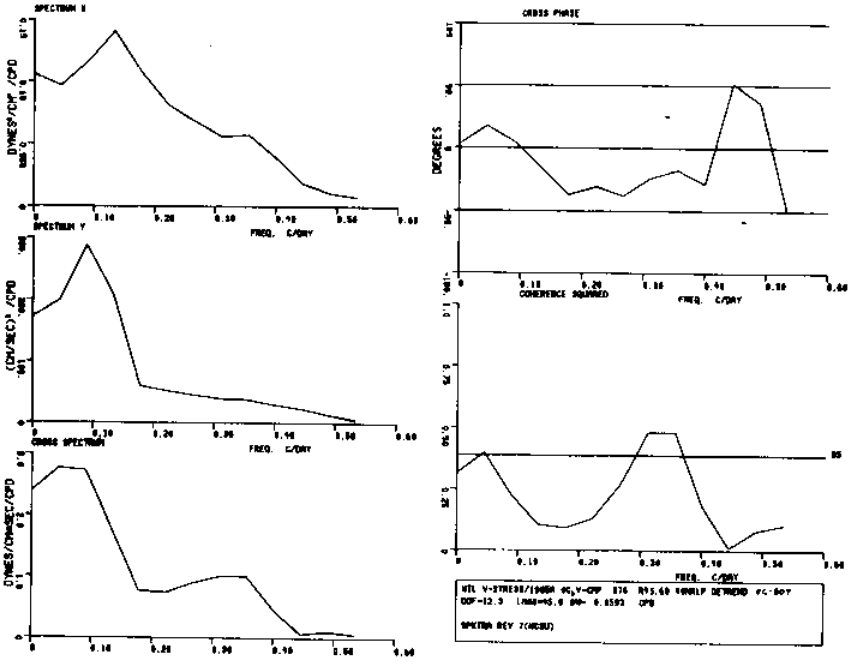

Figure 356 Spectra of the low pass wind stress v component at Wilmington, 18 June–26 September, and low pass current velocity v component from meter C_{bot}

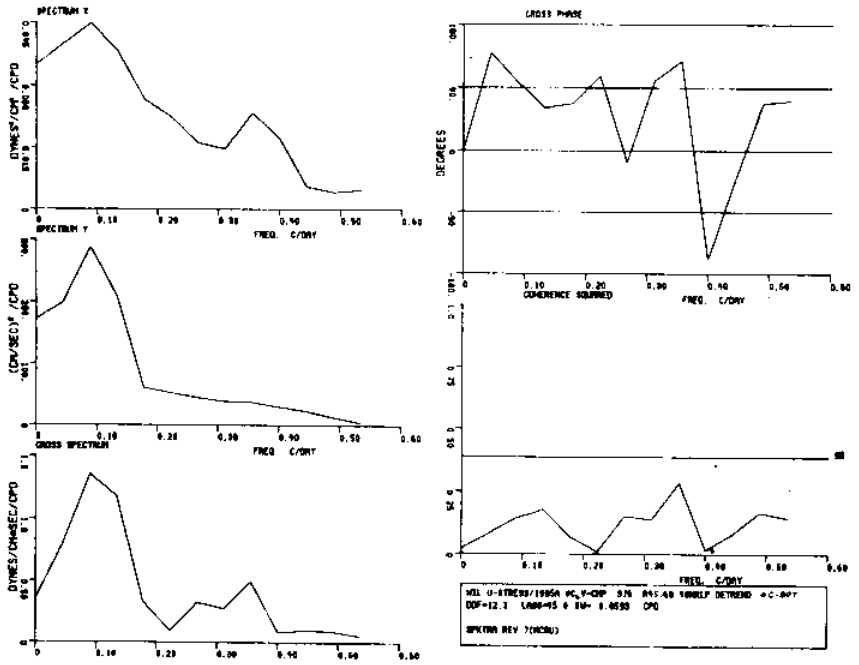

Figure 357 Spectra of the low pass wind stress u component at Wilmington, 18 June–26 September, and low pass current velocity v component from meter C_{bot}

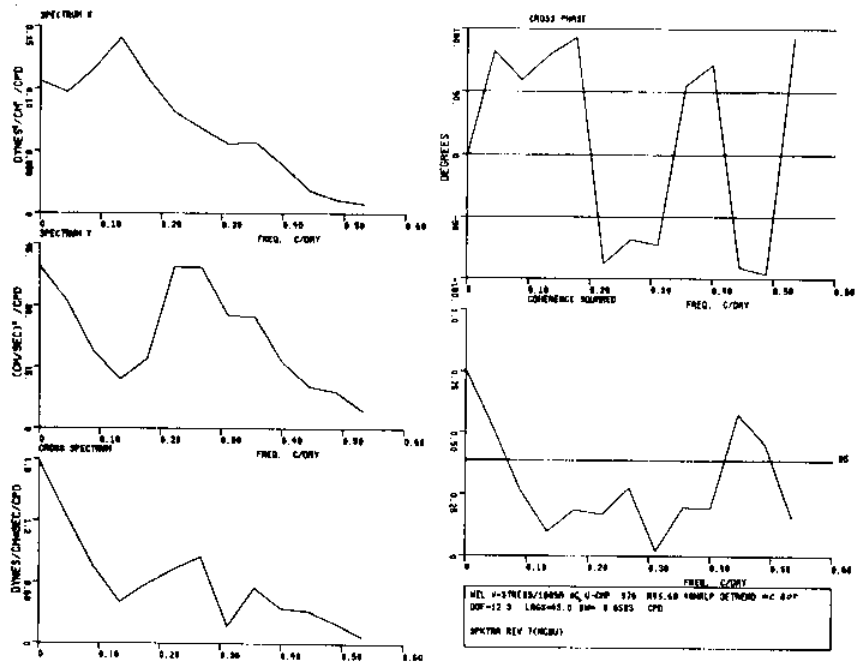

Figure 358 Spectra of the low pass wind stress v component at Wilmington, 18 June–26 September, 1976 and low pass current velocity u component from meter C_{bot}

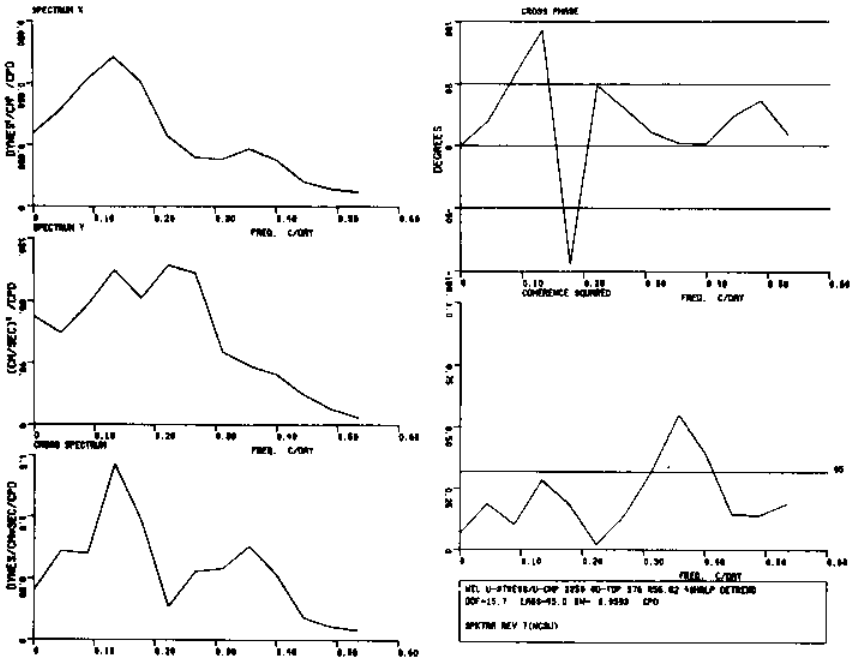

Figure 359 Spectra of the low pass wind stress u component at Wilmington, 18 June–26 September, 1976 and low pass current velocity u component from meter D_{top}

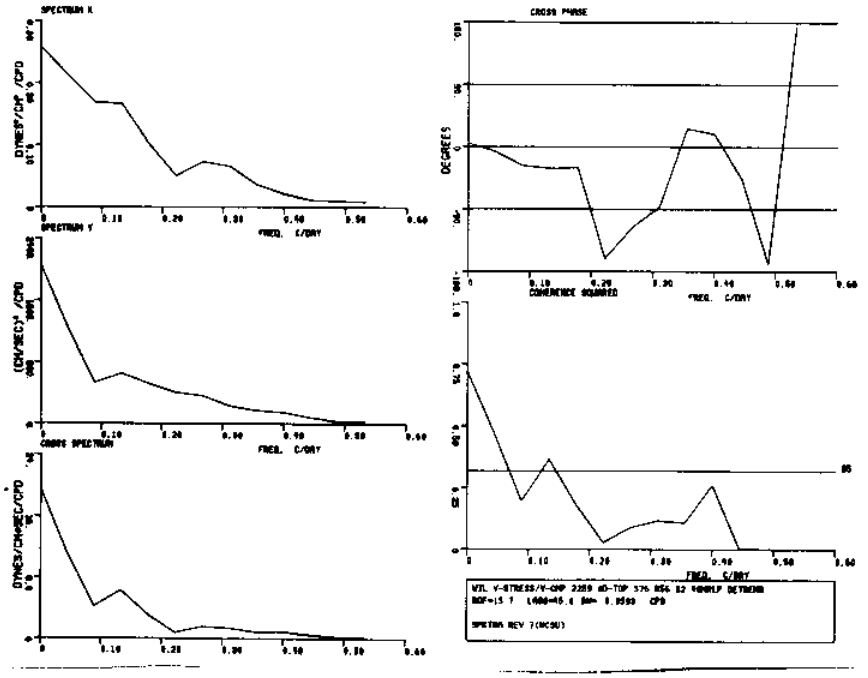

Figure 360 Spectra of the low pass wind stress v component at Wilmington, 18 June–26 September, 1976 and low pass current velocity v component from meter D_{top}

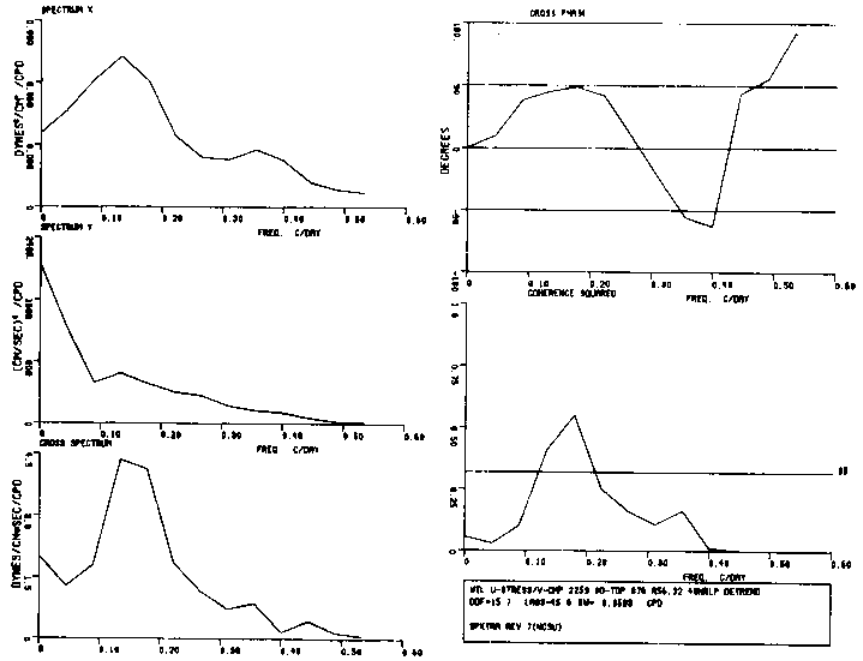

Figure 361 Spectra of the low pass wind stress u component at Wilmington, 18 June-26 September, 1976 and low pass current velocity v component from meter D_{top}

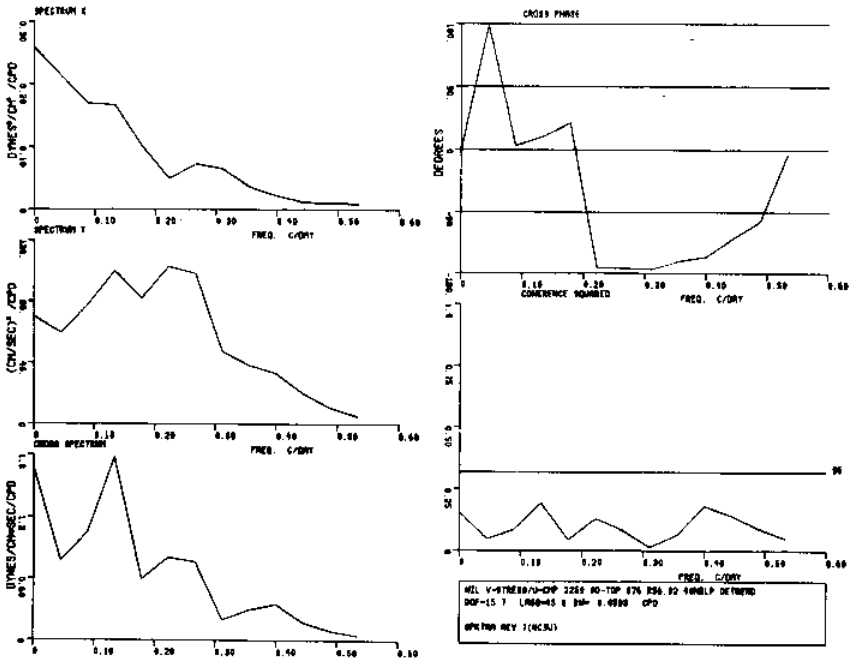

Figure 362 Spectra of the low pass wind stress v component at Wilmington, 18 June-26 September, 1976 and low pass current velocity u component from meter D_{top}

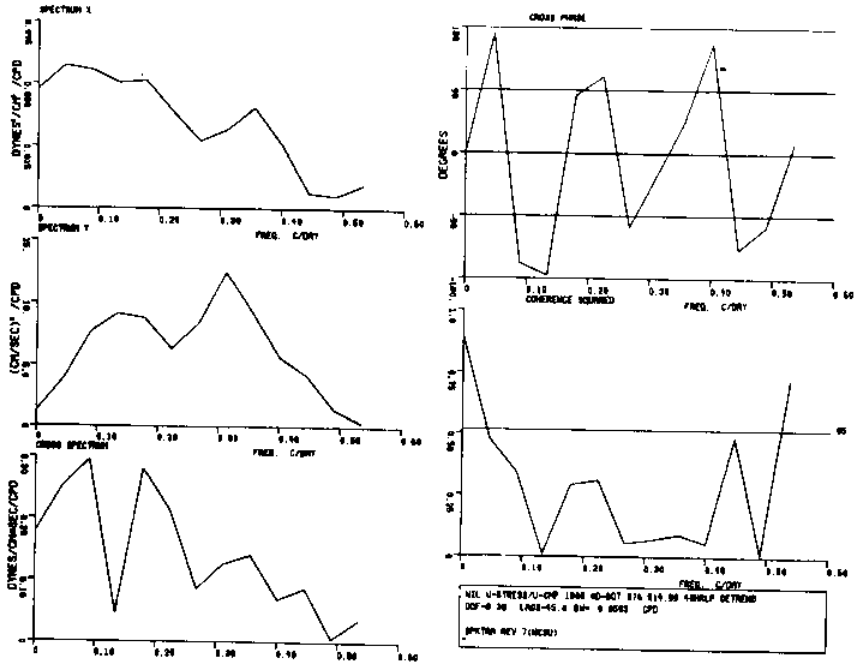

Figure 363 Spectra of the low pass wind stress u component at Wilmington, 18 June-26 September, 1976 and low pass current velocity u component from meter D_{bot}

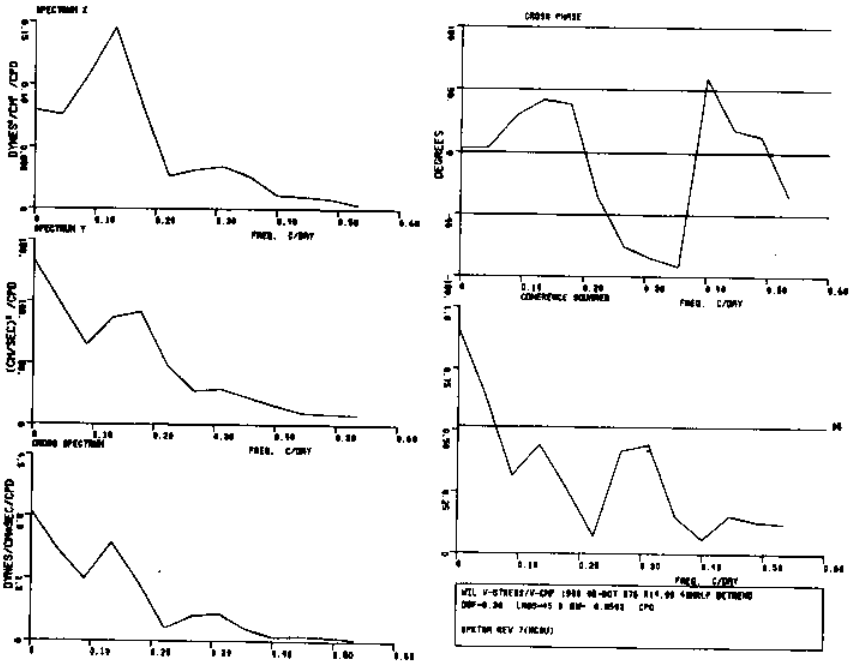

Figure 364 Spectra of the low pass wind stress v component at Wilmington, 18 June-26 September, 1976 and low pass current velocity v component from meter D_{bot}

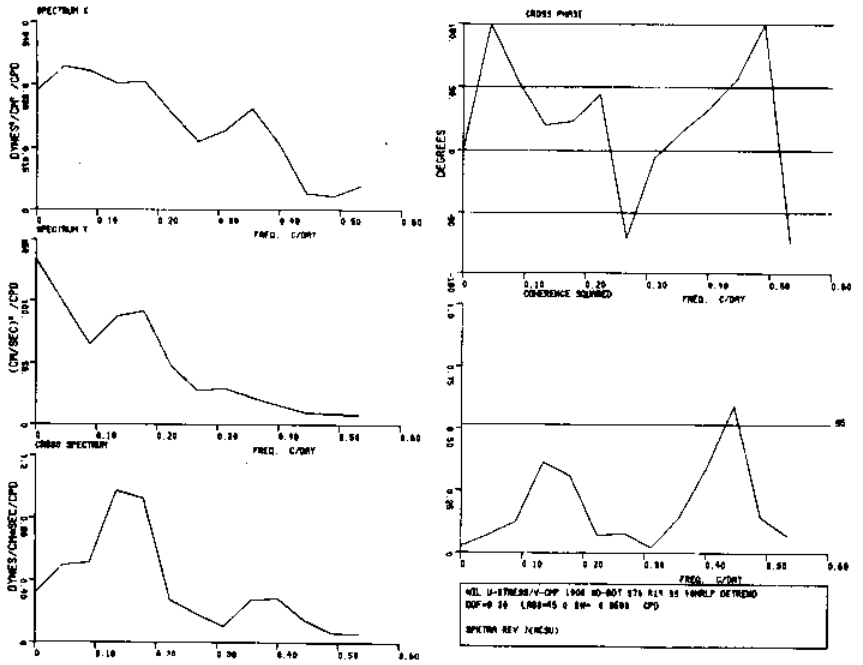

Figure 365 Spectra of the low pass wind stress u component at Wilmington, 18 June-26 September, 1976 and low pass current velocity v component from meter D_{bot}

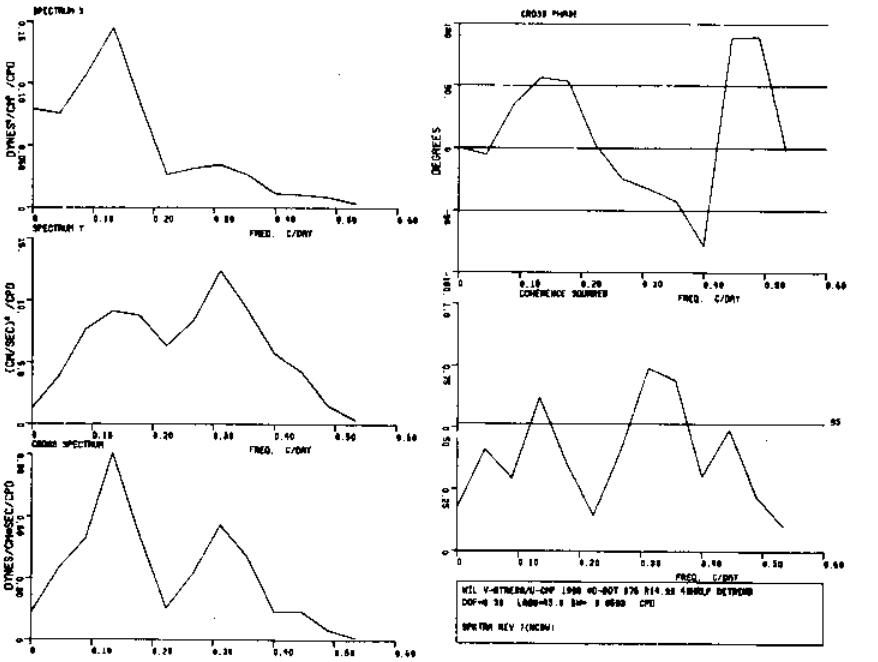

Figure 366 Spectra of the low pass wind stress v component at Wilmington, 18 June-26 September, 1976 and low pass current velocity u component from meter D_{bot}

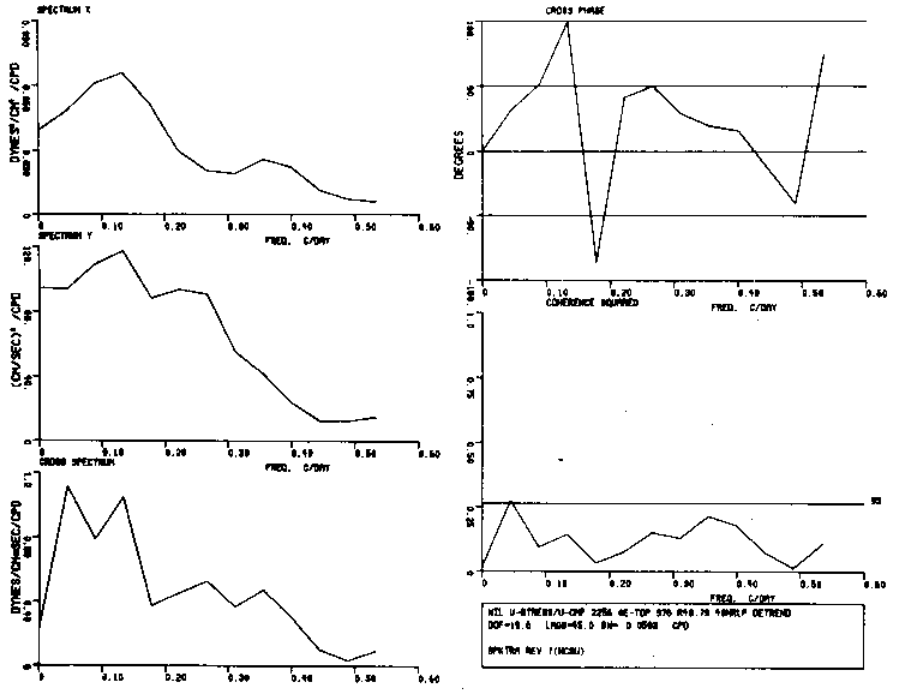

Figure 367 Spectra of the low pass wind stress u component at Wilmington, 18 June-26 September, 1976 and low pass current velocity u component from meter E_{top}

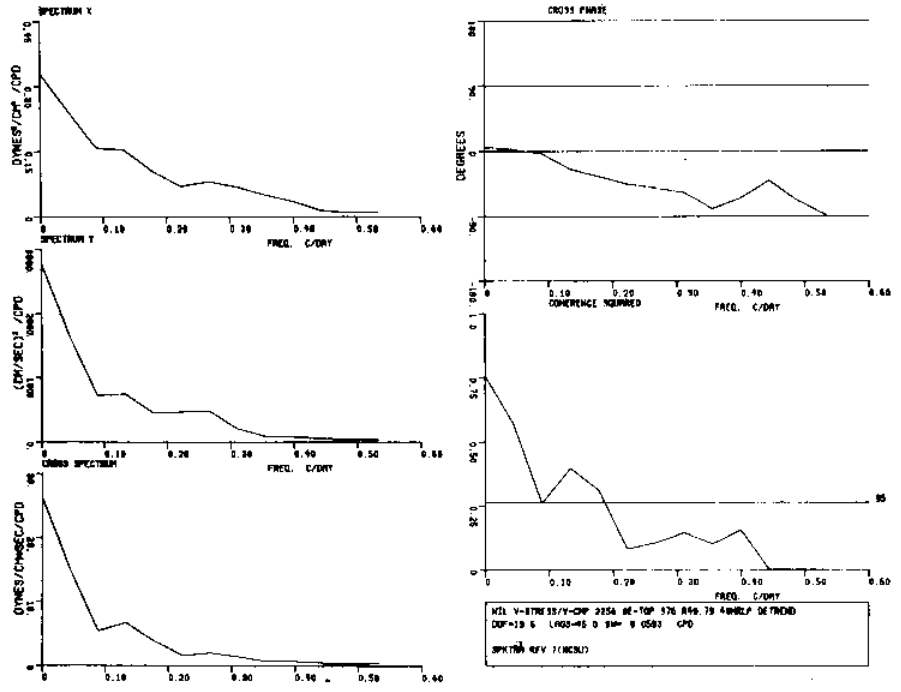

Figure 368 Spectra of the low pass wind stress v component at Wilmington, 18 June-26 September, 1976 and low pass current velocity v component from meter E_{top}

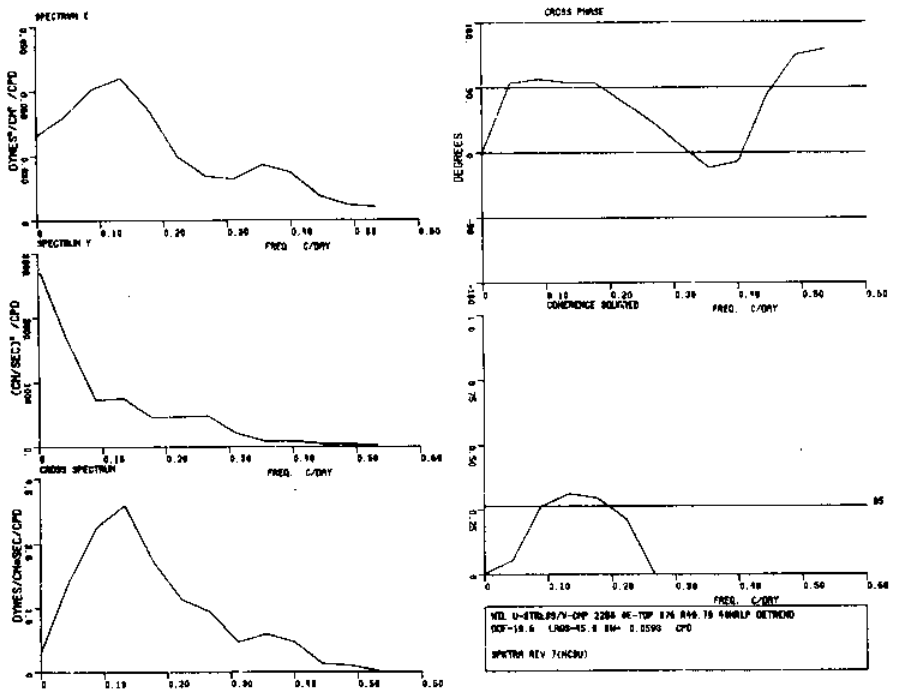

Figure 369 Spectra of the low pass wind stress u component at Wilmington, 18 June-26 September, 1976 and low pass current velocity v component from meter E_{top}

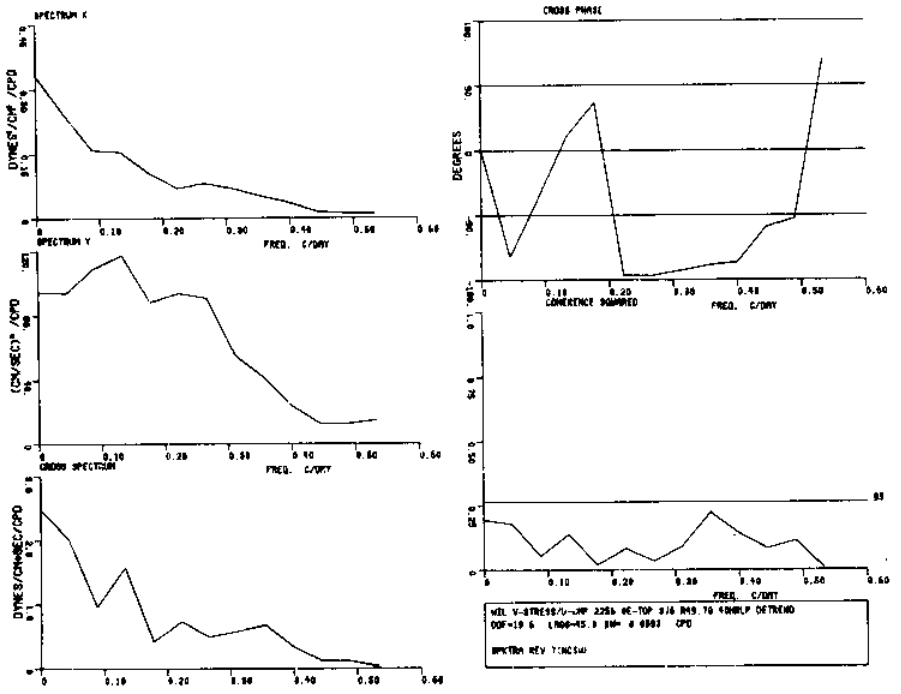

Figure 370 Spectra of the low pass wind stress v component at Wilmington, 18 June-26 September, 1976 and low pass current velocity u component from meter E_{top}

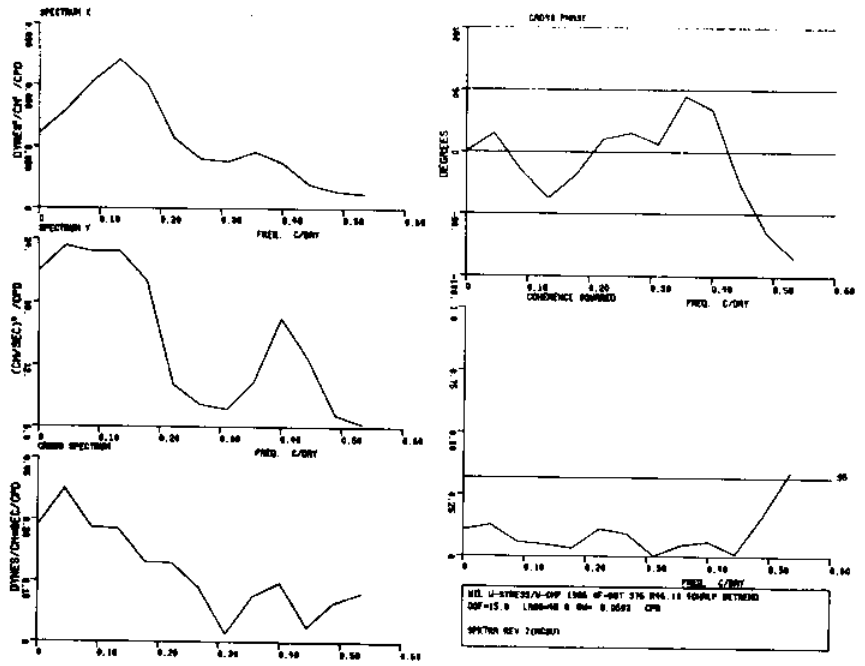

Figure 371 Spectra of the low pass wind stress u component at Wilmington, 18 June-26 September, 1976 and low pass current velocity u component from meter F_{bot}

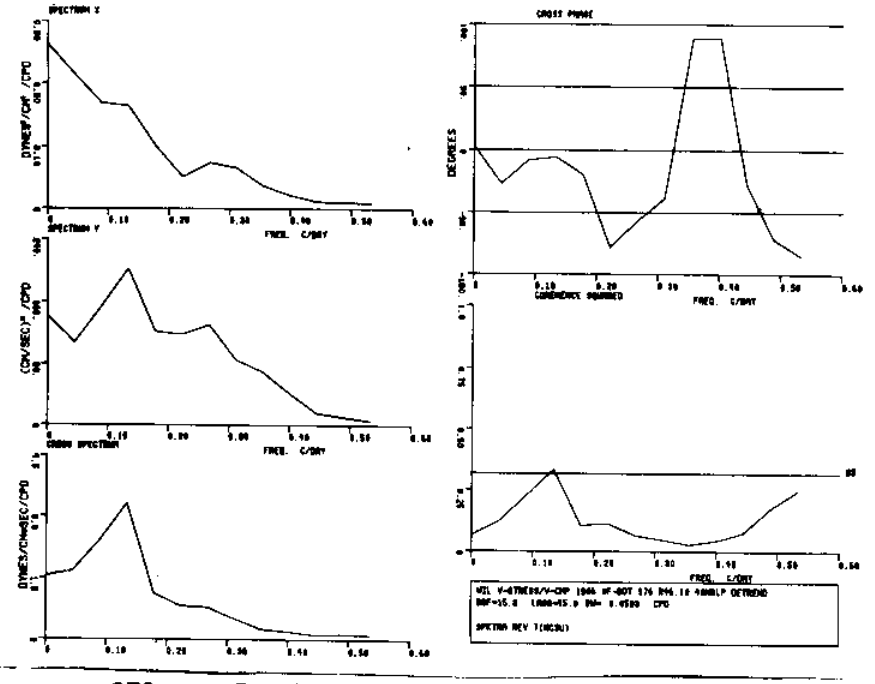

Figure 372 Spectra of the low pass wind stress v component at Wilmington, 18 June-26 September, 1976 and low pass current velocity v component from meter F_{bot}

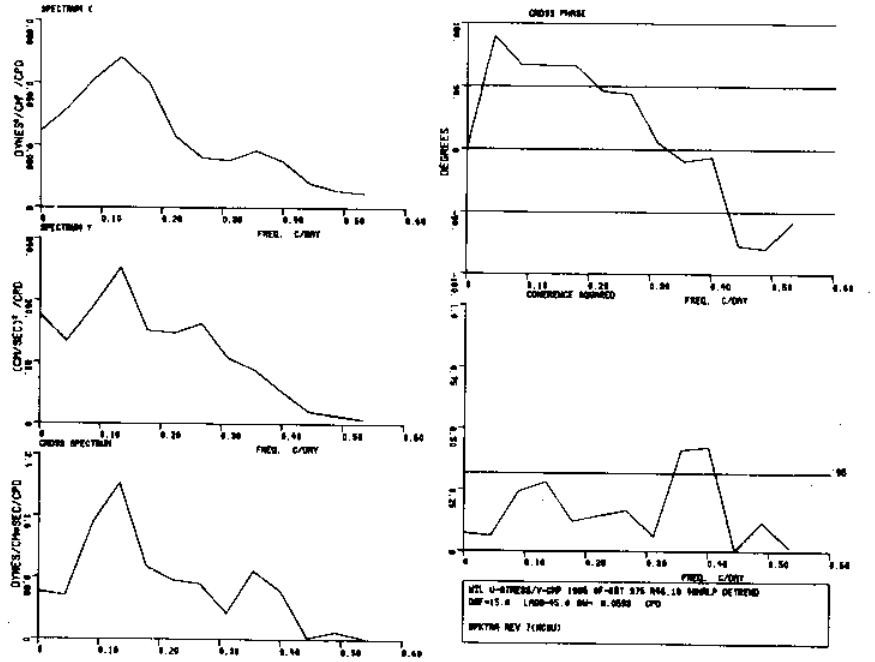

Figure 373 Spectra of the low pass wind stress u component at Wilmington, 18 June-26 September, 1976 and low pass current velocity v component from meter F_{bot}

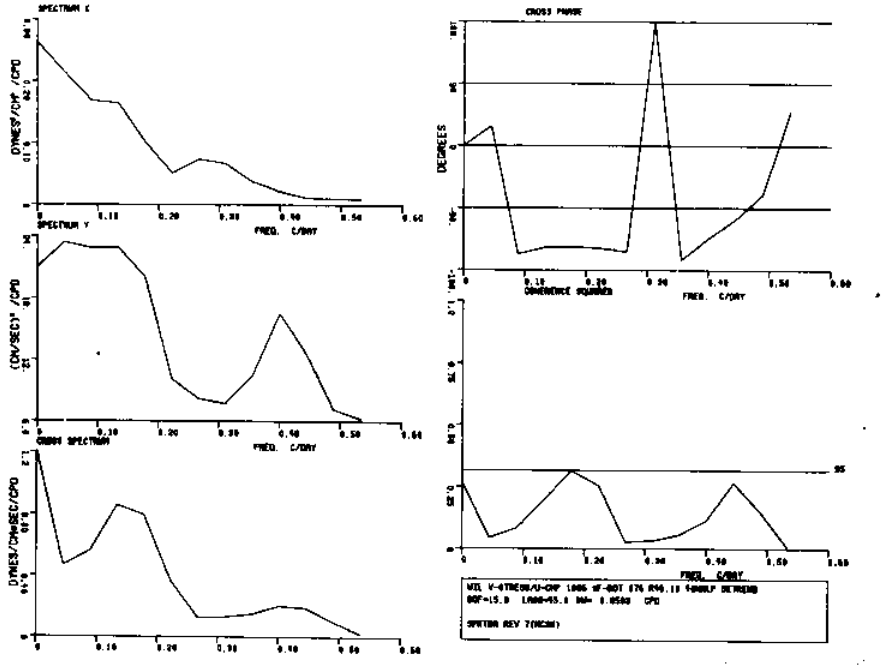

Figure 374 Spectra of the low pass wind stress v component at Wilmington, 18 June-26 September, 1976 and low pass current velocity u component from meter F_{bot}

References

Atkinson, L.P., J.J. Singer, W.M. Dunstan, L.J. Pietrafesa 1976a. Hydrography of Onslow Bay, North Carolina. September 1975 (OBIS II). Georgia Marine Science Center Technical Report, 76-2.

Atkinson, L.P., J.J. Singer, and L.J. Pietrafesa 1976b. Onslow Bay intrusion study. Hydrographic observations during current meter servicing cruises in August, October and December 1975 (OBIS I, III, and IV). Georgia Marine Science Center Technical Report 76-4.

Atkinson, L.P., J.O. Blanton, and E. Haines 1977. Shelf flushing rates based on the distribution of salinity and freshwater in the Georgia Bight. Coastal and Estuarine Marine Science (in press).

Beardsley, R.C., W. Boicourt, L.C. Huff, J. Scott 1977. CMICE 76: A current meter intercomparison experiment conducted off Long Island in February-March, 1976. Woods Hole Oceanographic Institute Technical Report 77-62.

Brooks, D.A. 1976. Festsa: fast and easy time series analysis at N.C.S.U. Center for Marine and Coastal Studies, North Carolina State University.

Dunstan, W.M. and L.P. Atkinson 1976. Sources of new nitrogen for the South Atlantic Bight. Proceedings of 3rd International Estuarine Research Conference, Galveston, Texas (Martin Wiley, ed.), 1, 69-78.

Fofonoff, N.P. 1969. Spectral characteristics of internal waves in the Ocean. Deep Sea Res. 16 (supplement, 59-72).

Gonella, J. 1972. A rotary-component method for analyzing meteorological and oceanographic vector time series. Deep Sea Res., 19 (12), 833-846.

LeBlond, P.H. and L.A. Mysac.1977. Trapped coastal waves and their role in shelf dynamics. The Sea, Vol. 6. pp. 459-495.

Lee, T.N. and R.L. Shutts 1977. Technical program for Aanderaa current meter moorings on continental shelves. University of Miami Technical Report. TR 77-5.

Mooers, C.N.K. 1973. A technique for the cross spectrum analysis of pairs of complex-valued time series, with emphasis on properties of polarized components and rotational invariants. Deep Sea Res., 20 (12), 1129-1142.

Pietrafesa, L.J. 1974. Continental Shelf processes affecting the Oceanography of the South Atlantic Bight. Proposal to Atomic Energy Commission.

Pietrafesa, L.J. and L.P. Atkinson 1975. Continental Shelf processes affecting the Oceanography of the South Atlantic Bight. Proposal to Energy Research and Development Administration.

Pietrafesa, L.J., D.A. Brooks, R.D'Amato, L.P. Atkinson 1978. Onslow Bay physical/dynamical experiments; summer - fall, 1975. Center for Marine and Coastal Studies, North Carolina State University. Technical Report, 78-04.

Redfield, A.C. 1958. The influence of the continental shelf on the tides of the Atlantic Coast of the U.S. J. Mar. Res., 17, 432-448.

Singer, J.J., L.P. Atkinson, W.S. Chandler, and P.G. O'Malley 1977. Hydrographic observations in Onslow Bay, North Carolina, July-August 1976 (OBIS V), Data Graphics. Georgia Marine Science Center Technical Report 77-6.

Appendix A

The speed and direction values were converted to u and v components in several ways. The Carolina Cape region is defined by an irregular, cuspate, scallop-like coastline which extends into shoals and consequently it is difficult to specify a spatial co-ordinate system. Coherency and phase relationships between components of a vector time series are functions of the co-ordinate system in which the components are specified. The natural tendencies are to choose either a north-south, east-west horizontal axis or to assume a straight coastline of uniform cross-section so that the horizontal co-ordinate system axes lie parallel to and perpendicular to the straight isobaths. Unfortunately, however, the isobaths in the Carolina Capes region are not uniform or straight and the choice of a co-ordinate system is less than obvious. Two tacks were taken herein. The first co-ordinate system chosen is one based on the direction of the local bathemetric contours at approximately mid shelf to the shelf break, which tend to run southwest to northeast at an angle 56° clockwise from North (quantitatively "alongshore"). The second co-ordinate system used is one oriented on a basis determined by the characteristics of the data itself. A co-ordinate system which maximizes the variance in any given direction gives the so called "Principal Axis" of variance. This system, in which the estimated phase difference between u and v is identically +90° is also called the "Normal" system (Fofonoff, 1969) and the "Hodograph" system (Mooers, 1970). As a function of the physical, dynamical processes causing the measured hydrodynamics, the principal axis of variance may vary with frequency and geographic location. The "Principal Axis" for a given vector time series is obtained by rotating the covariance matrix until the cross-covariance between orthogonal velocity components is zero. The rotation of the co-ordinate system into the principal axis does not fix the sign of the 90° phase shift between u and v. This is determined by the data. Since the principal axis for a given vector time series will vary with frequency, we can construct hodographs which will allow for the vector time series to be decomposed into cyclonic and anticyclonic rotating motions of different amplitude and phase. The sum of these two polarized motions yields an ellipse whose semi-major axis is oriented along the principal axis of variance at that particular frequency. The principal axis herein is given as a function of frequency rather than as an average over a large frequency band.

In this report the "alongshore" co-ordinate system was used on the meteorological data. It was also used to generate first order statistics for the current meter velocity data. However, the "Principal Axis" system was used exclusively with the current meter velocity data for all data plotting.

Appendix B

The current meter velocity information is presented in several forms. Displayed in unfiltered form are time series of current components u and v, FFT's, histograms and progressive vector diagrams (PVD'S). The PVD's are presented for the full time series and also for interesting and/or confusing subsets. Displayed in 3HRLP are time series of current components u and v and hodographs. 40HRLP records were used to produce time series of velocity components, vector stick diagrams, FFT's and spectra. The spectra series, Figures 244-251, crosses the velocity components for the top and bottom meters on the same mooring string. Figures 252-271 are spectra of meters located on a line perpendicular to the shoreline while Figures 272-303 are for meters on an alongshore line. All this current velocity data is presented in the "Principal Axis" system (see Appendix A) excepting for the hodographs and the histograms which are in a natural co-ordinate system.

It should be noted that meter E_{bot} lost its rotor early in its operation on location and, hence, no speed data was gathered. To facilitate the presentation of the valuable direction data in time series plots, histograms, PVD's etc. a constant 1.5 cm/sec dummy speed was inserted in the data processing programs for E_{bot}.

The information from Aanderaa temperature and pressure sensors is displayed in time series plots of unfiltered, 3HRLP and 40HRLP form. FFT's are presented of unfiltered and 40HRLP records. Spectras of temperature vs. velocity components are also given.

Meteorological data from two stations, Wilmington, N.C. and Cape Hatteras, N.C. are presented in several forms. Displayed in unfiltered form are the time series of wind velocity components and their FFT's. Displayed in 40HRLP form is the temperature, pressure, wind velocity components and wind stress time series with their FFT's. Stick vector plots of wind stress are also displayed. Figures 341 and 342 give a comparative look at the stick vector plots of current velocity and wind stress. A series of spectras are presented crossing wind stress with current velocity components (Figures 343-374).

Kinetic energy density spectra for current meter u, v and T are presented in Figures 19, 20, 29, 30, 61-63, 94-96, 124-126, 154-156, 184-186, 212-214, and 241-243 and of wind velocity and stress in Figures 321-324 and 337-340. Momentum and heat correlation variance plots are displayed for current meters C-F in Figures 50-58, 83-91, 113-121, 143-151, 173-181, 203-211, and 231-238. Cospectra of temperature vs. velocity components for current meters C-F are presented in Figures 59, 60, 92, 93, 122, 123, 152, 153, 182, 183, 239 and 240. Hodograph

parameters of current meter data is plotted in Figures 39, 72, 105, 135, 165, 195 and 223. Hodograph plots of wind velocity and stress are Figures 304 and 305, and tidal elipses are plotted in Figures 307 and 308 for the same periods. Energy fraction vs. frequency plots for the C mooring string for different current modes are Figures 40-42 and 73-75.